FACULTY OF ENGINEERING
AND ARCHITECTURE

Advanced Equalization and Crosstalk Suppression for High-Speed Communication

Jelle Bailleul

Doctoral dissertation submitted to obtain the academic degree of
Doctor of Electrical Engineering

Supervisors
Prof. Marc Moeneclaey, PhD - Lennert Jacobs, PhD

Department of Telecommunications and Information Processing
Faculty of Engineering and Architecture, Ghent University

April 2021

GHENT
UNIVERSITY

ISBN 978-94-6355-476-3
NUR 959
Wettelijk depot: D/2021/10.500/23

Members of the Examination Board

Chair

Prof. Patrick De Baets, PhD, Ghent University

Other members entitled to vote

Prof. Jérôme Louveaux, PhD, Université catholique de Louvain
Prof. Marc Moonen, PhD, KU Leuven
Prof. Nele Noels, PhD, Ghent University
Prof. Dries Vande Ginste, PhD, Ghent University

Supervisors

Prof. Marc Moeneclaey, PhD, Ghent University
Lennert Jacobs, PhD, Ghent University

Dankwoord

Graag zou ik hier enkele mensen bedanken die er elk op hun manier voor hebben gezorgd dat het gelukt is om mijn doctoraat tot een goed eind te brengen.

Ik wil graag Marc eerst en vooral bedanken voor de mogelijkheid die hij mij geboden heeft om te mogen doctoreren onder zijn hoede. Maar nog meer wil ik eigenlijk de belangrijke rol die hij gespeeld heeft in mijn ontwikkeling als onderzoeker benadrukken. Of het nu ging om een wiskundig probleem, het kritisch interpreteren van mijn resultaten of het nalezen van mijn tekst, Marc was altijd beschikbaar en bereid om waardevolle feedback te geven, hoe krap de deadline ook was. Ik heb een grote bewondering voor de motivatie en inzet die hij toont om al zijn doctoraatstudenten op een zo goed mogelijke manier te begeleiden.

Ook wens ik Lennert te bedanken voor zijn werk en papers waarop ik kon voortbouwen in dit doctoraat. Hij was ook altijd bereid om zijn Matlab code te delen en samen nieuwe ideeën uit te werken.

Next, I want to emphasize the importance of the input of Mamoun Guenach. His comments on the first drafts of my articles and his suggestions on how to reply to the remarks of the reviewers were always much appreciated.

Zonder data geen resultaten natuurlijk. Zonder het werk van de onderzoekers van de vakgroep informatietechnologie waren er dus geen numerieke resultaten voor een chip-naar-chip verbinding. In het bijzonder wil ik dr. ir. Paolo Manfredi en prof. dr. ir. Dries Vande Ginste bedanken voor het aanmaken en beschikbaar stellen van de verschillende datasets.

Verder wens ik ook uitdrukkelijk Patrick Schaillée en Sylvia Moeneclaey te bedanken voor al hun administratief werk in het secretariaat. Het is heel aangenaam dat wij als doctoraatstudent ons niet moeten bezighouden met het betalen van conferenties, het indienen van onkosten, etc. Ook de uitstekende IT-support van Davy Moreels en Philippe Serbruyns wordt enorm gewaardeerd. Telkens er een probleem was met mijn computer of met de simulatieservers waren zij daar om het probleem grondig aan te pakken en snel en efficiënt op te lossen.

Ik wil ook mijn collega's van TELIN bedanken voor de aangename werksfeer. Onder andere het samen lunchen in de Brug, de spelletjesavonden, het meedoen aan de sportnamiddagen en de fietstochten in de zomer maakten van TELIN een fijne vakgroep waar ik met plezier naar toe kwam om te werken. Het thuiswerken door corona heeft het belang van dit alles alleen maar bevestigd.

Verder heb ik ook het geluk dat mijn beide ouders mij al heel mijn leven

kansen bieden en onvoorwaardelijk steunen. Het is iets waar zij terecht trots op mogen zijn en ik ontzettend dankbaar voor ben. Ook de rest van mijn familie en vrienden wens ik te bedanken voor hun interesse in mijn werk, maar nog meer voor de ontspannende momenten die we samen doorgebracht hebben.

Ten slotte wens ik in het bijzonder mijn vriendin, Ella, te bedanken. Vijf jaar geleden begonnen we elk aan ons eigen doctoraat-avontuur, niet wetende wat ons te wachten stond. Nu kan ik zeggen dat jij voor het slagen mijn doctoraat een cruciale rol hebt gespeeld. Telkens als ik in een dip zat of gefrustreerd was over mijn doctoraat was het jij die mij weer moed insprak en motiveerde om verder te gaan. Maar het is vooral het geluk dat jij mij brengt naast het werk dat mij drijft om samen ons verhaal verder te schrijven.

Contents

List of Abbreviations **xi**

List of Symbols **xiii**

Nederlandse samenvatting **xvii**

English summary **xxi**

1 Introduction **1**
1.1 Background and motivation 1
1.2 Outline 3

2 Channel models **5**
2.1 General communication system 5
2.1.1 Channel description 5
2.1.2 Complex-valued baseband model 7
2.2 MIMO chip-to-chip interconnect 8
2.3 Multipath wideband channel 12

3 Overview of equalization schemes **15**
3.1 Problem statement 16
3.2 Equalization schemes 18
3.2.1 Optimal detection 18
3.2.2 Linear equalization 19
3.2.3 Decision-feedback equalization 22
3.2.4 Tomlinson-Harashima precoding 24
3.2.5 Partial-response signaling 26
3.2.6 Overview of the investigated equalization schemes . . . 29

4 Equalization strategies **31**
4.1 Adjustable and fixed parameters 31
4.2 Parameter optimization 32
4.3 Proposed equalization strategies 35

5 Stochastic channel: decision feedback equalization 39
5.1 System model . . . 41
5.1.1 Linear equalization scheme . . . 45
5.2 MMSE equalization . . . 45
5.2.1 Adjustable strategy . . . 48
5.2.2 Fixed strategy . . . 50
5.2.3 Hybrid strategy . . . 52
5.2.4 Suboptimal 1 . . . 53
5.2.5 Suboptimal 2 . . . 54
5.2.6 Linear equalization scheme . . . 55
5.2.7 Complexity considerations . . . 55
5.3 Baseband transmission . . . 56
5.4 SER and BER expression . . . 57
5.4.1 SER expression for M-PAM transmission . . . 57
5.4.2 BER expression for M-PAM transmission . . . 59
5.4.3 Numerical evaluation of the SER and BER expressions . 60
5.5 Numerical results and discussion . . . 63
5.5.1 Performance comparison of the different strategies . . . 64
5.5.2 Feedback filter: a detailed discussion . . . 72
5.5.3 Fractionally-spaced equalizers . . . 77
5.5.4 Convergence analysis . . . 81
5.5.5 Effect of constellation size for fixed bitrate . . . 83
5.5.6 Simulation accuracy of the BER . . . 85
5.6 Comparison of different optimization methods . . . 88
5.6.1 Alternating optimization method . . . 89
5.6.2 Saddle-free Newton optimization method . . . 90
5.6.3 Improved bidirectional random optimization method . . 91
5.6.4 MSE performance comparison . . . 92
5.6.5 Summary and remarks . . . 95
5.7 Conclusions . . . 96

6 Stochastic channel: Tomlinson-Harashima precoding 99
6.1 System model . . . 100
6.2 MMSE equalization . . . 102
6.2.1 Adjustable strategy . . . 104
6.2.2 Fixed strategy . . . 106
6.2.3 Hybrid strategy . . . 107
6.2.4 Suboptimal 1 . . . 109
6.2.5 Suboptimal 2 . . . 109
6.3 SER and BER expression . . . 110
6.3.1 SER expression for M-PAM transmission . . . 110
6.3.2 BER expression for M-PAM transmission . . . 112
6.3.3 Numerical evaluation of the SER and BER expression . 112
6.4 Numerical results and discussion . . . 113
6.5 Addition of a feedback filter at the receiver . . . 121

6.6 Conclusions . . . 128

7 Partial-response signaling **131**
7.1 System model . . . 132
7.2 MMSE equalization . . . 135
7.2.1 Optimization over **W** and **B** . . . 136
7.2.2 Optimization over **T** . . . 137
7.2.2.1 Algorithm 1 . . . 139
7.2.2.2 Algorithm 2 . . . 140
7.2.2.3 Algorithm 3 . . . 142
7.2.2.4 Complexity considerations . . . 143
7.2.2.5 Optimality and convergence considerations . . . 144
7.3 BER expression for PRS . . . 145
7.4 Numerical results and discussion . . . 146
7.4.1 Average performance . . . 147
7.4.2 Performance for individual channel realizations . . . 150
7.4.3 Convergence and complexity analysis . . . 153
7.4.4 Alternative selection criterion . . . 155
7.5 Conclusions . . . 156

8 Robust partial-response signaling **159**
8.1 Robust design . . . 160
8.2 System model . . . 160
8.3 Robust equalizer design . . . 164
8.3.1 General optimization problem . . . 164
8.3.2 MMSE optimization problem . . . 165
8.3.3 Calculation of the equalization parameters . . . 166
8.4 BER expression . . . 167
8.5 Numerical results and discussion . . . 168
8.6 Conclusions . . . 175

9 Stochastic channel: partial-response signaling **177**
9.1 System model . . . 178
9.2 MMSE optimization . . . 179
9.2.1 Adjustable strategy . . . 181
9.2.2 Fixed strategy . . . 183
9.2.3 Hybrid strategy . . . 185
9.3 BER expression for PRS . . . 186
9.4 Numerical results and discussion . . . 187
9.5 Conclusions . . . 195

10 Concluding remarks **197**
10.1 Main conclusions . . . 197
10.2 Future work . . . 201
10.2.1 Different objective functions . . . 201

10.2.2 Robust minimax design of PRS precoder 204
10.2.3 Extension of the ST-PRS precoder 205
10.3 Publications 206

11 Appendices **207**
11.1 Optimization problem with complex arguments 207
11.2 Optimization problem A 209
11.3 DFE: computation of adjustable parameters in S-H_{s2} 210
11.4 DFE: $BER^{(l)}_{\mathbf{g}_{ch}}$ expression for M-PAM transmission 212
11.5 THP: derivation of the $SER^{(l)}_{\mathbf{g}_{ch}}$ expression 213
11.6 THP: $BER^{(l)}_{\mathbf{g}_{ch}}$ expression for M-PAM transmission 214
11.7 THP-DFE: Computation of equalization parameters 215
11.8 PRS: proposition 1 220
11.9 PRS: proposition 2 220
11.10PRS: derivation of $BER^{(l)}$ expression for ST PRS 221
11.11Robust PRS: linear MMSE estimation from pilot symbols . . . 224
11.12Robust PRS: orthogonal pilot sequences 226

Bibliography **227**

List of Abbreviations

A/D Analog-to-Digital

AMSER Adaptive Minimum Symbol Error Rate

BER Bit Error Rate

BLAST Bell Laboratories Layered Space-Time

CSI Channel State Information

CSIT Channel State Information at the Transmitter

D/A Digital-to-Analog

DFE Decision Feedback Equalizer

IBI Interblock Interference

IBRO Improved Bidirectional Random Optimization

ISI Intersymbol Interference

FIR Finite Impulse Response

FRS Full-Response Signaling

MAP Maximum a Posteriori

MDist Minimum Distortion

MIMO Multiple-Input Multiple-Output

MLSD Maximum Likelihood Sequence Detector

MMnE Minimum mean nth power of the Error

MMSE Minimum Mean Square Error

MnE Mean nth power of the Error

MSE Mean Square Error

OFDM Orthogonal Frequency Division Multiplexing

PDF Probability Density Function

LLL Lenstra-Lenstra-Lovasz

LRA Lattice Reduction Aided

PAM Pulse Amplitude Modulation

PRS Partial-Response Signaling

RCC Root-Raised Cosine

SER Symbol Error Rate

SISO Single-Input Single-Output

SF Saddle-Free

SNR Signal-to-Noise Ratio

ST Spatio-Temporal

THP Tomlinson-Harashima Precoding

TIR Target Impulse Response

ZF Zero-Forcing

XT Crosstalk

List of Symbols

j	imaginary unit
x	a scalar
$\mathrm{Re}(x)$	the real part of x
$\mathrm{Im}(x)$	the imaginary part of x
$\lvert x \rvert$	absolute value of x
$x^\star$	optimized version of x
$\mathbf{X}$	a matrix
$(\mathbf{X})_{i,j}$	(i,j)th element of the matrix $\mathbf{X}$
$\mathrm{X}_{i,j}$	short notation for $(\mathbf{X})_{i,j}$
$\mathrm{X}_{i,\lvert}$	ith row of the matrix $\mathbf{X}$
$\mathrm{X}_{\lvert,j}$	jth column of the matrix $\mathbf{X}$
$[\mathbf{X}]_{i,j}$	(i,j)th matrix of the block matrix $\mathbf{X}$
$\mathbf{X}^{-1}$	inverse of the matrix $\mathbf{X}$
$\mathbf{X}^H$	Hermitian of the matrix $\mathbf{X}$
$\mathbf{X}^T$	transpose of the matrix $\mathbf{X}$
$\mathbf{X}^*$	complex conjugate of the matrix $\mathbf{X}$
$\det(\mathbf{X})$	determinant of the matrix $\mathbf{X}$
$\mathrm{adj}(\mathbf{X})$	adjugate matrix of the matrix $\mathbf{X}$
$\lVert\mathbf{X}\rVert$	Frobenius norm of the matrix $\mathbf{X}$
$\mathrm{Tr}(\mathbf{X})$	trace of the matrix $\mathbf{X}$
$\mathbf{x}$	a vector
$(\mathbf{x})_l$	lth element of the vector $\mathbf{x}$
x_l	short notation for $(\mathbf{x})_l$
$\lVert\mathbf{x}\rVert$	Euclidean norm of the vector $\mathbf{x}$
$\mathbf{0}$	matrix/vector whose entries are all 0
$\mathbf{1}$	matrix/vector whose entries are all 1
$\mathrm{diag}(\mathbf{X})$	vector with diagonal elements of the matrix $\mathbf{X}$
$\mathrm{diag}(\mathbf{x})$	diagonal matrix whose entries are specified by the vector $\mathbf{x}$
$\mathbf{J}_{l,q}$	matrix whose elements are all zero expect for the (l,q)th element that equals 1
$\mathbf{I}_L$	identity matrix of size $L \times L$
∇f	gradient of the function f
$\nabla^2 f$	Hessian of the function f
$\bar{f}$	average of the function f
$\mathbb{E}[\cdot]$	expectation operator
$\arg\min$	argument of the minimum of a set

$\max(\cdot,\cdot)$	maximum of two real-valued numbers
$\log_x(\cdot)$	logarithm with base x
$\exp(\cdot)$	exponential function
$\cos(\cdot)$	cosinus function
$\mathrm{Q}(x)$	probability that a zero-mean unit variance Gaussian random variable exceeds x
$\delta(x)$	Dirac delta function with argument x
δ_x	Kronecker delta function with argument x
$\otimes$	Kronecker product
$\mathbb{Z}$	set of all integers
$\mathbb{Z}^+$	set of strictly positive integers
$\mathbb{Z}[j]$	set of Gaussian integers
$\{a, \cdots, b\}$	set containing all integers from a to b
$A \cup B$	the union of set A and set B
$A \cap B$	the intersection of set A and set B
$\emptyset$	empty set
$B \setminus A$	the relative complement of set A with respect to set B
$\subseteq$	the subset operator
$\mathcal{D}(x)$	the decision area of the constellation point x
$N_{\neq}(x, y)$	the number of differences in the bit labels associated with constellation points x and y
$\lceil\cdot\rfloor_M$	the element-wise modulo reduction to the interval $[-M, M)$
$[\cdot]_M$	the element-wise modulo reduction to the interval $[0, M)$
$\lfloor\cdot\rceil$	operator that rounds both the real and the imaginary part to the nearest integer
$\lfloor\cdot\rfloor$	floor function
$[a, b)$	set of real-valued numbers lying between a (included) and b (excluded).
$\{\cdot\}_B$	filtering with ideal low-pass filter with bandwidth B
$\mathcal{O}(\cdot)$	the element-wise time complexity
$\binom{n}{x}$	number of k-combinations from a set with n elements
$\mathbf{a}(k)$	vector containing the data symbols at index k
$\hat{\mathbf{a}}(k)$	vector containing the detected data symbols at index k
$\mathbf{s}(t)$	vector containing the transmitted signal at time instant t
$\mathbf{n}(t)$	vector containing the noise signal at time instant t
$\mathbf{r}(t)$	vector containing the received signal at time instant t
$\mathbf{u}(k)$	vector containing the decision variables at index k
$\mathbf{e}(k)$	vector containing the error signal at index k
$\mathbf{T}(m)$	matrix containing the coefficients of the feedback filter or the target impulse response $\mathbf{T}$ at index m
$\mathbf{P}(n)$	matrix containing the coefficients of the filter $\mathbf{P}$ at index n
$\mathbf{W}(i)$	matrix containing the coefficients of the filter $\mathbf{W}$ at index i
α	the scaling factor at the receiver
$\mathbf{B}(m)$	matrix containing the coefficients of the feedback filter $\mathbf{B}$ at index m

$h_{\mathrm{TX}}(u)$	impulse response of the transmit filter
$\mathbf{H}_{\mathrm{ch}}(u)$	impulse response of the MIMO channel
$h_{\mathrm{RX}}(u)$	impulse response of the receive filter
L_{P}	number of nonzero matrices $\mathbf{P}(n)$
L_{W}	number of nonzero matrices $\mathbf{W}(i)$
L_{B}	number of nonzero matrices $\mathbf{B}(m)$
L_{T}	number of nonzero matrces $\mathbf{T}(m)$ with $m > 0$
$L_{\mathbf{X}}^{(1)}$	number of anti-causal taps in filter $\mathbf{X}$
$L_{\mathbf{X}}^{(2)}$	number of causal taps in filter $\mathbf{X}$
$L_{\mathrm{X}} = x$	$L_{\mathrm{P}}^{(1)} = L_{\mathrm{P}}^{(2)} = L_{\mathrm{W}}^{(1)} = L_{\mathrm{W}}^{(2)} = x$

Samenvatting

In de afgelopen decennia heeft een reeks van innovaties in de elektrotechniek de ontwikkeling van verschillende toepassingen versneld, gaande van lokalisatie aan de hand van satellieten tot slimme apparaten voor mobiele connectiviteit. Aangezien veel van deze toepassingen een snelle en betrouwbare overdracht van informatie vereisen, is de communicatietheorie één van de cruciale onderzoeksdomein om deze technologische vooruitgang mogelijk te maken. We zijn meer bepaald getuige geweest van een significante groei in de vraag voor bitsnelheid en bandbreedte. Één techniek om deze communicatie bij hoge snelheid mogelijk te maken is een communicatielink met meerdere ingangen en meerdere uitgangen (MIMO), waarbij meerdere datastromen tegelijk verzonden worden in dezelfde frequentieband. In het beste geval is het ontvangen signaal volledig identiek aan het verzonden signaal, maar verschillende beperkingen limiteren in de praktijk de kwaliteit van de MIMO informatieoverdracht. Omdat deze beperkingen prominenter worden bij hogere bitsnelheden, heeft hun beheer aan belang gewonnen in de communicatietheorie. De volgende beperkingen komen aan bod in dit proefschrift:

- Een eerste belangrijke beperking van het kanaal is intersymbool interferentie (ISI), wat veroorzaakt wordt door een frequentieselectief kanaal karakteristiek. Meer bepaald, de verschillende frequentiecomponenten van het verzonden signaal ervaren een verschillende kanaalversterking en/of kanaalfase, waardoor de verzonden pulsen worden uiteen gespreid in de tijd. Hierdoor interfereren naburige pulsen met elkaar, wat het moeilijker maakt om de verzonden data te extraheren uit het ontvangen signaal.

- Een tweede beperking dat eigen is aan MIMO communicatie is overspraak. Deze beperking treedt op wanneer het verzonden signaal horend bij de ene datastroom de data detectie van een andere datastroom verstoort. Men zou overspraak in feite kunnen interpreteren als ISI in de ruimte.

- Ten derde, elk kanaal heeft in de praktijk last van een ongewenst ruissignaal dat het ontvangen signaal verstoort. Deze ruis kan afkomstig zijn van zowel de omgeving als de elektronica componenten van de ontvanger. Het ruissignaal is normaal onafhankelijk van de verzonden data.

De hoofddoelstelling van de ontvanger is om de verzonden data te reconstrueren op basis van het vervormd ontvangen signaal dat ook ruis bevat. Optimale detectie in termen van bitfoutkans gebeurt in theorie door de a-posteriori-kans van de verzonden data voor het ontvangen signaal te maximaliseren, wat typisch kan geïmplementeerd worden aan de hand van een maximale waarschijnlijkheid sequentiedetector. Helaas is de complexiteit van dergelijke detectors in de praktijk vaak onaanvaardbaar groot zodat zijn prestaties vooral dienen als een theoretische maatstaf. In de literatuur zijn daarom al verschillende egalisatieschema's in combinatie met een symbool-per-symbool detector voorgesteld als alternatief. Deze egalisatieschema's hebben als doel om de kanaal beperkingen zo goed mogelijk te compenseren zodat een eenvoudige symbool-per-symbool detector resulteert in suboptimale maar bevredigende prestaties. Dit proefschrift behandelt de volgende egalisatieschema's: het lineaire egalisatieschema, het *decision-feedback equalization (DFE)* egalisatieschema, het *Tomlinson-Harashima precoding (THP)* egalisatieschema en het partiële responsie signalering (PRS) egalisatieschema. In het lineaire egalisatieschema, wordt een lineair filter met beperkte lengte gebruikt aan de zenderen/of ontvangerszijde om de ISI en de overspraak te verminderen en de ruisversterking te beperken. Het DFE egalisatieschema breidt het lineaire egalisatieschema uit door aan de ontvanger een terugkoppelingsfilter toe te voegen dat inwerkt op de eerder gedetecteerde data symbolen. Dit terugkoppelingsfilter is echter onderhevig aan foutpropagatie wat wordt vermeden in het THP egalisatieschema door het terugkoppelingsfilter te verplaatsen van de ontvangerszijde naar de zenderzijde. Ten slotte laat het PRS egalisatieschema een gecontroleerde hoeveelheid interferentie toe in het detectieproces wat de taak van de egalisatie filters vergemakkelijkt terwijl de eenvoud van de symbool-per-symbool detector behouden blijft.

De beste egalisatieprestatie wordt bereikt wanneer de kanaalkennis perfect is. In het bijzonder aan de zenderzijde is deze kanaalkennis helaas vaak niet perfect in de praktijk. De kanaalkennis kan enerzijds niet accuraat zijn omdat de ruis de kanaalschatting verstoort en de kanaalkennis kan anderzijds verouderd zijn omdat het kanaal tijdsvariant is. Een egalisatie ontwerp dat rekening houdt met deze imperfecties noemen we robuust.

In de eerste bijdrage van dit proefschrift worden het lineaire, het DFE en het THP egalisatieschema onderzocht in de context van een frequentieselectief MIMO kanaal dat onderhevig is aan kanaalvariabiliteit. Een algoritme om een algemene objectieve functie te optimaliseren wordt afgeleid en op basis daarvan worden drie egalisatiestrategieën geformuleerd: (i) de instelbare strategie waarin alle egalisatieparameters kunnen worden afgestemd op de kanaalschatting, (ii) de vaste strategie waarin alle egalisatieparameters zijn ontworpen op basis van de kanaalstatistiek en (iii) de hybride strategie dat zowel instelbare als vaste egalisatieparameters bevat. Daarnaast, worden ook eenvoudigere en suboptimale methodes voorgesteld om de vaste egalisatieparameters te bepalen. Vervolgens wordt dit optimalisatie kader met de gemiddelde kwadratische afwijking (GKA) als objectieve functie toegepast op het lineaire, het DFE en het

THP egalisatieschema. Verder wordt er ook een uitdrukking voor de bitfoutprobabiliteit (BER) opgesteld voor elk van deze egalisatieschema's, wat toelaat om de verschillende egalisatiestrategieën te onderzoeken in termen van zowel GKA als BER. Als voorbeeld wordt een chip-naar-chip verbinding geanalyseerd, waarvan verschillende geometrische parameters en verschillende materiaaleigenschappen beschouwd worden als Gaussiaanse toevalsgrootheden. Numerieke resultaten bevestigen dat de hybride strategie een goed alternatief met een lage complexiteit is voor de instelbare strategie, terwijl de degradatie van de vaste strategie snel stijgt met toenemende kanaalvariabiliteit.

De tweede bijdrage van dit proefschrift is de veralgemening van PRS naar een frequentieselectief MIMO systeem. In de literatuur is het doel impulsantwoord (TIR) beperkt tot zuiver temporele of zuiver ruimtelijke componenten. Bovendien, wordt de TIR vaak niet geoptimaliseerd zodat het volle potentieel van PRS niet benut wordt. Dit proefschrift breidt daarom eerst de PRS precoder uit tot een algemene tijdruimtelijke PRS precoder, wiens TIR bestaat uit zowel zuiver temporele en zuiver ruimtelijke componenten, alsook tijdruimtelijke componenten. Tevens worden er drie algoritmes voorgesteld om de TIR te optimaliseren en wordt er een nauwkeurige benadering van de uitdrukking voor de BER afgeleid. De prestatie van de algemene PRS precoder wordt eerst vergeleken met de traditionele volledige responsie signalering in het geval dat de kanaalkennis perfect is aan zowel de zenderzijde als de ontvangerszijde. In dit geval bevestigen numeriek resultaten horend bij een *multipath* breedband kanaal de superioriteit van de algemene PRS precoder. Vervolgens beschrijft dit proefschrift hoe het ontwerp van de PRS precoder robuust kan gemaakt worden tegen een verouderde kanaalschatting dat ruis bevat. Numerieke resultaten geven het voordeel van het robuuste ontwerp weer ten opzichte van het naïeve ontwerp. Ten slotte wordt het ontwerp van de algemene PRS precoder geschetst in de context van een frequentieselectief MIMO kanaal dat lijdt aan kanaalvariabiliteit. Meer bepaald impliceren numerieke resultaten met betrekking tot een chip-naar-chip verbinding dat ook voor het PRS egalisatieschema de hybride strategie een alternatief met een lage complexiteit is voor de instelbare strategie als de kanaalvariabiliteit laag is en/of voldoende egalisatieparameters instelbaar zijn.

Summary

During the last decades, a series of innovations in electrical engineering have accelerated the development of several applications, ranging from localization by means of satellites to smart devices for mobile connectivity. Since many of these applications require a fast and reliable transfer of information, the field of communication theory has been one of the crucial research domains to make these technological advancements possible. More precisely, we have witnessed a significant increase in the demand for bit rate and the associated bandwidth. One technique to provide this high-speed communication is a multiple-input multiple-output (MIMO) communication link, in which multiple data streams can be simultaneously transmitted in the same frequency interval. Ideally, the received signal is completely identical to the transmitted signal, but, in practice, several impairments limit the quality of the MIMO data transfer. Moreover, as these impairments are more prominent at higher bit rates, their management has become of particular importance in the field of communication theory. The following impairments are considered in this dissertation.

- A first important channel impairment is *intersymbol interference* (ISI), which is caused by a frequency-selective channel response. In this case, the different frequency components of the transmitted signal experience a different channel gain and/or channel phase, causing a transmitted pulse to spread out in time. As a result, neighboring pulses interfere with each other, making it more difficult to extract the transmitted data from the received signal.

- A second impairment that is specific to MIMO communication is *crosstalk* (XT), which arises when the transmitted signal associated with one data stream interferes with the data recovery of another symbol stream. In fact, one could interpret this XT as spatial ISI.

- Thirdly, any practical channel is affected by an unwanted *noise* signal that disturbs the received signal. This noise could be originated either from the environment or from the electronics components of the receiver. Normally, this noise signal is independent of the transmitted data.

The main objective of the receiver is to retrieve the transmitted data from the noisy and distorted received signal. In theory, optimal detection in terms of error performance is achieved by maximizing the a posteriori probability

of the transmitted data for a given received signal, which can typically be implemented by means of a maximum-likelihood sequence detector (MLSD). Unfortunately, the complexity of such a detector is often intolerably large in practice such that its performance mainly serves as a theoretical benchmark. As an alternative, different equalization schemes in combination with a symbol-by-symbol detector have been proposed in the literature. These equalization schemes aim to handle the channel impairments as good as possible such that a simple symbol-by-symbol detector results in suboptimal but still adequate performance. This dissertation discusses the following equalization schemes: the linear equalization scheme, the decision-feedback equalizer (DFE) equalization scheme, the Tomlinson-Harashima precoding (THP) equalization scheme, and the partial-response signaling (PRS) equalization scheme. In the linear equalization scheme, a (finite-length) linear filter at the transmitter and/or the receiver is employed to reduce the ISI and the XT, while limiting the noise enhancement. The DFE equalization scheme extends the linear equalization scheme by adding a (finite-length) feedback filter at the receiver that acts on the previously detected data symbols. However, this feedback filter is prone to error propagation, which is avoided in the THP equalization scheme by transferring the feedback filter from the receiver to the transmitter. Finally, the PRS equalization scheme allows a controlled amount of interference in the detection process, facilitating the tasks of the equalizers, while maintaining the simplicity of the symbol-by-symbol detector.

The best equalization performance is achieved when the channel state information (CSI) is perfectly known. Unfortunately, CSI is often imperfect in practice, especially at the transmitter; the CSI can be inaccurate because the noise affects the channel estimation, and/or the CSI can be outdated when the channel is time-variant. An equalizer design that takes these imperfections into account is called robust.

In the first contribution of this dissertation, the linear, the DFE and the THP equalization schemes are investigated in the context of a frequency-selective MIMO channel suffering from channel variability. An algorithm for optimizing a general objective function over the equalization parameters is derived, based on which three equalization strategies are formulated: (i) an adjustable strategy, in which all equalization parameters can adapt to the channel estimate; (ii) a fixed strategy, in which all equalization parameters are designed based on the channel statistics; and (iii) a hybrid strategy consisting of both adjustable and fixed equalization parameters. Additionally, less complicated suboptimal approaches to determine the fixed equalization parameters are presented as well. Next, taking the mean square error (MSE) as the objective function, this optimization framework is applied to the linear equalization scheme, the DFE equalization scheme and the THP equalization scheme. Moreover, an expression for the bit error rate (BER) for each of these equalization schemes is derived, allowing to investigate the different equalization strategies in terms of both MSE and BER. As an example, a chip-to-chip interconnect is analyzed from which several geometrical and material parameters are considered to be

Gaussian random variables. Numerical results confirm that the hybrid strategy is a low-complexity alternative to the adjustable strategy, whereas the degradation of the fixed strategy rapidly grows with increasing channel variability.

The second contribution of this dissertation is the generalization of PRS to a frequency-selective MIMO system. In the literature, the target impulse response (TIR) has been limited to temporal-only or spatial-only components. Moreover, the TIR is most often not optimized such that the full potential of PRS is not realized. This dissertation, therefore, first extends the PRS precoder to a general spatio-temporal (ST) PRS precoder, whose TIR comprises not only temporal and spatial components, but also ST components. Moreover, three different algorithms are proposed to optimize the TIR and an accurate approximation of the BER expression for the PRS system is derived. The performance of the general PRS precoder is first compared to traditional full-response signaling (FRS) in terms of MSE and BER when the CSI is perfect at both the transmitter and the receiver. In this case, numerical results related to a multipath wideband channel confirm the superiority of the general PRS precoder. Next, this dissertation describes how to make the design of the PRS precoder robust with respect to a noisy and/or outdated channel estimate. Numerical results indicate the benefits of the robust design compared to the naive design. Finally, the design of the general PRS precoder is outlined in the context of a frequency-selective MIMO channel suffering from channel variability. More specifically, numerical results pertaining to a chip-to-chip interconnect imply that also for the PRS equalization scheme the hybrid strategy is a low-complexity alternative to the adjustable strategy when the channel variability is small and/or enough equalization parameters are adjustable.

1 Introduction

1.1 Background and motivation

Today, it is almost impossible to imagine life without the numerous applications that rely on digital communications, ranging from localization by means of satellites, to mobile connectivity with smart portable devices, to autonomous driving, and to live streaming over the internet. In all these applications, vast amounts of data, mostly in the form of bits, must be reliably and efficiently transferred from point A to point B across some kind of communication channel. This transfer is schematically presented in Fig. 1.1. Mathematical modeling of the data transfer is one of the main topics of the field of communication theory. This dissertation is confined to digital communication, meaning that the data to be transmitted consist of digital data, typically a sequence of bits that can take either the value 0 or 1. The transmitter converts this data stream into a physical signal, e.g., an electromagnetic wave, and this signal subsequently travels across the transmission medium, which is also called the channel. The different types of channels define two groups of communication. For wireline communication, a conductor physically connects the transmitter and the receiver, e.g., a cable, whereas no physical connection is present for wireless communication, e.g., radio waves. The task of the receiver is to recover

Figure 1.1: General structure of a communication system.

the transmitted digital data sequence from the received signal.

In the early days of communication theory, the main focus lied on single-input single-output (SISO) communication channels, meaning that the data input stream, the transmitted signal, and the received signal contain all exactly one signal stream. Due to the demand for higher bit rates and good quality of service, multiple-input multiple-output (MIMO) communication is nowadays omnipresent, e.g., massive MIMO in 5G applications. Contrary to SISO communication, a MIMO channel has multiple inputs and multiple outputs such that the input data stream, the transmitted signal and the received signal consist all of multiple signal streams, allowing to either increase the data rate (spatial multiplexing), or to lower the error rates (spatial diversity), or to improve the signal-to-noise (SNR) ratios (beamforming)[1]. In this dissertation, MIMO communication is employed to increase the data rate by simultaneously transmitting multiple independent data sequences.

Unfortunately, communication channels are imperfect in practice, as they not only distort the transmitted signal, but also add a disturbance signal. For instance, frequency-selective MIMO channels introduce intersymbol interference (ISI) and crosstalk (XT) such that there is an overlap at the receiver of neighboring pulses in both space and time. On the other hand, the additive disturbance signal is often referred to as the noise, which is typically independent of the transmitted signal. The management of the ISI, the XT, and the noise at the transmitter and/or the receiver has already been extensively studied in the literature and several equalization mechanisms have been presented to improve the communication quality over these imperfect communication channels: THP at the transmitter is an example of pre-filtering at the transmitter, whereas a decision-feedback equalizer (DFE) performs post-filtering at the receiver.

In several applications, the channel realizations are not identical to each other, e.g., due to manufacturing tolerances, but these different channel realizations often still exhibit a moderate to large degree of similarity in their channel responses. Consequently, to lower the complexity of the equalization processing, one could benefit from this similarity by considering (part of) the equalization fixed, i.e., independent of the particular channel realization. Still, the performance degradation due to the fixed equalization part is expected to be limited as long as the deviations between the different channel realizations are sufficiently small. The main objective of the first part of this dissertation is to propose different equalization strategies that investigate this trade-off between low complexity and good performance. This dissertation therefore devises an optimization framework to determine MIMO equalization algorithms that are robust against this channel variability. This optimization framework is subsequently applied to the DFE equalization scheme and the Tomlinson-Harashima precoding (THP) equalization scheme, with the emphasis on a chip-to-chip interconnect suffering from manufacturing tolerances.

In standard full-response signaling (FRS), the equalization parameters attempt to reduce all ISI and XT as much as possible. On the other hand, partial response signaling (PRS) allows a controlled amount of residual interference,

with the aim of facilitating the equalization design and thereby improving the error performance. Hence, a second objective of this dissertation is to design a general PRS precoder for a MIMO frequency-selective channel. Unlike the PRS precoders proposed in the literature, the target impulse response (TIR) matrix of this precoder contains not only temporal and spatial, but also ST components. This dissertation considers the optimization of this TIR for three scenarios of channel knowledge. First, the theoretical case is investigated, in which the channel is assumed to be perfectly known and available at both the transmitter and the receiver. Second, the channel is assumed to be suffering from channel variability and the same equalization strategies that are proposed in the first part of this dissertation are applied to the optimization of the general PRS precoder. Third, the design of the PRS precoder with perfect channel state information (CSI) is revised by taking the imperfections of the channel estimation process into account, yielding a robust design of the TIR. This channel estimate is commonly acquired by means of pilot symbols, which experience the following limitations: (i) the noise introduced by the channel induces an estimation error, which becomes smaller when more pilot symbols are employed and/or the transmit energy is larger; and (ii) getting the channel estimate from the receiver to the transmitter requires a return channel with possibly limited bandwidth. As a result, the CSI at the transmitter (CSIT) is often inaccurate and/or delayed.

1.2 Outline

This dissertation is outlined as follows.

Chapter 2 first provides an overview of the channel impairments in a general communication system, after which two classes of channels are discussed: (i) a MIMO chip-to-chip interconnect and (ii) the multipath wideband channel.
Chapter 3 lists the different approaches that have been presented in the literature to manage the distortions induced by the communications channel. Moreover, the mechanisms of the different approaches are illustrated by an example.
Chapter 4 proposes different equalization strategies to face the performance-complexity trade-off when the communication channel is stochastic. To this end, a general iterative optimization algorithm is presented.
Chapter 5 applies the different equalization strategies from Chapter 4 to the DFE equalization scheme. For all equalization strategies, both the iterative mean square errror (MSE) minimization of the equalization parameters and the achieved performance in terms of MSE and bit error rate (BER) are investigated. Moreover, this chapter also studies two alternative optimization methods to solve the MSE minimization problem.
Chapter 6 studies the design and the performance of the various equalization strategies from Chapter 4 for the THP equalization scheme. Additionally, the

traditional THP equalization scheme is extended with a feedback filter at the receiver, thereby enhancing the performance of the hybrid strategy.
Chapter 7 introduces the design of a general spatio-temporal (ST) PRS precoder in the case of a frequency-selective MIMO channel. More precisely, three different iterative algorithms are developed to determine the optimal TIR.
Chapter 8 investigates the design of the PRS equalization scheme from Chapter 7 when the channel estimates are imperfect due to the noise and/or the latency. This chapter demonstrates that incorporating these imperfection into the design of the equalization parameters results in significantly better performance than naively assuming that the channel estimates are perfect.
Chapter 9 again focuses on the PRS equalization scheme, but assumes that the channel suffers from channel variability and thus applies the different equalization strategies from Chapter 4 to the PRS equalization scheme.
Chapter 10 summarizes the main conclusions of the obtained results. Moreover, several topics for future research are explored and a list of our publications is compiled.
Chapter 11 constitutes a collection of several appendices, providing some supplementary material for the other chapters.

2 Channel models

This chapter's objective is to describe the various channel models that are employed in this work. To this end, a general communication system is described in Section 2.1, in which not only the different imperfections of a communication channel are listed, but also the complex-valued baseband representation of a bandpass channel is introduced. Next, Section 2.2 provides some details on the first channel that is considered: a chip-to-chip interconnect consisting of four coupled microstrips. The main feature is that this channel is affected by manufacturing tolerances such that the time-invariant channel response must be treated as a random variable. Section 2.3 discusses a second channel model, i.e., the wireless multipath wideband channel, which is an example of a complex-valued MIMO frequency-selective time-variant channel.

2.1 General communication system

2.1.1 Channel description

Ideally, the output of a communication channel is identical to its input such that the received signal is equal to the transmitted signal. Unfortunately, perfect channels do not exist in reality because of the following channel impairments:

- *Frequency-selectivity*: In the case of a frequency-selective channel, the different frequency components of the transmitted signal experience a different channel gain and/or channel phase. Consequently, every pulse consisting of multiple frequencies in the transmitted signal is spread out in time, introducing interference between consecutive data symbols. This

interference is called ISI and can be described either by the channel impulse response $\mathbf{H}_{\mathrm{ch}}(u)$ or by the channel transfer function $\mathbf{H}_{\mathrm{ch}}(f)$, the latter being the Fourier transform of the former. This type of interference depends only on the causal and the anti-causal data symbols of the current data stream and is therefore denoted as *temporal* ISI.

- *Crosstalk*: Apart from the ISI due to the frequency-selectivity of the channel, interference can also be originated from other sources, e.g., other communication systems or another data stream in a MIMO system. This type of interference is generally called XT. In this work, only the XT generated by the other data streams in the MIMO system is considered and can also be derived from the channel impulse response $\mathbf{H}_{\mathrm{ch}}(u)$ or from the channel transfer function $\mathbf{H}_{\mathrm{ch}}(f)$. Moreover, the XT from a data symbol to the decision variable of another data symbol transmitted at the same time is called *spatial* interference, whereas this interference is called *ST* interference when both data symbols are transmitted on different time instants.

- *Noise*: All practical communication links suffer from some level of undesired interference that is random and independent from any other signal. This interference is called the noise and is often modeled as an additive noise source. The noise elements are randomly generated according to some distribution, whereas the power of the elements and the correlation between the different elements are defined by the power spectral density.

- *Time-variability*: Especially in the case of wireless channels, the impulse response of the channel and thus also the associated frequency response varies in time. One well-known channel suffering from time-variability is for example the (frequency-selective) fading channel. Consequently, the channel impulse response and the channel transfer function are dependent not only on the delay variable u and the associated frequency variable f, respectively, but also on the observation instant t, yielding $\mathbf{H}_{\mathrm{ch}}(u,t)$ and $\mathbf{H}_{\mathrm{ch}}(f,t)$. More precisely, $\mathbf{H}_{\mathrm{ch}}(u,t)$ represents the channel impulse response perceived by a signal applied at the time instant $t-u$ and observed at time instant t.

In summary, all these impairments can be captured by the following model of the MIMO channel:

$$\mathbf{r}(t) = \int_{-\infty}^{\infty} \mathbf{H}_{\mathrm{ch}}(u,t)\mathbf{s}(t-u)\ \mathrm{d}u + \mathbf{n}(t), \tag{2.1}$$

where $\mathbf{H}_{\mathrm{ch}}(u,t)$ is the $N_{\mathrm{R}} \times N_{\mathrm{T}}$ channel impulse response matrix with N_{T} and N_{R} denoting the number of channel inputs and the number of channel outputs, respectively. Moreover, all ISI and XT terms are characterized by the impulse response $\mathbf{H}_{\mathrm{ch}}(u,t)$, whereas the noise contribution is defined by the $N_{\mathrm{R}} \times 1$

vector $\mathbf{n}(t)$. In general, this noise vector is considered to follow a Gaussian distribution, which is defined by the mean $\boldsymbol{\mu}_{\mathbf{n}}(t)$ and the autocorrelation function $\mathbf{R}_{\mathbf{n}}(u) = \mathbb{E}\left[\mathbf{n}(t)\mathbf{n}^T(t+u)\right]$. In practice, the mean $\boldsymbol{\mu}_{\mathbf{n}}(t)$ is often equal to zero, i.e., $\boldsymbol{\mu}_{\mathbf{n}}(t) = \mathbf{0}$, and the noise is assumed to be white, meaning that its power spectral density is constant and equal to $\frac{N_0}{2}$ such that $\mathbf{R}_{\mathbf{n}}(u) = \frac{N_0}{2}\delta(u)\mathbf{I}_{N_{\mathrm{R}}}$.

When the channel response does not changes over time, i.e., when the channel is time-invariant, the argument t in $\mathbf{H}_{\mathrm{ch}}(u,t)$ in (2.1) can be dropped.

2.1.2 Complex-valued baseband model

This work considers both baseband transmission and bandpass transmission. In both cases, the physical signals (transmitted signals, noise, received signals) and the impulse responses of the physical channels are real-valued.

The main frequency content of the transmitted signal is in an interval $(-B, B)$ for baseband transmission, whereas for bandpass transmission the transmitted signal is mainly contained in a frequency interval $(-f_c - B, -f_c + B) \cup (f_c - B, f_c + B)$, with $f_c > B$. The baseband channel and the bandpass channel are responsive to the frequencies of the baseband signal and the bandpass signal, respectively.

However, to be able to describe the bandpass transmission with the same system model as the low-pass transmission, we represent all bandpass signals and all bandpass filters by their complex-valued baseband representations. As for a bandpass signal $x_{BP}(t)$ with center frequency f_c and bandwidth $B < f_c$, the complex-valued baseband signal $x_{LP}(t)$ is defined according to

$$x_{LP}(t) = \left\{ \sqrt{2} x_{BP}(t) \exp\left(-j2\pi f_c t\right) \right\}_B, \tag{2.2}$$

where $\{\cdot\}_B$ denotes the filtering by a perfect unit-gain low-pass filter with bandwidth B. For the impulse response $h_{\mathrm{BP}}(t)$ of a bandpass filter, its complex-valued baseband representation is similarly constructed as in (2.2), but with the factor $\sqrt{2}$ omitted. Moreover, when the signal $s_{BP}(t)$ is applied to the filter $h_{\mathrm{BP}}(t)$ with the additive noise term $n_{BP}(t)$, the complex-valued baseband representation $r_{LP}(t)$ of the output $r_{BP}(t)$ can be expressed as

$$r_{LP}(t) = \int_{-\infty}^{+\infty} h_{\mathrm{LP}}(u) s_{LP}(t-u)\, \mathrm{d}u + n_{LP}(t), \tag{2.3}$$

where $n_{LP}(t)$ is the complex-valued baseband representation of $n_{BP}(t)$. Importantly, when $n_{BP}(t)$ has a constant power spectral density equal to $\frac{N_0}{2}$, then $n_{LP}(t)$ has also a constant power spectral density in the interval $[-B, B]$, which is equal to N_0 rather than $\frac{N_0}{2}$ due to the factor $\sqrt{2}$ in (2.2). Of course, the filter input-output relationship from (2.3) can directly be extended to a time-varying MIMO bandpass channel. Consequently, when all bandpass signals and impulse responses are represent by their complex-valued baseband representations, the channel model of (2.1) is still valid. The main advantage of

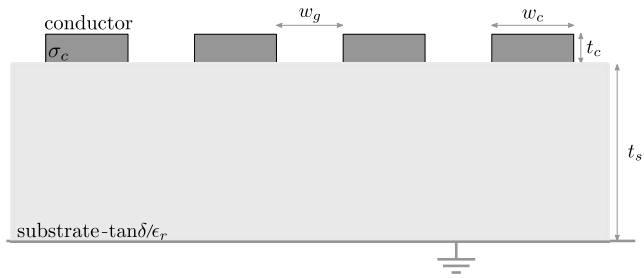

Figure 2.1: Cross section of chip-to-chip interconnect (not to scale).

employing this complex-valued baseband representation is that the description of the modulation (baseband-to-bandpass conversion) and the demodulation (bandpass-to-baseband conversion) can be omitted, allowing to describe bandpass transmission with the same system model as baseband transmission.

To avoid any ambiguity in the remainder of this work, we specifically clarify when baseband or bandpass transmission is considered.

2.2 MIMO chip-to-chip interconnect

The principal channel that is discussed in this work is an electrical chip-to-chip interconnect of 10 cm consisting of four parallel coupled microstrips between the transmitter and the receiver. The cross section of this interconnect is given in Fig. 2.1. This chip-to-chip interconnect is characterized by the following set of geometrical and material parameters:

- Gap between two signal conductors w_g
- Width of the signal conductor w_c
- Thickness of the signal conductor t_c
- Thickness of the dielectric substrate t_s
- Conductivity of the signal conductor σ_c
- Relative permittivity of the dielectric substrate ϵ_r
- Loss tangent of the dielectric substrate $\tan_\delta$

Due to manufacturing tolerances, the different realizations of this interconnect are not identical, so the listed parameters must be treated as random variables. As the sum of the gap between two signal conductors w_g and the width of the signal conductor w_c is considered to be constant, six parameters in total vary independently. These independent parameters, gathered in the vector $\boldsymbol{\phi}$, are treated as independent Gaussian random variables with a mean equal to

Table 2.1: Nominal values of the geometrical and the material parameters.

Parameter	Nominal value
w_g	$80\,\mu$m
w_c	$100\,\mu$m
t_c	$35\,\mu$m
t_s	$500\,\mu$m
σ_c	$58\,$MS/m
ϵ_r	4
$\tan_\delta$	0.02

the nominal values of Table 2.1 and a standard deviation σ_r expressed as a percentage of the mean. To investigate the impact of the level of variability on the performance of the different equalization schemes proposed in the Chapters below, different values for the standard deviation σ_r, ranging from 1% to 10%, are considered. For each value of σ_r, a data set consisting of 1000 channel realizations is constructed according to the approach outlined in [2, 3, 4], which is briefly summarized here. First, using polynomial chaos theory, the frequency-dependent RLGC parameters of the interconnect are represented as truncated multivariate expansions of the random parameters. Next, for each realization of the random parameters, the corresponding RLGC parameters are computed using these polynomial expansions. Finally, the corresponding realizations of the channel frequency response are obtained from the RLGC parameters using standard transmission line relations.

To gain a better understanding about both the frequency response of this chip-to-chip interconnect and the influence of the standard deviation σ_r, Fig. 2.2 depicts the frequency responses $|(\mathbf{H}_{\text{ch}}(f))_{1,1}|$ and $|(\mathbf{H}_{\text{ch}}(f))_{1,2}|$ in the case of $\sigma_r = 1\%$ and $\sigma_r = 10\%$ as a function of the frequency f. More precisely, all plots present the 10th percentile p_{10}, the 50th percentile p_{50}, and the 90th percentile p_{90} of the depicted frequency response. The following observations can be made:

- Based on the upper plots of Fig. 2.2, one can conclude that the channel response $(\mathbf{H}_{\text{ch}}(f))_{1,1}$ is a low-pass channel such that baseband transmission over this chip-to-chip interconnect is suitable. This low-pass frequency response can mainly be attributed to the attenuation caused by the skin effect and the dielectric loss that increases with signal frequency [5]. Moreover, $\left|(\mathbf{H}_{\text{ch}}(f))_{2,2}\right|$ is verified to exhibit a similar curve as $|(\mathbf{H}_{\text{ch}}(f))_{1,1}|$, whereas $(\mathbf{H}_{\text{ch}}(f))_{3,3}$ and $(\mathbf{H}_{\text{ch}}(f))_{4,4}$ are identical to $(\mathbf{H}_{\text{ch}}(f))_{2,2}$ and $(\mathbf{H}_{\text{ch}}(f))_{1,1}$, respectively, due to the symmetry in the geometry of this interconnect. To maximize the data rate, one must thus simultaneously transmit an unique data stream over each of the four microstrips. Due to the low-pass nature of the channel, larger temporal ISI

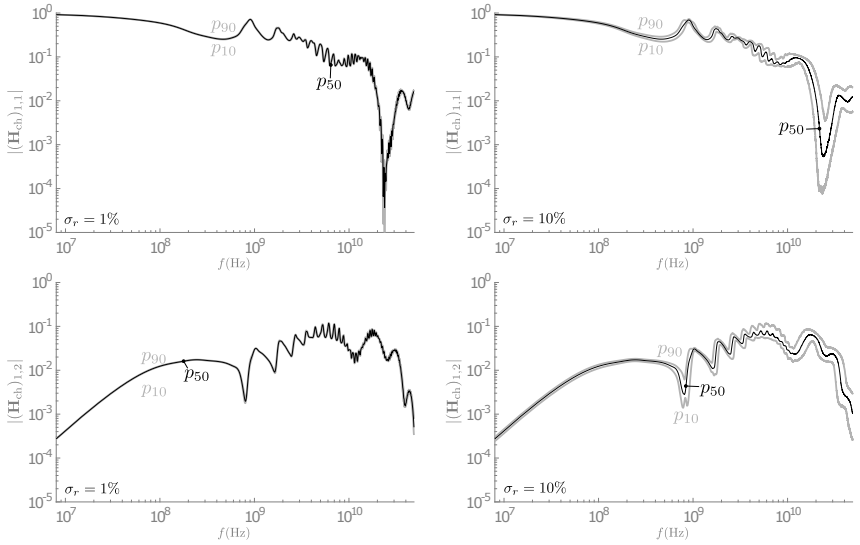

Figure 2.2: Chip-to-chip interconnect: visualization of the 10th percentile p_{10}, the 50th percentile p_{50}, and the 90th percentile p_{90} of the frequency responses $|(\mathbf{H}_{\mathrm{ch}}(f))_{1,1}|$ (upper plots) and $|(\mathbf{H}_{\mathrm{ch}}(f))_{1,2}|$ (lower plots) in the case of $\sigma_r = 1\%$ (left plots) and $\sigma_r = 10\%$ (right plots) as a function of the frequency f. The larger variability in the case of $\sigma_r = 10\%$ mainly manifests itself at larger frequencies.

is to be expected when the symbol rate is increased.

- The amount of XT in this chip-to-chip interconnect is characterized by the non-diagonal elements of $\mathbf{H}_{\mathrm{ch}}(f)$, i.e., $(\mathbf{H}_{\mathrm{ch}}(f))_{i,j}$ with $i \neq j$. XT in a chip-to-chip interconnect is caused by capacitive and inductive coupling between neighboring signals. Examination of all these frequency responses demonstrates that they are all nearly identical to each other. Consequently, Fig. 2.2 presents only the frequency response of one of them, i.e., $(\mathbf{H}_{\mathrm{ch}}(f))_{1,2}$. The plot of $|(\mathbf{H}_{\mathrm{ch}}(f))_{1,2}|$ indicates that the XT is more suppressed than the useful signal, but rises when the frequency increases. As a result, significantly more spatial and ST ISI is present at larger symbol rates such that the XT energy received can even exceed the energy of the useful signal at high frequencies [6].

- The amount of variability between the frequency responses of the different channels is limited when $\sigma_r = 1\%$. Indeed, p_{10}, p_{50}, and p_{90} lie all very close to each other in the left plots of Fig. 2.2, indicating that most frequency responses are nearly identical to each other. However, when σ_r is increased to 10% in the right plots of Fig. 2.2, more difference between p_{10} and p_{90} is present, especially at large frequencies. Consequently, the larger the symbol rate, the more the manufacturing tolerances are expected to (negatively) impact the quality of the communication link.

- In Fig. 2.3, the channel impulse response $(\mathbf{H}_{\mathrm{ch}}(u))_{1,1}$ is presented as a function of u in the case of $\sigma_r = 3\%$. More precisely, the 10th percentile p_{10}, the 50th percentile p_{50}, and the 90th percentile p_{90} of $(\mathbf{H}_{\mathrm{ch}}(u))_{1,1}$ are depicted. One of the main aspects of all impulse responses $(\mathbf{H}_{\mathrm{ch}}(u))_{i,j}$ is that they suffer from reflections due to impedance mismatch at both the transmitter and the receiver. The amplitude of these reflections gradually diminishes in time such that the first reflection is the largest and thus the most important. Fig. 2.3 confirms that this first reflection occurs approximately 1 ns after the main pulse, inducing a ripple with a period of approximately $1/1\,\mathrm{ns} = 1\,\mathrm{GHz}$ in the frequency responses of Fig. 2.2. In fact, this delay of 1 ns is approximately the time T_{r} required for a signal to propagate over 20 cm of the interconnect. Since an electromagnetic wave travels at the speed of light divided by the square root of the effective relative permittivity of the medium, in which this wave travels, this time is given by

$$T_{\mathrm{r}} = \sqrt{\epsilon_{r,I}}\,\frac{0.2\,\mathrm{m}}{3 \cdot 10^8\,\mathrm{m/s}}. \tag{2.4}$$

In (2.4), $\epsilon_{r,I}$ represents the effective dielectric constant of the microstrip interconnect, which is, for the non-homogeneous medium, between the permittivity of the air (= 1) and the permittivity of the dielectric (= 4). Subsequently, substituting $\epsilon_{r,I}$ with any value within this range confirms that the reflection is to be expected after approximately 1 ns.

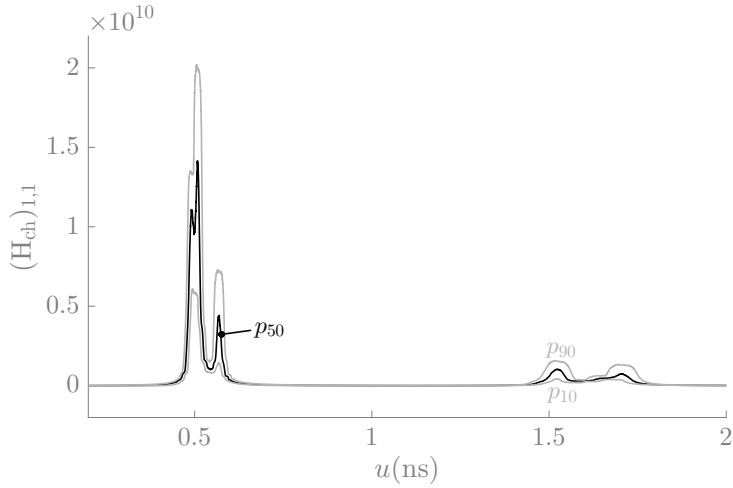

Figure 2.3: Chip-to-chip interconnect: visualization of the 10th percentile p_{10}, the 50th percentile p_{50}, and the 90th percentile p_{90} of the impulse response $(\mathbf{H}_{\mathrm{ch}}(u))_{1,1}$ in the case of $\sigma_r = 3\%$ as a function of u. This channel suffers from reflections with a period of approximately 1 ns.

Although manufacturing tolerances in the production process result in channel realizations that all (slightly) differ from each other, once in operation, the channel response of each particular channel is assumed to be constant in time, because external factors such as temperature only mildly influence the properties of the microstrip. Consequently, the sets of channel realizations corresponding to the different values of σ_r consist all of 1000 time-invariant channels.

The presented chip-to-chip interconnect above is an example channel of an electrical interconnect in chip-to-chip communication. In practice, these chip-to-chip interconnects can be found in processor-to-memory interfaces, and in the multi-layer backplanes of server/router systems and multi-processor systems. Recent research indicates that bit rates up to 100 Gb/s are targeted in the near future [7, 8, 9, 10, 11, 12].

The communication over this chip-to-chip interconnect is investigated in Chapters 5, 6, and 9.

2.3 Multipath wideband channel

In the wireless multipath channel [13], the moving receiver obtains multiple copies of the transmitted signal by means of several reflections, each with a distinct delay, magnitude and phase. Hence, the received pulse is a distorted version of the transmitted pulse due to the frequency-selective nature of the

channel. Moreover, the delays, the magnitudes, and the phases of the various reflections change in time due to the movement of the receiver such that the channel response also suffers from time-variability.

As the actual channel behavior cannot be exactly predicted, a statistical model must be employed to characterize the channel. Hence, the MIMO channel impulse response $\mathbf{H}_{\text{ch}}(u,t)$ (in complex-valued baseband notation) is assumed to be a zero-mean random process with the autocorrelation function $R_{\mathbf{H}_{\text{ch}}}(\cdot)$ defined by

$$R_{\mathbf{H}_{\text{ch}}}(u_1,u_2,t_1,t_2,i_1,i_2,j_1,j_2) = \mathbb{E}\left[\left(\mathbf{H}_{\text{ch}}(u_1,t_1)\right)_{i_1,j_1}\left(\mathbf{H}^*_{\text{ch}}(u_2,t_2)\right)_{i_2,j_2}\right]. \tag{2.5}$$

Expression (2.5) can be simplified by the following assumptions:

- The channel impulse response from channel input j_1 to channel output i_1 is assumed to be independent from all other channel impulse responses. Consequently, the autocorrelation function $R_{\mathbf{H}_{\text{ch}}}(\cdot)$ from (2.5) is different from zero only when $(i_1,j_1)=(i_2,j_2)$.
- The autocorrelation function $R_{\mathbf{H}_{\text{ch}}}(\cdot)$ from (2.5) does not depend on the separate values of t_1 and t_2, but only on the time difference Δt between t_2 and t_1, i.e., $\Delta t = t_2 - t_1$. A random process possessing this property is said to be wide-sense stationary.
- No correlation is present between the different reflections such that the amplitudes and the phases of the different paths are uncorrelated as well. As a result, the autocorrelation of the channel disappears when $u_1 \neq u_2$. This property is referred to as uncorrelated scattering.

Consequently, the autocorrelation function $R_{\mathbf{H}_{\text{ch}}}(\cdot)$ can be written as

$$R_{\mathbf{H}_{\text{ch}}}(u_1,u_2,t_1,t_2,i_1,i_2,j_1,j_2) = \hat{R}_{\mathbf{H}_{\text{ch}}}(u_1,\Delta t)\delta(u_1-u_2)\delta_{i_1-i_2}\delta_{j_1-j_2}. \tag{2.6}$$

Next, the correlation $\hat{R}_{\mathbf{H}_{\text{ch}}}(u,\Delta t)$ in (2.6) can be decomposed into two terms, i.e.,

$$\hat{R}_{\mathbf{H}_{\text{ch}}}(u,\Delta t) = p_d(u)R_t(\Delta t), \tag{2.7}$$

due to the assumption that the frequency-selectivity is independent from the time-selectivity. In (2.7), $p_d(u)$ is called the power delay profile, whose area is normalized to one, i.e., $\int_{-\infty}^{+\infty} p_d(u)\,\mathrm{d}u = 1$. The Fourier transform of $p_d(u)$, $R_f(\Delta f)$, is known as the frequency correlation function, from which the coherence bandwidth B_c is determined as the bandwidth over which the magnitude of $R_f(\Delta f)$ is more than half its maximum value. The function $R_t(\Delta t)$ in (2.7) is called the time correlation function and this function is equal to the inverse Fourier transform of the Doppler spectrum $p_D(\nu)$, whose area is again normalized to 1 ($\int_{-\infty}^{+\infty} p_D(\nu)\,\mathrm{d}\nu = 1$). Additionally, the coherence time T_c is analogously

defined as the coherence bandwidth, i.e., the interval over which the magnitude of the time correlation function is at least half its maximum value. This work considers only the case in which the symbol period is significantly smaller than the coherence time and the transmitted bandwidth is larger than the coherence bandwidth. Consequently, the MIMO channel is frequency-selective, but only shows weak time-variant behavior such that the MIMO channel can be assumed to be quasi-static during the transmission of a block of data symbols.

3

Overview of equalization schemes

This chapter concentrates on the different receiver and transmitter schemes that have been presented in the literature to handle the interference and the noise induced by a frequency-selective channel (Chapter 2). To this end, the general problem is formulated and commented on in Section 3.1 and the basic principles of various equalization schemes are subsequently presented in Section 3.2. First, the optimal detection in terms of error performance is considered in Subsection 3.2.1. Due to its large complexity, the resulting optimal receiver is most often not realizable in practice. Hence, the suboptimal equalization schemes from Subsections 3.2.2-3.2.5 are more suitable. For instance, the linear equalization scheme (Subsection 3.2.2) employs linear filters to reduce or even to completely eliminate the ISI, after which a symbol-by-symbol detector attempts to recover the original data. In the case of the DFE equalization scheme from Subsection 3.2.3, a linear feedback filter acting on the previously detected symbols tries to improve the performance of the linear equalization scheme. The resulting equalizer is referred to as nonlinear, because of the nonlinear operation involved in the symbol detection. Transferring this feedback filter from the receiver to the transmitter results in an equalization scheme called the THP equalization scheme (Subsection 3.2.4). As for PRS in Subsection 3.2.5, the coefficients of the feedback filter are limited to the set of integers, such that the symbol-by-symbol detector can directly act on the target response that possesses a controlled amount of ISI. The idea is that by allowing some ISI at the detector input, the task of the equalizers simplifies and the performance therefore improves. Finally, an overview is given of the equalization schemes that are considered in this dissertation.

To illustrate the different equalization schemes, each equalization scheme is

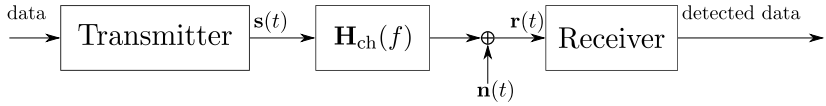

Figure 3.1: Problem statement: data transmission over a MIMO frequency-selective communication channel $\mathbf{H}_{\text{ch}}(f)$.

applied to a random SISO example channel such that its main characteristics are highlighted. In this chapter, no details are given on how to compute the optimal equalizers, as this becomes apparent in the chapters below.

For simplicity, this chapter assumes that the channel is time-invariant and employs the complex-valued baseband notation.

3.1 Problem statement

A general block diagram of the data transfer from the transmitter to the receiver over a frequency-selective MIMO channel $\mathbf{H}_{\text{ch}}(f)$ is shown in Fig. 3.1. The data typically consists of N_{dat} sequences of data symbols that are simultaneously applied to the transmitter at a symbol rate $1/T$. The task of the transmitter is to convert this input data sequence into a continuous $N_{\text{T}} \times 1$ transmitted signal $\mathbf{s}(t)$. Due to the XT and the frequency-selective nature of the $N_{\text{R}} \times N_{\text{T}}$ MIMO channel $\mathbf{H}_{\text{ch}}(f)$, this transmitted signal is linearly distorted, inducing ISI in the $N_{\text{R}} \times 1$ received signal $\mathbf{r}(t)$. Moreover, a noise vector $\mathbf{n}(t)$ is added to the received signal $\mathbf{r}(t)$. The task of the receiver is to correctly retrieve the N_{dat} original input data sequences from the noisy and linearly distorted signal $\mathbf{r}(t)$. Hence, the optimization problem to be solved essentially amounts to jointly designing the data conversion at the transmitter and the signal recovery at the receiver. Below, some fundamental principles of most transmitters and receivers are given.

At the transmitter, linear digital modulation is often employed to transform a discrete-time sequence $\{\mathbf{a}(k)\}$, whose elements are independently drawn from a finite set, into the continuous-time signal $\mathbf{s}(t)$ according to

$$\mathbf{s}(t) = \sum_{m=-\infty}^{+\infty} \mathbf{H}_{\text{TX}}(t - mT)\mathbf{a}(k - m). \tag{3.1}$$

In (3.1), the transmitted signal $\mathbf{s}(t)$ consists of a sum of multiple translated pulses characterized by the $N_{\text{T}} \times N_{\text{dat}}$ transmit filter $\mathbf{H}_{\text{TX}}(t)$. Indeed, the (i, j)th element of the matrix $\mathbf{H}_{\text{TX}}(t - mT)$ represents the contribution of the mth element of the jth data sequence to the ith element of the transmitted signal $\mathbf{s}$ at time instant t. The most elementary form of linear digital modulation occurs when all data symbol sequences are independently transmitted using the same SISO transmit filter $h_{\text{TX}}(t)$, meaning that $N_{\text{dat}} = N_{\text{T}}$ and only the

diagonal elements of $\mathbf{H}_{\mathrm{TX}}(t)$ are nonzero and equal to $h_{\mathrm{TX}}(t)$. This diagonal matrix $\mathbf{H}_{\mathrm{TX}}(t)$ is denoted by $\mathbf{H}_{\mathrm{TX}}^{(d)}(t)$.

The receiver aims to recover the original data sequence $\{\mathbf{a}(k)\}$ based on the received signal $\mathbf{r}(t)$, which is a noisy and linearly distorted version of the transmitted signal $\mathbf{s}(t)$. The typical structure of a receiver is as follows: first, a receive filter $\mathbf{H}_{\mathrm{RX}}(f)$, also called an anti-aliasing filter, selects the desired frequency interval from $\mathbf{r}(t)$, thereby suppressing any unwanted interference and noise contributions lying outside this frequency interval. Again, the simplest implementation of this receive filter is to filter each channel output individually with the receive filter $h_{\mathrm{RX}}(t)$. Similarly to $\mathbf{H}_{\mathrm{TX}}^{(d)}(t)$, the resulting diagonal matrix $\mathbf{H}_{\mathrm{RX}}(t)$ is denoted by $\mathbf{H}_{\mathrm{RX}}^{(d)}(t)$. Next, a sampler, possibly operating at a multiple of the symbol rate, generates a discrete-time version of the continuous-time and filtered received signal. Finally, a detection algorithm takes the sampled signal as input and computes the decisions $\hat{\mathbf{a}}(k)$.

To achieve ISI-free communication in the case of a SISO channel, the Nyquist criterion [14] dictates that the periodic extension with period $1/T$ of the overall frequency response, i.e., the cascade of the transmit filter, the channel, and the receive filter, must be constant and equal to T. This criterion is extended in [15] to MIMO channels. One immediate consequence of the Nyquist criterion is that the one-sided bandwidth of the transmit and the receive filter must be at least $1/2T$ if no ISI is allowed. In practice, the transmit filter $h_{\mathrm{TX}}(t)$ and the receive filter $h_{\mathrm{RX}}(t)$ are often chosen to be a root-raised-cosine (RRC) filter with bandwidth $1/T$ and a roll-off factor β with $0 \leq \beta \leq 1$, as their convolution is a raised-cosine pulse, and thus satisfies the Nyquist criterion.

In this dissertation, only uncoded transmission is considered. Moreover, the scope of this dissertation is limited to continuous transmission[1], meaning that only the steady-state performance of an infinite data sequence is investigated. Alternatively, one could envisage block transmission, in which the data stream is divided into data blocks that are separately transmitted over the channel. Examples of commonly employed block-based techniques to manage the ISI are orthogonal frequency division multiplexing (OFDM) [16] and frequency-domain equalization [17, 18], which divide a frequency-selective channel in many flat-fading subchannels. A long enough guard interval or cyclic prefix between the different blocks must be inserted to avoid interblock interference (IBI). For long channel responses, however, this long guard interval comes at the expense of either a decreased throughput or large symbol blocks; long blocks increase not only the latency, but also the memory requirements. Finally, the equalization problem to be solved in the case of block transmission is inherently

[1] In Chapter 8, block transmission is considered, as regular estimates of the channel must be computed by means of pilot symbols. However, the block length is chosen to be quite large and time-invariant (at least during one data block) equalization filters are employed to compensate for the channel impairments. Hence, no block-based techniques to manage the ISI are employed and as for the design of the equalization filters, the mathematical problem is identical as in the case of continuous transmission.

different from the one in the case of continuous transmission, as the former can be interpreted as a MIMO flat-fading channel [19], in which only XT and no temporal ISI is present.

3.2 Equalization schemes

This section reviews several equalization schemes and detection algorithms that have been presented in the literature to handle the ISI and the noise induced by the frequency-selective (MIMO) channel. First, the optimal detection in terms of error performance is summarized in Subsection 3.2.1. Its large complexity, however, motivates the usage of computationally less complex symbol-by-symbol detectors, combined with some kind of equalization. In total, four equalization schemes are discussed:(i) the linear equalization scheme in Subsection 3.2.2, (ii) the DFE equalization scheme in Subsection 3.2.3, (iii) the THP equalization scheme in Subsection 3.2.4, and (iv) the PRS equalization scheme in Subsection 3.2.5. Finally, Subsection 3.2.6 outlines not only which equalization schemes, but also which channel models are discussed in subsequent chapters.

The CSI is assumed to be perfectly known at both the transmitter and the receiver in the brief discussion below, as the emphasis lies on the different equalization schemes. In practice, this assumption is, especially at the transmitter, not always valid. The designs of the different equalization schemes can be adopted to take the imperfections of the CSI into account, as will be demonstrated in subsequent chapters.

3.2.1 Optimal detection

The goal of the receiver is to detect the transmitted sequence $\{\mathbf{a}(k)\}$ based on the received signal $\mathbf{r}(t)$. Due to the noise, completely error-free detection is impossible. Let us define the error probability as the probability that the detected sequence differs from the transmitted sequence. The error probability is minimized by taking the maximum a posteriori (MAP) decision. This decision is given by $\mathbf{a}_{\text{MAP}} = \arg\max_{\mathbf{a}} p(\mathbf{a}|\mathbf{r})$, where $p(\mathbf{a}|\mathbf{r})$ is the posterior probability of a symbol sequence $\mathbf{a}$, and the maximization is over all allowed data sequences. Interestingly, Bayes's theorem states that the posterior probability can be rewritten as

$$p(\mathbf{a}|\mathbf{r}) = \frac{p(\mathbf{r}|\mathbf{a})p(\mathbf{a})}{p(\mathbf{r})}. \tag{3.2}$$

Since the probability $p(\mathbf{r})$ is independent of the data symbols, the maximization of $p(\mathbf{a}|\mathbf{r})$ is equivalent to the maximization of $p(\mathbf{r}|\mathbf{a})p(\mathbf{a})$. When the prior probability $p(\mathbf{a})$ is uniform over all data symbol sequences, one could equivalently maximize the likelihood $p(\mathbf{r}|\mathbf{a})$ with respect to $\mathbf{a}$ instead of the posterior probability $p(\mathbf{a}|\mathbf{r})$. The corresponding optimal receiver is known as the maximum likelihood sequence detector (MLSD).

For both SISO and MIMO communication, the MLSD has been extensively studied in the literature [20, 21, 22, 23, 24]. The MLSD consists of a filter(bank) matched to the cascade of the transmit and channel filter, followed by a symbol-rate sampler and a sequence detection algorithm, of which the Viterbi algorithm is a well-known example. Considering a filter with impulse response $h(t)$ and transfer function $H(f)$, the corresponding matched filter has impulse response $h^*(-t)$ and transfer function $H^*(f)$. It has been shown that the symbol-rate sampled output of the matched filter(bank) forms a sufficient statistic of $\mathbf{r}(t)$. The noise samples at the output of the matched filter are often correlated. Therefore, it is convenient to add a whitening filter, which can be computed by means of spectral factorization. The complete chain of the transmit filter, the channel filter, the matched filter, the sampler and the whitening filter is then equivalent to a frequency-selective discrete-time causal channel with white noise such that the Viterbi algorithm can be applied to its output.

The main problem of the optimal detector is that the complexity of the Viterbi algorithm is *exponential* in both the channel memory and the number of data sequences, hence limiting the practicability of this detector. Therefore, less computationally complex but suboptimal alternative equalization schemes are proposed below.

3.2.2 Linear equalization

A more practically feasible alternative to the optimal detector is the linear equalization scheme, in which one or more linear equalization filters attempt to reduce or even completely eliminate the ISI induced by the MIMO frequency-selective channel. Afterwards, a simple symbol-by-symbol detector acts on the decision variable to recover the transmitted data symbol, by selecting the symbol that has the smallest Euclidean distance to the decision variable. The complexity of this detector is far less than the complexity of a sequence detector. As the symbol-by-symbol detector ignores the correlation of the noise contributions to the decision variables, only suboptimal performance is achieved.

For a given transmit filter $\mathbf{H}_{\mathrm{TX}}(f)$ and channel response $\mathbf{H}_{\mathrm{ch}}(f)$, the optimal linear receiver, for symbol-by-symbol detection, is given by the matched filter, cascaded with an infinite-length symbol-spaced tapped delay line [20, 21, 25], which can either be implemented as an analog filter or as a digital filter acting on the sampled output of the matched filter. It is of course desirable to select the coefficients of the tapped delay line such that the probability of a decision error is as small as possible, but this optimization is hard to implement as it is highly nonlinear [26, 27, 28]. In the literature, two common techniques have been proposed as an alternative, in the case of a infinite-length delay line. First, the zero-forcing (ZF) equalizer eliminates all ISI and XT by ensuring that the impulse response of the complete system fulfills the Nyquist criterion. However, this performance measure does not consider the noise, and the error performance could thus be impaired by an intolerably large noise enhancement. The second performance measure therefore minimizes the MSE between

the decision variable and the corresponding data symbol. The resulting minimum MSE (MMSE) equalizer ensures that the noise enhancement becomes not too large, at the expense of residual amount of ISI. At small and medium signal-to-noise ratio (SNR), the MMSE equalizer yields typically better performance than the zero-forcing equalizer. As the SNR approaches infinity, the MMSE equalizer converges to the zero-forcing equalizer. For each of the two performance measures, an additional optimization over the transmit filter is also possible [29, 30, 21].

Although the complexity in the case of the linear equalization scheme is drastically smaller than in the case of the MLSD receiver, the practical implementation of the former equalization scheme still requires some alterations to the optimal linear equalizer:

- As the matched filter(bank) and the symbol-spaced tapped delay line depend on the channel transfer function, these filters must be adjusted when the channel response changes. Especially for the continuous-time matched filter(bank), this adjustment is a difficult task in practice. As an alternative, the continuous-time matched filter(bank) is set to a fixed anti-aliasing filter, often matched to the known invariant transmit filter. In this case, however, the cascade of the fixed anti-aliasing filter with an adjustable tapped delay line with symbol-spaced coefficients is only suboptimal, and a high sensitivity to the sampling delay is perceived. Alternatively, optimal performance and robustness to the sampling delay can be achieved by considering a fractionally-spaced equalizer, e.g., a tapped delay line with multiple taps per symbol interval, because the cascade of a proper fixed anti-aliasing filter and an adjustable fractionally-spaced tapped delay line can be made equivalent to the cascade of the matched filter and the symbol-spaced tapped delay line [20, 21].

- The optimal transmit filter also depends on the channel response. Similar to the receiver, however, a more convenient practical approach is to implement this optimal transmit filter as a cascade of a fractionally-spaced tapped delay line and a fixed continuous-time transmit filter.

- All results regarding infinite-length tapped delay lines are essentially only a theoretical optimum, as any practical tapped delay line is restricted to a finite number of coefficients. When the delay-line has finite length, the ZF condition cannot always be met; therefore, the MMSE criterion is commonly used to determine the filter taps. For a given number of coefficients, the optimal tapped delay line is not simply constructed by truncating the optimum infinite-length tapped delay line, but by taking the exact number of coefficients into consideration during the equalizer design.

In Fig 3.2, the system model of the practical linear equalization scheme is presented. The fixed continuous-time transmit and continuous-time receive filter are symbolized by $\mathbf{H}_{\mathrm{TX}}(f)$ and $\mathbf{H}_{\mathrm{RX}}(f)$, respectively. In this dissertation,

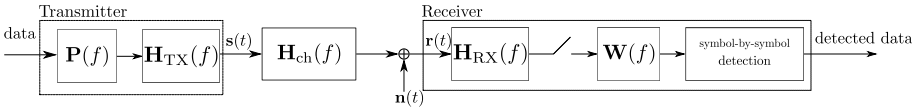

Figure 3.2: Conceptual block diagram of a practical linear equalization scheme. The fractionally-spaced equalization filters $\mathbf{P}(f)$ and $\mathbf{W}(f)$ have both a finite number of coefficients.

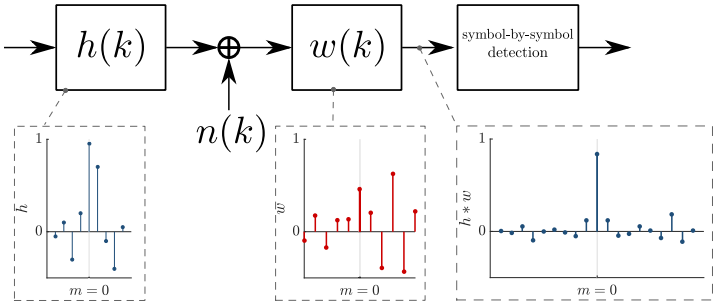

Figure 3.3: Linear equalization scheme applied to the example discrete-time SISO channel $h(k)$. The 11-tap linear FIR filter $w(k)$ is computed according to the MMSE criterion, i.e., the MSE between the decision variable and the transmitted data symbol is minimized, here, at a SNR of 15 dB.

these continuous-time transmit and receive filters are restricted to be diagonal, i.e., $\mathbf{H}_{\mathrm{TX}}(f) = \mathbf{H}^{(d)}_{\mathrm{TX}}(f)$ and $\mathbf{H}_{\mathrm{RX}}(f) = \mathbf{H}^{(d)}_{\mathrm{RX}}(f)$. The symbol-spaced or fractionally-spaced finite impulse response (FIR) tapped delay line at the transmitter and at the receiver are denoted as $\mathbf{P}(f)$ and $\mathbf{W}(f)$, respectively. For given $\mathbf{H}^{(d)}_{\mathrm{TX}}(f)$ and $\mathbf{H}^{(d)}_{\mathrm{RX}}(f)$, the optimization problem then in fact translates to computing the optimal value for the coefficients of $\mathbf{P}(f)$ and $\mathbf{W}(f)$, usually according to the MMSE criterion [29, 31, 28, 32]. The joint optimization of the coefficients of $\mathbf{P}(f)$ and $\mathbf{W}(f)$ is still an open problem and an iterative algorithm is recommended. When either $\mathbf{P}(f)$ or $\mathbf{W}(f)$ is absent, this optimization problem drastically simplifies and becomes fairly straightforward [33, 34] to solve. Still, when both $\mathbf{P}(f)$ and $\mathbf{W}(f)$ are present, a better performance is expected, as the task of equalization is split among the transmitter and the receiver.

The equalization by means of an 11-tap linear equalizer at the receiver is presented in Fig. 3.3, which considers a linear and practical FIR equalization filter $w(k)$ applied to a random SISO example channel characterized by a discrete-time response $h(k)$. This response can be interpreted as the sampled cascade of the transmit filter, the channel filter and the receive filter. The various impulse responses shown on these figures confirm that the linear equalizer $w(k)$ removes part of the ISI generated by the channel: using z-transforms, we

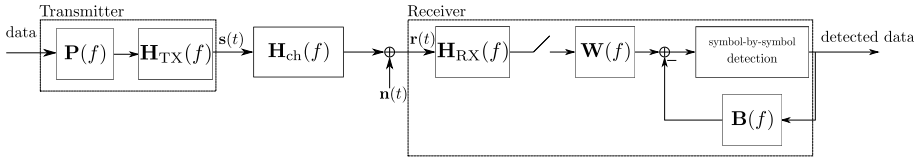

Figure 3.4: Conceptual block diagram of a practical DFE equalization scheme. Compared to the linear equalization scheme, the feedback filter $\mathbf{B}(f)$ now eliminates (part of) the causal ISI.

have $H(z)W(z) \approx 1$. The linear equalizer $w(k)$ in Fig. 3.3 minimizes the MSE between the decision variable and the transmitted data symbol.

In the remainder of this dissertation, we refer to this equalization scheme as the linear equalization scheme.

3.2.3 Decision-feedback equalization

At the cost of only a small increase in complexity, the performance of the linear equalization scheme can be significantly enhanced by adding a linear feedback filter $\mathbf{B}(f)$ that operates on the previously detected data symbols. As a result, the equalization structure at the receiver consists of a feedforward path between the received signal and the decision variable and a feedback path between the detected data and the decision variable. Because the symbol-by symbol decision device performs a nonlinear function on its input, the overall equalization scheme is referred to as nonlinear. Since this nonlinearity greatly complicates the exact computation of the optimal equalizers, this equalization scheme is typically designed while assuming that the previously detected symbols are correct. With this assumption, the equalizer design simplifies, as the relationship between the transmitted data and the input to the decision device becomes linear.

Similar to the linear equalization scheme, the optimization of the minimum error probability turns out to be relatively complicated [35] such that the ZF and the MMSE criterion are again more viable options in the case of infinite-length equalizers. The optimal feedforward equalizer at the receiver for both criteria has been shown to be equal to the matched filter(bank) followed by a tapped delay line [20, 21, 36, 37, 38, 39]. Contrary to the linear equalization scheme, however, the tapped delay line must only counteract the anti-causal ISI, because the feedback filter is able to eliminate all causal ISI. The ZF feedforward equalizer completely removes this anti-causal interference with the smallest amount of noise-enhancement possible, whereas the MMSE feedforward equalizer allows some residual anti-causal ISI with the aim of a lower noise enhancement. In general, less noise enhancement is to be expected for the DFE equalization scheme than for the linear equalization scheme as the noise enhancement associated with the reduction of the causal ISI is avoided.

For a given structure of the receiver, an additional optimization of the transmit filter $\mathbf{H}_{\mathrm{TX}}(t)$ has been proposed in [39, 40].

Just as for the the linear equalization scheme, the matched filter and the infinitely long feedforward and feedback tapped delay lines are not practical to implement. Therefore, the same modifications to the optimal equalization scheme as for the linear equalization scheme are proposed. First, the cascade of the matched filter(bank) and the feedforward tapped delay line is approximated by the fixed anti-aliasing filter $\mathbf{H}_{\mathrm{RX}}^{(d)}(f)$ followed by a (fractionally-spaced) FIR feedforward filter $\mathbf{W}(f)$. Moreover, the feedback filter $\mathbf{B}(f)$ is assumed to contain only a limited number of feedback taps, which implies that the finite-length feedback filter can remove only a part of the causal ISI. The resulting receiver optimized with the MMSE criterion has been previously investigated in [41, 42, 43]. At the transmitter, the linear filter is implemented as the cascade of a (fractionally-spaced) FIR filter $\mathbf{P}(f)$ followed by a fixed continuous-time filter $\mathbf{H}_{\mathrm{TX}}^{(d)}(f)$ [44]. Note that the joint optimization of a finite $\mathbf{W}(f)$, a finite $\mathbf{P}(f)$, and a finite $\mathbf{B}(f)$ is still an open problem. The resulting practical DFE equalization scheme is schematically depicted in Fig. 3.4.

In this dissertation, the feedback filter is assumed to be strictly causal, meaning that the output of the feedback filter at the current time instant is a weighted sum of decisions corresponding to past time instants only. In the case of MIMO communication, one could, however, perform the symbol-by-symbol detection of the different data streams successively, and extend this weighted sum to the decisions associated with the current time instant from the already detected data streams [41]. Naturally, this extended feedback filter is expected to yield better performance, especially when the order in which the different data streams are detected is optimized. For a flat-fading MIMO channel, this latter approach is known as Bell Laboratories Layered Space-Time (BLAST) [45]. A minor disadvantage of this feedback filter is that the various decisions at the current time instant must be made sequentially, such that the different symbol-by-symbol detectors cannot be implemented in parallel.

To correctly evaluate the error performance of this equalization scheme, one must consider the effect of error propagation at the receiver. Indeed, when (part of) the previously detected symbols are erroneous, the associated causal interference does not disappear and possibly even enlarges. The error propagation problem can be modeled as a stationary Markov chain. However, exactly computing the transitions probabilities becomes problematic for feedback filters with a large number of feedback taps. The easiest method to quantify the effect of the error propagation on the error performance is therefore either a Monte Carlo simulation or an upper bound [46].

Fig. 3.5 shows the optimal MMSE equalizer when the DFE equalization scheme is applied to the same example channel as in Fig. 3.3. Clearly, the feedback filter eliminates all causal ISI associated with the time delays on which it is active on the condition that the previously detected data symbols are correct. Consequently, the design of the feedforward equalizer could neglect

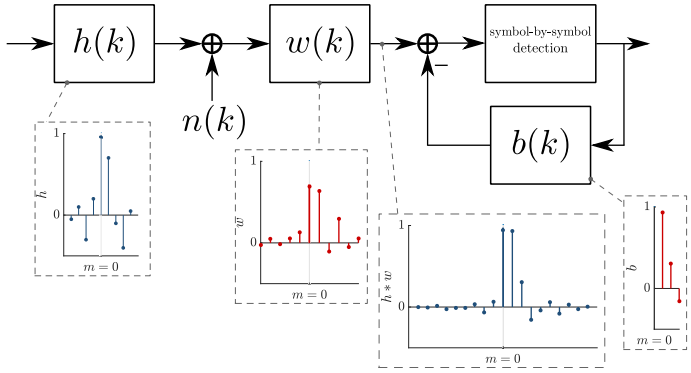

Figure 3.5: The DFE equalization scheme applied to the example discrete-time SISO channel $h(k)$. The linear FIR filters $w(k)$ and $b(k)$ are computed according to the MMSE criterion, i.e., the MSE between the decision variable and the transmitted data symbol is minimized, here, at a SNR of 15 dB. The 3-tap feedback filter clearly removes all ISI corresponding to the time delays on which it is active, whereas the 11-tap linear feedforward filter $\mathbf{w}(k)$ reduces the remaining ISI.

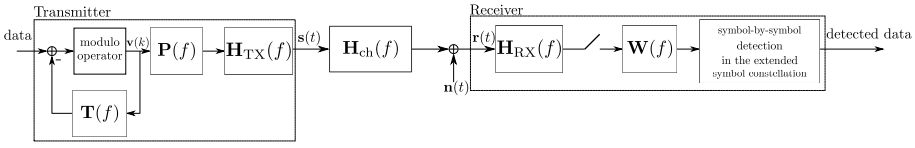

Figure 3.6: Conceptual block diagram of a practical THP equalization scheme. Compared to the DFE equalization scheme, the feedback filter is transferred from the receiver to the transmitter.

this causal ISI and thus completely focuses on the ISI that is not canceled by the feedback filter. Hence, compared to the linear equalizer, the task of the feedforward equalizer facilitates, yielding smaller noise enhancement and in general improved performance. In z-transform notation, we have $H(z)W(z) - B(z) \approx 1$, or, equivalently, $H(z)W(z) \approx 1 + B(z)$.

In the remainder of this dissertation, we refer to this equalization scheme as the DFE equalization scheme.

3.2.4 Tomlinson-Harashima precoding

THP has originally been proposed as an equalization technique at the transmitter to mitigate the causal ISI generated by a frequency-selective SISO channel [47, 48, 49, 50, 51, 52]. Basically, one can interpret this THP equalization scheme as the DFE equalization scheme, where the feedback filter is transferred from the receiver to the transmitter. Consequently, the design principles

of the DFE equalization scheme can be applied here as well, meaning that one can again employ either the ZF criterion (for infinite-length tapped delay lines) or the MMSE criterion (for infinite-length or finite-length delay lines) to compute the equalization parameters. The main advantage of moving the feedback filter to the transmitter is that error propagation is avoided, as data symbols are perfectly known at the transmitter. This feedback filter could, however, give rise to intolerably large transmit signals. The standard approach to face this problem is to apply a modulo operation at the transmitter, hence restricting the magnitude of the transmitted signal. The combination of the feedback structure at the transmitter with the modulo operator is often referred to as the THP precoder. At the receiver, the data is recovered by performing symbol-by-symbol detection in the extended symbol set, which is the periodical extension of the regular symbol set.

The THP at the transmitter has also some disadvantages. First of all, CSI must be available at the transmitter, which is not evident in practice as a this requires a return channel in most applications. Second, the transmitted energy increases beyond the energy of the regular symbol set, due to the modulo operator. This is referred to as the *power loss*. Interestingly, the impact of this power loss diminishes for larger symbol sets. Thirdly, the average number of nearest neighbors in the case of THP slightly increases as the symbol-by-symbol detection is now performed with respect to the extended symbol set instead of the regular symbol set; the corresponding degradation is referred to as the *modulo loss*.

In [53, 54, 55], the THP scheme has been extended to the flat fading MIMO channel to eliminate (part of) the XT caused by the channel. Similar to BLAST, the performance of this THP scheme can be improved by optimizing the order of the different symbol streams [56]. THP has been proposed for a frequency-selective MIMO channel [34, 56, 57, 58, 59] as well in the case of both point-to-point and point-to-multipoint transmission. In this case, the precoder possesses always a causal feedback filter to compensate for all ISI and XT generated by past data symbols, whereas it is possible to additionally eliminate the XT generated by simultaneous symbols in already processed data streams. In this dissertation, only the ISI and XT caused by past symbols are eliminated by the precoder.

A conceptual block diagram of the THP equalization is presented in Fig. 3.6. Comparing this block diagram with the block diagram of the DFE equalization, one can indeed interpret the THP equalization scheme as the DFE equalization with the feedback filter transferred from the receiver to the transmitter, since, apart from the feedback filter, the equalization schemes are very similar. The transmit and the receive filter are assumed to be independent from the specific channel, and the linear FIR equalizers $\mathbf{P}(f)$ and $\mathbf{W}(f)$ must tackle the ISI that is not removed by the feedback filter $\mathbf{T}(f)$. Again, the joint optimization of all filters is still an open problem.

Fig. 3.7 displays the different impulse responses acquired when the THP equalization scheme with an 11-tap linear filter $w(k)$ and a 3-tap feedback

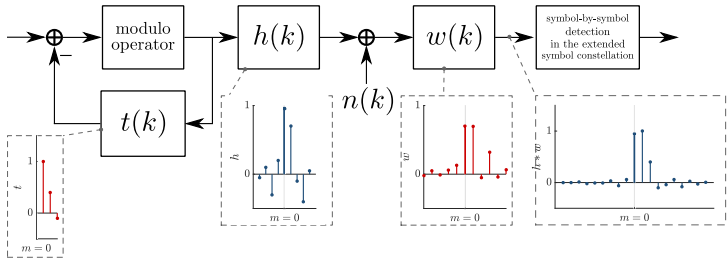

Figure 3.7: The THP equalization scheme applied to the example discrete-time SISO channel $h(k)$. The linear filters $w(k)$ and $t(k)$ are computed according to the MMSE criterion. The 3-tap feedback filter $t(k)$ and the 11-tap FIR filter $w(k)$ only slightly differ from the feedback and feedforward filter from the DFE equalization scheme due to the power loss.

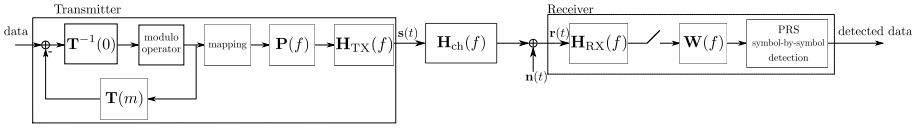

Figure 3.8: Conceptual block diagram of a practical generalized PRS equalization scheme. Contrary to the literature, the TIR matrix $\mathbf{T}$ contains spatial, temporal, and ST components.

filter $t(k)$ is applied to the SISO example channel $h(k)$. The similarities of the obtained $w(k)$ and $t(k)$ to the optimal $w(k)$ and $b(k)$ in the case of the DFE equalization scheme are apparent, as they only (slightly) differ due to the power loss induced by the modulo operator. In z-transform notation, we have $\frac{1}{1+T(z)}H(z)W(z) \approx 1$, or, equivalently, $H(z)W(z) \approx 1+T(z)$, so that $T(z)$ can be viewed as the feedback filter $B(z)$ from the DFE that is moved from the receiver to the transmitter.

In the remainder of this dissertation, we refer to this equalization scheme as the THP equalization scheme.

3.2.5 Partial-response signaling

All equalization schemes considered above aim to considerably reduce the ISI, such that the decision variable becomes a noisy observation of the transmitted data symbol; this is referred to as FRS. In the case of PRS [60, 20], the equalizer aims to produce a noisy version of a *specific linear combination* of the actual and some of the previous data symbols, hence allowing a controlled amount of residual ISI; the coefficients of this linear combination constitute the (finite-length causal) TIR. For the sake of a concise explanation, we consider SISO duobinary signaling [61, 62, 63, 64], with the z-transform of the TIR given by

$1 + z^{-1}$. Hence, the decision variable $u(k)$ at instant k is a noisy version of $u_{\mathrm{T}}(k) = a(k) + a(k-1)$. Assuming that $a(k) \in \{-1, 1\}$, we have $u_{\mathrm{T}}(k) \in \{-2, 0, 2\}$. The receiver then makes a decision $\hat{u}_{\mathrm{T}}(k)$ by selecting the element from $\{-2, 0, 2\}$ which is closest to $u(k)$, after which the symbol decisions $\hat{a}(k)$ are obtained from $\hat{u}_{\mathrm{T}}(k)$ using decision-feedback, i.e., $\hat{a}(k)$ is the element from {-1, 1} which is closest to $\hat{u}_{\mathrm{T}}(k) - \hat{a}(k-1)$. The advantage of PRS over FRS is that a better equalizer performance (in terms of MSE) can be obtained for a well-selected TIR. Unfortunately, the feedback structure that computes $\hat{a}(k)$ from $\hat{u}_{\mathrm{T}}(k)$ is prone to error propagation. Alternatively, one can transfer this feedback structure to the transmitter; the resulting structure is known as a PRS precoder. This PRS precoder has some resemblance with THP, but due to the integer coefficients of the feedback taps, the precoded data symbols are independent and uniformly distributed over the original symbol set. Hence, in contrast to the THP precoder, the PRS precoder does not induce any power loss.

Interestingly, a relation between PRS and lattice-reduction-aided (LRA) equalization has been established in [65, 66, 67]. The LRA equalization technique has been proposed in the context of flat fading MIMO channels, which induce only spatial XT. More precisely, LRA equalization expresses the channel matrix $\mathbf{H}$ as the product $\mathbf{H} = \mathbf{H}_{\mathrm{red}}\mathbf{T}$ of a reduced channel matrix $\mathbf{H}_{\mathrm{red}}$ and an unimodular matrix $\mathbf{T}$. Consequently, the matrices $\mathbf{H}$ and $\mathbf{H}_{\mathrm{red}}$ generate the same lattice. The receiver performs linear equalization with respect to the reduced channel, yielding an equalized channel output which is a noisy version of the transformed data $\mathbf{a}_T = \mathbf{T}\mathbf{a}$. Assuming that the components of $\mathbf{a}$ belong to the set $\{0, 1, ..., M-1\}$, the components of $\mathbf{a}_T$ are integers. The receiver makes a decision $\hat{\mathbf{a}}_T$ by rounding the components of the equalized channel output to the nearest integer. Finally, the decision $\hat{\mathbf{a}}$ is obtained by selecting the i-th component of $\hat{\mathbf{a}}$ as the element from $\{0, 1, ..., M-1\}$ that is closest to the i-th component of $\mathbf{T}^{-1}\hat{\mathbf{a}}_T$. The unimodular matrix $\mathbf{T}$ is computed by means of a lattice reduction algorithm, e.g, the Lenstra-Lenstra-Lovasz (LLL) algorithm [68] or the element-based reduction algorithm [69], typically yielding a reduced channel matrix that is better conditioned than the original channel matrix, i.e., closer to being orthogonal. Consequently, compared to equalizing the original channel matrix, better performance is achieved by equalizing this reduced channel matrix, for both the ZF and the MMSE criterion. This procedure has been applied to block transmission over frequency-selective SISO channels [70] and over frequency-selective MIMO channels [71] and to mitigate the XT in MIMO OFDM [72]. In this dissertation, the focus lies on continuous transmission over a frequency-selective MIMO channel with time-invariant filters such that these block transmission techniques cannot be applied. However, the proposed MIMO PRS system could be interpreted as a generalization of the LRA equalization to frequency-selective MIMO channels. s

Although PRS has already been described in the literature for the continuous transmission over the frequency-selective SISO channel and the flat-fading MIMO channel, no general PRS equalization scheme has been studied for the

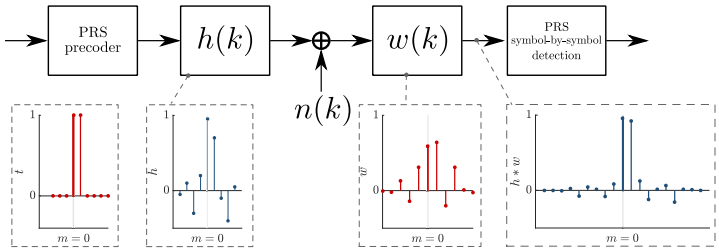

Figure 3.9: The PRS equalization scheme applied to the example discrete-time SISO channel $h(k)$. The 11-tap linear filter $w(k)$ is computed according to the MMSE criterion, whereas the TIR $t(k)$ is set to duo-binary. By allowing some residual interference, the TIR $t(k)$ can be designed to the specific channel, yielding a possibly lower MSE between the target response and the decision variable than for the linear equalization scheme with FRS.

frequency-selective MIMO channel, as previous studies confine the TIR either to temporal-only or spatial-only components. This dissertation therefore proposes a general PRS precoder whose TIR contains both spatial, temporal, and ST components. The definition of these components is similar to the definition of spatial, temporal, and ST interference in Subsection 2.1.1, since the TIR matrix $\mathbf{T} = [\mathbf{T}(0)\,\mathbf{T}(1)\,\cdots\mathbf{T}(L_{\mathrm{T}})]$ represents in fact the desired residual ISI. Hence, the desired XT originated from data symbols transmitted at the same time instant define the spatial components and are characterized by the matrix $\mathbf{T}(0)$. Moreover, all diagonal elements of the matrices $\{\mathbf{T}(m)|\, m > 0\}$ constitute the temporal components of the TIR, whereas all non-diagonal elements of the matrices $\{\mathbf{T}(m)|\, m > 0\}$ specify the desired XT from data symbols transmitted at different time instants. A conceptual block diagram of this general ST PRS precoder is presented Fig. 3.8. The linear equalizers $\mathbf{P}_f^\star$ and $\mathbf{W}_f^\star$ again attempt to eliminate any undesired ISI and can be computed by means of similar techniques as for the equalization schemes above. Remark that the TIR of the general ST PRS precoder simplifies to a temporal-only TIR when $\mathbf{T}(0) = \mathbf{I}$ and $\mathbf{T}(m)$ is diagonal and to a spatial-only TIR when $\mathbf{T}(m) = \mathbf{0}$. Additionally, most contributions in the literature assume that the TIR is given, and no optimization with respect to the TIR is performed at all, resulting in an inferior trial-and-error selection of the TIR. One goal of this dissertation is to propose an algorithm to optimize the TIR for a given frequency-selective MIMO channel.

The mechanism of PRS is illustrated in Fig. 3.9, which applies duo-binary precoding to the SISO example channel $h(k)$. Here, the aim of the 11-tap equalizer $w(k)$ is not to remove most of the ISI, but to ensure that the convolution $h * w$ matches the duo-binary target response $t(k) = \delta_k + \delta_{k-1}$ as closely as possible; in z-transform notation, $H(z)W(z) \approx T(z)$. Interestingly, the corresponding MSE between the target response and this convolution turns out

to be more than 25% smaller than the MSE in the case of FRS for the linear equalization scheme with an 11-tap equalizer $w(k)$ (Fig. 3.3), proving that allowing a controlled amount of interference can indeed improve the equalization performance.

In the remainder of this dissertation, we refer to this equalization scheme as the PRS equalization scheme.

3.2.6 Overview of the investigated equalization schemes

The purpose of this section is to provide an overview of the equalization schemes investigated in this dissertation. In total, three different types of channel knowledge are considered: (i) in the case of perfect CSI, the channel is perfectly known at both the transmitter and the receiver; (ii) in practice, this CSI is often acquired by means of channel estimation, which is never perfect, due to the noise and the (processing) latency; and (iii) in the case of small to moderate channel variability, different channel realizations could bear significant resemblance, which can be exploited to lower the complexity by considering fixed equalization parts, that are not adjusted according to the actual channel realization. For clarity, Table 3.1 displays which equalization schemes are investigated in the different chapters for the different types of channel knowledge. As for the linear equalization scheme, the DFE equalization scheme, and the THP equalization scheme, the case of perfect CSI and the case of imperfect channel estimation have already been well documented in the literature. In this dissertation, however, these equalization schemes are discussed in more detail in the case of channel variability in Chapters 5 and 6. The general MIMO PRS precoder for frequency-selective channels has not been previously discussed in the literature. This dissertation therefore first discusses the generalized PRS equalization scheme when the CSI is perfect in Chapter 7. Subsequently, Chapter 8 and Chapter 9 study the design of the equalization parameters of the generalized PRS scheme in the case of imperfect channel estimation and in the case of channel variability, respectively. In all Chapters, the focus lies entirely on practically realizable filters, i.e., finite-length filters, and all equalization parameters are designed according to the MMSE criterion.

In this dissertation, the focus lies on spatial multiplexing, meaning that N_{dat} is chosen to be as large as possible on the condition that decent (error) performance is still possible. As only symbol-by-symbol detectors are employed in this dissertation, one must therefore be able to spatially distinguish each data substream at the receiver. Hence, to be able to significantly reduce the ISI in each data stream N_{dat} is set equal to $\min(N_{\mathrm{T}}, N_{\mathrm{R}})$. Notably, this is also the factor by which the capacity of a flat-fading MIMO channel increases compared to a system with $N_{\mathrm{T}} = N_{\mathrm{R}} = 1$ [73].

Table 3.1: Overview of the investigated equalization schemes.

Equalization scheme	Perfect CSI	Imperfect channel estimation	Channel variability
Linear	[29]	[74]	Chapter 5
DFE	[41]	[75]	Chapter 5
THP	[34]	[76]	Chapter 6
generalized PRS	Chapter 7	Chapter 8	Chapter 9

4 Equalization strategies

The main goal of equalization is to counteract or even completely remove the ISI and the XT generated by the frequency-selective MIMO channel. This chapter investigates in general how to design all equalization parameters when the communication channel is time-invariant but stochastic. First, Section 4.1 briefly introduces the concept of adjustable and fixed equalization parameters. To design these equalization parameters, an optimization framework is subsequently provided in Section 4.2. More precisely, a general optimization problem is proposed, for which an iterative algorithm is developed to determine both the adjustable and the fixed equalization parameters. Finally, different optimal and suboptimal equalization strategies are discussed in Section 4.3.

4.1 Adjustable and fixed parameters

In general, the optimal setting for all equalization parameters depends on the specific channel realization $\mathbf{g}_{\mathrm{ch}}$ such that all equalization parameters are ideally determined for each channel realization $\mathbf{g}_{\mathrm{ch}}$ individually. In the remainder of this work, we call these parameters *adjustable equalization parameters* as they are adjusted to the channel realization $\mathbf{g}_{\mathrm{ch}}$. One major drawback of these adjustable parameters is their potentially intolerably large associated computational and/or implementational complexity. Alternatively, considering equalization parameters that remain constant for all channel realizations could significantly lower this complexity. Especially when the difference between the various channel realizations is small to moderate, the performance degradation compared to the adjustable equalization parameters is expected

to be limited. As these constant equalization parameters do not adjust to the specific channel realization, we call them *fixed equalization parameters* in the remainder of this work. One of the main objectives of this work is to closely examine the performance-complexity trade-off between the adjustable and the fixed equalization parameters by investigating several equalization strategies, in which either all equalization parameters are adjustable, or all equalization parameters are fixed, or some equalization parameters are adjustable, while others are fixed.

4.2 Parameter optimization

To compute the best-performing equalization setting, an objective function f_0 is optimized with respect to all equalization parameters, possibly subject to a constraint f_1. This objective function is obviously a function of the channel realization $\mathbf{g}_{\text{ch}}$ and all equalization parameters. More specifically, all adjustable parameters depend on the channel realization $\mathbf{g}_{\text{ch}}$ as well and they are collected in the vector $\mathbf{x}(\mathbf{g}_{\text{ch}})$, whereas all fixed parameters are collected in the vector $\mathbf{y}$. The notation $f_0(\mathbf{x}(\mathbf{g}_{\text{ch}}), \mathbf{y}, \mathbf{g}_{\text{ch}})$ then explicitly highlights all dependencies. When only adjustable equalization parameters are present, the optimal $\mathbf{x}^\star(\mathbf{g}_{\text{ch}})$ can of course be determined by directly optimizing the objective function f_0 corresponding to the specific channel realization $\mathbf{g}_{\text{ch}}$, i.e., $f_0(\mathbf{x}(\mathbf{g}_{\text{ch}}), \mathbf{g}_{\text{ch}})$. However, when fixed equalization parameters are present as well, the average (over the channel realizations) $\bar{f}_0$ must be optimized instead. Hence, the optimization problem that must be solved is the following:

$$\begin{aligned}(\mathbf{x}^\star(\mathbf{g}_{\text{ch}}), \mathbf{y}^\star) &= \arg \min_{\mathbf{x}(\mathbf{g}_{\text{ch}}), \mathbf{y}} \bar{f}_0(\mathbf{x}(\mathbf{g}_{\text{ch}}), \mathbf{y}) \\ &= \arg \min_{\mathbf{x}(\mathbf{g}_{\text{ch}}), \mathbf{y}} \int f_{\mathbf{G}_{\text{ch}}}(\mathbf{g}_{\text{ch}}) f_0(\mathbf{x}(\mathbf{g}_{\text{ch}}), \mathbf{y}, \mathbf{g}_{\text{ch}}) \, \mathrm{d}\mathbf{g}_{\text{ch}} \\ &\quad \text{subject to} \quad f_1(\mathbf{x}(\mathbf{g}_{\text{ch}}), \mathbf{y}) \leq 0,\end{aligned} \tag{4.1}$$

where $f_{\mathbf{G}_{\text{ch}}}(\mathbf{g}_{\text{ch}})$ denotes the probability density function (PDF) of the stochastic channel $\mathbf{G}_{\text{ch}}$. In this dissertation, the constraint f_1 is always a transmit energy constraint, which is not an explicit function of the channel, because the transmitted energy is affected only by the equalization parts at the transmitter. Moreover, all equalization parameters that are involved in this energy constraint are generally either all adjustable or all fixed in this work, simplifying the constraint to $f_1(\mathbf{x}(\mathbf{g}_{\text{ch}})) \leq 0$ or $f_1(\mathbf{y}) \leq 0$, respectively. Presenting the general optimization problem in (4.1) as a minimization problem is without loss of generality, as the maximization of a function f_0 is equivalent to the minimization of $-f_0$.

For most choices of f_0 and f_1, two difficulties prevent to easily solve the joint optimization problem from (4.1):

- First, a closed-form analytical solution is often particularly difficult or even impossible to derive. Numerical optimization algorithms could al-

ternatively be employed to search for the global optimum, but minimization problem (4.1) is in general a nonconvex optimization problem. This nonconvexity makes the search for the global optimum considerably more difficult as multiple local optima and saddle points co-exist such that the relatively simple convex optimization methods cannot be employed to solve this optimization problem. To overcome this difficulty in this dissertation, an *alternating* optimization method is proposed, in which the optimal adjustable parameters $\mathbf{x}^\star(\mathbf{g}_{\text{ch}})$ for given fixed parameters $\mathbf{y}$ (subproblem (i)) and the optimal fixed parameters $\mathbf{y}^\star$ for given adjustable parameters $\mathbf{x}(\mathbf{g}_{\text{ch}})$ (subproblem (ii)) are alternately determined. For some partitions of the equalization parameters into adjustable and fixed parameters and a right choice for the objective function f_0, e.g., MSE between a target variable and a decision variable, these subproblems become convex optimization problems for which an analytical solution can easily be derived, whereas for other partitions and/or more complicated objective functions, another (possibly iterative) algorithm must be proposed to solve the subproblems. It should be noted that the optimum solution of these subproblems does not imply that the set of all equalization parameters converges to the globally optimum solution of (4.1).

- A second difficulty is that the PDF $f_{\mathbf{G}_{\text{ch}}}(\mathbf{g}_{\text{ch}})$ is often not available or hard to determine accurately. The following approximation is therefore made:

$$\int f_{\mathbf{G}_{\text{ch}}}(\mathbf{g}_{\text{ch}}) f_0(\mathbf{x}(\mathbf{g}_{\text{ch}}), \mathbf{y}, \mathbf{g}_{\text{ch}}) \, \mathrm{d}\mathbf{g}_{\text{ch}} \approx \frac{1}{N_{\text{ch}}} \sum_{\mathbf{g}_{\text{ch}} \in \mathbb{G}_{\text{ch}}} f_0(\mathbf{x}(\mathbf{g}_{\text{ch}}), \mathbf{y}, \mathbf{g}_{\text{ch}}) \tag{4.2}$$

$$= \mathbb{E}_{\mathbf{G}_{\text{ch}}} \left[f_0(\mathbf{x}(\mathbf{g}_{\text{ch}}), \mathbf{y}, \mathbf{g}_{\text{ch}}) \right], \tag{4.3}$$

  where $\mathbb{G}_{\text{ch}}$ denotes a subset of N_{ch} channel realizations. The set $\mathbb{G}_{\text{ch}}$ is called representative when this set sufficiently captures the statistics of the channel PDF $f_{\mathbf{G}_{\text{ch}}}(\cdot)$. In practice, one method to construct such a set is to measure a considerable number N_{ch} of randomly selected interconnects. When this subset $\mathbb{G}_{\text{ch}}$ is representative, e.g., N_{ch} is sufficiently large, the arithmetic average in (4.2) is nearly identical to the integral on the left-hand side in (4.2). In (4.3), the shorthanded notation $\mathbb{E}_{\mathbf{G}_{\text{ch}}}[\cdot]$ is introduced to denote the arithmetic average over the channel realizations in the subset $\mathbb{G}_{\text{ch}}$.

Next, a more detailed description of the alternating optimization algorithm is provided with the assumption that the transmit energy constraint depends only on the adjustable equalization parameters. In the first step of each iteration, the optimal fixed $\mathbf{y}^\star$ is calculated for a given function $\mathbf{x}(\mathbf{g}_{\text{ch}})$ of the channel realization. As the fixed parameters do not influence the constraint, the optimal $\mathbf{y}^\star$ can directly be obtained by solving

$$\int f_{\mathbf{G}_{\text{ch}}}(\mathbf{g}_{\text{ch}}) \nabla_{\mathbf{y}} f_0(\mathbf{x}(\mathbf{g}_{\text{ch}}), \mathbf{y}, \mathbf{g}_{\text{ch}}) \, \mathrm{d}\mathbf{g}_{\text{ch}} = \mathbf{0}, \tag{4.4}$$

which is approximated by

$$\sum_{\mathbf{g}_{\text{ch}} \in \mathbb{G}_{\text{ch}}} \nabla_{\mathbf{y}} f_0(\mathbf{x}(\mathbf{g}_{\text{ch}}), \mathbf{y}, \mathbf{g}_{\text{ch}}) = \mathbf{0}. \tag{4.5}$$

where $\nabla_{\mathbf{y}}(\cdot)$ represents the column vector containing all first-order derivatives with respect to the different elements of $\mathbf{y}$.

The second step in each iteration is to determine the optimal function $\mathbf{x}^{\star}(\mathbf{g}_{\text{ch}})$ for a given $\mathbf{y}$. To handle the transmit energy constraint, the Lagrangian $\Lambda_{\mathbf{x}}$ is introduced, i.e.,

$$\Lambda_{\mathbf{x}}(\mathbf{x}(\mathbf{g}_{\text{ch}}), \lambda(\mathbf{g}_{\text{ch}}), \mathbf{g}_{\text{ch}}) = f_0(\mathbf{x}(\mathbf{g}_{\text{ch}}), \mathbf{y}, \mathbf{g}_{\text{ch}}) + \lambda(\mathbf{g}_{\text{ch}}) f_1(\mathbf{x}(\mathbf{g}_{\text{ch}})). \tag{4.6}$$

To find a stationary point of this function, both the gradient $\nabla_{\mathbf{x}}\Lambda_{\mathbf{x}}$ and the derivative $\frac{\partial \Lambda_{\mathbf{x}}}{\partial \lambda}$ are computed and equated to zero, i.e.,

$$\begin{cases} \nabla_{\mathbf{x}} f_0(\mathbf{x}(\mathbf{g}_{\text{ch}}), \mathbf{y}, \mathbf{g}_{\text{ch}}) + \lambda(\mathbf{g}_{\text{ch}}) \nabla_{\mathbf{x}} f_1(\mathbf{x}(\mathbf{g}_{\text{ch}})) = \mathbf{0} \\ f_1(\mathbf{x}(\mathbf{g}_{\text{ch}})) = 0 \end{cases}, \tag{4.7}$$

where, similarly to $\nabla_{\mathbf{y}}(\cdot)$, $\nabla_{\mathbf{x}}(\cdot)$ denotes the column vector consisting of all first-order derivatives with respect to the different elements of $\mathbf{x}$. The optimal adjustable parameters $\mathbf{x}^{\star}(\mathbf{g}_{\text{ch}})$ for the given parameter vector $\mathbf{y}$ are then the solution to the system from (4.7).

Algorithm 4.1 Description of the iterative optimization algorithm.

1: Initialize $\mathbf{x}_0(\mathbf{g}_{\text{ch}})$, $i = 1$, $\bar{f}_{0,0} = +\infty$, and $\varepsilon = 1$.
2: **while** $i \leq N_{\max}$ and $\varepsilon > \gamma_{\min}$ **do**
3: Obtain $\mathbf{y}_i$ by solving (4.5) with $\mathbf{x}_{i-1}(\mathbf{g}_{\text{ch}})$ given.
4: $\forall \mathbf{g}_{\text{ch}} \in \mathbb{G}_{\text{ch}}$: Obtain $\mathbf{x}_i(\mathbf{g}_{\text{ch}})$ by solving (4.7) with $\mathbf{y}_i$ given.
5: Calculate $\bar{f}_{0,i} = \frac{1}{N_{\text{ch}}} \sum_{\mathbf{g}_{\text{ch}} \in \mathbb{G}_{\text{ch}}.} f_0(\mathbf{x}_i(\mathbf{g}_{\text{ch}}), \mathbf{y}_i, \mathbf{g}_{\text{ch}})$.
6: $\varepsilon = \frac{\bar{f}_{0,i-1} - \bar{f}_{0,i}}{\bar{f}_{0,i-1}}$.
7: $i \leftarrow i + 1$.

Algorithm 4.1 presents a detailed description of the alternating optimization algorithm, about which the following comments can be formulated:

- Since the summation in the computation of the optimal fixed equalization parameters in (4.5) is restricted to the N_{ch} channel realizations from the set $\mathbb{G}_{\text{ch}}$, only the N_{ch} associated vectors $\mathbf{x}_{i-1}(\mathbf{g}_{\text{ch}})$ must be computed in the previous iteration. As a result, the optimal adjustable equalization parameters must be computed just N_{ch} times per iteration. Moreover, the iterative computation of the optimal fixed parameters could be performed offline, using a predetermined, representative subset $\mathbb{G}_{\text{ch}}$ of channels. During manufacturing or just before operation, the adjustable

equalization parameters for one specific channel realization $\mathbf{g}_{\text{ch}}$ are then obtained by solving the system from (4.7) just once. This optimization method scales very well in large bulk applications as the iterative algorithm is always performed using a set of N_{ch} channel realizations, irrespective of the total number of channel realizations.

- A combination of two common stopping criteria is employed to terminate the algorithm. First, the iterative algorithm stops when a predefined number of iterations, $N_{\max}$, is reached. Second, the iterative algorithm ends when the relative decrease in $\bar{f}_0$ is smaller than a particular $\gamma_{\min}$. The advantage of this approach is that both the complexity in terms of iterations and the accuracy can be easily controlled.

- The transmit energy constraint in Algorithm 4.1 is assumed to be dependent only on the adjustable parameters. When this constraint is influenced only by the fixed parameters, however, a similar algorithm can be proposed. More precisely, the optimal adjustable equalizers are obtained by equating $\nabla_{\mathbf{x}} f_0(\mathbf{x}(\mathbf{g}_{\text{ch}}), \mathbf{y}, \mathbf{g}_{\text{ch}})$ to zero, whereas the stationary points of the following Lagrangian must be determined to find the optimal $\mathbf{y}$ for given $\mathbf{x}(\mathbf{g}_{\text{ch}})$:

$$\Lambda_{\mathbf{y}}(\mathbf{y}, \lambda) = \bar{f}_0(\mathbf{y}) + \lambda f_1(\mathbf{y}). \tag{4.8}$$

4.3 Proposed equalization strategies

In the remainder of this thesis, several equalization schemes are presented to equalize the frequency-selective MIMO channel. For each of the investigated equalization schemes, the following strategies are proposed. In terms of performance, the optimal strategy is to adjust all equalization parameters to the specific channel realization, and we therefore call this strategy the *adjustable strategy*. The main disadvantage of this strategy is that accurate CSI must be available in the computation of the equalization parameters, inducing a possibly large complexity. Contrary, the strategy inducing the least complexity is the *fixed strategy*, in which all equalization parameters depend only on the channel statistics and not on the channel realization itself, avoiding the need for accurate CSI. When both adjustable and fixed equalization parameters are present, the strategy is called the *hybrid strategy*, which aims to combine low complexity with good performance. The iterations between the adjustable and the fixed parameters of course vanish for the adjustable and the fixed strategy, as all parameters are either adjustable or fixed. The resulting non-iterative algorithm is not necessarily less complicated, however, as a proper division between adjustable and fixed parameters in the hybrid strategy often yields relatively easy-to-solve subproblems compared to the joint optimization of all parameters in the case of either the adjustable or the fixed strategy.

The division in the hybrid strategy between the adjustable and the fixed equalization parameters is crucial for its performance and its complexity. This

dissertation mostly considers the equalization parameters corresponding to the transmitter as fixed and the equalization parameters related to the receiver as adjustable. This way, no accurate CSIT is required, making a return channel or expensive measurements unnecessary and thus significantly lowering the complexity. When making the division between the adjustable and the fixed equalization parameters, one must additionally ensure that the constraints in (4.1) depend solely on either the adjustable or the fixed equalization parameters as the alternating approach is otherwise not applicable when the constraints depend on both types of parameters. In the latter case, satisfying the constraint in the design of the fixed parameters for a given set of adjustable equalizers is in particular not straightforward.

In the adjustable, the hybrid, and the fixed strategy above, all equalization parameters are computed according to Algorithm 4.1 with the purpose of optimally solving the optimization problem from (4.1). These strategies are therefore called the *optimal* adjustable, the *optimal* hybrid, and the *optimal* fixed strategy. Alternatively, some *suboptimal* approaches can be formulated as well, where the objective function is simplified compared to (4.1). For example, the minimization process described above designs the fixed equalization parameters by minimizing the statistical average of an objective function, i.e., $\bar{f}_0$. Alternatively, one could neglect all channel variations and design the fixed equalization parameters by minimizing the objective function f_0 evaluated for the average channel $\bar{\mathbf{g}}_{\mathrm{ch}}$, defined by

$$\bar{\mathbf{g}}_{\mathrm{ch}} = \int \mathbf{g}_{\mathrm{ch}} f_{\mathbf{G}_{\mathrm{ch}}}(\mathbf{g}_{\mathrm{ch}}) \, \mathrm{d}\mathbf{g}_{\mathrm{ch}}. \tag{4.9}$$

This approach, referred to as *Suboptimal 1*, can first be interpreted as applying the optimization algorithm of the optimal adjustable strategy to the average channel, after which all fixed equalization parameters are set equal to the obtained parameters. A second interpretation of this suboptimal approach is that the set $\mathbb{G}_{\mathrm{ch}}$ contains only the average channel in the computation of the fixed equalization parameters in Algorithm 4.1, i.e., $\mathbb{G}_{\mathrm{ch}} = \{\bar{\mathbf{g}}_{\mathrm{ch}}\}$. This suboptimal approach can be applied to both the hybrid and the fixed strategy, yielding the strategies suboptimal hybrid 1 and suboptimal fixed 1, respectively. A second suboptimal approach, referred to as *Suboptimal 2*, first designs the fixed equalization parameters under the assumption that the adjustable equalization parameters are not present in the equalization scheme. Subsequently, the adjustable parameters are added to the equalization scheme and are designed to combat the residual ISI for each channel realization. The key feature of this suboptimal approach is that no iterations between the fixed and the adjustable parameters are required.

In summary, Table 4.1 gives an overview of the different considered strategies.

Table 4.1: Equalization strategies.

Strategy		Description
Optimal	Adjustable	all parameters are adjustable
	Fixed	all parameters are fixed
	Hybrid	both adjustable and fixed parameters
Suboptimal 1	Hybrid	channel variation is neglected in the computation of $\mathbf{y}^\star$
	Fixed	
Suboptimal 2	Hybrid	adjustable parameters are omitted in the computation of $\mathbf{y}^\star$

5

Stochastic channel: decision feedback equalization

This chapter investigates the equalization of a frequency-selective MIMO channel subject to channel variability in the context of continuous data transmission, i.e., the equalization scheme considered in this chapter consists of a pre-equalizer at the transmitter and a DFE at the receiver. More precisely, the pre-equalizer at the transmitter is a linear FIR MIMO filter that is fractionally spaced, meaning that this filter operates at a multiple of the symbol rate. The DFE at the receiver comprises (i) a linear, fractionally-spaced FIR filter called the feedforward filter and (ii) a linear symbol-spaced FIR filter called the feedback filter that operates on the previously detected symbols. Due to the filtering of the detected symbols, the equalization structure becomes nonlinear, complicating not only the implementation, but also the optimization of the equalization parameters and the accurate evaluation of the performance measures. With the omission of the feedback filter, the equalization scheme is completely linear and less complex, but its performance is generally inferior to the equalization scheme with the feedback filter. In Section 5.1, the system models of both equalization schemes are described in more detail.

With a proper set of equalization coefficients and sufficiently long filters, the equalization scheme presented here should be capable of counteracting most of the ISI and XT generated by the stochastic frequency-selective MIMO channel, while limiting the effects of the noise. For this purpose, the optimization procedure presented in Chapter 4 is applied to this equalization scheme. The MSE between the decision variable and the transmitted data symbols is an excellent choice for the objective function $f_0(\cdot)$, because it combines mathematical

simplicity with excellent performance. More specifically, Section 5.2 applies the different equalization strategies from Chapter 4, i.e., the adjustable, the hybrid, and the fixed strategy, to obtain the set of equalization coefficients for this stochastic channel. For optimal performance, all equalization parameters are adjustable to each individual channel realization (adjustable strategy) and these adjustable parameters are obtained by minimizing the MSE conditioned on the specific channel realization $\mathbf{g}_{\text{ch}}$. On the other hand, a significant reduction in complexity can be achieved by considering fixed equalizers that are independent to the specific channel realization (fixed strategy), as these fixed equalization parameters are determined by minimizing the MSE averaged over all channel realizations. Finally, the hybrid strategy has both adjustable and fixed equalization parameters. In all computations, the assumption of perfect decision feedback is made for mathematical simplicity. More precisely, this assumption neglects any error propagation in the feedback structure by assuming that all previous symbols are perfectly detected.

The description of the system model (Section 5.1) and the derivation of the MMSE equalizer coefficients (Section 5.2) assume bandpass transmission: the bandpass signals and bandpass filters are represented in complex-valued baseband notation. As explained in Section 5.3, the results for bandpass transmission are easily converted to apply to baseband transmission.

One of the key performance measures in any practical communication link is the probability of some type of transmission error. Therefore, Section 5.4 derives the BER and the symbol error rate (SER) expression for the uncoded pulse amplitude modulation (PAM) baseband transmission over the equalized MIMO chip-to-chip interconnect presented in Chapter 2. Additionally, several techniques are described to accurately numerically evaluate the obtained expressions.

To quantify and investigate the performance of the different proposed equalization strategies, numerical results are provided in Section 5.5. Both the (average) MSE and the (average) BER performance of the M-PAM transmission over the chip-to-chip interconnect described in Chapter 2 are examined in more detail.

The standard approach to solve the joint optimization of the MSE with respect to all equalization parameters is to alternately compute an optimal value of a subset of the parameters with the other parameters given. Section 5.6, however, discusses two alternative optimization methods, i.e., the saddle-free (SF) Newton method and the improved bidirectional random optimization (IBRO) method. Additionally, their advantages and disadvantages compared to the alternating optimization method are investigated by means of numerical results.

Finally, concluding remarks are given in Section 5.7.

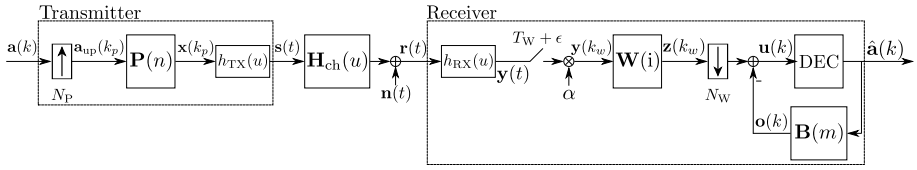

Figure 5.1: System model of the equalization scheme consisting of a linear pre-equalizer at the transmitter and a nonlinear DFE at the receiver.

5.1 System model

Fig. 5.1 displays the system model of a $L \times L$ MIMO frequency-selective communication link that is equalized by means of a fractionally-spaced linear FIR pre-equalizer $\mathbf{P}$ at the transmitter and a nonlinear DFE at the receiver. More specifically, the DFE at the receiver comprises two linear FIR filters: a fractionally-spaced feedforward filter $\mathbf{W}$ and a symbol-spaced feedback filter $\mathbf{B}$ operating on the previously detected symbols $\hat{\mathbf{a}}(k-m)$.

To transfer information over this communication link, a continuous stream of complex-valued data symbol vectors $\{\mathbf{a}(k)\}$ is applied to the transmitter. This data stream contains L spatially parallel substreams, each operating at a symbol rate $1/T$. More specifically, the lth stream is denoted by $\{\mathrm{a}_l(k)\}$, $l = 1, ..., L$, where $\mathrm{a}_l(k)$ denotes the lth component of the vector $\mathbf{a}(k)$. The data symbols are spatially and temporally independent, meaning that $\mathbb{E}[\mathrm{a}_{l_1}(k)\mathrm{a}_{l_2}(m)] = \sigma_{\mathrm{a}}^2 \delta_{l_1-l_2}\delta_{k-m}$, where σ_{a}^2 equals the average energy of the elements of the symbol set $\mathcal{C}$. Because the fractionally-spaced pre-equalizer $\mathbf{P}$ operates at a multiple N_{P} of the symbol rate $1/T$, the data input vector $\mathbf{a}(k)$ is first upsampled by a factor N_{P} by inserting $N_{\mathrm{P}} - 1$ zeros between all data symbol vectors, yielding the sequence $\{\mathbf{a}_{\mathrm{up}}(k_p)\}$. Next, this upsampled sequence is applied to the linear pre-equalizer with impulse response $\mathbf{P}(n)$ and tap spacing $T_{\mathrm{P}} = T/N_{\mathrm{P}}$, yielding the pre-equalizer's output $\mathbf{x}(k_p)$ given by

$$\mathbf{x}(k_p) = \sum_{n=-L_{\mathrm{P}}^{(1)}}^{L_{\mathrm{P}}^{(2)}} \mathbf{P}(n)\mathbf{a}_{\mathrm{up}}(k_p - n). \tag{5.1}$$

Since the pre-equalizer is finite in length, only L_{P} matrices $\mathbf{P}(n)$ are nonzero, i.e., $\mathbf{P}(n) = \mathbf{0}\ \forall n \notin \{-L_{\mathrm{P}}^{(1)}, \cdots, L_{\mathrm{P}}^{(2)}\}$ with $L_{\mathrm{P}} = L_{\mathrm{P}}^{(1)} + L_{\mathrm{P}}^{(2)} + 1$. Next, each of the L pre-equalizer's output streams is applied to a real-valued continuous-time SISO transmit filter with impulse response $h_{\mathrm{TX}}(u)$, yielding the transmitted signal

$$\mathbf{s}(t) = \sum_{\substack{n=-L_{\mathrm{P}}^{(1)} \\ k_p}}^{L_{\mathrm{P}}^{(2)}} h_{\mathrm{TX}}(t - (n + k_p)T_{\mathrm{P}})\mathbf{P}(n)\mathbf{a}_{\mathrm{up}}(k_p), \tag{5.2}$$

where all symbols from the stream $\{\mathbf{a}_{\mathrm{up}}(k_p)\}$ are included in the summation over k_p, i.e., k_p ranges from $-\infty$ to $+\infty$. To limit the average transmitted energy per data symbol, a constraint on the pre-equalizer taps ensures that this average energy does not exceed a predefined value E_{TX}:

$$\mathbb{E}\left[\int_0^T \|\mathbf{s}(t)\|^2 \,\mathrm{d}t\right] = \sigma_{\mathrm{a}}^2 \mathrm{Tr}\left[\sum_{n_1,n_2=-L_{\mathrm{P}}^{(1)}}^{L_{\mathrm{P}}^{(2)}} \mathbf{P}^H(n_1)(\tilde{\mathbf{R}}_{\mathrm{TX}})_{n_1,n_2}\mathbf{P}(n_2)\right] \tag{5.3}$$

$$= \sigma_{\mathrm{a}}^2 \mathrm{Tr}\left[\mathbf{P}^H \mathbf{R}_{\mathrm{TX}} \mathbf{P}\right] \tag{5.4}$$

$$\leq L E_{\mathrm{TX}}, \tag{5.5}$$

where the $(LL_{\mathrm{P}}) \times L$ stacked block matrix $\mathbf{P}$ comprises all pre-equalizer coefficients and is constructed by stacking all nonzero $\mathbf{P}(n)$ matrices into one matrix, i.e.,

$$\mathbf{P} = \left[\mathbf{P}^H(-L_{\mathrm{P}}^{(1)}) \cdots \mathbf{P}^H(L_{\mathrm{P}}^{(2)})\right]^H \tag{5.6}$$

and $\mathbf{R}_{\mathrm{TX}} = \tilde{\mathbf{R}}_{\mathrm{TX}} \otimes \mathbf{I}_L$. Moreover, all elements of the $L_{\mathrm{P}} \times L_{\mathrm{P}}$ Toeplitz matrix $\tilde{\mathbf{R}}_{\mathrm{TX}}$ are defined by

$$(\tilde{\mathbf{R}}_{\mathrm{TX}})_{n_1,n_2} = \int_{-\infty}^{+\infty} h_{\mathrm{TX}}(t) h_{\mathrm{TX}}(t - (n_1 - n_2)T_{\mathrm{P}}) \,\mathrm{d}t \tag{5.7}$$

$$= \int_{-\infty}^{+\infty} |H_{\mathrm{TX}}(f)|^2 \exp\left(j2\pi f(n_1 - n_2)T_{\mathrm{P}}\right) \mathrm{d}f. \tag{5.8}$$

Subsequently, all components of $\mathbf{s}(t)$ propagate over a frequency-selective MIMO channel suffering from channel variability as described in Chapter 2. Here, the main aspects of this channel are briefly recapitulated. Due to the frequency-selective nature and the mutual coupling of the channels, the transmitted signals are spread out in both time and space, producing ST ISI characterized by the channel impulse response matrix $\mathbf{H}_{\mathrm{ch}}(u)$, which is assumed to be time-limited. When the channel is stochastic, e.g., due to manufacturing tolerances, this impulse response $\mathbf{H}_{\mathrm{ch}}(u)$ should be considered as the outcome of a random process, resulting in channel realizations that all (slightly) differ from each other. Furthermore, the transmission over the channel is affected by an additive Gaussian circular symmetric stationary noise signal $\mathbf{n}(t)$ with zero mean and $\mathbb{E}[\mathbf{n}(t)\mathbf{n}^H(t+u)] = N_0\delta(u)\mathbf{I}_L$. The received signal can thus be expressed as

$$\mathbf{r}(t) = \int_{-\infty}^{+\infty} \mathbf{H}_{\mathrm{ch}}(u)\mathbf{s}(t-u) \,\mathrm{d}u + \mathbf{n}(t). \tag{5.9}$$

At the receiver, all L received signal streams are first individually filtered by an analog SISO receive filter specified by its impulse response $h_{\mathrm{RX}}(u)$, typically

matched to the transmit filter. These filtered signals are subsequently sampled at instants $k_w T_{\mathrm{W}} + \epsilon$, where $T_{\mathrm{W}} = T/N_{\mathrm{W}}$ denotes the tap spacing of the fractionally-spaced feedforward filter $\mathbf{W}$ with oversampling factor N_{W}. The sampling delay ϵ compensates for any delay introduced by $\mathbf{H}(u)$, which denotes the cascade of the transmit filter, the channel filter, and the receive filter. For simplicity, this sampling delay is identical for all symbol streams. Next, the sampled signal is multiplied with a scaling factor α to counteract the energy constraint imposed on the transmitter, yielding a signal $\mathbf{y}(k_w)$ that can be decomposed as

$$\mathbf{y}(k_w) = \alpha \sum_{\substack{n=-L_{\mathrm{P}}^{(1)} \\ m}}^{L_{\mathrm{P}}^{(2)}} \mathbf{H}(k_w T_{\mathrm{W}} + \epsilon - nT_{\mathrm{P}} - mT)\mathbf{P}(n)\mathbf{a}(m) + \alpha \mathbf{n}_{\mathrm{RX}}(k_w T_{\mathrm{W}} + \epsilon), \tag{5.10}$$

where

$$\mathbf{n}_{\mathrm{RX}}(t) = \int_{-\infty}^{+\infty} h_{\mathrm{RX}}(u)\mathbf{n}(t-u)\,\mathrm{d}u. \tag{5.11}$$

Subsequently, the receiver reduces the ISI and XT by means of a DFE comprising two linear FIR filters: a fractionally-spaced feedforward filter with impulse response matrices $\mathbf{W}(i)$ and tap spacing T_{W} operating on $\mathbf{y}(k_w)$ and a symbol-spaced feedback filter with impulse response matrices $\mathbf{B}(m)$ operating on the previously detected symbols $\hat{\mathbf{a}}(k-m)$. More specifically, the output $\mathbf{z}(k_w)$ of the feedforward filter is given by

$$\begin{aligned}\mathbf{z}(k_w) = \alpha \sum_{i=-L_{\mathrm{W}}^{(1)}}^{L_{\mathrm{W}}^{(2)}} \sum_{\substack{n=-L_{\mathrm{P}}^{(1)} \\ m}}^{L_{\mathrm{P}}^{(2)}} \mathbf{W}(i)\mathbf{H}((k_w - i)T_{\mathrm{W}} + \epsilon - nT_{\mathrm{P}} - mT)\mathbf{P}(n)\mathbf{a}(m) \\ + \alpha \sum_{i=-L_{\mathrm{W}}^{(1)}}^{L_{\mathrm{W}}^{(2)}} \mathbf{W}(i)\mathbf{n}_{\mathrm{RX}}((k_w - i)T_{\mathrm{W}} + \epsilon),\end{aligned} \tag{5.12}$$

where the feedforward filter is time-limited as only $L_{\mathrm{W}}^{(1)}$ anti-causal and $L_{\mathrm{W}}^{(2)}$ causal response matrices are assumed to be nonzero, i.e., $\mathbf{W}(i) = \mathbf{0}\ \forall i \notin \{-L_{\mathrm{W}}^{(1)}, \cdots, L_{\mathrm{W}}^{(2)}\}$. As for the feedback filter, its output is defined as the signal $\mathbf{o}(k)$, i.e.,

$$\mathbf{o}(k) = \sum_{m \in \Phi_{\mathbf{B}}} \mathbf{B}(m)\hat{\mathbf{a}}(k-m). \tag{5.13}$$

In (5.13), the set $\Phi_{\mathbf{B}}$ with L_{B} elements contains all active causal delays of the feedback filter $\mathbf{B}$, i.e., $\mathbf{B}(m) \neq \mathbf{0}\ \forall m \in \Phi_{\mathbf{B}} \subseteq \mathbb{Z}^+$, with $\mathbb{Z}^+$ denoting the strictly positive integers. Moreover, these active delays do not necessarily coincide with the time-delay indices $\{1, \cdots, L_{\mathrm{B}}\}$, but the only restriction, imposed by causality, is $\Phi_{\mathbf{B}}(i) \geq 1$ for $i = 1, \ldots, L_{\mathrm{B}}$. The decision variable $\mathbf{u}(k)$ is consecutively

constructed by subtracting the output of the feedback filter $\mathbf{o}(k)$ from $\mathbf{z}(k_w)$ that is downsampled by a factor N_{W}:

$$\mathbf{u}(k) = \mathbf{z}(kN_{\mathrm{W}}) - \mathbf{o}(k). \tag{5.14}$$

By plugging (5.13) and (5.12) into (5.14) and after some basic manipulations, $\mathbf{u}(k)$ can be written as

$$\mathbf{u}(k) = \alpha \sum_{m=-L_{\mathrm{G}}^{(1)}}^{L_{\mathrm{G}}^{(2)}} \mathbf{W}\mathbf{G}(m)\mathbf{P}\mathbf{a}(k-m) + \alpha\mathbf{W}\bar{\mathbf{n}}(k) - \sum_{m\in\Phi_{\mathbf{B}}} \mathbf{B}(m)\hat{\mathbf{a}}(k-m). \tag{5.15}$$

In (5.15), the $L \times (LL_{\mathrm{W}})$ augmented block matrix $\mathbf{W}$ and $(LL_{\mathrm{W}}) \times 1$ stacked vector $\bar{\mathbf{n}}(k)$ are obtained by combining all $\mathbf{W}(i)$ and all $\mathbf{n}_{\mathrm{RX}}((k_w - i)T_{\mathrm{W}} + \epsilon)$ into one matrix and vector, respectively, i.e.,

$$\mathbf{W} = \left[\mathbf{W}(-L_{\mathrm{W}}^{(1)}) \cdots \mathbf{W}(L_{\mathrm{W}}^{(2)})\right] \tag{5.16}$$

and

$$\bar{\mathbf{n}}(k) = \left[\mathbf{n}_{\mathrm{RX}}^{H}(kT + L_{\mathrm{W}}^{(1)}T_{\mathrm{W}} + \epsilon) \cdots \mathbf{n}_{\mathrm{RX}}^{H}(kT - L_{\mathrm{W}}^{(2)}T_{\mathrm{W}} + \epsilon)\right]^{H}. \tag{5.17}$$

Moreover, the block matrix $\mathbf{G}(m)$ in (5.15) is constructed as

$$\mathbf{G}(m) = \begin{bmatrix} \check{\mathbf{H}}_m(-L_{\mathrm{W}}^{(1)}, -L_{\mathrm{P}}^{(1)}) & \cdots & \check{\mathbf{H}}_m(-L_{\mathrm{W}}^{(1)}, L_{\mathrm{P}}^{(2)}) \\ \vdots & \ddots & \vdots \\ \check{\mathbf{H}}_m(L_{\mathrm{W}}^{(2)}, -L_{\mathrm{P}}^{(1)}) & \cdots & \check{\mathbf{H}}_m(L_{\mathrm{W}}^{(2)}, L_{\mathrm{P}}^{(2)}) \end{bmatrix} \tag{5.18}$$

with $\check{\mathbf{H}}_m(i,n) = \mathbf{H}(mT - iT_{\mathrm{W}} - nT_{\mathrm{P}} + \epsilon)$. With the assumption that the channel response is time-limited, i.e., $\mathbf{H}(u) = \mathbf{0}\ \forall u \notin [-L_{\mathrm{H}}^{(1)}T + \epsilon, L_{\mathrm{H}}^{(2)}T + \epsilon]$, the sequence $\{\mathbf{G}(m)\}$ must be finite in time as well. More precisely, the block matrix $\mathbf{G}(m)$ equals the zero matrix when m is not an element of the set $\Phi = \{-L_{\mathrm{G}}^{(1)}, \cdots, L_{\mathrm{G}}^{(2)}\}$, where

$$\begin{cases} L_{\mathrm{G}}^{(1)} &= \left\lfloor L_{\mathrm{H}}^{(1)} + \frac{L_{\mathrm{P}}^{(1)}}{N_{\mathrm{P}}} + \frac{L_{\mathrm{W}}^{(1)}}{N_{\mathrm{W}}} \right\rfloor \\ L_{\mathrm{G}}^{(2)} &= \left\lfloor L_{\mathrm{H}}^{(2)} + \frac{L_{\mathrm{P}}^{(2)}}{N_{\mathrm{P}}} + \frac{L_{\mathrm{W}}^{(2)}}{N_{\mathrm{W}}} \right\rfloor \end{cases}. \tag{5.19}$$

Moreover, the total number of elements in the set Φ is denoted by L_{G}, i.e., $L_{\mathrm{G}} = L_{\mathrm{G}}^{(1)} + L_{\mathrm{G}}^{(2)} + 1$. To recover the original data $\mathbf{a}(k)$, the symbol-by-symbol detector finally computes the decision $\hat{\mathbf{a}}(k)$, which is constructed by determining the closest constellation point to each of the elements of $\mathbf{u}(k)$, i.e.,

$$\hat{\mathrm{a}}_l(k) = \arg\min_{\mathfrak{a}\in\mathcal{C}} ||\mathrm{u}_l(k) - \mathfrak{a}||^2.\ \ \forall l \in \{1, \cdots, L\} \tag{5.20}$$

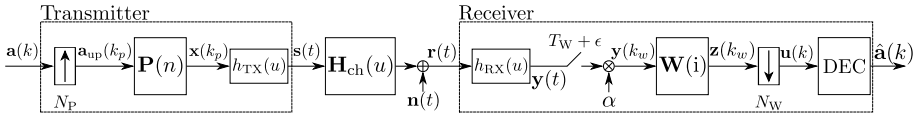

Figure 5.2: System model of the equalization scheme consisting of a linear equalizer at the transmitter and a linear equalizer at the receiver.

5.1.1 Linear equalization scheme

When the feedback filter is absent, an equalization scheme emerges that possesses a linear fractionally-spaced FIR equalizer at both the transmitter and the receiver. This equalization scheme is appropriately called the linear equalization scheme and its system model in Fig. 5.2 is comparable to the general system model from Fig. 5.1. Obviously, the expression for the decision variable $\mathbf{u}(k)$ in the linear equalization scheme is identical to (5.15) with all feedback taps set to zero, i.e., $\mathbf{B}(m) = \mathbf{0}\ \forall m$, yielding

$$\mathbf{u}(k) = \alpha \sum_{m \in \Phi} \mathbf{W}\mathbf{G}(m)\mathbf{P}\mathbf{a}(k-m) + \alpha \mathbf{W}\bar{\mathbf{n}}(k). \tag{5.21}$$

The main motivation to even consider this equalization scheme is its smaller complexity than the original equalization scheme as the decision feedback filter does not have to be computed nor have to be implemented.

5.2 MMSE equalization

To compute a suitable set of equalization parameters, this section applies the optimization procedure from Chapter 4 to the equalization scheme presented in the section above. As the channel suffers from channel variability, different equalization strategies are discussed to counteract the ISI and the XT.

In most practical communication systems, some type of error probability, e.g., BER, is the most important performance measure. Hence, this error probability is a good candidate for the objective function f_0, except that the minimization of such error probabilities is often mathematically challenging, making more tractable alternatives more suitable. The most commonly adopted objective function f_0 in the optimization of the equalizer coefficients is the MSE, which is defined here as the average squared difference between the decision variable $\mathbf{u}(k)$ and the input data symbols $\mathbf{a}(k)$. The main advantage of the MSE as the objective function is its combination of mathematical simplicity and a more than decent (error) performance.

For mathematical simplicity, all previously detected symbols are assumed to be perfect in the computation of the MSE such that the error propagation at the receiver is in fact neglected in the design of the equalization parameters.

Based on (5.15), the error $\mathbf{e}(k)$ between $\mathbf{u}(k)$ and $\mathbf{a}(k)$ can then be written as

$$\begin{aligned}\mathbf{e}(k) &= \mathbf{u}(k) - \mathbf{a}(k) \qquad (5.22)\\ &= \alpha \sum_{m\in\Phi} \left(\mathbf{W}\mathbf{G}(m)\mathbf{P} - \delta(m)\mathbf{I}_L\right)\mathbf{a}(k-m)\\ &\quad + \alpha\mathbf{W}\bar{\mathbf{n}}(k) - \sum_{m\in\Phi_{\mathbf{B}}} \mathbf{B}(m)\mathbf{a}(k-m). \qquad (5.23)\end{aligned}$$

The normalized MSE conditioned on the MIMO channel $\mathbf{g}_{\text{ch}}$, denoted by $\text{MSE}_{\mathbf{g}_{\text{ch}}}$ is defined as

$$\text{MSE}_{\mathbf{g}_{\text{ch}}} \triangleq \frac{\mathbb{E}\left[\|\mathbf{e}(k)\|^2\right]}{\mathbb{E}\left[\|\mathbf{a}(k)\|^2\right]} = \frac{\mathbb{E}\left[\|\mathbf{e}(k)\|^2\right]}{L\sigma_{\text{a}}^2}, \qquad (5.24)$$

where the expectation $\mathbb{E}[\cdot]$ is taken over both the data symbols and the noise. Since the data symbols and the noise are assumed to be uncorrelated, plugging (5.23) into (5.24) yields

$$\begin{aligned}\text{MSE}_{\mathbf{g}_{\text{ch}}} = \frac{1}{L}\Bigg(&\sum_{m\in\Phi_{\mathbf{N}}} \|\alpha\mathbf{W}\mathbf{G}(m)\mathbf{P} - \delta(m)\mathbf{I}_L\|^2 + \frac{|\alpha|^2}{\sigma_{\text{a}}^2}\text{Tr}\left(\mathbf{W}\mathbf{R}_{\bar{\mathbf{n}}}\mathbf{W}^H\right)\\ &+ \sum_{m\in\Phi_{\mathbf{B}}} \|\alpha\mathbf{W}\mathbf{G}(m)\mathbf{P} - \mathbf{B}(m)\|^2\Bigg), \qquad (5.25)\end{aligned}$$

where $\Phi_{\mathbf{N}}$ denotes the set of $L_{\text{N}} = L_{\text{G}} - L_{\text{B}}$ time instants, on which the feedback filter $\mathbf{B}$ is not active, i.e., $\Phi_{\mathbf{N}} = \Phi \setminus \Phi_{\mathbf{B}}$, and $\mathbf{R}_{\bar{\mathbf{n}}}$ is the $(LL_{\text{W}}) \times (LL_{\text{W}})$ autocorrelation matrix of the noise vector $\bar{\mathbf{n}}(k)$, i.e.,

$$\mathbf{R}_{\bar{\mathbf{n}}} \triangleq \mathbb{E}\left[\bar{\mathbf{n}}(k)\bar{\mathbf{n}}^H(k)\right]. \qquad (5.26)$$

This autocorrelation matrix is given by

$$\mathbf{R}_{\bar{\mathbf{n}}} = N_0\tilde{\mathbf{R}}_{\text{RX}} \otimes \mathbf{I}_L, \qquad (5.27)$$

where $\tilde{\mathbf{R}}_{\text{RX}}$ is obtained by replacing $H_{\text{TX}}(f)$ by $H_{\text{RX}}(f)$ in (5.8).

Since the frequency-selective MIMO channel is considered to be stochastic in this chapter, all equalization parameters are computed according to the optimization method from Chapter 4, which minimizes the objective function f_0 averaged over all channel realizations. In this section, f_0 is set equal to $\text{MSE}_{\mathbf{g}_{\text{ch}}}$ such that the optimal parameters $(\mathbf{P}^\star, \alpha^\star, \mathbf{W}^\star, \mathbf{B}^\star)$ are obtained by solving the following optimization problem

$$\begin{aligned}(\mathbf{P}^\star, \alpha^\star, \mathbf{W}^\star, \mathbf{B}^\star) = \arg\min_{\mathbf{P},\alpha,\mathbf{W},\mathbf{B}} \overline{\text{MSE}}(\mathbf{P}, \alpha, \mathbf{W}, \mathbf{B})\\ \text{subject to } \sigma_{\text{a}}^2\text{Tr}\left(\mathbf{P}^H\mathbf{R}_{\text{TX}}\mathbf{P}\right) \leq LE_{\text{TX}}\end{aligned}, \qquad (5.28)$$

where $\overline{\text{MSE}} = \mathbb{E}_{\mathbf{G}_{\text{ch}}}\left[\text{MSE}_{\mathbf{g}_{\text{ch}}}\right]$.

Due to two features of the $\text{MSE}_{\mathbf{g}_{\text{ch}}}$ expression in (5.25), this optimization problem can be somewhat simplified. First, inspection of (5.25) reveals that $\text{MSE}_{\mathbf{g}_{\text{ch}}}$ depends on the phase of the product of $\alpha\mathbf{W}$ and not on the individual phases of α and $\mathbf{W}$, allowing to restrict α to the set of positive real-valued numbers. Indeed, when the set $(\mathbf{P}^\star, |\alpha^\star| \exp(-j\theta_{\alpha^\star}), \mathbf{W}^\star, \mathbf{B}^\star)$ is optimal, the set $(\mathbf{P}^\star, |\alpha^\star|, \exp(-j\theta_{\alpha^\star})\mathbf{W}^\star, \mathbf{B}^\star)$ must be optimal as well because both sets yield identical $\text{MSE}_{\mathbf{g}_{\text{ch}}}$. Second, the average transmitted energy per data symbol induced by the optimal pre-equalizer $\mathbf{P}^\star$ must be equal to the maximum LE_{TX}, which can easily be verified by contradiction. Indeed, when the set $(\mathbf{P}^\star, \alpha^\star, \mathbf{W}^\star, \mathbf{B}^\star)$ is assumed to be optimal with $\sigma_{\text{a}}^2 \text{Tr}\left(\mathbf{P}^{\star,H}\mathbf{R}_{\text{TX}}\mathbf{P}^\star\right) = \beta^2 LE_{\text{TX}}$ with $0 < \beta < 1$, the set $\left(\frac{\mathbf{P}^\star}{\beta}, \beta\alpha^\star, \mathbf{W}^\star, \mathbf{B}^\star\right)$ produces a smaller $\text{MSE}_{\mathbf{g}_{\text{ch}}}$. Consequently, the inequality in the constraint can be replaced by an equality without loss of optimality.

The optimization method described in Chapter 4 proposes different strategies to determine the equalization parameters in the case of a stochastic channel, each corresponding to a distinct performance-complexity combination. Here, these different strategies are briefly discussed, after which the mathematical details of the optimal equalization parameters are provided for each strategy in the subsections below (Subsections 5.2.1-5.2.5). First, the best-performing strategy (adjustable strategy, denoted S-A) to solve minimization problem (5.28) is to allow all equalization parameters to be adjusted to the specific channel $\mathbf{g}_{\text{ch}}$. In contrast, the least complexity is induced when all equalization parameters are identical for all channel realizations (fixed strategy, denoted S-F). Furthermore, the hybrid strategy (denoted S-H) intends to approximate the performance of strategy S-A with a limited complexity by considering both adjustable and fixed equalization parameters. More precisely, the pre-equalizer $\mathbf{P}$ and its associated scaling factor α are fixed, whereas $\mathbf{W}$ and $\mathbf{B}$ are adjustable. In doing so, no CSIT is required and the subproblems in Algorithm 4.1 can be solved by means of closed-form expression, significantly simplifying the implementational and computational complexity. Moreover, two suboptimal approaches are discussed. In the first suboptimal approach, the design of the fixed equalization parameters is solely based on the average channel and thus completely ignores the channel variability (strategies S-F_{s1} and S-H_{s1}). The second suboptimal approach (strategy S-H_{s2}) acquires the fixed equalization parameters in the hybrid strategy under the assumption that all adjustable equalizers are not present, i.e., all coefficients of $\mathbf{W}_{\text{adj}}$ and $\mathbf{B}$ are zero except for $\mathbf{W}_{\text{adj}}(0)$, which is equal to $\mathbf{I}_L$. The different strategies are summarized in Table 5.1.

Additionally, the special case of the linear equalization scheme is investigated in Subsection 5.2.6. Finally, the complexity differences between all strategies are discussed in more detail in Subsection 5.2.7.

Table 5.1: Overview of the different equalization strategies.

Strategy	Notation	Adjustable parameters	Fixed parameters
Adjustable	S-A	$\mathbf{P}, \alpha, \mathbf{W}, \mathbf{B}$	/
Fixed	S-F	/	$\mathbf{P}, \alpha, \mathbf{W}, \mathbf{B}$
Hybrid	S-H	$\mathbf{W}, \mathbf{B}$	$\mathbf{P}, \alpha$
Fixed-suboptimal 1	S-$\mathrm{F_{s1}}$	/	$\mathbf{P}, \alpha, \mathbf{W}, \mathbf{B}$
Hybrid-suboptimal 1	S-$\mathrm{H_{s1}}$	$\mathbf{W}, \mathbf{B}$	$\mathbf{P}, \alpha$
Hybrid-suboptimal 2	S-$\mathrm{H_{s2}}$	$\mathbf{P}, \alpha, \mathbf{W}_{\mathrm{fix}}$	$\mathbf{W}_{\mathrm{adj}}, \mathbf{B}$

5.2.1 Adjustable strategy (S-A)

In this optimal strategy in terms of MSE performance, all equalization parameters are a function of the specific channel realization $\mathbf{g}_{\mathrm{ch}}$, implying that all equalization parameters are collected in the vector $\mathbf{x}(\mathbf{g}_{\mathrm{ch}})$. Consequently, no iterations are required between the adjustable and the fixed equalization parameters and the optimal set $(\mathbf{P}_a^\star, \alpha_a^\star, \mathbf{W}_a^\star, \mathbf{B}_a^\star)$ is acquired by minimizing $\mathrm{MSE}_{\mathbf{g}_{\mathrm{ch}}}$ for each channel realization $\mathbf{g}_{\mathrm{ch}}$ individually. Unfortunately, the joint optimization of (5.25) subject to the energy constraint is mathematically quite challenging and no analytical expression can be easily derived. An iterative algorithm is therefore proposed to find a suitable set of equalization parameters. More precisely, the optimal $\mathbf{B}_a^\star(m)$ can almost directly be identified as a function of the other parameters, yielding $\mathrm{MSE}_{\mathbf{g}_{\mathrm{ch}},\mathbf{B}_a^\star}$. Next, $\mathrm{MSE}_{\mathbf{g}_{\mathrm{ch}},\mathbf{B}_a^\star}$ is further reduced by alternately computing the optimal $(\mathbf{P}_a^\star, \alpha_a^\star)$ and optimal $\mathbf{W}_a^\star$ for given $\mathbf{W}$ and $(\mathbf{P}, \alpha)$, respectively, until a stopping criterion is met.

Closer inspection of (5.25) reveals that the optimal feedback filter $\mathbf{B}_a^\star(m)$ can be expressed as

$$\mathbf{B}_a^\star(m) = \alpha \mathbf{W}\mathbf{G}(m)\mathbf{P} \tag{5.29}$$

for $m \in \Phi_{\mathbf{B}}$. When (5.29) is plugged into (5.25), the summation over $\Phi_{\mathbf{B}}$ completely disappears since the adjustable $\mathbf{B}_a^\star$ eliminates all residual ISI on all active causal delays of the feedback filter. The resulting $\mathrm{MSE}_{\mathbf{g}_{\mathrm{ch}}}$ is denoted by $\mathrm{MSE}_{\mathbf{g}_{\mathrm{ch}},\mathbf{B}_a^\star}$ and given by

$$\mathrm{MSE}_{\mathbf{g}_{\mathrm{ch}},\mathbf{B}_a^\star} = \frac{1}{L}\left(\sum_{m\in\Phi_{\mathbf{N}}} \left\|\alpha\mathbf{W}\mathbf{G}(m)\mathbf{P} - \delta_m \mathbf{I}_L\right\|^2 + \frac{\alpha^2}{\sigma_{\mathrm{a}}^2}\mathrm{Tr}\left(\mathbf{W}\mathbf{R}_{\bar{\mathbf{n}}}\mathbf{W}^H\right)\right). \tag{5.30}$$

Next, the optimal set $(\mathbf{P}_a^\star, \alpha_a^\star)$ is determined for given $\mathbf{W}$ by minimizing $\mathrm{MSE}_{\mathbf{g}_{\mathrm{ch}},\mathbf{B}_a^\star}$ from (5.30), for which the $L \times (LL_{\mathrm{P}})$ matrix $\mathcal{G}(m) = \mathbf{W}\mathbf{G}(m)$ is introduced. The $(LL_{\mathrm{N}}) \times (LL_{\mathrm{P}})$ stacked block matrix $\mathcal{G}_{\mathrm{N}}$ is then constructed by stacking all $\mathcal{G}(m)$ contributing to the sum over $\Phi_{\mathbf{N}}$ into one matrix, i.e.,

$$\mathcal{G}_{\mathrm{N}} = \left[\mathcal{G}^H\left(\Phi_{\mathbf{N}}(1)\right)\cdots\mathcal{G}^H\left(\Phi_{\mathbf{N}}(L_{\mathrm{N}})\right)\right]^H. \tag{5.31}$$

The conditional $\mathrm{MSE}_{\mathbf{g}_{\mathrm{ch}},\mathbf{B}_a^\star}$ can then be rewritten as

$$\mathrm{MSE}_{\mathbf{g}_{\mathrm{ch}},\mathbf{B}_a^\star} = \frac{1}{L}\mathrm{Tr}\left[\alpha^2\mathbf{P}^H\mathcal{G}_{\mathrm{N}}^H\mathcal{G}_{\mathrm{N}}\mathbf{P} + \frac{\alpha^2}{\sigma_{\mathrm{a}}^2}\mathbf{W}\mathbf{R}_{\bar{\mathbf{n}}}\mathbf{W}^H - \alpha\mathcal{G}(0)\mathbf{P} - \alpha\mathbf{P}^H\mathcal{G}^H(0) + \mathbf{I}_L\right]. \tag{5.32}$$

The minimization of $\mathrm{MSE}_{\mathbf{g}_{\mathrm{ch}},\mathbf{B}_a^\star}$ from (5.32) with respect to $\mathbf{P}$ and α for a given $\mathbf{W}$ subject to the energy constraint is a specific case of the more general optimization problem presented in Appendix 11.2. Indeed, the variables $\mathbf{G}$, $\mathbf{A}_1$, $\mathbf{A}_2$, and $\mathbf{A}_3$ employed in this appendix can readily be identified by comparing (5.32) with (11.9). Based on Appendix 11.2, the optimal pre-equalizer $\mathbf{P}_a^\star$ and the optimal scaling factor $\alpha_a^\star$ are given by

$$\mathbf{P}_a^\star = \frac{1}{\alpha_a^\star}\mathbf{D}_a^{-1}\mathcal{G}^H(0) \tag{5.33}$$

and

$$\alpha_a^\star = \sqrt{\frac{\sigma_{\mathrm{a}}^2}{LE_{\mathrm{TX}}}\mathrm{Tr}\left(\mathcal{G}(0)\mathbf{D}_a^{-1}\mathbf{R}_{\mathrm{TX}}\mathbf{D}_a^{-1}\mathcal{G}^H(0)\right)} \tag{5.34}$$

with $\mathbf{D}_a = \mathcal{G}_{\mathrm{N}}^H\mathcal{G}_{\mathrm{N}} + \zeta_a\mathbf{R}_{\mathrm{TX}}$ and $\zeta_a = \frac{\mathrm{Tr}(\mathbf{W}\mathbf{R}_{\bar{\mathbf{n}}}\mathbf{W}^H)}{LE_{\mathrm{TX}}}$. The smallest $\mathrm{MSE}_{\mathbf{g}_{\mathrm{ch}},\mathbf{B}^\star}$ for a given $\mathbf{W}$ denoted by $\mathrm{MSE}_{\mathbf{g}_{\mathrm{ch}},\mathbf{P}_a^\star,\alpha_a^\star,\mathbf{B}_a^\star}$, is subsequently computed by replacing $\mathbf{P}$ and α in (5.32) by (5.33) and (5.34), respectively, which can be simplified to

$$\mathrm{MSE}_{\mathbf{g}_{\mathrm{ch}},\mathbf{P}_a^\star,\alpha_a^\star,\mathbf{B}_a^\star} = \frac{1}{L}\mathrm{Tr}\left[\mathbf{I}_L - \mathcal{G}(0)\mathbf{D}_a^{-1}\mathcal{G}^H(0)\right]. \tag{5.35}$$

The second task in each iteration is to compute the optimal $\mathbf{W}_a^\star$ for a given set $(\mathbf{P}, \alpha)$. Similar to the computation of $(\mathbf{P}_a^\star, \alpha_a^\star)$, the $(LL_{\mathrm{W}}) \times L$ matrix $\boldsymbol{\mathcal{G}}(m) = \alpha\mathbf{G}(m)\mathbf{P}$ is introduced and the related $(LL_{\mathrm{W}}) \times (LL_{\mathrm{N}})$ augmented block matrix $\boldsymbol{\mathcal{G}}_{\mathrm{N}}$ is constructed according to

$$\boldsymbol{\mathcal{G}}_{\mathrm{N}} = \left[\boldsymbol{\mathcal{G}}(\Phi_{\mathbf{N}}(1)) \cdots \boldsymbol{\mathcal{G}}(\Phi_{\mathbf{N}}(L_{\mathrm{N}}))\right]. \tag{5.36}$$

By means of these definitions, the conditional $\mathrm{MSE}_{\mathbf{g}_{\mathrm{ch}},\mathbf{B}_a^\star}$ for given $(\mathbf{P}, \alpha)$ can be expressed as

$$\mathrm{MSE}_{\mathbf{g}_{\mathrm{ch}},\mathbf{B}_a^\star} = \frac{1}{L}\mathrm{Tr}\left[\mathbf{W}\boldsymbol{\mathcal{G}}_{\mathrm{N}}\boldsymbol{\mathcal{G}}_{\mathrm{N}}^H\mathbf{W}^H + \frac{\alpha^2}{\sigma_{\mathrm{a}}^2}\mathbf{W}\mathbf{R}_{\bar{\mathbf{n}}}\mathbf{W}^H - \mathbf{W}\boldsymbol{\mathcal{G}}(0) - \boldsymbol{\mathcal{G}}^H(0)\mathbf{W}^H + \mathbf{I}_L\right]. \tag{5.37}$$

Since the optimization of (5.37) over $\mathbf{W}$ is not restricted by any constraints, the optimal $\mathbf{W}_a^\star$ can be found by equating the complex derivative $\frac{\partial \mathrm{MSE}_{\mathbf{g}_{\mathrm{ch}},\mathbf{B}_a^\star}}{\partial \mathbf{W}^*}$ (Appendix 11.1) to zero, yielding

$$\mathbf{W}_a^\star = \boldsymbol{\mathcal{G}}^H(0)\mathbf{C}_a^{-1}, \tag{5.38}$$

where $\mathbf{C}_a = \boldsymbol{\mathcal{G}}_{\mathrm{N}}\boldsymbol{\mathcal{G}}_{\mathrm{N}}^H + \frac{\alpha^2}{\sigma_{\mathrm{a}}^2}\mathbf{R}_{\tilde{\mathbf{n}}}$. Subsequently, the lowest $\mathrm{MSE}_{\mathbf{g}_{\mathrm{ch}},\mathbf{B}_a^\star}$ for given $(\mathbf{P},\alpha)$ is obtained by substituting $\mathbf{W}$ in (5.37) for $\mathbf{W}_a^\star$ from (5.38), which can be simplified to

$$\mathrm{MSE}_{\mathbf{g}_{\mathrm{ch}},\mathbf{W}_a^\star,\mathbf{B}_a^\star} = \frac{1}{L}\mathrm{Tr}\left[\mathbf{I}_L - \boldsymbol{\mathcal{G}}^H(0)\mathbf{C}_a^{-1}\boldsymbol{\mathcal{G}}(0)\right]. \tag{5.39}$$

In conclusion, the adjustable strategy S-A iteratively minimizes $\mathrm{MSE}_{\mathbf{g}_{\mathrm{ch}},\mathbf{B}_a^\star}$ for each channel realization $\mathbf{g}_{\mathrm{ch}}$ by alternately computing the optimal $(\mathbf{P}_a^\star,\alpha_a^\star)$, given by (5.33) and (5.34), and the optimal $\mathbf{W}_a^\star$, defined in (5.38), for given $\mathbf{W}$ and $(\mathbf{P},\alpha)$, respectively, until some stopping criterion is met. In principle, any matrix can be assigned to the initial feedforward filter $\mathbf{W}$, but the most reasonable choice is to set the initial $\mathbf{W}$ equal to the all-pass filter, i.e., $\mathbf{W}(i) = \mathbf{I}_L\delta_i$. As a stopping criterion, the algorithm could terminate when either a predefined number of iterations is reached, or when the relative decrease in $\mathrm{MSE}_{\mathbf{g}_{\mathrm{ch}},\mathbf{B}_a^\star}$ is smaller than a predetermined threshold. Of course, a combination of these two stopping criteria is also a possibility.

5.2.2 Fixed strategy (S-F)

The main purpose of this strategy is to significantly lower the complexity by considering only fixed equalization parameters. Hence, all coefficients of $\mathbf{P}$, $\mathbf{W}$, and $\mathbf{B}$ and the scaling factor α are contained in the vector $\mathbf{y}$ in the optimization algorithm presented in Algorithm 4.1. As a result, the optimal set $\left(\mathbf{P}_f^\star,\alpha_f^\star,\mathbf{W}_f^\star,\mathbf{B}_f^\star\right)$ is determined by minimizing the average $\mathrm{MSE}_{\mathbf{g}_{\mathrm{ch}}}$, i.e., $\overline{\mathrm{MSE}}$. Similar to the minimization of $\mathrm{MSE}_{\mathbf{g}_{\mathrm{ch}}}$ in the adjustable strategy, analytically solving the joint minimization of $\overline{\mathrm{MSE}}$ subject to the energy constraint is rather hard. As an alternative, an iterative algorithm that is similar to the iterative algorithm of the adjustable strategy is proposed. First, the optimal $\mathbf{B}_f^\star$ is expressed as a function of $\mathbf{P}$, α, and $\mathbf{W}$, yielding $\overline{\mathrm{MSE}}_{\mathbf{B}_f^\star}$. Next, $\overline{\mathrm{MSE}}_{\mathbf{B}_f^\star}$ is iteratively lowered by alternately computing the optimal $\left(\mathbf{P}_f^\star,\alpha_f^\star\right)$ and optimal $\mathbf{W}_f^\star$ for given $\mathbf{W}$ and $(\mathbf{P},\alpha)$, respectively, until a stopping criterion is met.

By applying the expectation $\mathbb{E}_{\mathbf{G}_{\mathrm{ch}}}[\cdot]$ to $\mathrm{MSE}_{\mathbf{g}_{\mathrm{ch}}}$ from (5.25), one can readily determine the optimal $\mathbf{B}_f^\star$ as

$$\mathbf{B}_f^\star(m) = \alpha\mathbf{W}\mathbb{E}_{\mathbf{G}_{\mathrm{ch}}}\left[\mathbf{G}(m)\right]\mathbf{P} \tag{5.40}$$

for $m \in \Phi_{\mathbf{B}}$. Contrary to the adjustable strategy, the fixed feedback filter is unable to eliminate all residual ISI on all active causal delays of the feedback filter. Indeed, the average MSE evaluated at $\mathbf{B}_f^\star$ is given by

$$\begin{aligned}\overline{\mathrm{MSE}}_{\mathbf{B}_f^\star} = \frac{1}{L}\Bigg(&\sum_{m\in\Phi_{\mathbf{N}}}\mathbb{E}_{\mathbf{G}_{\mathrm{ch}}}\left[\left\|\alpha\mathbf{W}\mathbf{G}(m)\mathbf{P} - \delta_m\mathbf{I}_L\right\|^2\right] + \frac{\alpha^2}{\sigma_{\mathrm{a}}^2}\mathrm{Tr}\left(\mathbf{W}\mathbf{R}_{\tilde{\mathbf{n}}}\mathbf{W}^H\right)\\ &+ \sum_{m\in\Phi_{\mathbf{B}}}\mathbb{E}_{\mathbf{G}_{\mathrm{ch}}}\left[\left\|\alpha\mathbf{W}\mathbf{G}(m)\mathbf{P} - \alpha\mathbf{W}\mathbb{E}_{\mathbf{G}_{\mathrm{ch}}}\left[\mathbf{G}(m)\right]\mathbf{P}\right\|^2\right]\Bigg).\end{aligned} \tag{5.41}$$

In each iteration, $\overline{\mathrm{MSE}}_{\mathbf{B}_f^\star}$ is first minimized with respect to $(\mathbf{P}, \alpha)$ for given $\mathbf{W}$. In this regard, the $(LL_\mathrm{B}) \times (LL_\mathrm{P})$ stacked block matrix $\mathcal{G}_\mathrm{B}$ is similarly defined as $\mathcal{G}_\mathrm{N}$, i.e.,

$$\mathcal{G}_\mathrm{B} = \left[\mathcal{G}^H\left(\Phi_{\mathbf{B}}(1)\right) \cdots \mathcal{G}^H\left(\Phi_{\mathbf{B}}(L_\mathrm{B})\right)\right]^H. \tag{5.42}$$

The average $\overline{\mathrm{MSE}}_{\mathbf{B}_f^\star}$ can then be rewritten as

$$\begin{aligned}\overline{\mathrm{MSE}}_{\mathbf{B}_f^\star} = \frac{1}{L}\mathrm{Tr}\Big[&\alpha^2\mathbf{P}^H\left(\mathbb{E}_{\mathbf{G}_\mathrm{ch}}\left[\mathcal{G}_\mathrm{N}^H\mathcal{G}_\mathrm{N} + \mathcal{G}_\mathrm{B}^H\mathcal{G}_\mathrm{B}\right] - \mathbb{E}_{\mathbf{G}_\mathrm{ch}}\left[\mathcal{G}_\mathrm{B}^H\right]\mathbb{E}_{\mathbf{G}_\mathrm{ch}}\left[\mathcal{G}_\mathrm{B}\right]\right)\mathbf{P} \\ &+\frac{\alpha^2}{\sigma_\mathrm{a}^2}\mathbf{W}\mathbf{R}_{\bar{\mathbf{n}}}\mathbf{W}^H - \alpha\mathbb{E}_{\mathbf{G}_\mathrm{ch}}\left[\mathcal{G}(0)\right]\mathbf{P} - \alpha\mathbf{P}^H\mathbb{E}_{\mathbf{G}_\mathrm{ch}}\left[\mathcal{G}^H(0)\right] + \mathbf{I}_L\Big].\end{aligned} \tag{5.43}$$

Structurally, $\overline{\mathrm{MSE}}_{\mathbf{B}_f^\star}$ from (5.43) is very similar to $\mathrm{MSE}_{\mathbf{g}_\mathrm{ch},\mathbf{B}_a^\star}$ from (5.32). Consequently, the minimization of (5.43) with respect to $\mathbf{P}$ and α subject to the energy constraint is again a specific case of the optimization problem discussed in Appendix 11.2. The optimal fixed pre-equalizer $\mathbf{P}_f^\star$ and the optimal fixed scaling factor $\alpha_f^\star$ can therefore be determined as

$$\mathbf{P}_f^\star = \frac{1}{\alpha_f^\star}\mathbf{D}_f^{-1}\mathbb{E}_{\mathbf{G}_\mathrm{ch}}\left[\mathcal{G}^H(0)\right] \tag{5.44}$$

and

$$\alpha_f^\star = \sqrt{\frac{\sigma_\mathrm{a}^2}{LE_\mathrm{TX}}\mathrm{Tr}\left(\mathbb{E}_{\mathbf{G}_\mathrm{ch}}\left[\mathcal{G}(0)\right]\mathbf{D}_f^{-1}\mathbf{R}_\mathrm{TX}\mathbf{D}_f^{-1}\mathbb{E}_{\mathbf{G}_\mathrm{ch}}\left[\mathcal{G}^H(0)\right]\right)} \tag{5.45}$$

with $\mathbf{D}_f = \mathbb{E}_{\mathbf{G}_\mathrm{ch}}\left[\mathcal{G}_\mathrm{N}^H\mathcal{G}_\mathrm{N} + \mathcal{G}_\mathrm{B}^H\mathcal{G}_\mathrm{B}\right] - \mathbb{E}_{\mathbf{G}_\mathrm{ch}}\left[\mathcal{G}_\mathrm{B}^H\right]\mathbb{E}_{\mathbf{G}_\mathrm{ch}}\left[\mathcal{G}_\mathrm{B}\right] + \zeta_f\mathbf{R}_\mathrm{TX}$ and $\zeta_f = \frac{\mathrm{Tr}\left(\mathbf{W}\mathbf{R}_{\bar{\mathbf{n}}}\mathbf{W}^H\right)}{LE_\mathrm{TX}}$. Moreover, the smallest average $\overline{\mathrm{MSE}}_{\mathbf{B}_f^\star}$ for given $\mathbf{W}$ is denoted by $\overline{\mathrm{MSE}}_{\mathbf{P}_f^\star,\alpha_f^\star,\mathbf{B}_f^\star}$ and given by

$$\overline{\mathrm{MSE}}_{\mathbf{P}_f^\star,\alpha_f^\star,\mathbf{B}_f^\star} = \frac{1}{L}\mathrm{Tr}\left[\mathbf{I}_L - \mathbb{E}_{\mathbf{G}_\mathrm{ch}}\left[\mathcal{G}(0)\right]\mathbf{D}_f^{-1}\mathbb{E}_{\mathbf{G}_\mathrm{ch}}\left[\mathcal{G}^H(0)\right]\right]. \tag{5.46}$$

The second step in each iteration is to derive the optimal fixed $\mathbf{W}_f^\star$ for a given set $(\mathbf{P}, \alpha)$. To derive a neat expression for $\overline{\mathrm{MSE}}_{\mathbf{B}_f^\star}$ as a function of $\mathbf{W}$, the $(LL_\mathrm{W}) \times (LL_\mathrm{B})$ augmented matrix $\boldsymbol{\mathcal{G}}_\mathrm{B}$ is similarly defined as $\boldsymbol{\mathcal{G}}_\mathrm{N}$, i.e.,

$$\boldsymbol{\mathcal{G}}_\mathrm{B} = \left[\boldsymbol{\mathcal{G}}\left(\Phi_{\mathbf{B}}(1)\right) \cdots \boldsymbol{\mathcal{G}}\left(\Phi_{\mathbf{B}}(L_\mathrm{B})\right)\right] \tag{5.47}$$

such that $\overline{\mathrm{MSE}}_{\mathbf{B}_f^\star}$ can be written as

$$\begin{aligned}\overline{\mathrm{MSE}}_{\mathbf{B}_f^\star} = \frac{1}{L}\mathrm{Tr}\Big[&\mathbf{W}\left(\mathbb{E}_{\mathbf{G}_\mathrm{ch}}\left[\boldsymbol{\mathcal{G}}_\mathrm{N}\boldsymbol{\mathcal{G}}_\mathrm{N}^H + \boldsymbol{\mathcal{G}}_\mathrm{B}\boldsymbol{\mathcal{G}}_\mathrm{B}^H\right] - \mathbb{E}_{\mathbf{G}_\mathrm{ch}}\left[\boldsymbol{\mathcal{G}}_\mathrm{B}\right]\mathbb{E}_{\mathbf{G}_\mathrm{ch}}\left[\boldsymbol{\mathcal{G}}_\mathrm{B}^H\right]\right)\mathbf{W}^H \\ &+ \frac{\alpha^2}{\sigma_\mathrm{a}^2}\mathbf{W}\mathbf{R}_{\bar{\mathbf{n}}}\mathbf{W}^H - \mathbf{W}\mathbb{E}_{\mathbf{G}_\mathrm{ch}}\left[\boldsymbol{\mathcal{G}}(0)\right] - \mathbb{E}_{\mathbf{G}_\mathrm{ch}}\left[\boldsymbol{\mathcal{G}}^H(0)\right]\mathbf{W}^H + \mathbf{I}_L\Big].\end{aligned} \tag{5.48}$$

Next, the optimal fixed $\mathbf{W}_f^\star$ is acquired by equating the complex derivative of $\overline{\text{MSE}}_{\mathbf{B}_f^\star}$ with respect to $\mathbf{W}^*$ to zero, resulting in

$$\mathbf{W}_f^\star = \mathbb{E}_{\mathbf{G}_{\text{ch}}}\left[\boldsymbol{\mathcal{G}}^H(0)\right]\mathbf{C}_f^{-1} \tag{5.49}$$

with $\mathbf{C}_f = \mathbb{E}_{\mathbf{G}_{\text{ch}}}\left[\boldsymbol{\mathcal{G}}_{\text{N}}\boldsymbol{\mathcal{G}}_{\text{N}}^H + \boldsymbol{\mathcal{G}}_{\text{B}}\boldsymbol{\mathcal{G}}_{\text{B}}^H\right] - \mathbb{E}_{\mathbf{G}_{\text{ch}}}\left[\boldsymbol{\mathcal{G}}_{\text{B}}\right]\mathbb{E}_{\mathbf{G}_{\text{ch}}}\left[\boldsymbol{\mathcal{G}}_{\text{B}}^H\right] + \frac{\alpha^2}{\sigma_{\text{a}}^2}\mathbf{R}_{\bar{\mathbf{n}}}$. The corresponding minimal value of $\overline{\text{MSE}}_{\mathbf{B}_f^\star}$ for given $(\mathbf{P}, \alpha)$ can be simplified to

$$\overline{\text{MSE}}_{\mathbf{W}_f^\star,\mathbf{B}_f^\star} = \frac{1}{L}\text{Tr}\left[\mathbf{I}_L - \mathbb{E}_{\mathbf{G}_{\text{ch}}}\left[\boldsymbol{\mathcal{G}}^H(0)\right]\mathbf{C}_f^{-1}\mathbb{E}_{\mathbf{G}_{\text{ch}}}\left[\boldsymbol{\mathcal{G}}(0)\right]\right]. \tag{5.50}$$

In summary, the structure of the algorithm to determine the fixed equalization parameters in the fixed strategy is quite similar to the algorithm to obtain the adjustable equalization parameters in the adjustable strategy such that the same stopping criteria and initialization of $\mathbf{W}$ can be employed. The only difference between the two algorithms is that in the fixed strategy the average $\overline{\text{MSE}}$ rather than the conditional $\text{MSE}_{\mathbf{g}_{\text{ch}}}$ is minimized. For this purpose, both the first-order and the second-order statistics of the channel must be available.

5.2.3 Hybrid strategy (S-H)

This strategy considers both adjustable and fixed equalization parameters. Most practical is to keep the pre-equalizer $\mathbf{P}$ and the scaling factor α fixed and the filters $\mathbf{W}$ and $\mathbf{B}$ at the receiver adjustable, because this configuration does not require any transfer of CSI from the receiver to the transmitter. In terms of the notations used in Algorithm 4.1, this means that the vector $\mathbf{y}$ consists of all coefficients of $\mathbf{P}$ and the scaling factor α, whereas the vector $\mathbf{x}(\mathbf{g}_{\text{ch}})$ contains all coefficients of $\mathbf{W}$ and $\mathbf{B}$. The optimization problem from (5.28) could then be solved by Algorithm 4.1, which must be slightly changed as the energy constraint depends on the fixed equalization parameters rather than the adjustable equalization parameters. Just as $\mathbf{B}_a^\star$, the optimal adjustable feedback filter $\mathbf{B}_h^\star$ can however directly be written as a function of the other parameters, i.e.,

$$\mathbf{B}_h^\star(m) = \alpha\mathbf{W}\mathbf{G}(m)\mathbf{P} \tag{5.51}$$

for $m \in \Phi_{\mathbf{B}}$, and the resulting $\text{MSE}_{\mathbf{g}_{\text{ch}},\mathbf{B}_h^\star}$ is completely identical to $\text{MSE}_{\mathbf{g}_{\text{ch}},\mathbf{B}_a^\star}$. Consequently, instead of applying the optimization algorithm from Algorithm 4.1 to $f_0 = \text{MSE}_{\mathbf{g}_{\text{ch}}}$, it is better to apply this algorithm to $f_0 = \text{MSE}_{\mathbf{g}_{\text{ch}},\mathbf{B}_h^\star}$, because this guarantees that the feedback filter is always optimal for given $(\mathbf{P}, \mathbf{W}, \alpha)$. Compared to the original approach, the vector $\mathbf{y}$ in this alternative approach does not alter, but the vector $\mathbf{x}(\mathbf{g}_{\text{ch}})$ now comprises only the coefficients of $\mathbf{W}$.

The first step in the optimization algorithm is to compute the optimal $\mathbf{y}_i^\star$ for given $\mathbf{x}_{i-1}(\mathbf{g}_{\text{ch}})$, i.e., the optimal $(\mathbf{P}_h^\star, \alpha_h^\star)$ for given $\mathbf{W}$ (for all channel

realizations in Gch). The average over the channel realizations of $\mathrm{MSE}_{\mathbf{g}_{\mathrm{ch}},\mathbf{B}_h^\star}$, $\overline{\mathrm{MSE}}_{\mathbf{B}_h^\star}$, is therefore expressed as

$$\overline{\mathrm{MSE}}_{\mathbf{B}_h^\star} = \frac{1}{L}\mathrm{Tr}\left[\alpha^2\mathbf{P}^H\mathbb{E}_{\mathbf{G}_{\mathrm{ch}}}\left[\mathcal{G}_{\mathrm{N}}^H\mathcal{G}_{\mathrm{N}}\right]\mathbf{P} + \frac{\alpha^2}{\sigma_{\mathrm{a}}^2}\mathbb{E}_{\mathbf{G}_{\mathrm{ch}}}\left[\mathbf{W}\mathbf{R}_{\bar{\mathbf{n}}}\mathbf{W}^H\right]\right.$$
$$\left. -\alpha\mathbb{E}_{\mathbf{G}_{\mathrm{ch}}}\left[\mathcal{G}(0)\right]\mathbf{P} - \alpha\mathbf{P}^H\mathbb{E}_{\mathbf{G}_{\mathrm{ch}}}\left[\mathcal{G}^H(0)\right] + \mathbf{I}_L\right]. \tag{5.52}$$

The minimization of (5.52) with respect to $\mathbf{P}$ and α subject to the energy constraint is once more a particular case of the optimization problem discussed in Appendix 11.2. The optimal $\mathbf{P}_h^\star$ and $\alpha_h^\star$ are thus given by

$$\mathbf{P}_h^\star = \frac{1}{\alpha_h^\star}\mathbf{D}_h^{-1}\mathbb{E}_{\mathbf{G}_{\mathrm{ch}}}\left[\mathcal{G}^H(0)\right] \tag{5.53}$$

and

$$\alpha_h^\star = \sqrt{\frac{\sigma_{\mathrm{a}}^2}{LE_{\mathrm{TX}}}\mathrm{Tr}\left(\mathbb{E}_{\mathbf{G}_{\mathrm{ch}}}\left[\mathcal{G}(0)\right]\mathbf{D}_h^{-1}\mathbf{R}_{\mathrm{TX}}\mathbf{D}_h^{-1}\mathbb{E}_{\mathbf{G}_{\mathrm{ch}}}\left[\mathcal{G}^H(0)\right]\right)} \tag{5.54}$$

with $\mathbf{D}_h = \mathbb{E}_{\mathbf{G}_{\mathrm{ch}}}\left[\mathcal{G}_{\mathrm{N}}^H\mathcal{G}_{\mathrm{N}}\right] + \zeta_h\mathbf{R}_{\mathrm{TX}}$ and $\zeta_h = \frac{\mathrm{Tr}\left(\mathbb{E}_{\mathbf{G}_{\mathrm{ch}}}\left[\mathbf{W}\mathbf{R}_{\bar{\mathbf{n}}}\mathbf{W}^H\right]\right)}{LE_{\mathrm{TX}}}$. Furthermore, evaluating $\overline{\mathrm{MSE}}_{\mathbf{B}_h^\star}$ from (5.52) at the optimal $\mathbf{P}_h^\star$ and $\alpha_h^\star$ yields an optimized $\overline{\mathrm{MSE}}_{\mathbf{P}_h^\star,\alpha_h^\star,\mathbf{B}_h^\star}$, which can be expressed as

$$\overline{\mathrm{MSE}}_{\mathbf{P}_h^\star,\alpha_h^\star,\mathbf{B}_h^\star} = \frac{1}{L}\mathrm{Tr}\left[\mathbf{I}_L - \mathbb{E}_{\mathbf{G}_{\mathrm{ch}}}\left[\mathcal{G}(0)\right]\mathbf{D}_h^{-1}\mathbb{E}_{\mathbf{G}_{\mathrm{ch}}}\left[\mathcal{G}^H(0)\right]\right]. \tag{5.55}$$

In the second step of the optimization algorithm, the optimal $\mathbf{x}_i^\star\left(\mathbf{g}_{\mathrm{ch}}\right)$ for given $\mathbf{y}_i$ must be determined by minimizing $\mathrm{MSE}_{\mathbf{g}_{\mathrm{ch}},\mathbf{B}_h^\star}$ with respect to $\mathbf{W}$ for given $(\mathbf{P},\alpha)$. This subproblem is identical to determining the optimal $\mathbf{W}_a^\star$ in the adjustable strategy as $\mathrm{MSE}_{\mathbf{g}_{\mathrm{ch}},\mathbf{B}_h^\star}$ is equal to $\mathrm{MSE}_{\mathbf{g}_{\mathrm{ch}},\mathbf{B}_a^\star}$. The optimal $\mathbf{W}_h^\star$ and the minimal $\mathrm{MSE}_{\mathbf{g}_{\mathrm{ch}},\mathbf{W}_h^\star,\mathbf{B}_h^\star}$ are thus respectively given by

$$\mathbf{W}_h^\star = \boldsymbol{\mathcal{G}}^H(0)\mathbf{C}_h^{-1} \tag{5.56}$$

and

$$\mathrm{MSE}_{\mathbf{g}_{\mathrm{ch}},\mathbf{W}_h^\star,\mathbf{B}_h^\star} = \frac{1}{L}\mathrm{Tr}\left[\mathbf{I}_L - \boldsymbol{\mathcal{G}}^H\left(0\right)\mathbf{C}_h^{-1}\boldsymbol{\mathcal{G}}(0)\right] \tag{5.57}$$

with $\mathbf{C}_h = \boldsymbol{\mathcal{G}}_{\mathrm{N}}\boldsymbol{\mathcal{G}}_{\mathrm{N}}^H + \frac{\alpha^2}{\sigma_{\mathrm{a}}^2}\mathbf{R}_{\bar{\mathbf{n}}}$.

To initialize $\mathbf{x}_0(\mathbf{g}_{\mathrm{ch}})$, all initial feedforward filters $\mathbf{W}$ are assumed to be equal to the all-pass filter.

5.2.4 Suboptimal 1 (S-F_{s1} and S-H_{s1})

A suboptimal approach to determine the fixed equalization parameters in both the fixed and the hybrid strategy is to ignore all channel variability, i.e., $\mathbf{G}(m)$

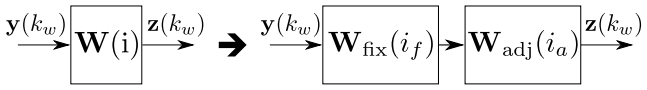

Figure 5.3: Partition of the linear filter $\mathbf{W}(i)$ into a fixed filter $\mathbf{W}_{\text{fix}}(i_{\text{f}})$ and an adjustable filter $\mathbf{W}_{\text{adj}}(i_{\text{a}})$ with $L_{\text{W,fix}}$ and $L_{\text{W,adj}}$ taps, respectively. The total number of taps does not change, such that $L_{\text{W}} = L_{\text{W,adj}} + L_{\text{W,fix}} - 1$.

is assumed to be equal to $\mathbb{E}_{\mathbf{G}_{\text{ch}}}[\mathbf{G}(m)]$. This assumption is equivalent to considering a channel set $\mathbb{G}_{\text{ch}}$ with the average channel $\mathbb{E}_{\mathbf{G}_{\text{ch}}}[\mathbf{g}_{\text{ch}}]$ as the only element. For this specific set $\mathbb{G}_{\text{ch}}$, all second order moments transform to a product of first order moments, e.g., $\mathbb{E}_{\mathbf{G}_{\text{ch}}}[\mathcal{G}_{\text{N}}^H \mathcal{G}_{\text{N}}]$ becomes $\mathbb{E}_{\mathbf{G}_{\text{ch}}}\left[\mathcal{G}_{\text{N}}^H\right] \mathbb{E}_{\mathbf{G}_{\text{ch}}}[\mathcal{G}_{\text{N}}]$. As a result, all terms with $\mathcal{G}_{\text{B}}$ and $\boldsymbol{\mathcal{G}}_{\text{B}}$ in $\mathbf{D}_f$ and $\mathbf{C}_f$, respectively, can be omitted in the fixed strategy such that the fixed strategy becomes in fact identical to the adjustable strategy applied to the average channel $\mathbb{E}_{\mathbf{G}_{\text{ch}}}[\mathbf{g}_{\text{ch}}]$. Moreover, the fixed equalization parameters of the suboptimal hybrid strategy are chosen to be equal to the corresponding fixed parameters of the suboptimal fixed strategy.

This suboptimal approach is denoted by S-F_{s1} and S-H_{s1} for the fixed and the hybrid strategy, respectively.

5.2.5 Suboptimal 2 (S-H_{s2})

Based on the optimization method from [53], a second suboptimal approach for the hybrid strategy, S-H_{s2}, is presented here. In this approach, the fixed equalization parameters are first computed, while completely neglecting the presence of the adjustable equalizers, i.e., the latter parameters are assumed to be not present. Afterwards, the adjustable parameters are designed to combat the residual ISI generated by the cascade of the fixed equalization filters and the channel $\mathbf{g}_{\text{ch}}$. To allow for additional design freedom, the linear feedforward filter $\mathbf{W}$ in the equalization scheme of Fig. 5.1 is divided into a fixed linear filter $\mathbf{W}_{\text{fix}}$ and an adjustable linear filter $\mathbf{W}_{\text{adj}}$ with $L_{\text{W,fix}}$ and $L_{\text{W,adj}}$ taps, respectively. This partitioning is schematically depicted in Fig. 5.3. Consequently, a fixed linear filter is now present at both the transmitter and the receiver, just as in [53]. When the fixed $\mathbf{W}_{\text{fix}}$ is bypassed, the set of adjustable parameters and the set of fixed parameters is of course the same as in the other hybrid strategies.

In this strategy, the fixed equalization parameters are determined under the assumption that the adjustable equalizers are not present. More precisely, this means that the adjustable feedforward filter $\mathbf{W}_{\text{adj}}$ is assumed to equal an all-pass filter, i.e., $\mathbf{W}_{\text{adj}}(m) = \mathbf{I}_L \delta_m$, while all coefficients of the adjustable feedback filter $\mathbf{B}$ are assumed to be zero. As a result, determining the fixed equalization parameters, i.e., $\mathbf{P}$, α, and $\mathbf{W}_{\text{fix}}$, can be achieved by applying the algorithm of the fixed strategy with $\mathbf{W} = \mathbf{W}_{\text{fix}}$ and $\Phi_{\mathbf{B}} = \emptyset$. Subsequently, the adjustable filters $\mathbf{W}_{\text{adj}}$ and $\mathbf{B}$ are obtained by minimizing $\text{MSE}_{\mathbf{g}_{\text{ch}}}$ for a given

channel realization $\mathbf{g}_{\text{ch}}$ and a given set $(\mathbf{P}, \alpha, \mathbf{W}_{\text{fix}})$. For this minimization, standard techniques can be employed as the cascade of the channel and the fixed $\mathbf{W}_{\text{fix}}$ can be interpreted as an equivalent channel $\mathbf{H}_{\mathbf{W}_{\text{fix}}}$. All details of the computation of $\mathbf{W}_{\text{adj}}$ and $\mathbf{B}$ are included in Appendix 11.3.

5.2.6 Linear equalization scheme

In the linear equalization scheme, the feedback filter is absent such that the optimal $(\mathbf{P}^\star, \mathbf{W}^\star, \alpha^\star)$ for all strategies are obtained by setting $\Phi_{\mathbf{B}} = \emptyset$ in the equations above. As a consequence $\Phi_{\mathbf{N}}$ becomes equal to Φ and $\mathcal{G}_{\text{B}}$ and $\boldsymbol{\mathcal{G}}_{\text{B}}$ are equal to the zero matrix $\mathbf{0}$.

5.2.7 Complexity considerations

This section compares the complexities of the equalization strategies above with a focus on the chip-to-chip interconnect affected by manufacturing tolerances. For any realization of the interconnect, the corresponding channel is considered essentially time-invariant, but some variability is present among the different realizations due to manufacturing tolerances.

Adjusting all equalizers to the actual realization $\mathbf{g}_{\text{ch}}$ of the interconnect could in principle be achieved as part of the manufacturing process, involving (i) the measurement of the transfer function matrix of the specific interconnect; (ii) the offline computation of the corresponding equalizer taps; and (iii) setting the taps on the transmitter/receiver chip accordingly before the interconnect is put in operation. However, this requires that each produced interconnect is measured, making the manufacturing very expensive and time-consuming. The alternative is that the equalizers are adjusted in real-time during operation, based on channel information which must be estimated at regular intervals by the receiver and passed to the transmitter. This alternative has the additional advantage that it adapts to slow variations of the channel (e.g., caused by temperature). However, this comes at the expense of a higher cost of the transmitter/receiver chip due to the increased implementation complexity (on-chip channel estimation circuit, channel information return channel from receiver to transmitter) and a higher computational complexity (e.g., on-chip iterative coefficient computation).

The high complexity and cost associated with the adjustable equalizer strategy can be avoided to a large extent by having (some of) the equalizers fixed. The fixed equalizers depend on the channel statistics rather than the actual realization of the interconnect. These statistics are obtained from the measurement of the individual channel transfer matrices corresponding to a sample consisting of N_{ch} interconnects; N_{ch} should be large enough to reliably capture

the statistics of the interconnects, but N_{ch} is typically much smaller than the total number of interconnects to be produced.

For the fixed and the hybrid equalization strategies, the offline iterative computation (based on the channel statistics) of the coefficients of the fixed equalizers has to be executed only once. The resulting fixed coefficients of each transmitter/receiver chip are set accordingly during the manufacturing process, irrespective of the actual realization of the interconnect. In the case of the fixed equalization strategy, no channel estimation nor channel information return channel needs to be implemented on-chip. As for the hybrid equalization strategy, on-chip channel estimation is required at the receiver, but the return channel is redundant, because the pre-equalizer at the transmitter is fixed. The receiver of the hybrid equalizer must perform on-chip adjustment of the feedforward equalizer according to the actual channel after the interconnect has been put in operation, but, unlike the adjustable equalizer strategy, these on-chip computations do not involve any iterations. In contrast to the fixed equalizer, the hybrid equalizer is also able to adapt to slow variation of the channel.

In the context of multi-Gbit/s electrical interconnects, advanced digital signal processing and high-precision analog-to-digital (A/D) and digital-to-analog (D/A) converters should be avoided, because of their high power consumption. Therefore, it is of interest to implement the FIR filters as *analog* tapped delay lines [10]. For the hybrid strategy, the on-chip complexity can be substantially reduced by using adaptive equalizers [20, 77] that could be determined by recursively updating the filter taps of the tapped delay lines by means of a simple stochastic gradient algorithm, rather than performing channel estimation and computing the feedforward equalizer taps. This way, no high-precision A/D and D/A converters are needed for the hybrid strategy, and the filter tap updating requires only low-complexity digital signal processing.

5.3 Baseband transmission

The system model (Section 5.1) and the derivation of the MMSE equalizer coefficients (Section 5.2) assume bandpass transmission: the bandpass signals and the bandpass filters are represented in complex-valued baseband notation.

In the case of baseband transmission, the transmitted symbols, the filter and channel impulse responses and the noise are real-valued instead of complex-valued. Hence, only minor alterations must be made to convert the results for bandpass transmission to baseband transmission:

- The Hermitian conjugate$(\cdot)^H$ is replaced by the transpose $(\cdot)^T$.
- The channel noise $\mathbf{n}(t)$ is zero-mean Gaussian with $\mathbb{E}[\mathbf{n}(t+u)\mathbf{n}^T(t)] = \frac{N_0}{2}\delta(u)\mathbf{I}_L$

As a result, $\mathbf{R}_{\bar{\mathbf{n}}}$ is obtained by replacing N_0 by $N_0/2$ in (5.27).

In baseband transmission, the elements of the symbol set $\mathcal{C}$ are real-valued. A typical constellation is the M-PAM constellation with the symbol set $\mathcal{C}_{M-\mathrm{PAM}}$ given by

$$\mathcal{C}_{M-\mathrm{PAM}} = \{(-M+1)\Delta, (-M+3)\Delta, \cdots, (-M+3)\Delta, (-M+1)\Delta\}, \quad (5.58)$$

where Δ is often chosen to normalize the constellation ($\sigma_{\mathrm{a}}^2 = 1$), i.e.,

$$\Delta = \sqrt{\frac{3}{M^2-1}}. \quad (5.59)$$

5.4 SER and BER expression

The probability of some type of error is often one of the key performance measures in any practical communication link. This section therefore derives and discusses both the SER and the BER expression for the system model from Fig. 5.1 in the case of uncoded *baseband* communication with M-PAM transmission.

5.4.1 SER expression for M-PAM transmission

The SER corresponding to the lth data symbol stream conditioned on the channel realization $\mathbf{g}_{\mathrm{ch}}$, $\mathrm{SER}_{\mathbf{g}_{\mathrm{ch}}}^{(l)}$, is defined as the probability that the decision $\hat{\mathrm{a}}_l(k)$ is different from the original data symbol $\mathrm{a}_l(k)$. This decision $\hat{\mathrm{a}}_l(k)$ is based on the lth entry of the decision variable $\mathbf{u}(k)$, $\mathrm{u}_l(k)$. With the assumption that the previous decisions are correctly detected, $\mathrm{u}_l(k)$ can be decomposed as

$$\mathrm{u}_l(k) = (1+\mathrm{e}_l)\mathrm{a}_l(k) + \mathrm{isi}_l(k) + \mathrm{w}_l(k), \quad (5.60)$$

where $\mathbf{e} = \mathrm{diag}\,(\alpha\mathbf{W}\mathbf{G}(0)\mathbf{P}) - \mathbf{1}$, $\mathbf{w}(k) = \alpha\mathbf{W}\bar{\mathbf{n}}(k)$, and

$$\begin{aligned}\mathbf{isi}(k) = &\sum_{m\in\Phi_{\mathbf{N}}} \alpha\mathbf{W}\mathbf{G}(m)\mathbf{P}\mathbf{a}(k-m) - \mathrm{diag}(\mathbf{e}+\mathbf{1})\mathbf{a}(k) \\ &+ \sum_{m\in\Phi_{\mathbf{B}}} \left(\alpha\mathbf{W}\mathbf{G}(m)\mathbf{P} - \mathbf{B}(m)\right)\mathbf{a}(k-m). \end{aligned} \quad (5.61)$$

For notational convenience, the symbol time index (k) is dropped in the remainder of this section. All data symbols present in isi_l in (5.60) are collected in the vector $\mathbf{a}_{\mathrm{ISI}}$, and this dependence is emphasized by the notation $\mathrm{isi}_l(\mathbf{a}_{\mathrm{ISI}})$. Note that the vector $\mathbf{a}_{\mathrm{ISI}}$ has $LL_{\mathrm{G}} - 1$ components. Furthermore, (5.60) illustrates that u_l can be written as the sum of (i) a useful term $(1+\mathrm{e}_l)\mathrm{a}_l$; (ii) an interference term $\mathrm{isi}_l(\mathbf{a}_{\mathrm{ISI}})$; and (iii) a Gaussian noise contribution w_l with variance $\sigma_{\mathrm{w}_l}^2 = \alpha^2\left(\mathbf{W}\mathbf{R}_{\bar{\mathbf{n}}}\mathbf{W}^H\right)_{l,l}$. In this section, all data symbols are assumed to belong to the M-PAM constellation $\mathcal{C}_{M-\mathrm{PAM}}$, which is schematically presented in Fig. 5.4. At the receiver, the symbol-by-symbol decoder processes each u_l

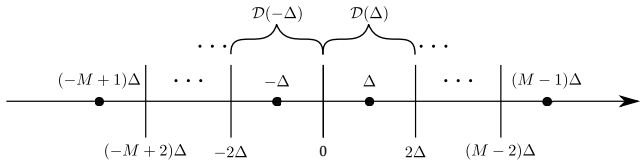

Figure 5.4: Visualization of the normalized M-PAM constellation. All constellation points are symbolized by the dots on the horizontal axis, whereas the boundaries of the decision areas $\mathcal{D}(\cdot)$ are indicated by the vertical lines. The scaling factor Δ is chosen such that the average symbol energy is equal to 1.

by mapping it to the closest constellation point, resulting in a decision area $\mathcal{D}(\cdot)$ for each constellation point $\mathfrak{c}$. An expression for $\mathrm{SER}_{\mathbf{g}_{\mathrm{ch}}}^{(l)}$ is then derived as follows:

$$\begin{aligned}\mathrm{SER}_{\mathbf{g}_{\mathrm{ch}}}^{(l)} &= \Pr\left(\hat{\mathrm{a}}_l \neq \mathrm{a}_l\right) && (5.62)\\ &= \Pr\left(\mathrm{u}_l \notin \mathcal{D}\left(\mathrm{a}_l\right)\right) && (5.63)\\ &= \frac{1}{M}\sum_{\mathfrak{c}} \mathbb{E}_{\mathbf{a}_{\mathrm{ISI}}}\left[P\left(\mathrm{error}|\mathfrak{c}, \mathbf{a}_{\mathrm{ISI}}\right)\right], && (5.64)\end{aligned}$$

where we made use of $\Pr\left(\mathrm{a}_l = \mathfrak{c}\right) = \frac{1}{M}$, $\mathbb{E}_{\mathbf{a}_{\mathrm{ISI}}}\left[\cdot\right]$ denotes the expectation over $\mathbf{a}_{\mathrm{ISI}}$, and $P\left(\mathrm{error}|\mathfrak{c}, \mathfrak{a}_{\mathrm{ISI}}\right)$ is defined as

$$P\left(\mathrm{error}|\mathfrak{c}, \mathfrak{a}_{\mathrm{ISI}}\right) = \Pr\left(\left(1+\mathrm{e}_l\right)\mathfrak{c} + \mathrm{isi}_l\left(\mathfrak{a}_{\mathrm{ISI}}\right) + \mathrm{w}_l \notin \mathcal{D}\left(\mathfrak{c}\right)\right), \tag{5.65}$$

with $\mathfrak{a}_{\mathrm{ISI}}$ denoting a realization of $\mathbf{a}_{\mathrm{ISI}}$. Since w_l has a Gaussian distribution with zero-mean and variance $\sigma_{\mathrm{w}_l}^2$, $P(\mathrm{error}|\mathfrak{c}, \mathfrak{a}_{\mathrm{ISI}})$ from (5.65) can easily be derived. Still, a distinction must be drawn between the outer and the inner constellation points. As for the outer constellation points, only one decision boundary is present, whereas the decision areas of the inner constellation points are bounded by two decision boundaries. First, $P(\mathrm{error}|\mathfrak{c}, \mathfrak{a}_{\mathrm{ISI}})$ for the outer constellation points, i.e., $\pm(M-1)\Delta$, can be derived as

$$P(\mathrm{error}|\mathfrak{c}, \mathfrak{a}_{\mathrm{ISI}}) = \begin{cases} \mathrm{Q}\left(\frac{\Delta+\mathrm{isi}_l(\mathfrak{a}_{\mathrm{ISI}})+\mathrm{e}_l(M-1)\Delta}{\sigma_{\mathrm{w}_l}}\right) & \mathfrak{c} = (M-1)\Delta \\ \mathrm{Q}\left(\frac{\Delta-\mathrm{isi}_l(\mathfrak{a}_{\mathrm{ISI}})+\mathrm{e}_l(M-1)\Delta}{\sigma_{\mathrm{w}_l}}\right) & \mathfrak{c} = (-M+1)\,\Delta \end{cases}, \tag{5.66}$$

where $\mathrm{Q}(\cdot) = 1 - \mathrm{F}(\cdot)$ with $\mathrm{F}(\cdot)$ representing the cumulative distribution function of the standard normal distribution. On the other hand, all inner constellation points, i.e., $(2m+1)\Delta$ with $m \in \{-\frac{M}{2}+1, \cdots, \frac{M}{2}-2\}$, result in a probability $P(\mathrm{error}|(2m+1)\Delta, \mathfrak{a}_{\mathrm{ISI}})$ given by

$$\begin{aligned}P(\mathrm{error}|(2m+1)\Delta, \mathfrak{a}_{\mathrm{ISI}}) &= \mathrm{Q}\left(\frac{\Delta + \mathrm{e}_l(2m+1)\Delta + \mathrm{isi}_l(\mathfrak{a}_{\mathrm{ISI}})}{\sigma_{\mathrm{w}_l}}\right)\\ &\quad + \mathrm{Q}\left(\frac{\Delta - \mathrm{e}_l(2m+1)\Delta - \mathrm{isi}_l(\mathfrak{a}_{\mathrm{ISI}})}{\sigma_{\mathrm{w}_l}}\right). \end{aligned}\tag{5.67}$$

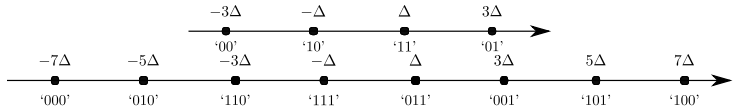

Figure 5.5: 4-PAM (upper plot) and 8-PAM (lower plot) constellation with Gray mapping.

Next, an expression for $\mathrm{SER}_{\mathbf{g}_{\mathrm{ch}}}^{(l)}$ can be derived by plugging (5.66) and (5.67) into (5.64). Interestingly, the obtained expression can be simplified by noting that $\Pr(\mathbf{a}_{\mathrm{ISI}} = \mathfrak{a}_{\mathrm{ISI}})$ is equal to $\Pr(\mathbf{a}_{\mathrm{ISI}} = -\mathfrak{a}_{\mathrm{ISI}})$ because all data symbols are independent and equally likely and the constellation is symmetric around zero. Consequently, $\mathrm{SER}_{\mathbf{g}_{\mathrm{ch}}}^{(l)}$ can be expressed as

$$\mathrm{SER}_{\mathbf{g}_{\mathrm{ch}}}^{(l)} = \frac{2}{M} \sum_{m=-\frac{M}{2}+1}^{\frac{M}{2}-1} \mathbb{E}_{\mathbf{a}_{\mathrm{ISI}}} \left[\mathrm{Q}\left(\frac{\Delta + \mathrm{e}_l(2m+1)\Delta + \mathrm{isi}_l(\mathbf{a}_{\mathrm{ISI}})}{\sigma_{\mathrm{w}_l}} \right) \right]. \tag{5.68}$$

The $\mathrm{SER}_{\mathbf{g}_{\mathrm{ch}}}^{(l)}$ from (5.68) is a performance measure related to the lth symbol stream and channel realization $\mathbf{g}_{\mathrm{ch}}$. From $\mathrm{SER}_{\mathbf{g}_{\mathrm{ch}}}^{(l)}$, the average SER, denoted as $\overline{\mathrm{SER}}$, is then derived by averaging $\mathrm{SER}_{\mathbf{g}_{\mathrm{ch}}}^{(l)}$ over all symbol streams and all channel realizations, i.e.,

$$\overline{\mathrm{SER}} = \mathbb{E}_{\mathbf{G}_{\mathrm{ch}}} \left[\frac{1}{L} \sum_{l=1}^{L} \mathrm{SER}_{\mathbf{g}_{\mathrm{ch}}}^{(l)} \right]. \tag{5.69}$$

When the condition $(1 + \mathrm{e}_l)\,\mathfrak{c} + \mathrm{isi}_l\,(\mathfrak{a}_{\mathrm{ISI}}) \in \mathcal{D}\,(\mathfrak{c})$ holds for all considered $\mathfrak{c}$ and $\mathfrak{a}_{\mathrm{ISI}}$, the arguments of the functions $\mathrm{Q}(\cdot)$ in (5.66) and (5.67) all take positive values. When this condition holds for vanishing σ_{w_l}, the corresponding SER goes to zero. When the condition does not hold for vanishing σ_{w_l}, the corresponding SER converges to a nonzero asymptotic value. This phenomenon is referred to as an error floor.

5.4.2 BER expression for M-PAM transmission

The BER of the lth symbol stream conditioned on the channel realization $\mathbf{g}_{\mathrm{ch}}$, $\mathrm{BER}_{\mathbf{g}_{\mathrm{ch}}}^{(l)}$, is defined as the probability that a transmitted bit is erroneously decoded at the receiver. Unlike $\mathrm{SER}_{\mathbf{g}_{\mathrm{ch}}}^{(l)}$, the mapping of the bit sequence on the data symbols does influence the expression for $\mathrm{BER}_{\mathbf{g}_{\mathrm{ch}}}^{(l)}$. Here, the binary labels associated with the elements from $\mathcal{C}_{M-\mathrm{PAM}}$ are according to the binary-reflected Gray mapping, meaning that the binary labels of neighboring symbols differ at exactly one position. As an example, Fig. 5.5 depicts a possible Gray mapping for the 4-PAM and the 8-PAM constellation. The derivation of an expression for $\mathrm{BER}_{\mathbf{g}_{\mathrm{ch}}}^{(l)}$ is very similar to the derivation of expression (5.64) for

$\mathrm{SER}^{(l)}_{\mathbf{g}_{\mathrm{ch}}}$. However, instead of considering the probability that a received symbol u_l is not an element of the correct decision area $\mathcal{D}(\mathfrak{c})$ as in (5.65), one must take a weighted sum over all erroneous symbols $\hat{\mathfrak{c}}$ of the probability that the received symbol is within the incorrect decision area $\mathcal{D}(\hat{\mathfrak{c}})$. In this sum, the weight coefficients are equal to the number of bit differences $N_{\neq}$ between the bit labels associated with $\mathfrak{c}$ and $\hat{\mathfrak{c}}$. Hence,

$$\mathrm{BER}^{(l)}_{\mathbf{g}_{\mathrm{ch}}} = \frac{1}{M}\frac{1}{\log_2(M)} \sum_{\substack{\mathfrak{c},\hat{\mathfrak{c}}\in\mathcal{C}_{M-\mathrm{PAM}} \\ \mathfrak{c}\neq\hat{\mathfrak{c}}}} N_{\neq}\left(\mathfrak{c},\hat{\mathfrak{c}}\right) \mathbb{E}_{\mathbf{a}_{\mathrm{ISI}}}\left[P(\hat{\mathfrak{c}}|\mathfrak{c},\mathbf{a}_{\mathrm{ISI}})\right], \tag{5.70}$$

where

$$P(\hat{\mathfrak{c}}|\mathfrak{c},\mathfrak{a}_{\mathrm{ISI}}) = \Pr\left(\left(1+\mathrm{e}_l\right)\mathfrak{c} + \mathrm{isi}_l\left(\mathfrak{a}_{\mathrm{ISI}}\right) + \mathrm{w}_l \in \mathcal{D}\left(\hat{\mathfrak{c}}\right)\right). \tag{5.71}$$

For larger M, the number of terms in $\mathrm{BER}^{(l)}_{\mathbf{g}_{\mathrm{ch}}}$ rapidly increases and the number of bit differences $N_{\neq}$ cannot be described in general, making it hard to further simplify expression (5.70). In Appendix 11.4, the $\mathrm{BER}^{(l)}_{\mathbf{g}_{\mathrm{ch}}}$ expression is made explicit for the 4-PAM and the 8-PAM constellation from Fig. 5.5.

As an alternative, a simple lower bound $\mathrm{BER}^{(l)}_{\mathbf{g}_{\mathrm{ch}},\mathrm{LB}}$ on $\mathrm{BER}^{(l)}_{\mathbf{g}_{\mathrm{ch}}}$ is constructed by setting $N_{\neq}$ in (5.70) equal to 1 as the bit labels of two data symbols differ at least at one position. Since

$$\sum_{\substack{\hat{\mathfrak{c}}\in\mathcal{C}_{M-\mathrm{PAM}} \\ \mathfrak{c}\neq\hat{\mathfrak{c}}}} P(\hat{\mathfrak{c}}|\mathfrak{c},\mathfrak{a}_{\mathrm{ISI}}) = P(\mathrm{error}|\mathfrak{c},\mathfrak{a}_{\mathrm{ISI}}), \tag{5.72}$$

this lower bound is actually equal to the $\mathrm{SER}^{(l)}_{\mathbf{g}_{\mathrm{ch}}}$ divided by $\log_2(M)$, i.e,

$$\mathrm{BER}^{(l)}_{\mathbf{g}_{\mathrm{ch}},\mathrm{MPAM,LB}} = \frac{\mathrm{SER}^{(l)}_{\mathbf{g}_{\mathrm{ch}}}}{\log_2(M)}. \tag{5.73}$$

When the SNR is large and $\left(1+\mathrm{e}_l\right)\mathfrak{c} + \mathrm{isi}_l\left(\mathfrak{a}_{\mathrm{ISI}}\right) \in \mathcal{D}\left(\mathfrak{c}\right)$ for all considered $\mathfrak{c}$ and $\mathfrak{a}_{\mathrm{ISI}}$, the lower bound from (5.73) is expected to be tight, because decision errors involving neighboring symbols are far more likely than errors involving non-neighboring symbols.

Similar to $\overline{\mathrm{SER}}$, the BER averaged over all symbol streams and channel realization, i.e., $\overline{\mathrm{BER}}$, is defined as

$$\overline{\mathrm{BER}} = \mathbb{E}_{\mathbf{G}_{\mathrm{ch}}}\left[\frac{1}{L}\sum_{l=1}^{L}\mathrm{BER}^{(l)}_{\mathbf{g}_{\mathrm{ch}}}\right]. \tag{5.74}$$

5.4.3 Numerical evaluation of the SER and BER expressions

Two important obstacles must be overcome when evaluating the $\overline{\mathrm{SER}}$ in (5.69).

- A closed-form expression of the expected value $\mathbb{E}_{\mathbf{G}_{\mathrm{ch}}}[\cdot]$ in (5.69) is almost impossible to derive, even when the channel distribution is perfectly known. A simple alternative that is employed here is to numerically approximate the expectation $\mathbb{E}_{\mathbf{G}_{\mathrm{ch}}}[\cdot]$ by the arithmetic average over a representative subset of N_{ch} channel realizations. When N_{ch} is large enough, this approach should yield reliable numerical results with satisfactory accuracy.

- A similar problem is encountered in the computation of $\mathbb{E}_{\mathbf{a}_{\mathrm{ISI}}}[\cdot]$ in (5.68), since the distribution of $\mathrm{isi}_l(k)$ does not allow to formulate a simple closed-form expression for (5.68). To evaluate (5.68), one could sum over all possible $\mathbf{a}_{\mathrm{ISI}}$. However, the number of terms in $\mathbb{E}_{\mathbf{a}_{\mathrm{ISI}}}[\cdot]$ is equal to $M^{LL_{\mathrm{G}}-1}$, which increases exponentially with the channel length, the equalizer length, and the number of data streams, limiting the practicality of this approach as excessive computation time would be required.

Instead, several alternatives are presented to evaluate $\mathrm{SER}_{\mathbf{g}_{\mathrm{ch}}}^{(l)}$ with a controlled amount of computational complexity.

First of all, the sum over all possible $\mathbf{a}_{\mathrm{ISI}}$ could be approximated by restricting the expectation to N randomly generated terms. Hence, the corresponding approximation of (5.68) becomes

$$\mathrm{SER}_{\mathbf{g}_{\mathrm{ch}}}^{(l)} \approx \frac{2}{MN} \sum_{m=-\frac{M}{2}+1}^{\frac{M}{2}-1} \sum_{n=1}^{N} \mathrm{Q}\left(\frac{\Delta + \mathrm{e}_l(2m+1)\Delta + \mathrm{isi}_l(\mathbf{a}_{\mathrm{ISI},n})}{\sigma_{\mathrm{w}_l}} \right). \tag{5.75}$$

For large N, a sufficiently accurate estimate of the $\mathrm{SER}_{\mathbf{g}_{\mathrm{ch}}}^{(l)}$ is achieved even when $N \ll M^{LL_{\mathrm{G}}-1}$, yielding a considerably smaller computation time compared to the exact evaluation of the expectation $\mathbb{E}_{\mathbf{a}_{\mathrm{ISI}}}[\cdot]$. Selecting an appropriate N thus involves a trade-off between accuracy and computing power/time. Averaging this approximation over the symbol streams and the channel realizations results in a approximation of $\overline{\mathrm{SER}}$, which is denoted as $\overline{\mathrm{SER}}_1$.

Second, the problem of the prohibitive computation time can be circumvented by computing an upper and a lower bound on $\mathrm{SER}_{\mathbf{g}_{\mathrm{ch}}}^{(l)}$ with manageable complexity [78]. To derive these bounds, $\mathrm{isi}_l(\mathbf{a}_{\mathrm{ISI}})$ is decomposed into two terms: $\mathrm{isi}_l^{(1)}(\mathbf{a}_{\mathrm{ISI}}^{(1)})$ and $\mathrm{isi}_l^{(2)}(\mathbf{a}_{\mathrm{ISI}}^{(2)})$, i.e.,

$$\mathrm{isi}_l(\mathbf{a}_{\mathrm{ISI}}) = \sum_{j=1}^{LL_{\mathrm{G}}-1} (\mathbf{d}_{\mathrm{isi}_l})_j (\tilde{\mathbf{a}}_{\mathrm{ISI}})_j \tag{5.76}$$

$$= \mathrm{isi}_l^{(1)}(\mathbf{a}_{\mathrm{ISI}}^{(1)}) + \mathrm{isi}_l^{(2)}(\mathbf{a}_{\mathrm{ISI}}^{(2)}). \tag{5.77}$$

In (5.76), $\mathbf{d}_{\mathrm{isi}_l}$ is a vector containing all the coefficients of isi_l, i.e., all $(\alpha \mathbf{WG}(m)\mathbf{P})_{l,l'}$ and $(\alpha \mathbf{WG}(m)\mathbf{P} - \mathbf{B}(\mathrm{m}))_{l,l'}$ in equation (5.61), ordered in magnitude from large to small in descending order. Moreover, $\tilde{\mathbf{a}}_{\mathrm{ISI}}$ is a vector containing all

data symbols in the same order. Second, $\mathrm{isi}_l^{(1)}$ in (5.77) represents the interference caused by the K most dominant symbols corresponding to the first K elements of the vector $\tilde{\mathbf{a}}_{\mathrm{ISI}}$, whereas $\mathrm{isi}_l^{(2)}$ denotes the contribution from the remaining symbols. All dominant symbols are collected in the vector $\mathbf{a}_{\mathrm{ISI}}^{(1)}$, whereas the other symbols are gathered in the vector $\mathbf{a}_{\mathrm{ISI}}^{(2)}$. As $\mathrm{Q}(\cdot)$ is a convex function for positive arguments, the following property holds:

$$\mathrm{Q}(x+y)+\mathrm{Q}(x-y)\geq 2\mathrm{Q}(x). \tag{5.78}$$

when $x\geq|y|\geq 0$. By construction, $\mathbf{a}_{\mathrm{ISI}}^{(2)}$ and $-\mathbf{a}_{\mathrm{ISI}}^{(2)}$ are equally likely and $\mathrm{isi}_l^{(2)}(\mathbf{a}_{\mathrm{ISI}}^{(2)})=-\mathrm{isi}_l^{(2)}(-\mathbf{a}_{\mathrm{ISI}}^{(2)})$ such that the inequality from (5.78) can be applied to $\mathrm{SER}_{\mathbf{g}_{\mathrm{ch}}}^{(l)}$ defined in (5.68), when $(1+\mathrm{e}_l)\,\mathfrak{c}+\mathrm{isi}_l(\mathfrak{a}_{\mathrm{ISI}})\in\mathcal{D}(\mathfrak{c})$ for all considered $\mathfrak{c}$ and $\mathfrak{a}_{\mathrm{ISI}}$. Indeed, setting $\sigma_{\mathrm{w}_l}x=\Delta+\mathrm{e}_l(2m+1)+\mathrm{isi}_l^{(1)}(\mathbf{a}_{\mathrm{ISI}}^{(1)})$ and $\sigma_{\mathrm{w}_l}y=\left|\mathrm{isi}_l^{(2)}\left(\mathbf{a}_{\mathrm{ISI}}^{(2)}\right)\right|$ yields the following lower bound

$$\mathrm{SER}_{\mathbf{g}_{\mathrm{ch}},\mathrm{LB}}^{(l)}=\frac{2}{M}\sum_{m=-\frac{M}{2}+1}^{\frac{M}{2}-1}\mathbb{E}_{\mathbf{a}_{\mathrm{ISI}}^{(1)}}\left[\mathrm{Q}\left(\frac{\Delta+\mathrm{e}_l(2m+1)\Delta+\mathrm{isi}_l^{(1)}(\mathbf{a}_{\mathrm{ISI}}^{(1)})}{\sigma_{\mathrm{w}_l}}\right)\right], \tag{5.79}$$

where $\mathbb{E}_{\mathbf{a}_{\mathrm{ISI}}^{(1)}}[\cdot]$ denotes the expectation over $\mathbf{a}_{\mathrm{ISI}}^{(1)}$ and the assumption is made that $x\geq 0$. In fact, this lower bound corresponds to taking $\mathrm{isi}_l^{(2)}(\mathbf{a}_{\mathrm{ISI}}^{(2)})=0$. Moreover, the function $\mathrm{Q}(x+y)+\mathrm{Q}(x-y)$ is an increasing function of y when $x\geq y\geq 0$ such that a simple upper bound of $\mathrm{SER}_{\mathbf{g}_{\mathrm{ch}}}^{(l)}$ is given by

$$\begin{aligned}\mathrm{SER}_{\mathbf{g}_{\mathrm{ch}},\mathrm{UB}}^{(l)}=\frac{1}{M}\sum_{m=-\frac{M}{2}+1}^{\frac{M}{2}-1}\mathbb{E}_{\mathbf{a}_{\mathrm{ISI}}^{(1)}}\Bigg[&\mathrm{Q}\left(\frac{\Delta+\mathrm{e}_l(2m+1)\Delta+\mathrm{isi}_l^{(1)}(\mathbf{a}_{\mathrm{ISI}}^{(1)})+\mathrm{isi}_{l,\max}^{(2)}}{\sigma_{\mathrm{w}_l}}\right)\\&+\mathrm{Q}\left(\frac{\Delta+\mathrm{e}_l(2m+1)\Delta+\mathrm{isi}_l^{(1)}(\mathbf{a}_{\mathrm{ISI}}^{(1)})-\mathrm{isi}_{l,\max}^{(2)}}{\sigma_{\mathrm{w}_l}}\right)\Bigg],\end{aligned} \tag{5.80}$$

where the variable $\mathrm{isi}_{l,\max}^{(2)}$ denotes the maximum of $\mathrm{isi}_l^{(2)}\left(\mathbf{a}_{\mathrm{ISI}}^{(2)}\right)$ over $\mathbf{a}_{\mathrm{ISI}}^{(2)}$. This upper bound corresponds to assuming that $\mathrm{isi}_l^{(2)}(\mathbf{a}_{\mathrm{ISI}}^{(2)})$ takes the values $\mathrm{isi}_{l,\max}^{(2)}$ and $-\mathrm{isi}_{l,\max}^{(2)}$, each with probability $1/2$.

Thirdly, another approximation $\overline{\mathrm{SER}}_2$ is also directly developed from the decomposition of $\mathrm{isi}_l(\mathbf{a}_{\mathrm{ISI}})$ into the two terms $\mathrm{isi}_l^{(1)}\left(\mathbf{a}_{\mathrm{ISI}}^{(1)}\right)$ and $\mathrm{isi}_l^{(2)}\left(\mathbf{a}_{\mathrm{ISI}}^{(2)}\right)$ in (5.77). For long equalizer lengths and/or long channel lengths, the second term typically consists of a sum of numerous relatively small terms such that the distribution of $\mathrm{isi}_l^{(2)}\left(\mathbf{a}_{\mathrm{ISI}}^{(2)}\right)$ could be approximated by a zero-mean Gaussian distribution. By means of the definition in (5.76), the variance of $\mathrm{isi}_l^{(2)}\left(\mathbf{a}_{\mathrm{ISI}}^{(2)}\right)$

can be expressed as

$$\sigma^2_{\mathrm{isi}_l^{(2)}} = \mathbb{E}_{\mathbf{a}_{\mathrm{ISI}}^{(2)}}\left[\left|\mathrm{isi}_l^{(2)}\left(\mathbf{a}_{\mathrm{ISI}}^{(2)}\right)\right|^2\right] \tag{5.81}$$

$$= \sigma_{\mathrm{a}}^2 \sum_{j=K+1}^{LL_{\mathrm{G}}-1} \left|(\mathbf{d}_{\mathrm{isi}_l})_j\right|^2 . \tag{5.82}$$

Consequently, the contribution of $\mathrm{isi}_l^{(2)}$ could be approximated by an additional Gaussian noise source, yielding the following approximation of $\mathrm{SER}_{\mathbf{g}_{\mathrm{ch}}}^{(l)}$:

$$\mathrm{SER}_{\mathbf{g}_{\mathrm{ch}}}^{(l)} \approx \frac{2}{M} \sum_{m=-\frac{M}{2}+1}^{\frac{M}{2}-1} \mathbb{E}_{\mathbf{a}_{\mathrm{ISI}}^{(1)}}\left[\mathrm{Q}\left(\frac{\Delta + \mathrm{e}_l(2m+1)\Delta + \mathrm{isi}_l^{(1)}(\mathbf{a}_{\mathrm{ISI}}^{(1)})}{\sqrt{\sigma^2_{\mathrm{w}_l} + \sigma^2_{\mathrm{isi}_l^{(2)}}}}\right)\right] . \tag{5.83}$$

Obviously, the accuracy of this approximation and the bounds in (5.79) and (5.80) improves with increasing K, and all three converge to $\mathrm{SER}_{\mathbf{g}_{\mathrm{ch}}}^{(l)}$ when K is maximum, i.e., $LL_{\mathrm{G}} - 1$, as all interference contributions are then included in $\mathrm{isi}_l^{(1)}(\mathbf{a}_{\mathrm{ISI}}^{(1)})$ and none in $\mathrm{isi}_l^{(2)}(\mathbf{a}_{\mathrm{ISI}}^{(2)})$. However, the larger K, the more terms in the expectation $\mathbb{E}_{\mathbf{a}_{\mathrm{ISI}}^{(1)}}[\cdot]$, and the more complex the evaluation of this expectation becomes. Indeed, this expectation contains M^K terms, which rapidly grows with K, but could also be much smaller than the $M^{LL_{\mathrm{G}}-1}$ terms in the expectation $\mathbb{E}_{\mathbf{a}_{\mathrm{ISI}}}[\cdot]$ in (5.68). In the selection of K, a trade-off between accuracy and computational complexity must thus be evaluated.

The $\mathrm{SER}_{\mathbf{g}_{\mathrm{ch}}}^{(l)}$ in (5.68) is derived with the assumption that all previously detected symbols are correct. In practice, detection errors, however, do occur and they could even induce errors in later decisions due to the feedback filter. This error propagation could significantly impact the error probability such that numerical simulations to verify this impact are important. Unfortunately, this error propagation is a complicated process to model [46], and the standard approach to obtain an accurate SER including the effect of error propagation is therefore to numerically simulate the transmission of a large number $N_{\mathrm{prop}} \gg 1/\mathrm{SER}_{\mathbf{g}_{\mathrm{ch}}}^{(l)}$ of data symbols and count the number of errors made. This approach is typically computationally more demanding and more time-consuming than evaluating the $\overline{\mathrm{SER}}$ with perfect feedback, especially for low SER values. Hence, most numerical results in Section 5.5 are obtained with perfect feedback and the impact of the error propagation is investigated separately.

To evaluate $\overline{\mathrm{BER}}$ in (5.74), identical problems are encountered as for $\overline{\mathrm{SER}}$, and thus similar numerical evaluation methods can be proposed.

5.5 Numerical results and discussion

To investigate the performance of the equalization scheme and of the different equalization strategies from Section 5.2 and Table 5.1, this section discusses

numerical results for baseband M-PAM transmission on the MIMO chip-to-chip interconnect that is affected by manufacturing tolerances and presented in Chapter 2. For convenience, the definitions of some notations are first repeated here. The number of causal and anti-causal taps of a filter $\mathbf{Y}$ is respectively defined as $L_{\mathrm{Y}}^{(1)}$ and $L_{Y}^{(2)}$, respectively, whereas the total number of filter taps is given by L_{Y}. Moreover the number of feedback taps of the feedback filter is defined as L_{B} and the corresponding set of active time delays is symbolized by $\Phi_{\mathbf{B}}$. Furthermore, the channel variability is characterized by the variable σ_r. Finally, the integer values N_{W} and N_{P} define the tap spacing of the filters $\mathbf{W}$ and $\mathbf{P}$, respectively, whereas the value of ϵ determines the sampling delay.

In this discussion below, the SNR is defined as the ratio of the transmit energy per bit, E_b, to the one-sided spectral density of the channel noise, N_0, i.e., $\mathrm{SNR} = \frac{\mathrm{E_{TX}}}{\mathrm{log_2(M)N_0}}$. Moreover, the notation $L_{\mathrm{X}} = x$ is employed as the shorthand notation for $L_{\mathrm{P}}^{(1)} = L_{\mathrm{P}}^{(2)} = L_{\mathrm{W}}^{(1)} = L_{\mathrm{W}}^{(2)} = x$.

The subsections below cover various aspects of the baseband data transmission over the stochastic chip-to-chip interconnect. First, Subsection 5.5.1 analyzes the relative performance of the different strategies. Second, the feedback filter is the focus of the numerical simulations conducted in Subsection 5.5.2, whereas fractionally-spaced equalizers are considered in Subsection 5.5.3. Next, Subsection 5.5.4 investigates the convergence of the iterative algorithms corresponding to the different equalization strategies and several conclusions are extended to a general M-PAM constellation in Subsection 5.5.5. Finally, the accuracy of the numerical evaluation of the $\overline{\mathrm{BER}}$ is the main topic of Subsection 5.5.6.

Unless mentioned otherwise, the following values for the system parameters are employed: $\epsilon = 0$, $M = 2$, $N_{\mathrm{W}} = 1$, and $N_{\mathrm{P}} = 1$. Moreover, most $\overline{\mathrm{BER}}$ values are obtained by employing an approximation similar to (5.83) with $K = 20$.

5.5.1 Performance comparison of the different strategies

In Fig. 5.6, the performance of all equalization strategies in terms of $\overline{\mathrm{MSE}}$ and $\overline{\mathrm{BER}}$ is depicted as a function of σ_r with $L_{\mathrm{X}} = 7$ and a SNR equal to 25 dB. Moreover, the impact of the feedback filter is investigated by comparing the performance achieved by the equalization scheme without the feedback filter, i.e., $\Phi_{\mathbf{B}} = \emptyset$, in the left plots with the performance of the equalization scheme with a 16-tap feedback filter, i.e., $\Phi_{\mathbf{B}} = \Phi_{\mathbf{B},16} = \{1, \cdots, 16\}$, in the right plots. Of course, better $\overline{\mathrm{MSE}}$ and $\overline{\mathrm{BER}}$ performance is to be expected with the feedback filter, but the addition of this feedback filter is also expected to alter the relative performance of the different strategies. In this regard, the following observations can be made:

- Unsurprisingly, the fully adjustable strategy S-A yields superior performance compared to the other strategies. It even maintains a fairly constant $\overline{\mathrm{MSE}}$ and $\overline{\mathrm{BER}}$, irrespective of the channel variability σ_r. Fur-

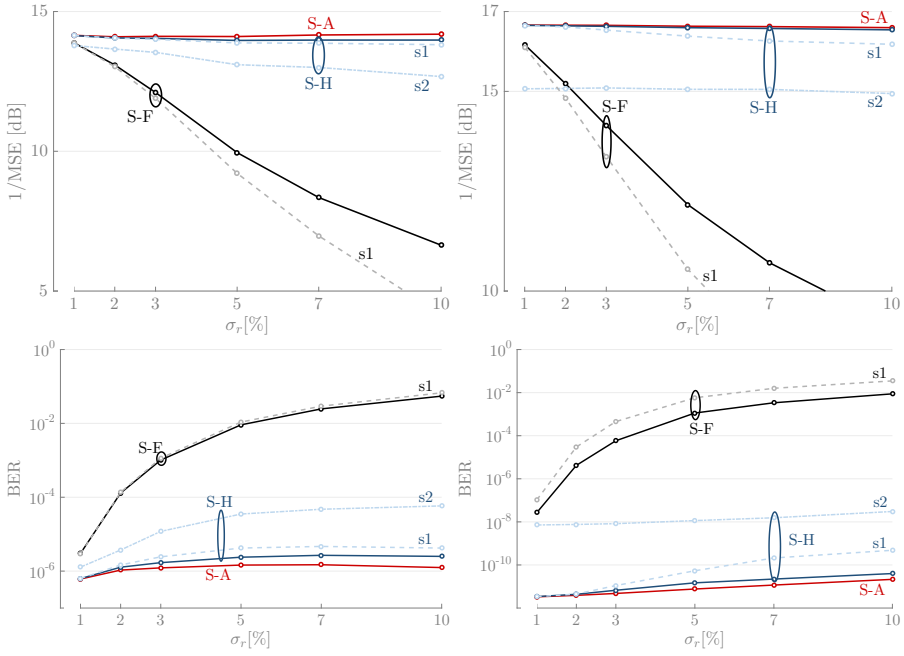

Figure 5.6: Performance of all equalization strategies in terms of both $1/\overline{\mathrm{MSE}}$ and $\overline{\mathrm{BER}}$ as a function of σ_r for SNR $= 25\,\mathrm{dB}$ and $L_\mathrm{X} = 7$. In the left plots, the feedback filter is omitted ($\Phi_\mathbf{B} = \emptyset$), whereas a 16-tap feedback filter is employed in the right plots ($\Phi_\mathbf{B} = \Phi_{\mathbf{B},16}$). Compared to the nearly constant performance of the adjustable strategy S-A, only a small decline is experienced by the hybrid strategy S-H, whereas the quality of the fixed strategy S-F rapidly deteriorates with increasing σ_r. The addition of an adjustable feedback filter provides a significant performance gain.

thermore, activating the feedback filter induces a significant performance improvement: a gain of approximately 2.5 dB in $\overline{\text{MSE}}$ and a substantial $\overline{\text{BER}}$ reduction by a factor up to 10^5, emphasizing the potential of an adjustable feedback filter.

- A small performance gap between the optimal hybrid strategy S-H and the adjustable strategy S-A is anticipated for small σ_r. When sufficient equalization parameters are adjustable, Fig. 5.6 confirms, however, that a partially adjustable equalization scheme is a suitable low-complexity alternative to the fully adjustable equalization scheme, even for larger σ_r, as the performance gap between S-H and S-A only slightly grows with increasing σ_r. When the feedback filter is present, the performance difference between the two strategies is even smaller as a relatively larger part of the equalization parameters is adjustable in the hybrid strategy.

- Especially at large σ_r, the optimal fixed strategy cannot compete with the adjustable strategy nor with the optimal hybrid strategy. Since the fixed strategy does not provide any mechanism to handle the variations between the channels, its performance rapidly degrades with increasing σ_r. Moreover, a fixed feedback filter sometimes even negatively impacts the $\text{BER}_{\mathbf{g}_{\text{ch}}}$ as it cannot adapt to the highly variable postcursor ISI (Fig. 2.3), thereby increasing (rather than reducing) the peak ISI for some channel realizations. When these channel realizations are dominant, the average $\overline{\text{BER}}$ increases.

- The importance of considering the second-order moments in the computation of the fixed equalization parameters is illustrated by the performance difference between the suboptimal approaches S-H_{s1} and S-F_{s1} and their optimal counterparts S-H and S-F. When the feedback filter is not active, this gap in performance slowly grows with increasing σ_r, but stays within limits even for large σ_r. On the other hand, when the feedback filter is present, the performance degradation is larger, because the full potential of the feedback filter is not unlocked in the computation of the fixed parts.

- To fairly compare the suboptimal strategy S-H_{s2} to the other strategies, the number of equalizer taps of the cascade of the fixed feedforward filter $\mathbf{W}_{\text{fix}}$ and the adjustable feedforward filter $\mathbf{W}_{\text{adj}}$ is kept at 15 taps, and divided as follows: $L^{(1)}_{\text{W,fix}} = L^{(2)}_{\text{W,fix}} = 2$ and $L^{(1)}_{\text{W,adj}} = L^{(2)}_{\text{W,adj}} = 5$. Even with this large number of adjustable taps, the performance of this suboptimal strategy is not satisfactory, emphasizing the positive impact of considering the adjustable equalization parameters in the design of the fixed parameters. A more detailed discussion on this suboptimal approach can be found below (Fig. 5.9).

When the amount of equalization resources, e.g., the length of the filters, is restricted or expensive, a proper balance between the cost and the performance

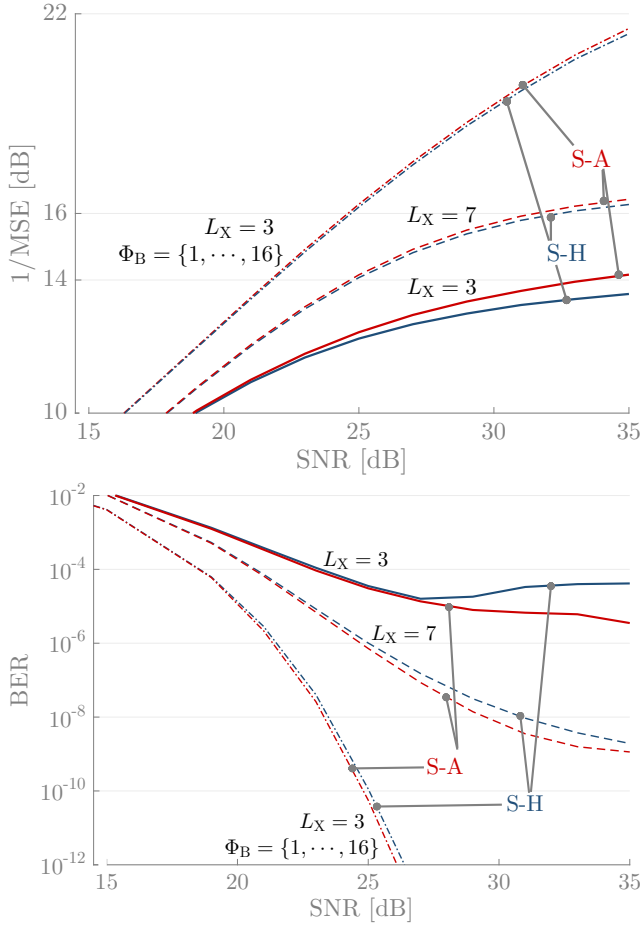

Figure 5.7: Performance of the adjustable and the hybrid strategy in terms of both $1/\overline{\text{MSE}}$ and $\overline{\text{BER}}$ as a function of SNR for $\sigma_r = 3\%$. Three sets of equalization parameters are considered: (i) $L_X = 3$ and $\Phi_{\mathbf{B}} = \emptyset$, (ii) $L_X = 7$ and $\Phi_{\mathbf{B}} = \emptyset$, and (iii) $L_X = 3$ and $\Phi_{\mathbf{B}} = \Phi_{\mathbf{B},16}$. The figure implies that short linear equalizers accompanied with a feedback filter are preferred to long linear equalizers without any feedback filter.

of the equalization is desirable. To evaluate this trade-off, a clear understanding is required of the impact of the different equalization filters on the performance. In this regard, Fig. 5.7 presents the performance of the adjustable and the hybrid strategy as a function of SNR for $\sigma_r = 3\%$ and for three equalization configurations: (i) a configuration with $L_{\mathrm{X}} = 3$, but without any feedback ($\Phi_{\mathbf{B}} = \emptyset$); (ii) a configuration that adds 16 additional taps to the linear equalization filters, but still without any feedback, i.e., $L_{\mathrm{X}} = 7$ and $\Phi_{\mathbf{B}} = \emptyset$; and (iii) a configuration with short linear equalization filters, but with a 16-tap feedback filter, i.e., $L_{\mathrm{X}} = 3$ and $\Phi_{\mathbf{B}} = \{1, \cdots, 16\}$. Particularly notable in Fig. 5.7 is the outstanding performance achieved in the third configuration, which can be contributed to the presence of the feedback filter. Indeed, increasing the filter length to $L_{\mathrm{X}} = 7$ only considerably lowers the $\overline{\mathrm{BER}}$ floor by a factor of 10^4, while this floor is completely eliminated when the feedback filter is active, illustrating that short linear equalizers with a feedback filter are to be preferred to long linear equalizers without any feedback.

An interesting question is how to choose the filter lengths of $\mathbf{P}$ and $\mathbf{W}$ when the total number of equalization taps of their cascade is predefined. For $\mathrm{SNR} = 25\,\mathrm{dB}$ and $\sigma_r = 5\%$, Fig. 5.8 focuses on this issue by presenting the $1/\overline{\mathrm{MSE}}$ and the $\overline{\mathrm{BER}}$ performance of the adjustable, the hybrid, and the fixed strategy as a function of L_{W}, while the cascade of $\mathbf{P}$ and $\mathbf{W}$ consists of 29 taps in total. In the left plots of Fig. 5.8, the feedback filter is absent ($\Phi_{\mathbf{B}} = \emptyset$), whereas a 16-tap feedback filter is active in the right plots ($\Phi_{\mathbf{B}} = \Phi_{\mathbf{B},16}$). The following observations hold:

- In terms of performance, the adjustable strategy is as expected superior to the hybrid and the fixed strategy for every L_{W}, irrespective whether the feedback filter is present or not. More interestingly, a distinct performance improvement is perceived when a linear filter is present at both the transmitter and the receiver compared to when only either $\mathbf{P}$ ($L_{\mathrm{W}} = 0$) or $\mathbf{W}$ ($L_{\mathrm{W}} = 29$) is active. One possible explanation for this observation is that when both $\mathbf{P}$ and $\mathbf{W}$ are active, the equalization task can be properly distributed between them such that this additional design freedom allows to lower the combined negative impact of the energy constraint and the noise enhancement. Finally, the performance of the adjustable strategy is fairly constant when both $\mathbf{P}$ and $\mathbf{W}$ are active, making the exact division of the equalizer taps between the transmitter and the receiver irrelevant, as long as both linear equalizers are present.

- As for the fixed equalization strategy, the performance is poor and L_{W} does not seem to positively nor negatively impact it.

- In the hybrid strategy, a complexity-performance trade-off is inherent to the division of the equalization coefficients between $\mathbf{P}$ and $\mathbf{W}$: the larger L_{W}, the better the performance but the larger the complexity. Indeed, when the feedback filter is omitted, the hybrid strategy is identical to the fixed strategy for $L_{\mathrm{W}} = 0$. When L_{W} increases, the performance of the

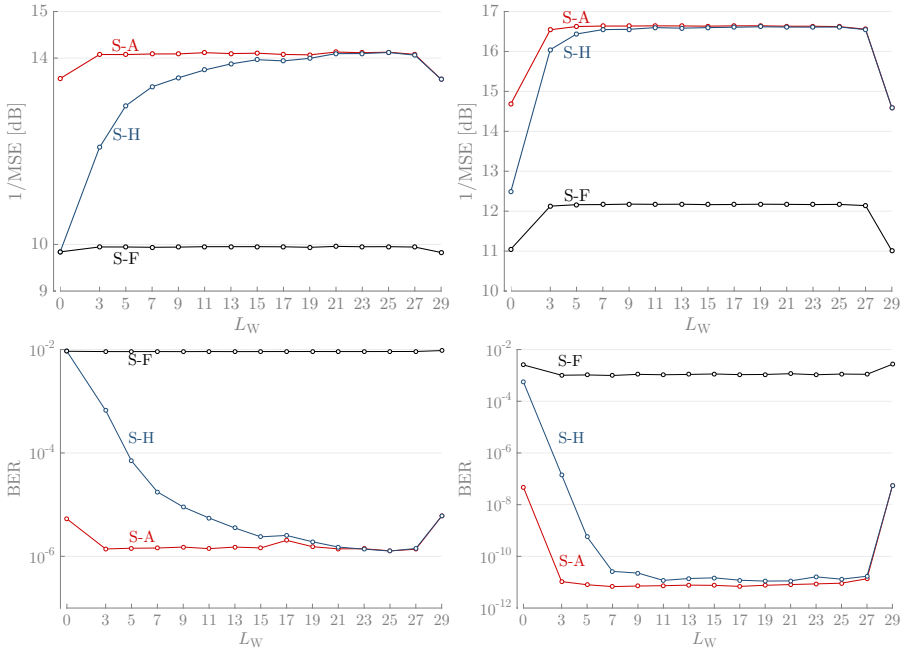

Figure 5.8: Performance of the adjustable, the hybrid, and the fixed strategy in terms of both $1/\overline{\text{MSE}}$ and $\overline{\text{BER}}$ as a function of L_W for SNR $= 25\,\text{dB}$ and $\sigma_r = 5\%$. While L_W varies, the total number of equalizer taps in the cascade of $\mathbf{P}$ and $\mathbf{W}$ is always 29. In the left plots, the feedback filter is omitted ($\Phi_\mathbf{B} = \emptyset$), whereas a 16-tap feedback filter is employed in the right plots ($\Phi_\mathbf{B} = \Phi_{\mathbf{B},16}$). Performance improves when both $\mathbf{P}$ and $\mathbf{W}$ are present, while the hybrid strategy performs nearly as good as the adjustable strategy when L_W is sufficiently large.

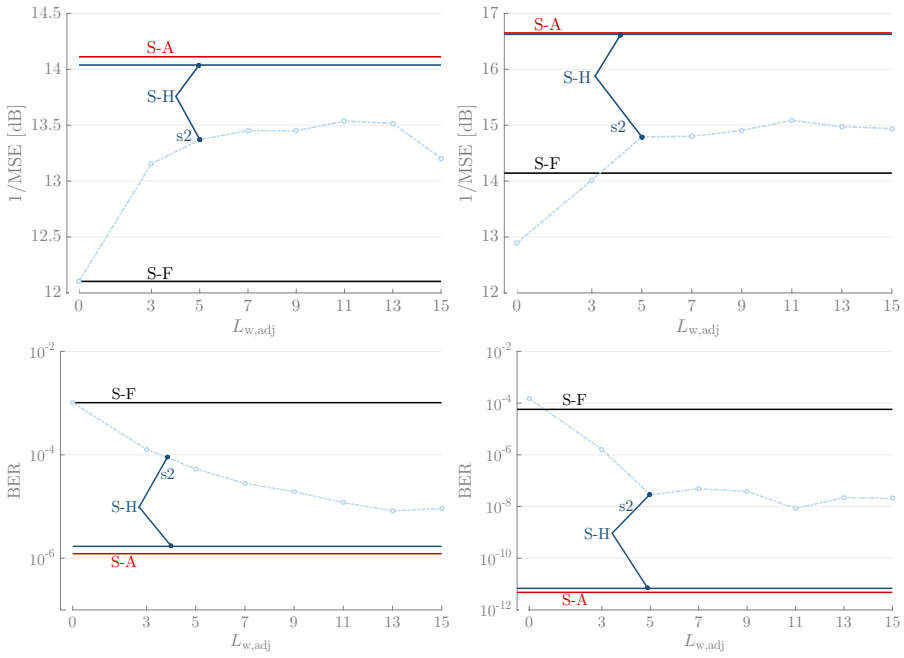

Figure 5.9: Performance of strategy S-H_{s2} in terms of both $1/\overline{\mathrm{MSE}}$ and $\overline{\mathrm{BER}}$ as a function of $L_{\mathrm{W,adj}}$ for $L_{\mathrm{P}}^{(1)} = L_{\mathrm{P}}^{(2)} = 7$, SNR $= 25\,\mathrm{dB}$, and $\sigma_r = 3\%$, while the total number of taps in $\mathbf{W}$ is equal to 15. As a reference, the performances of the optimal S-A, S-H, and S-F are included as well. In the left plots, the feedback filter is absent ($\Phi_{\mathbf{B}} = \emptyset$), whereas a 16-tap feedback filter is employed in the right plots ($\Phi_{\mathbf{B}} = \Phi_{\mathbf{B},16}$). Strategy S-$H_{s2}$ does not attain the performance levels of the optimal hybrid strategy, even when most of the taps of $\mathbf{W}$ are adjustable.

hybrid strategy gradually improves and converges to the performance of the adjustable strategy. For instance, when $L_{\mathrm{W}} \geq 11$, the hybrid strategy results in a $\overline{\mathrm{MSE}}$ and a $\overline{\mathrm{BER}}$ that is smaller than the $\overline{\mathrm{MSE}}$ and $\overline{\mathrm{BER}}$ achieved in the adjustable strategy with only one 29-tap linear equalizer. Consequently, a relatively large number of fixed equalizer taps in the hybrid strategy does not impede decent performance. Moreover, the performance difference between the adjustable and the hybrid strategy diminishes even further when the feedback filter is present.

To explore the influence of the number of adjustable taps $L_{\mathrm{W,adj}}$ on the performance of the suboptimal strategy S-H_{s2}, Fig. 5.9 shows the $1/\overline{\mathrm{MSE}}$ and the $\overline{\mathrm{BER}}$ performance of this strategy as a function of $L_{\mathrm{W,adj}}$ (from 0 to 15) for $L_{\mathrm{P}}^{(1)} = L_{\mathrm{P}}^{(2)} = 7$, SNR $= 25\,\mathrm{dB}$ and $\sigma_r = 3\%$, while the total number of taps of the filter $\mathbf{W}$, i.e., the cascade of $\mathbf{W}_{\mathrm{fix}}$ and $\mathbf{W}_{\mathrm{adj}}$, is kept constant to

15. Similar to Figs. 5.6 and 5.8, the feedback filter is excluded in the left plots ($\Phi_{\mathbf{B}} = \emptyset$) and a 16-tap is present in the right plots ($\Phi_{\mathbf{B}} = \Phi_{\mathbf{B},16}$). As a reference, the performance corresponding to the adjustable, the hybrid, and the fixed strategy with the same number of equalization parameters is included. Following observations can be made:

- As for $L_{\mathrm{W,adj}} = 0$, strategy S-H_{s2} is completely identical to the optimal fixed strategy when the feedback is omitted. In the case of $\Phi_{\mathbf{B}} = \Phi_{\mathbf{B},16}$, however, the feedback filter is adjustable in the former strategy, whereas it is fixed in the latter strategy. Nevertheless, S-H_{s2} performs worse than S-F, because the design of the fixed linear filters in S-H_{s2} does not consider the adjustable feedback filter, while the fixed feedback filter is considered in the design of the fixed linear filters in S-F.

- Irrespective of the number of feedback taps, increasing the number of variable taps, $L_{\mathrm{W,adj}}$ from small to larger values, positively influences the performance of S-H_{s2}. However, this suboptimal strategy never closely approximates the performance levels of the optimal hybrid strategy, even when $L_{\mathrm{W,adj}}$ is relatively large, e.g., more than 0.5 dB loss in $\overline{\mathrm{MSE}}$ when $\Phi_{\mathbf{B}} = \emptyset$ and more than 1.5 dB loss when $\Phi_{\mathbf{B}} = \Phi_{\mathbf{B},16}$. One possible explanation is that the iterative computation of the fixed pre-equalizer $\mathbf{P}$ in S-H_{s2} is performed with a feedforward filter, which is not only fixed, but also shorter than the adjustable and longer filter of the optimal hybrid strategy. Moreover, this iterative computation of $\mathbf{P}$ and $\mathbf{W}_{\mathrm{fix}}$ totally neglects any feedback in S-H_{s2}. Consequently, the resulting pre-equalizer $\mathbf{P}$ performs worse than the pre-equalizer $\mathbf{P}$ obtained by the optimal hybrid strategy.

- One exception to the observation above is that the performance of S-H_{s2} worsens when all coefficients of $\mathbf{W}$ are adjustable ($L_{\mathrm{W}} = L_{\mathrm{W,adj}}$). In this case, the fixed $\mathbf{W}_{\mathrm{fix}}$ is not present such that no iterations are involved in the computation of the fixed $\mathbf{P}$. The presence of the feedforward filter $\mathbf{W}$ and the feedback filter $\mathbf{B}$ at the receiver is then in fact completely ignored in the design of $\mathbf{P}$, yielding poor results.

In the computation of the fixed equalizer(s) in the hybrid and the fixed strategy, the number of channel realizations, N_{ch}, that are incorporated in the expectation $\mathbb{E}_{\mathbf{G}_{\mathrm{ch}}}[\cdot]$ is preferably as small as possible to attain low complexity and corresponding fast computation. However, when N_{ch} is too small, the subset of N_{ch} channel realizations cannot capture the full variability of the channel, risking unreliable and inferior average performance. This trade-off between performance and complexity is further illustrated in Fig. 5.10, which plots the $\overline{\mathrm{MSE}}$ performance as a function of N_{ch} for $\mathrm{SNR} = 25\,\mathrm{dB}$, $\sigma_r = 3\%$, $L_{\mathrm{X}} = 7$, and $\Phi_{\mathbf{B}} = \emptyset$. For each value of N_{ch}, 200 simulation runs are conducted. In each run, N_{ch} channels are randomly selected from a database of 1000 channel realizations to compute the fixed equalizers. Next, the $\overline{\mathrm{MSE}}$ is

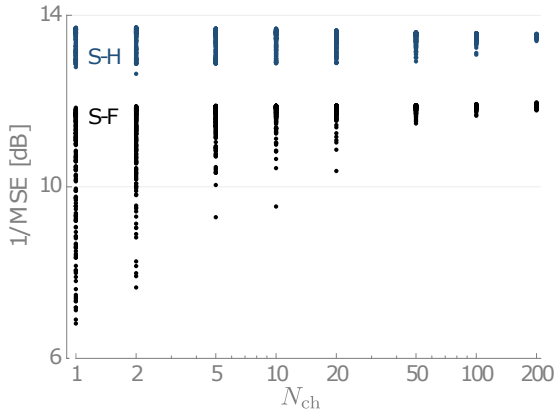

Figure 5.10: Performance of the hybrid and the fixed strategy in terms of $1/\overline{\mathrm{MSE}}$ as a function of the number of channel realizations N_{ch} incorporated in the expectation $\mathbb{E}_{\mathbf{G}_{\mathrm{ch}}}[\cdot]$ for SNR $= 25\,\mathrm{dB}$, $\sigma_r = 3\%$, $L_{\mathrm{X}} = 7$, and $\Phi_{\mathbf{B}} = \emptyset$. The performance of both strategies is sensitive to small N_{ch}, while reliable performance is only to be expected for sufficiently large N_{ch}.

evaluated based on the other $1000 - N_{\mathrm{ch}}$ channel realizations. Fig. 5.10 confirms that $\overline{\mathrm{MSE}}$ is sensitive to small N_{ch}, especially in the case of the fixed strategy. Reliable performance is to be expected only for sufficiently large N_{ch}, i.e., N_{ch} greater than a certain $N_{\mathrm{ch,min}}$. This threshold $N_{\mathrm{ch,min}}$ naturally depends on the channel characteristics, and can be visually determined in Fig. 5.10 as approximately 200.

5.5.2 Feedback filter: a detailed discussion

When the feedback filter $\mathbf{B}$ consists of L_{B} taps, deriving the set of L_{B} active time delays yielding the lowest $\overline{\mathrm{MSE}}$ is an interesting subject to study. Here, an active time delay m is defined as a causal time delay, on which the feedback filter is active, i.e., $\mathbf{B}(m) \neq \mathbf{0}$. Because the relationship between the performance, e.g., MSE, and the set of active time delays is complicated, analytical minimization is unfortunately not a viable option. Moreover, numerical evaluation of the performance corresponding to each possible set of L_{B} active time delays is not practical either, as the number of possible sets is equal to the number of L_{B}-combinations from a set with $L_{\mathrm{G}}^{(2)}$ elements, i.e., $\binom{L_{\mathrm{G}}^{(2)}}{L_{\mathrm{B}}}$, which is often impractically large. However, decent to excellent performance is to be expected when most of the dominant causal ISI components are eliminated by the feedback filter. In this regard, Fig. 5.11 plots the $1/\overline{\mathrm{MSE}}$ and the $\overline{\mathrm{BER}}$ performance of the adjustable, the hybrid, and the fixed strategy for an interconnect with $\sigma_r = 3\%$ as a function of the SNR with $L_{\mathrm{X}} = 3$. The set of active time delays and the feedback filter are computed according to one of the

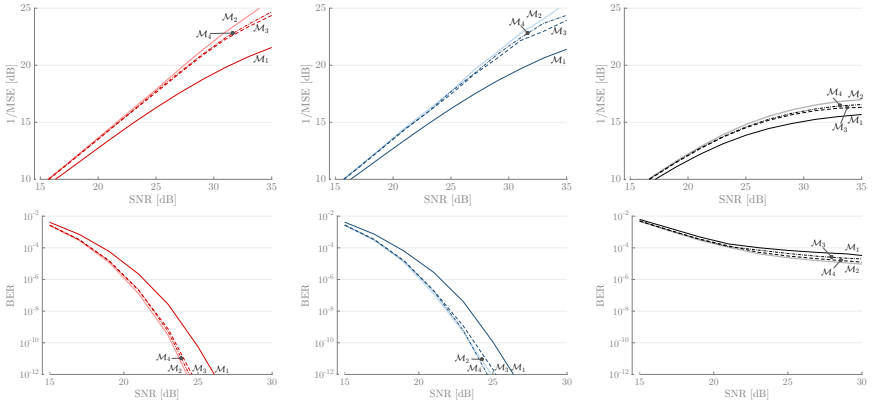

Figure 5.11: Performance of the adjustable (left), the hybrid (middle), and the fixed (right) strategy in terms of $1/\overline{\text{MSE}}$ and $\overline{\text{BER}}$ as a function of SNR for $\sigma_r = 3\%$ with $L_{\text{X}} = 3$. In total, four different methods to select the set of active time delays and to compute the feedback filter are examined. Determining the set $\Phi_{\mathbf{B}}$ by keeping only a select number of dominant taps of a long feedback filter does in general not induce a major performance loss.

following methods:

1. In the first method $\mathcal{M}_1$, all L_{B} feedback taps correspond to the first L_{B} causal time delays, as traditionally the largest causal ISI occurs close to the time delay on which the decision is based. In Fig. 5.11, L_{B} is equal to 16 such that $\Phi_{\mathbf{B}} = \Phi_{\mathbf{B},16}$. For the chip-to-chip interconnect, this method is generally not optimal as this communication channel suffers from reflections, whose ISI is not within the range of this $\Phi_{\mathbf{B}}$.

2. The performance of a long equalizer that eliminates all causal ISI is a lower bound on the performance of a feedback filter with a limited number of taps. To gain insight into how well the feedback filter with 16-taps performs compared to a long feedback filter, method $\mathcal{M}_2$ extends the feedback filter from $\mathcal{M}_1$ to $L_{\text{B}} = 100$ taps, i.e., $\Phi_{\mathbf{B}} = \{1, \cdots, 100\}$ such that the first reflection is within the range of $\Phi_{\mathbf{B}}$.

3. As for the long feedback filter in method $\mathcal{M}_2$, many taps are observed to be relatively small in magnitude, which is exploited by the third method $\mathcal{M}_3$. In this method, the feedback filter from method $\mathcal{M}_2$ is active only at the time delays corresponding to the $L_{\text{B}} = 16$ dominant feedback matrices, which are the 16 matrices with largest $\|\mathbf{B}(m)\|^2$. The resulting set $\Phi_{\mathbf{B},\mathcal{M}_3}$ depends on the channel realization in S-A and S-H, but is identical for all channel realizations in S-F. Compared to $\mathcal{M}_2$, both the number of active time delays and the complexity greatly reduce in $\mathcal{M}_3$, while the performance difference should be relatively small because both

methods are able to eliminate the largest dominant causal ISI generated by the direct pulse and the first reflection.

4. Except for the feedback filter, all equalization parameters in method $\mathcal{M}_3$ are specifically designed with the assumption that the feedback filter is active in the complete range of $\Phi_{\mathbf{B}} = \{1, \cdots, 100\}$. However, the feedback filter is only active in the set $\Phi_{\mathbf{B},\mathcal{M}_3}$ such that the equalization parameters are not necessarily optimal. In method $\mathcal{M}_4$, all equalization parameters are therefore recalculated with $\Phi_{\mathbf{B}} = \Phi_{\mathbf{B},\mathcal{M}_3}$, which should in theory yield superior performance. The full procedure to compute the equalization parameters in method $\mathcal{M}_4$ is presented in Algorithm 5.1. Interestingly, full convergence is not required in the computation of $(\mathbf{P}^\star, \alpha^\star, \mathbf{W}^\star, \mathbf{B}^\star)$ during the first step of the algorithm, as the relevant information, $\Phi_{\mathbf{B},\mathcal{M}_3}$, can generally be derived after only a few iterations between $(\mathbf{P}, \alpha)$ and $\mathbf{W}$.

Algorithm 5.1 Computation of the equalization parameters in $\mathcal{M}_4$.

1. Compute $(\mathbf{P}^\star, \alpha^\star, \mathbf{W}^\star, \mathbf{B}^\star)$ with $\Phi_{\mathbf{B}} = \{1, \cdots, 100\}$.
2. Determine $\Phi_{\mathbf{B},\mathcal{M}_3}$ by selecting the L_{B} dominant time delays of $\mathbf{B}^\star$.
3. Recompute $(\mathbf{P}^\star, \alpha^\star, \mathbf{W}^\star, \mathbf{B}^\star)$ with $\Phi_{\mathbf{B}} = \Phi_{\mathbf{B},\mathcal{M}_3}$.

As anticipated, Fig. 5.11 confirms that the shorter feedback filter of the first method $\mathcal{M}_1$ is outperformed by the longer feedback filter of the second method $\mathcal{M}_2$ regardless of the equalization strategy. More interesting is that selecting only the $L_{\mathrm{B}} = 16$ most dominant taps in method $\mathcal{M}_3$ causes only a minor performance loss compared to $\mathcal{M}_2$. Although the equalization parameters in $\mathcal{M}_3$ are not specifically designed for $\Phi_{\mathbf{B},\mathcal{M}_3}$, $\mathcal{M}_3$ achieves significantly better performance than $\mathcal{M}_1$, because the feedback filter in $\mathcal{M}_3$ reduces also the dominant causal interference of the first reflection. Based on the performance difference between $\mathcal{M}_4$ and $\mathcal{M}_3$, one can deduce that a only marginal gain is obtained by recomputing the equalization coefficients in $\mathcal{M}_4$ for the specific set of time delays $\Phi_{\mathbf{B},\mathcal{M}_3}$.

This performance difference between methods $\mathcal{M}_3$ and $\mathcal{M}_4$ is further investigated in Fig. 5.12, which plots the $1/\overline{\mathrm{MSE}}$ and the $\overline{\mathrm{BER}}$ performance of the adjustable, the hybrid, and the fixed strategy for both these methods as a function of L_{B} ranging from 1 to 100 with $\Phi_{\mathbf{B}} = \{1, \cdots, 100\}$. Other parameters such as σ_r, SNR, and L_{X} are respectively set to 3%, 20 dB, and 3. The following conclusions can be drawn:

- As for $\mathcal{M}_3$, increasing L_{B} implies that additional time delays are added to the set $\Phi_{\mathbf{B},\mathcal{M}_3}$ and thus more causal time delays become active. Consequently, $\overline{\mathrm{MSE}}$ must be a decreasing function of L_{B} as all other equalization parameters remain identical. This decrease is confirmed by Fig.

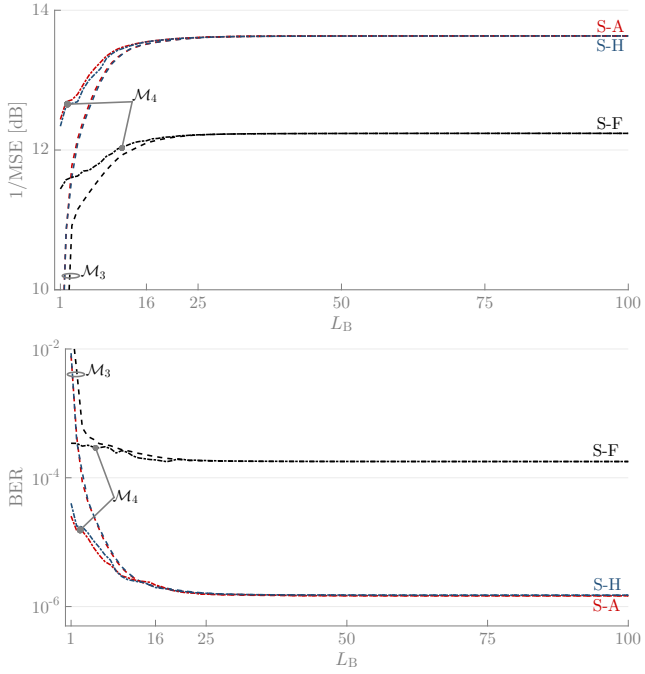

Figure 5.12: $1/\overline{\mathrm{MSE}}$ and $\overline{\mathrm{BER}}$ performance of S-A, S-H, and S-F for methods $\mathcal{M}_3$ and $\mathcal{M}_4$ as a function of L_{B} with $\Phi_{\mathbf{B}} = \{1, \cdots, 100\}$. Moreover, σ_r, SNR, and L_{X} are set to 3%, 20 dB, and 3, respectively. Method $\mathcal{M}_4$ clearly outperforms method $\mathcal{M}_3$ for small L_{B}, whereas the performance of both methods is nearly constant and identical for $L_{\mathrm{B}} > 25$.

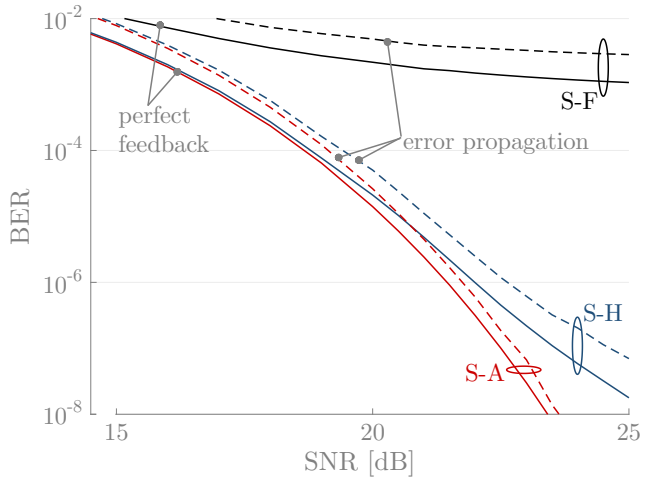

Figure 5.13: Comparison of $\overline{\text{BER}}$ achieved by a feedback filter with perfect feedback and by the realistic feedback filter suffering from error propagation as a function of SNR for strategies S-A, S-H, and S-F. Moreover, $\Phi_{\mathbf{B}} = \Phi_{\mathbf{B},16}$ and $\sigma_r = 5\%$. The impact of the error propagation is only small to moderate and fairly constant over the whole SNR range.

5.12, which also reveals that $\overline{\text{MSE}}$ converges fairly quickly to the lowest value reached at $L_{\text{B}} = 100$. Indeed, $\overline{\text{MSE}}$ at $L_{\text{B}} = 25$ is less than 1% larger than the $\overline{\text{MSE}}$ at $L_{\text{B}} = 100$. These results depend of course on the channel, but do illustrate that setting relatively small feedback taps to zero does not majorly impact the $\overline{\text{MSE}}$ performance. Furthermore, a similar reasoning holds for the $\overline{\text{BER}}$ performance.

- Recalculating all equalization parameters in method $\mathcal{M}_4$ improves the $\overline{\text{MSE}}$ and the $\overline{\text{BER}}$ performance compared to method $\mathcal{M}_3$, especially for low L_{B}, which can be explained by the following reasoning. In the design of $\mathbf{P}$ and $\mathbf{W}$ in $\mathcal{M}_3$, the residual ISI for all $m \in \Phi_{\mathbf{B}} \setminus \Phi_{\mathbf{B},\mathcal{M}_3}$ is not taken into account as this ISI is assumed to be neutralized by the feedback filter. In practice, only the ISI for $m \in \Phi_{\mathbf{B},\mathcal{M}_3}$ is eliminated and when L_{B} is too small not all dominant ISI is neutralized, inducing a considerable degradation to the MSE performance. In $\mathcal{M}_4$ however, all residual ISI for all $m \in \Phi_{\mathbf{B}} \setminus \Phi_{\mathbf{B},\mathcal{M}_3}$ is considered in the design of $\mathbf{P}$ and $\mathbf{W}$ such that excessively large residual ISI is avoided, even when L_{B} is small.

- The performance difference between S-A and S-H is almost negligible as the channel variance is only 3% and the length of the linear filters is moderately large, i.e., $L_{\text{X}} = 3$.

All $\overline{\text{BER}}$ results presented above are generated with the assumption that all decisions on previously transmitted symbols are correct, which is referred to

as 'perfect feedback'. In practice, this assumption does not hold and one erroneous decision could severely impair the error performance, since this decision error influences future decisions. This error propagation is difficult to model mathematically [46], and Fig. 5.13 therefore compares the $\overline{\text{BER}}$ in the case of perfect feedback with the simulated $\overline{\text{BER}}$ achieved by a realistic feedback filter suffering from error propagation. For both cases, the $\overline{\text{BER}}$ performance of S-A, S-H, and S-F is presented as a function of the SNR with $L_{\text{X}} = 3$, $\Phi_{\mathbf{B}} = \Phi_{\mathbf{B},16}$, and $\sigma_r = 5\%$. As for the perfect feedback, the $\overline{\text{BER}}$ is computed by means of the procedure described in Section 5.4, whereas the $\overline{\text{BER}}$ including the effect of error propagation is obtained by simulating the transmission of $1.2 \cdot 10^7$ random symbols over each of the 1000 channel realizations, yielding a total of $1.2 \cdot 10^{10}$ transmitted symbols. Following observations can be made:

- Only a small to moderate increase in $\overline{\text{BER}}$ is observed when error propagation is present. Indeed, the degradation in SNR is less than 0.5 dB and 1 dB in S-A and S-H, respectively, while maximum 3 times as much errors are present at high SNR in the case of S-F. This observation thus validates the assumption of perfect feedback when a fast and reliable indication of $\overline{\text{BER}}$ is required.

- The equalization scheme with a feedback filter affected by error propagation still outperforms the equalization scheme without any feedback (Fig. 5.2), even when the linear filters in the latter are relatively long. This observation is confirmed by comparing Fig. 5.13 with Fig. 5.7. Indeed, the $\overline{\text{BER}}$ achieved over the channel with $\sigma_r = 5\%$ equalized by a DFE with error propagation in Fig. 5.13 is lower than the $\overline{\text{BER}}$ achieved over the channel with $\sigma_r = 3\%$ equalized by means of linear filters with $L_{\text{X}} = 7$ in Fig. 5.7.

The impact of error propagation could of course also be dependent on the number of feedback taps and the placement of the active time delays. Fig. 5.14 therefore adds the $\overline{\text{BER}}$ with error propagation to the $\overline{\text{BER}}$ results of Fig. 5.12 in the case of method $\mathcal{M}_4$. This figure confirms that the performance difference between perfect and realistic feedback is not only fairly constant over the entire range of L_{B}, but also small to moderate for all equalization strategies. Moreover, similar results are obtained for configuration $\mathcal{M}_3$ (not shown).

In conclusion, the numerical results without error propagation provide a good indication of the actual error performance of the feedback filter with error propagation.

5.5.3 Fractionally-spaced equalizers

This subsection considers fractionally-spaced linear filters as a means to further improve the performance. In particular, Fig. 5.15 investigates the impact of doubling the operating rate of either $\mathbf{P}$ or $\mathbf{W}$ on $\overline{\text{MSE}}$ and $\overline{\text{BER}}$ as a function of

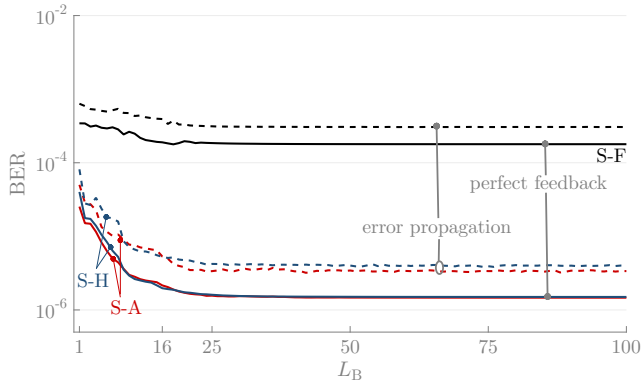

Figure 5.14: Influence of the error propagation on the $\overline{\text{BER}}$ performance as a function of L_B in the case of method $\mathcal{M}_4$, $\sigma_r = 3\%$, SNR $= 20\,\text{dB}$, and $L_\text{X} = 3$. The effect of the error propagation is fairly constant over the whole range of L_B.

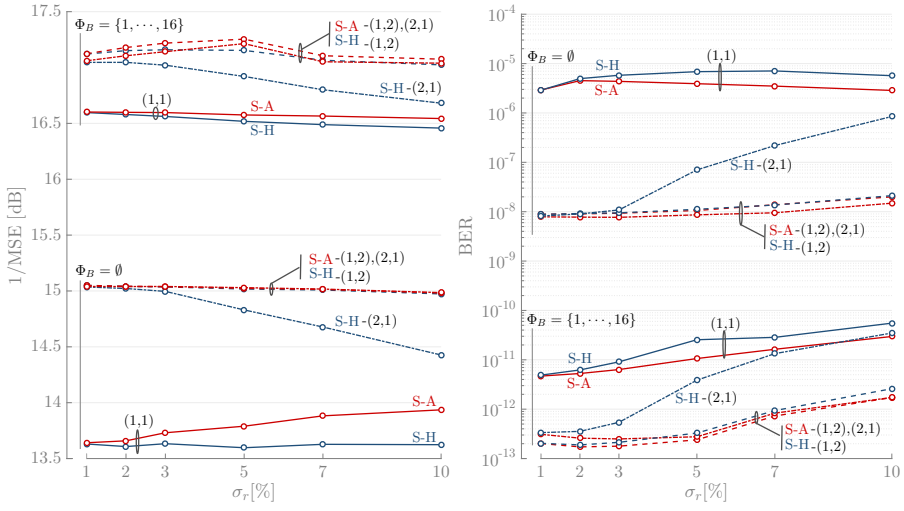

Figure 5.15: Performance of the adjustable and the hybrid strategy in terms of both $1/\overline{\text{MSE}}$ and $\overline{\text{BER}}$ with fractionally-spaced equalizers as a function of σ_r at SNR $= 25\,\text{dB}$. Three pairs of (N_P, N_W) are considered: $(1,1)$, $(2,1)$, and $(1,2)$. For the symbol-spaced equalizer, $L_\text{X} = 5$, whereas all fractionally-spaced equalizers possess the same time span. The feedback filter is either present ($\mathbf{\Phi_B} = \mathbf{\Phi}_{\mathbf{B},16}$) or not ($\mathbf{\Phi_B} = \emptyset$). Doubling the operating rate of either $\mathbf{P}$ or $\mathbf{W}$ clearly improves $\overline{\text{MSE}}$ and $\overline{\text{BER}}$ for both strategies.

σ_r at SNR = 25 dB for the adjustable and the hybrid strategy. In the former, $(N_\mathrm{P}, N_\mathrm{W}) = (2, 1)$, whereas $(N_\mathrm{P}, N_\mathrm{W}) = (1, 2)$ in the latter. As a reference, the case with solely symbol-spaced equalizers, i.e., $(N_\mathrm{P}, N_\mathrm{W}) = (1, 1)$, and $L_\mathrm{X} = 5$ is included as well. To allow for a fair comparison, the time span of the fractionally-spaced filters equals the time span of the symbol-spaced filters by doubling the number of causal and anti-causal taps. Moreover, the feedback filter $\mathbf{B}$ contains either 16-taps ($\Phi_\mathbf{B} = \Phi_{\mathbf{B},16}$), or is absent ($\Phi_\mathbf{B} = \emptyset$). Following observations can be made.

- Whether N_P or N_W is increased from 1 to 2, the $\overline{\mathrm{MSE}}$ and the $\overline{\mathrm{BER}}$ performance considerably improves in the case of the adjustable strategy. More precisely, a gain in $1/\overline{\mathrm{MSE}}$ of up to 1 dB and decreases in $\overline{\mathrm{BER}}$ by a factor 100 and more are observed. As both $\mathbf{P}$ and $\mathbf{W}$ are adjustable, both fractionally-spaced equalizers yield similar performance and no preference is given to either. The performance improvement in both $\overline{\mathrm{MSE}}$ and $\overline{\mathrm{BER}}$ seems to be larger when the feedback filter is absent, i.e., $\Phi_\mathbf{B} = \emptyset$, than when a 16-tap feedback filter is active, since in the former configuration doubling the operating rate of one of the linear filters has relatively more impact on the total equalization power than in the latter configuration.

- As for the hybrid strategy, the configuration with the fractionally-spaced $\mathbf{W}$, i.e., $(N_\mathrm{P}, N_\mathrm{W}) = (1, 2)$ yields superior performance compared to the configuration with the fractionally-spaced $\mathbf{P}$, i.e., $(N_\mathrm{P}, N_\mathrm{W}) = (2, 1)$, since the former filter is adjustable and the latter filter is fixed. This performance difference is especially pronounced for larger σ_r, for which a fractionally-spaced fixed $\mathbf{P}$ is less beneficial.

The sensitivity of the optimal equalization strategies to the sampling delay ϵ is illustrated in Fig. 5.16 for both symbol-spaced and fractionally-spaced equalizers with SNR = 25 dB, $\sigma_r = 5\%$, and $\Phi_\mathbf{B} = \emptyset$. In this figure, the $1/\overline{\mathrm{MSE}}$ and the $\overline{\mathrm{BER}}$ performance are plotted as a function of $\Delta\epsilon/T$. The deviation $\Delta\epsilon$ denotes the difference between ϵ and the delay ϵ_max, the latter being defined as the delay corresponding to the largest element of $\mathbf{H}(u)$. In total, three configurations are investigated: one with only symbol-spaced equalizers, i.e., $N_\mathrm{P} = N_\mathrm{W} = 1$, and two with one linear filter operating at twice the symbol rate, i.e., $(N_\mathrm{P}, N_\mathrm{W}) = (2, 1)$ and $(N_\mathrm{P}, N_\mathrm{W}) = (1, 2)$. All equalizer taps are equally distributed around the main tap of the filter and the time span of all equalizers is kept constant by considering 11-tap symbol-spaced filters and 21-tap fractionally-spaced filters. The following observations can be made:

- As for the adjustable strategy, only mild fluctuations in $\overline{\mathrm{MSE}}$ and $\overline{\mathrm{BER}}$ are perceived when both $\mathbf{P}$ and $\mathbf{W}$ are symbol-spaced equalizers. Moreover, the sampling delay $\epsilon = \epsilon_\mathrm{max}$ is not necessarily optimal such that an additional optimization over ϵ realizes potentially a marginal gain in $\overline{\mathrm{MSE}}$ and $\overline{\mathrm{BER}}$. However, this optimization requires the numerical evaluation of the performance for numerous values of ϵ, which often induces an excessive computational complexity, yielding only limited benefits.

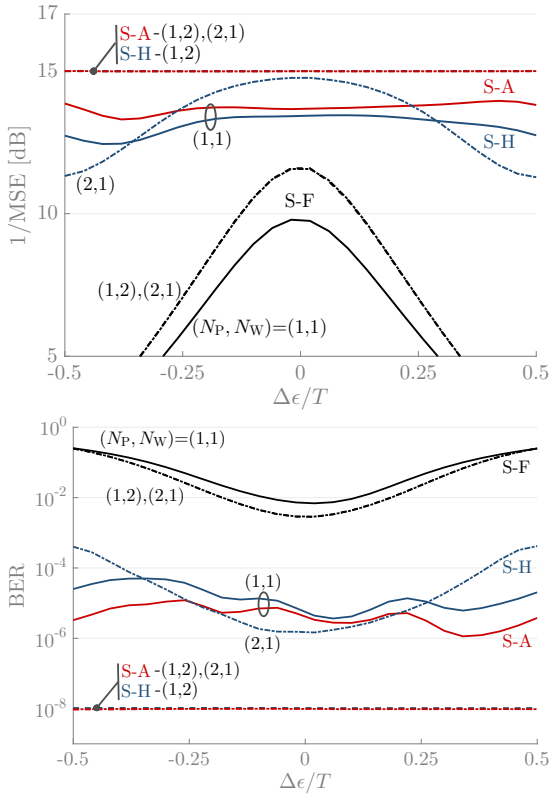

Figure 5.16: Performance of the adjustable, the hybrid, and the fixed strategy in terms of both $1/\overline{\text{MSE}}$ and $\overline{\text{BER}}$ as a function of $\Delta\epsilon/T$ for SNR $= 25\,\text{dB}$, $\sigma_r = 5\%$, and $\Phi_{\mathbf{B}} = \emptyset$. Three pairs of (N_P, N_W) are considered: $(1,1)$, $(2,1)$, and $(1,2)$. All symbol-spaced equalizers comprise 11 taps evenly spread around the center tap, while any fractionally-spaced equalizer operating at twice the symbol rate possesses 21 taps such that the time span of all filters is identical. In the case of an adjustable fractionally-spaced filter, the performance is constant with respect to $\Delta\epsilon$.

- More prominent is the nearly constant performance for different ϵ in the case of the adjustable strategy when a fractionally-spaced equalizer is present. Indeed, this fractionally-spaced equalizer is capable of introducing an arbitrary additional delay over the useful signal frequency-band $|f| < B$ (with B slightly exceeding $\frac{1}{2T}$ due to the transmit and receive filter rolloff), which is something a symbol-spaced equalizer cannot do.

- In the hybrid strategy, the iterative computation of the fixed $\mathbf{P}$ and the scaling factor α is performed with the assumption that $\epsilon = \epsilon_{\max}$. When the communication link is in operation, the sampling constant ϵ could of course be different to $\epsilon_{\max}$, which is subsequently taken into account in the design of all adjustable equalization parameters at the receiver. When both $\mathbf{P}$ and $\mathbf{W}$ are symbol-spaced, the sensitivity to ϵ is nearly identical compared to the adjustable strategy. Additionally, the performance is again constant for a fractionally-spaced $\mathbf{W}$ with $N_{\mathrm{W}} = 2$. However, a fractionally-spaced pre-equalizer $\mathbf{P}$ is designed for $\epsilon = \epsilon_{\max}$ and its superior performance compared to a symbol-spaced pre-equalizer only applies when ϵ slightly deviates from $\epsilon_{\max}$.

- Just as the hybrid strategy, the fixed strategy computes the fixed equalization parameters with respect to $\epsilon = \epsilon_{\max}$. Contrary to the hybrid strategy, this strategy has, however, no mechanism to cope with the mismatch between ϵ and $\epsilon_{\max}$. The performance of the fixed strategy therefore rapidly worsens with increasing $|\Delta\epsilon|$, even when a fractionally-spaced equalizer is present.

5.5.4 Convergence analysis

Irrespective of the presence of a feedback filter, all optimal equalization strategies proposed above obtain the equalization parameters by means of an iterative algorithm. The convergence of these iterative algorithms is investigated in Fig. 5.17. More precisely, this figure plots the $\overline{\mathrm{MSE}}$, the relative decrease γ in $\overline{\mathrm{MSE}}$, and the $\overline{\mathrm{SER}}$ corresponding to the adjustable, the hybrid, and the fixed strategy as a function of the number of iterations for $(N_{\mathrm{P}}, N_{\mathrm{W}}) = (1, 1)$, SNR $=$25 dB, $L_{\mathrm{X}} = 7$, $\Phi_{\mathbf{B}} = \emptyset$, and $\sigma_r = 3\%$. As for the hybrid strategy, the convergence when either $\mathbf{P}$ or $\mathbf{W}$ is fractionally-spaced with spacing T/2 is also included. Finally, the cross markers indicate the iteration index at which the relative decrease of $\overline{\mathrm{MSE}}$ is below $\gamma_{\min} = 10^{-4}$. The following observations hold:

- By design, $\overline{\mathrm{MSE}}$ is a nonincreasing function of the iteration index. Moreover, $\overline{\mathrm{MSE}}$ is lower bounded by 0 such that convergence is guaranteed. For all strategies, most improvement in both $\overline{\mathrm{MSE}}$ and $\overline{\mathrm{BER}}$ is observed in the first iterations, after which the performance gain gradually diminishes. Consequently, $\gamma_{\min}$ must be small enough such that convergence is reached after the initial performance improvement, but must be not too small either such that the computational complexity does not become

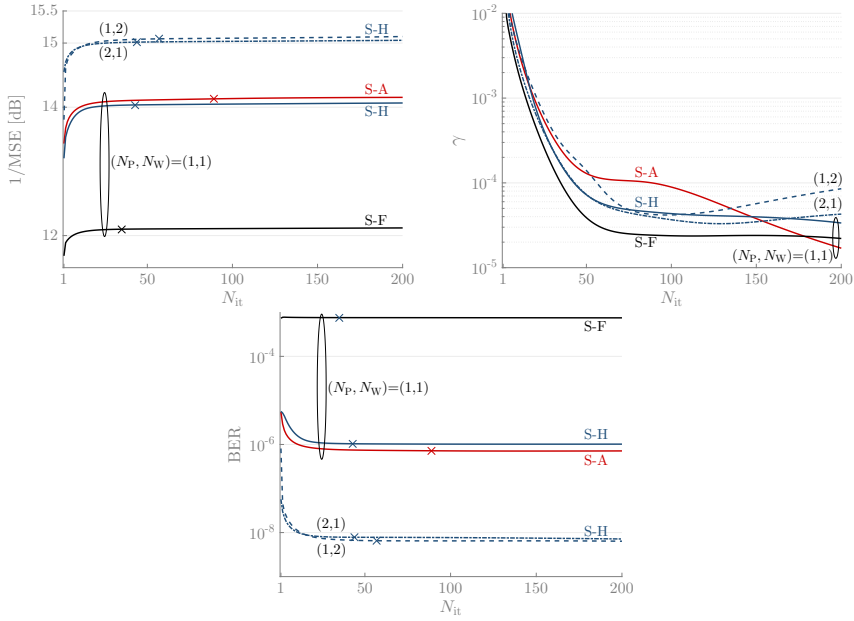

Figure 5.17: Performance of the optimal adjustable, the optimal hybrid, and the optimal fixed strategy in terms of $1/\overline{\mathrm{MSE}}$, γ, and $\overline{\mathrm{BER}}$ as a function of the number of iterations for $(N_{\mathrm{P}}, N_{\mathrm{W}}) = (1, 1)$, SNR =25 dB, $L_{\mathrm{X}} = 7$, $\Phi_{\mathbf{B}} = \emptyset$, and $\sigma_r = 3\%$. Moreover, the performance of the hybrid strategy is also included when either $\mathbf{P}$ or $\mathbf{W}$ is fractionally spaced with a factor 2. Additional cross markers indicate the iteration index at which convergence is achieved when $\gamma_{\min} = 10^{-4}$. The convergence is quite fast for all considered strategies and configurations.

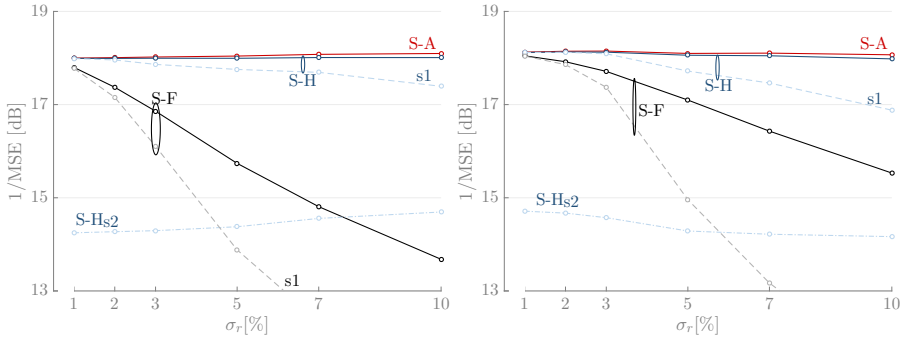

Figure 5.18: Performance of all equalization strategies in terms of $1/\overline{\text{MSE}}$ as a function of σ_r in the case of 4-PAM (left plot) and 8-PAM (right plot). Just as for the right plot of Fig. 5.6, SNR = 25 dB, $L_{\text{X}} = 7$, and $\Phi_{\mathbf{B}} = \Phi_{\mathbf{B},16}$. As for the $\overline{\text{MSE}}$ performance of the different strategies, similar conclusions can be drawn as in Fig. 5.6, irrespective of the value of M.

needlessly large. Nevertheless, a large number of iterations in the hybrid and the fixed strategy is less of a concern in practice, as these iterative computations can be performed offline.

- Whether or not a linear equalizer is fractionally spaced does not seem to have a profound impact on the convergence rate.

- No feedback filter is present in Fig. 5.17. However, the addition of a feedback filter does not alter the structure of the iterative algorithms. Additional simulations (not shown) indicate no meaningful difference in the convergence rate when the feedback filter is present.

5.5.5 Effect of constellation size for fixed bitrate

Fig. 5.18 presents the $1/\overline{\text{MSE}}$ performance of all equalization strategies as a function of σ_r for the 4-PAM (left plot) and the 8-PAM (right plot) constellation. The system parameters are identical to the right plot of Fig. 5.6, i.e., SNR = 25 dB, $L_{\text{X}} = 7$, and $\Phi_{\mathbf{B}} = \Phi_{\mathbf{B},16}$. For the different values of M, the bit rate is kept *constant* to 75 Gb/s by scaling the symbol rate $1/T$ (and, hence, the bandwidth of the transmitted signal) by a factor of $1/\log_2(M)$. The following statements can be made:

- The main conclusions drawn from Fig. 5.6 for $M = 2$ are also valid for larger M in Fig. 5.18, because the MSE performance is only indirectly influenced by the specific value of M in the case of a normalized M-PAM constellation. Indeed, for a given sequence of channel matrices $\{\mathbf{G}(m)\}$, the $\text{MSE}_{\mathbf{g}_{\text{ch}}}$ defined in (5.25) is only dependent on the constellation energy σ_{a}^2 and the correlation matrix of the noise such that the optimal

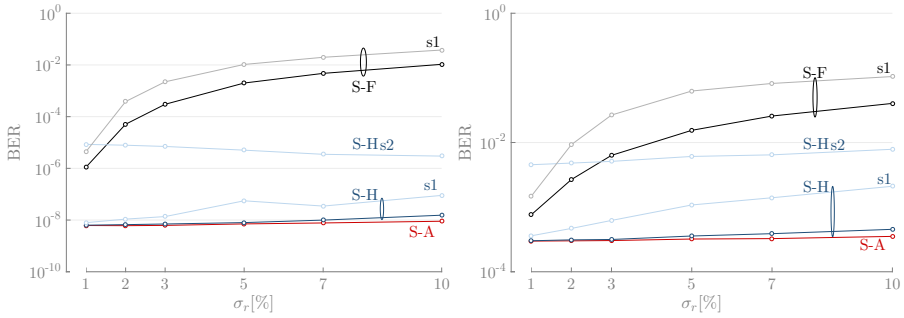

Figure 5.19: Performance of all equalization strategies in terms of $\overline{\text{BER}}$ as a function of σ_r in the case of 4-PAM (left plot) and 8-PAM (right plot) at SNR = 25 dB and $L_{\text{X}} = 7$. The same parameters as in Fig. 5.18 are employed except that the feedback filter is extended to 50 taps and 33 taps in the case of 4-PAM and 8-PAM, respectively. However, even with these longer feedback filters, the 4-PAM and the 8-PAM constellation result in inferior $\overline{\text{BER}}$ compared to the 2-PAM constellation.

equalization parameters are identical for all M. However, larger M does result in smaller symbol rates and thus different channel matrices $\{\mathbf{G}(m)\}$ and the MSE performance is therefore not exactly the same for different M.

- The degradation of the fixed strategy becomes considerably smaller for increasing M. For example, the $\overline{\text{MSE}}$ at $\sigma_r = 10\%$ of the fixed strategy is 7.4 dB, 4.4 dB, and 2.6 dB larger compared to the adjustable strategy for $M = 2$, $M = 4$, and $M = 8$, respectively. The main reason for this smaller performance gap is that most variability of this particular channel is situated at large frequencies (see Fig. 2.2). Because larger M results in smaller symbol rates, less variability among the channel realizations is present, and thus less degradation in the fixed strategy is to be expected.

To explore the impact of larger M on the $\overline{\text{BER}}$ performance, Fig. 5.19 depicts the $\overline{\text{BER}}$ as a function of σ_r for the 4-PAM (left plot) and the 8-PAM (right plot) constellation. Just as in Fig. 5.18, SNR = 25 dB, and $L_{\text{X}} = 7$, but the feedback filter is extended to 50 taps and to 33 taps in the case of 4-PAM and 8-PAM, respectively, such that the time span of the feedback filter also covers the first reflection. Based on Fig. 5.19, one can make the following observations:

- Similar conclusions can be made for the relative $\overline{\text{BER}}$ performance of the different strategies in the case of 4-PAM and 8-PAM as for 2-PAM, because the optimization method is not directly influenced by the specific value of M.

- Despite the longer feedback filters, the $\overline{\text{BER}}$ corresponding to both the 4-PAM and the 8-PAM constellation is worse compared to the $\overline{\text{BER}}$ achieved in the case of the 2-PAM constellation. To explain this observation, one must consider all following factors that are influenced by M. First of all, the distance between two neighboring constellation points becomes smaller for larger M due to the normalization of the constellation such that the noise margin declines. Moreover, the absolute value of the smallest and the largest constellation point is proportional to $\sqrt{M}$, resulting in larger maximal interference. Thirdly, a higher M requires a smaller symbol rate to achieve the same bit rate. Consequently, the bandwidth of the transmit and the receive filter is smaller such that less interference and XT are introduced by the channel as it possesses a low-pass characteristic. For identical SNR levels, the noise variance finally decreases for increasing M as the energy per bit is proportional to $1/\log_2(M)$ when the transmit energy is constant. The first two factors clearly have a negative impact on the $\overline{\text{BER}}$ when M increases, whereas the last two factors favorably influence the $\overline{\text{BER}}$. The negative factors are clearly dominant for the numerical results presented in Fig. 5.19.

5.5.6 Simulation accuracy of the BER

In Fig. 5.20, the accuracy of the different methods to approximate $\overline{\text{BER}}$ (as outlined in section 5.4.3) is investigated as a function of SNR for $\sigma_r = 3\%$, $L_{\text{X}} = 7$, and $\Phi_{\mathbf{B}} = \emptyset$ in the case of the adjustable strategy. To verify the correctness of these methods, this figure contains also the simulated $\overline{\text{BER}}_{\text{sim}}$, which is obtained by simulating the continuous transmission of $2 \cdot 10^6$ randomly generated data symbols over each trace of each channel realization, resulting in a total of $N_{\text{sim}} = 8 \cdot 10^9$ simulated data symbols. This simulation is in the literature often referred to as a Monte-Carlo simulation. As for $\overline{\text{BER}}_1$ and $\overline{\text{BER}}_2$, the variables N (the limited number of realizations of $\mathbf{a}_{\text{ISI}}$ used to compute $\overline{\text{BER}}_1$) and K (the number of symbols contained in the dominant ISI) are moderately large such that relatively accurate results are to be expected, e.g., $N = 10^6$ and $K = 24$. Moreover, the lower bound $\overline{\text{BER}}_{\text{LB}}$ and upper bound $\overline{\text{BER}}_{\text{UB}}$ are also considered: once for the small $K = 4$ and once for the larger $K = 24$. The following observations hold:

- Particularly prominent is that both $\overline{\text{BER}}_1$ and $\overline{\text{BER}}_2$ are nearly identical to the simulated $\overline{\text{BER}}_{\text{sim}}$, confirming the accuracy of both methods to evaluate the $\overline{\text{BER}}$. Only at low $\overline{\text{BER}}$, a difference is notable, which is caused by the unreliability of the simulated $\overline{\text{BER}}_{\text{sim}}$ rather than the inaccuracy of the approximations. In conclusion, both $\overline{\text{BER}}_1$ and $\overline{\text{BER}}_2$ can be employed to numerically compute an accurate approximation of the $\overline{\text{BER}}$, when N and K are large enough.

- In Fig. 5.20, the lower and especially the upper bound to $\overline{\text{BER}}$ are rather loose. Indeed, the convergence improvement for $K = 24$ compared to

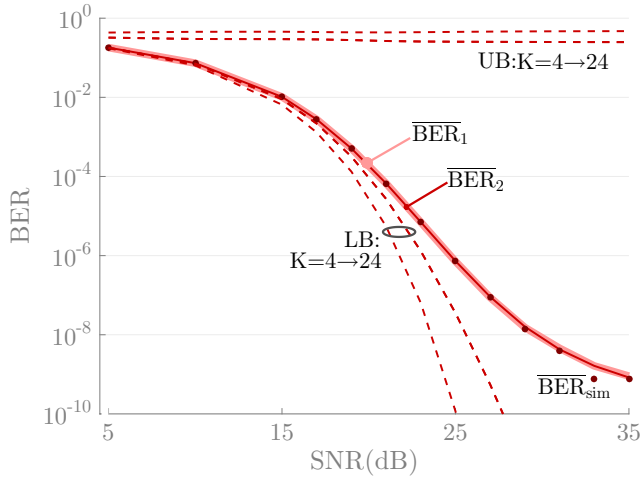

Figure 5.20: Comparison of the simulated $\overline{\text{BER}}_{\text{sim}}$ ($N_{\text{sim}} = 8 \cdot 10^9$, dark red dots), the approximation $\overline{\text{BER}}_1$ ($N = 2 \cdot 10^6$, thick light red line) and the approximation $\overline{\text{BER}}_2$ ($K = 24$, thin red line) as a function of SNR for $\sigma_r = 3\%$, $L_{\text{X}} = 7$, and $\Phi_{\mathbf{B}} = \emptyset$ in the case of the adjustable strategy. The lower bound $\overline{\text{BER}}_{\text{LB}}$ and the upper bound $\overline{\text{BER}}_{\text{UB}}$ are included as well for both $K = 4$ and $K = 24$. Both $\overline{\text{BER}}_1$ and $\overline{\text{BER}}_2$ are reliable approximations for $\overline{\text{BER}}$ in the complete SNR range, whereas the upper and lower bound are rather loose, even for large K.

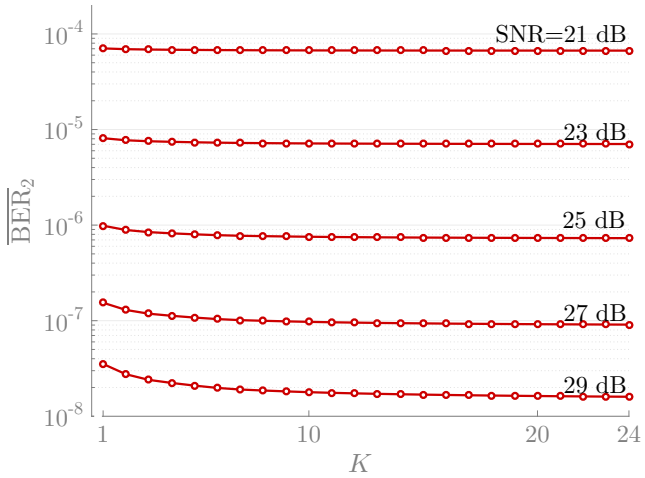

Figure 5.21: The approximation $\overline{\mathrm{BER}}_2$ as a function of K for various SNR levels in the case of the adjustable strategy, $\sigma_r = 3\%$, $L_{\mathrm{X}} = 7$, and $\Phi_{\mathbf{B}} = \emptyset$. The larger the SNR, the lower $\overline{\mathrm{BER}}$, and the larger K must be to reach convergence.

$K = 4$ is visible, but this improvement is not nearly enough to obtain tight bounds. By design, further increasing K should eventually yield bounds close to the actual value of $\overline{\mathrm{BER}}$, but this is not particularly attractive as the computational complexity grows exponentially with K. Moreover, the estimate $\overline{\mathrm{BER}}_2$ requires the same computational complexity and is already reliable for moderate K, making these tight bounds unnecessary.

To investigate the accuracy of the approximation $\overline{\mathrm{BER}}_2$ more thoroughly, Fig. 5.21 presents $\overline{\mathrm{BER}}_2$ as a function of K for different SNR levels with $\sigma_r = 3\%$, $L_{\mathrm{X}} = 7$, and $\Phi_{\mathbf{B}} = \emptyset$ in the case of the adjustable strategy. Visual inspection confirms that for large K, $\overline{\mathrm{BER}}_2$ converges to an asymptotic value. However, the SNR level affects the convergence rate: the larger the SNR and thus the lower $\overline{\mathrm{BER}}_2$, the slower the convergence becomes.

In Figs. 5.20 and 5.21, all results are limited to the 2-PAM constellation and no feedback filter is present. To verify whether the approximations of the $\overline{\mathrm{BER}}$ are still reliable for larger constellations and when the feedback filter is present, Fig. 5.22 compares the approximations $\overline{\mathrm{BER}}_1$ ($N = 10^6$) and $\overline{\mathrm{BER}}_2$ ($K = 11$) with the simulated $\overline{\mathrm{BER}}_1$ ($N_{\mathrm{sim}} = 10^9$) for 4-PAM transmission with $\Phi_{\mathbf{B}} = \{1, \cdots, 50\}$. Here, the approximations are obtained by applying the reasoning from Section 5.4.3 on the BER expression for the 4-PAM constellation from (11.25). Additionally, the figure includes the lower bound $\overline{\mathrm{BER}}_{\mathrm{4PAM,LB}}$, which is equal to $\overline{\mathrm{SER}}/2$ according to (5.73). Clearly, Fig. 5.22 confirms not only that the approximations are still well-defined, but also that the formulated lower bound is extremely tight.

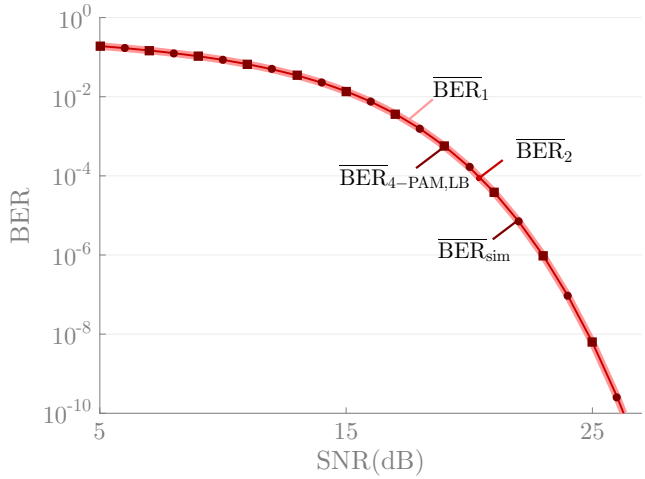

Figure 5.22: Comparison of the simulated $\overline{\text{BER}}_{\text{sim}}$ ($N_{\text{sim}} = 10^9$, dark red dots) and the approximations $\overline{\text{BER}}_1$ ($N = 10^6$, thick light red line) and $\overline{\text{BER}}_2$ ($K = 11$, thin red line), and the lower bound $\overline{\text{BER}}_{\text{4PAM,LB}}$ (dark red squares) as a function of SNR for $\sigma_r = 3\%$, $L_{\text{X}} = 7$, $\Phi_{\mathbf{B}} = \{1, \cdots, 50\}$, and 4-PAM transmission. All approximations of $\overline{\text{BER}}$ yield accurate results and the lower bound $\overline{\text{BER}}_{\text{4PAM,LB}}$ is extremely tight.

In conclusion, all numerical methods to evaluate the $\overline{\text{BER}}$ and the $\overline{\text{SER}}$ yield reliable and accurate results, except for the lower bound $\overline{\text{BER}}_{\text{LB}}$ and upper bound $\overline{\text{BER}}_{\text{UB}}$.

5.6 Comparison of different optimization methods

The joint optimization of the different equalization coefficients is solved for all strategies above by means of an iterative optimization method. However, other optimization methods could be employed, yielding possibly better performance as this iterative optimization algorithm does not necessarily converge to the global optimum. Here, two alternative optimization methods are briefly discussed: the SF Newton optimization method from [79, 80] and the IBRO method from [81, 82].

In this section, these two methods are applied to the linear equalization scheme presented in Section 5.2 and the discussion is limited to the adjustable strategy S-A. In this strategy, the optimal set $(\mathbf{P}^\star, \mathbf{W}^\star, \alpha^\star)$ is obtained by minimizing $\text{MSE}_{\mathbf{g}_{\text{ch}}}$ from (5.25) with $\Phi_{\mathbf{B}} = \emptyset$ subject to the energy constraint from (5.5). At optimum, this constraint is met with equality such that the

following relationship holds

$$\alpha^2 = \frac{\sigma_a^2}{LE_{\mathrm{TX}}} \mathrm{Tr}\left[\hat{\mathbf{P}}^H \mathbf{R}_{\mathrm{TX}} \hat{\mathbf{P}}\right] \tag{5.84}$$

with $\hat{\mathbf{P}} = \alpha \mathbf{P}$. Plugging (5.84) into (5.25) reveals that the solution of the constrained optimization problem can then also be obtained by minimizing the following expression for $\mathrm{MSE}_{\mathbf{g}_{\mathrm{ch}}}(\hat{\mathbf{P}}, \mathbf{W})$ with respect to $\hat{\mathbf{P}}$ and $\mathbf{W}$:

$$\mathrm{MSE}_{\mathbf{g}_{\mathrm{ch}}}(\hat{\mathbf{P}}, \mathbf{W}) = \frac{1}{L} \mathrm{Tr}\left[\sum_{m=-L_{\mathrm{G}}^{(1)}}^{L_{\mathrm{G}}^{(2)}} \left\| \mathbf{W}\mathbf{G}(m)\hat{\mathbf{P}} - \delta(m)\mathbf{I}_L \right\|^2 + \frac{\mathrm{Tr}\left[\hat{\mathbf{P}}^H \mathbf{R}_{\mathrm{TX}} \hat{\mathbf{P}}\right] \mathbf{W}\mathbf{R}_{\bar{\mathbf{n}}}\mathbf{W}^H}{LE_{\mathrm{TX}}} \right]. \tag{5.85}$$

5.6.1 Alternating optimization method

Despite the obvious similarity with the optimization of $\mathrm{MSE}_{\mathbf{g}_{\mathrm{ch}}, \mathbf{B}_a^\star}$ from (5.30) in Subsection 5.2.1, the alternating optimization of $\mathrm{MSE}_{\mathbf{g}_{\mathrm{ch}}}(\hat{\mathbf{P}}, \mathbf{W})$ from (5.85) is briefly discussed here to facilitate the comparison with the other optimization methods. In this iterative method, the optimal $\hat{\mathbf{P}}^\star$ and $\mathbf{W}^\star$ are alternately computed for given $\mathbf{W}$ and $\hat{\mathbf{P}}$, respectively. The optimal $\hat{\mathbf{P}}^\star$ for given $\mathbf{W}$ is given by

$$\hat{\mathbf{P}}^\star = \mathbf{D}^{-1}\mathcal{G}^H(0) \text{ with } \mathbf{D} = \mathcal{G}^H\mathcal{G} + \frac{\mathrm{Tr}\left(\mathbf{W}\mathbf{R}_{\bar{\mathbf{n}}}\mathbf{W}^H\right)}{LE_{\mathrm{TX}}}\mathbf{R}_{\mathrm{TX}}, \tag{5.86}$$

where the stacked matrix $\mathcal{G}$ is similarly defined as $\mathcal{G}_{\mathrm{N}}$ in (5.31), i.e.,

$$\mathcal{G} = \left[\mathcal{G}^H\left(-L_{\mathrm{G}}^{(1)}\right) \cdots \mathcal{G}^H\left(L_{\mathrm{G}}^{(2)}\right)\right]^H. \tag{5.87}$$

The corresponding minimal $\mathrm{MSE}_{\mathbf{G}, \hat{\mathbf{P}}^\star}$ can be expressed as

$$\mathrm{MSE}_{\mathbf{G}, \hat{\mathbf{P}}^\star} = \frac{1}{L}\mathrm{Tr}\left[\mathbf{I}_L - \mathcal{G}(0)\mathbf{D}^{-1}\mathcal{G}^H(0)\right]. \tag{5.88}$$

Second, the optimal $\mathbf{W}^\star$ for given $\hat{\mathbf{P}}$ is defined as

$$\mathbf{W}^\star = \boldsymbol{\mathcal{G}}^H(0)\mathbf{C}^{-1} \text{ with } \mathbf{C} = \boldsymbol{\mathcal{G}}\boldsymbol{\mathcal{G}}^H + \frac{\mathrm{Tr}\left(\hat{\mathbf{P}}^H \mathbf{R}_{\mathrm{TX}} \hat{\mathbf{P}}\right)}{LE_{\mathrm{TX}}}\mathbf{R}_{\bar{\mathbf{n}}}, \tag{5.89}$$

where the augmented matrix $\boldsymbol{\mathcal{G}}$ is defined as

$$\boldsymbol{\mathcal{G}} = \left[\boldsymbol{\mathcal{G}}(-L_{\mathrm{G}}^{(1)}) \cdots \boldsymbol{\mathcal{G}}(L_{\mathrm{G}}^{(2)})\right]. \tag{5.90}$$

The associated minimal $\text{MSE}_{\mathbf{G},\mathbf{W}^\star}$ can be written as

$$\text{MSE}_{\mathbf{G},\mathbf{W}^\star} = \frac{1}{L}\text{Tr}\left[\mathbf{I}_L - \boldsymbol{\mathcal{G}}(0)\mathbf{C}^{-1}\boldsymbol{\mathcal{G}}^H(0)\right]. \tag{5.91}$$

The computation of the optimal $\hat{\mathbf{P}}^\star$ and $\mathbf{W}^\star$ in each iteration of the iterative optimization method consists entirely of matrix multiplications and matrix inversions. Closer inspection of (5.86) and (5.89) reveals that the corresponding computational complexity of one iteration is of the order of $\mathcal{O}\left(L^3 L_\text{G} \max\left(L_\text{W}, L_\text{P}\right)^2\right)$.

5.6.2 Saddle-free Newton optimization method (SF-Newton)

Newton's method is a well-known, iterative general descent algorithm to find the root of a differentiable function [83]. When applied to the first-order derivative or to the gradient of the objective function f_0, this algorithm can be employed to find a critical point, i.e., a point $\mathbf{x}$ where the gradient of f_0 vanishes. In this algorithm, the search direction is defined as follows:

$$\Delta\mathbf{x}_\text{nt}(\mathbf{x}) = -\left(\nabla^2 f_0(\mathbf{x})\right)^{-1}\nabla f_0(\mathbf{x}), \tag{5.92}$$

where $\nabla f_0(\mathbf{x})$, and $\nabla^2 f_0(\mathbf{x})$ are the gradient and Hessian of f_0 at point $\mathbf{x}$, respectively. Newton's method is an effective algorithm to solve an unconstrained convex optimization problem, because the only critical point of a convex f_0 is equal to the global optimum ([83]). Unfortunately, directly applying Newton's method to a nonconvex objective function such as the $\text{MSE}_{\mathbf{g}_\text{ch}}(\hat{\mathbf{P}}, \mathbf{W})$ from (5.85) does not yield adequate performance as many critical points could be present and they are not all globally optimal. Indeed, depending on the eigenvalues of the Hessian, the critical point is either a local minimum (only positive eigenvalues), or a local maximum (only negative eigenvalues), or a saddle point (both positive and negative eigenvalues). The main drawback of Newton's method is that the saddle points act as attractors, since the search direction along each eigenvector is rescaled with the inverse of the corresponding eigenvalue. Consequently, the increment in Newton's method is directed towards saddle points as the negative eigenvalues reverse the sign of the gradient in the subspace in which the Hessian is negative definite. Based on the eigendecomposition $\nabla^2 f_0(\hat{\mathbf{x}}) = \mathbf{Q}\boldsymbol{\Lambda}\mathbf{Q}^T$, an alternative and better search direction $\Delta\mathbf{x}_\text{SF}$ is therefore defined as

$$\Delta\mathbf{x}_\text{SF} = -\left(\overline{\nabla^2 f_0}(\mathbf{x})\right)^{-1}\nabla f_0(\mathbf{x}), \tag{5.93}$$

where $\overline{\nabla^2 f_0}(\mathbf{x}) = \mathbf{Q}\overline{\boldsymbol{\Lambda}}\mathbf{Q}^T$ and the diagonal matrix $\overline{\boldsymbol{\Lambda}}$ is constructed by reversing the sign of all negative eigenvalues in $\boldsymbol{\Lambda}$, while the positive eigenvalues remain unaltered. With this modified search direction, the saddle points are no longer attractors and the resulting optimization method is called the SF Newton optimization method.

When the SF-Newton method is applied to the minimization of $\mathrm{MSE}_{\mathbf{g}_{\mathrm{ch}}}(\hat{\mathbf{P}}, \mathbf{W})$ from (5.85), the gradient and Hessian of $\mathrm{MSE}_{\mathbf{g}_{\mathrm{ch}}}$ must be computed with respect to both the real and the imaginary part of $\hat{\mathbf{P}}$ and $\mathbf{W}$. For conciseness, the exact expressions are not included. Nevertheless, the heaviest computational burden in each iteration is the eigendecomposition of the Hessian $\nabla^2 f_0(\cdot)$ and the inversion of $\overline{\nabla^2 f_0}(\cdot)$. Without proof, this results in a computational complexity equal to $\mathcal{O}\left(\left(L^2(L_{\mathrm{P}} + L_{\mathrm{W}})\right)^3\right)$, which is substantially larger than the computational complexity of one iteration of the alternating optimization method.

5.6.3 Improved bidirectional random optimization method (IBRO)

The IBRO method is an example of a random search algorithm, which aims to optimize an objective function $f_0(\mathbf{x})$. Conceptually, this method attempts to improve the estimate of the optimum, $\mathbf{x}_i$, by generating a random increment $\boldsymbol{\xi}_i$ according to a normal distribution with mean $\mathbf{b}_i$ and covariance matrix $\sigma^2\mathbf{I}$. Characteristic to the IBRO algorithm is that the possible reduction caused by the increment $\boldsymbol{\xi}_i$ is verified in two directions, i.e., $\mathbf{x}_i + \boldsymbol{\xi}_i$ and $\mathbf{x}_i - \boldsymbol{\xi}_i$, whereas even an additional increment is considered when the first increment fails to reduce $f_0(\mathbf{x}_i)$. Furthermore, when an increment successfully decreases f_0, the mean $\mathbf{b}_i$ is partially realigned to the direction of this increment. All details of the IBRO method can be found in [81].

One advantage of the IBRO method is that no gradient information is required in the optimization process. This method is therefore applicable to a broad class of objective functions, including non-differentiable functions. For instance, the minimization of $\mathrm{MSE}_{\mathbf{g}_{\mathrm{ch}}}(\hat{\mathbf{P}}, \mathbf{W})$ can be performed by minimizing either $\mathrm{MSE}_{\mathbf{G},\hat{\mathbf{P}}^\star}(\mathbf{W})$ from (5.88) or $\mathrm{MSE}_{\mathbf{G},\mathbf{W}^\star}\left(\hat{\mathbf{P}}\right)$ from (5.91) instead of $\mathrm{MSE}_{\mathbf{G},\mathbf{W}^\star}\left(\hat{\mathbf{P}}, \mathbf{W}\right)$ from (5.85), greatly reducing the dimensions of the search space as the minimization is only over the coefficients of $\mathbf{W}$ or $\hat{\mathbf{P}}$, respectively. Because of this smaller search space, smaller computational complexity and faster convergence is to be expected.

The optimization of $\mathrm{MSE}_{\mathbf{G},\mathbf{W}^\star}(\hat{\mathbf{P}})$ by means of the IBRO algorithm has in fact already been proposed in [82]. However, the discussion here has some noticeable differences to the optimization procedure from [82]. Unlike the optimization problem here, no energy constraint is considered at the transmitter in [82]. Second, the variance σ^2 is considered to be fixed in [82], whereas allowing the variance to change in each iteration yields better performance in terms of both convergence and accuracy. For example, [84] multiplies the variance by $\alpha_{\mathrm{suc}} > 1$ when N_{suc} consecutive iterations decrease f_0, whereas the variance is multiplied by $\alpha_{\mathrm{fail}} < 1$ when N_{fail} consecutive iterations fail to decrease f_0. Furthermore, convergence can be defined as the moment when σ^2 becomes smaller than a certain threshold. Thirdly, the optimization method

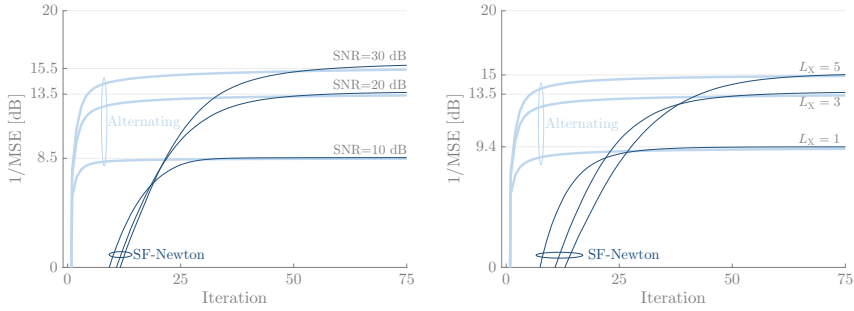

Figure 5.23: $\overline{\text{MSE}}$ performance of the SF-Newton and the alternating optimization method as a function of the iteration index. In the left plot, $L_{\text{X}} = 3$ and three SNR-levels are considered: SNR $= 10\,\text{dB}$, SNR $= 20\,\text{dB}$, and SNR $= 30\,\text{dB}$. In the right plot, SNR $= 20\,\text{dB}$ and three values for L_{X} are considered: $L_{\text{X}} = 1$, $L_{\text{X}} = 3$, and $L_{\text{X}} = 5$. The alternating method has a faster convergence, but the SF-Newton method achieves a smaller $\overline{\text{MSE}}$.

in [82] always opts to minimize $\text{MSE}_{\mathbf{G},\mathbf{W}^\star}(\hat{\mathbf{P}})$ rather than $\text{MSE}_{\mathbf{G},\hat{\mathbf{P}}^\star}(\mathbf{W})$. This strategy is reasonable when $L_{\text{P}} \leq L_{\text{W}}$, as the minimization is then over the smallest search space. However, minimizing $\text{MSE}_{\mathbf{G},\hat{\mathbf{P}}^\star}(\mathbf{W})$ is a better option when $L_{\text{W}} < L_{\text{P}}$.

The most computationally complex instruction in the IBRO method is the evaluation of either $\text{MSE}_{\mathbf{G},\mathbf{W}^\star}\left(\hat{\mathbf{P}}\right)$ or $\text{MSE}_{\mathbf{G},\hat{\mathbf{P}}^\star}(\mathbf{W})$, which both correspond to a maximum complexity of $\mathcal{O}\left(L^3 L_{\text{W}} L_{\text{P}} L_{\text{G}}\right)$. Hence, per iteration, this complexity is slightly smaller than the complexity of the alternating optimization method.

5.6.4 MSE performance comparison

To compare the performance of the alternating and the SF-Newton optimization method, Fig. 5.23 visualizes the $\overline{\text{MSE}}$ averaged over 1000 random frequency-selective 4×4 MIMO channels with an exponential power delay profile as a function of the iteration index. In the left plot, $L_{\text{X}} = 3$ and SNR is either $10\,\text{dB}$ or $20\,\text{dB}$ or $30\,\text{dB}$, whereas SNR is set to $20\,\text{dB}$ and L_{X} to either 1 or 3 or 5 in the right plot. Following observations can be made:

- At convergence, solving the optimization problem by means of the SF-Newton method yields slightly better average performance compared to the alternating optimization method. Consequently, this observation confirms that the alternating method is only locally optimum.

- The SF-Newton method converges more slowly than the alternating optimization method. Indeed, the numerical results demonstrate that the number of iterations needed for convergence in the case of the alternating

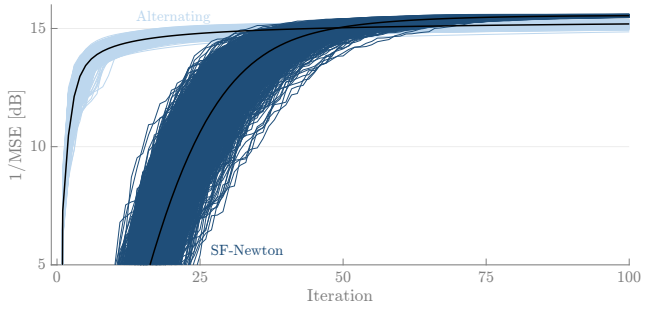

Figure 5.24: $\text{MSE}_{\mathbf{g}_{\text{ch}}}$ performance corresponding to 20000 different random initializations as a function of the iteration index for one specific channel realization with SNR = 20 dB and $L_{\text{X}} = 3$. The thick black lines show the $\text{MSE}_{\mathbf{g}_{\text{ch}}}$ averaged over the different initializations. Although the alternating algorithm converges relatively fast, a fairly large difference in $\text{MSE}_{\mathbf{g}_{\text{ch}}}$ is observed at convergence. Less difference is noticed for the SF-Newton method, but the convergence is slower and the convergence rate greatly depends on the initialization.

method for most channel realizations is considerably less than the number of iterations required on average to reach convergence in the SF-Newton method. Because the SF-Newton method not only requires more iterations, but also has a larger computational complexity per iteration, the SF-Newton method is considerably more computationally complex than the iterative optimization method.

- The higher the SNR level in the left plot of Fig. 5.23, the more iterations both algorithms need to reach convergence as the noise becomes less dominant. Furthermore, increasing the number of equalization parameters in the right plot of Fig. 5.23 naturally enlarges the design space, and more iterations are needed on average to reach convergence. This effect, however, is especially pronounced for the SF-Newton method, implying that the alternating method is better in handling large design spaces.

In conclusion, one must opt for the SF-Newton method when performance is essential, whereas the alternating method is to be preferred when the computational complexity is a limiting factor due to either a large design space or a limited amount of available computational resources.

Fig. 5.24 analyzes the performance of both the alternating and the SF-Newton method for one particular random channel realization $\mathbf{g}_{\text{ch}}$ with SNR = 20 dB and $L_{\text{X}} = 3$. In total, both algorithms are executed 20000 times, each time with a different random initialization. As above, the faster convergence of the alternating method and the lower $\text{MSE}_{\mathbf{g}_{\text{ch}}}$ achieved by the SF-Newton method are both directly observed in Fig 5.24 as well. Moreover, two additional findings can be derived.

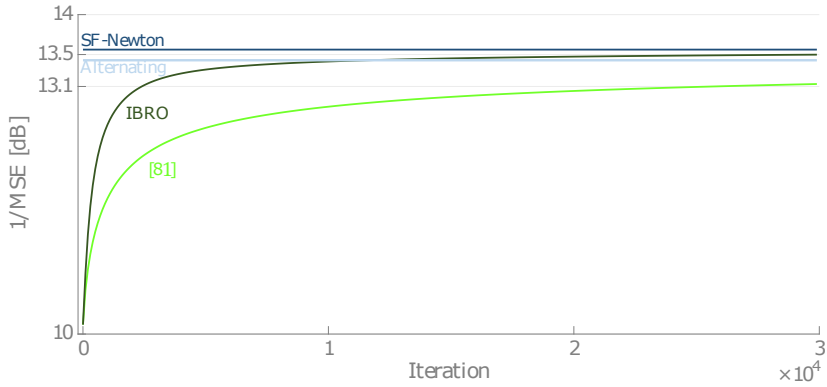

Figure 5.25: $1/\overline{\text{MSE}}$ performance of the IBRO method and the optimization method from [82]. For each channel, 20 runs of the algorithms are executed and all MSE results are averaged over 200 channel realizations. As a reference, the $\overline{\text{MSE}}$ obtained by the SF-Newton and the alternating optimization method are included as well. Clearly, the improved IBRO algorithm presented here outperforms the optimization method of [82].

- Fig. 5.24 first demonstrates that both algorithms cannot guarantee to converge to the global optimum. After 100 iterations, all $\text{MSE}_{\mathbf{g}_{\text{ch}}}$ computed by means of the alternating method are larger than all $\text{MSE}_{\mathbf{g}_{\text{ch}}}$ obtained by the SF-Newton method. Moreover, the different runs of the SF-Newton method do not converge to one optimum and some spread in the obtained $\text{MSE}_{\mathbf{g}_{\text{ch}}}$ values exists at convergence.
- Second, the influence of the exact value of the initialization on $\text{MSE}_{\mathbf{g}_{\text{ch}}}$ is opposite for the two methods. As for the alternating method, the convergence is fast irrespective of the initialization, but the final $\text{MSE}_{\mathbf{g}_{\text{ch}}}$ values differ relatively much from each other. In the case of the SF-Newton method, the convergence rate, however, greatly depends on the exact initialization but less difference between the final $\text{MSE}_{\mathbf{g}_{\text{ch}}}$ values is observed.

The average MSE performance of the IBRO method as a function of the iteration index is analyzed in Fig. 5.25. Here, $\overline{\text{MSE}}$ is obtained by averaging $\text{MSE}_{\mathbf{g}_{\text{ch}}}$ over 200 random channel realizations and, since the IBRO method is random by construction, over 20 executions of the IBRO method for each channel realization. In this figure, both the optimization method proposed in [82] and the improved IBRO method considered here are investigated. As a reference, the obtained $\overline{\text{MSE}}$ by the SF-Newton method and the alternating optimization method are included as well. Following observations can be made:

- The convergence rate of the IBRO method is much slower compared to the SF-Newton and the alternating optimization method. Indeed, the im-

proved IBRO method requires more than 100 times more iterations than the SF-Newton and the alternating method. Due to this large number of iterations, the total computational complexity of the IBRO algorithm is significantly larger compared to the alternating optimization method, and even the SF-Newton method when the number of data streams L and the filter lengths are relatively small.

- After approximately $1.2 \cdot 10^4$ iterations, the $\overline{\text{MSE}}$ obtained by the improved IBRO method is smaller than the $\overline{\text{MSE}}$ of the iterative optimization method, confirming that the improved IBRO method can compete with the other optimization methods in terms of performance. For other filter lengths, it is verified that the IBRO method could even outperform the SF-Newton method (not shown).

- Compared to the optimization method presented in [82], allowing the variance σ^2 to vary in the adjusted IBRO method greatly improves both the convergence speed and the $\overline{\text{MSE}}$ after 30000 iterations. At convergence, the IBRO method from [82] is up to 1.4 times larger than the MSE of the improved IBRO method. These results indicate that the proposed version of the IBRO algorithm is indeed better than the version of [82].

5.6.5 Summary and remarks

This section proposes two optimization methods as an alternative to the alternating optimization method. First, the SF-Newton method modifies the search direction of Newton's method to avoid convergence to saddle points. Numerical results confirm that the SF-Newton method outperforms the alternating method at convergence, but its convergence rate is slower and its computational complexity higher. Moreover, convergence to the global optimum is not guaranteed. Second, the IBRO method iteratively improves the current estimate of the optimum by exploring two or more random search directions. Although the IBRO method presented here performs better than the IBRO from [82], its convergence is far too slow such that the IBRO method is not a suitable alternative to the other methods.

This section considers the optimization of the equalization parameters from the linear equalization scheme (Fig. 5.2) for the adjustable strategy. However, the discussion can almost directly be extended to the equalization scheme with a DFE (Fig. 5.1), since the expression for $\text{MSE}_{\mathbf{g}_{\text{ch}}}$ is structurally identical. Moreover, the SF-Newton and IBRO method can also directly be applied to the fixed strategy, but not to the hybrid strategy. Indeed, alternately computing the fixed and adjustable equalization parameters is inherent to the hybrid strategy, impeding the joint optimization of all equalization parameters with either the SF-Newton or the IBRO method. Moreover, the subproblems of finding the optimal adjustable and the optimal fixed parameters in the hybrid strategy can be solved analytically such that there is no need for numerical optimization methods.

5.7 Conclusions

This chapter proposes different equalization strategies to equalize a stochastic frequency-selective MIMO channel suffering from channel variability by means of the equalization scheme presented in Fig. 5.1, which consists of a linear pre-equalizer at the transmitter and a DFE at the receiver. To obtain the optimal equalization parameters, the average MSE between the decision variable and the transmitted data is minimized according to the optimization framework of Chapter 4. Different equalization strategies are proposed, each with a distinct combination of performance and complexity. The best-performing strategy is to adjust all equalization parameters to the specific channel realization (strategy S-A), while the lowest-complexity strategy is to equalize all channel realizations with identical and fixed equalizers (strategy S-F). The hybrid strategy S-H, on the other hand, aims to approximate the good performance of S-A and the low complexity of S-F by combining adjustable and fixed equalization parameters. Moreover, two suboptimal approaches are considered. First, the channel variability is ignored in the computation of the fixed equalization parameters in the first suboptimal approach, while the adjustable equalization filters are neglected in the computation of the fixed equalization parameters in the second suboptimal approach.

Next, to evaluate the performance of the equalization scheme and the different equalization strategies, analytical expressions for the SER and the BER are derived in the case of M-PAM transmission. Moreover, several techniques are presented to numerically evaluate the obtained expressions. Numerical simulations confirm that these techniques yield reliable and accurate results.

Numerical results indicate that the adjustable strategy has a fairly constant performance for the different channel variability levels considered. Rather than long linear filters, an adjustable feedback filter is recommended when low error rates are required. Moreover, when the number of feedback taps is restricted, better performance is achieved when the feedback filter is obtained by selecting the dominant taps from a long feedback filter rather than setting $\Phi_{\mathbf{B}}$ to the first L_{B} causal time delays. As for the hybrid strategy, it could be a low-complexity alternative to the adjustable strategy with only a limited degradation, on the condition that enough equalization parameters are adjustable and enough channel realizations are incorporated in the expectation $\mathbb{E}_{\mathbf{G}_{\mathrm{ch}}}[\cdot]$. On the other hand, the fixed strategy cannot cope with the channel variability, yielding poor performance for moderate to large σ_r. As for the suboptimal strategies, ignoring the channel variability in the first suboptimal strategy results in a degradation that steadily increases for larger σ_r, whereas the second suboptimal strategy yields inadequate results, irrespective of the number of taps that are adjustable. This latter observation highlights the importance of considering the adjustable parameters in the design of the fixed parameters. These observations about the different strategies hold, irrespective of the constellation size M.

Fractionally-spaced equalizers could considerably improve the MSE and the BER performance. Especially interesting is an adjustable filter $\mathbf{W}$ operating

at twice the symbol rate in the adjustable and the hybrid strategy since this filter achieves not only a significant performance gain for all considered variability levels, but also a robustness to alterations in the sampling delay. This performance gain is notable also for a fractionally-spaced filter $\mathbf{P}$ in the hybrid strategy, but only when the channel variability is not too high and when the actual sampling instant does not deviate too much from the sampling moment assumed for the equalizer coefficient computation.

For the iterative algorithms, most of the performance improvement is observed in the first iterations such that one can safely terminate these algorithms after an adequate number of iterations.

Beside the iterative alternating optimization method, Section 5.6 proposes two alternative optimization methods to obtain the optimal equalization parameters: the SF-Newton method and the IBRO method. Although both methods yield on average slightly better performance, their convergence is slower (especially for the IBRO method) and their total computational complexity is noticeably larger.

6

Stochastic channel: Tomlinson-Harashima precoding

The aim of this chapter is to propose a second equalization scheme in the context of a frequency-selective MIMO channel that is affected by channel variability. More precisely, this equalization scheme consists of a THP and a linear fractionally-spaced equalizer at the transmitter, and a linear fractionally-spaced equalizer at the receiver. In fact, this equalization scheme with a THP can be interpreted as the DFE equalization scheme from Chapter 5, but with the feedback filter transferred from the receiver side to the transmitter side. One consequence of this transfer is that a modulo operator at the transmitter is required to limit the transmit energy, which could otherwise become very large due to the feedback. Section 6.1 discusses the system model of the considered equalization scheme in detail.

Next, Section 6.2 applies the optimization framework from Chapter 4 to obtain a set of well-performing equalization parameters by minimizing the MSE between the decision variable and the data symbol in the extended symbol constellation, while considering that the channel coefficients are random variables due to the channel variability. Similar to Chapter 5, the choice for the MSE as the objective function is motivated by its excellent performance and mathematical simplicity. We define several equalization strategies, each one with its own distinct performance-complexity combination. First, the adjustable strategy assumes that all equalization parameters adjust to the specific channel realization, allowing to directly minimize the conditional MSE and yielding the best performance, but also the highest complexity (Subsection 6.2.1). Next, all equalization parameters are independent of the channel realization in the fixed

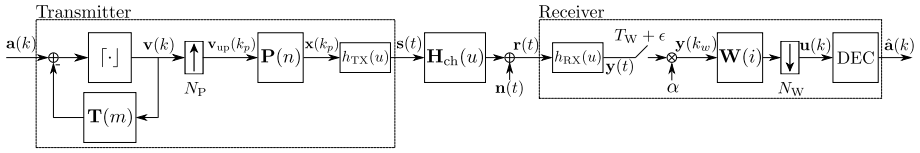

Figure 6.1: System model of the equalization scheme with a nonlinear THP and a linear equalizer at both the transmitter and the receiver.

strategy (Subsection 6.2.2), such that the complexity could be substantially lower at the cost of a performance degradation. Thirdly, the hybrid strategy (Subsection 6.2.3) aims to combine low-complexity with good performance. In this regard, all equalization parameters at the transmitter, i.e., the feedback filter and the linear equalizer, are assumed to be fixed, whereas the parameters of the linear equalizer at the receiver are adjustable. Finally, two suboptimal approaches (Subsections 6.2.4-6.2.5) are introduced to derive the fixed equalization parameters.

Section 6.3 first derives a closed-form expression for the SER and the BER corresponding to the investigated equalization scheme, after which numerical methods are considered to accurately evaluate the derived expressions.

Subsequently, numerical results are presented in Section 6.4, in which the performances of the proposed equalization scheme and the different equalization strategies are investigated in terms of (average) MSE and (average) SER/BER. As an example, M-PAM transmission over the stochastic chip-to-chip interconnect presented in Section 2.2 is considered.

To improve the performance of the investigated equalization scheme, one could add a feedback equalizer at the receiver such that both a THP precoder at the transmitter and a DFE at the receiver are present. This additional feedback filter could improve the performance, especially in the hybrid strategy as the extra filter is adjustable to the channel realization. All details of this equalization scheme can be found in Section 6.5.

Finally, conclusions are drawn in Section 6.6.

In this chapter, only baseband communication is considered. However, after only a few minor alterations, the derived results are also valid for the complex-valued baseband notation, commonly employed for representing bandpass signals and bandpass filters.

6.1 System model

Fig. 6.1 depicts the system model of the transmission over a frequency-selective MIMO channel equalized by means of a THP combined with a fractionally-spaced equalizer at the transmitter and a fractionally-spaced equalizer at the receiver. Below, this equalization scheme is referred to as the THP equalization scheme. In the case of baseband communication, the data symbol vector $\mathbf{a}(k)$

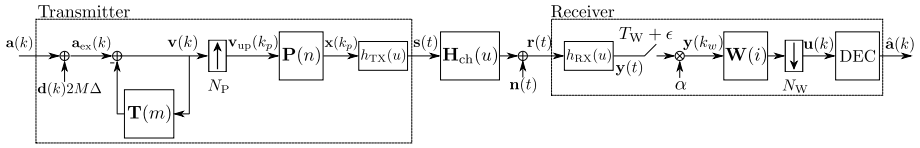

Figure 6.2: Linearized system model of the equalization scheme with a nonlinear THP and linear fractionally-spaced equalizer at both the transmitter and the receiver.

at the input of the transmitter consists of L symbol streams, whose elements $\mathrm{a}_l(k)$ are spatially and temporally uncorrelated and belong to the M-PAM constellation with symbol set $\mathcal{C}_{M-\mathrm{PAM}} = \{(-M+1)\Delta, (-M+3)\Delta, \cdots, (M-3)\Delta, (M-1)\Delta\}$. Consequently, $\mathbb{E}[\mathrm{a}_{l_1}(k)\mathrm{a}_{l_2}(m)] = \sigma_{\mathrm{a}}^2 \delta_{l_1-l_2}\delta_{k-m}$. As in (5.59), the factor Δ is typically chosen to normalize the average symbol energy σ_{a}^2 to one. At the transmitter, the THP is characterized by a feedback filter $\mathbf{T}$ with coefficient matrices $\mathbf{T}(m)$ corresponding to the active time delays $m \in \Phi_{\mathbf{T}}$. Here, $\Phi_{\mathbf{T}}$ represents the set of L_{T} strictly causal time delays, on which this feedback filter is active, i.e., $\mathbf{T}(m) \neq \mathbf{0}\ \forall m \in \Phi_{\mathbf{T}}$. The signal at the output of the THP, $\mathbf{v}(k)$, is then constructed as follows:

$$\mathbf{v}(k) = \left\lceil \mathbf{a}(k) - \sum_{m \in \Phi_{\mathbf{T}}} \mathbf{T}(m)\mathbf{v}(k-m) \right\rfloor_{M\Delta}, \tag{6.1}$$

where $\lceil \cdot \rfloor_{M\Delta}$ symbolizes the element-wise modulo operator restricting each element of $\mathbf{v}(k)$ to the interval $[-M\Delta, M\Delta)$. The main purpose of this modulo operator is to limit the energy of $\mathbf{v}(k)$, which could otherwise become excessively large. The effect of the modulo operator can also be captured by expressing $\mathbf{v}(k)$ as the summation of the modulo operator's input and the term $\mathbf{d}(k)2M\Delta$, where $\mathbf{d}(k) \in \mathbb{Z}^L$ is selected such that the elements of $\mathbf{v}(k)$ are constrained to the interval $[-M\Delta, M\Delta)$. Consequently, $\mathbf{v}(k)$ can be expressed as

$$\mathbf{v}(k) = \mathbf{a}(k) - \sum_{m \in \Phi_{\mathbf{T}}} \mathbf{T}(m)\mathbf{v}(k-m) + \mathbf{d}(k)2M\Delta \tag{6.2}$$

$$= \mathbf{a}_{\mathrm{ex}}(k) - \sum_{m \in \Phi_{\mathbf{T}}} \mathbf{T}(m)\mathbf{v}(k-m). \tag{6.3}$$

In this last expression, $\mathbf{v}(k)$ is interpreted as the sum of a symbol $\mathbf{a}_{\mathrm{ex}}(k) = \mathbf{a}(k) + \mathbf{d}(k)2M\Delta$ in the extended symbol set and a feedback term. The corresponding system model (Fig. 6.2) is generally called the linearized system model as the nonlinear modulo operator is absent.

The signal path from $\mathbf{v}(k)$ to $\mathbf{u}(k)$ in the equalization scheme investigated here is completely identical to the signal path from $\mathbf{a}(k)$ to $\mathbf{u}(k)$ in the linear equalization scheme presented in Fig. 5.2. Moreover, the noise contribution

to $\mathbf{u}(k)$ is identical in both system models. The decision variable $\mathbf{u}(k)$ can therefore be expressed as a function of $\mathbf{v}(k)$ and $\bar{\mathbf{n}}(k)$ by replacing $\mathbf{a}(k-m)$ in (5.21) by $\mathbf{v}(k-m)$, i.e.,

$$\mathbf{u}(k) = \alpha \sum_{m \in \Phi} \mathbf{W}\mathbf{G}(m)\mathbf{P}\mathbf{v}(k-m) + \alpha \mathbf{W}\bar{\mathbf{n}}(k), \tag{6.4}$$

where all notations are identical to those in Chapter 5.

To recover the original data symbols $\mathbf{a}(k)$, one could apply the modulo operator $\lceil \cdot \rfloor_{M\Delta}$ to the extended symbol $\mathbf{a}_{\text{ex}}(k)$. All equalization variables are therefore designed such that the decision variable $\mathbf{u}(k)$ at the receiver matches $\mathbf{a}_{\text{ex}}(k)$ as closely as possible. This approach enables to perform symbol-by-symbol detection on $\mathbf{u}(k)$ in the extended symbol set, yielding $\hat{\mathbf{a}}_{\text{ex}}(k)$, after which the estimate of the original data $\hat{\mathbf{a}}(k)$ is obtained as the output of the modulo operator applied to $\hat{\mathbf{a}}_{\text{ex}}(k)$.

In the case of bandpass communication, complex-valued symbol constellations are allowed as well. One condition is, however, that the periodic extension of the symbol constellation must completely fill the complex plane without any gaps or overlaps. For example, one possible symbol constellation is the M-QAM constellation. In this case, all equalization parameters are complex-valued as well and relation (6.1) must be reformulated as

$$\mathbf{v}(k) = \left\lceil \mathbf{a}(k) - \sum_{j \in \Phi_{\mathbf{T}}} \mathbf{T}(m)\mathbf{v}(k-j) \right\rfloor_{\sqrt{M}\Delta}, \tag{6.5}$$

where both the real and the imaginary part of the argument of $\lceil \cdot \rfloor_{\sqrt{M}\Delta}$ are restricted to the interval $[-\sqrt{M}\Delta, \sqrt{M}\Delta)$. As a result, the variable $\mathbf{d}(k)$ in (6.2) is now complex-valued as well, i.e., $\mathbf{d}(k) \in \mathbb{C}^L$.

6.2 MMSE equalization

In this section, the equalization parameters for the equalization scheme of Section 6.1 are derived for a baseband frequency-selective MIMO channel suffering from channel variability according to the optimization procedure from Chapter 4. Desirably, the objective function f_0 is equal to some kind of error probability, but this choice induces a considerable mathematical complexity. As an alternative, the MSE between $\mathbf{a}_{\text{ex}}(k)$ and $\mathbf{u}(k)$ is a well-defined performance measure to verify whether the set of equalization parameters ($\mathbf{T}$,$\mathbf{P}$,α,$\mathbf{W}$) yields adequate performance, because the original data symbol vector $\mathbf{a}(k)$ can be correctly retrieved from the decision variable $\mathbf{u}(k)$ by means of a symbol-by-symbol detector and a modulo operator, when $\mathbf{u}(k)$ is relatively close to the extended data symbol $\mathbf{a}_{\text{ex}}(k)$. For this equalization scheme, the MSE for a particular

channel realization $\mathbf{g}_{\text{ch}}$, $\text{MSE}_{\mathbf{g}_{\text{ch}}}$, is thus defined as

$$\text{MSE}_{\mathbf{g}_{\text{ch}}} = \frac{\mathbb{E}\left[\|\mathbf{u}(k) - \mathbf{a}_{\text{ex}}(k)\|^2\right]}{L\sigma_{\text{a}}^2} \tag{6.6}$$

$$= \frac{\mathbb{E}\left[\left\|\mathbf{u}(k) - \mathbf{v}(k) - \sum_{m\in\Phi_{\mathbf{T}}} \mathbf{T}(m)\mathbf{v}(k-m)\right\|^2\right]}{L\sigma_{\text{a}}^2} \tag{6.7}$$

$$= \frac{1}{L\sigma_{\text{a}}^2}\mathbb{E}\Bigg[\Bigg\|\alpha \sum_{m\in\Phi} \left(\mathbf{W}\mathbf{G}(m)\mathbf{P} - \delta_m\mathbf{I}_L\right)\mathbf{v}(k-m) -$$

$$- \sum_{m\in\Phi_{\mathbf{T}}} \mathbf{T}(m)\mathbf{v}(k-m) + \alpha\mathbf{W}\bar{\mathbf{n}}(k)\Bigg\|^2\Bigg], \tag{6.8}$$

where (6.8) follows from inserting (6.3) and (6.4) into (6.6) and (6.7), respectively. The expectation $\mathbb{E}[\cdot]$ is with respect to all $\mathbf{v}(k-m)$ with $m \in \Phi$ and all the noise samples. To evaluate the $\text{MSE}_{\mathbf{g}_{\text{ch}}}$ from (6.8), the statistical properties of the signal vector $\mathbf{v}(k)$ must be determined. Unfortunately, the exact PDF is rather complicated and depends on both the feedback taps $\mathbf{T}(m)$ and the size of the symbol constellation. In this regard, Theorem 3.1 of [50] states that the sequence $\mathbf{v}(k)$ generated by the THP precoder consists of almost independently and uniformly distributed variables over the interval $[-M\Delta, M\Delta)$. Based on this theorem, the second-order moments $\mathbb{E}[\mathbf{v}(k)\mathbf{v}(k-m)^T]$ can be approximated as follows:

$$\mathbb{E}[\mathbf{v}(k)\mathbf{v}(k-m)^T] \approx \sigma_{\text{v}}^2\delta_m\mathbf{I}_L, \tag{6.9}$$

where $\sigma_{\text{v}}^2 = \frac{M^2}{M^2-1}\sigma_{\text{a}}^2$. Compared to the average energy of the M-PAM constellation, σ_{a}^2, the average energy per sample in $\mathbf{v}(k)$, σ_{v}^2, is slightly larger, increasing the impact of energy constraint on the pre-equalizer $\mathbf{P}$. This effect is peculiar to THP, and is often referred to as the power loss. Remark that the ratio $\sigma_{\text{v}}^2/\sigma_{\text{a}}^2$ approaches 1 as M approaches $+\infty$.

Considering that the autocorrelation of the symbol stream $\mathbf{v}(k)$ is defined in (6.9) and the covariance matrix of the noise is given by (5.26), one can then rewrite the conditional $\text{MSE}_{\mathbf{g}_{\text{ch}}}$ as follows:

$$\text{MSE}_{\mathbf{g}_{\text{ch}}} = \frac{1}{L\sigma_{\text{a}}^2}\Bigg[\sum_{m\in\Phi_{\mathbf{N}}} \sigma_{\text{v}}^2 \left\|\alpha\mathbf{W}\mathbf{G}(m)\mathbf{P} - \delta_m\mathbf{I}_L\right\|^2 + \alpha^2\text{Tr}(\mathbf{W}\mathbf{R}_{\bar{\mathbf{n}}}\mathbf{W}^T)$$

$$+ \sum_{m\in\Phi_{\mathbf{T}}} \sigma_{\text{v}}^2 \left\|\alpha\mathbf{W}\mathbf{G}(m)\mathbf{P} - \mathbf{T}(m)\right\|^2\Bigg], \tag{6.10}$$

where $\Phi_{\mathbf{N}}$ is the set of $L_{\text{N}} = L_{\text{G}} - L_{\text{T}}$ time delays, for which the feedback equalizer $\mathbf{T}$ is not active, i.e., $\Phi_{\mathbf{N}} = \Phi \setminus \Phi_{\mathbf{T}}$.

Since the frequency-selective MIMO channel is assumed to be stochastic, the computational and the implementational complexity could again be lowered

by considering fixed equalizers that do not adapt to the channel realizations. The objective function corresponding to the MMSE equalizer is therefore not the conditional $\mathrm{MSE}_{\mathbf{g}_{\mathrm{ch}}}$, but the average $\overline{\mathrm{MSE}}$, which is defined as

$$\overline{\mathrm{MSE}} = \mathbb{E}_{\mathbf{G}_{\mathrm{ch}}}[\mathrm{MSE}_{\mathbf{g}_{\mathrm{ch}}}]. \tag{6.11}$$

Hence, the optimization problem to be solved is the following:

$$\begin{aligned}(\mathbf{P}^{\star}, \alpha^{\star}, \mathbf{W}^{\star}, \mathbf{T}^{\star}) = \arg \min_{\mathbf{P},\alpha,\mathbf{W},\mathbf{T}} \overline{\mathrm{MSE}}(\mathbf{P}, \alpha, \mathbf{W}, \mathbf{T}) \\ \text{subject to } \sigma_{\mathrm{v}}^2 \mathrm{Tr}\left[\mathbf{P}^T \mathbf{R}_{\mathrm{TX}} \mathbf{P}\right] \leq L E_{\mathrm{TX}}\end{aligned}, \tag{6.12}$$

where the energy constraint is similarly constructed as in (5.5), but with σ_{v}^2 substituted for σ_{a}^2.

Structurally, the MMSE optimization problem from (6.12) is analogous to the MMSE optimization problem from Chapter 5. Consequently, the remarks made in Chapter 5 are valid for this optimization problem as well. Hence, the scaling factor α could be restricted to the positive numbers and the optimal pre-equalizer $\mathbf{P}^{\star}$ satisfies the energy constraint with equality.

To illustrate the trade-off between the performance and the complexity, the optimization framework from Chapter 4 is employed to propose different equalization strategies to solve the constrained minimization of $\overline{\mathrm{MSE}}$. Optimal performance is achieved when all equalization coefficients are adjusted to the specific channel realization $\mathbf{g}_{\mathrm{ch}}$ (strategy S-A) but at the cost of a high complexity. Next, the least complexity is induced when all equalization parameters are fixed (strategy S-F), whereas a balance between performance and complexity is achieved in the hybrid strategy S-H. To avoid the need for accurate CSIT in this last strategy, all equalization parameters associated with the design of the transmitter, i.e., $\mathbf{P}, \alpha$, and $\mathbf{T}$, are fixed, while the linear filter $\mathbf{W}$ at the receiver is adjustable. Moreover, two suboptimal approaches will be formulated here as well: (i) all fixed equalization parameters are determined while neglecting the channel variability; and (ii) all fixed equalization parameters in the hybrid strategy are computed while assuming that no adjustable equalization parameters are present. The different equalization strategies are summarized in Table 6.1, and a more detailed discussion of each strategy is presented in the subsections below.

6.2.1 Adjustable strategy (S-A)

In this best-performing strategy, all equalization parameters, i.e., $\mathbf{P}, \alpha, \mathbf{W}, \mathbf{T}$, are adjustable to the specific channel realization $\mathbf{g}_{\mathrm{ch}}$, hence simplifying the minimization of the average $\overline{\mathrm{MSE}}$ to the minimization of $\mathrm{MSE}_{\mathbf{g}_{\mathrm{ch}}}$ from (6.8) for each channel realization $\mathbf{g}_{\mathrm{ch}}$. In terms of the optimization framework from Chapter 4, all equalization parameters are collected in the vector $\mathbf{x}(\mathbf{g}_{\mathrm{ch}})$, making any iterations between the adjustable and the fixed equalization parameters of course irrelevant. Still, an iterative algorithm is required to find the optimal

Table 6.1: Overview of the different equalization strategies.

Strategy	Notation	Adjustable parameters	Fixed parameters
Adjustable	S-A	$\mathbf{P}, \alpha, \mathbf{W}, \mathbf{T}$	/
Fixed	S-F	/	$\mathbf{P}, \alpha, \mathbf{W}, \mathbf{T}$
Hybrid	S-H	$\mathbf{W}$	$\mathbf{P}, \alpha, \mathbf{T}$
Fixed-suboptimal 1	S-F_{s1}	/	$\mathbf{P}, \alpha, \mathbf{W}, \mathbf{T}$
Hybrid-suboptimal 1	S-H_{s1}	$\mathbf{W}$	$\mathbf{P}, \alpha, \mathbf{T}$
Hybrid-suboptimal 2	S-H_{s2}	$\mathbf{W}_{\text{adj}}$	$\mathbf{P}, \alpha, \mathbf{W}_{\text{fix}}, \mathbf{T}$

$(\mathbf{P}_a^\star, \alpha_a^\star, \mathbf{W}_a^\star, \mathbf{T}_a^\star)$ as the joint optimization of (6.10) has no straightforward analytical solution. More precisely, the optimal $\mathbf{T}_a^\star$ is easily expressed as a function of the other equalization parameters, because the feedback filter $\mathbf{T}$ is only involved in the last term of (6.10), i.e.,

$$\mathbf{T}_a^\star(m) = \alpha \mathbf{W}\mathbf{G}(m)\mathbf{P}. \tag{6.13}$$

for $m \in \Phi_{\mathbf{T}}$. When (6.13) is plugged into (6.10), the last term in (6.10) is canceled and the resulting $\text{MSE}_{\mathbf{g}_{\text{ch}}}$ optimized over $\mathbf{T}$, $\text{MSE}_{\mathbf{g}_{\text{ch}},\mathbf{T}_a^\star}$, simplifies to

$$\text{MSE}_{\mathbf{g}_{\text{ch}},\mathbf{T}_a^\star} = \frac{1}{L\sigma_{\text{a}}^2}\left(\sum_{m\in\Phi_{\mathbf{N}}} \sigma_{\text{v}}^2 \left\|\alpha\mathbf{W}\mathbf{G}(m)\mathbf{P} - \delta_m \mathbf{I}_L\right\|^2 + \alpha^2 \text{Tr}(\mathbf{W}\mathbf{R}_{\bar{\mathbf{n}}}\mathbf{W}^T)\right). \tag{6.14}$$

The expression for $\text{MSE}_{\mathbf{g}_{\text{ch}},\mathbf{T}_a^\star}$ from (6.14) is in essence equal to the expression for $\text{MSE}_{\mathbf{g}_{\text{ch}},\mathbf{B}_a^\star}$ from (5.30). Consequently, an effective algorithm to acquire the optimal set $(\mathbf{P}_a^\star, \alpha_a^\star, \mathbf{W}_a^\star)$ is to alternately compute the optimal $(\mathbf{P}_a^\star, \alpha_a^\star)$ for given $\mathbf{W}$ and the optimal $\mathbf{W}_a^\star$ for given $(\mathbf{P}, \alpha)$ by minimizing $\text{MSE}_{\mathbf{g}_{\text{ch}},\mathbf{T}_a^\star}$. Because of the similarity with the subproblems handled in Subsection 5.2.1, only the expressions for $(\mathbf{P}_a^\star, \alpha_a^\star, \mathbf{W}_a^\star)$ are explicitly given here. First, the optimal $(\mathbf{P}_a^\star, \alpha_a^\star)$ for given $\mathbf{W}$ is given by

$$\mathbf{P}_a^\star = \frac{1}{\alpha_a^\star}\mathbf{D}_a^{-1}\mathcal{G}(0) \tag{6.15}$$

and

$$\alpha_a^\star = \sqrt{\frac{\sigma_{\text{v}}^2}{LE_{\text{TX}}}\text{Tr}\left(\mathcal{G}(0)\mathbf{D}_a^{-1}\mathbf{R}_{\text{TX}}\mathbf{D}_a^{-1}\mathcal{G}^T(0)\right)} \tag{6.16}$$

with $\mathbf{D}_a = \mathcal{G}_{\text{N}}^T\mathcal{G}_{\text{N}} + \zeta_a\mathbf{R}_{\text{TX}}$, $\zeta_a = \frac{\text{Tr}(\mathbf{W}\mathbf{R}_{\bar{\mathbf{n}}}\mathbf{W}^T)}{LE_{\text{TX}}}$, $\mathcal{G}(m) = \mathbf{W}\mathbf{G}(m)$, and $\mathcal{G}_{\text{N}} = \left[\mathcal{G}^T\left(\Phi_{\mathbf{N}}(1)\right)\cdots\mathcal{G}^T\left(\Phi_{\mathbf{N}}(L_{\text{N}})\right)\right]^T$. The corresponding minimum $\text{MSE}_{\mathbf{g}_{\text{ch}},\mathbf{P}_a^\star,\alpha_a^\star,\mathbf{T}_a^\star}$ can then be simplified to

$$\text{MSE}_{\mathbf{g}_{\text{ch}},\mathbf{P}_a^\star,\alpha_a^\star,\mathbf{T}_a^\star} = \frac{\sigma_{\text{v}}^2}{L\sigma_{\text{a}}^2}\text{Tr}\left(\mathbf{I}_L - \mathcal{G}(0)\mathbf{D}_a^{-1}\mathcal{G}^T(0)\right). \tag{6.17}$$

Second, the optimal linear equalizer, $\mathbf{W}_a^\star$, for a given set $(\mathbf{P}, \alpha)$ is given by

$$\mathbf{W}_a^\star = \boldsymbol{\mathcal{G}}^T(0)\mathbf{C}_a^{-1}, \tag{6.18}$$

where $\mathbf{C}_a = \boldsymbol{\mathcal{G}}_{\mathrm{N}}\boldsymbol{\mathcal{G}}_{\mathrm{N}}^T + \frac{\alpha^2\mathbf{R}_{\bar{\mathbf{n}}}}{\sigma_{\mathrm{v}}^2}$, $\boldsymbol{\mathcal{G}}(m) = \alpha\mathbf{P}\mathbf{G}(m)$, and $\boldsymbol{\mathcal{G}}_{\mathrm{N}} = [\boldsymbol{\mathcal{G}}(\Phi_{\mathbf{N}}(1)) \cdots \boldsymbol{\mathcal{G}}(\Phi_{\mathbf{N}}(L_{\mathrm{N}}))]$. The corresponding minimum $\mathrm{MSE}_{\mathbf{g}_{\mathrm{ch}},\mathbf{W}_a^\star,\mathbf{T}_a^\star}$ then follows from inserting (6.18) into (6.14), and simplifying the result leads to

$$\mathrm{MSE}_{\mathbf{g}_{\mathrm{ch}},\mathbf{W}_a^\star,\mathbf{T}_a^\star} = \frac{\sigma_{\mathrm{v}}^2}{L\sigma_{\mathrm{a}}^2}\mathrm{Tr}\left(\mathbf{I}_L - \boldsymbol{\mathcal{G}}^T(0)\mathbf{C}_a^{-1}\boldsymbol{\mathcal{G}}(0)\right). \tag{6.19}$$

Due to the similarity between $\mathrm{MSE}_{\mathbf{g}_{\mathrm{ch}},\mathbf{T}_a^\star}$ and $\mathrm{MSE}_{\mathbf{g}_{\mathrm{ch}},\mathbf{B}_a^\star}$ from (5.30), the same stopping criteria and initialization of $\mathbf{W}$ as for the DFE equalization scheme (Subsection 5.2.1) can be used here as well.

6.2.2 Fixed strategy (S-F)

To lower the complexity, the equalization parameters in the fixed strategy do not depend on the specific channel realization, meaning that all coefficients of $(\mathbf{P}, \mathbf{W}, \alpha, \mathbf{T})$ belong to the vector $\mathbf{y}$ in the optimization algorithm from Chapter 4. Consequently, no iterations between the adjustable and the fixed equalization parameters are required. However, similar to the adjustable strategy, an iterative algorithm is particularly suitable to solve the joint optimization problem from (6.12), because an analytical solution is not readily available. This iterative algorithm exhibits a similar structure to the iterative algorithm of the adjustable strategy. Indeed, first the optimal $\mathbf{T}_f^\star$ is expressed as a function of the other equalization parameters, after which the optimal $\left(\mathbf{P}_f^\star, \alpha_f^\star\right)$ for given $\mathbf{W}$ and the optimal $\mathbf{W}_f^\star$ for given $(\mathbf{P}, \alpha)$ are alternately determined.

The optimal feedback filter $\mathbf{T}_f^\star$ is easily determined as

$$\mathbf{T}_f^\star(m) = \alpha\mathbf{W}\mathbb{E}_{\mathbf{G}_{\mathrm{ch}}}\left[\mathbf{G}(m)\right]\mathbf{P} \tag{6.20}$$

for $m \in \Phi_{\mathbf{T}}$. Inserting (6.20) into (6.11) yields the corresponding minimum $\overline{\mathrm{MSE}}_{\mathbf{T}_f^\star}$, which is given by

$$\begin{aligned}\overline{\mathrm{MSE}}_{\mathbf{T}_f^\star} = \frac{1}{L\sigma_{\mathrm{a}}^2}\Bigg(&\mathbb{E}_{\mathbf{G}_{\mathrm{ch}}}\left[\sum_{m\in\Phi_{\mathbf{N}}}\sigma_{\mathrm{v}}^2\left\|\alpha\mathbf{W}\mathbf{G}(m)\mathbf{P} - \delta_m\mathbf{I}_L\right\|^2\right] + \alpha^2\mathrm{Tr}\left(\mathbf{W}\mathbf{R}_{\bar{\mathbf{n}}}\mathbf{W}^T\right)\\ &+ \mathbb{E}_{\mathbf{G}_{\mathrm{ch}}}\left[\sum_{m\in\Phi_{\mathbf{T}}}\sigma_{\mathrm{v}}^2\left\|\alpha\mathbf{W}\mathbf{G}(m)\mathbf{P} - \alpha\mathbf{W}\mathbb{E}_{\mathbf{G}_{\mathrm{ch}}}[\mathbf{G}(m)]\mathbf{P}\right\|^2\right]\Bigg).\end{aligned} \tag{6.21}$$

One can note that $\overline{\mathrm{MSE}}_{\mathbf{T}_f^\star}$ is very similar to the $\overline{\mathrm{MSE}}_{\mathbf{B}_f^\star}$ from (5.41) such that the same iterative procedure can be employed, i.e., alternately computing the optimal $\left(\mathbf{P}_f^\star, \alpha_f^\star\right)$ and $\mathbf{W}_f^\star$ for given $\mathbf{W}$ and $\left(\mathbf{P}_f^\star, \alpha_f^\star\right)$, respectively. Due to

this similarity, the mathematical details are omitted and only the expressions for the optimal parameters are given.

The optimal $\mathbf{P}_f^\star$ and $\alpha_f^\star$ for given $\mathbf{W}$ are respectively given by

$$\mathbf{P}_f^\star = \frac{1}{\alpha_f^\star}\mathbf{D}_f^{-1}\mathbb{E}_{\mathbf{G}_{\text{ch}}}\left[\mathcal{G}^T(0)\right] \tag{6.22}$$

and

$$\alpha_f^\star = \sqrt{\frac{\sigma_{\text{v}}^2}{LE_{\text{TX}}}\text{Tr}\left(\mathbb{E}_{\mathbf{G}_{\text{ch}}}[\mathcal{G}(0)]\mathbf{D}_f^{-1}\mathbf{R}_{\text{TX}}\mathbf{D}_f^{-1}\mathbb{E}_{\mathbf{G}_{\text{ch}}}\left[\mathcal{G}^T(0)\right]\right)} \tag{6.23}$$

with

$$\mathbf{D}_f = \mathbb{E}_{\mathbf{G}_{\text{ch}}}\left[\mathcal{G}_{\text{N}}^T\mathcal{G}_{\text{N}} + \mathcal{G}_{\text{T}}^T\mathcal{G}_{\text{T}}\right] - \mathbb{E}_{\mathbf{G}_{\text{ch}}}\left[\mathcal{G}_{\text{T}}^T\right]\mathbb{E}_{\mathbf{G}_{\text{ch}}}\left[\mathcal{G}_{\text{T}}\right] + \zeta_f\mathbf{R}_{\text{TX}}, \tag{6.24}$$

$\zeta_f = \frac{\text{Tr}(\mathbf{W}\mathbf{R}_{\tilde{\mathbf{n}}}\mathbf{W}^T)}{LE_{\text{TX}}}$, and $\mathcal{G}_{\text{T}} = \left[\mathcal{G}^T\left(\Phi_{\mathbf{T}}(1)\right)\cdots\mathcal{G}^T\left(\Phi_{\mathbf{T}}(L_{\text{T}})\right)\right]^T$. Furthermore, the minimized $\overline{\text{MSE}}_{\mathbf{P}_f^\star,\alpha_f^\star,\mathbf{T}_f^\star}$ can be written as

$$\overline{\text{MSE}}_{\mathbf{P}_f^\star,\alpha_f^\star,\mathbf{T}_f^\star} = \frac{\sigma_{\text{v}}^2}{L\sigma_{\text{a}}^2}\text{Tr}\left(\mathbf{I}_L - \mathbb{E}_{\mathbf{G}_{\text{ch}}}\left[\mathcal{G}\left(0\right)\right]\mathbf{D}_f^{-1}\mathbb{E}_{\mathbf{G}_{\text{ch}}}\left[\mathcal{G}^T\left(0\right)\right]\right). \tag{6.25}$$

The optimal $\mathbf{W}_f^\star$ for given $(\mathbf{P}, \alpha)$ is acquired by minimizing $\overline{\text{MSE}}_{\mathbf{T}_f^\star}$ with respect to $\mathbf{W}$, yielding

$$\mathbf{W}_f^\star = \mathbb{E}_{\mathbf{G}_{\text{ch}}}[\boldsymbol{\mathcal{G}}^T(0)]\mathbf{C}_f^{-1} \tag{6.26}$$

with

$$\mathbf{C}_f = \mathbb{E}_{\mathbf{G}_{\text{ch}}}[\boldsymbol{\mathcal{G}}_{\text{N}}\boldsymbol{\mathcal{G}}_{\text{N}}^T + \boldsymbol{\mathcal{G}}_{\text{T}}\boldsymbol{\mathcal{G}}_{\text{T}}^T] - \mathbb{E}_{\mathbf{G}_{\text{ch}}}\left[\boldsymbol{\mathcal{G}}_{\text{T}}\right]\mathbb{E}_{\mathbf{G}_{\text{ch}}}\left[\boldsymbol{\mathcal{G}}_{\text{T}}^T\right] + \frac{\alpha^2\mathbf{R}_{\tilde{\mathbf{n}}}}{\sigma_{\text{v}}^2} \tag{6.27}$$

and $\boldsymbol{\mathcal{G}}_{\text{T}} = [\boldsymbol{\mathcal{G}}\left(\Phi_{\mathbf{T}}(1)\right)\cdots\boldsymbol{\mathcal{G}}\left(\Phi_{\mathbf{T}}\left(L_{\text{T}}\right)\right)]$. The corresponding minimal value of $\overline{\text{MSE}}_{\mathbf{T}_f^\star}$, $\overline{\text{MSE}}_{\mathbf{W}_f^\star,\mathbf{T}_f^\star}$ can then be expressed as

$$\overline{\text{MSE}}_{\mathbf{W}_f^\star,\mathbf{T}_f^\star} = \frac{\sigma_{\text{v}}^2}{L\sigma_{\text{a}}^2}\text{Tr}\left(\mathbf{I}_L - \mathbb{E}_{\mathbf{G}_{\text{ch}}}\left[\boldsymbol{\mathcal{G}}^T\left(0\right)\right]\mathbf{C}_f^{-1}\mathbb{E}_{\mathbf{G}_{\text{ch}}}\left[\boldsymbol{\mathcal{G}}(0)\right]\right). \tag{6.28}$$

Just as for the adjustable strategy, the stopping criteria and the initialization of $\mathbf{W}$ is the same as for the DFE equalization scheme.

6.2.3 Hybrid strategy (S-H)

In the hybrid strategy, all equalization parameters at the transmitter are fixed such that only the linear filter $\mathbf{W}$ at the receiver can adjust to the specific channel realization $\mathbf{g}_{\text{ch}}$. Similar to the other strategies, one could first derive the optimal feedback filter $\mathbf{T}_h^\star$ as a function of the other parameters by minimizing $\overline{\text{MSE}}$ from (6.11), i.e.,

$$\mathbf{T}_h^\star(m) = \alpha \mathbb{E}_{\mathbf{G}_{\text{ch}}}\left[\mathbf{W}\mathbf{G}(m)\right]\mathbf{P} \tag{6.29}$$

for $m \in \Phi_{\mathbf{T}}$. Consequently, the $\text{MSE}_{\mathbf{g}_{\text{ch}}}$ after optimizing over $\mathbf{T}$, $\text{MSE}_{\mathbf{g}_{\text{ch}},\mathbf{T}_h^\star}$, can be written as

$$\begin{aligned}\text{MSE}_{\mathbf{g}_{\text{ch}},\mathbf{T}_h^\star} = \frac{1}{L\sigma_{\text{a}}^2}\Bigg(&\sum_{m\in\Phi_{\mathbf{N}}} \sigma_{\text{v}}^2 \left\|\alpha\mathbf{W}\mathbf{G}(m)\mathbf{P} - \delta_m\mathbf{I}_L\right\|^2 + \alpha^2\text{Tr}\left(\mathbf{W}\mathbf{R}_{\bar{\mathbf{n}}}\mathbf{W}^T\right)\\ &+ \sum_{m\in\Phi_{\mathbf{T}}} \sigma_{\text{v}}^2 \left\|\alpha\mathbf{W}\mathbf{G}(m)\mathbf{P} - \alpha\mathbb{E}_{\mathbf{G}_{\text{ch}}}\left[\mathbf{W}\mathbf{G}(m)\right]\mathbf{P}\right\|^2\Bigg).\end{aligned} \tag{6.30}$$

Next, the optimal $(\mathbf{P}_h^\star, \alpha_h^\star)$, and $\mathbf{W}_h^\star$ can be obtained by applying the optimization framework described in Algorithm 4.1 to $\mathbb{E}_{\mathbf{G}_{\text{ch}}}\left[\text{MSE}_{\mathbf{g}_{\text{ch}},\mathbf{T}_h^\star}\right]$ from (6.30), where the vector $\mathbf{y}$ consists of all coefficients of $\mathbf{P}$ and the scaling factor α, whereas the vector $\mathbf{x}\left(\mathbf{g}_{\text{ch}}\right)$ contains all coefficients of $\mathbf{W}$. However, this optimization procedure is quite challenging as the minimization of $\text{MSE}_{\mathbf{g}_{\text{ch}},\mathbf{T}_h^\star}$ over the filter $\mathbf{W}$ requires the derivative of $\mathbb{E}_{\mathbf{G}_{\text{ch}}}\left[\mathbf{W}\mathbf{G}(m)\right]$ with respect to $\mathbf{W}$, which cannot be readily obtained. Alternatively, it is mathematically more tractable to apply the optimization framework from Algorithm 4.1 to $\overline{\text{MSE}}$ from (6.11) such that the coefficients of $\mathbf{T}$ are added to the vector $\mathbf{y}$, while the vector $\mathbf{x}\left(\mathbf{g}_{\text{ch}}\right)$ remains unaltered.

Regarding the joint optimization of $(\mathbf{P}, \alpha, \mathbf{T})$ for given $\mathbf{W}$, the optimal $\mathbf{T}_h^\star$ is still given by (6.29), whereas the optimal $\mathbf{P}_h^\star$ and $\alpha_h^\star$ are computed by minimizing $\mathbb{E}_{\mathbf{G}_{\text{ch}}}\left[\text{MSE}_{\mathbf{g}_{\text{ch}},\mathbf{T}_h^\star}\right]$ subject to the energy constraint. This optimization is similar to deriving $\left(\mathbf{P}_f^\star, \alpha_f^\star\right)$ in the fixed strategy such that $\mathbf{P}_h^\star$ and $\alpha_h^\star$ are given by

$$\mathbf{P}_h^\star = \frac{1}{\alpha_h^\star}\mathbf{D}_h^{-1}\mathbb{E}_{\mathbf{G}_{\text{ch}}}[\mathcal{G}^T(0)] \tag{6.31}$$

and

$$\alpha_h^\star = \sqrt{\frac{\sigma_{\text{v}}^2}{LE_{\text{TX}}}\text{Tr}\left(\mathbb{E}_{\mathbf{G}_{\text{ch}}}\left[\mathcal{G}(0)\right]\mathbf{D}_h^{-1}\mathbf{R}_{\text{TX}}\mathbf{D}_h^{-1}\mathbb{E}_{\mathbf{G}_{\text{ch}}}\left[\mathcal{G}^T(0)\right]\right)} \tag{6.32}$$

with

$$\mathbf{D}_h = \mathbb{E}_{\mathbf{G}_{\text{ch}}}\left[\mathcal{G}_{\text{N}}^T\mathcal{G}_{\text{N}} + \mathcal{G}_{\text{T}}^T\mathcal{G}_{\text{T}}\right] - \mathbb{E}_{\mathbf{G}_{\text{ch}}}\left[\mathcal{G}_{\text{T}}^T\right]\mathbb{E}_{\mathbf{G}_{\text{ch}}}\left[\mathcal{G}_{\text{T}}\right] + \zeta_h\mathbf{R}_{\text{TX}}, \tag{6.33}$$

and $\zeta_h = \frac{\mathbb{E}_{\mathbf{G}_{\text{ch}}}\left[\text{Tr}\left(\mathbf{W}\mathbf{R}_{\bar{\mathbf{n}}}\mathbf{W}^T\right)\right]}{LE_{\text{TX}}}$. The evaluation of $\overline{\text{MSE}}$ from (6.11) at $(\mathbf{P}_h^\star, \alpha_h^\star, \mathbf{W}, \mathbf{T}_h^\star)$ results in the following expression for the optimized $\overline{\text{MSE}}_{\mathbf{P}_h^\star,\alpha_h^\star,\mathbf{T}_h^\star}$:

$$\overline{\text{MSE}}_{\mathbf{P}_h^\star,\alpha_h^\star,\mathbf{T}_h^\star} = \frac{\sigma_{\text{v}}^2}{L\sigma_{\text{a}}^2}\text{Tr}\left(\mathbf{I}_L - \mathbb{E}_{\mathbf{G}_{\text{ch}}}\left[\mathcal{G}(0)\right]\mathbf{D}_h^{-1}\mathbb{E}_{\mathbf{G}_{\text{ch}}}\left[\mathcal{G}^T(0)\right]\right). \tag{6.34}$$

Next, to derive the optimal linear equalizer $\mathbf{W}_h^\star$ for given $(\mathbf{P}, \alpha, \mathbf{T})$, the $\mathrm{MSE}_{\mathbf{g}_{\mathrm{ch}}}$ from (6.10) must be minimized with respect to $\mathbf{W}$, yielding

$$\mathbf{W}_h^\star = \left(\boldsymbol{\mathcal{G}}^T(0) + \mathbf{T}\boldsymbol{\mathcal{G}}_{\mathrm{T}}^T\right)\mathbf{C}_h^{-1} \tag{6.35}$$

with $\mathbf{C}_h^{-1} = \boldsymbol{\mathcal{G}}_{\mathrm{N}}\boldsymbol{\mathcal{G}}_{\mathrm{N}}^T + \boldsymbol{\mathcal{G}}_{\mathrm{T}}\boldsymbol{\mathcal{G}}_{\mathrm{T}}^T + \frac{\alpha^2\mathbf{R}_{\tilde{\mathbf{n}}}}{\sigma_{\mathrm{v}}^2}$. After plugging (6.35) into (6.10) and simplifying the obtained expression, the optimized $\mathrm{MSE}_{\mathbf{g}_{\mathrm{ch}},\mathbf{W}_h^\star}$ can be written as

$$\mathrm{MSE}_{\mathbf{g}_{\mathrm{ch}},\mathbf{W}_h^\star} = \frac{\sigma_{\mathrm{v}}^2}{L\sigma_{\mathrm{a}}^2}\mathrm{Tr}\left(\mathbf{I}_L + \mathbf{T}\mathbf{T}^T - (\boldsymbol{\mathcal{G}}^T(0) + \mathbf{T}\boldsymbol{\mathcal{G}}_{\mathrm{T}}^T)\mathbf{C}^{-1}\left(\boldsymbol{\mathcal{G}}(0) + \boldsymbol{\mathcal{G}}_{\mathrm{T}}\mathbf{T}^T\right)\right). \tag{6.36}$$

To initialize $\mathbf{x}_0(\mathbf{g}_{\mathrm{ch}})$, the initial feedforward filter $\mathbf{W}$ is assumed to be equal to the all-pass filter, i.e., $\mathbf{W}(i) = \mathbf{I}_L\delta_i$.

6.2.4 Suboptimal 1 (S-F_{s1} and S-H_{s1})

Similar to the first suboptimal approach in the case of the DFE equalization scheme, all fixed equalization parameters in either the fixed or the hybrid strategy are determined, while the channel variability is ignored. More precisely, all channel matrices $\mathbf{G}(m)$ are assumed to be equal to $\mathbb{E}_{\mathbf{G}_{\mathrm{ch}}}[\mathbf{G}(m)]$, which is equivalent to considering a channel set $\mathbb{G}_{\mathrm{ch}}$ containing only $\mathbb{E}_{\mathbf{G}_{\mathrm{ch}}}[\mathbf{g}_{\mathrm{ch}}]$. As a result, all second order moments simplify to a product of first order moments such that all terms containing $\mathcal{G}_{\mathrm{T}}$ and $\boldsymbol{\mathcal{G}}_{\mathrm{T}}$ in $\mathbf{D}_f$ and $\mathbf{C}_f$, respectively, disappear. With this assumption, the fixed strategy becomes in fact equal to the adjustable strategy applied to the average channel $\mathbb{E}_{\mathbf{G}_{\mathrm{ch}}}[\mathbf{g}_{\mathrm{ch}}]$. As for the hybrid strategy, the fixed equalization parameters are obtained by the same procedure, after which the adjustable filter $\mathbf{W}$ is computed once for each channel realization $\mathbf{g}_{\mathrm{ch}}$.

This suboptimal approach is denoted by S-F_{s1} and S-H_{s1} for the fixed and the hybrid strategy, respectively.

6.2.5 Suboptimal 2 (S-H_{s2})

Similar to the suboptimal approach presented in Section 5.2.5, one can follow the optimization method from [53] by computing first the fixed equalization parameters in the hybrid strategy with the assumption that the adjustable filter $\mathbf{W}$ at the receiver is not present, i.e., equal to an all-pass filter. After the design of the fixed parameters, the adjustable filter $\mathbf{W}$ is then designed to combat the residual ISI. Just as in Section 5.2.5, additional design freedom is established by dividing the adjustable filter $\mathbf{W}$ into a fixed linear filter $\mathbf{W}_{\mathrm{fix}}$ and an adjustable linear filter $\mathbf{W}_{\mathrm{adj}}$ with $L_{\mathrm{W,fix}}$ and $L_{\mathrm{W,adj}}$ taps, respectively. The fixed parameters can then be computed by applying the optimization algorithm of the fixed algorithm with $\mathbf{W} = \mathbf{W}_{\mathrm{fix}}$, after which $\mathbf{W}_{\mathrm{adj}}$ can be obtained by means of standard techniques.

The corresponding suboptimal hybrid strategy is denoted by S-$\mathrm{H}_{\mathrm{s}2}$.

6.3 SER and BER expression

To be able to investigate the error probability performance of the presented equalization scheme and the different equalization strategies, this section derives the SER and the BER expression for the system model from Fig. 6.1. More precisely, this discussion considers uncoded M-PAM transmission over a frequency-selective MIMO baseband channel.

6.3.1 SER expression for M-PAM transmission

The SER conditioned on the channel realization $\mathbf{g}_{\mathrm{ch}}$ and corresponding to the lth symbol stream, $\mathrm{SER}_{\mathbf{g}_{\mathrm{ch}}}^{(l)}$, is defined as the probability that the decision $\hat{\mathrm{a}}_l(k)$ differs from the original data symbol $\mathrm{a}_l(k)$. The first step in the derivation of the $\mathrm{SER}_{\mathbf{g}_{\mathrm{ch}}}^{(l)}$ expression is to rewrite the decision variable $\mathbf{u}(k)$ by replacing the quantity $\mathbf{v}(k)$ in the term with $m = 0$ in (6.4) with the expression for $\mathbf{v}(k)$ from (6.3), yielding

$$\mathbf{u}(k)=\breve{\mathbf{G}}_0\mathbf{a}_{\mathrm{ex}}(k)+\sum_{m\in\Phi_0}\alpha\mathbf{W}\mathbf{G}(m)\mathbf{P}\mathbf{v}(k-m)-\sum_{m\in\Phi_{\mathbf{T}}}\breve{\mathbf{G}}_0\mathbf{T}(m)\mathbf{v}(k-m)+\mathbf{w}(k) \tag{6.37}$$

with $\breve{\mathbf{G}}_0 = \alpha\mathbf{W}\mathbf{G}(0)\mathbf{P}$, $\Phi_0 = \Phi \setminus \{0\}$, and $\mathbf{w}(k) = \alpha\mathbf{W}\bar{\mathbf{n}}(k)$. Consequently, the lth element of $\mathrm{u}_l(k)$ can be rewritten as

$$\mathrm{u}_l(k) = (1+\mathrm{e}_l)\,(\mathbf{a}_{\mathrm{ex}}(k))_l + \mathrm{isi}_l(k)(\mathbf{v}_{\mathrm{ISI}}, \mathbf{a}_{\mathrm{ex}}^{(\mathrm{ISI})}) + \mathrm{w}_l(k), \tag{6.38}$$

where $\mathbf{e} = \mathrm{diag}\left(\breve{\mathbf{G}}_0\right) - \mathbf{1}$, and

$$\begin{aligned}\mathbf{isi}(k)(\mathbf{v}_{\mathrm{ISI}}, \mathbf{a}_{\mathrm{ex}}^{(\mathrm{ISI})}) = &\sum_{m\in\Phi_{\mathbf{N}}\setminus\{0\}}\alpha\mathbf{W}\mathbf{G}(m)\mathbf{P}\mathbf{v}(k-m)\\ &+\sum_{m\in\Phi_{\mathbf{T}}}\left(\alpha\mathbf{W}\mathbf{G}(m)\mathbf{P}-\breve{\mathbf{G}}_0\mathbf{T}(m)\right)\mathbf{v}(k-m)\\ &+\left(\breve{\mathbf{G}}_0-\mathrm{diag}\,(\mathbf{e}+1)\right)\mathbf{a}_{\mathrm{ex}}(k).\end{aligned} \tag{6.39}$$

To allow for simpler notations, the time variable (k) is omitted in the remainder of this section. In (6.38), the interference term isi_l depends not only on the elements of all causal and anti-causal signals $\mathbf{v}(k-m)$, but also on the elements of the current extended data symbol $\mathbf{a}_{\mathrm{ex}}$ except for $(\mathbf{a}_{\mathrm{ex}})_l$. The former are collected in the vector $\mathbf{v}_{\mathrm{ISI}}$, whereas the latter are gathered in the vector $\mathbf{a}_{\mathrm{ex}}^{(\mathrm{ISI})}$. Similar to (5.60), (6.38) demonstrates that the decision variable u_l is in fact a summation of three terms: (i) a useful term $(1+\mathrm{e}_l)\,(\mathbf{a}_{\mathrm{ex}})_l$,

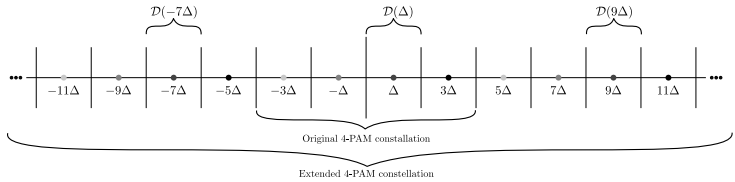

Figure 6.3: Visualization of the extended 4-PAM constellation. All constellation points are symbolized by the dots on the horizontal axis, whereas the boundaries of the decision regions $\mathcal{D}(\cdot)$ are indicated by the vertical lines.

(ii) an ISI term $\text{isi}_l(\mathbf{v}_{\text{ISI}}, \mathbf{a}_{\text{ex}}^{(\text{ISI})})$ and a Gaussian noise term w_l with variance $\sigma_{\text{w}_l}^2 = \alpha^2 \left(\mathbf{W}\mathbf{R}_{\bar{\mathbf{n}}}\mathbf{W}^T\right)_{l,l}$. Although the structure of u_l is similar to the structure of u_l in the case of the equalization scheme investigated in Chapter 5, the derivation of the $\text{SER}_{\mathbf{g}_{\text{ch}}}^{(l)}$ here is somewhat different. Indeed, the decision on u_l must be performed in the extended symbol constellation instead of the standard M-PAM constellation, i.e., the symbol-by-symbol detector maps u_l to the closest constellation point $(\hat{\mathbf{a}}_{\text{ex}})_l$ in the extended symbol set, after which the modulo operator retrieves the corresponding decision of the original data symbol $\hat{\text{a}}_l$. Consequently, multiple constellation points $(\hat{\mathbf{a}}_{\text{ex}})_l$ yield the same $\hat{\text{a}}_l$ such that a correct $\hat{\text{a}}_l$ is obtained when u_l is inside the union of multiple decision regions. For example, Fig. 6.3 presents the extended symbol constellation of the 4-PAM constellation. When a_l is for instance equal to Δ, the decision $\hat{\text{a}}_l$ is correct if and only if u_l is an element of $\cup_{q\in\mathbb{Z}}\mathcal{D}(\Delta + 2qM\Delta)$. Based on this reasoning, an expression for $\text{SER}_{\mathbf{g}_{\text{ch}}}^{(l)}$ can be derived as follows:

$$\text{SER}_{\mathbf{g}_{\text{ch}}}^{(l)} = \Pr\left(\hat{\text{a}}_l \neq \text{a}_l\right) = 1 - \Pr\left(\hat{\text{a}}_l = \text{a}_l\right) \tag{6.40}$$

$$= 1 - \sum_{q\in\mathbb{Z}} \Pr\left(\text{u}_l \in \mathcal{D}\left((\mathbf{a}_{\text{ex}})_l + 2qM\Delta\right)\right). \tag{6.41}$$

In Appendix 11.5, an elaborate discussion is given on how to derive the following expression for $\text{SER}_{\mathbf{g}_{\text{ch}}}^{(l)}$:

$$\text{SER}_{\mathbf{g}_{\text{ch}}}^{(l)} = 1 - \left(\mathbb{E}_{\mathbf{a}_{\text{ex}},\mathbf{v}_{\text{isi}}}\left[\sum_{q\in\mathbb{Z}} \text{Q}\left(\frac{-\Delta + 2qM\Delta - \text{e}_l\left(\mathbf{a}_{\text{ex}}\right)_l - \text{isi}_l\left(\mathbf{v}_{\text{ISI}}, \mathbf{a}_{\text{ex}}^{(\text{ISI})}\right)}{\sigma_{\text{w}_l}}\right)\right.\right.$$
$$\left.\left. - \text{Q}\left(\frac{\Delta + 2qM\Delta - \text{e}_l\left(\mathbf{a}_{\text{ex}}\right)_l - \text{isi}_l\left(\mathbf{v}_{\text{ISI}}, \mathbf{a}_{\text{ex}}^{(\text{ISI})}\right)}{\sigma_{\text{w}_l}}\right)\right]\right), \tag{6.42}$$

where the expectation $\mathbb{E}_{\mathbf{a}_{\text{ex}},\mathbf{v}_{\text{isi}}}[\cdot]$ denotes the expectation over all possible $\mathbf{v}_{\text{ISI}}$, and all possible vectors $\mathbf{a}_{\text{ex}}$, i.e., both $(\mathbf{a}_{\text{ex}})_l$ and $\mathbf{a}_{\text{ex}}^{(\text{ISI})}$. Averaging the $\text{SER}_{\mathbf{g}_{\text{ch}}}^{(l)}$

from (6.42) over all symbol streams and all channel realizations then results in the average $\overline{\mathrm{SER}}$, i.e.,

$$\overline{\mathrm{SER}} = \mathbb{E}_{\mathbf{G}_{\mathrm{ch}}}\left[\frac{1}{L}\sum_{l=1}^{L}\mathrm{SER}_{\mathbf{g}_{\mathrm{ch}}}^{(l)}\right]. \tag{6.43}$$

6.3.2 BER expression for M-PAM transmission

Similar to the derivation in Section 5.4.2, $\mathrm{BER}_{\mathbf{g}_{\mathrm{ch}}}^{(l)}$ can be expressed as

$$\mathrm{BER}_{\mathbf{g}_{\mathrm{ch}}}^{(l)} = \frac{1}{\log_2(M)}\sum_{\mathfrak{a}_{\mathrm{ex}},\mathfrak{a}} N_{\neq}\left(\mathfrak{a}_{\mathrm{ex}},\mathfrak{a}\right)\Pr\left(\mathrm{u}_l \in \mathcal{D}(\mathfrak{a}_{\mathrm{ex}}), \mathrm{a}_l = \mathfrak{a}\right), \tag{6.44}$$

where the summation is over all elements $\mathfrak{a}_{\mathrm{ex}}$ in the extended symbol set and all $\mathfrak{a}$ in the symbol set $\mathcal{C}_{M-\mathrm{PAM}}$. Hence, contrary to the SER, not only whether or not the symbol $\hat{\mathrm{a}}_l$ is correctly decoded is important, but also the number of bit differences between $\hat{\mathrm{a}}_l$ and a_l in the case of an incorrect decision influences $\mathrm{BER}_{\mathbf{g}_{\mathrm{ch}}}^{(l)}$. To evaluate (6.44), the repetitive nature of the extended symbol constellation, the uniform distribution of a_l, and the symmetry in both the symbol constellation and the PDF of isi_l can be exploited to express $\mathrm{BER}_{\mathbf{g}_{\mathrm{ch}}}^{(l)}$ as a sum of Q-functions. However, the number of terms in this summation rapidly increases with M, making it difficult to derive a general and compact expression for $\mathrm{BER}_{\mathbf{g}_{\mathrm{ch}}}^{(l)}$. Nevertheless, an expression for $\mathrm{BER}_{\mathbf{g}_{\mathrm{ch}}}^{(l)}$ in the case of 4-PAM and 8-PAM is developed in Appendix 11.6.

As an alternative, one can, similarly as in Section 5.4.2, assume that an erroneous decision will result in just one erroneous bit error, as neighboring symbols differ only at one bit position in the case of Gray mapping. With this assumption, $N_{\neq}$ in (6.44) is always equal to one, resulting in a lower bound on $\mathrm{BER}_{\mathbf{g}_{\mathrm{ch}}}^{(l)}$ that equals $\mathrm{SER}_{\mathbf{g}_{\mathrm{ch}}}^{(l)}$ divided by $\log_2(M)$, i.e.,

$$\mathrm{BER}_{\mathbf{g}_{\mathrm{ch}},\mathrm{LB}}^{(l)} \approx \frac{1}{\log_2(M)}\mathrm{SER}_{\mathbf{g}_{\mathrm{ch}}}^{(l)}. \tag{6.45}$$

Again, averaging the $\mathrm{BER}_{\mathbf{g}_{\mathrm{ch}},\mathrm{LB}}^{(l)}$ over all symbol streams and channel realizations yields a lower bound on the average $\overline{\mathrm{BER}}$.

6.3.3 Numerical evaluation of the SER and BER expression

When evaluating $\overline{\mathrm{SER}}$ from (6.43), not only the same two difficulties as in Section 5.4.3 must be faced, but also the infinite summation over q can of course not be exactly assessed. The following approximations are therefore employed to overcome these difficulties:

- The expectation $\mathbb{E}_{\mathbf{G}_{\mathrm{ch}}}[\cdot]$ over the different channel realizations is again approximated by taking the arithmetic average over a representative subset of N_{ch} channel realizations.

- An analytical expression for the average of the Q-functions in (6.42) over the joint distribution of $\mathbf{a}_{\text{ex}}$ and $\mathbf{v}_{\text{ISI}}$ is not readily available. Moreover, since $\mathbf{v}_{\text{ISI}}$ is a continuous-time vector, the number of different possible isi_l terms is in principle infinitely large such that one cannot simply sum over all $\mathbf{v}_{\text{ISI}}$. Still, one can easily approximate the expectation $\mathbb{E}_{\mathbf{a}_{\text{ex}},\mathbf{v}_{\text{isi}}}[\cdot]$ by generating a large number N of different values for $\mathbf{a}_{\text{ex}}$ and $\mathbf{v}_{\text{ISI}}$ by means of (6.1) and subsequently averaging all Q-functions over the obtained set of values.

- As for the infinite summation over q, the terms corresponding to $q = 0$ are dominant such that all other terms can be disregarded.

Based on these last two approximations, a reliable indication of $\text{SER}_{\mathbf{g}_{\text{ch}}}^{(l)}$ is given by

$$\text{SER}_{\mathbf{g}_{\text{ch}}}^{(l)} \approx 1 - \frac{1}{N}\left(\sum_{n=1}^{N} \text{Q}\left(\frac{-\Delta - \text{e}_l\left(\mathbf{a}_{\text{ex},n}\right)_l - \text{isi}_l\left(\mathbf{a}_{\text{ex},n}^{(\text{ISI})}, \mathbf{v}_{\text{ISI},n}\right)}{\sigma_{\text{w}_l}}\right)\right.$$
$$\left. -\text{Q}\left(\frac{\Delta - \text{e}_l\left(\mathbf{a}_{\text{ex},n}\right)_l - \text{isi}_l\left(\mathbf{a}_{\text{ex},n}^{(\text{ISI})}, \mathbf{v}_{\text{ISI},n}\right)}{\sigma_{\text{w}_l}}\right)\right). \tag{6.46}$$

Subsequently, averaging (6.46) over all symbol streams and all channel realizations results in a numerical approximation of $\overline{\text{SER}}$ denoted by $\overline{\text{SER}}_1$.

As for $\overline{\text{BER}}$, the same approximations as for the SER can be applied to $\text{BER}_{\mathbf{g}_{\text{ch}},\text{LB}}^{(l)}$, yielding an approximation $\overline{\text{BER}}_1$.

6.4 Numerical results and discussion

To illustrate the performance of the equalization scheme and equalization strategies proposed in this chapter, this section presents, similar to Section 5.5, several numerical results for baseband M-PAM transmission over the MIMO chip-to-chip interconnect that is affected by manufacturing tolerances (Chapter 2). The SNR is again defined as the ratio of the transmitted energy per bit to the one-sided spectral density of the channel noise, i.e., $\text{SNR} = \frac{E_{\text{TX}}}{\log_2(M)N_0}$. Unless mentioned otherwise, 2-PAM transmission is employed with the sampling delay ϵ set to 0. Moreover, the linear equalizers are restricted to be symbol-spaced and at least $N = 10^6$ terms are employed in the determination of $\text{SER}_{\mathbf{g}_{\text{ch}}}^{(l)}$.

Below, the different equalization strategies are first compared by plotting their performance as a function of σ_r and L_{W} in Figs. 6.4 and 6.5, respectively, after which the convergence of the different equalization strategies is discussed in Fig. 6.6. Next, the BER achieved by means of this equalization scheme is compared with the BER achieved by the equalization schemes from Chapter 5 (Figs. 6.7 and 6.8). In addition, the accuracy of the numerical evaluation of

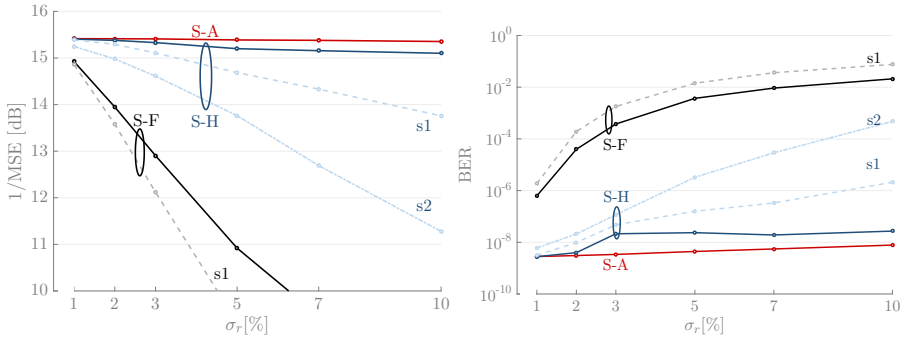

Figure 6.4: Performance of all equalization strategies in terms of both $1/\overline{\text{MSE}}$ (left plot) and $\overline{\text{BER}}$ (right plot) as a function of σ_r for SNR $= 25\,\text{dB}$, $L_{\text{X}} = 7$, and $\Phi_{\mathbf{T}} = \Phi_{\mathbf{T},16}$. Similar relative performance as for the DFE equalization scheme can be observed.

the BER is investigated in Fig. 6.9. Finally, the assumption that each element of $\mathbf{v}(k)$ is uniformly distributed over $[-M\Delta, M\Delta)$ is verified in Fig. 6.10.

To facilitate the comparison of the different equalization strategies in terms of performance, Fig. 6.4 presents both $\overline{\text{MSE}}$ and $\overline{\text{BER}}$ for all strategies as a function of σ_r when SNR $= 25\,\text{dB}$ and $L_{\text{X}} = 7$, while the feedback filter of the THP consists of 16 taps, i.e., $\Phi_{\mathbf{T}} = \Phi_{\mathbf{T},16} = \{1, \cdots, 16\}$. In general, the different strategies exhibit similar relative performance as in the case of the equalization scheme from Chapter 5 (Fig. 5.6). The following observations can be made:

- In terms of performance, the adjustable strategy is superior to all other equalization strategies, and this performance is fairly constant over the whole range of σ_r. Moreover, the $\overline{\text{MSE}}$ performance of the adjustable strategy in Fig. 6.4 and the $\overline{\text{MSE}}$ performance of the adjustable strategy in the case of the DFE equalization scheme in Fig 5.6 are related in a simple way, when the lengths of the corresponding linear equalizers are the same and $\Phi_{\mathbf{T}} = \Phi_{\mathbf{B}}$. Indeed, under this condition, it can be verified that, after optimization, the system with a DFE and the system with a THP yield the same feedback filter and the same linear equalizer at the receiver; for the THP equalization scheme, the coefficients of the linear equalizer at the transmitter and the scaling factor at the receiver are obtained by multiplying the corresponding quantities of the DFE equalization scheme by a factor $\frac{\sigma_a}{\sigma_v}$ (because of the power loss of the THP system) and a factor $\frac{\sigma_v}{\sigma_a}$, respectively. As result, the minimized MSE of the system with THP is larger by a factor $\frac{\sigma_v^2}{\sigma_a^2}$, compared to the system with DFE. For 2-PAM, this factor amounts to $4/3$ (or about 1.25 dB), which corresponds to the difference observed when comparing Fig. 5.6 (right plot) and Fig. 6.4.

- Fig. 6.4 further demonstrates that the optimal hybrid strategy performs only slightly worse than the optimal adjustable strategy when σ_r is relatively small. Compared to the DFE equalization scheme, the performance gap between the hybrid and the adjustable strategy, however, grows faster with increasing σ_r in the case of the THP equalization scheme considered here, because more equalization parameters are fixed.

- The performance of the optimal fixed strategy is again not competitive with the adjustable, nor with the optimal hybrid strategy, since both $\overline{\text{MSE}}$ and $\overline{\text{BER}}$ corresponding to the fixed strategy quickly rise with increasing σ_r. Just as for the adjustable strategy, the $\overline{\text{MSE}}$ of the fixed strategy in the case of the THP equalization scheme is in fact larger by a factor $\frac{\sigma_v^2}{\sigma_a^2}$ (1.25 dB for 2-PAM) than in the case of the DFE equalization scheme from Chapter 5.

- Because the feedback filter $\mathbf{T}$ is fixed in the hybrid strategy, considering the second-order moments in the design of the fixed filters in the hybrid strategy is more important for the THP equalization scheme than for the DFE equalization scheme from Chapter 5. Indeed, the performance difference between the optimal hybrid strategy and the suboptimal approach S-H_{s1} is insignificant for small σ_r, but intolerably increases for larger σ_r. For example, the $\overline{\text{BER}}$ is more than a factor 100 larger for S-H_{s1} compared to the optimal hybrid strategy at $\sigma_r = 10\%$. As for the fixed strategy, the relative performance of the optimal fixed strategy and the suboptimal S-F_{s1} is similar to Fig. 5.6.

- Just as the filter $\mathbf{W}$ in the other strategies, the cascade of $\mathbf{W}_{\text{fix}}$ and $\mathbf{W}_{\text{adj}}$ contains 15 taps in the second suboptimal strategy S-H_{s2}. More precisely, $L_{\text{W,fix}}^{(1)} = L_{\text{W,fix}}^{(2)} = 2$ and $L_{\text{W,adj}}^{(1)} = L_{\text{W,adj}}^{(2)} = 5$. Fig. 6.4 demonstrates that this suboptimal approach yields unsatisfactory performance that is even worse than the performance of the first suboptimal approach S-H_{s1}. While the performance gap between the adjustable strategy and the suboptimal S-H_{s2} is quite large and constant in the case of the DFE equalization scheme (right plot of Fig. 5.6), this performance gap in the case of the THP equalization scheme is relatively small for small σ_r and quickly grows with increasing σ_r, indicating the optimization approach from [53] is not suitable for larger levels of variability.

Similar to Fig. 5.8 from Chapter 5, the performance of the different strategies as a function of L_{W} is interesting to investigate when the total number of taps in the cascade of the linear filters $\mathbf{P}$ and $\mathbf{W}$ remains constant. To this end, Fig 6.5 presents both the $\overline{\text{MSE}}$ and the $\overline{\text{BER}}$ performance for all three optimal equalization strategies as a function of L_{W} in the case of $\sigma_r = 5\%$, SNR = 25 dB, and $\Phi_{\mathbf{T}} = \Phi_{\mathbf{T},16}$, while the cascade of $\mathbf{P}$ and $\mathbf{W}$ always contains 29 taps. In general, the same conclusions as for the DFE equalization scheme from Chapter 5 can be drawn. Indeed, the adjustable strategy has a

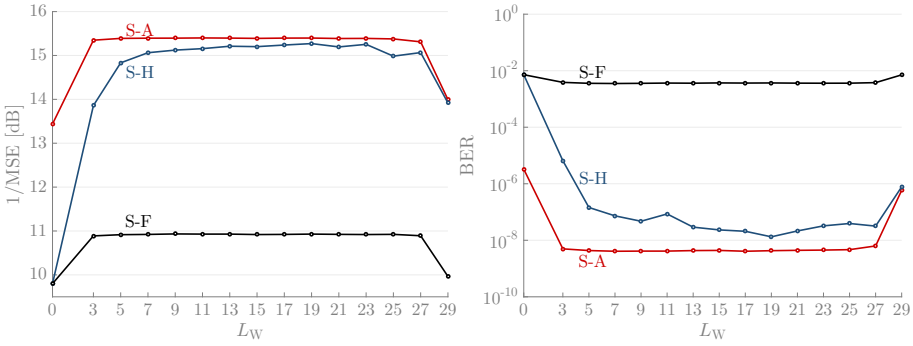

Figure 6.5: Performance of the adjustable, the hybrid, and the fixed strategy in terms of both $1/\overline{\mathrm{MSE}}$ and $\overline{\mathrm{BER}}$ as a function of L_{W} for $\sigma_r = 5\%$, $\mathrm{SNR} = 25\,\mathrm{dB}$, and $\Phi_{\mathbf{T}} = \Phi_{\mathbf{T},16}$, while the total number of taps in the cascade of $\mathbf{P}$ and $\mathbf{W}$ remains constant and equal to 29. Similar conclusions as in Fig. 5.8 can be drawn.

nearly constant performance, except when only one the of the linear filters is present. The performance of the fixed strategy is inferior to the performance of the adjustable strategy in the whole range of L_{W}. As for the hybrid strategy, a sharp performance gain is observed when going from small to moderate L_{W}, while the hybrid strategy only marginally performs worse than the adjustable strategy at larger L_{W}. Compared to the right plot in Fig. 5.8, however, the performance gain at low L_{W} is less sharp and the performance gap between the adjustable and the hybrid strategy at moderate to large L_{W} is slightly larger, because relatively more equalization parameters are fixed in the THP equalization scheme. Still, competitive performance can be achieved by the hybrid strategy with a relatively small number of adjustable equalization coefficients.

For each strategy, the alternating optimization algorithm presented here to minimize $\overline{\mathrm{MSE}}$ is structurally identical to the alternating optimization algorithm proposed in Chapter 5 to minimize $\overline{\mathrm{MSE}}$ in the case of the DFE equalization scheme. Unsurprisingly, the convergence of both alternating algorithms is similar as well. More precisely, the largest decrease in $\overline{\mathrm{MSE}}$ is observed in the first iterations, whereas later iterations yield only marginal performance gains. Fig. 6.6 confirms these observations by presenting $\overline{\mathrm{MSE}}$ and the relative decrease γ as a function of the number of iterations N_{it} in the case of $\sigma_r = 3\%$, $\mathrm{SNR} = 25\,\mathrm{dB}$, $L_{\mathrm{X}} = 7$, and $\Phi_{\mathbf{T}} = \Phi_{\mathbf{T},16}$. Still, this figure indicates that the hybrid strategy requires slightly more iterations to reach convergence than the adjustable and the fixed strategy, which is probably because the feedback filter $\mathbf{T}$ is also iteratively obtained in the hybrid strategy, whereas this feedback filter $\mathbf{T}$ is always optimal for given $(\mathbf{P}, \alpha, \mathbf{W})$ in the case of the adjustable and the fixed strategy.

The goal of Figs. 6.7 and 6.8 is to compare the BER performance achieved

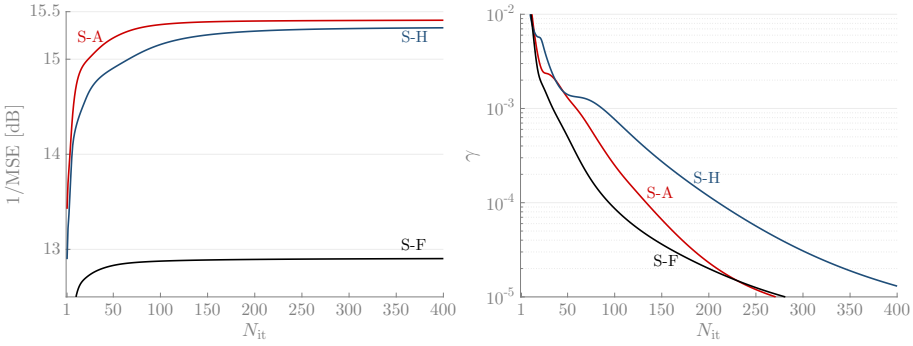

Figure 6.6: Performance of the adjustable, the hybrid, and the fixed strategy in terms of $\overline{\text{MSE}}$ and relative decrease γ as a function of N_{it} when $\sigma_r = 3\%$, SNR $= 25\,\text{dB}$, $L_{\text{X}} = 7$, and $\Phi_{\mathbf{T}} = \Phi_{\mathbf{T},16}$. Evidently, most performance improvement is achieved in the first iterations of the alternating optimization algorithms.

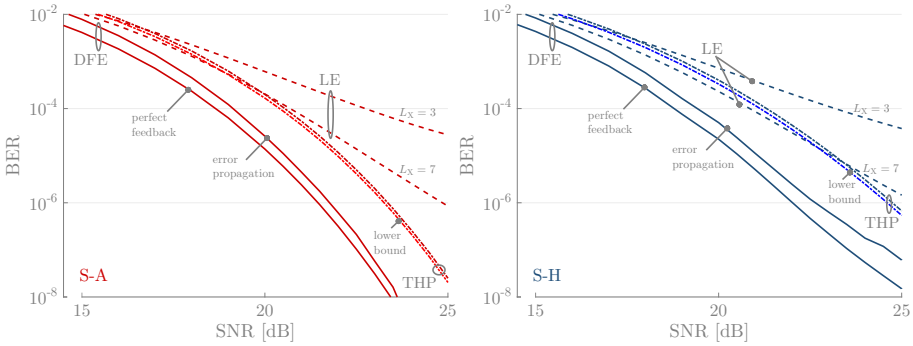

Figure 6.7: Performance of the adjustable (left) and the hybrid (right) strategy in terms of $\overline{\text{BER}}$ as a function of SNR in the case of 2-PAM transmission and $\sigma_r = 5\%$. In total, three configurations are considered: (i) the linear equalization scheme ($L_{\text{X}} = 3$ or $L_{\text{X}} = 7$), (ii) the DFE equalization scheme ($L_{\text{X}} = 3$ and $\Phi_{\mathbf{B}} = \Phi_{\mathbf{B},16}$), and (iii) the THP equalization scheme ($L_{\text{X}} = 3$ and $\Phi_{\mathbf{T}} = \Phi_{\mathbf{T},16}$). For 2-PAM transmission, the DFE equalization scheme results in the best performance.

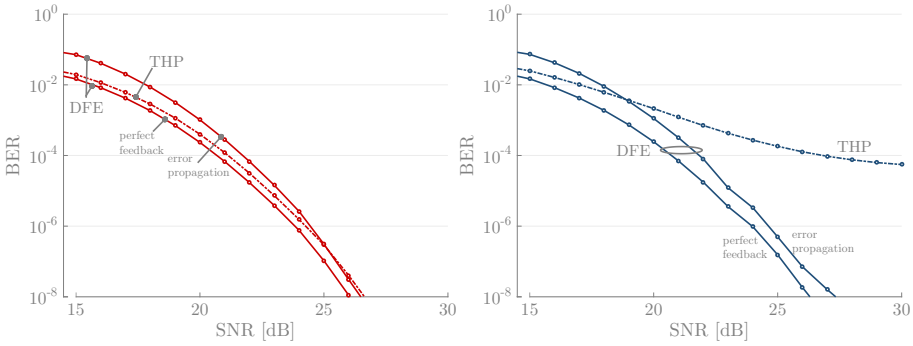

Figure 6.8: Performance of the adjustable (left) and the hybrid (right) strategy in terms of $\overline{\text{BER}}$ as a function of SNR in the case of 4-PAM transmission and $\sigma_r = 3\%$. Two equalization schemes are considered: (i) the DFE equalization scheme ($L_{\text{X}} = 7$ and $\Phi_{\mathbf{B}} = \{16 \text{ dominant feedback taps}\}$) and (ii) the THP equalization scheme ($L_{\text{X}} = 3$ and $\Phi_{\mathbf{T}} = \{16 \text{ dominant feedback taps}\}$). Due to the larger constellation size, the power loss is smaller than in Fig. 6.7 and, at moderate SNR, the THP equalization scheme performs better than the DFE equalization scheme with error propagation in the case of S-A.

in the case of the THP equalization scheme with the BER performance corresponding to the linear equalization scheme and the DFE equalization scheme, presented in Chapter 5, for 2-PAM and 4-PAM transmission, respectively. In Fig. 6.7, σ_r is set to 5% and both the adjustable (left plot) and the hybrid strategy (right plot) are considered for the following three equalizer configurations: (i) the linear equalization scheme ($L_{\text{X}} = 3$ or $L_{\text{X}} = 7$), (ii) the DFE equalization scheme ($L_{\text{X}} = 3$ and $\Phi_{\mathbf{B}} = \Phi_{\mathbf{B},16}$), and (iii) the THP equalization scheme ($L_{\text{X}} = 3$ and $\Phi_{\mathbf{T}} = \Phi_{\mathbf{T},16}$). On the other hand, the BER associated with only equalizer configurations (ii) and (iii) are included in the case of $\sigma_r = 3\%$ in Fig. 6.8, where now $L_{\text{X}} = 7$ and the various feedback equalizers are obtained by selecting the 16 most dominant taps of a long feedback filter with 100 active time delays. Note that for a fair comparison, the number of equalization parameters is the same for the DFE equalization scheme and the THP equalization scheme. In the case of a DFE, the figures include both the BER assuming perfect feedback and the simulated BER with error propagation. In the case of 2-PAM transmission, a lower bound that excludes the effect of the modulo loss is added in the case of THP in Fig. 6.7. This lower bound is only valid for 2-PAM and constructed by assuming that each decision region possesses only one decision boundary instead of two. The following remarks can be made:

- As for the adjustable strategy in the case of 2-PAM signaling (Fig. 6.7), the BER associated with the THP equalization scheme is smaller for medium to larger SNR compared to the linear equalization scheme with

long equalizers ($L_{\mathrm{X}} = 7$), indicating that, in this SNR range, the THP equalization scheme is preferred to the linear equalization scheme with long linear equalizers. Still, the THP equalization scheme is clearly outperformed by the DFE equalization scheme, even when the error propagation of the latter is taken into account. Comparing the expression for $\overline{\mathrm{SER}}$ of both equalization schemes, this performance gap can mainly be attributed to the power loss (1.25 dB for 2-PAM) and the larger values of $\mathbf{isi}(k)$, because $\mathbf{v}(k)$ can assumes larger values than $\mathbf{a}(k)$ when a THP precoder is present. The impact of the modulo loss is verified to be minor as the gap between the lower bound and the actual performance is small. Hence, the DFE equalization scheme is the most favorable in terms of performance in the case of 2-PAM transmission.

- The influence of the power loss dramatically reduces for larger constellations, e.g., for the 4-PAM transmission in Fig. 6.8 this power loss equals 16/15 or 0.28 dB, which is almost 1 dB lower than in the case of the 2-PAM constellation from Fig. 6.7. By comparing these two figures, one can clearly see that the performance gap between the THP equalization scheme and the DFE equalization scheme considerably reduces. In the case of the adjustable strategy and 4-PAM transmission, the THP equalization scheme yields even better performance at moderate SNR than the DFE equalization scheme when the effect of the error propagation in the latter scheme is taken into consideration.

- The performance gap between the THP equalization scheme and DFE equalization scheme is larger in the case of the hybrid strategy than in the case of the adjustable strategy, as the feedback filter is fixed in the former equalization scheme and adjustable in the latter equalization scheme. Due to the smaller decision areas corresponding to the 4-PAM constellation, the THP equalization scheme cannot even remove enough ISI to avoid an error floor in the right plot of Fig. 6.8.

The accuracy of the approximation $\overline{\mathrm{BER}}_1$ is examined in Fig. 6.9, which presents first $\overline{\mathrm{BER}}_1$ as a function of the SNR when $\sigma_r = 3\%$, $L_{\mathrm{X}} = 7$, $\Phi_{\mathbf{T}} = \Phi_{\mathbf{T},16}$, and $N = 2 \cdot 10^6$. Additionally, the simulated $\overline{\mathrm{BER}}_{\mathrm{sim}}$ is included as well and this value is obtained by counting the bit errors in a numerical simulation of the transmission of $2 \cdot 10^6$ symbols over each trace of all channel realizations, yielding a total of $8 \cdot 10^9$ transmitted symbols. Thirdly, Fig. 6.9 also presents $\overline{\mathrm{BER}}_{1,q}$, which is similarly constructed as $\overline{\mathrm{BER}}_1$ but in the case of $\overline{\mathrm{BER}}_{1,q}$ all terms corresponding to $q \in \{-1, 0, 1\}$ are included in the summation in (6.42) rather than only the terms corresponding to $q = 0$. Clearly, Fig. 6.9 indicates that all three computation methods yield similar numerical results in the entire range of SNR, confirming that $\overline{\mathrm{BER}}_1$ is a good approximation of $\overline{\mathrm{BER}}$. Moreover, this figure demonstrates that the terms corresponding to $q = 0$ are indeed dominant in (6.42).

In the computation of the optimal equalization parameters, all elements of

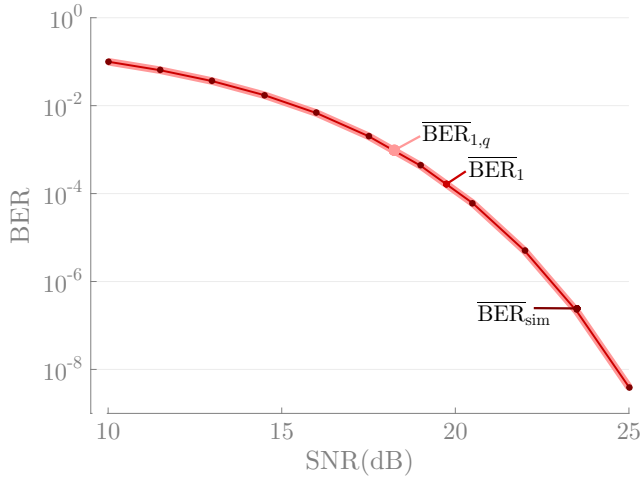

Figure 6.9: Investigation of the accuracy of $\overline{\text{BER}}_1$ (thin line) as a function of the SNR for $\sigma_r = 3\%$, $L_{\text{X}} = 7$, $\Phi_{\mathbf{T}} = \Phi_{\mathbf{T},16}$, and $N = 2 \cdot 10^6$. For verification, the simulated $\overline{\text{BER}}_{\text{sim}}$ (circular markers) and the $\overline{\text{BER}}_{1,q}$ (thick line) are added. This plot confirms that the numerical approximation of $\overline{\text{BER}}_1$ is reliable when N is sufficiently large.

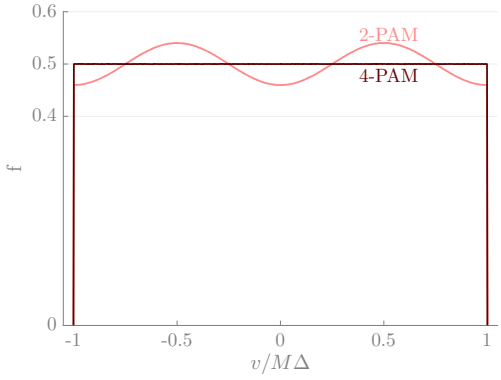

Figure 6.10: Simulated distribution $f(\cdot)$ of $(\mathbf{v}(k))_{1,1}$ in the case of the 2-PAM and the 4-PAM constellation for $\sigma_r = 3\%$, SNR $= 25\,\text{dB}$, $L_{\text{X}} = 7$, and $\Phi_{\mathbf{T}} = \Phi_{\mathbf{T},16}$. The assumption of the uniform distribution holds better for larger constellations as stated by Theorem 3.1 of [21].

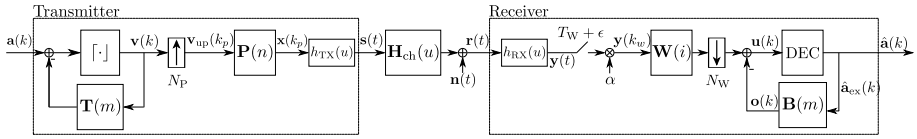

Figure 6.11: System model of the equalization scheme with a nonlinear THP and a linear equalizer at the transmitter, and a nonlinear DFE at the receiver.

the vector $\mathbf{v}(k)$ are assumed to be independent and uniformly distributed over the interval $[-M\Delta, M\Delta)$ as stated by Theorem 3.1 of [21]. The assumption of this uniform distribution is verified in Fig. 6.10, which plots the simulated distribution $f(\cdot)$ of $(\mathbf{v}(k))_{1,1}$ in the case of the 2-PAM and the 4-PAM constellation for the adjustable strategy with $\sigma_r = 3\%$, SNR $= 25\,\mathrm{dB}$, $L_\mathrm{X} = 7$, and $\Phi_\mathbf{T} = \Phi_{\mathbf{T},16}$. These results are valid for the hybrid and the fixed strategies as well.

Several observations made in Chapter 5 for the DFE equalization scheme can be made here as well, since both MSE optimization problems are structurally similar. For example, the computation of the optimal set of active time delays $\Phi_\mathbf{T}$ for the feedback filter $\mathbf{T}$ can be obtained by a similar approach as for the feedback filter $\mathbf{B}$ in Subsection 5.5.2. Moreover, no significant different behavior in performance is observed compared to Subsection 5.5.3 when one of the linear equalizers is fractionally spaced, i.e., especially an adjustable fractionally-spaced linear equalizer induces a performance gain for all variability levels and has a robustness to different sampling moments. Additionally, the same behavior as in Subsection 5.5.5 is observed when increasing the constellation size, i.e., the BER performance becomes worse when M is increased when the equalization lengths remains the same.

6.5 Addition of a feedback filter at the receiver

Either to improve the performance of the THP equalization scheme from Fig. 6.1, or to reduce the performance gap between the adjustable and the hybrid strategy, the signal processing at the receiver could be enriched by an additional feedback filter $\mathbf{B}$ operating on the decisions $\hat{\mathbf{a}}_\mathrm{ex}(k-m)$ in the extended symbol set (Fig. 6.11). In this section, a brief overview is first given on how this additional feedback filter affects the system equations, the MMSE optimization procedure and the SER expression, compared to the equalization scheme without the feedback filter $\mathbf{B}$. Afterwards, numerical results explore the possible improvements in performance as a result of this decision-feedback filter. In this section, the abbreviation THP-DFE refers to the equalization scheme from Fig. 6.11.

First of all, the decision-feedback filter $\mathbf{B}$ acts on the previously detected extended symbols $\hat{\mathbf{a}}_\mathrm{ex}(k-m)$, where all active causal time delays $m > 0$ are

collected in the set $\Phi_{\mathbf{B}}$. As a result, the decision variable in the system model of Fig. 6.11 can be written as

$$\mathbf{u}(k) = \alpha \sum_{m \in \Phi} \mathbf{W}\mathbf{G}(m)\mathbf{P}\mathbf{v}(k-m) + \alpha \mathbf{W}\bar{\mathbf{n}}(k) - \sum_{m \in \Phi_{\mathbf{B}}} \mathbf{B}(m)\hat{\mathbf{a}}_{\text{ex}}(k-m). \quad (6.47)$$

As the decision-feedback filter does not alter the fact that the decision $\hat{\mathbf{a}}(k)$ is obtained by performing symbol-by-symbol detection on $\mathbf{u}(k)$ in the extended symbol set, the MSE between $\mathbf{u}(k)$ and $\hat{\mathbf{a}}_{\text{ex}}(k)$ is still a proper objective function to derive an appropriate set of equalization coefficients. For a given channel realization $\mathbf{g}_{\text{ch}}$ the $\text{MSE}_{\mathbf{g}_{\text{ch}}}$ is thus defined as

$$\text{MSE}_{\mathbf{g}_{\text{ch}}} = \frac{1}{L\sigma_{\text{a}}^2}\mathbb{E}\left[\left\| \alpha \sum_{m \in \Phi} \mathbf{W}\mathbf{G}(m)\mathbf{P}\mathbf{v}(k-m) + \alpha \mathbf{W}\bar{\mathbf{n}}(k) - \sum_{m \in \Phi_{\mathbf{B}}} \mathbf{B}(m)\hat{\mathbf{a}}_{\text{ex}}(k-m) - \mathbf{a}_{\text{ex}}(k) \right\|^2\right]. \quad (6.48)$$

Just as for the decision-feedback filter in Chapter 5, the decisions $\hat{\mathbf{a}}_{\text{ex}}(k-m)$ are assumed to be correct in the design of the equalization coefficients, as the minimization of $\text{MSE}_{\mathbf{g}_{\text{ch}}}$ is otherwise too complicated to solve. Moreover, expressing $\mathbf{a}_{\text{ex}}(k-m)$ and $\mathbf{a}_{\text{ex}}(k)$ in (6.48) as a function of the sequence $\{\mathbf{v}(k)\}$ using (6.3), the $\text{MSE}_{\mathbf{g}_{\text{ch}}}$ expression becomes

$$\text{MSE}_{\mathbf{g}_{\text{ch}}} = \frac{1}{L\sigma_{\text{a}}^2}\mathbb{E}\left[\left\| \alpha \sum_{m \in \Phi} \mathbf{W}\mathbf{G}(m)\mathbf{P}\mathbf{v}(k-m) + \alpha \mathbf{W}\bar{\mathbf{n}}(k) - \mathbf{v}(k) - \sum_{m \in \Phi_{\mathbf{B}}} \mathbf{B}(m)\Big(\mathbf{v}(k-m) + \sum_{j \in \Phi_{\mathbf{T}}} \mathbf{T}(j)\mathbf{v}(k-m-j)\Big) - \sum_{j \in \Phi_{\mathbf{T}}} \mathbf{T}(j)\mathbf{v}(k-j) \right\|^2\right]. \quad (6.49)$$

Since the channel considered in this chapter is assumed to be random, the equalization parameters associated with this equalization scheme are again obtained by following the optimization procedure from Chapter 4. More precisely, the objective function f_0 is equal to the $\text{MSE}_{\mathbf{g}_{\text{ch}}}$ from (6.49), whereas the energy constraint is the same as in optimization problem (6.12). In total, three equalization strategies (Table 6.2) are examined in more detail: the adjustable, the fixed and the hybrid strategy. As above, all equalization parameters, including the coefficients of the decision-feedback filter, are adjustable in the adjustable strategy and thus belong to the vector $\mathbf{x}(\mathbf{g}_{\text{ch}})$, whereas all equalization parameters are fixed in the fixed strategy and thus belong to the vector $\mathbf{y}$. In the hybrid strategy, the decision-feedback filter is adjustable to the channel, implying that the performance gap between the adjustable and the hybrid strategy should reduce compared to the THP equalization scheme.

For conciseness and clarity, the mathematical derivation of the optimal equalization parameters in the considered strategies is omitted here, but one

Table 6.2: Overview of the different equalization strategies.

Strategy	Notation	Adjustable parameters	Fixed parameters
Adjustable	S-A	$\mathbf{P}, \alpha, \mathbf{W}, \mathbf{T}, \mathbf{B}$	/
Fixed	S-F	/	$\mathbf{P}, \alpha, \mathbf{W}, \mathbf{T}, \mathbf{B}$
Hybrid	S-H	$\mathbf{W}, \mathbf{B}$	$\mathbf{P}, \alpha, \mathbf{T}$

can resort to Appendix 11.7 for more details. One important remark is, however, that in each equalization strategy the optimal equalization parameters are again the result of an iterative algorithm. As for the adjustable strategy, the feedback filter in the equalization schemes above, i.e., $\mathbf{B}$ in the DFE equalization scheme (Fig. 5.1) and $\mathbf{T}$ in the THP equalization scheme (Fig. 6.1), could directly be expressed as a function of the other equalization parameters, which are subsequently obtained by iteratively minimizing the $\mathrm{MSE}_{\mathbf{g}_{\mathrm{ch}}}$ optimized over this feedback filter. This optimization approach is unfortunately not possible for the THP-DFE equalization scheme of Fig. 6.11, because the optimal feedback filters $\mathbf{T}$ and $\mathbf{B}$ are not independent from each other as the $\mathrm{MSE}_{\mathbf{g}_{\mathrm{ch}}}$ in (6.49) is composed of several product terms in which both the $\mathbf{T}$ and $\mathbf{B}$ are present. As an alternative, $\mathrm{MSE}_{\mathbf{g}_{\mathrm{ch}}}$ is optimized by alternately computing the optimal $(\mathbf{P}_a^\star, \alpha_a^\star, \mathbf{T}_a^\star)$ and optimal $(\mathbf{W}_a^\star, \mathbf{B}_a^\star)$ for given $(\mathbf{W}, \mathbf{B})$ and $(\mathbf{P}, \alpha, \mathbf{T})$, respectively. Similar remarks can be made for the fixed strategy.

The SER for the system model corresponding to Fig. 6.11 can be deduced by means of a similar derivation as the SER for the THP equalization scheme without the feedback filter $\mathbf{B}$ (Section 6.3). Indeed, the decision corresponding to the kth symbol of the lth data streams, i.e., $\hat{\mathrm{a}}_l(k)$, is still based on $\mathrm{u}_l(k)$ and must be performed in the extended symbol set. However, the decision-feedback filter $\mathbf{B}$ does change the expression for $\mathrm{u}_l(k)$. More precisely, with the assumption that all previously detected extended data symbols $\hat{\mathbf{a}}_{\mathrm{ex}}(k-m)$ are correct, the decomposition of $\mathrm{u}_l(k)$ from (6.38) still holds, but $\mathbf{isi}(k)(\mathbf{v}_{\mathrm{ISI}}, \mathbf{a}_{\mathrm{ex}}^{(\mathrm{ISI})})$ is now defined as

$$\begin{aligned}\mathbf{isi}(\mathbf{v}_{\mathrm{ISI}}, \mathbf{a}_{\mathrm{ex}}^{(\mathrm{ISI})}) = &\sum_{m\in\Phi\setminus\{0\}} \alpha\mathbf{W}\mathbf{G}(m)\mathbf{P}\mathbf{v}(k-m) + \left(\breve{\mathbf{G}}_0 - \mathrm{diag}\left(\mathbf{e}+\mathbf{1}\right)\right)\mathbf{a}_{\mathrm{ex}}(k) \\ &- \sum_{m\in\Phi_{\mathbf{T}}} \breve{\mathbf{G}}_0\mathbf{T}(m)\mathbf{v}(k-m) - \sum_{m\in\Phi_{\mathbf{B}}} \mathbf{B}(m)\mathbf{v}(k-m) \\ &- \sum_{m_1\in\Phi_{\mathbf{B}}}\sum_{m_2\in\Phi_{\mathbf{T}}} \mathbf{B}(m_1)\mathbf{T}(m_2)\mathbf{v}(k-m_1-m_2). \end{aligned} \tag{6.50}$$

The remainder of the reasoning in Section 6.3 applies here as well, such that the $\mathrm{SER}_{\mathbf{g}_{\mathrm{ch}}}^{(l)}$ corresponding to the THP-DFE equalization scheme is given by (6.42), where $\mathrm{isi}_l\left(\mathbf{v}_{\mathrm{ISI}}, \mathbf{a}_{\mathrm{ex}}^{(\mathrm{ISI})}\right)$ is now equal to the lth component of $\mathbf{isi}\left(\mathbf{v}_{\mathrm{ISI}}, \mathbf{a}_{\mathrm{ex}}^{(\mathrm{ISI})}\right)$ defined in (6.50).

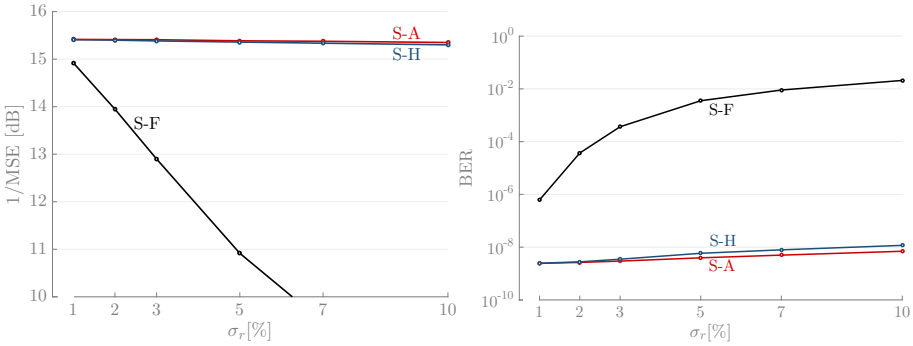

Figure 6.12: Performance of S-A, S-H, and S-F for the THP-DFE equalization scheme, in terms of both $1/\overline{\text{MSE}}$ (left plot) and $\overline{\text{BER}}$ (right plot) as a function of σ_r for SNR $= 25\,\text{dB}$, $L_{\text{X}} = 7$, and $\Phi_{\mathbf{T}} = \Phi_{\mathbf{B}} = \{1, \cdots, 8\}$. The performance gap between the adjustable and the hybrid strategy is smaller than in Fig. 6.4, where $\Phi_{\mathbf{T}} = \Phi_{\mathbf{T},16}$ and $\Phi_{\mathbf{B}} = \emptyset$.

Next, numerical results are provided to investigate the performance of the THP-DFE equalization scheme. Comparing the THP-DFE equalization scheme with the THP equalization scheme is, however, not really fair when assuming that $\Phi_{\mathbf{T}}$ is the same in both equalization schemes and the feedback filter $\mathbf{B}$ is just added in the case of the THP-DFE equalization scheme, as the THP-DFE equalization scheme then obviously outperforms the THP equalization scheme. Therefore, this section compares the THP and the THP-DFE equalization only when the *total* number of feedback taps is identical. First, Fig. 6.12 depicts the performance of the different strategies in the case of the THP-DFE equalization scheme. Second, Fig. 6.13 investigates the effect of considering more and more adjustable taps in the feedback filter at the receiver in the case of the adjustable and the hybrid strategy. Finally, several configurations are considered in Fig. 6.14 to determine the optimal set of active time delays and to compute the equalization parameters.

Fig. 6.12 presents the performance in terms of both $1/\overline{\text{MSE}}$ and $\overline{\text{BER}}$ in the case of the adjustable, the hybrid, and the fixed strategy for the THP-DFE equalization scheme. The system parameters are identical to those from Fig. 6.4, expect for $\Phi_{\mathbf{T}}$, as the 16 feedback taps are equally divided between the transmitter and the receiver. Consequently, the set of active causal delays for both $\mathbf{T}$ and $\mathbf{B}$ is given by $\{1, \cdots, 8\}$. Compared to Fig. 6.4, the addition of the decision-feedback filter $\mathbf{B}$ has the following impact:

- For the adjustable strategy S-A, approximately identical $\overline{\text{MSE}}$ and $\overline{\text{BER}}$ is achieved for both the THP-DFE and the THP equalization schemes. More comments on this observation can be found below.

- Compared to the performance gap between the hybrid and the adjustable

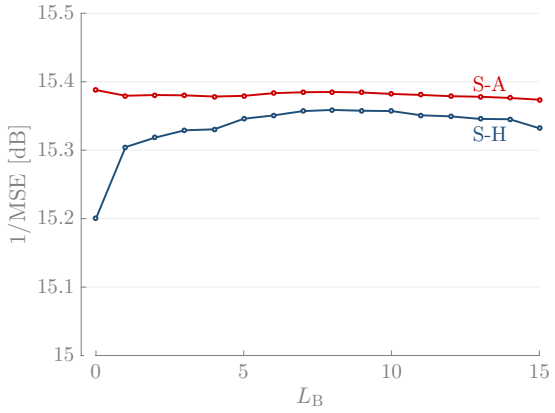

Figure 6.13: Performance of the adjustable and the hybrid strategy in terms of $1/\overline{\mathrm{MSE}}$ as a function of L_{B} for $\sigma_r = 5\%$, SNR $= 25\,\mathrm{dB}$, and $L_{\mathrm{X}} = 7$. The sets $\Phi_{\mathbf{T}}$ and $\Phi_{\mathbf{B}}$ are given by $\{1, \cdots, 16 - L_{\mathrm{B}}\}$ and $\{1, \cdots, L_{\mathrm{B}}\}$, respectively. The adjustable strategy has a nearly constant performance, whereas the hybrid strategy mainly improves for small L_{B}.

strategy for the THP equalization scheme (see Fig. 6.4), the gap for the THP-DFE equalization scheme is significantly smaller (see Fig. 6.12). Because all feedback coefficients are fixed in the former equalization scheme and half of them are adjustable in the latter equalization scheme, this reduction in the performance gap is thus not surprising.

- Regarding the fixed strategy S-F, the same inferior performance is achieved in the case of the THP-DFE equalization scheme as in the case of the THP equalization scheme.

Next, Fig. 6.13 more closely examines the performance difference between the adjustable and the hybrid strategy for the THP-DFE equalization scheme. To this end, this figure plots the $1/\overline{\mathrm{MSE}}$ as a function of the number of taps of the decision-feedback filter $\mathbf{B}$, i.e., L_{B}. Moreover, the number of taps of the feedback filter $\mathbf{T}$, L_{T}, is equal to $16 - L_{\mathrm{B}}$ such that the total number of feedback taps is constant and equal to 16. The sets of active causal delay $\Phi_{\mathbf{T}}$ and $\Phi_{\mathbf{B}}$ are $\{1, \cdots, L_{\mathrm{T}}\}$ and $\{1, \cdots, L_{\mathrm{B}}\}$, respectively, while $\sigma_r = 5\%$, SNR $= 25\,\mathrm{dB}$, and $L_{\mathrm{X}} = 7$. The following can be noted:

- This figure shows that the $\overline{\mathrm{MSE}}$ of the adjustable strategy is practically the same for all values of L_{B}, implying that the performance of the adjustable strategy is influenced mainly by the total number of feedback taps and not by the specific division of these taps over the transmitter and the receiver.

- Since the feedback filter at the receiver is adjustable in the hybrid strat-

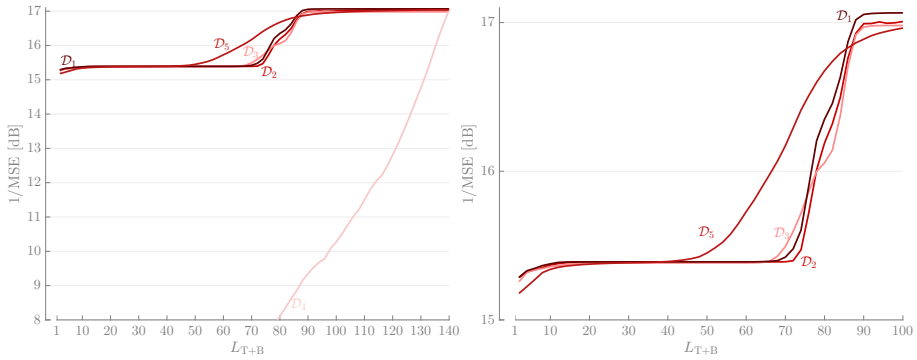

Figure 6.14: Performance of S-A in terms of $1/\overline{\text{MSE}}$ as a function of $L_{\text{T+B}}$ for $\sigma_r = 5\%$, SNR $= 25\,\text{dB}$ and $L_{\text{X}} = 7$. In total, five different methods $\mathcal{D}$ to compute the equalization parameters and the sets $\Phi_{\mathbf{T}}$ and $\Phi_{\mathbf{B}}$ are included. A general overview is given in the left plot, whereas the right plot contains a more detailed view.

egy, better $\overline{\text{MSE}}$ performance is to be expected when L_{B} rises. Fig. 6.13 not only confirms this expectation, but also reveals that most performance improvement is achieved for small L_{B}. Indeed, considering only one adjustable tap at the receiver yields a decrease in the performance gap between the adjustable and the hybrid strategy of almost 60% compared to the case of the THP equalization scheme ($L_{\text{B}} = 0$). Moreover, the smallest performance gap between the adjustable and the hybrid strategy is only slightly more than 10% of the original performance gap corresponding to $L_{\text{B}} = 0$.

Just as for the equalization schemes from Figs. 5.1 and 6.1, in which a feedback filter is included at either the transmitter or the receiver, the selection of the optimal sets of active time delays, i.e., $\Phi_{\mathbf{T}}$ and $\Phi_{\mathbf{B}}$, for a given total number of feedback taps $L_{\text{T+B}} = L_{\text{T}} + L_{\text{B}}$ is extremely hard as many possible combinations exist. As an alternative, five different possible methods $\mathcal{D}$ to determine these active time delays and to compute the corresponding equalization parameters are proposed below, after which their performances are discussed by means of Fig. 6.14.

1. In the first method $\mathcal{D}_1$, only the feedback filter $\mathbf{T}$ at the transmitter is active and all feedback taps correspond to the first $L_{\text{T}} = L_{\text{T+B}}$ causal time delays, meaning that $\Phi_{\mathbf{T}} = \{1, \cdots, L_{\text{T+B}}\}$ and $\Phi_{\mathbf{B}} = \emptyset$. In this case, the THP-DFE equalization scheme of course reduces to the THP equalization scheme and the optimization method from Subsection 6.2.1 is thus applied to compute all equalization parameters.

2. The feedback taps are equally divided between the transmitter and the receiver in the second method $\mathcal{D}_2$ such that $L_{\text{T}} = L_{\text{B}} = \frac{L_{\text{T+B}}}{2}$. More-

over, only the first L_{T} and first L_{B} causal time delays are active in both feedback filters such that $\Phi_{\mathbf{T}} = \{1, \cdots, L_{\mathrm{T}}\}$ and $\Phi_{\mathbf{B}} = \{1, \cdots, L_{\mathrm{B}}\}$, respectively.

3. The third method $\mathcal{D}_3$ again assumes that both feedback filters possess the same number of feedback taps, i.e., $L_{\mathrm{T}} = L_{\mathrm{B}} = \frac{L_{\mathrm{T+B}}}{2}$, but the set $\Phi_{\mathbf{B}}$ is chosen differently than in method $\mathcal{D}_2$. Indeed, the feedback filter $\mathbf{T}$ is active at the first L_{T} causal time delays, whereas the feedback filter $\mathbf{B}$ is active at the subsequent L_{B} causal time delays. Consequently, $\Phi_{\mathbf{T}} = \{1, \cdots, L_{\mathrm{T}}\}$ and $\Phi_{\mathbf{B}} = \{L_{\mathrm{T}} + 1, \cdots, L_{\mathrm{T+B}}\}$.

4. In the fourth method $\mathcal{D}_4$, all equalization parameters are first computed assuming that both feedback equalizers are quite long, i.e., $\Phi_{\mathbf{T}} = \Phi_{\mathbf{B}} = \{1, \cdots, L_{\gg}\}$. Afterwards, the $L_{\mathrm{T+B}}$ active time delays are determined by searching for the L_{T} and L_{B} dominant taps of the feedback filter $\mathbf{T}$ and the feedback filter $\mathbf{B}$, respectively, and the resulting sets $\Phi_{\mathbf{T}}$ and $\Phi_{\mathbf{B}}$ are denoted by $\Phi_{\mathbf{T},\mathcal{D}_4}$ and $\Phi_{\mathbf{B},\mathcal{D}_4}$. Here, $L_{\mathrm{T}} = L_{\mathrm{B}} = \frac{L_{\mathrm{T+B}}}{2}$. The final feedback filter $\mathbf{T}$ ($\mathbf{B}$) is then obtained by keeping all taps corresponding to $\Phi_{\mathbf{T},\mathcal{D}_4}$ ($\Phi_{\mathbf{B},\mathcal{D}_4}$), while setting all other taps to $\mathbf{0}$. Interestingly, the system with the long feedback filters by design outperforms all considered methods $\mathcal{D}$.

5. For the sets $\Phi_{\mathbf{T},\mathcal{D}_4}$ and $\Phi_{\mathbf{B},\mathcal{D}_4}$, the equalization parameters computed by means of method $\mathcal{D}_4$ are not optimal as they are derived with the assumption that $\Phi_{\mathbf{T}} = \Phi_{\mathbf{B}} = \{1, \cdots, L_{\gg}\}$. In this method $\mathcal{D}_5$, the sets $\Phi_{\mathbf{T},\mathcal{D}_4}$ and $\Phi_{\mathbf{B},\mathcal{D}_4}$ are first identically computed as in $\mathcal{D}_4$, but all equalization parameters are afterwards recalculated with $\Phi_{\mathbf{T}} = \Phi_{\mathbf{T},\mathcal{D}_4}$ and $\Phi_{\mathbf{B}} = \Phi_{\mathbf{B},\mathcal{D}_4}$ such that the obtained equalization parameters are optimal for the considered sets of active time delays.

In Fig. 6.14, the $1/\overline{\mathrm{MSE}}$ performance achieved by these different methods $\mathcal{D}$ are presented as a function of $L_{\mathrm{T+B}}$ when $\sigma_r = 5\%$, $\mathrm{SNR} = 25\,\mathrm{dB}$, $L_{\mathrm{X}} = 7$, and $L_{\gg} = 70$. Based on this figure, the following conclusions can be drawn.

- The first three methods $\mathcal{D}_1$-$\mathcal{D}_3$ yield approximately identical performance such that the gain of the additional decision-feedback $\mathbf{B}$ filter is rather small. For all three methods, a gain in MSE performance is noticed around $L_{\mathrm{T+B}} = 80$, since, in contrast to short feedback filters, the ISI caused by the first reflection can be targeted as well (Fig. 2.3). Remarkably, this performance gain in the case of method $\mathcal{D}_3$ is perceived for (slightly) smaller values of $L_{\mathrm{T+B}}$ than in the case of methods $\mathcal{D}_1$ and $\mathcal{D}_2$, since the feedback filters in method $\mathcal{D}_3$ has a larger range of causal time instants from which they can reduce the corresponding interference. Indeed, this range is equal to $m \in \{1, \cdots, L_{\mathrm{T+B}}\}$ in the case of methods $\mathcal{D}_1$ and $\mathcal{D}_2$, whereas this range is equal to $m \in \{1, \cdots, 1.5L_{\mathrm{T+B}}\}$ in the case of method $\mathcal{D}_3$.

- Although selecting the largest taps from a long feedback filter is a suitable method to determine a proper set of active time delays when either the

feedback filter $\mathbf{T}$ or the feedback filter $\mathbf{B}$ is present (Fig. 5.11), method $\mathcal{D}_4$ results in poor performance when both these filters are present, e.g., only good performance in Fig. 6.14 is obtained only when almost all feedback taps are active. Indeed, the effect on the $\mathrm{MSE}_{\mathbf{g}_{\mathrm{ch}}}$ of setting relatively small feedback taps to $\mathbf{0}$ is hard too predict and could be relatively large, because each feedback tap influences more than one term in (6.49) as product terms of different feedback taps are present. Consequently, method $\mathcal{D}_4$ is not a practical option when both feedback filters are present.

- This poor performance encountered $\mathcal{D}_4$ can be significantly enhanced by recomputing all equalization parameters in method $\mathcal{D}_5$ with $\Phi_{\mathbf{T}} = \Phi_{\mathbf{T},\mathcal{D}_4}$ and $\Phi_{\mathbf{B}} = \Phi_{\mathbf{B},\mathcal{D}_4}$. Still, this method performs (slightly) worse than methods $\mathcal{D}_1$-$\mathcal{D}_3$ for small values of $L_{\mathrm{T+B}}$, implying that $\Phi_{\mathbf{T},\mathcal{D}_4}$ and $\Phi_{\mathbf{B},\mathcal{D}_4}$ are far from optimal. When $L_{\mathrm{T+B}} > 50$, the performance of $\mathcal{D}_5$ rapidly improves, indicating that the feedback filters are capable of removing most of the larger ISI contributions, including the ISI from the first reflection. At larger, $L_{\mathrm{T+B}}$, the methods $\mathcal{D}_1$-$\mathcal{D}_3$, however, results again in better performance.

In conclusion, the presented methods to determine a good set of active time instants thus all result in acceptable performance, apart from method $\mathcal{D}_4$. However, neither of these method outperforms all others and determining the optimal set of active time instants for both feedback filters is still an open problem.

Additional simulations give rise to similar curves as in Fig. 6.6 when plotting $\overline{\mathrm{MSE}}$ as a function of the iteration index, which indicates that the added decision-feedback filter at the receiver does not have a significant impact on the convergence of the iterative algorithms for the MMSE optimization. For conciseness, these figures are not shown here.

6.6 Conclusions

This chapter investigates the equalization of a stochastic frequency-selective MIMO channel by means of a THP and two linear equalizers: one at the transmitter and one at the receiver. In fact, this equalization scheme can be interpreted as the DFE equalization scheme from Chapter 5 when the feedback filter is moved from the receiver to the transmitter. As the channel is stochastic, the optimization framework from Chapter 4 is applied and the MSE between the decision variable and the extended data symbol is selected as the objective function. In this regard, three equalization strategies are proposed. First, all equalization parameters are adjustable to the specific channel realization in the adjustable strategy, resulting in optimal performance and largest complexity. To lower this complexity, all equalization parameters are independent of the channel realization in the fixed strategy, while adjustable and fixed equalization parameters are both present in the hybrid strategy to combine relatively low

complexity with good performance. More precisely, this hybrid equalization scheme consists of a fixed THP and a fixed linear equalizer at the transmitter, while the linear equalizer at the receiver is adjustable.

Numerical results confirm that several conclusions drawn in the case of the DFE equalization scheme hold here as well, because both MMSE optimization algorithms are quite similar and sometimes directly related to each other. For instance, the adjustable strategy achieves superior and nearly constant performance in the considered channel variability range, whereas the degradation of the fixed strategy quickly rises with increasing σ_r. The hybrid strategy could still be a low-complexity alternative to the adjustable strategy, but the performance difference between these two strategies is larger in the case of the THP equalization scheme than in the case of the DFE equalization scheme because more equalization parameters are fixed. Consequently, the number of adjustable equalization taps in the equalizer $\mathbf{W}$ becomes more important to achieve a decent performance. Additionally, the convergence of the hybrid strategy is (slightly) slower in the case of the THP equalization scheme than in the case of the DFE equalization scheme, because not only the linear equalizers, but also the feedback filter is iteratively obtained.

The THP equalization scheme yields better performance than the linear equalization scheme with long linear equalizers. Compared to the DFE equalization scheme, however, the THP equalization scheme yields inferior performance for 2-PAM transmission due to the negative effect of the power loss. However, this effect reduces for increasing M such that the THP equalization achieves a lower BER than the DFE equalization scheme for the 4-PAM constellation when the impact of the error propagation is taken into account in the latter equalization scheme.

To reduce the performance gap between the adjustable and the hybrid strategy, a more general equalization scheme THP-DFE is introduced, where a feedback filter is present at both the transmitter and the receiver. As this additional decision-feedback filter at the receiver alters the expression for the decision variable, a modified iterative algorithm based on the optimization framework from Chapter 4 has been proposed. As for all strategies, both feedback filters are iteratively obtained, along with the coefficients of the linear equalizers. Numerical results indicate that the addition of a feedback filter at the receiver significantly reduces the gap between the adjustable and the hybrid strategy. This reduction is already observable when the adjustable feedback filter at the receiver contains only a few taps. Nevertheless, selecting the optimal sets of active time delays for both feedback filters is not straightforward, as just selecting the largest taps from long feedback filters yield inadequate performance, such that a recalculation of the equalization parameters corresponding to the obtained sets is recommended.

7 Partial-response signaling

This chapter examines the design of the adjustable equalization parameters for an equalization scheme with PRS applied to a frequency-selective MIMO channel, which is assumed to be perfectly known in the design of all equalization parameters.

First, an equalization scheme consisting of a PRS precoder at the transmitter and a nonlinear DFE at the receiver is introduced in Section 7.1. One noticeable feature of the TIR of the considered PRS precoder is that it contains both temporal, spatial, and ST components, making it more general than the PRS precoders with either temporal or spatial components, encountered in the literature.

Next, the primary focus of Section 7.2 lies on the design of the TIR and all filter coefficients by means of minimizing the MSE. The first step in this optimization is to derive the optimal DFE for a given TIR (Subsection 7.2.1), after which the resulting MSE must be further minimized over the TIR (Subsection 7.2.2). As this last optimization is not straightforward, three iterative algorithms, each with a different complexity, are proposed to obtain an optimized TIR. These algorithms reduce the MSE by incrementing in each iteration one row of the TIR matrix. In the first and the second algorithm (Sections 7.2.2.1 and 7.2.2.2, respectively) only part of the row is incremented. These algorithms differ only regarding the criterion for selecting the part of the row to be updated. The third algorithm increments in each iteration an entire row of the TIR matrix by reformulating the optimization problem as a lattice decoding algorithm (Section 7.2.2.3).

To allow for an in-depth investigation of the error performance achieved by the PRS precoder and the different optimization algorithms, Section 7.3 derives

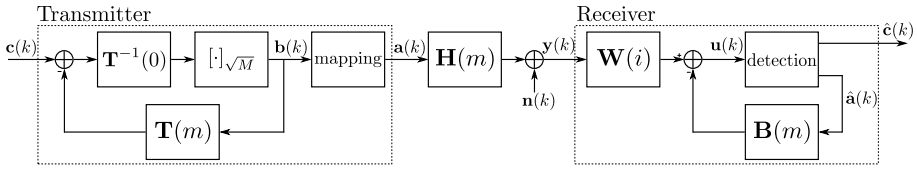

Figure 7.1: System model of the equalization scheme consisting of a PRS precoder at the transmitter and a nonlinear DFE at the receiver.

an accurate approximation for the BER.

Next, the numerical results presented in Section 7.4 reveal first that PRS is capable of inducing a considerable performance improvement compared to FRS. Second, the numerical results indicate that algorithm A3 is superior to algorithms A1 and A2 in terms of performance, but at the cost of a much larger computational complexity.

Finally, conclusions are drawn in Section 7.5.

7.1 System model

Fig. 7.1 displays the system model of an equalized MIMO $N_{\mathrm{R}} \times N_{\mathrm{T}}$ bandpass communication channel with a ST PRS (PRS-ST) precoder at the transmitter and a nonlinear DFE at the receiver. For the bandpass channel, the complex-valued baseband notation is employed.

The input at the transmitter consists of N_{T} complex-valued data symbol streams, i.e., $\mathbf{c}(k) = [\mathrm{c}_1(k) \dots \mathrm{c}_{N_{\mathrm{T}}}(k)]^T$ with $\mathrm{c}_l(k)$ denoting the kth symbol from the lth data symbol stream. All data symbols are independently and uniformly drawn from the complex symbol set $\mathcal{C}_{\mathrm{PRS}} = \{0, \cdots, \sqrt{M}-1\} + j\{0, \cdots, \sqrt{M}-1\}$, where M is assumed to be an integer power of 4. Moreover, the binary labels associated with the elements from $\mathcal{C}_{\mathrm{PRS}}$ are according to the binary-reflected Gray mapping. Next, the data symbol vectors $\mathbf{c}(k)$ are applied to the MIMO ST PRS precoder at the symbol rate $1/T$. This ST PRS precoder is characterized by the target polynomial $\boldsymbol{T}_{\mathrm{tar}} = \sum_{m=0}^{L_{\mathrm{T}}} \mathbf{T}(m) D^m$ of degree L_{T} with coefficients that are Gaussian integer matrices $\mathbf{T}(m)$, $m = 0, \dots, L_{\mathrm{T}}$, of dimension $N_{\mathrm{T}} \times N_{\mathrm{T}}$. A Gaussian integer is defined as a complex-valued number whose real and imaginary part are both integer, i.e., $\mathbf{T}(m) \in \mathbb{Z}[j]^{N_{\mathrm{T}} \times N_{\mathrm{T}}}$ with $\mathbb{Z}[j] = \{a + jb | a, b \in \mathbb{Z}\}$. Remember that the spatial components of the TIR are characterized by the matrix $\mathbf{T}(0)$ and defined as the desired XT originated from data symbols transmitted at the same time instant. Moreover, all diagonal elements of the matrices $\{\mathbf{T}(m) | \, m > 0\}$ constitute the temporal components of the TIR, whereas all non-diagonal elements of the matrices $\{\mathbf{T}(m) | \, m > 0\}$ specify the desired XT from data symbols transmitted at different time instants. In contrast to previous work on PRS that mainly focused either

on SISO channels ($N_{\mathrm{T}} = N_{\mathrm{R}} = 1$), or on strictly temporal partial response (diagonal $\mathbf{T}(m)$), or on strictly spatial partial response ($\mathbf{T}(m) = \mathbf{0}$ for $m > 0$), the more general complex MIMO precoder here allows ST components (with spatial-only and temporal-only components as particular cases). The input sequence $\{\mathbf{c}(k)\}$ is converted by the ST PRS precoder into the precoded output sequence $\{\mathbf{b}(k)\}$ according to

$$\mathbf{b}(k) = \left[\mathbf{T}^{-1}(0) \left(\mathbf{c}(k) - \sum_{m=1}^{L_{\mathrm{T}}} \mathbf{T}(m)\mathbf{b}(k-m) \right) \right]_{\sqrt{M}}, \tag{7.1}$$

where $[\cdot]_X$ symbolizes the element-wise modulo reduction to the interval $[0, X)$ of both the real and the imaginary part. To avoid any power loss as in THP, PRS requires that all entries of the precoded sequence $\mathbf{b}(k)$ are independently and uniformly drawn from the same symbol set, $\mathcal{C}_{\mathrm{PRS}}$, as the one containing the elements of $\mathbf{c}(k)$. This property is acquired when all entries of $\mathbf{T}(m)$ are Gaussian integers and $\mathbf{T}(0)$ is a complex-valued unimodular matrix (Appendix 11.9), since one can easily prove that $\mathbf{T}^{-1}(0) \in \mathbb{Z}[j]^{N_{\mathrm{T}} \times N_{\mathrm{T}}}$ if and only if the determinant of the Gaussian integer matrix $\mathbf{T}(0)$ is restricted to the set $\{1, -1, j, -j\}$ (Appendix 11.8). Next, the components from $\mathbf{b}(k)$ are mapped to the normalized M-QAM constellation, i.e.,

$$\mathbf{a}(k) = 2\Delta\mathbf{b}(k) + (1+j)\Delta(-\sqrt{M}+1)\mathbf{1}, \tag{7.2}$$

where $\Delta = \sqrt{\frac{3}{2(M-1)}}$ such that the symbol energy is normalized, i.e., $\mathbb{E}\big[\mathbf{a}(k)\,\mathbf{a}^H(k)\big] = \mathbf{I}_{N_{\mathrm{T}}}$.

The sequence $\mathbf{a}(k)$ is then transmitted over the discrete-time frequency-selective $N_{\mathrm{R}} \times N_{\mathrm{T}}$ MIMO channel, which encompasses both the complex-valued impulse response matrices $\mathbf{H}(m)$ of dimension $N_{\mathrm{R}} \times N_{\mathrm{T}}$ and the zero-mean circular symmetric additive complex-valued Gaussian noise vector $\mathbf{n}(k)$ characterized by the autocorrelation matrices $\mathbf{R}_{\mathbf{n}}(m) = \mathbb{E}\left[\mathbf{n}(k)\mathbf{n}(k+m)^H\right]$. The channel input-output relationship is given by

$$\mathbf{y}(k) = \sum_{m=-L_{\mathrm{H}}^{(1)}}^{L_{\mathrm{H}}^{(2)}} \mathbf{H}(m)\mathbf{a}(k-m) + \mathbf{n}(k). \tag{7.3}$$

In (7.3), the channel response is assumed to be time-limited, i.e., $\mathbf{H}(m) = \mathbf{0}\ \forall m \notin \{-L_{\mathrm{H}}^{(1)}, \cdots, L_{\mathrm{H}}^{(2)}\}$.

At the receiver, the channel output $\mathbf{y}(k)$ is equalized by means of a DFE. More precisely, this DFE consists of a linear MIMO feedforward equalization filter $\mathbf{W}$ characterized by the impulse response matrices $\mathbf{W}(i)$ of dimension $N_{\mathrm{T}} \times N_{\mathrm{R}}$ and a linear MIMO feedback filter $\mathbf{B}$ with impulse response matrices $\mathbf{B}(m)$ of dimension $N_{\mathrm{T}} \times N_{\mathrm{T}}$. The feedforward filter $\mathbf{W}$ and the feedback filter $\mathbf{B}$ operate on the received signal $\mathbf{y}(k)$ and on the previously detected symbols

$\hat{\mathbf{a}}(k)$, respectively. Consequently, the decision variable $\mathbf{u}(k)$ can be formulated as

$$\mathbf{u}(k) = \sum_{i=-L_{\mathrm{W}}^{(1)}}^{L_{\mathrm{W}}^{(2)}} \sum_{m=-L_{\mathrm{H}}^{(1)}}^{L_{\mathrm{H}}^{(2)}} \mathbf{W}(i)\mathbf{H}(m)\mathbf{a}(k-m-i) + \sum_{i=-L_{\mathrm{W}}^{(1)}}^{L_{\mathrm{W}}^{(2)}} \mathbf{W}(i)\mathbf{n}(k-i) - \sum_{m\in\Phi_{\mathbf{B}}} \mathbf{B}(m)\hat{\mathbf{a}}(k-m), \tag{7.4}$$

where both filters are assumed to have finite length, i.e., $\mathbf{W}(i) = \mathbf{0}\ \forall i \notin \{-L_{\mathrm{W}}^{(1)}, \cdots, L_{\mathrm{W}}^{(2)}\}$ and $\mathbf{B}(m) = \mathbf{0}\ \forall m \notin \Phi_{\mathbf{B}}$. As in Section 5.1 above, the set $\Phi_{\mathbf{B}}$ consists of L_{B} causal time delays and is not necessarily equal to the set $\{1, \cdots, L_{\mathrm{B}}\}$. To simplify the notations in (7.4), the $N_{\mathrm{T}} \times (N_{\mathrm{R}} L_{\mathrm{W}})$ augmented matrix $\mathbf{W}$ is similarly constructed as in (5.16), whereas $\mathbf{G}(m)$ and $\bar{\mathbf{n}}(k)$ are now respectively given by

$$\mathbf{G}(m) = \left[\mathbf{H}^H(m + L_{\mathrm{W}}^{(1)}) \cdots \mathbf{H}^H(m - L_{\mathrm{W}}^{(2)})\right]^H \tag{7.5}$$

and

$$\bar{\mathbf{n}}(k) = \left[\mathbf{n}^H(k + L_{\mathrm{W}}^{(1)}) \cdots \mathbf{n}^H(k - L_{\mathrm{W}}^{(2)})\right]^H. \tag{7.6}$$

Based on these shorthand notations, the decision variable $\mathbf{u}(k)$ defined in (7.4) can be rewritten as

$$\mathbf{u}(k) = \sum_{m\in\Phi} \mathbf{W}\mathbf{G}(m)\mathbf{a}(k-m) + \mathbf{W}\bar{\mathbf{n}}(k) - \sum_{m\in\Phi_{\mathbf{B}}} \mathbf{B}(m)\hat{\mathbf{a}}(k-m). \tag{7.7}$$

As in Chapter 5, Φ is defined as the set $\{-L_{\mathrm{G}}^{(1)}, \cdots, L_{\mathrm{G}}^{(2)}\}$, but $L_{\mathrm{G}}^{(1)}$ and $L_{\mathrm{G}}^{(2)}$ are here equal to

$$\begin{cases} L_{\mathrm{G}}^{(1)} & = L_{\mathrm{H}}^{(1)} + L_{\mathrm{W}}^{(1)} \\ L_{\mathrm{G}}^{(2)} & = L_{\mathrm{H}}^{(2)} + L_{\mathrm{W}}^{(2)} \end{cases}. \tag{7.8}$$

According to (7.1), the target response

$$\mathbf{u}_{\mathrm{T}}(k) = \sum_{m=0}^{L_{\mathrm{T}}} \mathbf{T}(m)\mathbf{a}(k-m) \tag{7.9}$$

and the original sequence $\mathbf{c}(k)$ are related by

$$\mathbf{c}(k) = \left[\frac{\mathbf{u}_{\mathrm{T}}(k)}{2\Delta} + \mathbf{c}_{\mathrm{off}}\right]_{\sqrt{M}}, \tag{7.10}$$

where the offset $\mathbf{c}_{\mathrm{off}}$ is given by

$$\mathbf{c}_{\mathrm{off}} = \frac{(1+j)(\sqrt{M}-1)}{2} \sum_{m=0}^{L_{\mathrm{T}}} \mathbf{T}(m)\mathbf{1}. \tag{7.11}$$

The equalization coefficients are therefore selected such that the decision variable $\mathbf{u}(k)$ from (7.7) approaches the target response vector $\mathbf{u}_{\mathrm{T}}(k)$ defined in (7.9) as close as possible (in a MSE sense). Consequently, the decision on $\mathbf{c}(k)$, $\hat{\mathbf{c}}(k)$, follows from replacing the quantity $\frac{\mathbf{u}_{\mathrm{T}}(k)}{2\Delta} + \mathbf{c}_{\mathrm{off}}$ in the right-hand side of (7.10) by the Gaussian integer vector which is nearest to $\frac{\mathbf{u}(k)}{2\Delta} + \mathbf{c}_{\mathrm{off}}$, after which the modulo operator maps all elements of this decision to the original constellation $\mathcal{C}_{\mathrm{PRS}}$. The input of the feedback filter, i.e., the decision on $\mathbf{a}(k)$, $\hat{\mathbf{a}}(k)$, is constructed by substituting $\mathbf{c}(k)$ for $\hat{\mathbf{c}}(k)$ in the precoder equation (7.1), yielding the decision on the vectors $\mathbf{b}(k)$, $\hat{\mathbf{b}}(k)$, which are then mapped to the corresponding M-QAM symbols $\hat{\mathbf{a}}(k)$.

Note that the number of data streams N_{dat} in this equalization scheme must be equal to N_{T} as all matrices $\mathbf{T}(m)$ of the PRS precoder are $N_{\mathrm{T}} \times N_{\mathrm{T}}$ square matrices. For decent performance, N_{R} is therefore assumed to be larger or equal to N_{T}, i.e., $N_{\mathrm{R}} \geq N_{\mathrm{T}}$.

Similar to the feedforward filter in the equalization scheme examined in Chapter 5, the feedforward filter $\mathbf{W}$ could be extended to a fractionally-spaced equalizer, but as this only marginally impacts the main focus of this chapter, a symbol-spaced filter $\mathbf{W}$ is considered for simplicity.

7.2 MMSE equalization

The goal of this section is to derive the optimal target response matrix $\mathbf{T}^{\star}$, the optimal feedforward filter $\mathbf{W}^{\star}$, and the optimal feedback filter $\mathbf{B}^{\star}$ for a given channel realization $\mathbf{g}_{\mathrm{ch}}$. For this joint optimization, the MSE is again particularly suitable as the objective function because it unites excellent performance with mathematical simplicity. For convenience, we denote by MSE (rather than $\mathrm{MSE}_{\mathbf{g}_{\mathrm{ch}}}$) the MSE conditioned on the channel realization. Since all equalization parameters are adjustable in this chapter, there is no need to consider the average (over the channel realizations) MSE in the optimization problem. With $\mathbf{e}(k) = \mathbf{u}(k) - \mathbf{u}_{\mathrm{T}}(k)$ representing the difference between the decision variable $\mathbf{u}(k)$ and the target response vector $\mathbf{u}_{\mathrm{T}}(k)$, the corresponding normalized MSE is defined as

$$\mathrm{MSE} \triangleq \frac{\mathbb{E}\left[\|\mathbf{e}(k)\|^2\right]}{\mathbb{E}\left[\|\mathbf{a}(k)\|^2\right]} = \frac{\mathrm{Tr}\left(\mathbf{R}_{\mathbf{e}}\right)}{\mathbb{E}\left[\|\mathbf{a}(k)\|^2\right]} = \frac{1}{N_{\mathrm{T}}} \sum_{l=1}^{N_{\mathrm{T}}} \mathrm{MSE}^{(l)}. \tag{7.12}$$

Similar to (5.24), the expectation $\mathbb{E}[\cdot]$ in (7.12) is taken over both the data symbols and the noise. Moreover, the error covariance matrix $\mathbf{R}_{\mathbf{e}}$ is defined as $\mathbb{E}\left[\mathbf{e}(k)\mathbf{e}^H(k)\right]$. The lth diagonal element of $\mathbf{R}_{\mathbf{e}}$ is denoted by $\mathrm{MSE}^{(l)}$, which equals the MSE corresponding to the lth data stream. The total MSE then equals the arithmetic average of all $\mathrm{MSE}^{(l)}$.

To solve the minimization of (7.12), first a simplified notation is developed. More precisely, the vector $\mathbf{y}_{\mathrm{W}}$ contains all channel output samples contributing

to the decision variable $\mathbf{u}(k)$. Stacked vectors $\mathbf{a}_{\mathrm{T}}$ and $\mathbf{a}_{\mathrm{B}}$ comprise all symbols contributing to $\mathbf{u}_{\mathrm{T}}(k)$ and to the input of the feedback filter, respectively, whereas all remaining data symbols are collected in the stacked vector $\mathbf{a}_{\mathrm{N}}$, i.e.,

$$\mathbf{y}_{\mathrm{W}} = \left[\mathbf{y}^H(k + L_{\mathrm{W}}^{(1)}) \cdots \mathbf{y}^H(k - L_{\mathrm{W}}^{(2)})\right]^H, \tag{7.13}$$

$$\mathbf{a}_{\mathrm{B}} = \left[\mathbf{a}^H(k - \Phi_{\mathbf{B}}(1)) \cdots \mathbf{a}^H(k - \Phi_{\mathbf{B}}(L_{\mathrm{B}}))\right]^H, \tag{7.14}$$

$$\mathbf{a}_{\mathrm{T}} = \left[\mathbf{a}^H(k) \cdots \mathbf{a}^H(k - L_{\mathrm{T}})\right]^H \tag{7.15}$$

$$\mathbf{a}_{\mathrm{N}} = \left[\cdots \mathbf{a}^H(k-m) \cdots\right]^H \ \forall m \in \Phi \setminus \{\Phi_{\mathbf{T}} \cup \Phi_{\mathbf{B}}\}. \tag{7.16}$$

Since all symbols in $\mathbf{a}(k)$ are spatially and temporally uncorrelated, all cross correlations between $\mathbf{a}_{\mathrm{T}}$, $\mathbf{a}_{\mathrm{B}}$, and $\mathbf{a}_{\mathrm{N}}$ are zero and the autocorrelation matrix of each of these vectors equals the identity matrix, e.g., $\mathbb{E}\left[\mathbf{a}_{\mathrm{T}}\mathbf{a}_{\mathrm{T}}^H\right] = \mathbf{I}_{L(L_{\mathrm{T}}+1)}$. In this section, the intersection of $\Phi_{\mathbf{T}} = \{0, \cdots, L_{\mathrm{T}}\}$ and $\Phi_{\mathbf{B}}$ is assumed to be empty by design. Otherwise, the target response matrices $\mathbf{T}(m)\ \forall m \in \{\Phi_{\mathbf{T}} \cap \Phi_{\mathbf{B}}\}$ would not influence the equalization performance at all, as the feedback equalizer is capable of removing the contribution from $\mathbf{a}(k-m)$ to $\mathbf{e}(k)$ for any $m \in \Phi_{\mathbf{B}}$. Based on (7.3) and the notations in (7.13)-(7.16), the relationship between $\mathbf{y}_{\mathrm{W}}$ and all data symbols can be rewritten as

$$\mathbf{y}_{\mathrm{W}} = \mathbf{G}_{\mathrm{T}}\mathbf{a}_{\mathrm{T}} + \mathbf{G}_{\mathrm{B}}\mathbf{a}_{\mathrm{B}} + \mathbf{G}_{\mathrm{N}}\mathbf{a}_{\mathrm{N}}, \tag{7.17}$$

where

$$\mathbf{G}_{\mathrm{T}} = \left[\mathbf{G}(0) \cdots \mathbf{G}(L_{\mathrm{T}})\right], \tag{7.18}$$

$$\mathbf{G}_{\mathrm{B}} = \left[\mathbf{G}(\Phi_{\mathrm{B}}(1)) \cdots \mathbf{G}(\Phi_{\mathrm{B}}(L_{\mathrm{B}}))\right], \tag{7.19}$$

$$\mathbf{G}_{\mathrm{N}} = \left[\cdots \mathbf{G}(m) \cdots\right]\ \forall m \in \Phi \setminus \{\Phi_{\mathbf{T}} \cup \Phi_{\mathbf{B}}\}. \tag{7.20}$$

Consequently, the MSE defined in (7.12) can be expressed as

$$\mathrm{MSE} = \frac{1}{N_{\mathrm{T}}}\mathbb{E}\left[\left\|\mathbf{W}\left(\mathbf{G}_{\mathrm{T}}\mathbf{a}_{\mathrm{T}} + \mathbf{G}_{\mathrm{B}}\mathbf{a}_{\mathrm{B}} + \mathbf{G}_{\mathrm{N}}\mathbf{a}_{\mathrm{N}} + \bar{\mathbf{n}}(k)\right) - \mathbf{B}\hat{\mathbf{a}}_{\mathrm{B}} - \mathbf{T}\mathbf{a}_{\mathrm{T}}\right\|^2\right], \tag{7.21}$$

where the augmented $\mathbf{T} = [\mathbf{T}(0) \cdots \mathbf{T}(L_{\mathrm{T}})]$, and the stacked $\hat{\mathbf{a}}_{\mathrm{B}}$ is similarly constructed as $\mathbf{a}_{\mathrm{B}}$ but with the decisions $\hat{\mathbf{a}}(k)$ instead of the actual symbols $\mathbf{a}(k)$. Below, the optimal $\mathbf{W}$ and $\mathbf{B}$ are first formulated for a given target response matrix $\mathbf{T}$ in Subsection 7.2.1, after which three algorithms are presented in Subsection 7.2.2 to optimize the target response matrix $\mathbf{T}$.

7.2.1 Optimization over W and B

Similar to the MMSE optimization from Section 5.2, the presence of the decision vector $\hat{\mathbf{a}}_{\mathrm{B}}$ complicates the minimization of MSE from (7.21) with respect to $\mathbf{W}$ and $\mathbf{B}$ for given $\mathbf{T}$. For mathematical simplicity, all previously detected symbols are therefore assumed to be correct such that $\hat{\mathbf{a}}_{\mathrm{B}}$ can be replaced

with $\mathbf{a}_{\mathrm{B}}$ in (7.21). The optimal coefficients $\mathbf{W}^{\star}$ and $\mathbf{B}^{\star}$, for given $\mathbf{T}$, are then straightforwardly obtained by equating the derivatives of the MSE with respect to $\mathbf{W}$ and $\mathbf{B}$ to zero, yielding

$$\mathbf{W}^{\star} = \mathbf{T}\mathbf{G}_{\mathrm{T}}^{H}\left(\mathbf{G}_{\mathrm{T}}\mathbf{G}_{\mathrm{T}}^{H} + \mathbf{G}_{\mathrm{N}}\mathbf{G}_{\mathrm{N}}^{H} + \mathbf{R}_{\bar{\mathbf{n}}}\right)^{-1} \text{ and } \mathbf{B}^{\star} = \mathbf{W}^{\star}\mathbf{G}_{\mathrm{B}}, \tag{7.22}$$

where $\mathbf{R}_{\bar{\mathbf{n}}} \triangleq \mathbb{E}\left[\bar{\mathbf{n}}(k)\bar{\mathbf{n}}^{H}(k)\right]$. Subsequently, the minimal MSE for given $\mathbf{T}$, denoted by $\mathrm{MSE}_{\mathbf{W}^{\star},\mathbf{B}^{\star}}$, is obtained by plugging (7.22) in (7.21), and the resulting expression can be simplified to

$$\mathrm{MSE}_{\mathbf{W}^{\star},\mathbf{B}^{\star}} = \frac{1}{N_{\mathrm{T}}}\mathrm{Tr}\left(\mathbf{T}\mathbf{G}\mathbf{T}^{H}\right), \tag{7.23}$$

where

$$\mathbf{G} = \mathbf{I}_{N_{\mathrm{T}}(L_{\mathrm{T}}+1)} - \mathbf{G}_{\mathrm{T}}^{H}\left(\mathbf{G}_{\mathrm{T}}\mathbf{G}_{\mathrm{T}}^{H} + \mathbf{G}_{\mathrm{N}}\mathbf{G}_{\mathrm{N}}^{H} + \mathbf{R}_{\bar{\mathbf{n}}}\right)^{-1}\mathbf{G}_{\mathrm{T}}. \tag{7.24}$$

Note that the matrix $\mathbf{G}$ is a positive Hermitian matrix.

For FRS, i.e., $\mathbf{T} = [\mathbf{I}_{N_{\mathrm{T}}} \ \mathbf{0}_{N_{\mathrm{T}}\times N_{\mathrm{T}}L_{\mathrm{T}}}]$, the expressions in (7.22) and (7.23) are verified to simplify to the standard expressions for the MMSE equalizer (see Section 5.2.1).

7.2.2 Optimization over T

Instead of considering a channel-independent TIR $\mathbf{T}$, as for FRS or duobinary ($\mathbf{T} = [\mathbf{I}\ \mathbf{I}\ \mathbf{0}]$), this section optimizes $\mathbf{T}$ by minimizing $\mathrm{MSE}_{\mathbf{W}^{\star},\mathbf{B}^{\star}}$ from (7.23) subject to two constraints: (i) all entries of $\mathbf{T}$ must belong to $\mathbb{Z}[j]$ and (ii) $\det(\mathbf{T}(0))$ must belong to the set $\{1, -1, j, -j\}$. TIRs satisfying these constraints are called feasible, and ensure that $\mathbf{b}(k)$ and $\mathbf{c}(k)$ possess identical statistics.

Expression (7.23) for $\mathrm{MSE}_{\mathbf{W}^{\star},\mathbf{B}^{\star}}$ reveals that the lth row of $\mathbf{T}$ influences only $\mathrm{MSE}^{(l)} = \left(\mathbf{T}\mathbf{G}\mathbf{T}^{H}\right)_{l,l}$, i.e., the MSE corresponding to the lth data stream. Hence, when the constraint on the determinant of $\mathbf{T}(0)$ is satisfied, constructing a new TIR matrix $\mathbf{T}'$ by multiplying one row of $\mathbf{T}$ with the complex conjugate of $\det(\mathbf{T}(0))$ results in $\det\left(\mathbf{T}'(0)\right) = 1$, while the MSE remains unaltered. Without loss of generality, the second constraint is therefore replaced by $\det(\mathbf{T}(0)) = 1$ in the sequel.

Although the lth row of $\mathbf{T}$ affects only $\mathrm{MSE}^{(l)}$, the rows of $\mathbf{T}$ cannot be chosen independently from each other due to the constraint on the determinant of $\mathbf{T}(0)$, impeding the optimization of each row individually. As an alternative, this subsection discusses three iterative algorithms to compute an optimized TIR $\mathbf{T}^{\star}$. In the ith iteration of each algorithm, the TIR $\mathbf{T}_i$ is incremented with the increment $\mathbf{T}_{\mathrm{inc}}$, i.e.,

$$\mathbf{T}_{i+1} = \mathbf{T}_i + \mathbf{T}_{\mathrm{inc}}. \tag{7.25}$$

In (7.25) the $N_\mathrm{T} \times N_\mathrm{T}(L_\mathrm{T}+1)$ increment matrix $\mathbf{T}_\mathrm{inc}$ is a function of $\mathbf{T}_i$ and the corresponding incremented MSE_{i+1} is given by

$$\mathrm{MSE}_{i+1} = \frac{1}{N_\mathrm{T}} \mathrm{Tr}\left(\mathbf{T}_{i+1}\mathbf{G}\mathbf{T}_{i+1}^H\right) \tag{7.26}$$

$$= \mathrm{MSE}_i + \frac{1}{N_\mathrm{T}} \mathrm{Tr}\left(\mathbf{T}_i\mathbf{G}\mathbf{T}_\mathrm{inc}^H + \mathbf{T}_\mathrm{inc}\mathbf{G}\mathbf{T}_i^H + \mathbf{T}_\mathrm{inc}\mathbf{G}\mathbf{T}_\mathrm{inc}^H\right). \tag{7.27}$$

In the ith iteration, $\mathbf{T}_\mathrm{inc}$ is restricted to possess only one nonzero row, namely the row with index $l_i^\star$. Hence, the ith iteration focuses entirely on the reduction of $\mathrm{MSE}_i^{(l_i^\star)}$, while the other $\mathrm{MSE}_i^{(l)}$ remain unaltered. Moreover, $l_i^\star$ is selected such that $\mathrm{MSE}_i^{(l_i^\star)}$ is the largest among the *reducible* MSE_i, i.e., $\mathrm{MSE}_i^{(l_i^\star)}$ is the largest diagonal element of the error covariance matrix that can be reduced by an increment $\mathbf{T}_\mathrm{inc}$ that is computed by a specific algorithm. More precisely, when the sequence $\left(\mathrm{MSE}_i^{(m_1)}, \ldots, \mathrm{MSE}_i^{(m_{N_\mathrm{T}})}\right)$ is sorted from large to small, i.e., $\mathrm{MSE}_i^{(m_n)} \geq \mathrm{MSE}_i^{(m_{n+1})}$ for $n \in \{1, \cdots, N_\mathrm{T}-1\}$, $l_i^\star = m_n$ if and only if $\mathrm{MSE}_i^{(l)}$ is not reducible for $l \in \{m_1, \cdots, m_{n-1}\}$ and $\mathrm{MSE}_i^{(m_n)}$ is reducible. Furthermore, to guarantee the feasibility of $\mathbf{T}_{i+1}$, each entry of $\mathbf{T}_\mathrm{inc}$ must be a Gaussian integer, i.e., $(\mathbf{T}_\mathrm{inc})_{l,q} \in \mathbb{Z}[j]$, and, when updating a certain row of $\mathbf{T}_i(0)$, the first N_T elements of the nonzero row of the increment $\mathbf{T}_\mathrm{inc}$ must additionally be a linear combination of the other rows of $\mathbf{T}_i(0)$ such that $\det(\mathbf{T}_i(0))$ does not alter. Initializing $\mathbf{T}_0$ to a random feasible TIR results then obviously in an optimized $\mathbf{T}^\star$, since convergence to a (local) optimum is guaranteed because the MSE is lowered in each iteration and bounded below by 0. However, convergence to the global optimum is not guaranteed by this optimization algorithm, making the initialization and the computation of $\mathbf{T}_\mathrm{inc}$ crucial for the quality of $\mathbf{T}^\star$. Initializing $\mathbf{T}_0$ as FRS is the most logical choice, because the resulting MSE is then upper bounded by the MSE achieved in the case of FRS.

Below, three different algorithms to compute the increment $\mathbf{T}_\mathrm{inc}$ are presented. The first algorithm A1 (Subsection 7.2.2.1) updates the $l_i^\star$th row of $\mathbf{T}_i$ with an increment from a predefined subset that induces the largest decrease in $\mathrm{MSE}_i^{(l_i^\star)}$, yielding a fast and low-complexity algorithm. The second algorithm A2 is similar to algorithm A1, but it updates the element(s) of the $l_i^\star$th row of $\mathbf{T}_i$ yielding the largest *guaranteed* decrease, which is defined in Subsection 7.2.2.2. This largest guaranteed decrease does not only depend on the current $\mathbf{T}_i$, but also on the potential of future TIR increments. Due to this extra information, convergence to a better (local) optimum is expected at the cost of a slightly larger computation complexity. In the last algorithm A3 (Subsection 7.2.2.3), even better performance is expected as the entire $l_i^\star$th row is updated by solving a relatively complicated lattice decoding problem.

7.2.2.1 Algorithm 1 (A1)

In algorithm A1, $\mathbf{T}_{\text{inc}}$ is restricted to the set $\left\{\mathbf{T}_{\text{inc}}^{(l,q)} | l \in \{1, \cdots, N_{\text{T}}\}, q \in \{1, \cdots, (L_{\text{T}}+1)N_{\text{T}}\}\right\}$. When $q > N_{\text{T}}$, $\mathbf{T}_{\text{inc}}^{(l,q)}$ updates the (l,q)th element of $\mathbf{T}_i$, i.e,

$$\mathbf{T}_{\text{inc}}^{(l,q)} = \lambda_{l,q}\mathbf{J}_{l,q} \quad q > N_{\text{T}}. \tag{7.28}$$

When $q \leq N_{\text{T}}$, $\mathbf{T}_{\text{inc}}^{(l,q)}$ adds a multiple of row q of $\mathbf{T}_i(0)$ to row l of $\mathbf{T}_i(0)$, i.e.,

$$\mathbf{T}_{\text{inc}}^{(l,q)} = [\lambda_{l,q}\mathbf{J}_{l,q}\mathbf{T}_i(0)\ \mathbf{0}] \quad q \leq N_{\text{T}},\ l \neq q. \tag{7.29}$$

In (7.28) and (7.29), the matrix $\mathbf{J}_{l,q}$ is defined as a matrix whose elements are all equal to zero except for the (l,q)th element that equals 1. Moreover, the factor $\lambda_{l,q}$ must be a Gaussian integer, and its optimum value, $\lambda_{l,q}^{\star}$, is determined by maximizing the decrease $\delta_{l,q} = \text{MSE}_i - \text{MSE}_{i+1}$, where MSE_{i+1} is obtained by plugging (7.28) and (7.29) into (7.27). After some mathematical manipulation, this decrease (as a function of $\lambda_{l,q}$) is verified to be

$$\delta_{l,q} = -2\text{Re}\left[\lambda_{l,q}A_{l,q}\right] - |\lambda_{l,q}|^2 B_q \tag{7.30}$$

with

$$A_{l,q} = \begin{cases} (\mathbf{G}\mathbf{T}_i^H)_{q,l} & q > N_{\text{T}} \\ \left(\mathbf{T}_i(0)\mathbf{G}_{N_T}\mathbf{T}_i^H\right)_{q,l} & q \leq N_{\text{T}},\ l \neq q \end{cases}, \tag{7.31}$$

$$B_q = \begin{cases} (\mathbf{G})_{q,q} & q > N_{\text{T}} \\ \left(\mathbf{T}_i(0)\mathbf{G}_{N_T,N_T}\mathbf{T}_i^H(0)\right)_{q,q} & q \leq N_{\text{T}}, \end{cases}, \tag{7.32}$$

where $\mathbf{G}_{N_T}$ and $\mathbf{G}_{N_T,N_T}$ are constructed by keeping the first N_{T} rows from $\mathbf{G}$ and the first N_{T} columns of $\mathbf{G}_{N_T}$, respectively. Since the maximum of the second order function in (7.30) is reached at $\lambda_{l,q} = -\frac{A_{l,q}^*}{B_q}$, the Gaussian integer inducing the largest $\delta_{l,q}$ is given by

$$\lambda_{l,q}^{\star} = \left\lfloor \frac{-A_{l,q}^*}{B_q} \right\rceil, \tag{7.33}$$

where $\lfloor\cdot\rceil$ rounds both the real and the imaginary part to the nearest integer. For given (l,q), the largest decrease of $\text{MSE}_i^{(l)}$ corresponding to the increment $\mathbf{T}_{\text{inc}}^{(l,q)}$ with $\lambda_{l,q} = \lambda_{l,q}^{\star}$ is then given by inserting (7.33) into (7.30), yielding

$$\delta_{l,q}^{\star} = -2\text{Re}\left[\lambda_{l,q}^{\star}A_{l,q}\right] - |\lambda_{l,q}^{\star}|^2 B_q. \tag{7.34}$$

For given l, $\text{MSE}_i^{(l)}$ is called reducible when the largest reduction of $\text{MSE}_i^{(l)}$ resulting from an increment matrix $\mathbf{T}_{\text{inc}}^{(l,q)}$, i.e., $\max_q \delta_{l,q}^{\star}$, is larger than 0. Otherwise, $\text{MSE}_i^{(l)}$ is irreducible. As pointed out above, A1 determines the index

Algorithm 7.1 Pseudocode algorithm A1.

1: $\mathbf{T}_0 = [\mathbf{I}_{N_\mathrm{T}}\ \mathbf{0}]$, $i = 0$.
2: **while** $\exists\, l : \mathrm{MSE}_i^{(l)}$ reducible **do**
3: Select $l_i^\star$ as largest reducible $\mathrm{MSE}_i^{(l)}$
4: $q_i^\star = \arg\max_q \delta_{l_i^\star,q}^\star$
5: Compute $\mathbf{T}_{i+1} = \mathbf{T}_i + \mathbf{T}_{\mathrm{inc}}^{(l_i^\star,q_i^\star)}$ with $\mathbf{T}_{\mathrm{inc}}^{(l_i^\star,q_i^\star)}$ given by (7.28)-(7.29)
6: $i \leftarrow i + 1$
7: **end**
8: $\mathbf{T}^\star = \mathbf{T}_i$

$l_i^\star$ such that $\mathrm{MSE}_i^{(l_i^\star)}$ is the largest of the reducible $\mathrm{MSE}_i^{(l)}$. The algorithm then increments $\mathbf{T}_i$ with $\mathbf{T}_{\mathrm{inc}}^{(l_i^\star,q_i^\star)}$, where $q_i^\star = \arg\max_q \delta_{l_i^\star,q}^\star$ such that $\mathrm{MSE}_i^{(l_i^\star)}$ is reduced by an amount $\delta_{l_i^\star,q_i^\star}^\star$. Algorithm A1 terminates when none of the $\mathrm{MSE}_i^{(l)}$ can be further reduced. The pseudocode of A1 is listed in Algorithm 7.1.

7.2.2.2 Algorithm 2 (A2)

Algorithms A1 and A2 are completely identical except that the selection criterion for $q_i^\star$ (line 4 in Algorithm 7.1) exercises more caution in algorithm A2. Instead of opting for the TIR increment $\mathbf{T}_{\mathrm{inc}}^{(l,q)}$ inducing the largest decrease in the largest reducible $\mathrm{MSE}_i^{(l_i^\star)}$ as in algorithm A1, algorithm A2 selects the most promising TIR increment. More precisely, algorithm A2 opts for the TIR increment $\mathbf{T}_{\mathrm{inc}}^{(l,q)}$ inducing the largest *guaranteed* decrease rather than the largest current decrease. This guaranteed decrease $d_{l,q}^\star$ is defined as the following sum of two terms:

$$d_{l,q}^\star = \delta_{l,q}^\star + \delta_{l,q,\mathrm{LB}}^\star. \tag{7.35}$$

The first term, $\delta_{l,q}^\star$, is already defined in (7.34) and represents the optimal decrease achieved by the increment $\mathbf{T}_{\mathrm{inc}}^{(l,q)}$ in iteration i. The second term, $\delta_{l,q,\mathrm{LB}}^\star$, is a lower bound on the maximal realizable decrease achievable by all possible TIR increments in future iterations $i+1, i+2$, etc, when the optimal increment $\mathbf{T}_{\mathrm{inc}}^{(l,q)}$ is selected in iteration i. Note that these increments in future iterations are not limited to row l, since this lower bound considers *all* possible TIR increments. For given $\mathbf{T}_{i+1}$, the reduction of the MSE realized during iteration $i+1+m$, with $m > 0$, usually depends on the increments previously performed during iterations $i+1, \ldots, i+m$. To compute the lower bound $\delta_{l,q,\mathrm{LB}}^\star$, the increments are *constrained* in iterations $i+2$, $i+3$, etc. such that, for all $m > 0$ the decrease achieved in iteration $i+1+m$ is influenced only by $\mathbf{T}_{i+1}$ and by the increment made in iteration $i+1+m$, but not by the increments of iterations $i+1, \ldots, i+m$. This way, the sum of all future decreases computed

subject to this constraint represents a lower bound on the maximum possible decrease, which would be accomplished by unconstrained increments.

Algorithm 7.2 Calculation of $\delta^{\star}_{l,q,\mathrm{LB}}$.

Input: $\mathbf{T}_i, \mathbf{T}_{\mathrm{inc}}^{(l,q)}$
$\mathbf{T}_{i+1} = \mathbf{T}_i + \mathbf{T}_{\mathrm{inc}}^{(l,q)}$, $\delta^{\star}_{l,q,\mathrm{LB}} = 0$, $m = 0$
Construct matrix $\mathbf{\Delta}$: compute $\Delta_{l,q} = \delta^{\star}_{l,q}$ using (7.34) with $\mathbf{T}_i$ replaced by $\mathbf{T}_{i+1}$
while $m < N_{\mathrm{T}}$ **do**
    $l_{i+1+m}, q_{i+1+m} = \arg\max_{l,q} \Delta_{l,q}$
    $\delta^{\star}_{l,q,\mathrm{LB}} \leftarrow \delta^{\star}_{l,q,\mathrm{LB}} + \Delta_{l_{i+1+m},q_{i+1+m}}$
    $\Delta_{l_{i+1+m},|} = \mathbf{0}$
    if $q_{i+1+m} \leq N_{\mathrm{T}}$ **then**
        $\Delta_{|,l_{i+1+m}} = \mathbf{0}$
    end
    $m \leftarrow m + 1$
end

For each increment $\mathbf{T}_{\mathrm{inc}}^{(l,q)}$ in iteration i, the lower bound $\delta^{\star}_{l,q,\mathrm{LB}}$ must be computed according to the algorithm presented in Algorithm 7.2. In this algorithm, the matrix $\mathbf{T}_i$ and the update $\mathbf{T}_{\mathrm{inc}}^{(l,q)}$ are given such that the $\mathbf{T}_{i+1}$ is equal to the sum $\mathbf{T}_i + \mathbf{T}_{\mathrm{inc}}^{(l,q)}$. Moreover, the quantities $l_{i+n} \in \{1, \cdots, N_{\mathrm{T}}\}$ and $q_{i+n}\{1, \cdots, (L_{\mathrm{T}}+1)\, N_{\mathrm{T}}\}$ here define the increment matrix $\mathbf{T}_{\mathrm{inc}}^{(l,q)}$ in iteration $i+n$. Equations (7.31) and (7.32) indicate that the MSE reduction in iteration $i+n$ depends on the l_{i+n}th row of $\mathbf{T}_{i+n}$ and if $q_{i+n} \leq N_{\mathrm{T}}$ also on the q_{i+n}th row of $\mathbf{T}_{i+n}(0)$ for all n> 0. Hence, with the purpose that the MSE reduction in iteration $i+1+m$ is not influenced by the increments made in iterations $i+1, \ldots, i+m$ for any $m > 0$, the quantities l_{i+1+m} and q_{i+1+m} must be outside the sets $\{l_{i+n} | n = 1, \cdots, m\}$ and $\{l_{i+n} | q_{i+n} \leq N_{\mathrm{T}}, n = 1, \ldots, m\}$, respectively. As a result, the largest value of m to be considered cannot exceed $N_{\mathrm{T}}-1$. When $\{(l_{i+1+m}, q_{i+1+m}) | m > 0\}$ is constructed this way, the MSE reduction corresponding to iteration $i+1+m$ can be computed from (7.34) by substituting the matrices $\mathbf{T}_{i+1}$ and $\mathbf{T}_{i+1}(0)$ (rather than $\mathbf{T}_{i+1+m}$ and $\mathbf{T}_{i+1+m}(0)$) for $\mathbf{T}_i$ and $\mathbf{T}_i(0)$, respectively, in (7.31) and (7.32). For given $\mathbf{T}_i$ and $\mathbf{T}_{\mathrm{inc}}^{(l,q)}$, the suboptimal greedy algorithm from Algorithm 7.2 selects in each iteration from the set $\{i+1, \cdots, i+N_{\mathrm{T}}\}$ the constrained increment that achieves the largest decrease, and subsequently sums these decreases to obtain $\delta^{\star}_{l,q,\mathrm{LB}}$. Because the MSE reduction in iteration $i+1+m$ is not influenced by the increments in made in iterations $i+1, \ldots, i+m$ for any $m > 0$, all reductions can be computed before determining all quantities $\{l_{i+1+m}, q_{i+1+m} | m \geq 0\}$. These reductions could be stored in the matrix $\mathbf{\Delta}$, where $\Delta_{l,q}$ is set to the maximal reduction for the incre-

ment $\mathbf{T}_{\text{inc}}^{(l,q)}$ in iteration $i+1$. The quantities $\{l_{i+1+m}, q_{i+1+m} | m \geq 0\}$ could then iteratively be selected according to $l_{i+1+m}, q_{i+1+m} = \arg\max_{l,q} \Delta_{l,q}$.Afterwards, the corresponding row of $\Delta_{l,q}$, i.e., $\Delta_{l_{i+1+m},|}$, is set equal to $\mathbf{0}$ and also the corresponding column of $\Delta_{l,q}$, i.e., $\Delta_{|,l_{i+1+m}} = \mathbf{0}$, when $q_{i+i+m} \leq 0$, because these reductions associated with these elements of $\mathbf{\Delta}$ cannot be chosen in later iterations as otherwise the different increments would not be independent.

Algorithm A2 opts in the ith iteration for the increment matrix that induces the largest guaranteed reduction, denoted by $d_{l_i^\star,q_i^\star}^\star$, of $\text{MSE}_i^{(l_i^\star)}$, where $l_i^\star$ equals the index of the largest of the reducible $\text{MSE}_i^{(l)}$. As in algorithm A1, $\text{MSE}_i^{(l)}$ is called reducible when $\max_q \delta_{l,q}^\star > 0$. Moreover, $q_i^\star$ is then selected such that the largest guaranteed decreased is maximized, i.e., $q_i^\star = \arg\max_q d_{l_i^\star,q}^\star$. Consequently, the pseudocode of A2 differs from A1 only in the selection criterion for $q_i^\star$ (line 4 in Algorithm 7.1).

7.2.2.3 Algorithm 3 (A3)

In algorithm A3, the ith iteration determines the optimized increment for an entire row of $\mathbf{T}_i$ rather than only a part of a row of $\mathbf{T}_i$ as in the algorithms above. In this regard, the Hermitian positive-definite matrix $\mathbf{G}$ is first factorized according to its Cholesky decomposition, i.e., $\mathbf{G} = \mathbf{L}\mathbf{L}^H$, where $\mathbf{L}$ is a lower triangular matrix. Based on (7.23), the MSE after iteration i, i.e., MSE_{i+1}, can thus be rewritten as

$$\text{MSE}_{i+1} = \frac{1}{N_\text{T}} \text{Tr}\left(\mathbf{T}_{i+1}\mathbf{L}\mathbf{L}^H\mathbf{T}_{i+1}^H\right) \tag{7.36}$$

$$= \frac{1}{N_\text{T}} \sum_{l=1}^{N_\text{T}} \left\|\mathbf{t}_{l,i+1}\mathbf{L}\right\|^2, \tag{7.37}$$

where $\mathbf{t}_{l,i+1}$ equals the lth row of the TIR matrix $\mathbf{T}_{i+1}$. As this algorithm increments an entire row l_i in iteration i, the updated row $\mathbf{t}_{l_i,i+1}$ can be expressed as

$$\mathbf{t}_{l_i,i+1} = \mathbf{t}_{l_i,i} + \mathbf{t}_\text{inc}, \tag{7.38}$$

while all the other rows of $\mathbf{T}_i$ remain unaltered. To satisfy the constraints, all components of the row increment $\mathbf{t}_\text{inc}$ must first belong to $\mathbb{Z}[j]$. Second, its first N_T elements must be a linear combination of the first N_T elements of the other rows of $\mathbf{T}_i$, i.e, $\mathbf{t}_{l,i}$ with $l \neq l_i$. For a more mathematical description $\mathbf{t}_\text{inc}$ and $\mathbf{L}$ are first decomposed as

$$\mathbf{t}_\text{inc} = \left[\mathbf{t}_\text{inc}^{(0)} \;\; \mathbf{t}_\text{inc}^{(1)}\right], \tag{7.39}$$

$$\mathbf{L} = \left[(\mathbf{L}^{(0)})^H \;\; (\mathbf{L}^{(1)})^H\right]^H, \tag{7.40}$$

where $\mathbf{t}_{\text{inc}}^{(0)}$ and $\mathbf{t}_{\text{inc}}^{(1)}$ contain the first N_{T} and the last $N_{\text{T}}L_{\text{T}}$ elements of $\mathbf{t}_{\text{inc}}$, respectively, whereas $\mathbf{L}^{(0)}$ and $\mathbf{L}^{(1)}$ comprise the first N_{T} and last $N_{\text{T}}L_{\text{T}}$ rows of $\mathbf{L}$, respectively. To met the requirements, $\mathbf{t}_{\text{inc}}^{(0)}$ in (7.39) must be a linear combination with Gaussian integer coefficients of the first N_{T} elements of $\mathbf{t}_{l,i}$ with $l \neq l_i$ and all elements of $\mathbf{t}_{\text{inc}}^{(1)}$ must be Gaussian integers as well. These requirements can then be expressed as

$$\mathbf{t}_{\text{inc}}^{(0)} = \sum_{\substack{l=1 \\ l \neq l_i}}^{N_{\text{T}}} \left(\boldsymbol{\lambda}_{\text{inc}}^{(0)}\right)_l \mathbf{t}_{l,i}^{(0)} = \boldsymbol{\lambda}_{\text{inc}}^{(0)} \mathbf{T}_{l_i,i}^{(0)}, \tag{7.41}$$

$$\mathbf{t}_{\text{inc}}^{(1)} = \boldsymbol{\lambda}_{\text{inc}}^{(1)}, \tag{7.42}$$

where $\mathbf{t}_{l,i}^{(0)}$ consists of the first N_{T} elements of $\mathbf{t}_{l,i}$, and $\mathbf{T}_{l_i,i}^{(0)}$ is constructed by removing the l_ith row from $\mathbf{T}_i(0)$. In (7.41) and (7.42) all elements of the vectors $\boldsymbol{\lambda}_{\text{inc}}^{(0)}$ and $\boldsymbol{\lambda}_{\text{inc}}^{(1)}$ must be Gaussian integers and can be combined into the single vector $\boldsymbol{\lambda}_{\text{inc}} = \left[\boldsymbol{\lambda}_{\text{inc}}^{(0)} \;\; \boldsymbol{\lambda}_{\text{inc}}^{(1)}\right]$. For a given $\mathbf{T}_i$ and l_i, the vector $\boldsymbol{\lambda}_{\text{inc}}$ must be selected such that the $\text{MSE}_{i+1}^{(l_i)}$ becomes as small as possible. To this purpose, (7.41) and (7.42) are first substituted in (7.39), after which (7.38)-(7.40) are employed to reformulate the minimization of $\text{MSE}_{i+1}^{(l_i)}$, i.e., the l_ith term in the summation from (7.37), into the following closest point search:

$$\boldsymbol{\lambda}_{\text{inc}}^{\star} = \underset{\boldsymbol{\lambda}_{\text{inc}} \in \mathbb{Z}[j]^{(L_{\text{T}}+1)N_{\text{T}}-1}}{\arg\min} \left\| \boldsymbol{\lambda}_{\text{inc}} \mathbf{G}_{\text{lat}} - \mathbf{x} \right\|^2, \tag{7.43}$$

where $\mathbf{x} = -\mathbf{t}_{l_i,i}^{(0)} \mathbf{L}$ and

$$\mathbf{G}_{\text{lat}} = \begin{bmatrix} \mathbf{T}_{l_i,i}^{(0)} \mathbf{L}^{(0)} \\ \mathbf{L}^{(1)} \end{bmatrix}. \tag{7.44}$$

To solve the minimization problem of (7.43), the lattice decoding algorithm presented in [85] is applied after decomposing all complex-valued quantities into their real and their imaginary parts. This algorithm searches for a point $\hat{\mathbf{x}}$ from a lattice with generator matrix $\mathbf{G}_{\text{lat}}$ that is closest to $\mathbf{x}$, by recursively decomposing the lattice into lower-dimensional sublattices.

In algorithm A3, $\text{MSE}_i^{(l)}$ is called reducible when the corresponding $\boldsymbol{\lambda}_{\text{inc}}^{\star}$ has at least one nonzero element. The pseudocode of A3 (Algorithm 7.3) is similar to algorithms A1 and A2 except that A3 updates in each iteration an entire row of $\mathbf{T}_i$, making the selection of $q_i^{\star}$ pointless.

7.2.2.4 Complexity considerations

This subsection provides some general remarks on the complexity per iteration of the proposed algorithms.

For algorithm A1, at most $\left((L_{\text{T}}+1)\,N_{\text{T}}^2 - N_{\text{T}}\right)$ optimal $\lambda_{l,q}^{\star}$ from (7.33) must be calculated per iteration, which is of course feasible in polynomial time.

Algorithm 7.3 Pseudocode of Algorithm A3.

$\mathbf{T}_0 = [\mathbf{I}_{N_\mathrm{T}}\ \mathbf{0}]$, $i = 0$.
while $\exists\, l : \mathrm{MSE}_i^{(l)}$ reducible **do**
    Select $l_i^\star$ as largest reducible $\mathrm{MSE}_i^{(l)}$
    Compute row increment $\mathbf{t}_\mathrm{inc}$ by solving optimization problem (7.43)
    Update $\mathbf{T}_{i+1}$ by computing $\mathbf{t}_{l_i,i+1}$ using (7.38)
    $i \leftarrow i + 1$
end
$\mathbf{T}^\star = \mathbf{T}_i$

To compute the largest guaranteed decrease $d_{l,q}^\star$ in A2 for all possible (l, q), not only all optimal $\lambda_{l,q}^\star$ for $\mathbf{T}_i$ must be determined, but one must compute also all $\lambda_{l,q}^\star$ of the next iteration for each increment $\mathbf{T}_\mathrm{inc}^{(l,q)}$ in the current iteration. Consequently, at most $\left((L_\mathrm{T}+1)\,N_\mathrm{T}^2 - N_\mathrm{T}\right)^2$ different $\lambda_{l,q}^\star$ must be determined, yielding, compared to A1, a larger complexity that is still polynomial in N_T and L_T.

Clearly, algorithm A3 is the most complex, as each iteration must solve multiple closest point problems. Unfortunately, this problem is NP-hard and no polynomial time algorithm is available (yet) to resolve it. Indeed, the search time of the lattice decoding algorithm in [85] rises exponentially with the problem's dimensions, i.e., $(L_\mathrm{T}+1)N_\mathrm{T} - 1$.

7.2.2.5 Optimality and convergence considerations

Due to the greedy nature of algorithm A1, the obtained $\mathbf{T}^\star$ is not guaranteed to be globally optimal. For example, several small decreases may be better than one large decrease, or one small decrease in the current iteration could enable a large decrease in future iterations. Both these events are completely ignored by this greedy algorithm.

Although the selection criterion in algorithm A2 more carefully selects the optimal $q_i^\star$, the obtained $\mathbf{T}^\star$ is still not guaranteed to be globally optimum, as algorithm A2 is essentially still a greedy algorithm. Nevertheless, algorithm A2 is expected to yield better performance than A1, as it can only benefit from the additional information in the selection of the increment. Moreover, the convergence conditions of algorithms A1 and A2 are identical, i.e., both algorithms terminate when none of the $\mathrm{MSE}_i^{(l)}$ can be further reduced. Hence neither algorithm is able to further lower the MSE when one algorithm is initialized with the TIR $\mathbf{T}$ obtained by means of the other algorithm.

When comparing algorithms A1 and A2 with algorithm A3, one can readily comprehend that the increments $\mathbf{T}_\mathrm{inc}^{(l,q)}$, allowed in A1 and A2, corresponds to a vector $\boldsymbol{\lambda}_\mathrm{inc}^\star$ with exactly one nonzero element in A3. The possible increments in A1 and A2 form thus a small subset of all increments allowed in A3. As

a consequence, running algorithm A1 or A2 initialized with the TIR matrix obtained by means of A3 will not further drop the MSE, whereas the reverse does not necessarily hold, implying that algorithm A3 has superior performance compared to A1 and A2.

7.3 BER expression for PRS

In this section, the BER expression for the ST PRS over a frequency-selective MIMO channel is derived. In [78], the SER of SISO PRS with an M-PAM constellation has already been discussed in detail. Here, this work is extended to obtain the BER for the general MIMO PRS with an M-QAM constellation using a two-dimensional binary reflected Gray mapping. Actually, this two-dimensional Gray mapping consists of two binary reflected Gray codes with halved dimension, as the real part and the imaginary part of the data symbol specify each $\frac{\log_2(M)}{2}$ bits.

First, a scaled and translated version $\mathbf{v}(k)$ of the decision variable $\mathbf{u}(k)$ is introduced, i.e.,

$$\mathbf{v}(k) = \frac{\mathbf{u}(k)}{2\Delta} + \mathbf{c}_{\text{off}}, \tag{7.45}$$

with $\mathbf{c}_{\text{off}}$ defined in (7.11). Based on the decomposition of $\mathbf{u}(k)$ from (7.7), the target response vector $\mathbf{u}_{\text{T}}(k)$ from (7.9), and the mapping rule from (7.2), $\mathbf{v}(k)$ can be expressed as

$$\mathbf{v}(k) = \sum_{m=0}^{L_{\text{T}}} \mathbf{T}(m)\mathbf{b}(k-m) + \mathbf{isi}(k) + \mathbf{n}_{\text{v}}(k), \tag{7.46}$$

where $\mathbf{n}_{\text{v}}(k) = \frac{\mathbf{W}\bar{\mathbf{n}}(k)}{2\Delta}$ and $\mathbf{isi}(k) = \sum_{m\in\Phi} \mathbf{E}(m)\mathbf{a}(k-m)$ with

$$2\Delta\mathbf{E}(m) = \begin{cases} \mathbf{WG}(m) - \mathbf{T}(m) & m \in \Phi_{\mathbf{T}} \\ \mathbf{WG}(m) - \mathbf{B}(m) & m \in \Phi_{\mathbf{B}} \\ \mathbf{WG}(m) & m \in \Phi \backslash \{\Phi_{\mathbf{T}} \cup \Phi_{\mathbf{B}}\} \end{cases}. \tag{7.47}$$

Because (7.1) yields

$$\sum_{m=0}^{L_{\text{T}}} \mathbf{T}(m)\mathbf{b}(k-m) = \mathbf{c}(k) + \mathbf{T}(0)\mathbf{d}(k)\sqrt{M}, \tag{7.48}$$

where the components of $\mathbf{d}(k)$ are Gaussian integers, $\mathbf{v}(k)$ from (7.45) reduces to

$$\mathbf{v}(k) = \mathbf{c}_{\text{ex}}(k) + \mathbf{isi}(k) + \mathbf{n}_{\text{v}}(k) \tag{7.49}$$

with $\mathbf{c}_{\text{ex}}(k) = \mathbf{c}(k) + \mathbf{T}(0)\mathbf{d}(k)\sqrt{M}$. At the receiver, the symbol-by-symbol detector makes a decision $\hat{\mathbf{c}}_{\text{ex}}(k)$ of $\mathbf{c}_{\text{ex}}(k)$ in the extended symbol set by rounding

$\mathbf{v}(k)$ to the closest Gaussian integer. As this procedure is performed for each data stream individually, the decision of the received symbol at instant k in the lth stream, $(\hat{\mathbf{c}}_{\rm ex}(k))_l$ is based on

$$\mathrm{v}_l(k) = (\mathbf{c}_{\rm ex}(k))_l + \mathrm{isi}_l(k) + (\mathbf{n}_{\rm v}(k))_l\,, \tag{7.50}$$

where $\mathrm{v}_l(k)$, $(\mathbf{c}_{\rm ex}(k))_l$, $\mathrm{isi}_l(k)$, and $(\mathbf{n}_{\rm v}(k))_l$ equal the lth component of the associated vectors $\mathbf{v}(k)$, $\mathbf{c}_{\rm ex}(k)$, $\mathbf{isi}(k)$, and $\mathbf{n}_{\rm v}(k)$, respectively. Afterwards, the modulo operator $[\cdot]_{\sqrt{M}}$ is applied to $(\hat{\mathbf{c}}_{\rm ex}(k))_l$, yielding the decisions $\hat{\mathrm{c}}_l(k) \in \mathcal{C}_{\rm PRS}$ of the transmitted symbol $\mathrm{c}_l(k)$ transmitted in the lth data stream at instant k. As the error performance does not depend on the symbol index k, this index is dropped in the sequel for notational conciseness. The BER of the lth data stream, $\mathrm{BER}^{(l)}$, can be expressed as

$$\mathrm{BER}^{(l)} = \sum_{(\mathfrak{c},\hat{\mathfrak{c}})} \frac{N_{\neq}(\mathfrak{c},\hat{\mathfrak{c}})}{\log_2(M)} \Pr\left(\mathrm{c}_l = \mathfrak{c}, \hat{c}_l = \hat{\mathfrak{c}}\right), \tag{7.51}$$

where $N_{\neq}(\mathfrak{c},\hat{\mathfrak{c}})$ represents the number of bits by which the binary labels of $\mathfrak{c}$ and $\hat{\mathfrak{c}}$ differ. In Appendix 11.10, an elaborate discussion is given on how the following simple but accurate approximation for $\mathrm{BER}^{(l)}$ is derived from (7.51):

$$\mathrm{BER}^{(l)} \approx \frac{1}{\log_2(M)} \mathbb{E}_{\mathbf{a}_{\rm ISI}}\left[4\mathrm{Q}\left(\frac{0.5 - \mathrm{Re}\left[\mathrm{isi}_l(\mathbf{a}_{\rm ISI})\right]}{\sigma_{(\mathbf{n}_{\rm v})_l}}\right)\right], \tag{7.52}$$

where $\mathrm{Q}(\cdot)$ once more represents the tail distribution of the standard normal distribution, $\sigma_{(\mathbf{n}_{\rm v})_l}$ equals the standard deviation of the real part of $(\mathbf{n}_{\rm v}(k))_l$, and $\mathbb{E}_{\mathbf{a}_{\rm ISI}}[\cdot]$ denotes the expectation over all symbols contributing to $\mathrm{Re}[\mathrm{isi}_l(\mathbf{a}_{\rm ISI})]$. The computational complexity in (7.52) rises exponentially with the channel and the filter length, thus rapidly becoming prohibitively large in numerical simulations. As an alternative, similar techniques as in Subsection 5.4.3 can be proposed to numerically evaluate this expression. For instance, a large number of N realizations of $\mathrm{Re}\left[\mathrm{isi}_l(\mathbf{a}_{\rm ISI})\right]$ could be generated, after which the expectation in (7.52) is replaced by the arithmetical average.

7.4 Numerical results and discussion

This section characterizes the performance of the optimization algorithms (A1, A2, and A3) discussed in Subsections 7.2.2.1-7.2.2.3 by numerical results for three scenarios, of which the simulation settings are summarized in Table 7.1. In all scenarios, the channel $\mathbf{H}(m)$ is a complex-valued frequency-selective Rayleigh-fading MIMO channel with $N_{\rm R} = N_{\rm T} = 4$ and an exponentially decaying power delay profile with base μ, i.e., $\mathbb{E}\left[\left|(\mathbf{H}(m))_{p,q}\right|^2\right] = \mu^{-(m+L_{\rm H}^{(1)})}$, $p, q \in \{1, \cdots, 4\}$ and $m \in \{-L_{\rm H}^{(1)}, \cdots, L_{\rm H}^{(2)}\}$. All channels taps are further assumed to be spatially and temporally uncorrelated. Moreover, all components of the

Table 7.1: Simulation settings of the different scenarios.

• 4-QAM constellation	• $\Phi_{\mathbf{B}} = \{4, 5\}$
• 3500 channel realizations	• $L_{\mathrm{H}}^{(1)} = 0$, $L_{\mathrm{H}}^{(2)} = 25$
• PRS settings:	• Scenarios:
FRS ($L_{\mathrm{T}} = 0$, $\mathbf{T}(0) = \mathbf{I}$)	S1: $\mu = 2$, $L_{\mathrm{W}}^{(1)} + L_{\mathrm{W}}^{(2)} + 1 = 13$
PRS-S ($L_{\mathrm{T}} = 0$; A1, A2, and A3)	S2: $\mu = 2$, $L_{\mathrm{W}}^{(1)} + L_{\mathrm{W}}^{(2)} + 1 = 21$
PRS-ST($L_{\mathrm{T}} = 3$; A1, A2, and A3)	S3: $\mu = 5$, $L_{\mathrm{W}}^{(1)} + L_{\mathrm{W}}^{(2)} + 1 = 13$

circular symmetric Gaussian noise $\mathbf{n}(k)$ are spatially and temporally uncorrelated and possess variance N_0, i.e., $\mathbf{R}_{\mathbf{n}}(m) = N_0 \delta_m \mathbf{I}_4$, whereas the components of $\mathbf{a}(k)$ belong to a Gray-mapped 4-QAM constellation. In the first scenario S1, a severely frequency-selective channel ($\mu = 2$) is equalized by means of a DFE consisting of a 13-tap feedforward filter and a 2-tap feedback filter with $\Phi_{\mathbf{B}} = \{4, 5\}$. Extending the feedforward filter to 21 taps in the second scenario S2 evidently improves the performance at the cost of a larger complexity. The third scenario S3 is identical to S1, except that the frequency-selectivity of the channel is less severe ($\mu = 5$). In all scenarios, a comparison is made between: (i) traditional FRS; (ii) spatial-only PRS (PRS-S), whose TIR possesses only spatial components ($L_{\mathrm{T}} = 0$); and (iii) ST PRS, whose TIR consists of both spatial, temporal, and ST components ($L_{\mathrm{T}} = 3$).

First, Subsection 7.4.1 issues several statements on the average performance of the different algorithms for the three considered scenarios. While the average performance is certainly one of the key performance indicators, the behavior of the different algorithms for individual channel realizations is also of particular importance. Hence, this performance aspect is the subject of Subsection 7.4.2. Moreover, the convergence and the complexity of the different algorithms is compared in Subsection 7.4.3 in terms of the number of iterations and the relative runtime. Finally, Subsection 7.4.4 investigates whether an alternative selection criterion for the row index l yields better performance.

7.4.1 Average performance

This discussion principally focuses on the average performance in terms of MSE and BER, because the former is the objective function of the optimization problem, whereas the latter is an important performance measure in practice. In this regard, Figs. 7.2, 7.3, and 7.4 respectively depict the 1/MSE and BER performances averaged over 3500 channel realizations in scenarios S1, S2, and S3, respectively, as a function of SNR $= \frac{E_b}{N_0} = \frac{E_{\mathrm{TX}}}{\log_2(M) N_0}$, where E_b and E_{TX} denote the transmitted energy per bit and per symbol, respectively. Furthermore, Table 7.2 lists the SNR in dB needed to achieve an average BER of 10^{-8} in the considered scenarios. The significant performance improvement achieved

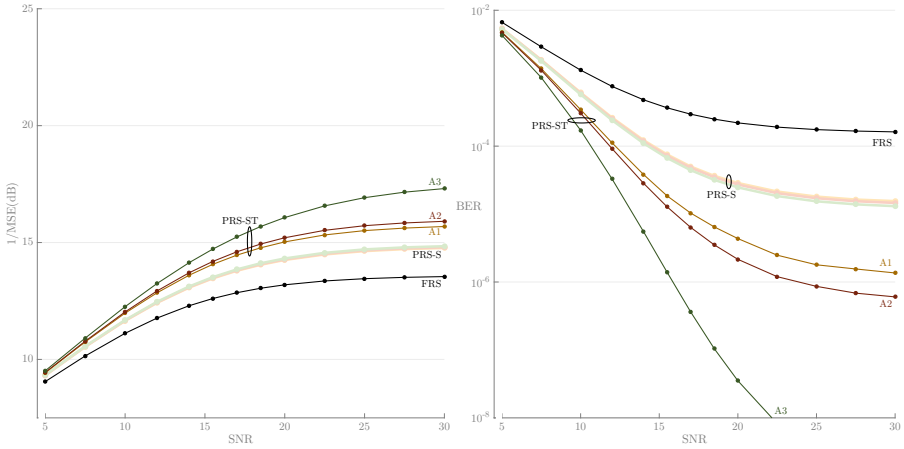

Figure 7.2: Scenario S1: average MSE (left) and average BER (right) as a function of the SNR with $\mu = 2$ and a 13-tap $\mathbf{W}$. Compared to FRS, PRS drastically improves the performance. In particular, PRS-ST optimized using A3 considerably reduces the BER floor.

by PRS compared to FRS is immediately apparent. Indeed, the smaller MSE accomplished by PRS is of course a direct consequence of the additional optimization of $\mathbf{T}$, but, more interestingly, the BER plots and Table 7.2 indicate that also the BER of the PRS is significantly lower compared to FRS. One noteworthy example is the drastic reduction of the error floor by considering PRS instead of FRS in S1 (Fig. 7.2). Moreover, the longer feedforward filter in S2 allows PRS even to completely remove the error floor encountered by FRS or at least to lower it to below 10^{-8} (Fig. 7.3). Finally, compared to FRS, PRS accomplishes a reduction up to 16 dB in SNR to reach a target BER of 10^{-8} in S3 (Fig. 7.4).

Significant differences in average performance between the three algorithms A1, A2, and A3 occur when the TIR has spatial, temporal, and ST components ($L_{\mathrm{T}} = 3$). In this configuration, algorithm A3 not only yields an average MSE that is smaller than the MSEs of algorithms A1 and A2, but, more importantly, also drastically lowers the BER. For instance, only algorithm A3 is able to reduce the error floor below 10^{-8} in scenario S1. Further, its SNR required to reach a BER of 10^{-8} in scenario S2 is approximately 2.8 dB and 2.5 dB lower compared to algorithms A1 and A2, respectively, whereas the gain of algorithm A3 compared to algorithms A1 and A2 in scenario S3 is about 2.3 dB and 1.5 dB, respectively. These results therefore imply not only that algorithms A1 and A2 do not yield the global optimum, but also that algorithm A3 is to be preferred when performance is essential. Furthermore, these numerical results confirm our expectation that algorithm A2 outperforms algorithm A1 on average, yet the gain of A2 compared to A1 turns out to be quite moderate: a lower error

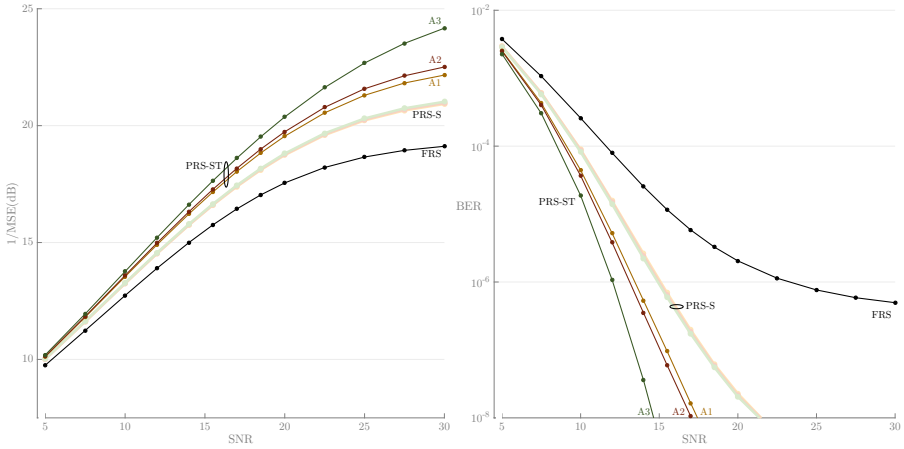

Figure 7.3: Scenario S2: average MSE (left) and average BER (right) as a function of the SNR with $\mu = 2$ and a 21-tap $\mathbf{W}$. Compared to S1 (Fig. 7.2), increasing the length of $\mathbf{W}$ results in remarkably better performance.

Table 7.2: SNR in dB needed to reach an average BER $= 10^{-8}$.

Scenario	FRS	PRS-S			PRS-ST		
		A1	A2	A3	A1	A2	A3
S1	-	-	-	-	-	-	22.17
S2	-	21.44	21.43	21.37	17.40	17.10	14.64
S3	31.69	18.65	18.51	18.40	17.79	17.00	15.53

floor is achieved in S1 (factor 2), whereas the SNR required to meet the BER target decreases by less than 0.8 dB in scenarios S2 and S3.

When the TIR possesses only spatial components, i.e., $L_{\mathrm{T}} = 0$, the performance difference between algorithms A1, A2, and A3 is almost negligible for all scenarios. In this case, $\mathbf{T}$ contains only $\mathbf{T}(0)$, limiting the possible increments in all algorithms to the set of consecutive row additions. All algorithms are therefore similar, resulting in nearly identical average MSE and BER performance. In this case, the least complicated algorithm A1 is the most attractive. For $L_{\mathrm{T}} = 0$, the minimization of (7.23) is structurally identical to the lattice reduction problem from [69]. Indeed, algorithm A1 corresponds to the element-based lattice reduction (ELR) algorithm from [69], while algorithm A3 is similar to the improved ELR algorithm from [69].

At low SNR, the matrix $\mathbf{G}$ in (7.24) closely resembles an identity matrix. Consequently, the optimized PRS converges to FRS for low SNR. The performance improvement of PRS over FRS is therefore mainly noticeable at high SNR.

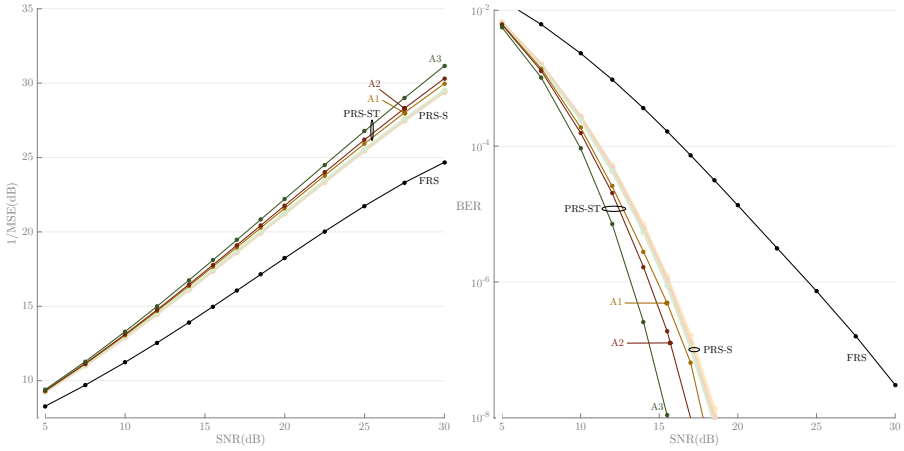

Figure 7.4: Scenario S3: average MSE (left) and average BER (right) as a function of the SNR with $\mu = 5$ and a 13-tap $\mathbf{W}$. Due to the mild frequency-selectivity of the channel, the difference between PRS-S and PRS-ST is considerably smaller.

As for the mildly selective channel in scenario S3, all PRS configurations outperform FRS, but the difference between PRS-S and PRS-ST is less significant. Hence, the improvement of PRS can mainly be attributed to the spatial components in $\mathbf{T}(0)$ and to a lesser extent to the temporal and ST components in $\{\mathbf{T}(m)|m > 0\}$. As the mildly frequency-selective channel generates relatively small temporal ISI and ST ISI, this observation is not unexpected.

7.4.2 Performance for individual channel realizations

Section 7.4.1 above considers only numerical results that are averaged over 3500 channel realizations. To better understand how FRS and PRS affect the BER performance for individual channel realizations, $\mathrm{SNR}_{\mathrm{FR}}$, $\mathrm{SNR}_{\mathrm{A1}}^{\mathrm{PR}}$, $\mathrm{SNR}_{\mathrm{A2}}^{\mathrm{PR}}$, and $\mathrm{SNR}_{\mathrm{A3}}^{\mathrm{PR}}$ are defined as the SNR required for a *particular* channel realization to reach a BER of 10^{-8} in the case of FRS and the three algorithms for PRS, respectively. The scatter plots from Fig. 7.5 compare $\mathrm{SNR}_{\mathrm{A3}}^{\mathrm{PR}}$ to $\mathrm{SNR}_{\mathrm{FR}}$, to $\mathrm{SNR}_{\mathrm{A1}}^{\mathrm{PR}}$, and to $\mathrm{SNR}_{\mathrm{A2}}^{\mathrm{PR}}$, for 3500 channel realizations in the case of S2 and $L_{\mathrm{T}} = 3$ (PRS-ST). In these plots, a scatter point is labeled as 'floor' when the target of 10^{-8} cannot be reached due to an error floor. Immediately evident from the plots is that nearly all scatter points are above the line connecting all points where the SNR on the ordinate equals $\mathrm{SNR}_{\mathrm{A3}}^{\mathrm{PR}}$. Hence, apart from some exceptions, PRS optimized with algorithm A3 requires the lowest SNR to reach the target BER. Additionally, the MSE achieved by means of algorithm A3, $\mathrm{MSE}_{\mathrm{A3}}^{\mathrm{PR}}$, has been numerically verified to be the lowest for all channel realizations (not shown). These observations not only corroborate the superiority

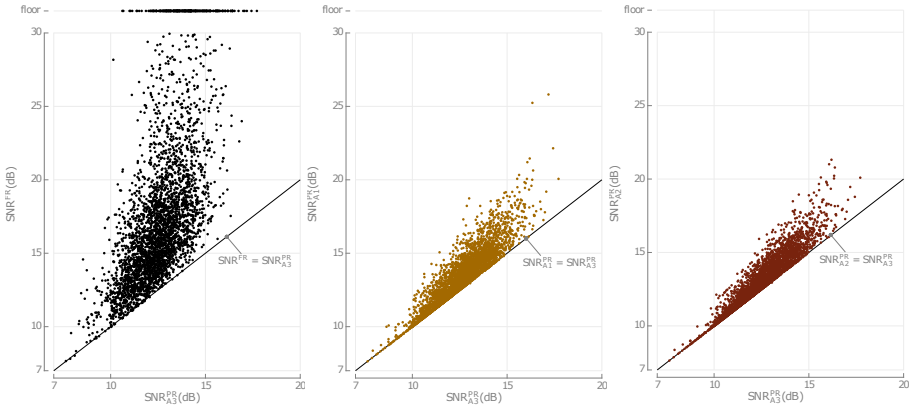

Figure 7.5: Scenario S2: scatter plot of the points ($\mathrm{SNR}^{\mathrm{PR}}_{\mathrm{A3}}$,$\mathrm{SNR}_{\mathrm{Y}}$), where $\mathrm{SNR}_{\mathrm{Y}}$ equals $\mathrm{SNR}_{\mathrm{FR}}$, $\mathrm{SNR}^{\mathrm{PR}}_{\mathrm{A1}}$ and $\mathrm{SNR}^{\mathrm{PR}}_{\mathrm{A2}}$ in the left, the middle, and the right plot, respectively. All points above/below the solid straight line represent channel realizations for which $\mathrm{SNR}_{\mathrm{Y}}$ is larger/smaller than $\mathrm{SNR}^{\mathrm{PR}}_{\mathrm{A3}}$.

of algorithm A3 in terms of MSE, but also illustrate that a smaller MSE does not necessarily guarantee a smaller BER. Next, the largest gain from applying A3 is observed for unfavorable channels, i.e., channel realizations requiring a rather large $\mathrm{SNR}_{\mathrm{FR}}$, $\mathrm{SNR}^{\mathrm{PR}}_{\mathrm{A1}}$, and $\mathrm{SNR}^{\mathrm{PR}}_{\mathrm{A2}}$, whereas only minor gains are obtained for favorable realizations with smaller values for $\mathrm{SNR}_{\mathrm{FR}}$, $\mathrm{SNR}^{\mathrm{PR}}_{\mathrm{A1}}$, and $\mathrm{SNR}^{\mathrm{PR}}_{\mathrm{A2}}$. Additional simulations confirm that all conclusions drawn here apply also to scenarios with different filter lengths and/or base μ (not shown).

While the MSE of algorithm A3, $\mathrm{MSE}^{\mathrm{PR}}_{\mathrm{A3}}$, is numerically verified to be the lowest for all channel realizations, algorithms A1 and A2 yield only locally optimal MSEs. As for their relative performance, results above confirm that algorithm A2 outperforms algorithm A1 on average as expected. However, this observation does not impede that algorithm A1 could yield better performance than algorithm A2 for a specific channel realization, because a sequence of increments in algorithm A1 could for example enable a large future decrease that was not considered by algorithm A2. This claim is supported by Fig. 7.5, which compares the MSE achieved by algorithm A1, i.e., $\mathrm{MSE}^{\mathrm{PR}}_{\mathrm{A1}}$, with the MSE achieved by algorithm A2, i.e, $\mathrm{MSE}^{\mathrm{PR}}_{\mathrm{A2}}$, by means of a scatter plot in the case of scenario S2 at $\mathrm{SNR} = 20\,\mathrm{dB}$. For about 92.5% of the channels, the outcome of algorithms A1 and A2 is identical, while algorithm A2 is superior for 6.5% of the channels and algorithm A1 outperforms algorithm A2 for only $< 1\%$ of the channel realizations. Consequently, neither algorithm A1 nor algorithm A2 is superior to the other in terms of minimal MSE for all channel realizations.

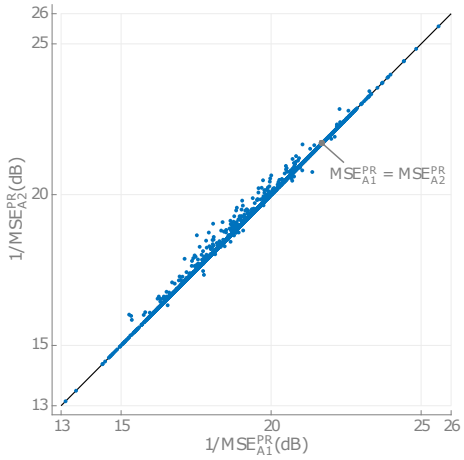

Figure 7.6: Scenario S2: scatter plot of the points $(\mathrm{MSE}_{\mathrm{A1}}^{\mathrm{PR}}, \mathrm{MSE}_{\mathrm{A2}}^{\mathrm{PR}})$ at SNR = 20 dB. For most channel realizations, algorithm A1 and algorithm A2 yield identical performance.

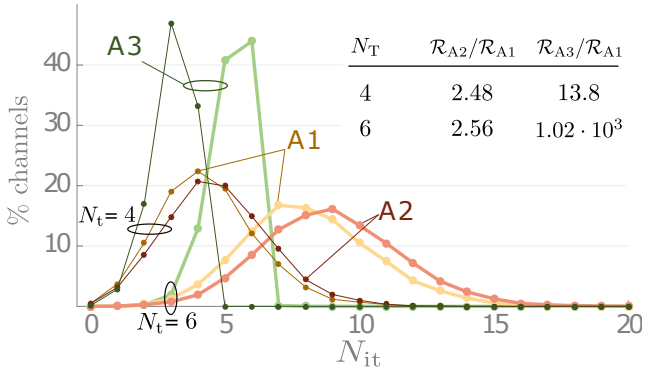

Figure 7.7: Histogram of the number of iterations required for convergence of algorithms A1-A3 in the case of scenario S2 with $L_{\mathrm{T}} = 2$ and SNR = 20 dB for both $N_{\mathrm{T}} = N_{\mathrm{R}} = 4$ and $N_{\mathrm{T}} = N_{\mathrm{R}} = 6$. Moreover, the relative runtimes with respect to algorithm A1 are also listed for A2 and A3. A small number of high-complexity iterations results in almost instant convergence for algorithm A3, whereas algorithms A1 and A2 require more, but significantly less complex iterations.

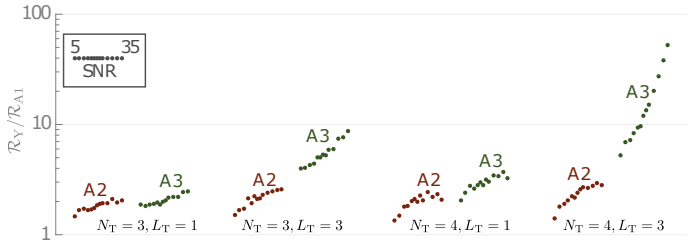

Figure 7.8: Scenario S2: average runtime of algorithms A2 and A3 relative to the runtime of algorithm A1 as a function of SNR for $N_T = N_R \in \{3, 4\}$ and $L_T \in \{1, 3\}$. Especially at high SNR, the runtime of algorithm A3 quickly rises with increasing N_T and L_T.

7.4.3 Convergence and complexity analysis

One key feature of all algorithms is their computational complexity. Fig. 7.7 therefore presents the histogram (3500 channels) of the number of iterations required for convergence in the case of scenario S2 with $L_T = 2$ and SNR = 20 dB for both $N_T = N_R = 4$ and $N_T = N_R = 6$. Moreover, an additional table lists the runtimes $\mathcal{R}$ of algorithms A2 and A3 relative to the runtime of algorithm A1, i.e., $\mathcal{R}_{A1}$. In this discussion, only the relative and not the absolute runtime of an algorithm is considered, because the latter is hugely dependent on the specific implementation and the computing power of the simulation machine, whereas the former is expected to be less influenced by these parameters. The following remarks can be made:

- In the case of both algorithm A1 and algorithm A2, convergence is reached for at least 90% of the channels after $2N_T$ iterations, but the runtime of A2, $\mathcal{R}_{A2}$, is approximately 2.5 times as large as the runtime of A1, $\mathcal{R}_{A1}$. This last observation has two reasons: (i) algorithm A2 requires on average slightly more iterations than algorithm A1; and (ii) one iteration of algorithm A2 is somewhat more complex than one iteration of algorithm A1 as possibly more increments must be computed.

- As for algorithm A3, only approximately N_T iterations are needed for convergence. Nevertheless, $\mathcal{R}_{A3}$ is significantly larger than both $\mathcal{R}_{A1}$ and $\mathcal{R}_{A2}$, because the complexity of the lattice decoding problem rises exponentially with the product $N_T L_T$, and the complexity of one iteration thus rapidly becomes substantial.

In conclusion, algorithms A1 and A2 are to be preferred when either performance is subordinated to complexity or when all algorithms yield similar performance, e.g., at low SNR or in the case of PRS-S. Yet, when performance is critical, algorithm A3 should be employed.

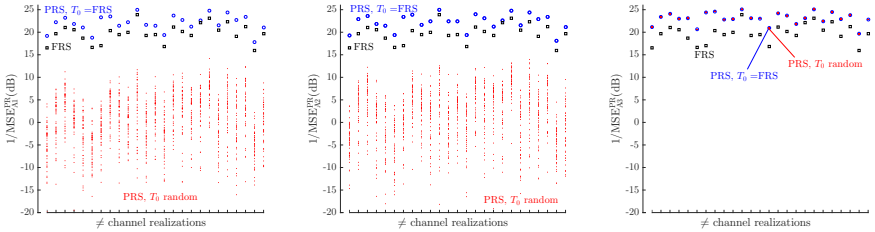

Figure 7.9: Scenario S2: comparison of the achieved MSE at SNR = 20 dB for 25 channel realizations in the case of algorithm A1 (left plot), algorithm A2 (middle plot), and algorithm A3 (right plot) for PRS-ST ($L_{\mathrm{T}} = 3$) with $\mathbf{T}_0$ either randomly initialized (50 realizations of $\mathbf{T}_0$ per channel realization) or initialized as FRS. As a reference, the MSE achieved by FRS is included as well. Clearly, the performance of algorithms A1 and A2 is highly susceptible to the initialization, whereas algorithm A3 yields excellent performance compared to FRS, irrespective of the initialization.

A more detailed insight into the runtime of the different algorithms is gained in Fig. 7.8, in which both the ratio $\mathcal{R}_{\mathrm{A2}}/\mathcal{R}_{\mathrm{A1}}$ and the ratio $\mathcal{R}_{\mathrm{A3}}/\mathcal{R}_{\mathrm{A1}}$ are investigated as a function of the SNR for different values of N_{T} and L_{T} in the case of scenario S2. The following observations hold:

- Algorithm A1 is executed the fastest because the ratios $\mathcal{R}_{\mathrm{A2}}/\mathcal{R}_{\mathrm{A1}}$ and $\mathcal{R}_{\mathrm{A3}}/\mathcal{R}_{\mathrm{A1}}$ are always larger than 1, irrespective of the SNR, N_{T} and L_{T}.
- The execution of algorithm A2 takes on average approximately two and maximally three times as much time as the execution of Algorithm A1. Compared to A1, the runtime of A2 is larger, especially at high SNR, whereas N_{T} and L_{T} do not have a major impact on the ratio $\mathcal{R}_{\mathrm{A2}}/\mathcal{R}_{\mathrm{A1}}$.
- The runtime of algorithm A3 is clearly the largest, confirming that its iterations are indeed more complex compared to the iterations of algorithms A1 and A2, since less iteration are generally required in algorithm A3. Just as for A2, the ratio $\mathcal{R}_{\mathrm{A3}}/\mathcal{R}_{\mathrm{A1}}$ increases with larger SNR, but the number of symbol streams N_{T} and the length of the target response L_{T} have also a profound impact on $\mathcal{R}_{\mathrm{A3}}/\mathcal{R}_{\mathrm{A1}}$. Especially at high SNR, the runtime of A3 quickly rises for increasing N_{T} and L_{T}. These observations are not unexpected as the complexity of the lattice decoding algorithm rises exponentially with the problem's dimensions, i.e., $N_{\mathrm{T}}(L_{\mathrm{T}}+1)-1$.

The effect of the initialization of $\mathbf{T}_0$ on the obtained MSE is investigated in Fig. 7.9 for algorithms A1 (left plot), A2 (middle plot), and A3 (right plot) in the case of scenario S2 at SNR = 20 dB. More specifically, this figure depicts for 25 random channel realizations: (i) the MSE achieved by means of all three algorithms when $\mathbf{T}_0$ is initialized as FRS, i.e., $\mathbf{T}_0 = [\mathbf{I}\ \mathbf{0}]$; (ii) the MSE achieved

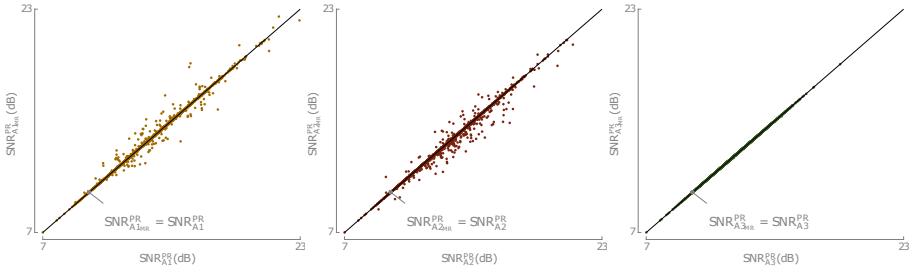

Figure 7.10: Scenario S2: scatter plots of the points $(\mathrm{SNR}^{\mathrm{PR}}_{\mathrm{Y}}, \mathrm{SNR}^{\mathrm{PR}}_{\mathrm{Y_{MR}}})$ for 3500 channel realizations, where Y equals A1, A2, and A3 in the left, middle, and right plot. More than 90% of all scatter points lie very close to the line connecting all points for which $\mathrm{SNR}^{\mathrm{PR}}_{\mathrm{Y}} = \mathrm{SNR}^{\mathrm{PR}}_{\mathrm{Y_{MR}}}$, indicating that $\mathrm{SNR}^{\mathrm{PR}}_{\mathrm{A1}} \approx \mathrm{SNR}^{\mathrm{PR}}_{\mathrm{A1_{MR}}}$, $\mathrm{SNR}^{\mathrm{PR}}_{\mathrm{A2}} \approx \mathrm{SNR}^{\mathrm{PR}}_{\mathrm{A2_{MR}}}$, and $\mathrm{SNR}^{\mathrm{PR}}_{\mathrm{A3}} \approx \mathrm{SNR}^{\mathrm{PR}}_{\mathrm{A3_{MR}}}$. Consequently, the performance is roughly identical with respect to the selection criterion of $l_i^\star$.

when $\mathbf{T}_0$ is set to a random feasible TIR (50 realizations of $\mathbf{T}_0$ per channel realization); and (iii) the MSE achieved in the case of FRS. When $\mathbf{T}_0$ is initialized as FRS, the MSE obtained by all three algorithms is of course smaller than the MSE in the case of FRS, simply because an additional optimization over $\mathbf{T}$ is performed. In the case of the random initialization of $\mathbf{T}_0$, however, algorithms A1 and A2 get trapped in local minima whose performance is often significantly worse than the performance of FRS, emphasizing the importance of good initialization in algorithms A1 and A2. On the other hand, the performance of algorithm of A3 is essentially unaffected by the value of $\mathbf{T}_0$, because all different $\mathbf{T}_0$ yield the same results.

7.4.4 Alternative selection criterion

In all the results above, the optimal row index $l_i^\star$ corresponds to the largest reducible $\mathrm{MSE}_i^{(l)}$. However, an alternative selection criterion for $l_i^\star$ could be envisaged as well. For instance, the row $l_i^\star$ could be chosen more aggressively such that the increment is selected to maximally decrease $\mathrm{MSE}_i^{(l)}$, e.g., $(l_i^\star, q_i^\star) = \arg\max_{l,q} \delta_{l,q}^\star$ in algorithm A1. The resulting algorithms with this alternative selection criterion are denoted by $\mathrm{A1_{MR}}$, $\mathrm{A2_{MR}}$, and $\mathrm{A3_{MR}}$. To compare the two selection criteria in terms of performance, Fig. 7.10 presents three scatter plots in which the tuples $(\mathrm{SNR}^{\mathrm{PR}}_{\mathrm{Y}}, \mathrm{SNR}^{\mathrm{PR}}_{\mathrm{Y_{MR}}})$ are presented. More specifically, $\mathrm{SNR}^{\mathrm{PR}}_{\mathrm{Y_{MR}}}$ is analogously defined as $\mathrm{SNR}^{\mathrm{PR}}_{\mathrm{Y}}$, i.e, the SNR required for a particular channel realization to reach a target BER of 10^{-8} when algorithm $\mathrm{Y_{MR}}$ is employed. In Fig. 7.10, Y is equal to A1, A2, and A3 in the left, the middle, and the right plot, respectively. Moreover, a straight line, connecting all points for which $\mathrm{SNR}^{\mathrm{PR}}_{\mathrm{Y}} = \mathrm{SNR}^{\mathrm{PR}}_{\mathrm{Y_{MR}}}$ is added to facilitate the performance comparison. Immediately noticeable on the scatter plots is that

almost all scatter points are close to or even lie on this straight line, especially in the case of algorithm A3, indicating that algorithms Y and $\mathrm{Y_{MR}}$ yield similar performance for most channel realizations. This statement is confirmed by the MSE performance (not shown), as the MSE of at least 85% of the channel realizations is identical for algorithms Y and $\mathrm{Y_{MR}}$. As for the channel realizations whose performances differ, algorithm Y is superior for roughly half of them, whereas algorithm $\mathrm{Y_{MR}}$ is superior for the other half. Hence, on average, the performances of algorithms Y and $\mathrm{Y_{MR}}$ are nearly identical.

In terms of MSE, algorithms A3 and $\mathrm{A3_{MR}}$ almost always yield identical performance and thus also identical TIRs. However, a few exceptions exists, where either algorithm A3 or algorithm $\mathrm{A3_{MR}}$ achieves a smaller MSE than the other algorithm. This numerical results indicates that neither algorithm converges to the global optimum for all channel realizations, but we strongly believe that the global minimum is reached for most channel realizations.

Irrespective of the considered algorithm, additional simulations reveal that both selection criteria require on average approximately the same number of iterations to converge. Consequently, the selection criterion requiring the least computations per iteration is expected to be executed the fastest and is thus preferred. In the case of algorithm $\mathrm{Y_{MR}}$, the largest decrease must be computed for each $l \in \{1, \cdots, N_{\mathrm{T}}\}$ such that the increment inducing the largest reduction in MSE_i can be selected. On the other hand, algorithm Y must compute only $L \leq N_{\mathrm{T}}$ largest decreases per iteration, where L is such that the Lth largest $\mathrm{MSE}_i^{(l)}$ is reducible and the $L-1$ larger $\mathrm{MSE}_i^{(l)}$ are irreducible. Consequently, the computational complexity per iteration is larger for algorithm $\mathrm{Y_{MR}}$ than for algorithm Y, making the latter the better choice.

7.5 Conclusions

This chapter discusses an equalization scheme with a ST MIMO PRS precoder, where a frequency-selective MIMO channel is equalized with respect to a general TIR that contains both temporal, spatial, and ST components. This TIR and all equalization coefficients of the DFE are jointly optimized according to the MMSE criterion. First, the optimal DFE for a given TIR is derived. Next, three iterative algorithms are described that perform a row-by-row optimization of the TIR by updating the row of the TIR matrix corresponding to the largest reducible $\mathrm{MSE}^{(l)}$. The least complex algorithm A1 selects from a predefined set of allowed increments the one yielding the largest decrease of the largest reducible MSE. The allowed increment either alters exactly one element of the TIR matrix, or adds an Gaussian integer multiple of one row of $\mathbf{T}(0)$ to another row of $\mathbf{T}(0)$. Algorithm A2 employs the same set of increments, and is structurally similar to A1, but its selection criterion considers also the potential of future increments. The most complex A3 updates in each iteration an entire row of the TIR matrix by solving a lattice decoding problem. Next, this chapter derives the BER expression along with an accurate approximation. The nu-

merical results confirm that PRS considerably outperforms FRS, not only when the TIR contains ST components (PRS-ST), but also when the TIR contains only spatial components (PRS-S). Interestingly, the performance improvement of PRS-ST compared to PRS-S becomes more prominent for severely distorted channel as the ST components of the TIR are more pronounced. As for the different algorithms, especially algorithm A3 achieves superior average performances, justifying its larger complexity, whereas algorithm A2 only slightly outperforms algorithm A1. However, the average performance difference between the different algorithms is negligibly small for a spatial-only TIR or at low SNR, making the low-complexity A1 most preferable in this situation. The performance of individual channel realizations confirms the superiority of algorithm A3 and also reveals that algorithm A2 yield not necessarily better performance than algorithm A1. A disadvantage of algorithm A3 is that its runtime quickly grows with increasing N_{T} or L_{T}, while this increase is far less noticeable for algorithms A1 and A2. Moreover, simulations show that algorithms A1 and A2 are susceptible to the initialization. Algorithm A3, on the other hand, does not suffer from this as it converges to the same optimum for all different initializations. Finally, an alternative selection criterion for $l_i^\star$ is proposed, which essentially results in approximately identical performance for all algorithms.

8

Robust partial-response signaling

This chapter discusses the equalizer design in the case of PRS over a frequency-selective and time-variant MIMO channel, just as Chapter 7. In contrast to Chapter 7, the design of the equalization parameters is based on estimates of the channel rather than the actual channel realization itself. As these estimates are noisy and/or delayed, a statistically robust optimization framework is proposed in this chapter. First, the concept of robustness is introduced in Section 8.1. Second, Section 8.2 presents the equalization scheme consisting of a PRS precoder and a linear filter at the transmitter. Next, Section 8.3 describes, in general, the optimization problem that must be solved in the robust design (Subsection 8.3.1), after which this general optimization framework is applied to the MSE corresponding to the considered equalization scheme (Subsection 8.3.2). Mathematical details of this MMSE optimization are given in Subsection 8.3.3, whereas Section 8.4 briefly discusses how the BER for this equalization scheme can be numerically obtained. In Section 8.5, numerical results illustrate that the robust PRS design offers several performance improvements compared to the case of naively assuming that the channel estimates are perfect. Finally, conclusions are drawn in Section 8.6.

In this chapter, only bandpass transmission is considered, and all bandpass signals and all bandpass filters are represented in complex-valued baseband notation.

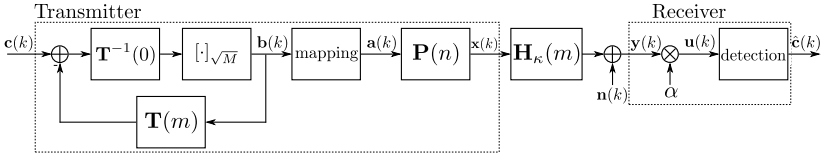

Figure 8.1: System model of the equalization scheme consisting of a PRS precoder and a linear equalizer at the transmitter.

8.1 Robust design

All equalization and TIR parameters are ideally computed with perfect CSI. However, the assumption of perfect CSI is often unrealistic in practice, especially at the transmitter. Indeed, several different elements could impact the quality of the CSI: channel noise during the estimation process, intolerably large processing delays, and limited bandwidth of the return channel, causing quantization errors and/or propagation delay. Consequently the CSIT, is often a noisy and/or delayed version of the actual channel. In general, the naive approach of determining the equalization and TIR parameters without taking these estimation imperfections into account results in adequate performance only when the available CSIT is sufficiently accurate. Alternatively, superior performance is usually attained by robust equalization design, because it incorporates the imperfections of the CSIT in the design of the equalization and the TIR parameters. As a result, the performance of the robust equalization and TIR parameters is more conservative, but also far less sensitive to the imperfections of the CSIT. Two main classes of robust designs exist. As for the worst-case designs, the channel estimation error is assumed to be within a bounded uncertainty region, e.g., due to quantization noise. Next, a minimax optimization problem is solved to guarantee a certain performance level for all estimation errors within that region [86, 87, 88, 89, 90, 91]. As an alternative to the worst-case design, the estimation error could also be modeled statistically, allowing to design the equalization and TIR parameters by optimizing a performance measure averaged over the joint distribution of the channel and the CSI [74, 54, 75, 92, 91]. In this chapter, the latter concept of robustness is employed and applied to the general ST PRS precoder.

8.2 System model

Fig. 8.1 shows the block diagram of the communication system considered in this chapter. More specifically, a frequency-selective MIMO channel with N_{T} inputs and N_{R} outputs is equalized by means of a ST PRS precoder and a linear FIR MIMO equalizer at the transmitter, and the data is recovered by means of a symbol-by-symbol detector at the receiver that operates on a scaled version of the received signal. This equalization scheme is quite similar to the equalization

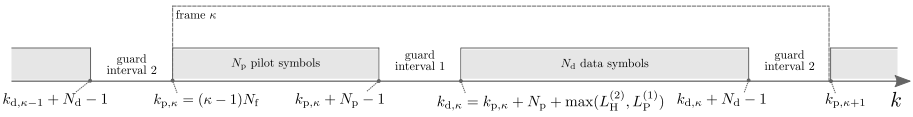

Figure 8.2: Structure of the κth frame of the block transmission scheme (sequence $\mathbf{c}(k)$) . The transmitter generates alternately a block of pilot symbols and a block of data symbols with guard intervals between them such that no IBI occurs at the receiver.

scheme discussed in Chapter 7, but with the DFE at the receiver in the latter scheme being replaced by a linear FIR MIMO equalizer at the transmitter. Moreover, the frequency-selective channel in this chapter is assumed to be wide-sense stationary slowly Rayleigh-fading, meaning that the optimal equalization coefficients must change over time as well. To this end, regularly updated and reliable CSI must be available at the transmitter. Here, this requirement is fulfilled by considering block transmission, in which the consecutively transmit frames span each N_f symbols and contain pilot symbols and data symbols. The pilot symbols are employed to perform channel estimation at the receiver, after which the acquired estimate is fed back to the transmitter over a return channel with possibly limited bandwidth. The obtained CSIT is, however, often inaccurate (because of channel estimation errors caused by noise) and/or delayed (because of the propagation delay on the actual and the return channel, and the processing time required for computing the estimate at the receiver).

The structure of the block transmission is now discussed in more detail by means of Fig. 8.2, which schematically illustrates the κth frame in the sequence $\mathbf{c}(k)$. Clearly, the sequence $\mathbf{c}(k)$ is composed of a stream of blocks that alternately span N_p symbols periods and N_d symbol periods. The former blocks are filled with pilot symbols, whereas the latter blocks contain data symbols. In each frame, two guard intervals are present with a duration of $N_{\mathrm{g},1}T$ and $N_{\mathrm{g},2}T$, respectively. These guard times must be large enough to ensure that the receiver does not suffer from interference between pilot symbols and data symbols, but must also be as small as possible to maximize the channel throughput. As for the pilot symbols, both the PRS precoder and the linear equalizer are bypassed such that these symbols are directly applied to the channel in frame κ from time index $k_{\mathrm{p},\kappa}=(\kappa-1)N_\mathrm{f}$ up to and including time index $k_{\mathrm{p},\kappa}+N_\mathrm{p}-1$. Consequently, the received data block corresponding to these pilot symbols ranges from $k_{\mathrm{p},\kappa}-L_\mathrm{H}^{(1)}$ up to and including $k_{\mathrm{p},\kappa}+N_\mathrm{p}-1+L_\mathrm{H}^{(2)}$, from which, however, only the part ranging from $k_{\mathrm{p},\kappa}+L_\mathrm{H}^{(2)}$ till $k_{\mathrm{p},\kappa}+N_\mathrm{p}-1-L_\mathrm{H}^{(1)}$ is used in the channel estimation process (Appendix 11.11). On the other hand, the data symbols of frame κ in the sequence $\mathbf{c}(k)$ correspond to the time index interval $I_{\mathrm{d},\kappa}=[k_{\mathrm{d},\kappa}=k_{\mathrm{p},\kappa}+N_\mathrm{P}-1+N_{\mathrm{g},1},k_{\mathrm{d},\kappa}+N_\mathrm{d}-1]$. In contrary to the pilot symbols, this block of data symbols is precoded and pre-equalized by the PRS precoder and the linear filter, respectively, after

which the resulting signal is transmitted over the channel. This results in a received data block starting at time index $k_{\mathrm{d},\kappa} - L_{\mathrm{G}}^{(1)}$ and ending at time index $k_{\mathrm{d},\kappa} + N_{\mathrm{d}} - 1 + L_{\mathrm{G}}^{(2)}$. Still, only the scaled received samples in the interval $I_{\mathrm{d},\kappa}$ are applied to the symbol-by-symbol detector to recover the data symbols. Next, $N_{\mathrm{g},1}$ and $N_{\mathrm{g},2}$ are equal to the smallest values that ensure that the useful part of the received samples from both the block with pilot symbols and the block with data symbols is not corrupted by interference of any other blocks. To satisfy this requirement, one could derive that $N_{\mathrm{g},1} = \max\left(L_{\mathrm{H}}^{(2)}, L_{\mathrm{P}}^{(1)}\right) + 1$ and $N_{\mathrm{g},2} = \max\left(L_{\mathrm{H}}^{(1)}, L_{\mathrm{P}}^{(2)}\right) + 1$. The total duration of one frame is then given by $N_{\mathrm{f}}T = (N_{\mathrm{P}} + N_{\mathrm{d}} + N_{\mathrm{g},1} + N_{\mathrm{g},2})\,T$. In the following, we describe both the transmitter and the receiver processing related to the data symbols in a generic frame.

As for the PRS precoder characterized by the target response vector $\mathbf{T}$, the description given in Chapter 7 applies here as well, with the exception that N_{R} instead of N_{T} symbol streams are considered here. Indeed, the linear equalization filter is situated here at the transmitter instead of the receiver. As a result, the symbol-by-symbol detector directly operates on a scaled version of each channel output. Therefore, the number of data streams N_{dat} is set equal to N_{R} and the assumption is made that $N_{\mathrm{T}} \geq N_{\mathrm{R}}$. So, the input at the transmitter consists of N_{R} independent complex-valued data symbol streams, whose entries are all an element of the constellation $\mathcal{C}_{\mathrm{PRS}}$. Moreover, the relationship specified in (7.1) and (7.2) between the data input symbol vector $\mathbf{c}(k)$ and the vector $\mathbf{a}(k)$ still holds here, but the matrices $\mathbf{T}(m)$ now belong to the set $\mathbb{Z}[j]^{N_{\mathrm{R}} \times N_{\mathrm{R}}}$. After the PRS precoder, the obtained symbol sequence $\{\mathbf{a}(k)\}$ is equalized by means of the equalizer $\mathbf{P}$, which represents a linear symbol-spaced FIR filter, yielding the signal $\mathbf{x}(k)$. This equalizer is characterized by the $N_{\mathrm{T}} \times N_{\mathrm{R}}$ impulse response matrices $\mathbf{P}(n)$ such that $\mathbf{x}(k)$ can be expressed as

$$\mathbf{x}(k) = \sum_{n=-L_{\mathrm{P}}^{(1)}}^{L_{\mathrm{P}}^{(2)}} \mathbf{P}(n)\mathbf{a}(k-n), \tag{8.1}$$

where all active delay indices n of the equalizer $\mathbf{P}$ are limited to the set $\{-L_{\mathrm{P}}^{(1)}, \cdots, L_{\mathrm{P}}^{(2)}\}$. Analogous to the equalizer $\mathbf{P}$ in the equalization schemes from the previous chapters, an energy constraint must ensure that the transmitted energy per symbol does not become excessive. This energy constraint is given by

$$\sigma_{\mathrm{a}}^2 \mathrm{Tr}\left[\mathbf{P}^H \mathbf{R}_{\mathrm{TX}} \mathbf{P}\right] \leq N_{\mathrm{R}} E_{\mathrm{TX}}, \tag{8.2}$$

where $\mathbf{R}_{\mathrm{TX}}$ is defined in (5.8).

Subsequently, the signal $\mathbf{x}$(k) propagates over a wide-sense stationary frequency-selective Rayleigh fading $N_{\mathrm{R}} \times N_{\mathrm{T}}$ MIMO channel that is characterized by the discrete-time channel impulse response matrices $\mathbf{H}(m, k)$. These

matrices $\mathbf{H}(m,k)$ are related to the impulse response matrix $\mathbf{H}_{\mathrm{ch}}(u,t)$ of the underlying continuous-time Rayleigh fading channel according to the following relationship:

$$\mathbf{H}(m,k) = \int_{-\infty}^{+\infty} h_{\mathrm{c}}(mT + \epsilon - u)\mathbf{H}_{\mathrm{ch}}(u, kT)\,\mathrm{d}u, \tag{8.3}$$

where $h_{\mathrm{c}}(u)$ denotes the impulse response of the cascade of the transmit and the receive filter. Since the channel is assumed to be slowly fading, its associated coherence time is assumed to be much larger than the symbol period such that the frame duration, i.e., $N_{\mathrm{f}}T$, can be chosen to be considerably smaller than the coherence time. As a result, $\mathbf{H}(m,k)$ is quasi-static during the transmission of one frame, allowing to approximate $\mathbf{H}(m,k)$ by $\mathbf{H}_\kappa(m) = \mathbf{H}(m, \kappa N_{\mathrm{f}})$ during the κth frame, i.e., for $\kappa N_{\mathrm{f}} \leq k < (\kappa+1)N_{\mathrm{f}}$. Moreover, as the duration of the channel impulse response is essentially finite in practice, $L_{\mathrm{H}}^{(1)}$ and $L_{\mathrm{H}}^{(2)}$ are again defined such that $\mathbf{H}_\kappa(m) = \mathbf{0}\ \forall m \notin \{-L_{\mathrm{H}}^{(1)}, \cdots, L_{\mathrm{H}}^{(2)}\}$. The channel also adds a noise vector $\mathbf{n}(k)$, whose components are zero-mean Gaussian distributed variables that are temporally and mutually uncorrelated such that $\mathbb{E}\left[\mathbf{n}(k)\mathbf{n}(k-m)^H\right] = N_0\delta_m\mathbf{I}$. The channel input-output relationship is thus given by

$$\mathbf{y}(k) = \sum_{m=-L_{\mathrm{H}}^{(1)}}^{L_{\mathrm{H}}^{(2)}} \mathbf{H}_\kappa(m)\mathbf{x}(k-m) + \mathbf{n}(k). \tag{8.4}$$

All channel coefficients $\mathbf{H}_\kappa(m)$ are collected in a single matrix $\mathbf{H}_\kappa = [\mathbf{H}_\kappa(-L_{\mathrm{H}}^{(1)}) \cdots \mathbf{H}_\kappa(-L_{\mathrm{H}}^{(2)})]$. For notational convenience, the frame index κ is omitted in the following when the dependency on the frame index is evident.

The signal processing at the receiver is kept to the strict minimum. The signal $\mathbf{y}(k)$ is first multiplied by a factor α to compensate for the constrained transmit energy per symbol, yielding the decision variable $\mathbf{u}(k)$, i.e.,

$$\mathbf{u}(k) = \alpha \sum_{m=-L_{\mathrm{G}}^{(1)}}^{L_{\mathrm{G}}^{(2)}} \mathbf{G}(m)\mathbf{P}\mathbf{a}(k-m) + \alpha\mathbf{n}(k), \tag{8.5}$$

where $\mathbf{G}(m) = \left[\mathbf{H}(m - L_{\mathrm{P}}^{(1)}) \cdots \mathbf{H}(m + L_{\mathrm{P}}^{(2)})\right]$ and

$$\begin{cases} L_{\mathrm{G}}^{(1)} & = L_{\mathrm{H}}^{(1)} + L_{\mathrm{P}}^{(1)} \\ L_{\mathrm{G}}^{(2)} & = L_{\mathrm{H}}^{(2)} + L_{\mathrm{P}}^{(2)} \end{cases}. \tag{8.6}$$

Subsequently, the symbol-by-symbol detector retrieves the original data from $\mathbf{u}(k)$ similarly as in Chapter 7 by means of the relationship between the original data and the target response $\mathbf{u}_{\mathrm{T}}(k)$ defined in (7.10) and (7.11).

8.3 Robust equalizer design

This section first discusses the general optimization problem that must be solved in the statistically robust equalizer design in Subsection 8.3.1. Next, this general optimization procedure is applied to the communication system from Fig. 8.1 by opting for the MSE between $\mathbf{u}(k)$ and $\mathbf{u}_{\mathrm{T}}(k)$ as the objective function (Subsection 8.3.2), after which the mathematical details of this minimization are further examined in Subsection 8.3.3.

In the following, the channel vector $\mathbf{h}_\kappa$ is defined as the result of stacking the columns of $\mathbf{H}_\kappa$ into one single column vector with $N_{\mathrm{T}}N_{\mathrm{R}}L_{\mathrm{H}}$ components. Moreover, the estimate of $\mathbf{h}_\kappa$ is denoted as $\hat{\mathbf{h}}_\kappa$, while the vector containing the CSIT that is available for the design of the equalization parameters for frame κ is symbolized by the vector $\hat{\bar{\mathbf{h}}}_\kappa$.

8.3.1 General optimization problem

All equalization parameters are collected into the vector $\mathbf{z}$. Because only the CSIT $\hat{\bar{\mathbf{h}}}_\kappa$ is assumed to be available in the design of the equalization parameters associated with frame κ, $\mathbf{z}$ is a function of $\hat{\bar{\mathbf{h}}}_\kappa$, which is highlighted by the notation $\mathbf{z}(\hat{\bar{\mathbf{h}}}_\kappa)$.

To obtain an optimal $\mathbf{z}^\star(\hat{\bar{\mathbf{h}}}_\kappa)$ in frame κ, one must optimize an objective function f_0 that is possibly subject to one or more constraints, e.g., the energy constraint from (8.2). In general, this objective function depends on both the channel vector $\mathbf{h}_\kappa$ and the equalization parameters, leading to the notation $f_0(\mathbf{z}(\hat{\bar{\mathbf{h}}}_\kappa), \mathbf{h}_\kappa)$. In the case of perfect CSIT, $\hat{\bar{\mathbf{h}}}_\kappa$ is equal to $\mathbf{h}_\kappa$ such that for a given $\mathbf{h}_\kappa$, one can directly minimize $f_0(\mathbf{z}(\mathbf{h}_\kappa), \mathbf{h}_\kappa)$. However, as in practice the CSIT is imperfect, the robust equalizer design takes this imperfection into account by minimizing $\bar{f}_0$, which is defined as the expected value of f_0 with respect to joint distribution of $\mathbf{h}_\kappa$ and $\hat{\bar{\mathbf{h}}}_\kappa$. Consequently, the objective function in the case of imperfect CSIT is given by

$$\bar{f}_0 = \int\int f_{\mathbf{G}_{\mathrm{ch}},\hat{\bar{\mathbf{G}}}_{\mathrm{ch}}}(\mathbf{h}_\kappa, \hat{\bar{\mathbf{h}}}_\kappa) f_0(\mathbf{z}(\hat{\bar{\mathbf{h}}}_\kappa), \mathbf{h}_\kappa)\, \mathrm{d}\mathbf{h}_\kappa\, \mathrm{d}\hat{\bar{\mathbf{h}}}_\kappa, \tag{8.7}$$

where $f_{\mathbf{G}_{\mathrm{ch}},\hat{\bar{\mathbf{G}}}_{\mathrm{ch}}}(\mathbf{h}_\kappa, \hat{\bar{\mathbf{h}}}_\kappa)$ represents the joint PDF of the channel vector $\mathbf{h}_\kappa$ and the available CSIT $\hat{\bar{\mathbf{h}}}_\kappa$. In (8.7), $\mathbf{G}_{\mathrm{ch}}$ and $\hat{\bar{\mathbf{G}}}_{\mathrm{ch}}$ denote the random variables corresponding to the channel vector $\mathbf{h}_\kappa$ and the channel estimation vector $\hat{\bar{\mathbf{h}}}_\kappa$, respectively. By expressing the joint PDF $f_{\mathbf{G}_{\mathrm{ch}},\hat{\bar{\mathbf{G}}}_{\mathrm{ch}}}(\cdot)$ as the product of the conditional PDF $f_{\mathbf{G}_{\mathrm{ch}}|\hat{\bar{\mathbf{G}}}_{\mathrm{ch}}}(\cdot|\cdot)$ and the PDF $f_{\hat{\bar{\mathbf{G}}}_{\mathrm{ch}}}(\cdot)$, one can rewrite $\bar{f}_0$ as

$$\bar{f}_0 = \int f_{\hat{\bar{\mathbf{G}}}_{\mathrm{ch}}}(\hat{\bar{\mathbf{h}}}_\kappa) \bar{f}_{0|\hat{\bar{\mathbf{G}}}_{\mathrm{ch}}}(\mathbf{z}(\hat{\bar{\mathbf{h}}}_\kappa), \hat{\bar{\mathbf{h}}}_\kappa)\, \mathrm{d}\hat{\bar{\mathbf{h}}}_\kappa, \tag{8.8}$$

where the a posteriori expectation $\bar{f}_{0|\hat{\mathbf{G}}_{\mathrm{ch}}}(\mathbf{z}(\hat{\mathbf{h}}_\kappa), \hat{\mathbf{h}}_\kappa)$ of f_0 is given by

$$\bar{f}_{0|\hat{\mathbf{G}}_{\mathrm{ch}}}(\mathbf{z}(\hat{\mathbf{h}}_\kappa), \hat{\mathbf{h}}_\kappa) = \int f_{\mathbf{G}_{\mathrm{ch}}|\hat{\mathbf{G}}_{\mathrm{ch}}}(\mathbf{h}_\kappa|\hat{\mathbf{h}}_\kappa) f_0(\mathbf{z}(\hat{\mathbf{h}}_\kappa), \mathbf{h}_\kappa)\, \mathrm{d}\mathbf{h}_\kappa. \tag{8.9}$$

Because $f_{\hat{\mathbf{G}}_{\mathrm{ch}}}(\hat{\mathbf{h}}_\kappa) \geq 0$ for all $\hat{\mathbf{h}}_\kappa$, the optimal $\bar{f}_0$ can be determined by minimizing $\bar{f}_{0|\hat{\mathbf{G}}_{\mathrm{ch}}}(\mathbf{z}(\hat{\mathbf{h}}_\kappa), \hat{\mathbf{h}}_\kappa)$ for each $\hat{\mathbf{h}}_\kappa$. Consequently, the optimal equalization parameters $\mathbf{z}^\star(\hat{\mathbf{h}}_\kappa)$ for a given vector $\hat{\mathbf{h}}_\kappa$ result from solving the following optimization problem:

$$\mathbf{z}^\star(\hat{\mathbf{h}}_\kappa) = \arg\min_{\mathbf{z}(\hat{\mathbf{h}}_\kappa)} \bar{f}_{0|\hat{\mathbf{G}}_{\mathrm{ch}}}(\mathbf{z}(\hat{\mathbf{h}}_\kappa), \hat{\mathbf{h}}_\kappa), \tag{8.10}$$

possibly subject to one or more constraints.

In the case of perfect CSIT, we have $\hat{\mathbf{h}}_\kappa = \mathbf{h}_\kappa$, in which case (8.9) and (8.10) reduce to

$$\bar{f}_{0|\hat{\mathbf{G}}_{\mathrm{ch}}}(\mathbf{h}_\kappa) = f_0(\mathbf{z}(\mathbf{h}_\kappa), \mathbf{h}_\kappa) \tag{8.11}$$

and

$$\mathbf{z}^\star(\mathbf{h}_\kappa) = \arg\min_{\mathbf{z}(\mathbf{h}_\kappa)} f_0(\mathbf{z}(\mathbf{h}_\kappa), \mathbf{h}_\kappa) \tag{8.12}$$

The resulting equalizer coefficients are the same as those obtained from the optimization (3.1), when all equalizer coefficients are adjustable in the latter optimization, i.e., $\mathbf{y} = \{\emptyset\}$.

8.3.2 MMSE optimization problem

In the MMSE optimization problem, the objective function $f_0(\mathbf{z}(\hat{\mathbf{h}}_\kappa), \mathbf{h}_\kappa)$ equals the MSE between the decision variable $\mathbf{u}(k)$ and the target response $\mathbf{u}_{\mathrm{T}}(k)$. This MSE is denoted by $\mathrm{MSE}_{\mathbf{h}_\kappa}$ and, for a specific realization of $\mathbf{h}_\kappa$, $\mathrm{MSE}_{\mathbf{h}_\kappa}$ is defined as

$$\mathrm{MSE}_{\mathbf{h}_\kappa} = \frac{1}{N_{\mathrm{R}}\sigma_{\mathrm{a}}^2}\mathbb{E}\left[\|\mathbf{u}(k) - \mathbf{u}_{\mathrm{T}}(k)\|^2\right]. \tag{8.13}$$

$$= \frac{1}{N_{\mathrm{R}}}\mathrm{Tr}\left[\alpha\mathbf{P}^H\mathbf{G}_\kappa^H\mathbf{G}_\kappa\mathbf{P} + \alpha^2\frac{N_0}{\sigma_{\mathrm{a}}^2}\mathbf{I}_{N_{\mathrm{R}}} + \mathbf{T}^H\mathbf{T} - \alpha\mathbf{T}^H\mathbf{G}_{\mathrm{T},\kappa}\mathbf{P} - \alpha\mathbf{P}^H\mathbf{G}_{\mathrm{T},\kappa}^H\mathbf{T}\right] \tag{8.14}$$

with

$$\mathbf{G}_\kappa = \left[\mathbf{G}_\kappa^H(-L_{\mathrm{G}}^{(1)}) \cdots \mathbf{G}_\kappa^H(L_{\mathrm{G}}^{(2)})\right]^H \tag{8.15}$$

and

$$\mathbf{G}_{\mathrm{T},\kappa} = \left[\mathbf{G}_\kappa^H(0) \cdots \mathbf{G}_\kappa^H(L_{\mathrm{T}})\right]^H. \tag{8.16}$$

Moreover, the matrix $\mathbf{T}$ is obtained in this chapter by stacking all matrices $\mathbf{T}(m)$ into a $(L_{\mathrm{T}}+1)N_{\mathrm{R}} \times N_{\mathrm{R}}$ stacked matrix, i.e., $\mathbf{T} = \left[\mathbf{T}^H(0) \cdots \mathbf{T}^H(L_{\mathrm{T}})\right]^H$.

When the available CSIT is imperfect, Section 8.3.1 states that the robust design of the equalization parameters takes $\overline{\mathrm{MSE}}_{\hat{\hat{\mathbf{h}}}_\kappa}$ as the objective function. This $\overline{\mathrm{MSE}}_{\hat{\hat{\mathbf{h}}}_\kappa}$ is defined as the a posteriori expectation of $\mathrm{MSE}_{\mathbf{h}_\kappa}$, i.e.,

$$\overline{\mathrm{MSE}}_{\hat{\hat{\mathbf{h}}}_\kappa} = \int f_{\mathbf{G}_{\mathrm{ch}}|\hat{\hat{\mathbf{G}}}_{\mathrm{ch}}}(\mathbf{h}_\kappa|\hat{\hat{\mathbf{h}}}_\kappa)\mathrm{MSE}_{\mathbf{h}_\kappa}\ \mathrm{d}\mathbf{h}_\kappa \tag{8.17}$$

$$= \frac{1}{N_{\mathrm{R}}}\mathrm{Tr}\Big[\alpha^2\mathbf{P}^H\mathbf{E}_{\mathrm{GG}}(\hat{\hat{\mathbf{h}}}_\kappa)\mathbf{P} + \alpha^2\frac{N_0}{\sigma_{\mathrm{a}}^2}\mathbf{I}_{N_{\mathrm{R}}} + \mathbf{T}^H\mathbf{T} - \alpha\mathbf{T}^H\mathbf{E}_{\mathrm{GT}}(\hat{\hat{\mathbf{h}}}_\kappa)\mathbf{P} - \alpha\mathbf{P}^H\mathbf{E}_{\mathrm{GT}}^H(\hat{\hat{\mathbf{h}}}_\kappa)\mathbf{T}\Big], \tag{8.18}$$

where

$$\mathbf{E}_{\mathrm{GG}}(\hat{\hat{\mathbf{h}}}_\kappa) = \int f_{\mathbf{G}_{\mathrm{ch}}|\hat{\hat{\mathbf{G}}}_{\mathrm{ch}}}(\mathbf{h}_\kappa|\hat{\hat{\mathbf{h}}}_\kappa)\mathbf{G}_\kappa^H\mathbf{G}_\kappa\ \mathrm{d}\mathbf{h}_\kappa \tag{8.19}$$

and

$$\mathbf{E}_{\mathrm{GT}}(\hat{\hat{\mathbf{h}}}_\kappa) = \int f_{\mathbf{G}_{\mathrm{ch}}|\hat{\hat{\mathbf{G}}}_{\mathrm{ch}}}(\mathbf{h}_\kappa|\hat{\hat{\mathbf{h}}}_\kappa)\mathbf{G}_{\mathrm{T},\kappa}\ \mathrm{d}\mathbf{h}_\kappa. \tag{8.20}$$

Consequently, the robust equalization coefficients in frame κ for a given $\hat{\hat{\mathbf{h}}}_\kappa$ are computed by solving the following optimization problem:

$$(\mathbf{P}_\kappa^\star, \alpha_\kappa^\star, \mathbf{T}_\kappa^\star) = \arg\min_{\mathbf{P},\alpha,\mathbf{T}} \overline{\mathrm{MSE}}_{\hat{\hat{\mathbf{h}}}_\kappa} \quad \text{subject to } \sigma_{\mathrm{a}}^2\mathrm{Tr}\left[\mathbf{P}^H\mathbf{R}_{\mathrm{TX}}\mathbf{P}\right] \leq N_{\mathrm{R}}E_{\mathrm{TX}}. \tag{8.21}$$

This chapter considers three particular types of CSIT, which differ in the available channel estimates at the transmitter: (C1) both the current estimate $\hat{\mathbf{h}}_\kappa$ and the past $\mathcal{K}$ estimates, i.e., $\hat{\mathbf{h}}_{\kappa-1}, \cdots, \hat{\mathbf{h}}_{\kappa-\mathcal{K}}$, are available; (C2) only the current estimate is available; and (C3) only the past $\mathcal{K}$ estimates are available. Hence, the vector $\hat{\hat{\mathbf{h}}}_\kappa$ depends on the considered type of CSIT, according to

$$\hat{\hat{\mathbf{h}}}_\kappa = \begin{cases} [\hat{\mathbf{h}}_\kappa^H \cdots \hat{\mathbf{h}}_{\kappa-\mathcal{K}}^H]^H & \text{C1} \\ \hat{\mathbf{h}}_\kappa & \text{C2} \\ [\hat{\mathbf{h}}_{\kappa-1}^H \cdots \hat{\mathbf{h}}_{\kappa-\mathcal{K}}^H]^H & \text{C3} \end{cases}. \tag{8.22}$$

For each type of available CSIT, Appendix 11.11 explains how to analytically obtain the a posteriori expectations $\mathbf{E}_{\mathrm{GG}}(\hat{\hat{\mathbf{h}}}_\kappa)$ and $\mathbf{E}_{\mathrm{GT}}(\hat{\hat{\mathbf{h}}}_\kappa)$, defined in respectively (8.19) and (8.20), in the case of MMSE channel estimation from pilot symbols.

8.3.3 Calculation of the equalization parameters

To solve optimization problem (8.21), first the optimal filter $\mathbf{P}^\star$ and the optimal scaling factor $\alpha^\star$ are expressed as a function of $\mathbf{T}$. To this end, $\overline{\mathrm{MSE}}_{\hat{\hat{\mathbf{h}}}_\kappa}$ from

(8.18) is minimized with respect to $\mathbf{P}$ and α for given $\mathbf{T}$ subject to the energy constraint. This optimization problem is noteworthy a particular case of the general optimization problem described in Appendix 11.2. More precisely, the matrices $\mathbf{G}$, $\mathbf{A}_1$, $\mathbf{A}_2$, and $\mathbf{A}_3$ from this appendix correspond to the matrices $\mathbf{E}_{\mathrm{GG}}(\hat{\hat{\mathbf{h}}}_\kappa)$, $\mathbf{T}^H\mathbf{E}_{\mathrm{GT}}(\hat{\hat{\mathbf{h}}}_\kappa)$, $\mathbf{T}^H\mathbf{T}$, and $N_0\mathbf{I}_{N_\mathrm{R}}$, respectively. Consequently, the optimal $\mathbf{P}^\star$ and $\alpha^\star$ can be expressed as

$$\mathbf{P}_\kappa^\star = \frac{1}{\alpha_\kappa^\star}\mathbf{D}^{-1}\mathbf{E}_{\mathrm{GT}}^H(\hat{\hat{\mathbf{h}}}_\kappa)\mathbf{T} \tag{8.23}$$

and

$$\alpha_\kappa^\star = \sqrt{\frac{\sigma_\mathrm{a}^2}{N_\mathrm{R}E_\mathrm{TX}}\mathrm{Tr}\left(\mathbf{T}^H\mathbf{E}_{\mathrm{GT}}\left(\hat{\hat{\mathbf{h}}}_\kappa\right)\mathbf{D}^{-1}\mathbf{R}_\mathrm{TX}\mathbf{D}^{-1}\mathbf{E}_{\mathrm{GT}}^H(\hat{\hat{\mathbf{h}}}_\kappa)\mathbf{T}\right)} \tag{8.24}$$

with $\mathbf{D} = \mathbf{E}_{\mathrm{GG}}\left(\hat{\hat{\mathbf{h}}}_\kappa\right) + \frac{N_0}{E_\mathrm{TX}}\mathbf{R}_\mathrm{TX}$. After plugging (8.23) and (8.24) into (8.18), the $\overline{\mathrm{MSE}}_{\hat{\hat{\mathbf{h}}}_\kappa}$ optimized over $\mathbf{P}$ and α, i.e., $\overline{\mathrm{MSE}}_{\hat{\hat{\mathbf{h}}}_\kappa,\mathbf{P}^\star,\alpha^\star}$ can be simplified to

$$\overline{\mathrm{MSE}}_{\hat{\hat{\mathbf{h}}}_\kappa,\mathbf{P}^\star,\alpha^\star} = \frac{1}{N_\mathrm{R}}\mathrm{Tr}\left(\mathbf{T}^H\mathbf{G}\mathbf{T}\right) \tag{8.25}$$

with $\mathbf{G} = \mathbf{I} - \mathbf{E}_{\mathrm{GT}}\left(\hat{\hat{\mathbf{h}}}_\kappa\right)\mathbf{D}^{-1}\mathbf{E}_{\mathrm{GT}}^H\left(\hat{\hat{\mathbf{h}}}_\kappa\right)$. Next, $\overline{\mathrm{MSE}}_{\hat{\hat{\mathbf{h}}}_\kappa,\mathbf{P}^\star,\alpha^\star}$ from (8.25) must be optimized with respect to the TIR $\mathbf{T}$. This optimization problem is, however, identical to optimizing $\mathrm{MSE}_{\mathbf{W}^\star,\mathbf{B}^\star}$ from (7.23) such that the optimization algorithms presented in Section 7.2.2 can be employed here as well.

8.4 BER expression

The goal of this section is to derive an expression for the BER corresponding to the system model of Fig. 8.1 with Gray-mapped M-QAM transmission. For this purpose, we define, analogously to Section 7.3, the translated version $\mathbf{v}(k)$ of the decision variable $\mathbf{u}(k)$ as follows:

$$\mathbf{v}(k) = \frac{\mathbf{u}(k)}{2\Delta} + \mathbf{c}_\mathrm{off}, \tag{8.26}$$

where $\mathbf{u}(k)$ is now given by (8.5), while $\mathbf{c}_\mathrm{off}$ is defined in (7.11). Just as in Section 7.3, $\mathbf{v}(k)$ can be decomposed as

$$\mathbf{v}(k) = \sum_{m=0}^{L_\mathrm{T}} \mathbf{T}(m)\mathbf{b}(k-m) + \mathbf{isi}(k) + \mathbf{n}_\mathrm{v}(k), \tag{8.27}$$

where now $\mathbf{n}_\mathrm{v}(k) = \frac{\alpha\mathbf{n}(k)}{2\Delta}$ and $\mathbf{isi}(k) = \sum_{m\in\Phi}\mathbf{E}(m)\mathbf{a}(k-m)$ with

$$2\Delta\mathbf{E}(m) = \begin{cases} \alpha\mathbf{G}(m)\mathbf{P} - \mathbf{T}(m) & m \in \Phi_\mathbf{T} \\ \alpha\mathbf{G}(m)\mathbf{P} & m \in \Phi \setminus \Phi_\mathbf{T} \end{cases}. \tag{8.28}$$

Because the decompositions of $\mathbf{v}(k)$ in (7.46) and (8.27) are structurally the same, the derivation of the BER expression is completely identical to the derivation of the BER expression in Section 7.3 such that expression (7.52) for $\mathrm{BER}^{(l)}$ holds here as well, but with the above definitions of $\mathbf{n}_{\mathrm{v}}(k)$ and $\mathbf{isi}(k)$.

8.5 Numerical results and discussion

To investigate the performance of the proposed robust design of the general MIMO ST PRS precoder and the accompanying linear equalizer, this section presents numerical results pertaining to the transmission of precoded 4-QAM symbols over a frequency-selective Rayleigh fading channel at a symbol rate $1/T = 20\,\mathrm{MHz}$. In all results, the transmitter is assumed to consist of (i) a ST PRS precoder with $L_{\mathrm{T}} = 2$ feedback taps, (ii) a 21-tap linear equalizer ($L_{\mathrm{P}}^{(1)} = L_{\mathrm{P}}^{(2)} = 10$), and (iii) $N_{\mathrm{T}} = N_{\mathrm{R}} = 3$ antennas. To determine the optimal TIR $\mathbf{T}$, algorithm A3 from Section 7.2.2.3 is employed, because this algorithm yields the best performance. The considered frequency-selective Rayleigh fading channel is an example of the multipath wideband channel from Section 2.3. Here, the power delay profile $p_d(u)$ is assumed to be exponentially decreasing, i.e., $p_d(u) = (1/T)\exp(-u/T)$, whereas the Doppler spectrum $p_D(\nu)$ is selected as a zero-mean Gaussian with a standard deviation of $f_{\mathrm{D}} = 50\,\mathrm{Hz}$. Taking symbol blocks of $N_{\mathrm{f}} = 10^4$ symbols, one obtains $N_{\mathrm{f}} T f_{\mathrm{D}} = 0.025 \ll 1$, indicating that the channel variations over a symbol block are indeed small. The relation given in (8.3) between $\mathbf{H}_{\mathrm{ch}}(u,t)$ and $\mathbf{H}(m,k)$ and the property from (2.6) allow to numerically evaluate the covariance between $(\mathbf{H}_{\kappa_1}(m_1))_{l_1,l_2}$ and $(\mathbf{H}_{\kappa_2}(m_2))_{l_1,l_2}$ for the relevant values of m_1, m_2, and $\kappa_1 - \kappa_2$, for example in (11.96) of Appendix 11.11; these covariances do not depend on (l_1, l_2). Consequently, Moreover, channel estimation is accomplished by means of Zadoff-Chu (ZC) sequences, with $\bar{E}_{\mathrm{p}} = 10E_{\mathrm{TX}}$ or $\bar{E}_{\mathrm{p}} = 100E_{\mathrm{TX}}$ (see Appendix 11.12), where $\bar{E}_{\mathrm{p}}$ denotes the useful portion of the energy of the pilot symbols.

Figs. 8.3 - 8.6 depict the MSE and the BER performance, both averaged over 2000 channel realizations, as a function of SNR. More precisely, Figs. 8.3 and 8.4 consider the cases of PRS with $\bar{E}_{\mathrm{p}} = 10E_{\mathrm{TX}}$ and $\bar{E}_{\mathrm{p}} = 100E_{\mathrm{TX}}$, respectively, whereas Figs. 8.5 and 8.6 examine the performance in the case of FRS with $\bar{E}_{\mathrm{p}} = 10E_{\mathrm{TX}}$ and $\bar{E}_{\mathrm{p}} = 100E_{\mathrm{TX}}$, respectively. Similar to the chapters above, the SNR is again defined as the ratio $\frac{E_{\mathrm{TX}}}{\log_2(M)N_0}$. In all figures, the performances resulting from the robust equalization designs for the CSIT types C1, C2, and C3 (with $\mathcal{K} = 2$) are compared to the following cases:

- Perfect CSIT, where the actual channel $\mathbf{h}_\kappa$ is available. This case obviously outperforms all other scenarios.

- Delayed CSIT, where the $\mathcal{K}$ previous channel realizations are perfectly known at the transmitter. These $\mathcal{K}$ channel states are collected in the vector $\bar{\mathbf{h}}_{\kappa,\mathcal{K}} = \left[\mathbf{h}_{\kappa-1}^H \cdots \mathbf{h}_{\kappa-\mathcal{K}}^H\right]^H$. To determine the optimal equalizer

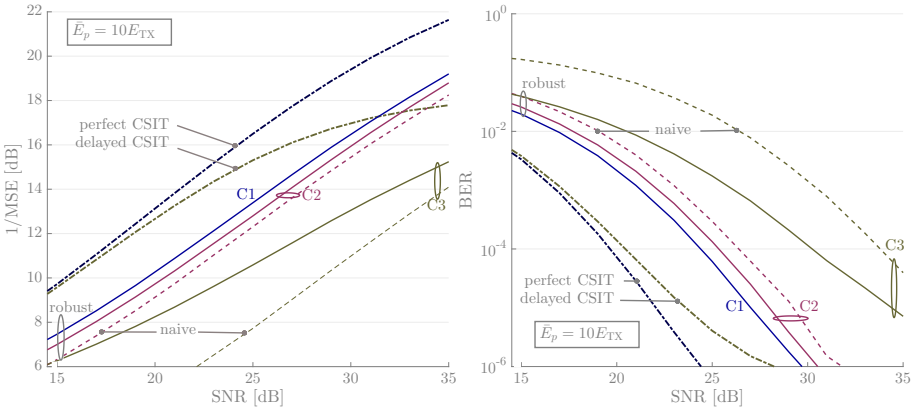

Figure 8.3: MSE (left plot) and BER (right plot) performance as a function of SNR in the case of ST PRS with $\bar{E}_{\mathrm{p}} = 10E_{\mathrm{TX}}$. The CSIT types C1, C2, and C3 are compared to the cases of perfect CSIT and delayed CSIT ($\mathcal{K} = 2$) and to the naive approach that ignores channel estimation errors.

and TIR, the a posteriori expectation $\mathbb{E}\left[\cdot|\hat{\bar{\mathbf{h}}}_\kappa\right]$ in (8.19) and (8.20) must be replaced by the a posteriori expectation $\mathbb{E}\left[\cdot|\bar{\mathbf{h}}_{\kappa,\mathcal{K}}\right]$, such that $\overline{\mathrm{MSE}}_{\hat{\bar{\mathbf{h}}}_\kappa}$ defined in (8.18) becomes a function of $\bar{\mathbf{h}}_{\kappa,\mathcal{K}}$ instead of $\hat{\bar{\mathbf{h}}}_\kappa$, which is emphasized by the notation $\overline{\mathrm{MSE}}_{\bar{\mathbf{h}}_{\kappa,\mathcal{K}}}$. The associated conditional PDF can directly be derived from the channel statistics. For CSIT type C3, the performance limit for E_{p} approaching infinity equals the performance achieved for delayed CSIT.

- The naive approach, in which one could naively derive the optimal equalization parameters by ignoring the channel state estimation errors such that $\hat{\mathbf{h}}_\kappa$ for CSIT types C1 and C2 and $\hat{\bar{\mathbf{h}}}_{\kappa,\mathcal{K}} = [\hat{\mathbf{h}}_{\kappa-1}^H \cdots \hat{\mathbf{h}}_{\kappa-\mathcal{K}}^H]^H$ for CSIT type C3 are assumed to be perfect. As a consequence, $(\mathbf{P}_\kappa^\star, \alpha_\kappa^\star, \mathbf{T}_\kappa^\star)$ are obtained in this naive approach by minimizing $\mathrm{MSE}_{\mathbf{h}_\kappa}$ but with $\mathbf{h}_\kappa$ replaced by the estimate $\hat{\mathbf{h}}_\kappa$ (types C1 and C2) and by minimizing $\overline{\mathrm{MSE}}_{\bar{\mathbf{h}}_{\kappa,\mathcal{K}}}$ but with $\bar{\mathbf{h}}_{\kappa,\mathcal{K}}$ replaced by the delayed estimates $\hat{\bar{\mathbf{h}}}_{\kappa,\mathcal{K}}$ (type C3). By design, the naive approach is inferior to the robust design, for all three types of CSIT.

Just as in Chapter 7, an especially noteworthy observation is the significant performance gain of PRS compared to FRS. For the cases with perfect CSIT and delayed CSIT, PRS indeed achieves not only a considerably lower MSE than FRS in the high SNR region, but also significantly lowers the BER floor (of the order of 10^{-5} for FRS) to (far) below 10^{-6}, demonstrating the potential of ST PRS. Likewise, the robust design in the case of PRS not only outperforms the robust design in FRS for a given type of CSIT, but also achieves

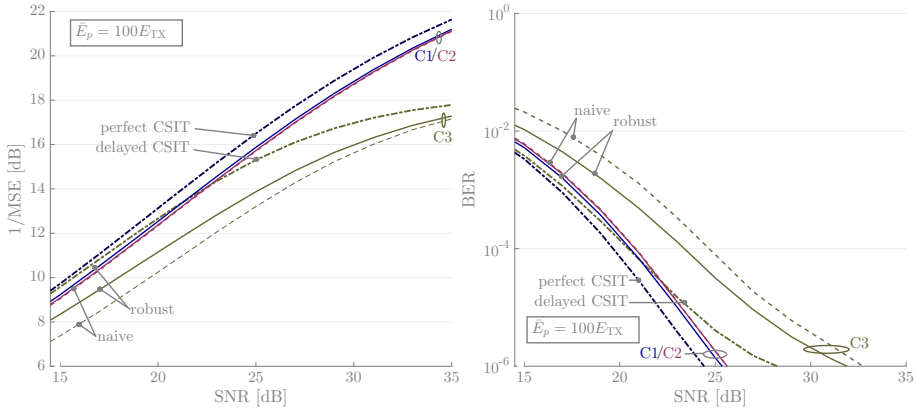

Figure 8.4: MSE (left plot) and BER (right plot) performance as a function of SNR in the case of ST PRS with $\bar{E}_{\mathrm{p}} = 100E_{\mathrm{TX}}$. The same scenarios as in Fig. 8.3 are compared.

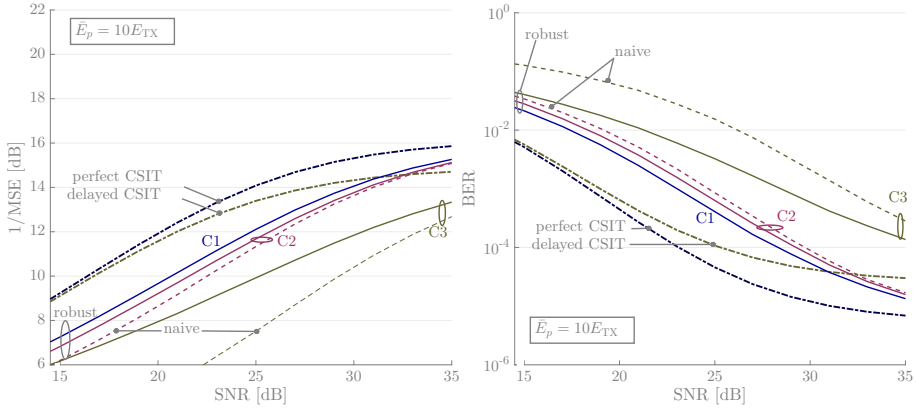

Figure 8.5: MSE (left plot) and BER (right plot) performance as a function of SNR in the case of FRS with $\bar{E}_{\mathrm{p}} = 10E_{\mathrm{TX}}$. The same scenarios as in Fig. 8.3 are compared.

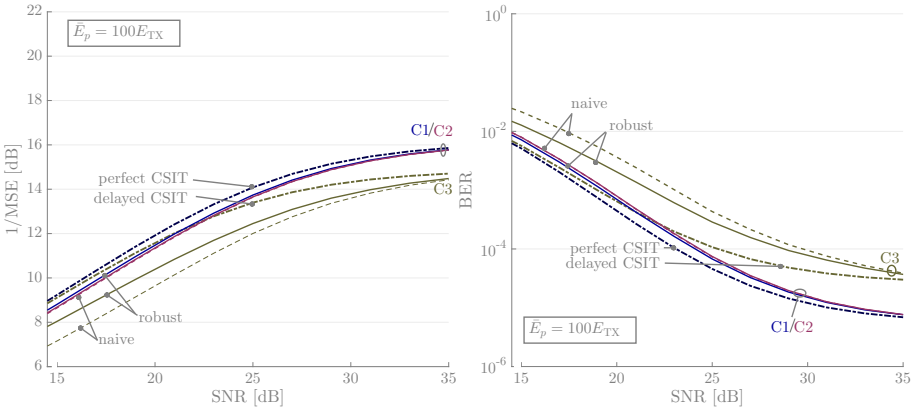

Figure 8.6: MSE (left plot) and BER (right plot) performance as a function of SNR in the case of FRS with $\bar{E}_{\mathrm{p}} = 100E_{\mathrm{TX}}$. The same scenarios as in Fig. 8.3 are compared.

(considerably) lower BER values (at high SNR) than FRS with perfect CSIT, even for the rather poor estimation quality of $\bar{E}_{\mathrm{p}} = 10E_{\mathrm{TX}}$. This observation thus confirms that a suitable TIR $\mathbf{T}$ and a suitable linear filter $\mathbf{P}$ are obtained by all robust PRS configurations.

Not surprisingly, the more channel estimates that are available at the TX, the better the performance of the robust configurations becomes, which is illustrated in all figures by the superior performance of C1 and C2 compared to C2 and C3, respectively. When the estimation quality improves, e.g., $\bar{E}_{\mathrm{p}} = 100E_{\mathrm{TX}}$ in Figs. 8.4 and 8.6, the performance gap between robust C1 and robust C2 diminishes and both configurations perform almost as well as in the case with perfect CSIT, because an (excellent) estimate of the current channel is available. Although the MSE and the BER of C3 reduce with increasing $\bar{E}_{\mathrm{p}}$, a performance loss compared to C1/C2 is notable for both PRS and FRS. Moreover, a similar observation holds when comparing perfect CSIT with delayed CSIT (which are the performance limits for C1/C2 and C2 when $\bar{E}_{\mathrm{p}}$ grows infinitely large). This performance gap between C1/C2 and C3 is explained by the rather large uncertainty about the current channel given the estimates of only $\mathcal{K} = 2$ prior channel realizations, as this gap is confirmed to disappear for increasing $\mathcal{K}$ in Fig. 8.7. Indeed, this figure shows the MSE performance as a function of SNR in the case of configuration C3. In total, three values of $\mathcal{K}$, i.e., $\mathcal{K} \in \{1, 2, 4\}$, and two values of $\bar{E}_{\mathrm{p}}$, i.e., $\bar{E}_{\mathrm{p}} \in \{10E_{\mathrm{TX}}, 100E_{\mathrm{TX}}\}$, are considered. Moreover, the cases with perfect CSIT and with delayed CSIT are added as a reference. This figure demonstrates not only that the difference between perfect CSIT and delayed CSIT diminishes for growing $\mathcal{K}$ and even almost vanishes for $\mathcal{K} = 4$, but also that the larger $\mathcal{K}$, the larger $\bar{E}_{\mathrm{p}}$ must be to approximate the performance limit in the case of configuration C3.

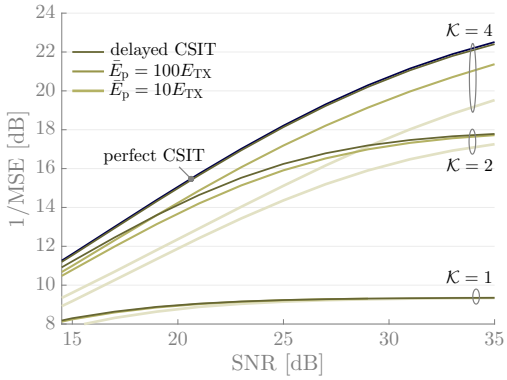

Figure 8.7: MSE performance as a function of SNR in the case of the robust configuration C3 for various $\mathcal{K}$ and $\bar{E}_\mathrm{p}$. As a reference the case when the channel is perfectly known is also incorporated. For larger $\mathcal{K}$, the performance gap between perfect CSIT and delayed CSIT reduces, but larger $\bar{E}_\mathrm{p}$ is required to reach the performance level of delayed CSIT in the case of the robust configuration C3.

Comparing the results for PRS (Figs. 8.3 and 8.4) with the results for FRS (Figs. 8.5 and 8.6) reveals that the performance difference between the robust configurations (C1/C2 and C3) and their limits for infinite $\bar{E}_\mathrm{p}$, i.e., perfect CSIT and delayed CSIT, is larger in the case of PRS than in the case of FRS. This is caused by the additional optimization over the TIR in PRS. Indeed, whereas the TIR for FRS is the same for all strategies, the robust TIR in the case of PRS is not necessarily identical to the TIR derived with perfect CSIT or delayed CSIT. These TIR differences could induce a considerable difference in both MSE and BER, since both the real and the imaginary part of the TIR are not continuous as the TIR assumes integer values only.

In the naive approach, the equalization parameters are computed with the assumption that the current estimate $\hat{\mathbf{h}}_\kappa$ (C1/C2) or the previous estimates $\hat{\bar{\mathbf{h}}}_{\kappa,\mathcal{K}}$ are without estimation error. Figs. 8.3 - 8.6 clearly demonstrate that the naive approach is inferior to the robust approach. The difference between the robust and the naive approach is particularly prominent when the channel estimates are rather poor, whereas the difference between the two approaches reduces with increasing $\bar{E}_\mathrm{p}$. Hence, the robust design is preferable, especially since the computational complexity of both approaches is comparable, as this complexity is dominated by the computation of $\mathbf{T}$ and not by the evaluation of the expectations in (8.19) and (8.20).

The numerical results above clearly indicate that better estimation quality, i.e., larger $\bar{E}_\mathrm{p}$, results in better performance of the robust and the naive design. However, the larger $\bar{E}_\mathrm{p}$, the more resources, i.e., bandwidth and/or energy, that must be allocated to the pilot symbols, which in practice often comes at the

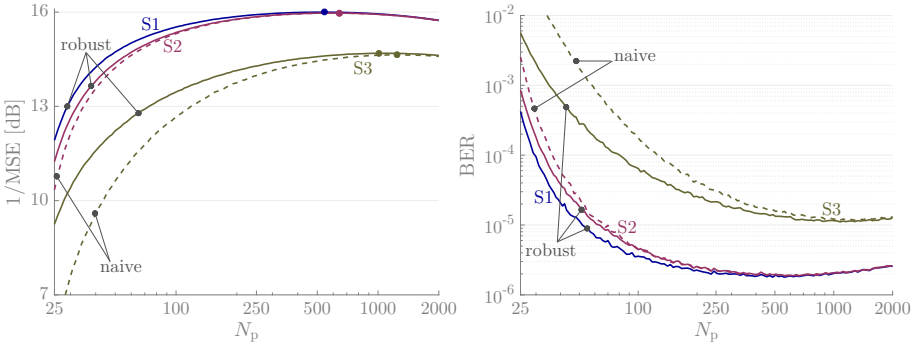

Figure 8.8: MSE (left plot) and BER (right plot) performance as a function of N_p in the case of PRS for $\mathrm{SNR_f} = 25\,\mathrm{dB}$. The MSE for optimal N_p is indicated with a small circle.

cost of a decrease in the available resources for the data symbols. Therefore, an additional constraint is defined here, imposing that the total energy of a frame must be constant. Consequently, an optimum division of this frame energy between the pilot symbols and the data symbols must be determined. Indeed, when $\bar{E}_\mathrm{p}$ is too low, the quality of the channel estimate is not sufficient, whereas when $\bar{E}_\mathrm{p}$ is too high, the energy available for data transmission decreases, inducing larger error performance. To investigate this trade-off in more detail, the energy per pilot symbol and the energy per data symbol are, for simplicity, assumed to be equal to E_TX. Hence, the total energy E_f of one frame is equal to $(N_\mathrm{p} + N_\mathrm{d})E_\mathrm{TX}$, whereas $\bar{E}_\mathrm{p} = (N_\mathrm{p} - L_\mathrm{H} + 1)\,E_\mathrm{TX}$. The effective energy per data symbol is then given by the ratio $\frac{N_\mathrm{d}}{N_\mathrm{p}+N_\mathrm{d}}E_\mathrm{TX}$, based on which the $\mathrm{SNR_f}$ is defined as

$$\mathrm{SNR_f} = \frac{E_\mathrm{TX}}{\log_2(M)N_0}\left(1 + \frac{N_\mathrm{p}}{N_\mathrm{d}}\right). \tag{8.29}$$

$$= \frac{E_f}{N_\mathrm{d}\log_2(M)N_0}. \tag{8.30}$$

For a given value of N_d, M, and N_0, keeping the energy E_f fixed is equivalent with keeping $\mathrm{SNR_f}$ fixed. To visualize the trade-off between the estimation quality and the data symbol energy, Fig. 8.8 displays the MSE and the BER performance of all configurations for $N_\mathrm{p} = 25$ up to $N_\mathrm{p} = 2000$ for both the robust and the naive approach, while the $\mathrm{SNR_f}$ is kept fixed at 25 dB and $N_\mathrm{d} = 10^4$. The following observations hold:

- In terms of both MSE and BER, the optimal value $N_\mathrm{p}^\star$ is reached around $N_\mathrm{p} = 600$ for configurations C1 and C2, whereas the optimal $N_\mathrm{p}^\star$ is approximately 1.7 times larger for configuration C3. One possible reason for this larger optimal $N_\mathrm{p}^\star$ is that unlike configurations C1 and C2, no

Table 8.1: Overview of the optimal $N_{\mathrm{p}}^{\star}$ and the associated ϵ_d for various N_{d}.

Configuration	$N_{\mathrm{d}} = 10000$	$N_{\mathrm{d}} = 1000$	$N_{\mathrm{d}} = 500$
robust C1	541 / 0.95	173 / 0.83	121 / 0.77
robust C2	643 / 0.94	191 / 0.82	143 / 0.74
robust C3	1007 / 0.91	309 / 0.75	231 / 0.66

estimate of the current channel state is available in configuration C3 such that a prediction of the current channel state based on estimates of the previous states is required. Apparently, to make this prediction reliable, more pilot symbols are needed than when an estimate of the current channel is available.

- Just as above, one intuitively expects that the performance difference between the robust and the naive approach diminishes for increasing N_{p} as the estimates are more reliable for larger N_{p}. This expectation is met in Fig. 8.8.

- The slope of the performance increase at low N_{p} is much steeper than the slope of the performance decrease at large N_{p}, which can mainly be contributed to the fact that $\bar{E}_{\mathrm{p}}$ is directly related to N_{p}, whereas the energy per data bit linearly decrease with N_{p} but at a much slower slope given by $-N_{\mathrm{p}}/N_{\mathrm{d}}$.

- Additional simulations, whose results are not shown here, reveal that the optimal value $N_{\mathrm{p}}^{\star}$ is relatively independent of the precise value of $\mathrm{SNR}_{\mathrm{f}}$.

- At optimal $N_{\mathrm{p}}^{\star}$, the performance difference between the robust and the naive approach is nearly invisible in Fig. 8.8. In this figure, the block length N_{d} is relatively large such that the optimal values $N_{\mathrm{p}}^{\star}$ still results in a acceptable ratio ϵ_d, which is defined as the fraction of one frame that is dedicated to the transmission of data symbols, i.e., $\epsilon_d = N_{\mathrm{d}}/N_{\mathrm{f}}$. For smaller N_{d}, the optimal $N_{\mathrm{p}}^{\star}$ decreases, but not linearly with N_{d} such that the ratio ϵ_d decreases and the throughput thus reduces. To illustrate this reasoning, Table 8.1 lists the optimal $N_{\mathrm{p}}^{\star}$ and the associated ϵ_d for various N_{d} for all configurations. When for small N_{d} the throughput becomes too small, one must opt for an N_{p} that is significantly smaller than the optimal $N_{\mathrm{p}}^{\star}$. For these smaller N_{p}, the performance difference between the robust and the naive design is more prominent, making the former clearly preferable to the latter.

8.6 Conclusions

This chapter applies the concept of statistically robust equalization to ST PRS over a frequency-selective and time-variant MIMO channel. More precisely, the transmitter designs both the TIR associated with PRS and the linear equalizer $\mathbf{P}$ based solely on the available imperfect CSIT, which consists of noisy estimates of the MIMO channel of the current and/or previous frames. The robustness in the design is accomplished by statistically modeling the channel estimation error and subsequently minimizing the average MSE between the decision variable and the target response, where the average is with respect to the joint PDF of the actual channel realization and the available CSIT. In total, three types of CSIT are investigated: (i) the estimates of the current channel state and $\mathcal{K}$ previous channel states are available in type C1; (ii) only the current channel state estimate is known in type C2; and (iii) the robust design is based on only the channel estimates of the $\mathcal{K}$ previous channel states in type C3. Numerical results confirm that the proposed robust PRS significantly improves the performance compared to the naive approach that ignores channel estimation errors, when the quality of the available CSIT is rather poor. As a result, the robust design is preferable, as the computational complexity of the robust and the naive approaches are similar. Compared to FRS, PRS yields a decrease in both MSE and BER for both the robust design and the design with perfect CSIT. Moreover, the robust PRS with poor estimation quality is even capable of outperforming FRS with perfect CSIT. Finally, a trade-off between the estimation quality on the one side and the energy per data symbol and/or the throughput on the other side has to be faced when the resources for one frame, e.g., E_f, is fixed.

9

Stochastic channel: partial-response signaling

This chapter focuses on the design and the performance of the general ST PRS precoder presented in Chapter 7 in the context of a stochastic channel suffering from channel variability. Moreover, the PRS equalization scheme investigated in Chapter 7 is expanded in this chapter with a linear pre-equalizer at the transmitter.

This chapter is organized as follows. Firstly, the impact of this additional linear filter on the system's equations is discussed in Section 9.1. Secondly, the main topic of Section 9.2 is the design of the equalization parameters according to the MMSE criterion. The choice for the MSE as the objective function is again justified by its combination of decent performance with mathematical simplicity. As the channel is assumed to be stochastic, the optimization procedure from Chapter 4 is applied to the considered equalization scheme. In total, three equalization strategies are proposed: the adjustable (Subsection 9.2.1), the fixed (Subsection 9.2.2), and the hybrid (Subsection 9.2.3) equalization strategy. The adjustable strategy aims for optimal performance by considering only adjustable equalization parameters, whereas the fixed strategy minimizes the complexity as its equalization parameters are fixed. A performance-complexity trade-off is inherent to the hybrid strategy, as the equalization parameters associated with the receiver are adjustable, and those at the transmitter are fixed. Thirdly, the derivation of the BER expression for the expanded ST PRS equalization scheme follows the same reasoning as in Section 7.3. Still, some minor differences can be distinguished, which are listed in Section 9.3. Fourthly, Section 9.4 presents the performance achieved by the MMSE design

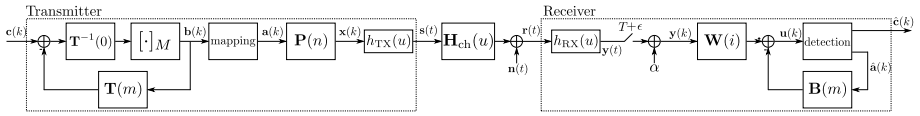

Figure 9.1: System model of the equalization scheme consisting of a ST PRS precoder and a linear equalizer at the transmitter and a nonlinear DFE at the receiver.

in the case of the chip-to-chip interconnect from Chapter 2 by means of numerical results. For instance, this section not only discusses the sensitivity of all equalization strategies to the amount of variability, but also compares the performances achieved by PRS and by FRS. Finally, conclusions are drawn in Section 9.5.

All system equations and expressions in this chapter are specifically derived in the context of baseband communication.

9.1 System model

The system model of the equalization scheme considered in this Chapter is presented in Fig. 9.1. At the transmitter, the entries of the vector $\mathbf{c}(k)$ are independently and uniformly drawn from the set $\{0, \cdots, M-1\}$, where M is assumed to be an integer power of 2. Just as in Chapters 7 and 8, the ST PRS precoder, characterized by the TIR $\mathbf{T}$, transforms the input stream $\mathbf{c}(k)$ into the stream $\mathbf{b}(k)$. In contrast to the chapters above, however, real-valued M-PAM transmission is considered instead of complex-valued M-QAM transmission. As a result, the TIR is real-valued and the relationship between $\mathbf{b}(k)$ and $\mathbf{c}(k)$ given in (7.1) still holds, but with M substituted for $\sqrt{M}$. Moreover $\mathbf{a}(k)$ is then constructed as follows

$$\mathbf{a}(k) = 2\Delta\mathbf{b}(k) + (-M+1)\Delta\mathbf{1}, \tag{9.1}$$

where Δ is often selected to normalize the M-PAM constellation. All entries from the TIR matrix $\mathbf{T}$ are restricted to be integer, and the $L \times L$ matrix $\mathbf{T}(0)$ is unimodular, ensuring that all elements of $\mathbf{a}(k)$ are independently and uniformly drawn from the M-PAM constellation such that $\mathbb{E}\left[\mathbf{a}(k)\mathbf{a}^T(k)\right] = \sigma_{\mathrm{a}}^2\mathbf{I}_L$.

This equalization scheme considers both a linear FIR pre-equalizer $\mathbf{P}$ at the transmitter and a nonlinear DFE, consisting of a feedforward FIR filter $\mathbf{W}$ and a feedback FIR filter $\mathbf{B}$, at the receiver. Comparing the system models from Fig. 9.1 and Fig. 5.1 confirms that the signal path from $\mathbf{a}(k)$ to $\mathbf{u}(k)$ is the same in both figures. Consequently, $\mathbf{u}(k)$ can be similarly expressed as (5.15), i.e.,

$$\mathbf{u}(k) = \alpha \sum_{m=-L_{\mathrm{G}}^{(1)}}^{L_{\mathrm{G}}^{(2)}} \mathbf{W}\mathbf{G}(m)\mathbf{P}\mathbf{a}(k-m) + \alpha\mathbf{W}\bar{\mathbf{n}}(k) - \sum_{m\in\Phi_{\mathbf{B}}} \mathbf{B}(m)\hat{\mathbf{a}}(k-m), \tag{9.2}$$

where the notations are the same as in Chapter 5.

The original data $\mathbf{c}(k)$ can again be retrieved from the target response $\mathbf{u}_{\mathrm{T}}(k)$ from (7.9), since they are related as follows

$$\mathbf{c}(k) = \left[\frac{\mathbf{u}_{\mathrm{T}}(k)}{2\Delta} + \mathbf{c}_{\mathrm{off}} \right]_M, \tag{9.3}$$

where the offset $\mathbf{c}_{\mathrm{off}}$ is now given by

$$\mathbf{c}_{\mathrm{off}} = \frac{M-1}{2} \sum_{m=0}^{L_{\mathrm{T}}} \mathbf{T}(m)\mathbf{1}. \tag{9.4}$$

Analogous to Chapter 7, the equalization coefficients are designed such that $\mathbf{u}(k)$ is as close as possible to $\mathbf{u}_{\mathrm{T}}(k)$ in a MSE sense. This equalizer design then allows to perform symbol-by-symbol detection by replacing the quantity $\frac{\mathbf{u}_{\mathrm{T}}(k)}{2\Delta} + \mathbf{c}_{\mathrm{off}}$ with the integer vector closest to $\frac{\mathbf{u}(k)}{2\Delta} + \mathbf{c}_{\mathrm{off}}$ in the right-hand side of (9.3), yielding the decision $\hat{\mathbf{c}}(k)$.

Interestingly, the baseband transmission variants of the equalization schemes with bandpass transmission from Chapters 7 and 8 are in fact special cases from the system model above. Indeed, the system equations can be derived by simply setting either $(L_{\mathrm{P}}, \mathbf{P}) = (1, \mathbf{I})$ or $(L_{\mathrm{W}}, \mathbf{W}, \mathbf{B}) = (1, \mathbf{I}, \mathbf{0})$, respectively.

9.2 MMSE optimization

As this chapter discusses the design of the equalization parameters for a channel subject to channel variability, the optimization framework from Chapter 4 is applied to the considered equalization scheme. For mathematical simplicity, the MSE between the decision variable $\mathbf{u}(k)$ and the target response $\mathbf{u}_{\mathrm{T}}(k)$ is selected as the objective function f_0. Moreover, the design of the equalizers assumes that all decisions at the receiver are correct. The MSE for one particular channel realization $\mathbf{g}_{\mathrm{ch}}$ is again denoted by $\mathrm{MSE}_{\mathbf{g}_{\mathrm{ch}}}$ and defined as

$$\mathrm{MSE}_{\mathbf{g}_{\mathrm{ch}}} = \frac{\mathbb{E}\left[\left\| \mathbf{u}(k) - \mathbf{u}_{\mathrm{T}}(k) \right\|^2 \right]}{L\sigma_{\mathrm{a}}^2} \tag{9.5}$$

$$\begin{aligned} &= \frac{1}{L} \Bigg[\sum_{m \in \Phi_{\mathbf{T}}} \left\| \alpha \mathbf{W}\mathbf{G}(m)\mathbf{P} - \mathbf{T}(m) \right\|^2 \\ &\quad + \sum_{m \in \Phi_{\mathbf{B}}} \left\| \alpha \mathbf{W}\mathbf{G}(m)\mathbf{P} - \mathbf{B}(m) \right\|^2 \\ &\quad + \sum_{m \in \Phi_{\mathbf{N}}} \left\| \alpha \mathbf{W}\mathbf{G}(m)\mathbf{P} \right\|^2 + \frac{\alpha^2}{\sigma_{\mathrm{a}}^2} \mathrm{Tr}\left(\mathbf{W}\mathbf{R}_{\bar{\mathbf{n}}}\mathbf{W}^T \right) \Bigg], \end{aligned} \tag{9.6}$$

where $\mathbf{R}_{\bar{\mathbf{n}}} \triangleq \mathbb{E}\left[\bar{\mathbf{n}}(k)\bar{\mathbf{n}}^T(k) \right]$, $\Phi_{\mathbf{N}} = \{-L_{\mathrm{G}}^{(1)}, \cdots, L_{\mathrm{G}}^{(2)}\} \setminus (\Phi_{\mathbf{B}} \cup \Phi_{\mathbf{T}})$, and the assumption is made that all previously detected symbols are correct. Just as

Table 9.1: Overview of the different equalization strategies.

Strategy	Notation	Adjustable parameters	Fixed parameters
Adjustable	S-A	$\mathbf{P}, \alpha, \mathbf{W}, \mathbf{T}, \mathbf{B}$	/
Fixed	S-F	/	$\mathbf{P}, \alpha, \mathbf{W}, \mathbf{T}, \mathbf{B}$
Hybrid	S-H	$\mathbf{W}, \mathbf{B}$	$\mathbf{P}, \alpha, \mathbf{T}$

in Chapter 7, the intersection between $\Phi_{\mathbf{T}}$ and $\Phi_{\mathbf{B}}$ is assumed to be empty by design, since, for a specific causal time delay $m \in \Phi_{\mathbf{B}} \cap \Phi_{\mathbf{T}}$, the feedback filter is capable of removing all causal interference, irrespective of the value of the TIR matrix $\mathbf{T}(m)$.

When (part of) the equalization parameters are fixed, not the $\mathrm{MSE}_{\mathbf{g}_{\mathrm{ch}}}$, but the average $\overline{\mathrm{MSE}} = \mathbb{E}_{\mathbf{G}_{\mathrm{ch}}}\left[\mathrm{MSE}_{\mathbf{g}_{\mathrm{ch}}}\right]$ must be minimized subject to the energy constraint, resulting in the following optimization problem:

$$\begin{aligned}(\mathbf{P}^{\star}, \alpha^{\star}, \mathbf{W}^{\star}, \mathbf{T}^{\star}, \mathbf{B}^{\star}) = \arg \min_{\mathbf{P},\alpha,\mathbf{W},\mathbf{T},\mathbf{B}} \overline{\mathrm{MSE}}(\mathbf{P}, \alpha, \mathbf{W}, \mathbf{T}, \mathbf{B}) \\ \text{subject to } \sigma_{\mathrm{a}}^2 \mathrm{Tr}\left[\mathbf{P}^T \mathbf{R}_{\mathrm{TX}} \mathbf{P}\right] \leq L E_{\mathrm{TX}}\end{aligned} . \tag{9.7}$$

For this optimization problem, one can argue similarly to optimization problem (5.28) that a necessary condition for optimality is that the energy constraint is met with equality. Moreover, the real-valued α can be restricted to be positive without loss of generality.

This chapter discusses the same three equalization strategies as the chapters above that study an equalization design in the context of a channel suffering from channel variability, i.e., the adjustable, the hybrid, and the fixed strategy. In the adjustable strategy, the TIR and all equalization coefficients are adjustable and therefore, in terms of the optimization procedure from Chapter 4, belong to the vector $\mathbf{x}(\mathbf{g}_{\mathrm{ch}})$. On the other hand, all equalization parameters in the fixed strategy are determined based on solely the channel statistics, meaning that all equalization parameters are fixed and thus belong to the vector $\mathbf{y}$. As for the hybrid strategy, all equalization parameters associated with the receiver are adjustable, i.e., $\mathbf{W}$ and $\mathbf{B}$, whereas all equalization parameters corresponding to the design of the transmitter are fixed, i.e., $\mathbf{P}$, α, and $\mathbf{T}$. Hence, the former parameters belong to the vector $\mathbf{x}(\mathbf{g}_{\mathrm{ch}})$, and the latter parameters are part of the vector $\mathbf{y}$. In summary, Table 9.1 provides an overview of the considered equalization strategies. In the subsections below, a detailed discussion is given on how the equalization parameters are derived for all equalization strategies by minimizing $\overline{\mathrm{MSE}}$.

9.2.1 Adjustable strategy

In the adjustable strategy, all equalization parameters are adjustable, implying that no iterations between the adjustable and the fixed parameters are required. As a result, one can directly minimize the conditional $\text{MSE}_{\mathbf{g}_{\text{ch}}}$ from (9.6) instead of the average $\overline{\text{MSE}}$ to find the optimal set of adjustable equalization parameters, i.e., $\mathbf{x}^\star(\mathbf{g}_{\text{ch}})$. To perform this minimization of $\text{MSE}_{\mathbf{g}_{\text{ch}}}$ subject to the energy constraint, an iterative optimization algorithm is recommended here as the analytical minimization is too complicated. The disadvantage of this iterative approach, however, is that convergence to the global optimum is not guaranteed. First, the optimal feedback filter $\mathbf{B}_a^\star$ is expressed as a function of the other equalization parameters, after which the resulting $\text{MSE}_{\mathbf{g}_{\text{ch}},\mathbf{B}_a^\star}$ is reduced by alternately determining the optimal $(\mathbf{P}_a^\star, \alpha_a^\star, \mathbf{T}_a^\star)$ and optimal $(\mathbf{W}_a^\star, \mathbf{T}_a^\star)$ for given $\mathbf{W}$ and $(\mathbf{P}, \alpha)$, respectively, until convergence is reached.

The feedback filter $\mathbf{B}(m)$ appears only in the second term of (9.6), allowing to easily express the optimal $\mathbf{B}_a^\star$ as

$$\mathbf{B}_a^\star(m) = \alpha \mathbf{W}\mathbf{G}(m)\mathbf{P} \tag{9.8}$$

for $m \in \Phi_{\mathbf{B}}$. When $\text{MSE}_{\mathbf{g}_{\text{ch}}}$ is evaluated at $\mathbf{B}_a^\star$, the second term in (9.6) vanishes such that the optimal $\text{MSE}_{\mathbf{g}_{\text{ch}},\mathbf{B}_a^\star}$ can be written as

$$\begin{aligned}\text{MSE}_{\mathbf{g}_{\text{ch}},\mathbf{B}_a^\star} = \frac{1}{L}\Bigg[&\sum_{m\in\Phi_{\mathbf{T}}} \left\|\alpha\mathbf{W}\mathbf{G}(m)\mathbf{P} - \mathbf{T}(m)\right\|^2 \\ &+ \sum_{m\in\Phi_{\mathbf{N}}} \left\|\alpha\mathbf{W}\mathbf{G}(m)\mathbf{P}\right\|^2 + \frac{\alpha^2}{\sigma_{\text{a}}^2}\text{Tr}\left(\mathbf{W}\mathbf{R}_{\bar{\mathbf{n}}}\mathbf{W}^T\right)\Bigg].\end{aligned} \tag{9.9}$$

To obtain the optimal $(\mathbf{P}_a^\star, \alpha_a^\star, \mathbf{T}_a^\star)$ for given $\mathbf{W}$ in the first step of each iteration, $\text{MSE}_{\mathbf{g}_{\text{ch}},\mathbf{B}^\star}$ from (9.9) is first rewritten as

$$\begin{aligned}\text{MSE}_{\mathbf{g}_{\text{ch}},\mathbf{B}_a^\star} = \frac{1}{L}\text{Tr}\Bigg(&\mathbf{T}_{\text{P}}^T\mathbf{T}_{\text{P}} + \alpha^2\mathbf{P}^T\left(\mathcal{G}_{\text{N}}^T\mathcal{G}_{\text{N}} + \mathcal{G}_{\text{T}}^T\mathcal{G}_{\text{T}}\right)\mathbf{P} + \frac{\alpha^2}{\sigma_{\text{a}}^2}\mathbf{W}\mathbf{R}_{\bar{\mathbf{n}}}\mathbf{W}^T \\ &- \alpha\mathbf{T}_{\text{P}}^T\mathcal{G}_{\text{T}}\mathbf{P} - \alpha\mathbf{P}^T\mathcal{G}_{\text{T}}^T\mathbf{T}_{\text{P}}\Bigg),\end{aligned} \tag{9.10}$$

where the stacked matrix $\mathbf{T}_{\text{P}}$ is constructed by stacking all matrices $\mathbf{T}(m)$, i.e., $\mathbf{T}_{\text{P}} = \left[\mathbf{T}(0)^T \cdots \mathbf{T}(L_{\text{T}})^T\right]^T$, $\mathcal{G}_{\text{N}} = \left[\mathcal{G}^T\left(\Phi_{\mathbf{N}}(1)\right) \cdots \mathcal{G}^T\left(\Phi_{\mathbf{N}}(L_{\text{N}})\right)\right]^T$, and $\mathcal{G}_{\text{T}} = \left[\mathcal{G}^T\left(\Phi_{\mathbf{T}}(1)\right) \cdots \mathcal{G}^T\left(\Phi_{\mathbf{T}}(L_{\text{T}})\right)\right]^T$. The minimization of (9.10) subject to the energy constraint with respect to $(\mathbf{P}, \alpha, \mathbf{T}_{\text{P}})$ for given $\mathbf{W}$ is performed in two steps: (i) the optimal $(\mathbf{P}_a^\star, \alpha_a^\star)$ is determined as a function of $\mathbf{T}_{\text{P}}$ and (ii) the optimized $\mathbf{T}_{\text{P},a}^\star$ is obtained by minimizing $\text{MSE}_{\mathbf{g}_{\text{ch}},\mathbf{P}_a^\star,\alpha_a^\star,\mathbf{B}_a^\star}$. The first step is in fact a particular case of the optimization problem from Appendix 11.2.

The optimal $\mathbf{P}_a^\star$ and $\alpha_a^\star$ are thus given by

$$\mathbf{P}_a^\star = \frac{1}{\alpha_a^\star}\mathbf{D}_a^{-1}\mathcal{G}_{\mathrm{T}}^T\mathbf{T}_{\mathrm{P}} \tag{9.11}$$

and

$$\alpha_a^\star = \sqrt{\frac{\sigma_{\mathrm{a}}^2}{LE_{\mathrm{TX}}}\mathrm{Tr}\left(\mathbf{T}_{\mathrm{P}}^T\mathcal{G}_{\mathrm{T}}\mathbf{D}_a^{-1}\mathbf{R}_{\mathrm{TX}}\mathbf{D}_a^{-1}\mathcal{G}_{\mathrm{T}}^T\mathbf{T}_{\mathrm{P}}\right)} \tag{9.12}$$

with $\mathbf{D}_a = \mathcal{G}_{\mathrm{N}}^T\mathcal{G}_{\mathrm{N}} + \mathcal{G}_{\mathrm{T}}^T\mathcal{G}_{\mathrm{T}} + \zeta_a\mathbf{R}_{\mathrm{TX}}$ and $\zeta_a = \frac{\mathrm{Tr}\left(\mathbf{W}\mathbf{R}_{\bar{\mathbf{n}}}\mathbf{W}^T\right)}{LE_{\mathrm{TX}}}$, yielding

$$\mathrm{MSE}_{\mathbf{g}_{\mathrm{ch}},\mathbf{P}_a^\star,\alpha_a^\star,\mathbf{B}_a^\star} = \frac{1}{L}\mathrm{Tr}\left(\mathbf{T}_{\mathrm{P}}^T\mathbf{G}_{\mathrm{P},a}\mathbf{T}_{\mathrm{P}}\right), \tag{9.13}$$

where $\mathbf{G}_{\mathrm{P},a} = \mathbf{I}_L - \mathcal{G}_{\mathrm{T}}\mathbf{D}_a^{-1}\mathcal{G}_{\mathrm{T}}^T$. Interestingly, the minimization of $\mathrm{MSE}_{\mathbf{g}_{\mathrm{ch}},\mathbf{P}_a^\star,\alpha_a^\star,\mathbf{B}_a^\star}$ from (9.13) with respect to $\mathbf{T}_{\mathrm{P}}$ shares a similar structure with the minimization of $\mathrm{MSE}_{\mathbf{W}^\star,\mathbf{B}^\star}$ from (7.23) in Subsection 7.2.2 with respect to $\mathbf{T}$. Consequently, all three algorithms proposed in Subsection 7.2.2 can be employed to compute $\mathbf{T}_{\mathrm{P},a}^\star$. In the remainder of this chapter, algorithm A3 is preferred to the other two algorithms as it achieves the best performance of the three algorithms.

The goal of the second stage of each iteration is to determine the optimal $(\mathbf{W}_a^\star, \mathbf{T}_a^\star)$ for given $(\mathbf{P}, \alpha)$. In this regard, the $\mathrm{MSE}_{\mathbf{g}_{\mathrm{ch}},\mathbf{B}_a^\star}$ from (9.9) is reformulated as

$$\mathrm{MSE}_{\mathbf{g}_{\mathrm{ch}},\mathbf{B}_a^\star} = \frac{1}{L}\mathrm{Tr}\Bigg(\mathbf{T}_{\mathrm{W}}\mathbf{T}_{\mathrm{W}}^T + \mathbf{W}\left(\boldsymbol{\mathcal{G}}_{\mathrm{N}}\boldsymbol{\mathcal{G}}_{\mathrm{N}}^T + \boldsymbol{\mathcal{G}}_{\mathrm{T}}\boldsymbol{\mathcal{G}}_{\mathrm{T}}^T\right)\mathbf{W}^T + \frac{\alpha^2}{\sigma_{\mathrm{a}}^2}\mathbf{W}\mathbf{R}_{\bar{\mathbf{n}}}\mathbf{W}^T$$
$$- \mathbf{W}\boldsymbol{\mathcal{G}}_{\mathrm{T}}\mathbf{T}_{\mathrm{W}}^T - \mathbf{T}_{\mathrm{W}}\boldsymbol{\mathcal{G}}_{\mathrm{T}}^T\mathbf{W}^T\Bigg), \tag{9.14}$$

where the augmented $\mathbf{T}_{\mathrm{W}} = [\mathbf{T}(0)\cdots\mathbf{T}(L_{\mathrm{T}})]$, $\boldsymbol{\mathcal{G}}_{\mathrm{N}} = [\boldsymbol{\mathcal{G}}(\Phi_{\mathbf{N}}(1))\cdots\boldsymbol{\mathcal{G}}(\Phi_{\mathbf{N}}(L_{\mathrm{N}}))]$, and $\boldsymbol{\mathcal{G}}_{\mathrm{T}} = [\boldsymbol{\mathcal{G}}(\Phi_{\mathbf{T}}(1))\cdots\boldsymbol{\mathcal{G}}(\Phi_{\mathbf{T}}(L_{\mathrm{T}}))]$. First, the optimal $\mathbf{W}_a^\star$ can be derived by equating the derivative $\frac{\partial \mathrm{MSE}_{\mathbf{g}_{\mathrm{ch}},\mathbf{B}_a^\star}}{\partial \mathbf{W}}$ to zero, yielding

$$\mathbf{W}_a^\star = \mathbf{T}_{\mathrm{W}}\boldsymbol{\mathcal{G}}_{\mathrm{T}}^T\mathbf{C}_a^{-1}, \tag{9.15}$$

where $\mathbf{C}_a = \boldsymbol{\mathcal{G}}_{\mathrm{N}}\boldsymbol{\mathcal{G}}_{\mathrm{N}}^T + \boldsymbol{\mathcal{G}}_{\mathrm{T}}\boldsymbol{\mathcal{G}}_{\mathrm{T}}^T + \frac{\alpha^2}{\sigma_{\mathrm{a}}^2}\mathbf{R}_{\bar{\mathbf{n}}}$. Second, $\mathbf{T}_{\mathrm{W},a}^\star$ is determined by minimizing $\mathrm{MSE}_{\mathbf{g}_{\mathrm{ch}},\mathbf{W}_a^\star,\mathbf{B}_a^\star}$, which equals $\mathrm{MSE}_{\mathbf{g}_{\mathrm{ch}},\mathbf{B}_a^\star}$ evaluated at $\mathbf{W}_a^\star$, i.e.,

$$\mathrm{MSE}_{\mathbf{g}_{\mathrm{ch}},\mathbf{W}_a^\star,\mathbf{B}_a^\star} = \frac{1}{L}\mathrm{Tr}\left(\mathbf{T}_{\mathrm{W}}\mathbf{G}_{\mathrm{W},a}\mathbf{T}_{\mathrm{W}}^T\right) \tag{9.16}$$

with $\mathbf{G}_{\mathrm{W},a} = \mathbf{I}_L - \boldsymbol{\mathcal{G}}_{\mathrm{T}}^T\mathbf{C}_a^{-1}\boldsymbol{\mathcal{G}}_{\mathrm{T}}$. Just as the minimization of $\mathrm{MSE}_{\mathbf{g}_{\mathrm{ch}},\mathbf{P}_a^\star,\alpha_a^\star,\mathbf{B}_a^\star}$, minimizing $\mathrm{MSE}_{\mathbf{g}_{\mathrm{ch}},\mathbf{W}_a^\star,\mathbf{B}_a^\star}$ from (9.16) with respect to $\mathbf{T}_{\mathrm{W}}$ can be performed by means of algorithm A3 from Subsection 7.2.2.3.

Remark that the algorithm presented here is identical to the algorithm employed to determine the equalization parameters of the adjustable strategy in the DFE equalization scheme of Section 5.2.1 when $L_{\mathrm{T}} = 0$ and $\mathbf{T}_{\mathrm{P}} = \mathbf{T}_{\mathrm{W}} = \mathbf{I}_L$.

Regarding the initialization, the initial feedforward filter $\mathbf{W}$ is chosen to be the all-pass filter, i.e., $\mathbf{W}(i) = \mathbf{I}_L \delta_i$. Iterations can be stopped after a fixed number of iterations or when the relative decrease of the $\mathrm{MSE}_{\mathbf{g}_{\mathrm{ch}}}$ is small enough.

9.2.2 Fixed strategy

In the fixed strategy, the average $\overline{\mathrm{MSE}}$ must be minimized subject to the energy constraint to design all (fixed) equalization parameters, i.e., to determine the vector $\mathbf{y}^\star$. Therefore, an iterative algorithm is proposed below, which is structurally identical to the algorithm associated with the adjustable strategy. First, the optimal $\mathbf{B}_f^\star$ is derived, after which the resulting $\overline{\mathrm{MSE}}_{\mathbf{B}_f^\star}$ is iteratively reduced by alternately computing the optimal $\left(\mathbf{P}_f^\star, \alpha_f^\star, \mathbf{T}_f^\star\right)$ and the optimal $\left(\mathbf{W}_f^\star, \mathbf{T}_f^\star\right)$ for given $\mathbf{W}$ and $(\mathbf{P}, \alpha)$, respectively.

By equating the partial derivative of $\overline{\mathrm{MSE}}$ with respect to the components of $\mathbf{B}$ to zero, one can readily determine $\mathbf{B}_f^\star$ as

$$\mathbf{B}_f^\star(m) = \alpha \mathbf{W} \mathbb{E}_{\mathbf{G}_{\mathrm{ch}}} \left[\mathbf{G}(m)\right] \mathbf{P} \tag{9.17}$$

for $m \in \Phi_{\mathbf{B}}$. Due to the fixed nature of this feedback filter, not all causal interference can be removed for all channel realizations and the $\overline{\mathrm{MSE}}$ evaluated at $\mathbf{B}_f^\star$ is given by

$$\begin{aligned}\overline{\mathrm{MSE}}_{\mathbf{B}_f^\star} = \frac{1}{L}\Bigg[& \sum_{m \in \Phi_{\mathbf{T}}} \mathbb{E}_{\mathbf{G}_{\mathrm{ch}}} \left[\left\| \alpha \mathbf{W} \mathbf{G}(m) \mathbf{P} - \mathbf{T}(m) \right\|^2 \right] \\ & + \sum_{m \in \Phi_{\mathbf{B}}} \mathbb{E}_{\mathbf{G}_{\mathrm{ch}}} \left[\left\| \alpha \mathbf{W} \mathbf{G}(m) \mathbf{P} - \alpha \mathbf{W} \mathbb{E}_{\mathbf{G}_{\mathrm{ch}}} \left[\mathbf{G}(m)\right] \mathbf{P} \right\|^2 \right] \\ & + \sum_{m \in \Phi_{\mathbf{N}}} \mathbb{E}_{\mathbf{G}_{\mathrm{ch}}} \left[\left\| \alpha \mathbf{W} \mathbf{G}(m) \mathbf{P} \right\|^2 \right] + \frac{\alpha^2}{\sigma_{\mathrm{a}}^2} \mathrm{Tr}\left(\mathbf{W} \mathbf{R}_{\bar{\mathbf{n}}} \mathbf{W}^H \right) \Bigg]. \end{aligned} \tag{9.18}$$

To compute the optimal $\left(\mathbf{P}_f^\star, \alpha_f^\star, \mathbf{T}_f^\star\right)$ for given $\mathbf{W}$ in the first step of each iteration, $\overline{\mathrm{MSE}}_{\mathbf{B}_f^\star}$ is rewritten as

$$\begin{aligned}\overline{\mathrm{MSE}}_{\mathbf{B}_f^\star} = \frac{1}{L} \mathrm{Tr} \Bigg(& \alpha^2 \mathbf{P}^T \Big(\mathbb{E}_{\mathbf{G}_{\mathrm{ch}}} \left[\mathcal{G}_{\mathrm{N}}^T \mathcal{G}_{\mathrm{N}} + \mathcal{G}_{\mathrm{T}}^T \mathcal{G}_{\mathrm{T}} + \mathcal{G}_{\mathrm{B}}^T \mathcal{G}_{\mathrm{B}} \right] - \mathbb{E}_{\mathbf{G}_{\mathrm{ch}}} \left[\mathcal{G}_{\mathrm{B}}^T \right] \mathbb{E}_{\mathbf{G}_{\mathrm{ch}}} \left[\mathcal{G}_{\mathrm{B}} \right] \Big) \mathbf{P} \\ & + \frac{\alpha^2}{\sigma_{\mathrm{a}}^2} \mathbf{W} \mathbf{R}_{\bar{\mathbf{n}}} \mathbf{W}^T - \alpha \mathbf{T}_{\mathrm{P}}^T \mathbb{E}_{\mathbf{G}_{\mathrm{ch}}} \left[\mathcal{G}_{\mathrm{T}} \right] \mathbf{P} - \alpha \mathbf{P}^T \mathbb{E}_{\mathbf{G}_{\mathrm{ch}}} \left[\mathcal{G}_{\mathrm{T}}^T \right] \mathbf{T}_{\mathrm{P}} + \mathbf{T}_{\mathrm{P}}^T \mathbf{T}_{\mathrm{P}} \Bigg). \end{aligned} \tag{9.19}$$

As $\overline{\mathrm{MSE}}_{\mathbf{B}_f^\star}$ from (9.19) is structurally identical to $\mathrm{MSE}_{\mathbf{g}_{\mathrm{ch}},\mathbf{B}_a^\star}$ from (9.10), the minimization of (9.19) subject to the energy constraint with respect to $(\mathbf{P},\alpha)$ can again be solved with the aid of Appendix 11.2, yielding

$$\mathbf{P}_f^\star = \frac{1}{\alpha_f^\star}\mathbf{D}_f^{-1}\mathbb{E}_{\mathbf{G}_{\mathrm{ch}}}\left[\mathcal{G}_{\mathrm{T}}^T\right]\mathbf{T}_{\mathrm{P}} \tag{9.20}$$

and

$$\alpha_f^\star = \sqrt{\frac{\sigma_{\mathrm{a}}^2}{LE_{\mathrm{TX}}}\mathrm{Tr}\left(\mathbf{T}_{\mathrm{P}}^T\mathbb{E}_{\mathbf{G}_{\mathrm{ch}}}\left[\mathcal{G}_{\mathrm{T}}\right]\mathbf{D}_f^{-1}\mathbf{R}_{\mathrm{TX}}\mathbf{D}_f^{-1}\mathbb{E}_{\mathbf{G}_{\mathrm{ch}}}\left[\mathcal{G}_{\mathrm{T}}^T\right]\mathbf{T}_{\mathrm{P}}\right)} \tag{9.21}$$

with $\mathbf{D}_f = \mathbb{E}_{\mathbf{G}_{\mathrm{ch}}}\left[\mathcal{G}_{\mathrm{N}}^T\mathcal{G}_{\mathrm{N}} + \mathcal{G}_{\mathrm{T}}^T\mathcal{G}_{\mathrm{T}} + \mathcal{G}_{\mathrm{B}}^T\mathcal{G}_{\mathrm{B}}\right] - \mathbb{E}_{\mathbf{G}_{\mathrm{ch}}}\left[\mathcal{G}_{\mathrm{B}}^T\right]\mathbb{E}_{\mathbf{G}_{\mathrm{ch}}}[\mathcal{G}_{\mathrm{B}}] + \zeta_f\mathbf{R}_{\mathrm{TX}}$ and $\zeta_f = \frac{\mathrm{Tr}\left(\mathbf{W}\mathbf{R}_{\bar{\mathbf{n}}}\mathbf{W}^T\right)}{LE_{\mathrm{TX}}}$. The resulting average $\overline{\mathrm{MSE}}_{\mathbf{B}_f^\star}$ optimized over $\mathbf{P}$ and α for given $\mathbf{W}$ is symbolized by $\overline{\mathrm{MSE}}_{\mathbf{P}_f^\star,\alpha_f^\star,\mathbf{B}_f^\star}$ and given by

$$\overline{\mathrm{MSE}}_{\mathbf{P}_f^\star,\alpha_f^\star,\mathbf{B}_f^\star} = \frac{1}{L}\mathrm{Tr}\left(\mathbf{T}_{\mathrm{P}}^T\mathbf{G}_{\mathrm{P},f}\mathbf{T}_{\mathrm{P}}\right), \tag{9.22}$$

where $\mathbf{G}_{\mathrm{P},f} = \mathbf{I}_L - \mathbb{E}_{\mathbf{G}_{\mathrm{ch}}}\left[\mathcal{G}_{\mathrm{T}}\right]\mathbf{D}_f^{-1}\mathbb{E}_{\mathbf{G}_{\mathrm{ch}}}\left[\mathcal{G}_{\mathrm{T}}^T\right]$. The similarities between $\mathrm{MSE}_{\mathbf{g}_{\mathrm{ch}},\mathbf{P}_a^\star,\alpha_a^\star,\mathbf{B}_a^\star}$ from (9.13) and $\overline{\mathrm{MSE}}_{\mathbf{P}_f^\star,\alpha_f^\star,\mathbf{B}_f^\star}$ from (9.22) are apparent and algorithm A3 from Section 7.2.2.3 can thus be applied to compute $\mathbf{T}_{\mathrm{P},f}^\star$.

The second step in each iteration of the optimization of $\overline{\mathrm{MSE}}_{\mathbf{B}_f^\star}$ is to compute the optimal $\left(\mathbf{W}_f^\star,\mathbf{T}_f^\star\right)$ for given $(\mathbf{P},\alpha)$. To this end, $\overline{\mathrm{MSE}}_{\mathbf{B}_f^\star}$ is first rewritten as

$$\begin{aligned}\overline{\mathrm{MSE}}_{\mathbf{B}_f^\star} = \frac{1}{L}\mathrm{Tr}\Bigg(&\mathbf{W}\Big(\mathbb{E}_{\mathbf{G}_{\mathrm{ch}}}\left[\boldsymbol{\mathcal{G}}_{\mathrm{N}}\boldsymbol{\mathcal{G}}_{\mathrm{N}}^T + \boldsymbol{\mathcal{G}}_{\mathrm{T}}\boldsymbol{\mathcal{G}}_{\mathrm{T}}^T + \boldsymbol{\mathcal{G}}_{\mathrm{B}}\boldsymbol{\mathcal{G}}_{\mathrm{B}}^T\right] - \mathbb{E}_{\mathbf{G}_{\mathrm{ch}}}[\boldsymbol{\mathcal{G}}_{\mathrm{B}}]\mathbb{E}_{\mathbf{G}_{\mathrm{ch}}}\left[\boldsymbol{\mathcal{G}}_{\mathrm{B}}^T\right]\Big)\mathbf{W}^T \\ &+ \frac{\alpha^2}{\sigma_{\mathrm{a}}^2}\mathbf{W}\mathbf{R}_{\bar{\mathbf{n}}}\mathbf{W}^T - \mathbf{W}\mathbb{E}_{\mathbf{G}_{\mathrm{ch}}}[\boldsymbol{\mathcal{G}}_{\mathrm{T}}]\mathbf{T}_{\mathrm{W}}^T - \mathbf{T}_{\mathrm{W}}\mathbb{E}_{\mathbf{G}_{\mathrm{ch}}}\left[\boldsymbol{\mathcal{G}}_{\mathrm{T}}^T\right]\mathbf{W}^T + \mathbf{T}_{\mathrm{W}}\mathbf{T}_{\mathrm{W}}^T\Bigg).\end{aligned} \tag{9.23}$$

Equating the derivatives of $\overline{\mathrm{MSE}}_{\mathbf{B}_f^\star}$ from (9.23) with respect to the feedforward filter to zero then yields

$$\mathbf{W}_f^\star = \mathbf{T}_{\mathrm{W}}\mathbb{E}_{\mathbf{G}_{\mathrm{ch}}}\left[\boldsymbol{\mathcal{G}}_{\mathrm{T}}^T\right]\mathbf{C}_f^{-1} \tag{9.24}$$

with $\mathbf{C}_f = \mathbb{E}_{\mathbf{G}_{\mathrm{ch}}}\left[\boldsymbol{\mathcal{G}}_{\mathrm{N}}\boldsymbol{\mathcal{G}}_{\mathrm{N}}^T + \boldsymbol{\mathcal{G}}_{\mathrm{T}}\boldsymbol{\mathcal{G}}_{\mathrm{T}}^T + \boldsymbol{\mathcal{G}}_{\mathrm{B}}\boldsymbol{\mathcal{G}}_{\mathrm{B}}^T\right] - \mathbb{E}_{\mathbf{G}_{\mathrm{ch}}}[\boldsymbol{\mathcal{G}}_{\mathrm{B}}]\mathbb{E}_{\mathbf{G}_{\mathrm{ch}}}\left[\boldsymbol{\mathcal{G}}_{\mathrm{B}}^T\right] + \alpha^2\mathbf{R}_{\bar{\mathbf{n}}}$. Consequently, the optimized $\overline{\mathrm{MSE}}_{\mathbf{W}_f^\star,\mathbf{B}_f^\star}$ can then be simplified to

$$\overline{\mathrm{MSE}}_{\mathbf{W}_f^\star,\mathbf{B}_f^\star} = \frac{1}{L}\mathrm{Tr}\left(\mathbf{T}_{\mathrm{W}}\mathbf{G}_{\mathrm{W},f}\mathbf{T}_{\mathrm{W}}^T\right) \tag{9.25}$$

with $\mathbf{G}_{\mathrm{W},f} = \mathbf{I}_L - \mathbb{E}_{\mathbf{G}_{\mathrm{ch}}}\left[\boldsymbol{\mathcal{G}}_{\mathrm{T}}^T\right] \mathbf{C}_f^{-1} \mathbb{E}_{\mathbf{G}_{\mathrm{ch}}}\left[\boldsymbol{\mathcal{G}}_{\mathrm{T}}\right]$. To obtain $\mathbf{T}_{\mathrm{W},f}^\star$, algorithm A3 is applied to $\overline{\mathrm{MSE}}_{\mathbf{W}_f^\star, \mathbf{B}_f^\star}$.

Finally, similar remarks as for the adjustable strategy can be made. Firstly, the algorithm presented here reduces to the algorithm of the fixed strategy in the DFE equalization scheme (Section 5.2.2) when $L_{\mathrm{T}} = 0$ and $\mathbf{T}_{\mathrm{P}} = \mathbf{T}_{\mathrm{W}} = \mathbf{I}_L$. Secondly, the initial feedforward filter $\mathbf{W}$ is set to the all-pass filter. Thirdly, iterations are stopped either after a certain number of iterations or when the relative decrease of $\overline{\mathrm{MSE}}$ is smaller than a predefined threshold.

9.2.3 Hybrid strategy

The hybrid strategy consists of both adjustable, i.e., $\mathbf{W}$ and $\mathbf{B}$, and fixed, i.e., $\mathbf{P}$, α, and $\mathbf{T}$, equalization parameters. Consequently, all equalization parameters are designed according to the iterative algorithm from Chapter 4, which alternately computes the optimal $\mathbf{y}^\star$ for given $\mathbf{x}\left(\mathbf{g}_{\mathrm{ch}}\right)$ and the optimal $\mathbf{x}^\star\left(\mathbf{g}_{\mathrm{ch}}\right)$ for given $\mathbf{y}$. Just as for the hybrid strategy in the case of the DFE equalization scheme from Chapter 5, however, the optimal adjustable $\mathbf{B}_h^\star$ is easily expressed as a function of the other equalization parameters, yielding the optimized $\mathrm{MSE}_{\mathbf{g}_{\mathrm{ch}}, \mathbf{B}_h^\star}$. In fact, $\mathbf{B}_h^\star$ and $\mathrm{MSE}_{\mathbf{g}_{\mathrm{ch}}, \mathbf{B}_h^\star}$ are identical to $\mathbf{B}_a^\star$ and $\mathrm{MSE}_{\mathbf{g}_{\mathrm{ch}}, \mathbf{B}_a^\star}$ from (9.8) and (9.9), respectively. Hence, instead of executing the iterative algorithm with $f_0 = \mathrm{MSE}_{\mathbf{g}_{\mathrm{ch}}}$, one could apply the algorithm to $f_0 = \mathrm{MSE}_{\mathbf{g}_{\mathrm{ch}}, \mathbf{B}_h^\star}$, where the vector $\mathbf{y}$ contains all coefficients of $\mathbf{P}$, α, and $\mathbf{T}$ and the vector $\mathbf{x}\left(\mathbf{g}_{\mathrm{ch}}\right)$ comprises all coefficients of the feedforward filter $\mathbf{W}$.

To compute the optimal $\mathbf{y}^\star$, i.e., $(\mathbf{P}_h^\star, \alpha_h^\star, \mathbf{T}_h^\star)$, for given $\mathbf{W}$, the average $\overline{\mathrm{MSE}}_{\mathbf{B}_h^\star} = \mathbb{E}_{\mathbf{G}_{\mathrm{ch}}}[\mathrm{MSE}_{\mathbf{g}_{\mathrm{ch}}, \mathbf{B}_h^\star}]$ is first rewritten as

$$\overline{\mathrm{MSE}}_{\mathbf{B}_h^\star} = \frac{1}{L}\mathrm{Tr}\Bigg(\alpha^2 \mathbf{P}^T \mathbb{E}_{\mathbf{G}_{\mathrm{ch}}}\left[\mathcal{G}_{\mathrm{N}}^T \mathcal{G}_{\mathrm{N}} + \mathcal{G}_{\mathrm{T}}^T \mathcal{G}_{\mathrm{T}}\right] \mathbf{P} + \frac{\alpha^2}{\sigma_{\mathrm{a}}^2} \mathbb{E}_{\mathbf{G}_{\mathrm{ch}}}\left[\mathbf{W}\mathbf{R}_{\bar{\mathbf{n}}}\mathbf{W}^T\right] - \alpha \mathbf{T}_{\mathrm{P}}^T \mathbb{E}_{\mathbf{G}_{\mathrm{ch}}}\left[\mathcal{G}_{\mathrm{T}}\right] \mathbf{P} - \alpha \mathbf{P}^T \mathbb{E}_{\mathbf{G}_{\mathrm{ch}}}\left[\mathcal{G}_{\mathrm{T}}^T\right] \mathbf{T}_{\mathrm{P}} + \mathbf{T}_{\mathrm{P}}^T \mathbf{T}_{\mathrm{P}} \Bigg). \tag{9.26}$$

Analogous to the adjustable and the fixed strategy, the optimal pre-equalizer $\mathbf{P}_h^\star$ and the optimal scaling factor $\alpha_h^\star$ again directly follow from Appendix 11.2, as optimizing (9.26) subject to the energy constraint is a particular case of the optimization problem considered in this appendix. Consequently, $\mathbf{P}_h^\star$ and $\alpha_h^\star$ are respectively derived as

$$\mathbf{P}_h^\star = \frac{1}{\alpha_h^\star} \mathbf{D}_h^{-1} \mathbb{E}_{\mathbf{G}_{\mathrm{ch}}}\left[\mathcal{G}_{\mathrm{T}}^T\right] \mathbf{T}_{\mathrm{P}} \tag{9.27}$$

and

$$\alpha_h^\star = \sqrt{\frac{\sigma_{\mathrm{a}}^2}{L E_{\mathrm{TX}}} \mathrm{Tr}\left(\mathbf{T}_{\mathrm{P}}^T \mathbb{E}_{\mathbf{G}_{\mathrm{ch}}}\left[\mathcal{G}_{\mathrm{T}}\right] \mathbf{D}_h^{-1} \mathbf{R}_{\mathrm{TX}} \mathbf{D}_h^{-1} \mathbb{E}_{\mathbf{G}_{\mathrm{ch}}}\left[\mathcal{G}_{\mathrm{T}}^T\right] \mathbf{T}_{\mathrm{P}} \right)} \tag{9.28}$$

with $\mathbf{D}_h^{-1} = \mathbb{E}_{\mathbf{G}_{\text{ch}}}\left[\mathcal{G}_{\text{N}}^T\mathcal{G}_{\text{N}} + \mathcal{G}_{\text{T}}^T\mathcal{G}_{\text{T}}\right] + \zeta_h\mathbf{R}_{\text{TX}}$ and $\zeta_h = \frac{\text{Tr}\left(\mathbb{E}_{\mathbf{G}_{\text{ch}}}\left[\mathbf{W}\mathbf{R}_{\tilde{\mathbf{n}}}\mathbf{W}^T\right]\right)}{LE_{\text{TX}}}$. The associated minimum $\overline{\text{MSE}}_{\mathbf{P}_h^\star,\alpha_h^\star,\mathbf{B}_h^\star}$ can be written as

$$\overline{\text{MSE}}_{\mathbf{P}_h^\star,\alpha_h^\star,\mathbf{B}_h^\star} = \frac{1}{L}\text{Tr}\left(\mathbf{T}_{\text{P}}^T\mathbf{G}_{\text{P},h}\mathbf{T}_{\text{P}}\right) \tag{9.29}$$

with $\mathbf{G}_{\text{P},h} = \mathbf{I}_L - \mathbb{E}_{\mathbf{G}_{\text{ch}}}\left[\mathcal{G}_{\text{T}}\right]\mathbf{D}_h^{-1}\mathbb{E}_{\mathbf{G}_{\text{ch}}}\left[\mathcal{G}_{\text{T}}^T\right]$. Similar to $\mathbf{T}_{\text{P},a}^\star$ and $\mathbf{T}_{\text{P},f}^\star$ in the adjustable and the fixed strategy, respectively, the optimized $\mathbf{T}_{\text{P},h}^\star$ is derived by applying algorithm A3 to $\overline{\text{MSE}}_{\mathbf{P}_h^\star,\alpha_h^\star,\mathbf{B}_h^\star}$ from (9.29).

The second step in each iteration is to compute the optimal adjustable feedforward filter $\mathbf{W}_h^\star$ for a fixed vector $\mathbf{y}$, i.e., the set $(\mathbf{P},\alpha,\mathbf{T})$. This subproblem is in fact identical to determining the optimal feedforward filter $\mathbf{W}_a^\star$ in the adjustable strategy when the TIR $\mathbf{T}_{\text{W}}$ is given. Consequently, the optimal $\mathbf{W}_h^\star$ is given by

$$\mathbf{W}_h^\star = \mathbf{T}_{\text{W}}\boldsymbol{\mathcal{G}}_{\text{T}}^T\mathbf{C}_h^{-1} \tag{9.30}$$

with $\mathbf{C}_h = \mathbf{C}_a$ and the corresponding $\text{MSE}_{\mathbf{g}_{\text{ch}},\mathbf{W}_h^\star,\mathbf{B}_h^\star}$ is then given by

$$\text{MSE}_{\mathbf{g}_{\text{ch}},\mathbf{W}_h^\star,\mathbf{B}_h^\star} = \frac{1}{L}\text{Tr}\left(\mathbf{T}_{\text{W}}\mathbf{G}_{\text{W},h}\mathbf{T}_{\text{W}}^T\right), \tag{9.31}$$

where $\mathbf{G}_{\text{W},h} = \mathbf{I}_L - \boldsymbol{\mathcal{G}}_{\text{T}}^T\mathbf{C}_h^{-1}\boldsymbol{\mathcal{G}}_{\text{T}}$.

When $L_{\text{T}} = 0$ and $\mathbf{T}_{\text{W}} = \mathbf{I}_L$, the algorithm reduces to the algorithm of the hybrid strategy in the DFE equalization scheme (Section 5.2.3).

To initialize $\mathbf{x}\left(\mathbf{g}_{\text{ch}}\right)$, all initial feedforward filters $\mathbf{W}$ are again assumed to be equal to the all-pass filter.

9.3 BER expression for PRS

Compared to the derivation of the BER expression from Section 7.3, two differences can be noticed here. First, this chapter considers baseband communication and M-PAM transmission rather than bandpass communication and M-QAM transmission. Second, the added pre-equalizer $\mathbf{P}$ alters the expression for the decision variable $\mathbf{u}(k)$. Still, to derive the BER expression for the equalization scheme from Fig. 9.1, a procedure similar to the one in Section 7.3 can be followed, hence merely the differences are highlighted here.

First, the variable $\mathbf{v}(k)$ is again a scaled and translated version of the decision variable $\mathbf{u}(k)$, but the offset vector $\mathbf{c}_{\text{off}}$ is now defined in (9.4). The decomposition of $\mathbf{v}(k)$ in (7.46) still holds but $\mathbf{E}(m)$ in the definition of $\mathbf{isi}(k)$ is now given by

$$2\Delta\mathbf{E}(m) = \begin{cases} \mathbf{W}\mathbf{G}(m)\mathbf{P} - \mathbf{T}(m) & m \in \Phi_{\mathbf{T}} \\ \mathbf{W}\mathbf{G}(m)\mathbf{P} - \mathbf{B}(m) & m \in \Phi_{\mathbf{B}} \\ \mathbf{W}\mathbf{G}(m)\mathbf{P} & m \in \Phi \backslash \{\Phi_{\mathbf{T}} \cup \Phi_{\mathbf{B}}\} \end{cases}. \tag{9.32}$$

The symbol-by-symbol detector makes a decision $(\hat{\mathbf{c}}_{\mathrm{ex}}(k))_l$ of $(\mathbf{c}_{\mathrm{ex}}(k))_l$ in the extended symbol set based on $\mathrm{v}_l(k)$ for each data stream individually, after which the modulo operator $[\cdot]_M$ is applied to $(\hat{\mathbf{c}}_{\mathrm{ex}}(k))_l$, yielding the decision $\hat{\mathrm{c}}_l(k) \in \{0, \cdots, M-1\}$. Consequently, the definition for $\mathrm{BER}^{(l)}$ is identical to the one from (7.51). To construct an accurate approximation similar to (7.52), one could follow an analogous derivation as in Appendix 11.10, bearing in mind that M-PAM transmission is considered here instead of M-QAM transmission. More precisely, the approximation is made that the symbol $\hat{\mathrm{c}}_l(k)$ is correctly detected only when $\mathrm{v}_l(k)$ is an element of the decision region of $(\hat{\mathbf{c}}_{\mathrm{ex}}(k))_l$, whereas exactly one bit error is assumed to occur when $\mathrm{v}_l(k)$ lies in any other decision region, yielding the approximation

$$\mathrm{BER}^{(l)} \approx \frac{1}{\log_2(M)} \mathbb{E}_{\mathbf{a}_{\mathrm{ISI}}} \left[2\mathrm{Q}\left(\frac{0.5 - \mathrm{Re}\left[\mathrm{isi}_l(\mathbf{a}_{\mathrm{ISI}})\right]}{\sigma_{(\mathbf{n}_{\mathrm{v}})_l}} \right) \right]. \tag{9.33}$$

To numerically evaluate $\mathrm{BER}^{(l)}$ from (9.33), one could again approximate the expectation $\mathbb{E}_{\mathbf{a}_{\mathrm{ISI}}}[\cdot]$ by the arithmetical average over a large number of N realizations of $\mathrm{Re}\left[\mathrm{isi}_l(\mathbf{a}_{\mathrm{ISI}})\right]$.

9.4 Numerical results and discussion

This section discusses the performance of the investigated equalization scheme and the proposed equalization strategies in terms of $\overline{\mathrm{MSE}}$ and $\overline{\mathrm{BER}}$ in the case of the frequency-selective chip-to-chip interconnect of Chapter 2. Similar to the chapters above, the SNR is defined as the ratio of the transmitted energy per bit to the one-sided spectral density of the channel-noise, i.e., $\mathrm{SNR} = \frac{E_{\mathrm{TX}}}{\log_2(M) N_0}$. As the influence of M is not the main objective of this section, only 2-PAM transmission is considered.

First Fig. 9.2 compares the $\overline{\mathrm{MSE}}$ and the $\overline{\mathrm{BER}}$ performance of the different strategies as a function of the channel deviation σ_r for different equalization scenarios. A remarkable result is that the hybrid strategy has sometimes a better performance than the adjustable strategy, which is more closely investigated in Fig. 9.3 by plotting $\overline{\mathrm{MSE}}$ against the iteration index. Next, the performance difference between PRS and FRS as a function of the SNR is visualized in Figs. 9.4 and 9.5 for the the linear and DFE equalization scheme, respectively. Finally, the importance of the order, in which $(\mathbf{W}^\star, \mathbf{B}^\star)$ and $(\mathbf{P}^\star, \alpha^\star, \mathbf{T}^\star)$ are computed, is highlighted in Fig. 9.6.

Fig. 9.2 displays the MSE and the BER performance averaged over 1000 channel realizations at $\mathrm{SNR} = 25\,\mathrm{dB}$ as a function of σ_r for both FRS and PRS. In the latter case, $L_{\mathrm{T}} = 3$, whereas the number of taps in the pre-equalizer and the feedforward filter are selected such that the convolution of both linear filters has 13 taps. In the left plots of Fig. 9.2, the feedforward filter is omitted such that all 13 taps are placed at the transmitter, i.e., $L_{\mathrm{P}}^{(1)} = L_{\mathrm{P}}^{(2)} = 6$. On the other hand, the pre-equalizer is bypassed in the right plots of Fig. 9.2, implying

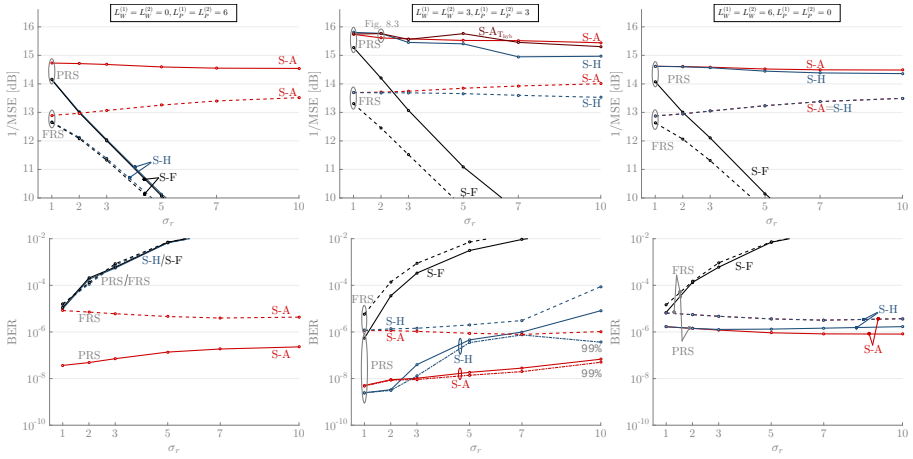

Figure 9.2: Performance of all equalization strategies in terms of both $1/\overline{\text{MSE}}$ and $\overline{\text{BER}}$ as a function of σ_r for SNR $= 25\,\text{dB}$ and $\Phi_{\mathbf{B}} = \{4, \cdots, 19\}$. Both FRS (dashed lines) and PRS with $L_{\text{T}} = 3$ (solid lines) are considered. The linear feedforward filter $\mathbf{W}$ and the pre-equalizer $\mathbf{P}$ are omitted in the left and the right plots, respectively, whereas the equalization taps in the middle plots are equally split between the feedforward filter and the pre-equalizer. Mostly, best performance is achieved in the case of the adjustable strategy with PRS.

that the feedforward filter consists of all 13 taps, i.e., $L_{\text{W}}^{(1)} = L_{\text{W}}^{(2)} = 6$. In the middle plots of Fig. 9.2, the taps are equally divided between $\mathbf{P}$ and $\mathbf{W}$, i.e., $L_{\text{P}}^{(1)} = L_{\text{P}}^{(2)} = L_{\text{W}}^{(1)} = L_{\text{W}}^{(2)} = 3$. Moreover, the feedback equalizer has 16 taps, corresponding to the time delays of the set $\Phi_{\mathbf{B}} = \{4, \cdots, 19\}$. Based on a closer examination of Fig. 9.2, one could derive the following observations:

- Due to the additional optimization over $\mathbf{T}$, PRS clearly outperforms FRS in terms of $\overline{\text{MSE}}$ with a gain up to 2 dB. Despite the larger number of neighboring symbols in PRS, a significant decrease in BER is observed as well, especially for the hybrid and the adjustable equalization strategy, illustrating the superiority of PRS over FRS. To compute the optimal filter taps when the TIR is predefined to a specific target response, the proposed optimization algorithm is easily modified by ignoring the optimization over $\mathbf{T}$ and setting $\mathbf{T}$ to the appropriate value. In practice, duo-binary is a commonly employed TIR ($\mathbf{T} = [\mathbf{I}_L \;\; \mathbf{I}_L]$) for low-pass channels. However, the performance of duo-binary (not shown) applied to the considered interconnect and equalization scheme is actually considerably worse compared to FRS, emphasizing the main feature of the proposed optimization algorithm, i.e., it computes a suitable $\mathbf{T}$ for every possible channel realization.

- Comparing the three equalization configurations considered in Fig. 9.2

confirms that the best $\overline{\text{MSE}}$ and the best $\overline{\text{BER}}$ performance are achieved when both the pre-equalizer and the feedforward filter are present. When all taps of the linear equalizers are placed at either the transmitter or the receiver, the performance of strategy S-A is impeded by the energy constraint or the noise enhancement, respectively. Dividing the equalization taps between the pre-equalizer and the feedforward filter, however, results in a better trade-off between the energy constraint and the noise enhancement, yielding superior overall performance.

- Regarding the relative performance of the different equalization strategies achieved by the PRS equalization scheme, similar remarks as for the DFE and the THP equalization scheme hold. More precisely, the performance of the adjustable strategy is mostly superior to the performance of the other strategies, whereas the performance of the fixed strategy considerably deteriorates with increasing σ_r, making this equalization strategy unattractive in practice. As for the hybrid strategy, its performance is close to or almost equal to the performance of the adjustable strategy when the variability is relatively low and/or enough equalization parameters are adjustable. Otherwise, the degradation of the hybrid strategy rapidly grows with increasing variability levels. Indeed, when the feedforward filter $\mathbf{W}$ at the receiver is bypassed (left plots of Fig. 9.2), the hybrid strategy performs only marginally better than the fixed strategy as in this case the feedback filter $\mathbf{B}$ is the only adjustable filter in the hybrid strategy. On the other hand, both the $\overline{\text{MSE}}$ and the $\overline{\text{BER}}$ corresponding to the hybrid strategy approach the performance of the adjustable strategy, when the pre-equalizer at the transmitter is bypassed (right plots of Fig. 9.2). This observation is anticipated, since the only difference between strategies S-A and S-H in this case is the (in)ability to adjust the TIR to the specific channel realization. A direct consequence is that identical performance is attained when the TIRs of these strategies are equal, which of course holds for FRS. When both the pre-equalizer and the feedforward filter are present (middle plots of Fig. 9.2), the performance of the hybrid strategy for small σ_r is close to or even better than the performance of the adjustable strategy (see discussion below) in the case of PRS. However, the hybrid strategy becomes less attractive for large σ_r, as its degradation compared to the adjustable strategy rapidly grows with increasing σ_r, especially in terms of $\overline{\text{BER}}$. To explain this observation $\overline{\text{BER}}^{(99\%)}$ is defined as the BER averaged over the 99% of the channel realizations with the smallest BER. As for the adjustable strategy, the relative difference $(\overline{\text{BER}}\text{-}\overline{\text{BER}}^{(99\%)})/\overline{\text{BER}}$ is fairly constant with respect to the channel variability and rather limited, whereas $\overline{\text{BER}}^{(99\%)}$ is sometimes substantially smaller than $\overline{\text{BER}}$ for the hybrid strategy, indicating that only a limited number of channel outliers negatively impact the $\overline{\text{BER}}$. For these outliers, the fixed $\mathbf{T}$ in the hybrid strategy is not a

suitable choice, resulting in inferior performance compared to the other realizations. One main drawback of the hybrid strategy, is that probably for any $\mathbf{T}$ some channel realizations yielding poor BER performance exist, especially when σ_r is moderate to high. As the proposed algorithm minimizes the average MSE, no guarantee can be given that these large BER values are minimized.

- One remarkable result in Fig. 9.2 is that for small σ_r the hybrid strategy possesses a lower $\overline{\text{MSE}}$ than the adjustable strategy when both $\mathbf{P}$ and $\mathbf{W}$ are active (middle plots). This observation results from the inability of the iterative optimization algorithms to converge to the global optimum. Indeed, although alternately computing $(\mathbf{P}^\star, \alpha^\star, \mathbf{T}^\star)$ and $(\mathbf{W}^\star, \mathbf{T}^\star)$ is a fairly straightforward approach to determine a set of suitable equalization parameters, its main drawback is that the convergence in the case of PRS is particularly sensitive to the specific value of $\mathbf{T}$ and the optimization algorithm gets trapped in a local minimum. Consequently, the iterative algorithm does not necessarily guarantee that the adjustable strategy results in a lower $\overline{\text{MSE}}$ than the hybrid strategy, especially when the channel variability is small. The main reason for this local convergence is that due to the discrete nature of $\mathbf{T}$, the final value of the TIR is mostly set during the first few iterations, and then does not alter during later iterations, even though a lower $\overline{\text{MSE}}$ can possibly be achieved by other TIRs. Indeed, because either $\mathbf{P}$ or $\mathbf{W}$ is given in the computation of $\mathbf{T}^\star$ and both filters $\mathbf{P}$ and $\mathbf{W}$ are already reasonably adapted to the current TIR after a few iterations, a strong preference to keep the current TIR is inherent to the computation of the next TIR. In other words, it is unlikely that $\mathbf{T}$ will change after a few iterations. For example, assume that, after the first iterations, the MSE associated with the TIR $\mathbf{T}_1$ is lower than the MSE corresponding to the TIR $\mathbf{T}_2$, then the iterative algorithm will probably pick $\mathbf{T}_1$ as the optimal TIR, even though the final MSE after many iterations could be smaller in the case of $\mathbf{T}_2$ than in the case of $\mathbf{T}_1$.

This last remark is more thoroughly investigated in Fig. 9.3, which displays the $\overline{\text{MSE}}$ achieved by PRS as a function of the iteration index for the adjustable and the hybrid strategy in the case of $\sigma_r = 2\%$, $L_{\text{X}} = 3$, $\text{SNR} = 25\,\text{dB}$, $L_{\text{T}} = 3$, and $\Phi_{\mathbf{B}} = \{4, \cdots, 19\}$. Remark that these parameters are the same as in the middle plots of Fig. 9.2. More precisely, the left plot of Fig. 9.3 gives an overview of the convergence of $\overline{\text{MSE}}$, whereas the right plot of Fig. 9.3 focuses on the first iterations. To facilitate the comparison between these two strategies, the $\overline{\text{MSE}}$ performance of the adjustable strategy is also included when the adjustable TIR is set to the fixed TIR computed by the hybrid strategy. This equalization strategy is denoted by $\text{S-A}_{\mathbf{T}_{\text{hyb}}}$ and its $\overline{\text{MSE}}$ performance is also added in the middle plot of Fig. 9.2. Fig. 9.3 demonstrates that, by design, the adjustable strategy S-A indeed achieves the lowest $\overline{\text{MSE}}$ after the first iteration. However, the hybrid strategy not only achieves a lower $\overline{\text{MSE}}$ than the adjustable strategy after only a couple of iterations, but it also converges to

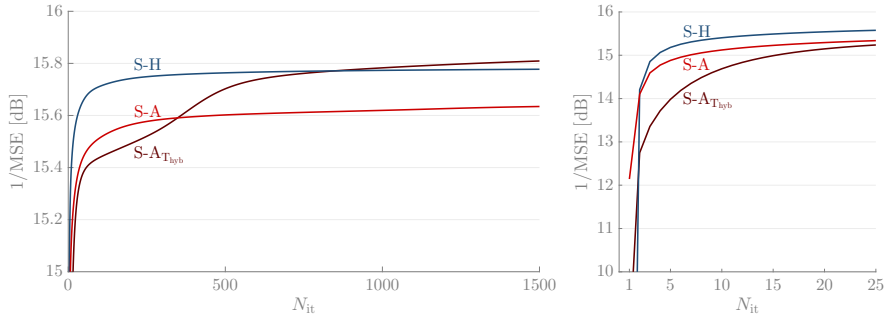

Figure 9.3: Performance in terms of $\overline{\text{MSE}}$ as a function of the iteration index for the strategies S-A, S-H, and S-A$_{\mathbf{T}_{\text{hyb}}}$ in the case of $\sigma_r = 2\%$, $L_{\text{X}} = 3$, SNR $= 25\,\text{dB}$, $L_{\text{T}} = 3$, and $\Phi_{\mathbf{B}} = \{4, \cdots, 19\}$. Initially, the adjustable strategy S-A achieves the best performance, but at convergence the strategies S-H and S-A$_{\mathbf{T}_{\text{hyb}}}$ achieve lower $\overline{\text{MSE}}$, since strategy S-A suffers from convergence to a local optimum.

a $\overline{\text{MSE}}$ which is smaller than the $\overline{\text{MSE}}$ resulting from the adjustable strategy, suggesting that the adjustable strategy suffers in this case from convergence to a local minimum. This latter observation is confirmed by the performance of S-A$_{\mathbf{T}_{\text{hyb}}}$, because this variant of the adjustable strategy also converges, after many iterations, to a lower $\overline{\text{MSE}}$ than the original adjustable and the hybrid strategy. Finally, it is important to stress that the performances of S-A$_{\mathbf{T}_{\text{hyb}}}$ and S-H are not necessarily optimal either and thus not necessarily better than the performance of strategy S-A, for other σ_r or other channels.

To visualize the effect of the addition of the PRS precoder to the linear equalization scheme, i.e., $\Phi_{\mathbf{B}} = \emptyset$, on the performance, Fig. 9.4 plots the performance in terms of $\overline{\text{MSE}}$ (left plot) and $\overline{\text{BER}}$ (right plot) of the linear equalization scheme as a function of the SNR for the adjustable and the hybrid strategy in the case of both FRS and PRS, which are labeled as 'LE-FRS' and 'LE-PRS', respectively. More precisely, $L_{\text{X}} = 7$, $\sigma_r = 5\%$, and the PRS is restricted to spatial-only PRS, i.e., $L_{\text{T}} = 0$. Fig. 9.4 implies that the performances of LE-FRS and LE-PRS are identical at lower SNR, because the noise is dominant in expressions (9.13), (9.16), (9.29), and (9.31) such that the TIR corresponding to PRS coincides with FRS. At larger SNR, the gain of the spatial-only PRS compared to FRS is, however, unmistakable. Indeed, both the $\overline{\text{MSE}}$ and the $\overline{\text{BER}}$ of both the adjustable and the hybrid strategy are considerably better in the case of spatial-only PRS compared to FRS. For example, to reach a target $\overline{\text{BER}}$ of 10^{-8}, the adjustable and the hybrid strategy in the case of PRS achieve a gain in SNR of approximately 5 dB and 3 dB, respectively, compared to the adjustable strategy in the case of FRS.

Another potential benefit of PRS is that it could be used to alleviate the latency constraint imposed by the feedback filter $\mathbf{B}$ on the receiver. To illustrate

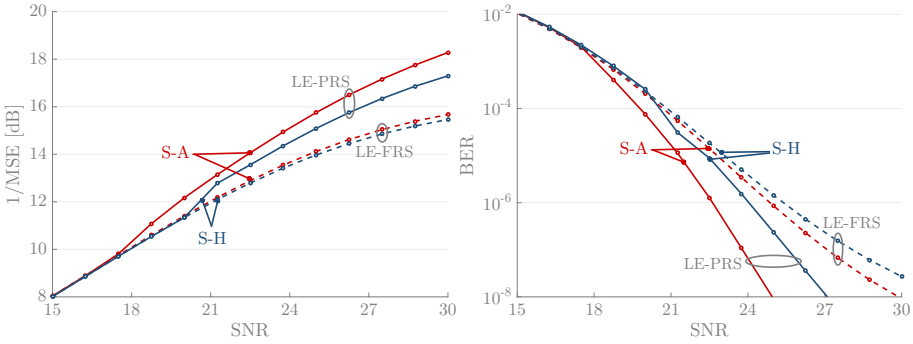

Figure 9.4: Performance of the adjustable and the hybrid strategy in terms of $1/\overline{\text{MSE}}$ (left plot) and $\overline{\text{BER}}$ (right plot) as a function of SNR for $\sigma_r = 5\%$, $L_{\text{X}} = 7$, and $\Phi_{\mathbf{B}} = \emptyset$. Both the performances of FRS ('LE-FRS') and PRS ('LE-PRS' - $L_{\text{T}} = 0$) are included.

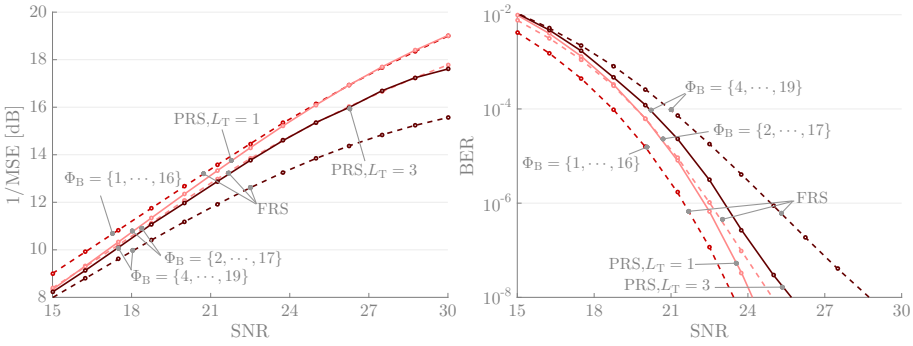

Figure 9.5: Performance of the adjustable strategy in terms of $1/\overline{\text{MSE}}$ (left plot) and $\overline{\text{BER}}$ (right plot) for a 16-tap feedback filter with $m_{\mathbf{B},\min} \in \{1, 2, 4\}$ in the case of both FRS and PRS with $L_{\text{X}} = 3$ and $\sigma_r = 5\%$. Compared to FRS with $m_{\mathbf{B},\min} = 1$, PRS results in less performance loss than FRS when $m_{\mathbf{B},\min} = 2$ and $m_{\mathbf{B},\min} = 4$.

this point, $m_{\mathbf{B},\min}$ is first defined as the smallest causal time delay that is part of the set $\Phi_{\mathbf{B}}$, i.e., $m_{\mathbf{B},\min} = \min \Phi_{\mathbf{B}}$. Traditionally, all L_{B} feedback taps correspond to the first L_{B} causal time delays such that $\Phi_{\mathbf{B}} = \{1, \cdots, L_{\mathrm{B}}\}$ and $m_{\mathbf{B},\min} = 1$. One consequence of this choice is that the decision on the current symbol must be available to the input of the feedback filter $\mathbf{B}$ within one symbol period, which could be cumbersome in practice, especially in high-speed applications. When PRS with $L_{\mathrm{T}} > 0$ is considered, the associated $\Phi_{\mathbf{T}}$ is equal to the set $\{0, \cdots, L_{\mathrm{T}}\}$. Recall that the intersection between $\Phi_{\mathbf{T}}$ and $\Phi_{\mathbf{B}}$ is empty by design, since otherwise all TIR matrices $\mathbf{T}(m)$ with $m \in \Phi_{\mathbf{T}} \cap \Phi_{\mathbf{B}}$ have no effect. Therefore, $m_{\mathbf{B},\min}$ in the case of PRS is equal to or larger than $L_{\mathrm{T}} + 1$, granting the receiver more time to make the decisions available to the feedback filter. The set of the L_{B} active time delays is then given by $\{m_{\mathbf{B},\min}, \cdots, m_{\mathbf{B},\min} + L_{\mathrm{B}} - 1\}$. To examine the effect of different $m_{\mathbf{B},\min}$ and how PRS could be beneficial, Fig. 9.5 shows the $1/\overline{\mathrm{MSE}}$ (left plot) and the $\overline{\mathrm{BER}}$ (right plot) performance of the adjustable strategy as a function of the SNR for a 16-tap feedback filter with $m_{\mathbf{B},\min} \in \{1, 2, 4\}$ in the case of both FRS and PRS. As for FRS, best performance is reached when $m_{\mathbf{B},\min} = 1$, which is logical, as this feedback filter can eliminate the relatively large ISI caused by the most recent past data symbols. When $m_{\mathbf{B},\min}$ must be set larger than 1 due to implementation constraints, a significant deterioration in performance of FRS is observed in Fig. 9.5 in terms of both $\overline{\mathrm{MSE}}$ and $\overline{\mathrm{BER}}$, e.g., to reach a target $\overline{\mathrm{BER}}$ of 10^{-8} an increase in SNR of approximately 1.5 dB and 5.3 dB compared to $m_{\mathbf{B},\min} = 1$ is required for $m_{\mathbf{B},\min} = 2$ and $m_{\mathbf{B},\min} = 4$, respectively. This performance gap between $m_{\mathbf{B},\min} = 1$ and $m_{\mathbf{B},\min} = 2/4$ can, however, be significantly reduced by considering PRS. Indeed, the additional SNR in dB needed compared to FRS with $m_{\mathbf{B},\min} = 1$ to attain a target $\overline{\mathrm{BER}}$ of 10^{-8} is at least 50% smaller for both $m_{\mathbf{B},\min} = 2$ and $m_{\mathbf{B},\min} = 4$, suggesting that the PRS can better handle the ISI generated by the symbols $\mathbf{a}(k-m)$ with $m \in \{1, \cdots, L_{\mathrm{T}}\}$ than FRS, when $m_{\mathbf{B},\min} = L_{\mathrm{T}} + 1$. .

In Fig. 9.6, the sensitivity to the TIR is once more illustrated by comparing the $\overline{\mathrm{MSE}}$ performances of the adjustable and the hybrid strategy as a function of L_{W} for two different iterative algorithms. The first algorithm, labeled as 'First $\mathbf{P}$' is equal to the algorithm proposed in Section 9.2, whereas the second algorithm 'First $\mathbf{W}$' is identical to the first one expect that the order of computing the equalization coefficients in each iteration is interchanged: $(\mathbf{W}^{\star}, \mathbf{T}^{\star})/\mathbf{W}^{\star}$ is first computed for given $(\mathbf{P}, \alpha)$ and then $(\mathbf{P}^{\star}, \alpha^{\star}, \mathbf{T}^{\star})$ for given $\mathbf{W}$. In both plots of Fig. 9.6, the convolution of the equalizers $\mathbf{P}$ and $\mathbf{W}$ contains 29 taps in total and the feedback filter $\mathbf{B}$ possesses 16 taps. In the left plot, the PRS precoder is present with $L_{\mathrm{T}} = 3$ and the active time delays of the feedback filter are given by $\Phi_{\mathbf{B}} = \{4, \cdots, 19\}$, whereas in the right plot FRS is considered, meaning that the PRS precoder is inactive, i.e., $\mathbf{T} = \mathbf{I}_L$, and $\Phi_{\mathbf{B}} = \{1, \cdots, 16\}$. In this case, the PRS equalization scheme in fact simplifies to DFE equalization scheme from Chapter 5. The following remarks can be made.

- When L_{P} and L_{W} somewhat differ, the performance gap between the

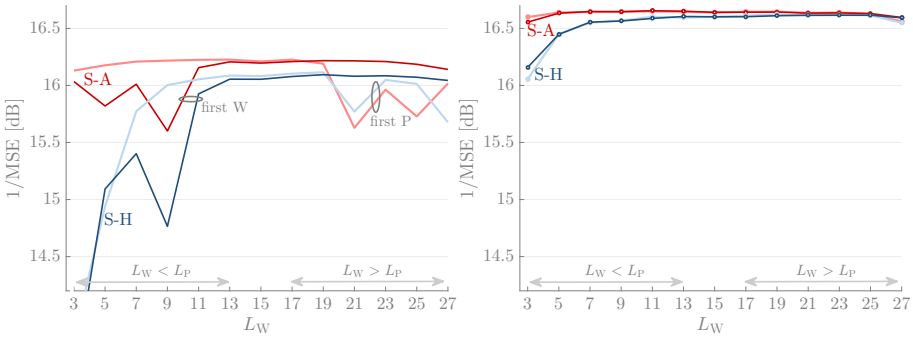

Figure 9.6: Performance of the adjustable and the hybrid strategy in terms of $1/\overline{\text{MSE}}$ as a function of L_{W} with SNR = 25 dB and a 16-tap feedback filter, while the convolution of $\mathbf{P}$ and $\mathbf{W}$ consists of 29 taps in total. In the left plot, the PRS precoder is active ($L_{\text{T}} = 3$, $\Phi_{\mathbf{B}} = \{4, \cdots, 19\}$), whereas the PRS precoder is inactive in the right plot ($\Phi_{\mathbf{B}} = \{1, \cdots, 16\}$). Two iterative optimization algorithms are considered: (i) 'First $\mathbf{P}$' and (ii) 'First $\mathbf{W}$'. Due to the selectivity to the TIR in the case of PRS, the best performance is achieved when the TIR and the longest linear equalizer is computed first.

algorithms 'First $\mathbf{P}$' and 'First $\mathbf{W}$' is apparent in the case of the active PRS precoder (left plot of Fig. 9.6). This performance gap suggests that different TIRs are obtained by the two algorithms. Clearly, the best $\overline{\text{MSE}}$ performance for both the adjustable and the hybrid strategy is achieved when the TIR and the longest linear filter are computed first in each iteration, i.e., algorithm 'First $\mathbf{P}$' when $L_{\text{P}} > L_{\text{W}}$ and algorithm 'First $\mathbf{W}$' when $L_{\text{W}} > L_{\text{P}}$.

- When $L_{\text{P}} = L_{\text{W}} = 7$ in the case of PRS, the average performance of the algorithms 'First $\mathbf{P}$' and 'First $\mathbf{W}$' is approximately identical. By no means, this implies that both algorithms yield nearly identical $\text{MSE}_{\mathbf{g}_{\text{ch}}}$ for each channel realization. To support this claim, Fig. 9.7 plots the histogram of the ratio $\text{MSE}_{\text{W}}/\text{MSE}_{\text{P}}$, where MSE_{W} and MSE_{P} denote the $\text{MSE}_{\mathbf{g}_{\text{ch}}}$ obtained by the algorithms 'First $\mathbf{W}$' and 'First $\mathbf{P}$', respectively. Clearly, for some channel realizations $\text{MSE}_{\text{W}} < \text{MSE}_{\text{P}}$, while for others $\text{MSE}_{\text{W}} > \text{MSE}_{\text{P}}$ such that neither algorithm is in general preferred.

- In the case of FRS, i.e., when the PRS precoder is inactive, the TIR must not be optimized and the sensitivity to the TIR then of course vanishes. This statement is corroborated by the right plot of Fig. 9.6, in which the algorithms 'First $\mathbf{P}$' and 'First $\mathbf{W}$' yield nearly identical performance for all values of L_{W}.

- As for PRS, similar conclusions can be made for the performance regarding the influence of L_{W} as in the FRS case (Fig. 5.8). More precisely,

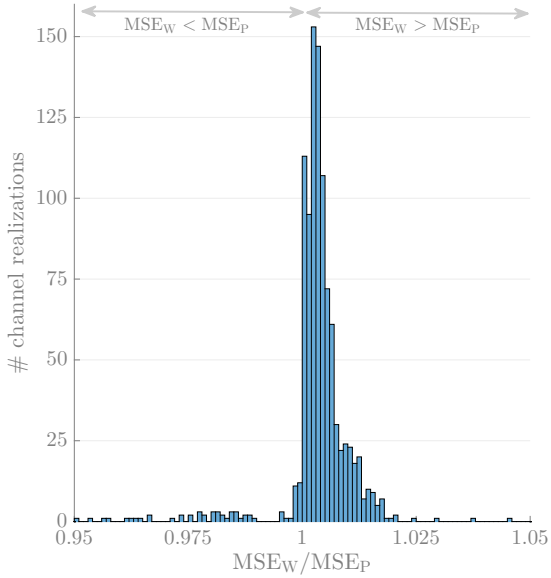

Figure 9.7: Histogram of the ratio $\mathrm{MSE_W}/\mathrm{MSE_P}$ in the case of PRS for 1000 channel realization with $\sigma_r = 5\%$, $L_\mathrm{X} = 7$, SNR $= 25\,\mathrm{dB}$, $\Phi_\mathbf{B} = \{4, \cdots, 19\}$ and $L_\mathrm{T} = 3$. Neither the first algorithm 'First $\mathbf{P}$' nor the second algorithm 'First $\mathbf{W}$' yields the global optimum for all channel realizations.

the performance for the adjustable strategy is reasonably constant when the best-performing algorithm is selected, whereas the performance of the hybrid strategy is poor for low L_W, but quickly improves when L_W increases.

9.5 Conclusions

This chapter expands the PRS equalization scheme from Chapter 7 with a linear pre-equalizer at the transmitter and discusses the performance of the resulting equalization scheme in the case of a communication channel suffering from channel variability. Therefore, the equalization procedure from Chapter 4 is put into practice, yielding three equalization strategies, whose optimized equalization parameters are derived according to the MMSE criterion. In the adjustable strategy, all equalization parameters are designed with respect to the specific channel realization, implying optimal performance at the cost of a relatively large complexity. The fixed strategy induces less complexity, e.g., no return channel between receiver and transmitter, by considering only fixed equalization parameters. However, the fixed strategy possesses an inherent and high sensitivity to the channel variability making this strategy mostly

inadequate in practice. Finally, the goal of the hybrid strategy is to combine low complexity with good performance. To this end, only the transmitter is fixed, whereas the receiver is adjustable to the channel realization.

Numerical results pertaining to the chip-to-chip interconnect from Chapter 2 reveal that PRS indeed outperforms FRS for all proposed equalization strategies, especially at moderate and large SNR. Unsurprisingly, the adjustable equalization strategy yields mostly the best performance, whereas the performance of the fixed strategy rapidly deteriorates with increasing variability. More interesting is that the performance difference between the hybrid strategy and the adjustable strategy is limited when the channel variability is low and/or enough adjustable equalization parameters are present. Moreover, just as in the case of FRS, better performance is achieved in the case of PRS when both the pre-equalizer and the feedforward filter are present. The proposed iterative algorithms, however, do not guarantee convergence to the global optimum. Due to the discrete nature of the TIR, determining the optimal TIR is especially challenging such that the hybrid strategy in some cases even outperforms the adjustable strategy. Moreover, different iterative algorithms could be proposed, but none of them outperforms the others in all cases.

10 Concluding remarks

In this chapter, Section 10.1 first formulates the main conclusions from this dissertation, after which some possible future research topics are briefly explored in Section 10.2. Finally, Section 10.3 provides an overview of our publications regarding this dissertation.

10.1 Main conclusions

The first part of this dissertation focuses on the equalization of a frequency-selective MIMO channel suffering from channel variability. The principle idea is to lower the computational and the implementational complexity of the equalization while preserving a good equalization quality, by adapting only part of the equalization parameters to the channel realization and taking fixed values for remaining equalization parameters. These fixed values are independent of the specific channel realization and, therefore, completely determined by the channel statistics. In this regard, an optimization framework is proposed, in which a general objective function is optimized by alternately determining the optimal adjustable and the optimal fixed equalization parameters. Based on this framework, different equalization strategies can be formulated. First, the adjustable strategy has the best performance but the highest complexity, as all equalization parameters are adjustable to the specific channel realization. Second, all equalization parameters are fixed in the fixed strategy, avoiding the need for channel estimation. Lastly, the hybrid strategy combines adjustable with fixed equalization parameters and thus aims to combine the low complexity of the fixed strategy with the good performance of the adjustable strategy.

Furthermore, two simplifications regarding the computation of the fixed equalization parameters are proposed, yielding two suboptimal approaches. The first suboptimal approach neglects any channel variability, whereas the second suboptimal approach ignores the potential of the adjustable equalization parameters in the computation of the fixed equalization parameters.

This optimization framework is subsequently applied to the linear, the DFE and the THP equalization scheme with linear FIR filters. More precisely, the objective function is selected as the MSE between the transmitted symbol (in the extended symbol set) and the decision variable, as it combines good performance with mathematical simplicity. Moreover, expressions for the SER and the BER for all equalization schemes are derived, after which the performance of the different equalization strategies is illustrated by means of some numerical results for a MIMO chip-to-chip interconnect. From the resulting performance results, one can draw the following conclusions:

- In the considered range of channel variability, the adjustable strategy yields a fairly constant performance that is superior to the performance of the other strategies. The fixed strategy, on the other hand, cannot cope with channel variability, as its performance rapidly deteriorates with increasing channel variability. The hybrid strategy could be a low-complexity alternative to the adjustable strategy with only a limited performance degradation for all channel variability levels, on the condition that (i) enough equalization parameters are adjustable and (ii) the computed channel statistics are based on a representative subset of channel realizations. The performance difference between the adjustable and the hybrid strategy is in general larger in the case of the THP equalization scheme than in the case of the DFE equalization scheme, since the feedback filter is fixed in the former equalization scheme and adjustable in the latter equalization scheme.

- The suboptimal approaches to compute the fixed equalization parameters induce a significant performance loss, especially at higher channel variability. This observation highlights the importance of taking into account the channel variability and the adjustable parameters in the design of the fixed equalization parameters.

- When only limited equalization resources are available, a short feedback filter is to be preferred to long linear filters for both the DFE and THP equalization scheme as the short feedback filter yields better performance. Moreover, to derive the active causal delays associated with this limited number of feedback taps, a simple suboptimal technique that yields nearly optimal performance is to select the dominant taps from a long feedback filter.

- For the investigated equalization schemes, the MMSE equalization parameters are derived by means of an iterative algorithm that alternately

computes a set of optimal parameters. Numerical results confirm that the performance improvement of this iterative algorithm is the highest in the first few iterations, since only marginal performance improvements are noticed after reasonable number of iterations. Only in the case of the hybrid strategy of the THP equalization scheme, the convergence is slightly slower as also the feedback filter is iteratively determined.

- Two alternative optimization methods are proposed to solve the MMSE optimization problem in the case of the adjustable strategy in the DFE equalization scheme: the SF-Newton method and the IBRO method. Although both methods yield on average slightly better performance, their convergence is slower and their computational complexity is larger, making them less attractive in practice. Moreover, these methods are not suitable to compute the equalization parameters for the hybrid strategy.

- To reduce the performance gap between the adjustable and the hybrid strategy in the case of the THP equalization scheme, an adjustable feedback filter is added to the receiver. Numerical results imply that this additional feedback does not alter the performance of the adjustable strategy, but does improve the performance of the hybrid strategy, even when the feedback filter at the receiver contains only a few taps. Unfortunately, selecting the optimal sets of active time delays for both feedback filters is not straightforward, as selecting the largest taps from long feedback filters yields inadequate performance for this equalization scheme; therefore, it is recommended to first determine the sets of all active time delays of the feedback filters and then perform a (re)calculation of all other equalization parameters.

The second part of this dissertation completely focuses on PRS, in which, in contrast to FRS, a controlled amount of interference is allowed at the input of the symbol-by-symbol detector. First, the traditional PRS precoders presented in the literature are generalized to a ST PRS precoder such that the TIR matrix contains not only temporal or only spatial components, but also ST components.

Next, the MMSE design of the equalization coefficients and the TIR parameters is considered in the case of perfect CSI at both the transmitter and the receiver. In this regard, the MSE is first minimized for a given TIR matrix, after which the TIR matrix is optimized. In total, three row-by-row TIR matrix optimization algorithms are proposed. The least complicated algorithm A1 selects the increment from a predefined set that yields the largest decrease of the largest reducible MSE. Structurally, algorithm A2 is identical to algorithm A2, but it opts for the increment inducing the largest guaranteed decrease such that also the potential of future increments is included in the selection criterion. Thirdly, the most complex algorithm A3 updates in each iteration an entire row of the TIR matrix by reformulating the TIR optimization problem as a series of lattice decoding problems. Numerical results regarding a complex-

valued frequency-selective Rayleigh-fading MIMO channel lead to the following conclusions:

- In the case that the active time delays of the feedback filter at the receiver is identical for both FRS and PRS, the general ST PRS precoder is able to significantly outperform FRS for various amounts of distortion in the frequency-selective channel, even when its TIR matrix is restricted to spatial components.

- Both the average performance and the performance associated with individual channel realizations show that algorithm A3 achieves superior performance compared to algorithms A1 and A2, but this superiority comes at the cost of a large complexity that quickly rises with the number of elements in the TIR matrix.

- Algorithm A2 only slightly outperforms the more basic algorithm A1, even though the potential of future updates is incorporated in the selection criterion of the former algorithm. Moreover, both algorithms achieve nearly identical performance as algorithm A3 in the case of low SNR and/or spatial-only TIR. In these situations, the least complicated algorithm A1 is then of course to be preferred.

The assumption of perfect CSIT is often unrealistic in practice, such that naively optimizing the equalization parameters and the TIR matrix, while assuming that the available channel estimate equals the actual channel realization, is often suboptimal. Because of channel estimation errors, the available CSIT is noisy and/or outdated and therefore, a robust design of both the equalization and the TIR parameters is derived for a frequency-selective and time-variant MIMO channel. Here, robustness is defined in a statistical way, meaning that one must optimize the objective function, e.g., the MSE, averaged over the joint PDF of the actual channel and the available CSIT. Numerical results first confirm that the robust design yields indeed better results than the naive approach that ignores all channel estimation errors, especially when the channel estimation quality is poor. Second, the superiority in MSE and BER of the proposed PRS precoder compared to traditional FRS is confirmed for the robust design when the the active time delays of the feedback filter at the receiver is identical for both FRS and PRS. Notable, the robust PRS with poor estimation quality is capable of outperforming FRS with perfect CSIT.

Finally, the design of the general ST PRS precoder is investigated for the channel model that is considered in the first part of this dissertation: a frequency-selective MIMO channel suffering from channel variability. More precisely, the optimization framework used in the first part of this dissertation is applied to the ST PRS precoder. For this channel model, two linear equalizers are assumed to be present, i.e., one at the transmitter and one at the receiver, whereas only one of these linear equalizers are considered to be present in the case of a frequency-selective Rayleigh-fading MIMO channel.

Subsequently, three equalization strategies are proposed: (i) the adjustable strategy possesses only adjustable parameters; (ii) the fixed strategy considers only fixed parameters; and (iii) all parameters associated with the transmitter are fixed in the hybrid strategy, whereas all parameters corresponding to the receiver are adjustable. Again, numerical results confirm the superiority of PRS compared to FRS in MSE and BER performance for all equalization strategies. Just as in the first part of this dissertation, the adjustable strategy yields the best performance, whereas the fixed strategy already results in poor performance for moderate channel variability. Moreover, the performance difference between the hybrid and the adjustable equalization strategy is limited when the variability is small and/or enough equalization parameters are adjustable. However, the iterative algorithms do not guarantee convergence to the global optimum. In particular, determining the optimal TIR is challenging due to its discrete nature such that the hybrid strategy in some cases even outperforms the adjustable strategy.

10.2 Future work

This sections lists and briefly discusses three topics that may constitute the object of future studies.

10.2.1 Different objective functions

In this dissertation, the objective function f_0 is equal to the MSE between the data symbol (in the extended symbol set) and the decision variable. However, this objective function does not guarantee optimal error performance such that other choices for the objective function could in principle result in superior performance. Here several alternatives are explored.

- Instead of minimizing the averaged square of the magnitude of the error signal, one could minimize the average of the nth power of the magnitude of the error signal with $n \in \mathbb{N}_0$, i.e., $\arg\min \mathbb{E}\left[\|\mathbf{e}(k)\|^n\right]$. Analogous to the abbreviation MSE, the average of the nth power is denoted here as MnE. The main motivation to consider $n > 2$ is that the relative weight of the larger errors compared to the smaller errors grows for increasing n. Consequently, the minimum MnE (MMnE) equalizer is expected to induce more smaller but fewer larger errors than the MMSE equalizer. Because the BER at large SNR is typically dominated by the larger errors, better error performance is to be expected for larger n. A closed-form analytical expression for the optimal equalization parameters for $n > 2$ is often unavailable, such that numerical optimization algorithms must be adapted to compute the optimal equalization parameters. As the MnE in general is not convex, the SF-Newton method could be employed to converge to a (local) optimum. Unfortunately, the computational complexity of

evaluating the gradient and the modified Hessian in this method exponentially increases with n such that the maximum value of n is limited by the available computational resources.

- One could also directly minimize the SER or the BER, which has previously been studied in [26, 27]. However, no closed-form analytical solution can be derived and two factors hinder the effective use of numerical methods: (i) the convergence to local optima and (ii) the expectation with respect to all data symbols that contribute to the ISI, which is essentially impossible to compute exactly for channels and/or equalizers with large memory. To overcome these difficulties, the authors in [26, 27] (i) approximate the condition for minimum SER such that global convergence is guaranteed; and (ii) propose a stochastic gradient algorithm to iteratively minimize the SER. The resulting algorithm is called the adaptive minimum-SER (AMSER) algorithm. The main disadvantage of this algorithm, is, however, that many iterations are needed to reach convergence for low SER values.

When all equalization parameters are adjustable to a specific channel realization $\mathbf{g}_{\mathrm{ch}}$, one could also opt for determining the equalization parameters by solving a minimax design.

- One example of a minimax design is the minimization of the maximum ISI, which is also called the distortion. Here, the resulting algorithm is denoted as the minimum distortion (MDist). In fact, MDist has already been presented in [93] for a linear equalizer at the receiver, and can easily be extended to the DFE equalization scheme. One can show that the optimal set of equalization parameters in this case is the solution of a linear program. The main disadvantage of this design is that the effect of the equalization on the noise variance is not taken into account, which could result in an intolerably large noise amplification.

- Another possibility to determine the equalization parameters is to minimize the worst-case SER (w.c. SER), i.e., minimizing the SER corresponding to the symbol sequence inducing the largest SER, which is typically equal to the symbol sequence inducing the largest ISI. Since the SER at high SNR is often dominated by the largest few terms, this equalization design is expected to yield excellent results. Because $\mathrm{Q}(\cdot)$ is a monotonically decreasing function, minimizing the worst-case SER is equivalent to maximizing the argument of the Q-function associated with the worst-case SER. On closer inspection, this argument is usually equal to the ratio of a concave numerator and convex denominator, e.g., (5.68), such that the problem of minimizing the worst-case SER can be expressed as a nonlinear fractional programming problem. A parametric method to solve this type of problems has been presented in [94]. In fact, the w.c. SER equalization design could be interpreted as a generalization

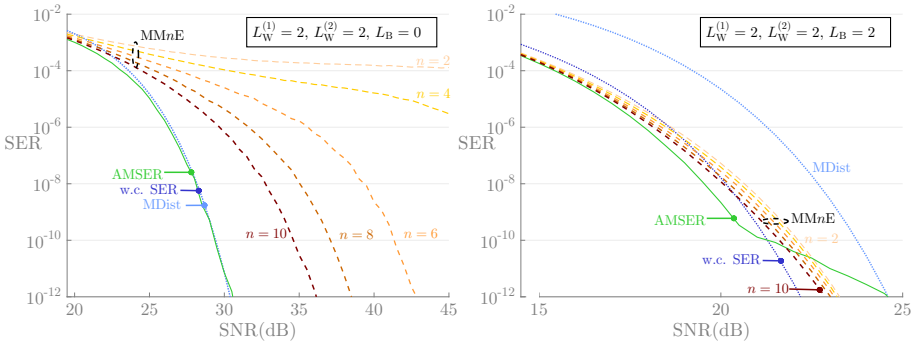

Figure 10.1: SER of an SISO example channel for various alternative methods to compute the equalization parameters. In the left plot, only a 5-tap linear filter at the receiver is present, whereas an additional 2-tap feedback filter is added in the right plot.

of the MDist equalization design, as the parametric method repeatedly solves the minimization of the weighted sum of the distortion and the noise variance.

To illustrate the performance differences between the alternative optimization methods, Fig. 10.1 shows the SER performance when these methods are applied to a SISO example channel that is equalized by means of the DFE equalization scheme, assuming perfect CSI. This channel is characterized by the frequency response $H(z)$ of the cascade of the transmit, the channel and the receive filter. In Fig. 10.1, 4-PAM signaling over the channel that has been studied in [27] is considered, i.e., $H(z) = 0.66 + z^{-1} - 0.66z^{-2}$. In the left plot of Fig. 10.1, only a 5-tap linear filter at the receiver is present in the equalization scheme, whereas an additional 2-tap feedback filter is added in the right plot of Fig. 10.1. Interestingly, these two plots illustrate the weaknesses and strengths of the different optimization methods

- An increase of n in the MnE equalizer results in noticeable lower SER values, especially when the equalization resources are limited. In this case (left plot), the larger n, the more the focus lies on the larger errors that dominate the error performance. When sufficient equalization resources are available (right plot), the equalizer is able to reduce all possible errors, irrespective of the precise value of n. In this case, the performance is less dependent of n.

- The MDist equalizer yields excellent performance in the left plot of Fig. 10.1, whereas it suffers from a prohibitively large noise enhancement in the right plot of Fig. 10.1.

- For the example channel, the SER performance reached by the w.c. SER equalizer is found to be competitive and close to the SER performance

when the SER is directly minimized. Moreover, the w.c. SER equalizer is nearly identical to the MDist equalizer when the latter yields excellent performance, whereas the worst-case SER equalizer avoids an intolerably large noise enhancement when the performance of the MDist equalizer is not good.

- When convergence is reached, the equalization parameters computed with the AMSER algorithm achieve indeed the smallest SER. However, the problem of insufficient convergence is clearly visible for small SER in the right plot of Fig. 10.1.

The numerical results here are restricted to the equalization of a SISO example channel with perfect CSI. Moreover, the equalization scheme solely contains equalization filters at the receiver. The aim of future research could be to expand the various methods presented here to (i) MIMO channels suffering from channel variability and (ii) all equalization schemes considered in this dissertation, where equalization filters could be present at both the transmitter and the receiver. In particular, the application of the minimax design to a channel suffering from channel variability is interesting as the optimization procedure from Chapter 4 is not directly applicable.

10.2.2 Robust minimax design of PRS precoder

In Chapter 8, robustness is defined in a statistical way, i.e., the robust equalization parameters for the PRS equalization scheme are derived by minimizing the MSE averaged over the joint PDF of the channel and the channel estimate. However, robustness can also be defined in a worst-case sense. In this case, the channel estimation error is assumed to be within a bounded uncertainty region. The equalization design then optimizes the performance level that is guaranteed for all estimation errors within that region. More precisely, one could express the channel vector $\mathbf{h}_\kappa$ as the sum of the channel estimate $\hat{\mathbf{h}}_\kappa$ and a bounded error vector $\Delta\mathbf{h}_\kappa$, i.e., $\mathbf{h}_\kappa = \hat{\mathbf{h}}_\kappa + \Delta\mathbf{h}_\kappa$ with $\|\Delta\mathbf{h}_\kappa\|^2 < \epsilon$. The minimax problem that subsequently must be solved is the following :

$$\begin{aligned}(\mathbf{P}_\kappa^\star, \alpha_\kappa^\star, \mathbf{T}_\kappa^\star) = \arg \min_{\mathbf{P},\alpha,\mathbf{T}} \max \ & \mathrm{MSE}_{\mathbf{h}_\kappa} \\ \text{subject to} \ \ & \sigma_\mathrm{a}^2 \mathrm{Tr}\left[\mathbf{P}^H \mathbf{R}_\mathrm{TX} \mathbf{P}\right] \leq N_\mathrm{R} E_\mathrm{TX}. \\ & \|\Delta\mathbf{h}_\kappa\|^2 \leq \epsilon\end{aligned} \tag{10.1}$$

For a given $\mathbf{T}$, one can derive the optimal $(\mathbf{P}_\kappa^\star, \alpha_\kappa^\star)$ by means of a similar reasoning as in [95] that reformulates this optimization problem as a semidefinite programming problem [83]. The optimization over $\mathbf{T}$, however, is still an open problem. One possibility is to optimize $\mathbf{T}$ while naively assuming that the channel estimate is perfect, but this approach is obviously not optimal.

10.2.3 Extension of the ST-PRS precoder

The TIR of the general ST PRS precoder, presented in Chapter 7 and characterized by (7.1), has two constraints: (i) all elements of $\mathbf{T}$ must be Gaussian integers and (ii) the $N_\mathrm{T} \times N_\mathrm{T}$ matrix $\mathbf{T}(0)$ must be unimodular. However, this last constraint could be slightly relaxed by proposing a different relationship between the input sequence $\{\mathbf{c}(k)\}$ and the precoded sequence $\{\mathbf{b}(k)\}$, i.e.,

$$\bar{\mathbf{D}}\mathbf{T}(0)\mathbf{b}(k) \equiv \mathbf{c}(k) - \sum_{m=1}^{L_\mathrm{T}} \mathbf{T}(m)\mathbf{b}(k-m) \pmod{\sqrt{M}}, \tag{10.2}$$

where the integer elements d_i of the diagonal matrix $\bar{\mathbf{D}}$, i.e., $\bar{\mathbf{D}} = \mathrm{diag}(d_1, \cdots, d_{N_\mathrm{T}})$ are all relatively prime to $\sqrt{M}$. Moreover, the precoded symbol vector $\mathbf{b}(k)$ must be an element of the set $\mathcal{C}_\mathrm{PRS}^{N_\mathrm{T}}$. Similar to the relationship from (7.1), one can prove that for each possible $\mathbf{c}(k)$ a unique $\mathbf{b}(k) \in \mathcal{C}_\mathrm{PRS}^{N_\mathrm{T}}$ exists that fulfills the relationship in (10.2). As a result, all elements of the vector $\mathbf{b}(k)$ are then uniformly and independently drawn from the symbol set $\mathcal{C}_\mathrm{PRS}$, just as for the vector $\mathbf{c}(k)$. In fact, the PRS precoder defined in Chapter 7 is equal to the PRS precoder resulting from the relationship from (10.2) when $\bar{\mathbf{D}} = \mathbf{I}_{N_\mathrm{T}}$.

Due to the additional $\bar{\mathbf{D}}$ in (10.2), the target response $\mathbf{u}_\mathrm{T}(k)$ for the PRS precoder presented here must be altered compared to (7.9), i.e.,

$$\mathbf{u}_\mathrm{T}(k) = \bar{\mathbf{D}}\mathbf{T}(0)\mathbf{a}(k) + \sum_{m>0}^{L_\mathrm{T}} \mathbf{T}(m)\mathbf{a}(k-m). \tag{10.3}$$

The relationship between the original data $\mathbf{c}(k)$ and the target response $\mathbf{u}_\mathrm{T}(k)$ is then again given by

$$\mathbf{c}(k) = \left\lfloor \frac{\mathbf{u}_\mathrm{T}(k)}{2\Delta} + \mathbf{c}_\mathrm{off} \right\rfloor_{\sqrt{M}}, \tag{10.4}$$

but with $\mathbf{c}_\mathrm{off}$ now defined as

$$\mathbf{c}_\mathrm{off} = \frac{(1+j)(-\sqrt{M}+1)}{2} \left(\bar{\mathbf{D}}\mathbf{T}(0) + \sum_{m>0}^{L_\mathrm{T}} \mathbf{T}(m) \right) \mathbf{1}. \tag{10.5}$$

Based on the relationship in (10.4), one could optimize the equalization parameters such that the decision variable $\mathbf{u}(k)$ resembles the target response $\mathbf{u}_\mathrm{T}(k)$ as much as possible, allowing to perform symbol-by-symbol detection on the vector $\frac{\mathbf{u}(k)}{2\Delta} + \mathbf{c}_\mathrm{off}$. Just as in Chapter 7, the MSE between $\mathbf{u}(k)$ and $\mathbf{u}_\mathrm{T}(k)$ is a good candidate for the objective function f_0. For this PRS precoder, however, one must not only minimize the coefficients of the linear filters and the TIR matrix $\mathbf{T}$, but also the elements of the diagonal matrix $\bar{\mathbf{D}}$. Consequently, the algorithms presented in Section 7.2 are not applicable anymore. Future research, therefore, could focus on the design and the performance evaluation of an optimization algorithm that jointly minimizes the MSE with respect to all equalization parameters, including the matrix $\bar{\mathbf{D}}$.

10.3 Publications

Our work has been been presented in the following refereed international journals and conference publications:

Journal Publications

- Computers and Electrical Engineering: [96]
- IEEE Transactions on Communications: [97]
- IEEE Transactions on Wireless Communications: [98]

Conference Publications

- IEEE Symposium on Communications and Vehicular Technologies in the Benelux: [99]
- IEEE Global Communications Conference (GLOBECOM): [100]
- European Signal Processing Conference (EUSIPCO): [61]
- IEEE International Symposium on Personal, Indoor, and Mobile Radio Communications (PIMRC): [101]

11 Appendices

11.1 Optimization problem with complex arguments

First, the optimization of a real-valued function $f(z)$ with respect to one complex-valued argument $z = x + jy$ is considered. This function can of course be interpreted as a real-valued function of two real-valued variables, i.e., the real part, x, and the imaginary part y. Consequently, a stationary point of this function can be determined by equating the derivatives of $f(z)$ to both real-valued variables to zero, i.e.,

$$\begin{cases} \frac{\partial f(z)}{\partial x} & = 0 \\ \frac{\partial f(z)}{\partial y} & = 0 \end{cases}. \tag{11.1}$$

The main drawback of this approach is that the function $f(z)$ must be explicitly written as function of x and y before these derivatives can be determined. Alternatively, one could interpreted the function $f(z)$ as a function of two complex variables z and z^*, i.e., $f(z, z^*)$. The derivatives from (11.1) can then be reformulated as

$$\begin{cases} \frac{\partial f(z,z^*)}{\partial x} & = \frac{\partial f(z,z^*)}{\partial z}\frac{\partial z}{\partial x} + \frac{\partial f(z,z^*)}{\partial z^*}\frac{\partial z^*}{\partial x} = \frac{\partial f(z,z^*)}{\partial z} + \frac{\partial f(z,z^*)}{\partial z^*} \\ \frac{\partial f(z,z^*)}{\partial y} & = \frac{\partial f(z,z^*)}{\partial z}\frac{\partial z}{\partial y} + \frac{\partial f(z,z^*)}{\partial z^*}\frac{\partial z^*}{\partial y} = j\frac{\partial f(z,z^*)}{\partial z} - j\frac{\partial f(z,z^*)}{\partial z^*} \end{cases}. \tag{11.2}$$

The derivatives $\frac{\partial f(z,z^*)}{\partial z}$ and $\frac{\partial f(z,z^*)}{\partial z^*}$ are also called the Wirtinger derivatives [20] and can be found by solving the system in (11.2), yielding

$$\begin{cases} \frac{\partial f(z,z^*)}{\partial z} = & \frac{1}{2}\left(\frac{\partial f(z,z^*)}{\partial x} - j\frac{\partial f(z,z^*)}{\partial y}\right) \\ \frac{\partial f(z,z^*)}{\partial z^*} = & \frac{1}{2}\left(\frac{\partial f(z,z^*)}{\partial x} + j\frac{\partial f(z,z^*)}{\partial y}\right) \end{cases}. \tag{11.3}$$

Closer inspection of (11.3) reveals that the condition for a stationary point from (11.1) is equivalent to equating either $\frac{\partial f(z,z^*)}{\partial z}$ or $\frac{\partial f(z,z^*)}{\partial z^*}$ to zero. To compute the Writinger derivatives, the function $f(z)$ must be expressed as a function of z and z^*, which is in general more convenient than expressing $f(z)$ as a function of x and y.

For example, assume that the condition for the stationary points of $f(z) = |z|^4$ must be defined. In the first approach, this $f(z)$ is reformulated as a function $f(x, y)$ of the real part x and the imaginary part y, which results in

$$\begin{aligned} f(x,y) &= (x^2+y^2)^2 \\ &= x^4 + 2x^2y^2 + y^4. \end{aligned} \tag{11.4}$$

Equating the derivatives of (11.4) with respect to x and y to zero then yields the following system of equations:

$$\begin{cases} \frac{\partial f(x,y)}{\partial x} = 4x^3 + 4xy^2 = 0 \\ \frac{\partial f(x,y)}{\partial y} = 4y^3 + 4x^2y = 0 \end{cases}. \tag{11.5}$$

In the second approach, $f(z)$ is first expressed as a function of z and z^*, i.e.,

$$f(z, z^*) = zz^*zz^* \tag{11.6}$$

such that the derivative with respect to $z*$ can be determined by as

$$\begin{aligned} \frac{\partial f(z,z^*)}{\partial z^*} &= 2zzz^*. \\ &= 2\left((x^3+xy^2) + j(x^2y+y^3)\right). \end{aligned} \tag{11.7}$$

Expression (11.7) confirms that equating $\frac{\partial f(z,z^*)}{\partial z^*}$ to zero is indeed equivalent with the system from (11.5).

The function f could also be dependent on a $M \times N$ matrix $\mathbf{Z}$. Of course, to determine a stationary point of the function $f(\mathbf{Z})$, one should equate the derivatives with respect to all elements of $\mathbf{Z}$ to zero. For convenience, the notation $\frac{\partial f(\mathbf{Z})}{\partial \mathbf{Z}^*}$ is introduced, which is defined as

$$\frac{\partial f(\mathbf{Z})}{\partial \mathbf{Z}^*} = \begin{bmatrix} \frac{\partial f(z)}{\partial (\mathbf{Z})^*_{1,1}} & & \frac{\partial f(z)}{\partial (\mathbf{Z})^*_{1,n}} \\ \vdots & \ddots & \vdots \\ \frac{\partial f(z)}{\partial (\mathbf{Z})^*_{m,1}} & & \frac{\partial f(z)}{\partial (\mathbf{Z})^*_{m,n}} \end{bmatrix} \tag{11.8}$$

Table 11.1: Examples of the derivative $\frac{\partial f(\mathbf{Z})}{\partial \mathbf{Z}^*}$.

$f(\mathbf{Z})$	$\frac{\partial f(\mathbf{Z})}{\partial \mathbf{Z}^*}$	additional information
$\mathrm{Tr}\left(\mathbf{Z}\mathbf{A}\mathbf{Z}^H\right)$	$\mathbf{Z}\mathbf{A}$	$\mathbf{A}$ is Hermitian $N \times N$ matrix
$\mathrm{Tr}\left(\mathbf{Z}^H\mathbf{A}\mathbf{Z}\right)$	$\mathbf{A}\mathbf{Z}$	$\mathbf{A}$ is Hermitian $M \times M$ matrix
$\mathrm{Tr}\left(\mathbf{A}\mathbf{Z} + \mathbf{Z}^H\mathbf{A}^H\right)$	$\mathbf{A}^H$	

and the stationary points can then be found by solving

$$\frac{\partial f(\mathbf{Z})}{\partial \mathbf{Z}^*} = \mathbf{0}.$$

Table 11.1 lists the derivative $\frac{\partial}{\partial \mathbf{Z}^*}$ of several example functions encountered in this dissertation.

11.2 Optimization problem A

In this appendix, the following optimization problem is solved with respect to the $(LL_\mathrm{P}) \times L$ matrix $\mathbf{P}$ and the real-valued α:

$$\begin{aligned}(\mathbf{P}^\star, \alpha^\star) = \arg\min_{\mathbf{P},\alpha} \frac{1}{L}\mathrm{Tr}\left(\alpha^2\mathbf{P}^H\mathbf{G}\mathbf{P} - \alpha\mathbf{A}_1\mathbf{P} - \alpha\mathbf{P}^H\mathbf{A}_1^H + \mathbf{A}_2 + \frac{\alpha^2}{\sigma_\mathrm{a}^2}\mathbf{A}_3\right),\\ \text{s. t.}\quad \sigma_\mathrm{a}^2\mathrm{Tr}\left[\mathbf{P}^H\mathbf{R}_\mathrm{TX}\mathbf{P}\right] \leq LE_\mathrm{TX}\end{aligned} \tag{11.9}$$

where $\mathbf{G}$ is a positive semidefinite Hermitian $(LL_\mathrm{P}) \times (LL_\mathrm{P})$ matrix, $\mathbf{A}_1$ is a $L \times (LL_\mathrm{P})$ matrix, $\mathbf{A}_2$ is a $L \times L$ matrix, $\mathbf{A}_3$ is $L \times L$ Hermitian matrix, and $\mathbf{R}_\mathrm{TX}$ is a positive definite $(LL_\mathrm{P}) \times (LL_\mathrm{P})$ Hermitian matrix. The energy constraint is integrated in the design of $(\mathbf{P}^\star, \alpha^\star)$ by considering the Lagrangian Λ with the Lagrangian multiplier λ, which is given by

$$\begin{aligned}\Lambda = &\frac{1}{L}\mathrm{Tr}\left(\alpha^2\mathbf{P}^H\mathbf{G}\mathbf{P} - \alpha\mathbf{A}_1\mathbf{P} - \alpha\mathbf{P}^H\mathbf{A}_1^H + \mathbf{A}_2 + \frac{\alpha^2}{\sigma_\mathrm{a}^2}\mathbf{A}_3\right)\\ &+ \lambda\left(\sigma_\mathrm{a}^2\mathrm{Tr}\left[\mathbf{P}^H\mathbf{R}_\mathrm{TX}\mathbf{P}\right] - LE_\mathrm{TX}\right).\end{aligned} \tag{11.10}$$

At optimum, the complex derivative of Λ with respect to the components of $\mathbf{P}$, α, and λ must be equal to zero, yielding the following system of equations:

$$\begin{cases} \frac{\partial \Lambda}{\partial \mathbf{P}^*} = \frac{1}{L}\left(\alpha^2 \mathbf{G}\mathbf{P} - \alpha \mathbf{A}_1^H\right) + \lambda \sigma_{\mathrm{a}}^2 \mathbf{R}_{\mathrm{TX}}\mathbf{P} = 0 \\ \frac{\partial \Lambda}{\partial \alpha} = \frac{1}{L}\mathrm{Tr}\left(2\alpha \mathbf{P}^H \mathbf{G}\mathbf{P} - \mathbf{A}_1\mathbf{P} - \mathbf{P}^H\mathbf{A}_1^H + \frac{2\alpha}{\sigma_{\mathrm{a}}^2}\mathbf{A}_3\right) = 0. \\ \frac{\partial \Lambda}{\partial \lambda} = \sigma_{\mathrm{a}}^2 \mathrm{Tr}\left[\mathbf{P}^H \mathbf{R}_{\mathrm{TX}}\mathbf{P}\right] - LE_{\mathrm{TX}} = 0 \end{cases} \tag{11.11}$$

Subsequently, equating $\mathrm{Tr}\left(\mathbf{P}^H \frac{\partial \Lambda}{\partial \mathbf{P}^*} + \left(\mathbf{P}^H \frac{\partial \Lambda}{\partial \mathbf{P}^*}\right)^H\right)$ to $\alpha \frac{\partial \Lambda}{\partial \alpha}$ results in

$$2\lambda \sigma_{\mathrm{a}}^2 \mathrm{Tr}\left[\mathbf{P}^H \mathbf{R}_{\mathrm{TX}}\mathbf{P}\right] = \frac{1}{L}\frac{2\alpha^2}{\sigma_{\mathrm{a}}^2}\mathrm{Tr}\left(\mathbf{A}_3\right) \tag{11.12}$$

such that the optimal $\lambda^\star$ is given by

$$\lambda^\star = \frac{\alpha^2}{L\sigma_a^2}\zeta, \tag{11.13}$$

with $\zeta = \frac{\mathrm{Tr}(\mathbf{A}_3)}{LE_{\mathrm{TX}}}$ as $\sigma_{\mathrm{a}}^2 \mathrm{Tr}\left[\mathbf{P}^H \mathbf{R}_{\mathrm{TX}}\mathbf{P}\right]$ can be replaced by LE_{TX} due to the constraint. Next, $\lambda^\star$ from (11.13) is substituted for λ in the first equation of (11.11), after which the optimal $\mathbf{P}^\star$ can be determined as

$$\mathbf{P}^\star = \frac{1}{\alpha}\left(\mathbf{G} + \zeta \mathbf{R}_{\mathrm{TX}}\right)^{-1} \mathbf{A}_1^H. \tag{11.14}$$

The optimal $\alpha^\star$ is then obtained by plugging (11.14) into the energy constraint (last equation of (11.11)), yielding

$$\alpha^\star = \sqrt{\frac{\sigma_{\mathrm{a}}^2}{LE_{\mathrm{TX}}}\mathbf{A}_1\left(\mathbf{G} + \zeta \mathbf{R}_{\mathrm{TX}}\right)^{-1}\mathbf{R}_{\mathrm{TX}}\left(\mathbf{G} + \zeta \mathbf{R}_{\mathrm{TX}}\right)^{-1}\mathbf{A}_1^H}. \tag{11.15}$$

Evaluating the objective function at the optimal $\mathbf{P}^\star$ and optimal $\alpha^\star$ results of course in the minimum value of the objective function $f_{0,\min}$, which can be written as

$$f_{0,\min} = \frac{1}{L}\mathrm{Tr}\left(\mathbf{A}_2 - \mathbf{A}_1\left(\mathbf{G} + \zeta \mathbf{R}_{\mathrm{TX}}\right)^{-1}\mathbf{A}_1^H\right). \tag{11.16}$$

11.3 DFE: computation of adjustable parameters in S-H_{s2}

In this section, expressions are derived for the adjustable $(\mathbf{W}_{\mathrm{adj}}, \mathbf{B})$ for given $(\mathbf{P}, \alpha, \mathbf{W}_{\mathrm{fix}})$ in case of the suboptimal S-H_{s2} approach presented in Subsection 5.2.5.

First of all, the signal $\mathbf{z}(k_w)$ at the output of the adjustable filter $\mathbf{W}_{\rm adj}$ can be written as

$$\begin{aligned}\mathbf{z}(k_w) = &\sum_{\substack{i_{\rm a}\in\Phi_{\mathbf{W}_{\rm adj}}\\ i_{\rm f}\in\Phi_{\mathbf{W}_{\rm fix}}\\ n\in\Phi_{\mathbf{P}}\\ m}} \alpha\mathbf{W}_{\rm adj}(i_{\rm a})\mathbf{W}_{\rm fix}(i_{\rm f})\mathbf{H}(sT_{\rm W}+\epsilon-nT_{\rm P}-mT)\mathbf{P}(n)\mathbf{a}(m)\\ &+\sum_{\substack{i_{\rm a}\in\Phi_{\mathbf{W}_{\rm adj}}\\ i_{\rm f}\in\Phi_{\mathbf{W}_{\rm fix}}}} \alpha\mathbf{W}_{\rm adj}(i_{\rm a})\mathbf{W}_{\rm fix}(i_{\rm f})\mathbf{n}_{\rm RX}(sT_{\rm W}+\epsilon). \end{aligned} \tag{11.17}$$

where $\Phi_{\mathbf{W}_{\rm adj}} = \{-L^{(1)}_{\rm W,adj},\cdots,L^{(2)}_{\rm W,adj}\}$, $\Phi_{\mathbf{W}_{\rm fix}} = \{-L^{(1)}_{\rm W,fix},\cdots,L^{(2)}_{\rm W,fix}\}$, $\Phi_{\mathbf{P}} = \{-L^{(1)}_{\rm P},\cdots,L^{(2)}_{\rm P}\}$, and $s = k_w - i_{\rm a} - i_{\rm f}$. With the assumption that all previously detected symbols are correct, the decision variable $\mathbf{u}(k)$ can then be expressed as

$$\begin{aligned}\mathbf{u}(k) &= \mathbf{z}(kN_{\rm W}) - \sum_{m\in\Phi_{\mathbf{B}}}\mathbf{B}(m)\mathbf{a}(k-m)\\ &= \sum_{m=-L^{(1)}_{\rm G}}^{L^{(2)}_{\rm G}} \alpha\mathbf{W}_{\rm adj}\mathbf{G}_{\mathbf{W}_{\rm fix}}(m)\mathbf{P}\mathbf{a}(k-m) + \alpha\mathbf{W}\bar{\mathbf{n}}_{\mathbf{W}_{\rm fix}}(k) - \sum_{m\in\Phi_{\mathbf{B}}}\mathbf{B}(m)\mathbf{a}(k-m),\end{aligned} \tag{11.18}$$

where $\mathbf{G}_{\mathbf{W}_{\rm fix}}(m)$ is similarly defined as $\mathbf{G}(m)$ in (5.18), but with $\check{\mathbf{H}}_m(i_{\rm a},n)$ replaced by

$$\check{\mathbf{H}}_{m,\mathbf{W}_{\rm fix}}(i_{\rm a},n) = \sum_{i_{\rm f}\in\Phi_{\mathbf{W}_{\rm fix}}} \mathbf{W}_{\rm fix}(i_{\rm f})\mathbf{H}(mT - i_{\rm a}T_{\rm W} - i_{\rm f}T_{\rm W} - nT_{\rm P} + \epsilon).$$

Furthermore, the sequence $\{\mathbf{G}_{\mathbf{W}_{\rm fix}}(m)\}$ has again a limited time duration, i.e., $\mathbf{G}_{\mathbf{W}_{\rm fix}}(m) = \mathbf{0}\ \forall m \notin \{-L^{(1)}_{\rm G},\cdots,L^{(2)}_{\rm G}\}$ with

$$\begin{cases} L^{(1)}_{\rm G} &= \left\lfloor L^{(1)}_{\rm H} + \frac{L^{(1)}_{\rm P}}{N_{\rm P}} + \frac{L^{(1)}_{\rm W,adj}}{N_{\rm W}} + \frac{L^{(2)}_{\rm W,fix}}{N_{\rm W}} \right\rfloor \\ L^{(2)}_{\rm G} &= \left\lfloor L^{(2)}_{\rm H} + \frac{L^{(2)}_{\rm P}}{N_{\rm P}} + \frac{L^{(2)}_{\rm W,adj}}{N_{\rm W}} + \frac{L^{(2)}_{\rm W,fix}}{N_{\rm W}} \right\rfloor \end{cases}. \tag{11.19}$$

Finally, the noise variable $\bar{\mathbf{n}}_{\mathbf{W}_{\rm fix}}(k)$ in (11.18) is constructed as the following stacked vector:

$$\bar{\mathbf{n}}^H_{\mathbf{W}_{\rm fix}}(k) = \left[\mathbf{n}^H_{\mathbf{W}_{\rm fix}}(k,-L^{(1)}_{\rm W,adj})\cdots\mathbf{n}^H_{\mathbf{W}_{\rm fix}}(k,L^{(2)}_{\rm W,adj})\right]^H \tag{11.20}$$

with

$$\mathbf{n}_{\mathbf{W}_{\rm fix}}(k,i) = \sum_{i_{\rm f}=-L^{(1)}_{\rm W,fix}}^{L^{(2)}_{\rm W,fix}} \mathbf{W}_{\rm fix}(i_{\rm f})\mathbf{n}_{\rm RX}(kT - iT_{\rm W} - i_{\rm f}T_{\rm W} + \epsilon). \tag{11.21}$$

Since the expression for $\mathbf{u}(k)$ in (11.18) is structurally identical to the expression for $\mathbf{u}(k)$ in (5.15), the optimal $\mathbf{W}_{\text{adj}}^{\star}$ and $\mathbf{B}^{\star}$ that minimize the conditional $\text{MSE}_{\mathbf{g}_{\text{ch}}}$ for given $(\mathbf{P}, \alpha, \mathbf{W})$ are similarly derived as the optimal $\mathbf{W}^{\star}$ and $\mathbf{B}^{\star}$ in the optimal adjustable and the optimal hybrid strategy, i.e.,

$$\mathbf{B}^{\star}(m) = \alpha \mathbf{W}_{\text{adj}}^{\star} \mathbf{G}_{\mathbf{W}_{\text{fix}}}(m)\mathbf{P} \quad \text{and} \quad \mathbf{W}_{\text{adj}}^{\star} = \mathcal{G}^{H}(0)\mathbf{C}^{-1}. \tag{11.22}$$

In (11.22), $\mathcal{G}(m) = \alpha \mathbf{G}_{\mathbf{W}_{\text{fix}}}(m)\mathbf{P}$ and $\mathbf{C} = \mathcal{G}_{\text{N}}\mathcal{G}_{\text{N}}^{H} + \frac{\alpha^2}{\sigma_{\text{a}}^2}\mathbf{R}_{\bar{\mathbf{n}}_{\mathbf{W}_{\mathbf{fix}}}}$, in which $\mathcal{G}_{\text{N}}$ is constructed as in (5.31) and $\mathbf{R}_{\bar{\mathbf{n}}_{\mathbf{W}_{\mathbf{fix}}}}$ is defined as the autocorrelation of $\bar{\mathbf{n}}_{\mathbf{W}_{\text{fix}}}^{H}(k)$, which can be constructed on the basis of the following correlation matrix:

$$\mathbb{E}\left[\mathbf{n}_{\mathbf{W}_{\text{fix}}}(k,i)\mathbf{n}_{\mathbf{W}_{\text{fix}}}^{H}(k,i')\right] = \sum_{i_{\text{f}}=-L_{\text{W,fix}}^{(1)}}^{L_{\text{W,fix}}^{(2)}} \mathbf{W}_{\text{fix}}(i_{\text{f}}) N_0 \tilde{\mathbf{R}}_{\text{RX}} \mathbf{W}_{\text{fix}}^{H}(i_{\text{f}}+i-i'). \tag{11.23}$$

11.4 DFE: $\text{BER}_{\mathbf{g}_{\text{ch}}}^{(l)}$ expression for M-PAM transmission

In this appendix, the expression for $\text{BER}_{\mathbf{g}_{\text{ch}}}^{(l)}$ from (5.70) is resolved for 4-PAM and 8-PAM constellation with the Gray mapping presented in Fig. 5.5. Only the resulting expression are included here, as the derivations itself are not difficult nor interesting.

First, the shorthanded notation $\text{Q}(a,b)$ is introduced and equal to

$$\text{Q}(a,b) = \text{Q}\left(\frac{a\Delta + b\text{e}_l\Delta + \text{isi}_l(\mathbf{a}_{\text{ISI}})}{\sigma_{\text{w}_l}}\right). \tag{11.24}$$

The $\text{BER}_{\mathbf{g}_{\text{ch}}}^{(l)}$ in case of 4-PAM can then be written as

$$\text{BER}_{\mathbf{g}_{\text{ch}},\text{4-PAM}}^{(l)} = \frac{1}{4}\left[\text{Q}(1,3) + \text{Q}(3,3) - \text{Q}(5,3) + \text{Q}(3,1) + \text{Q}(1,1) + \text{Q}(1,-1)\right], \tag{11.25}$$

whereas the $\text{BER}_{\mathbf{g}_{\text{ch}}}^{(l)}$ in case of 8-PAM is given by

$$\begin{aligned}\text{BER}_{\mathbf{g}_{\text{ch}},\text{8-PAM}}^{(l)} = \frac{1}{12}\big[&\text{Q}\,(1,7) + \text{Q}\,(3,7) - \text{Q}\,(5,7) + \text{Q}\,(7,7) - \text{Q}\,(9,7) \\ &+ \text{Q}\,(11,7) + \text{Q}\,(13,7) + \text{Q}\,(1,-5) + \text{Q}\,(1,5) + \text{Q}\,(3,5) \\ &+ \text{Q}\,(5,5) - \text{Q}\,(7,5) - \text{Q}\,(9,5) + \text{Q}\,(11,5) + \text{Q}\,(3,-3) \\ &+ \text{Q}\,(1,-3) + \text{Q}\,(1,3) + \text{Q}\,(3,3) + \text{Q}\,(5,3) - \text{Q}\,(7,3) \\ &- \text{Q}\,(9,3) - \text{Q}\,(5,-1) + \text{Q}\,(3,-1) + \text{Q}\,(1,-1) + \text{Q}\,(1,1) \\ &+ \text{Q}\,(3,1) + \text{Q}\,(5,1) - \text{Q}\,(7,1)\big].\end{aligned} \tag{11.26}$$

When no error floor is present and the SNR approaches zero, the terms with the smallest argument of $\mathrm{Q}(\cdot)$ are dominant in (11.25) and in (11.26) due to the rapid decrease of $\mathrm{Q}(x)$ for large positive x. Since e_l is typically much smaller than 1, this means that only the terms with $a = 1$ must be considered in this case. Unsurprisingly, the expressions (11.25) and (11.26) then reduce to $\mathrm{SER}_{\mathbf{g}_{\mathrm{ch}}}^{(l)} / \log_2(M)$.

11.5 THP: derivation of the $\mathrm{SER}_{\mathbf{g}_{\mathrm{ch}}}^{(l)}$ expression

The goal of this section is to derive expression (6.42) for the SER of the lth symbol stream conditioned on the channel realization $\mathbf{g}_{\mathrm{ch}}$ in case of the THP equalization scheme from Chapter 6.

First, expression (6.41) is reformulated as

$$\mathrm{SER}_{\mathbf{g}_{\mathrm{ch}}}^{(l)} = 1 - \sum_{q\in\mathbb{Z}} \Pr\left(\mathrm{u}_l \in \mathcal{D}\left((\mathbf{a}_{\mathrm{ex}})_l + 2qM\Delta\right)\right) \tag{11.27}$$

$$= 1 - \sum_{q\in\mathbb{Z}} \Pr\left((1+\mathrm{e}_l)(\mathbf{a}_{\mathrm{ex}})_l + \mathrm{ISI}_l\left(\mathbf{a}_{\mathrm{ex}}^{(\mathrm{ISI})}, \mathbf{v}_{\mathrm{ISI}}\right) + \mathrm{w}_l \in \mathcal{D}((\mathbf{a}_{\mathrm{ex}})_l, q)\right), \tag{11.28}$$

where $\mathcal{D}((\mathbf{a}_{\mathrm{ex}})_l, q)$ denotes the decision area corresponding to $(\mathbf{a}_{\mathrm{ex}})_l + 2qM\Delta$, i.e.,

$$\mathcal{D}((\mathbf{a}_{\mathrm{ex}})_l, q) = [(\mathbf{a}_{\mathrm{ex}})_l + 2qM\Delta - \Delta, (\mathbf{a}_{\mathrm{ex}})_l + 2qM\Delta + \Delta). \tag{11.29}$$

Deriving a closed-form analytical expression for $\mathrm{SER}_{\mathbf{g}_{\mathrm{ch}}}^{(l)}$ from (11.28) is complicated, since both the exact distribution of $(\mathbf{a}_{\mathrm{ex}})_l$ and the exact PDF of $\mathrm{ISI}_l\left(\mathbf{a}_{\mathrm{ex}}^{(\mathrm{ISI})}, \mathbf{v}_{\mathrm{ISI}}\right)$ are hard to obtain and quite complex. However, the probability in (11.28) can be rewritten as the conditional probability for given $(\mathbf{a}_{\mathrm{ex}})_l$, $\mathbf{a}_{\mathrm{ex}}^{(\mathrm{ISI})}$ and $\mathbf{v}_{\mathrm{ISI}}$ summed over all possible $(\mathbf{a}_{\mathrm{ex}})_l$ and $\mathbf{a}_{\mathrm{ex}}^{(\mathrm{ISI})}$ and integrated over all $\mathbf{v}_{\mathrm{ISI}}$. Consequently, $\mathrm{SER}_{\mathbf{g}_{\mathrm{ch}}}^{(l)}$ can be rewritten as

$$\mathrm{SER}_{\mathbf{g}_{\mathrm{ch}}}^{(l)} = 1 - \int \sum_{\substack{\mathfrak{a}_{\mathrm{ex}}, \mathfrak{a}_{\mathrm{ex}}^{(\mathrm{ISI})} \\ q\in\mathbb{Z}}} P\left(\mathfrak{a}_{\mathrm{ex}}, \mathfrak{a}_{\mathrm{ex}}^{(\mathrm{ISI})}, \mathfrak{v}_{\mathrm{ISI}}, q\right) f_{\mathbf{v}_{\mathrm{ISI}}}\left((\mathbf{a}_{\mathrm{ex}})_l = \mathfrak{a}_{\mathrm{ex}}, \mathbf{a}_{\mathrm{ex}}^{(\mathrm{ISI})} = \mathfrak{a}_{\mathrm{ex}}^{(\mathrm{ISI})}, \mathfrak{v}_{\mathrm{ISI}}\right) \mathrm{d}\mathfrak{v}_{\mathrm{ISI}}, \tag{11.30}$$

where the conditional probability $P(\mathfrak{a}_{\mathrm{ex}}, \mathfrak{a}_{\mathrm{ex}}^{(\mathrm{ISI})}, \mathfrak{v}_{\mathrm{ISI}})$ is given by

$$P(\mathfrak{a}_{\mathrm{ex}}, \mathfrak{a}_{\mathrm{ex}}^{(\mathrm{ISI})}, \mathfrak{v}_{\mathrm{ISI}}, q) = \Pr\left(\mathrm{u}_l \in \mathcal{D}\left((\mathbf{a}_{\mathrm{ex}})_l, q\right) \,|\, (\mathbf{a}_{\mathrm{ex}})_l = \mathfrak{a}_{\mathrm{ex}}, \mathbf{a}_{\mathrm{ex}}^{(\mathrm{ISI})} = \mathfrak{a}_{\mathrm{ex}}^{(\mathrm{ISI})}, \mathfrak{v}_{\mathrm{ISI}}\right) \tag{11.31}$$

$$= \Pr\left(\mathrm{e}_l \mathfrak{a}_{\mathrm{ex}} + \mathrm{ISI}_l\left(\mathfrak{a}_{\mathrm{ex}}^{(\mathrm{ISI})}, \mathfrak{v}_{\mathrm{ISI}}\right) + \mathrm{w}_l \in [2qM\Delta - \Delta, 2qM\Delta + \Delta)\right) \tag{11.32}$$

and $f_{\mathbf{v}_{\mathrm{ISI}}}((\mathbf{a}_{\mathrm{ex}})_l{=}\mathfrak{a}_{\mathrm{ex}}, \mathbf{a}_{\mathrm{ex}}^{(\mathrm{ISI})}{=}\mathfrak{a}_{\mathrm{ex}}^{(\mathrm{ISI})}, \mathfrak{v}_{\mathrm{ISI}})$ denotes the joint PDF over $(\mathbf{a}_{\mathrm{ex}})_l$, $\mathbf{a}_{\mathrm{ex}}^{(\mathrm{ISI})}$, and $\mathbf{v}_{\mathrm{ISI}}$. Since w_l is Gaussian distributed with zero-mean and standard deviation σ_{w_l}, one can express the conditional PDF from (11.32) in terms of the Q-function, yielding the following expression for $\mathrm{SER}_{\mathbf{g}_{\mathrm{ch}}}^{(l)}$:

$$\mathrm{SER}_{\mathbf{g}_{\mathrm{ch}}}^{(l)} = 1 - \left(\mathbb{E}_{\mathbf{a}_{\mathrm{ex}},\mathbf{v}_{\mathrm{isi}}} \left[\sum_{q\in\mathbb{Z}} \mathrm{Q}\left(\frac{2qM\Delta - \Delta - \mathrm{e}_l\,(\mathbf{a}_{\mathrm{ex}})_l - \mathrm{ISI}_l\left(\mathbf{a}_{\mathrm{ex}}^{(\mathrm{ISI})}, \mathbf{v}_{\mathrm{ISI}}\right)}{\sigma_{\mathrm{w}_l}} \right) \right.\right.$$
$$\left.\left. -\mathrm{Q}\left(\frac{2qM\Delta + \Delta - \mathrm{e}_l\,(\mathbf{a}_{\mathrm{ex}})_l - \mathrm{ISI}_l\left(\mathbf{a}_{\mathrm{ex}}^{(\mathrm{ISI})}, \mathbf{v}_{\mathrm{ISI}}\right)}{\sigma_{\mathrm{w}_l}} \right) \right] \right). \tag{11.33}$$

In (11.33), the expectation $\mathbb{E}_{\mathbf{a}_{\mathrm{ex}},\mathbf{v}_{\mathrm{isi}}}[\cdot]$ denotes the expectation over all possible $\mathbf{a}_{\mathrm{ex}}$, i.e., both $(\mathbf{a}_{\mathrm{ex}})_l$ and $\mathbf{a}_{\mathrm{ex}}^{(\mathrm{ISI})}$, and $\mathbf{v}_{\mathrm{ISI}}$.

11.6 THP: $\mathrm{BER}_{\mathbf{g}_{\mathrm{ch}}}^{(l)}$ expression for M-PAM transmission

This appendix resolves the $\mathrm{BER}_{\mathbf{g}_{\mathrm{ch}}}^{(l)}$ expression from (6.44) in case of the 4-PAM and 8-PAM constellation with Gray mapping, which are depicted in Fig. 5.5.

An interesting property of the 4-PAM constellation with Gray mapping is that $N_{\neq}(x,y)$ in (6.44) depends only on the difference between two constellation points and not on their exact values. As a result, $\mathrm{BER}_{\mathbf{g}_{\mathrm{ch}},\text{4-PAM}}^{(l)}$ can be expressed as follows

$$\mathrm{BER}_{\mathbf{g}_{\mathrm{ch}},\text{4-PAM}}^{(l)} = \frac{1}{2}\sum_{n\in\mathbb{Z}} N_{\neq}(n2\Delta)\,\Pr\left(\mathrm{u}_l \in \mathcal{D}((\mathbf{a}_{\mathrm{ex}})_l + n2\Delta)\right) \tag{11.34}$$

with

$$N_{\neq}(x) = \begin{cases} 0 & x = 8q\Delta \\ 1 & x = 2\Delta + 4q\Delta \\ 2 & x = 4\Delta + 8q\Delta \end{cases} \quad \text{with } q \in \mathbb{Z}. \tag{11.35}$$

Hence, $\mathrm{BER}_{\mathbf{g}_{\mathrm{ch}},\text{4-PAM}}^{(l)}$ can be rewritten as

$$\begin{aligned} \mathrm{BER}_{\mathbf{g}_{\mathrm{ch}},\text{4-PAM}}^{(l)} = \frac{1}{2}\Big(&\sum_{q\in\mathbb{Z}} \Pr\left(\mathrm{u}_l \in \mathcal{D}\left((\mathbf{a}_{\mathrm{ex}})_l + 2\Delta + 8q\Delta\right)\right) \\ &+ \quad 2\Pr\left(\mathrm{u}_l \in \mathcal{D}\left((\mathbf{a}_{\mathrm{ex}})_l + 4\Delta + 8q\Delta\right)\right) \\ &+ \quad \Pr\left(\mathrm{u}_l \in \mathcal{D}\left((\mathbf{a}_{\mathrm{ex}})_l + 6\Delta + 8q\Delta\right)\right)\Big). \end{aligned} \tag{11.36}$$

Similarly as in Appendix 11.5, the three different terms in (11.5), can be expressed as the expected value of the corresponding conditional probability

for given $(\mathbf{a}_{\text{ex}})_l$, $\mathbf{a}_{\text{ex}}^{(\text{ISI})}$, and $\mathbf{v}_{\text{ISI}}$. Using the symmetry property of the PDF of $(\mathbf{a}_{\text{ex}})_l$ and isi_l, $\text{BER}_{\mathbf{g}_{\text{ch}},4\text{-PAM}}^{(l)}$ can then be written as

$$\text{BER}_{\mathbf{g}_{\text{ch}},4\text{-PAM}}^{(l)} = \mathbb{E}_{\mathbf{a}_{\text{ex}},\mathbf{v}_{\text{isi}}}\Bigg[\sum_{q\in\mathbb{Z}^+}\Big(\text{Q}_{4\text{-PAM}}(1) + \text{Q}_{4\text{-PAM}}(3) - \text{Q}_{4\text{-PAM}}(5) - \text{Q}_{4\text{-PAM}}(7)\Big)\Bigg], \tag{11.37}$$

where the shorthanded notation $\text{Q}_{4\text{-PAM}}$ is defined by

$$\text{Q}_{4\text{-PAM}}(x) = \text{Q}\left(\frac{x\Delta + 8q\Delta - \text{e}_l(\mathbf{a}_{\text{ex}})_l - \text{isi}_l\left(\mathbf{a}_{\text{ex}}^{(\text{ISI})}, \mathbf{v}_{\text{ISI}}\right)}{\sigma_{\text{w}_l}}\right). \tag{11.38}$$

A similar reasoning holds for 8-PAM, yielding

$$\text{BER}_{\mathbf{g}_{\text{ch}},8\text{-PAM}}^{(l)} = \mathbb{E}_{\mathbf{a}_{\text{ex}},\mathbf{v}_{\text{isi}}}\Bigg[\sum_{q\in\mathbb{Z}^+}\Big(\text{Q}_{8\text{-PAM}}(1) + \text{Q}_{8\text{-PAM}}(3) - \text{Q}_{8\text{-PAM}}(13) - \text{Q}_{8\text{-PAM}}(15)\Big)\Bigg], \tag{11.39}$$

where

$$\text{Q}_{8\text{-PAM}}(x) = \text{Q}\left(\frac{x\Delta + 16q\Delta - \text{e}_l(\mathbf{a}_{\text{ex}})_l - \text{isi}_l\left(\mathbf{a}_{\text{ex}}^{(\text{ISI})}, \mathbf{v}_{\text{ISI}}\right)}{\sigma_{\text{w}_l}}\right). \tag{11.40}$$

11.7 THP-DFE: Computation of equalization parameters

The goal of this appendix is to derive the iterative algorithm for all equalization strategies in the case of the THP-DFE equalization scheme, in which a feedback filter at the receiver is added to the equalization scheme with a THP precoder from Chapter 6. More precisely, this appendix discusses the minimization of $\overline{\text{MSE}} = \mathbb{E}_{\mathbf{G}_{\text{ch}}}\left[\text{MSE}_{\mathbf{g}_{\text{ch}}}\right]$, with $\text{MSE}_{\mathbf{g}_{\text{ch}}}$ defined in (6.49), subject to the energy constraint $\sigma_{\text{v}}^2\text{Tr}\left[\mathbf{P}^T\mathbf{R}_{\text{TX}}\mathbf{P}\right] \leq LE_{\text{TX}}$. The following sections present this minimization in the context of the adjustable, the fixed, and the hybrid strategy.

The matrices $\mathbf{B}$ and $\mathbf{T}$ are defined in this section as follows. When the equalization parameters corresponding to the transmitter, i.e., $(\mathbf{P}, \alpha, \mathbf{T})$, are computed for a given set of equalization parameters corresponding to the receiver, i.e., $(\mathbf{W}, \mathbf{B})$, the $L_{\text{B}}L \times L$ stacked matrix $\mathbf{B}$ and the $L_{\text{T}}L \times L$ stacked

matrix $\mathbf{T}$ are constructed by stacking respectively all $\mathbf{B}(m)$ and $\mathbf{T}(m)$, i.e., $\mathbf{B} = [\mathbf{B}^H(\Phi_{\mathbf{B}}(1)) \cdots \mathbf{B}^H(\Phi_{\mathbf{B}}(L_{\mathrm{B}}))]^H$ and $\mathbf{T} = [\mathbf{T}^H(\Phi_{\mathbf{T}}(1)) \cdots \mathbf{T}^H(\Phi_{\mathbf{T}}(L_{\mathrm{T}}))]^H$. On the other hand, when the equalization parameters corresponding to the receiver, i.e., $(\mathbf{W}, \mathbf{B})$, are determined for a given set of equalization parameters corresponding to the transmitter, i.e., $(\mathbf{P}, \alpha, \mathbf{T})$, the $L \times LL_{\mathrm{B}}$ augmented matrix $\mathbf{B}$ and the $L \times LL_{\mathrm{T}}$ augmented matrix $\mathbf{T}$ are constructed as $\mathbf{B} = [\mathbf{B}(\Phi_{\mathbf{B}}(1)) \cdots \mathbf{B}(\Phi_{\mathbf{B}}(L_{\mathrm{B}}))]$ and $\mathbf{T} = [\mathbf{T}(\Phi_{\mathbf{T}}(1)) \cdots \mathbf{T}(\Phi_{\mathbf{T}}(L_{\mathrm{T}}))]$.

Adjustable strategy (S-A)

Because all equalization parameters are adjustable to the channel realization $\mathbf{g}_{\mathrm{ch}}$, i.e., belong to the vector $\mathbf{x}(\mathbf{g}_{\mathrm{ch}})$, $\overline{\mathrm{MSE}}$ can be minimized in this strategy by individually minimizing $\mathrm{MSE}_{\mathbf{g}_{\mathrm{ch}}}$ for each channel realization $\mathbf{g}_{\mathrm{ch}}$. Just as for other equalization schemes, the joint optimization of $\mathrm{MSE}_{\mathbf{g}_{\mathrm{ch}}}$ with respect to all equalization parameters is mathematically too difficult and an iterative optimization algorithm is proposed as an alternative. More precisely, all equalization parameters corresponding to the transmitter, i.e., $(\mathbf{P}, \alpha, \mathbf{T})$, and all equalization parameters corresponding to the receiver, i.e., $(\mathbf{W}, \mathbf{B})$ are alternately computed while the other parameters are assumed to be given and fixed. To compute the optimal $(\mathbf{P}_a^\star, \alpha_a^\star, \mathbf{T}_a^\star)$, the $\mathrm{MSE}_{\mathbf{g}_{\mathrm{ch}}}$ from (6.49) is first rewritten as

$$\begin{aligned}\mathrm{MSE}_{\mathbf{g}_{\mathrm{ch}}} = \frac{1}{L}\mathrm{Tr}\Big[&\mathbf{I}_L + \alpha^2\mathbf{P}^H\boldsymbol{\mathcal{G}}^H\boldsymbol{\mathcal{G}}\mathbf{P} + \frac{\alpha^2}{\sigma_{\mathrm{v}}^2}\mathbf{W}\mathbf{R}_{\tilde{\mathbf{n}}}\mathbf{W}^H + \mathbf{B}^H\mathbf{B} + \mathbf{T}^H\mathbf{Y}_{\mathrm{T}}\mathbf{T} \\ &- \alpha\boldsymbol{\mathcal{G}}(0)\mathbf{P} - \alpha\mathbf{P}^H\boldsymbol{\mathcal{G}}^H(0) - \alpha\mathbf{P}^H\boldsymbol{\mathcal{G}}_{\mathrm{B}}^H\mathbf{B} - \alpha\mathbf{B}^H\boldsymbol{\mathcal{G}}_{\mathrm{B}}\mathbf{P} \\ &- \mathbf{T}^H(\alpha\mathbf{C}_{\mathrm{T}}\mathbf{P} - \mathbf{D}_{\mathrm{T}}) - \left(\alpha\mathbf{P}^H\mathbf{C}_{\mathrm{T}}^H - \mathbf{D}_{\mathrm{T}}^H\right)\mathbf{T}\Big],\end{aligned} \tag{11.41}$$

where

$$\mathbf{Y}_{\mathrm{T}} = \mathbf{I}_{LL_{\mathrm{T}}} + \bar{\mathbf{B}}_1 + \bar{\mathbf{B}}_1^H + \bar{\mathbf{B}}_2, \tag{11.42}$$

$$\mathbf{C}_{\mathrm{T}} = \boldsymbol{\mathcal{G}}_{\mathrm{T}} + \overline{\mathbf{B}\boldsymbol{\mathcal{G}}}, \tag{11.43}$$

and

$$\mathbf{D}_{\mathrm{T}} = \mathbf{I}_{\mathrm{BT}}\mathbf{B} + \bar{\mathbf{B}}_3\mathbf{B}. \tag{11.44}$$

In (11.42), the $LL_{\mathrm{T}} \times LL_{\mathrm{T}}$ block matrices $\bar{\mathbf{B}}_1$ and $\bar{\mathbf{B}}_2$ are defined as follows:

$$\left[\bar{\mathbf{B}}_1\right]_{i,j} = \mathbf{B}^H(j-i) \;\text{ and }\; \left[\bar{\mathbf{B}}_2\right]_{i,j} = \sum_{m\in\Phi_{\mathbf{B}}} \mathbf{B}^H(m+i-j)\mathbf{B}(m) \;\; \forall i,j \in \Phi_{\mathbf{T}}. \tag{11.45}$$

Moreover, the $LL_{\mathrm{T}} \times LL_{\mathrm{P}}$ block matrix $\overline{\mathbf{B}\boldsymbol{\mathcal{G}}}$ in (11.43) is determined according to

$$\left[\overline{\mathbf{B}\boldsymbol{\mathcal{G}}}\right]_{i,1} = \sum_{m\in\Phi_{\mathbf{B}}} \mathbf{B}^H\left(m - \Phi_{\mathbf{T}}(j)\right)\boldsymbol{\mathcal{G}}(m) \;\; \forall i \in \Phi_{\mathbf{T}}, \tag{11.46}$$

whereas the $LL_{\mathrm{T}} \times LL_{\mathrm{B}}$ block matrices $\mathbf{I}_{\mathrm{BT}}$ and $\bar{\mathbf{B}}_3$ in (11.44) are constructed by means of the following relationships:

$$[\mathbf{I}_{\mathrm{BT}}]_{i,j} = \mathbf{I}_L \delta_{\Phi_{\mathbf{T}}(i)-\Phi_{\mathbf{B}}(j)} \text{ and } \left[\bar{\mathbf{B}}_3\right]_{i,j} = \mathbf{B}^H(j-i)\ \forall i \in \Phi_{\mathbf{T}}, j \in \Phi_{\mathbf{B}}. \quad (11.47)$$

The optimal set $(\mathbf{P}_a^\star, \alpha_a^\star, \mathbf{T}_a^\star)$ is subsequently obtained by minimizing $\mathrm{MSE}_{\mathbf{g}_{\mathrm{ch}}}$ from (11.41) first with respect to $\mathbf{T}$, after which $(\mathbf{P}_a^\star, \alpha_a^\star)$ is the result of the minimization of the resulting $\mathrm{MSE}_{\mathbf{g}_{\mathrm{ch}},\mathbf{T}_a^\star}$ subject to the energy constraint. One could verify that this latter minimization problem is again an example of the optimization problem from Appendix 11.2. Applying this optimization procedure then yields

$$\mathbf{T}_a^\star = \mathbf{Y}_{\mathrm{T}}^{-1}\left(\alpha \mathbf{C}_{\mathrm{T}} \mathbf{P}_a^\star - \mathbf{D}_{\mathrm{T}}\right), \quad (11.48)$$

$$\mathbf{P}_a^\star = \frac{1}{\alpha_a^\star} \mathbf{Y}_{\mathrm{P}}^{-1} \mathbf{X}_{\mathrm{P}}, \quad (11.49)$$

and

$$\alpha_a^\star = \sqrt{\frac{\sigma_{\mathrm{v}}^2}{\sigma_{\mathrm{a}}^2 L E_{\mathrm{TX}}} \mathbf{X}_{\mathrm{P}}^H \mathbf{Y}_{\mathrm{P}}^{-1} \mathbf{R}_{\mathrm{TX}} \mathbf{Y}_{\mathrm{P}}^{-1} \mathbf{X}_{\mathrm{P}}}, \quad (11.50)$$

where

$$\mathbf{Y}_{\mathrm{P}} = \frac{\mathrm{Tr}\left(\mathbf{W}\mathbf{R}_{\bar{\mathbf{n}}}\mathbf{W}^H\right)}{L E_{\mathrm{TX}}} \mathbf{R}_{\mathrm{TX}} + \boldsymbol{\mathcal{G}}^H \boldsymbol{\mathcal{G}} - \mathbf{C}_{\mathrm{T}}^H \mathbf{Y}_{\mathrm{T}}^{-1} \mathbf{C}_{\mathrm{T}} \quad (11.51)$$

and

$$\mathbf{X}_{\mathrm{P}} = \boldsymbol{\mathcal{G}}^H(0) + \boldsymbol{\mathcal{G}}_{\mathrm{B}}^H \mathbf{B} - \mathbf{C}_{\mathrm{T}}^H \mathbf{Y}_{\mathrm{T}}^{-1} \mathbf{D}_{\mathrm{T}}. \quad (11.52)$$

After plugging (11.48)-(11.50) into (11.41), the resulting optimized $\mathrm{MSE}_{\mathbf{g}_{\mathrm{ch}},\mathbf{P}_a^\star,\alpha_a^\star,\mathbf{T}_a^\star}$ can be simplified to

$$\mathrm{MSE}_{\mathbf{g}_{\mathrm{ch}},\mathbf{P}_a^\star,\alpha_a^\star,\mathbf{T}_a^\star} = \frac{1}{L}\mathrm{Tr}\left[\mathbf{I}_L + \mathbf{B}^H\mathbf{B} - \mathbf{D}_{\mathrm{T}}^H \mathbf{Y}_{\mathrm{T}}^{-1} \mathbf{D}_{\mathrm{T}} - \mathbf{X}_{\mathrm{P}}^H \mathbf{Y}_{\mathrm{P}}^{-1} \mathbf{X}_{\mathrm{P}}\right]. \quad (11.53)$$

The second step in each iteration is to compute the optimal $(\mathbf{W}_a^\star, \mathbf{B}_a^\star)$ for a given set $(\mathbf{P}, \alpha, \mathbf{T})$. To this end, $\mathrm{MSE}_{\mathbf{g}_{\mathrm{ch}}}$ is first rewritten as

$$\begin{aligned}\mathrm{MSE}_{\mathbf{g}_{\mathrm{ch}}} = \frac{1}{L}\mathrm{Tr}\Big[&\mathbf{I}_L - \alpha^2 \mathbf{W}\mathcal{G}\mathcal{G}^H\mathbf{W}^H + \frac{\alpha^2}{\sigma_{\mathrm{v}}^2}\mathbf{W}\mathbf{R}_{\bar{\mathbf{n}}}\mathbf{W}^H + \mathbf{T}\mathbf{T}^H + \mathbf{B}\mathbf{Y}_{\mathrm{B}}\mathbf{B}^H \\ &- \alpha\mathcal{G}^H(0)\mathbf{W}^H - \alpha\mathbf{W}\mathcal{G}(0) - \alpha\mathcal{G}_{\mathrm{T}}\mathbf{T}^H - \alpha\mathbf{T}\mathcal{G}_{\mathrm{T}}^H\mathbf{W}^H \\ &- \left(\alpha\mathbf{W}\mathbf{C}_{\mathrm{B}} - \mathbf{D}_{\mathrm{B}}\right)\mathbf{B}^H - \mathbf{B}\left(\alpha\mathbf{C}_{\mathrm{B}}^H\mathbf{W}^H - \mathbf{D}_{\mathrm{B}}^H\right)\Big], \end{aligned} \quad (11.54)$$

where

$$\mathbf{Y}_{\mathrm{B}} = \mathbf{I}_{LL_{\mathrm{B}}} + \bar{\mathbf{T}}_1 + \bar{\mathbf{T}}_1^H + \bar{\mathbf{T}}_2, \quad (11.55)$$

$$\mathbf{C}_{\mathrm{B}} = \mathcal{G}_{\mathrm{B}} + \overline{\mathcal{G}\mathbf{T}}, \quad (11.56)$$

and

$$\mathbf{D}_{\mathrm{B}} = \mathbf{T}\mathbf{I}_{\mathrm{BT}} + \mathbf{T}\bar{\mathbf{T}}_3. \quad (11.57)$$

In (11.55), the different matrices in the $LL_{\mathrm{B}} \times LL_{\mathrm{B}}$ block matrices $\bar{\mathbf{T}}_1$ and $\bar{\mathbf{T}}_2$ are given by

$$\left[\bar{\mathbf{T}}_1\right]_{i,j} = \mathbf{T}^H(i-j) \text{ and } \left[\bar{\mathbf{T}}_1\right]_{i,j} = \sum_{m \in \Phi_{\mathbf{T}}} \mathbf{T}(m)\mathbf{T}^H(m+i-j) \ \forall i,j \in \Phi_{\mathbf{B}}. \tag{11.58}$$

Moreover, the $LL_{\mathrm{W}} \times LL_{\mathrm{B}}$ block matrix $\overline{\mathcal{G}\mathbf{T}}$ in (11.56) is defined according to

$$\left[\overline{\mathcal{G}\mathbf{T}}\right]_{1,j} = \sum_{m \in \Phi_{\mathbf{T}}} \mathcal{G}(m)\mathbf{T}^H\left(m - \Phi_{\mathbf{B}}(j)\right) \ \forall j \in \Phi_{\mathbf{B}}, \tag{11.59}$$

while the $LL_{\mathrm{T}} \times LL_{\mathrm{B}}$ block matrix $\bar{\mathbf{T}}_3$ in (11.57) is constructed as follows:

$$\left[\bar{\mathbf{T}}_3\right]_{i,j} = \mathbf{T}^H(i-j) \ \forall i \in \Phi_{\mathbf{T}}, j \in \Phi_{\mathbf{B}}. \tag{11.60}$$

The joint minimization of $\mathrm{MSE}_{\mathbf{g}_{\mathrm{ch}}}$ from (11.54) with respect to $\mathbf{B}$ and $\mathbf{W}$ can easily be performed by first minimizing $\mathrm{MSE}_{\mathbf{g}_{\mathrm{ch}}}$ with respect to $\mathbf{B}$, after which one can further reduce the obtained $\mathrm{MSE}_{\mathbf{g}_{\mathrm{ch}},\mathbf{B}_a^\star}$ by means of a minimization over $\mathbf{W}$. The following optimized variables are obtained:

$$\mathbf{B}_a^\star = (\alpha \mathbf{W}\mathbf{C}_{\mathrm{B}} - \mathbf{D}_{\mathrm{B}})\mathbf{Y}_{\mathrm{B}}^{-1} \text{ and } \mathbf{W}_a^\star = \frac{1}{\alpha}\mathbf{X}_{\mathrm{W}}\mathbf{Y}_{\mathrm{W}}^{-1}, \tag{11.61}$$

where

$$\mathbf{Y}_{\mathrm{W}} = \mathcal{G}\mathcal{G}^H + \frac{\mathbf{R}_{\bar{\mathbf{n}}}}{\sigma_{\mathrm{v}}^2} - \mathbf{C}_{\mathrm{B}}\mathbf{Y}_{\mathrm{B}}^{-1}\mathbf{C}_{\mathrm{B}}^H \tag{11.62}$$

and

$$\mathbf{X}_{\mathrm{W}} = \mathcal{G}^H(0) + \mathbf{T}\mathcal{G}_{\mathrm{T}}^H - \mathbf{D}_{\mathrm{B}}\mathbf{Y}_{\mathrm{B}}^{-1}\mathbf{C}_{\mathrm{B}}^H. \tag{11.63}$$

The corresponding minimized $\mathrm{MSE}_{\mathbf{g}_{\mathrm{ch}}}$ denoted by $\mathrm{MSE}_{\mathbf{g}_{\mathrm{ch}},\mathbf{W}_a^\star,\mathbf{B}_a^\star}$ can then be expressed as

$$\mathrm{MSE}_{\mathbf{g}_{\mathrm{ch}},\mathbf{W}_a^\star,\mathbf{B}_a^\star} = \frac{1}{L}\mathrm{Tr}\left[\mathbf{I}_L + \mathbf{T}\mathbf{T}^H - \mathbf{D}_{\mathrm{B}}\mathbf{Y}_{\mathrm{B}}^{-1}\mathbf{D}_{\mathrm{B}}^H - \mathbf{X}_{\mathrm{W}}\mathbf{Y}_{\mathrm{W}}^{-1}\mathbf{X}_{\mathrm{W}}^H\right]. \tag{11.64}$$

Fixed strategy (S-F)

As all equalization parameters are assumed to be fixed in this strategy, the equalization parameters must be obtained by minimizing the average $\overline{\mathrm{MSE}}$. Similar to the adjustable strategy, this optimization problem is solved by alternately computing the optimal $\left(\mathbf{P}_f^\star, \alpha_f^\star, \mathbf{T}_f^\star\right)$ and the optimal $\left(\mathbf{W}_f^\star, \mathbf{B}_f^\star\right)$ for given $(\mathbf{W}, \mathbf{B})$ and $(\mathbf{P}, \alpha, \mathbf{T})$, respectively.

First, the optimal $\left(\mathbf{P}_f^\star, \alpha_f^\star, \mathbf{T}_f^\star\right)$ and associated minimal $\overline{\mathrm{MSE}}_{\mathbf{P}_f^\star,\alpha_f^\star,\mathbf{T}_f^\star}$ for given $(\mathbf{W}, \mathbf{B})$ are in fact identical to $(\mathbf{P}_a^\star, \alpha_a^\star, \mathbf{T}_a^\star)$ and $\mathrm{MSE}_{\mathbf{g}_{\mathrm{ch}},\mathbf{P}_a^\star,\alpha_a^\star,\mathbf{T}_a^\star}$, but with $\mathbf{C}_{\mathrm{T}}$, $\mathbf{Y}_{\mathrm{P}}$, and $\mathbf{X}_{\mathrm{P}}$ now defined as

$$\mathbf{C}_{\mathrm{T}} = \mathbb{E}_{\mathbf{G}_{\mathrm{ch}}}\left[\mathcal{G}_{\mathrm{T}}\right] + \mathbb{E}_{\mathbf{G}_{\mathrm{ch}}}\left[\overline{\mathbf{B}\mathcal{G}}\right], \tag{11.65}$$

$$\mathbf{Y}_{\mathrm{P}} = \frac{\sigma_{\mathrm{v}}^2 \mathrm{Tr}\left(\mathbf{W}\mathbf{R}_{\bar{\mathbf{n}}}\mathbf{W}^H\right)}{\sigma_{\mathrm{a}}^2 E_{\mathrm{TX}}}\mathbf{R}_{\mathrm{TX}} + \mathbb{E}_{\mathbf{G}_{\mathrm{ch}}}\left[\boldsymbol{\mathcal{G}}^H\boldsymbol{\mathcal{G}}\right] - \mathbf{C}_{\mathrm{T}}^H\mathbf{Y}_{\mathrm{T}}^{-1}\mathbf{C}_{\mathrm{T}}, \tag{11.66}$$

and

$$\mathbf{X}_{\mathrm{P}} = \mathbb{E}_{\mathbf{G}_{\mathrm{ch}}}\left[\boldsymbol{\mathcal{G}}^H(0)\right] + \mathbb{E}_{\mathbf{G}_{\mathrm{ch}}}\left[\boldsymbol{\mathcal{G}}_{\mathrm{B}}^H\right]\mathbf{B} - \mathbf{C}_{\mathrm{T}}^H\mathbf{Y}_{\mathrm{T}}^{-1}\mathbf{D}_{\mathrm{T}}. \tag{11.67}$$

Second, the optimal $\left(\mathbf{W}_f^\star, \mathbf{B}_f^\star\right)$ and corresponding minimal $\overline{\mathrm{MSE}}_{\mathbf{W}_f^\star,\mathbf{B}_f^\star}$ for given $(\mathbf{P}, \alpha, \mathbf{T})$ is respectively given by the expressions (11.61) and (11.64), but with $\mathbf{C}_{\mathrm{B}}$, $\mathbf{Y}_{\mathrm{W}}$, and $\mathbf{X}_{\mathrm{W}}$ defined as

$$\mathbf{C}_{\mathrm{B}} = \mathbb{E}_{\mathbf{G}_{\mathrm{ch}}}\left[\mathcal{G}_{\mathrm{B}}\right] + \mathbb{E}_{\mathbf{G}_{\mathrm{ch}}}\left[\overline{\mathcal{G}\mathbf{T}}\right], \tag{11.68}$$

$$\mathbf{Y}_{\mathrm{W}} = \mathbb{E}_{\mathbf{G}_{\mathrm{ch}}}\left[\mathcal{G}\mathcal{G}^H\right] + \frac{\mathbf{R}_{\bar{\mathbf{n}}}}{\sigma_{\mathrm{v}}^2} - \mathbf{C}_{\mathrm{B}}\mathbf{Y}_{\mathrm{B}}^{-1}\mathbf{C}_{\mathrm{B}}^H, \tag{11.69}$$

and

$$\mathbf{X}_{\mathrm{W}} = \mathbb{E}_{\mathbf{G}_{\mathrm{ch}}}\left[\mathcal{G}^H(0)\right] + \mathbf{T}\mathbb{E}_{\mathbf{G}_{\mathrm{ch}}}\left[\mathcal{G}_{\mathrm{T}}^H\right] - \mathbf{D}_{\mathrm{B}}\mathbf{Y}_{\mathrm{B}}^{-1}\mathbf{C}_{\mathrm{B}}^H. \tag{11.70}$$

Hybrid strategy (S-H)

In the hybrid strategy, all equalization parameters corresponding to the transmitter are fixed, i.e., $(\mathbf{P}, \alpha, \mathbf{T})$, whereas all equalization parameters associated with the receiver are adjustable, i.e., $(\mathbf{W}, \mathbf{B})$. In terms of the optimization procedure from Chapter 4, this means that the former parameters are collected in the vector $\mathbf{y}$, while the latter parameters are the elements of the vector $\mathbf{x}\left(\mathbf{g}_{\mathrm{ch}}\right)$. To determine the optimal $(\mathbf{P}_h^\star, \alpha_h^\star, \mathbf{T}_h^\star, \mathbf{W}_h^\star, \mathbf{B}_h^\star)$, the optimization algorithm from Algorithm 4.1 is applied and the two subproblems therein are discussed below.

First, the optimal $\mathbf{y}^\star$ must be computed for given $\mathbf{x}\left(\mathbf{g}_{\mathrm{ch}}\right)$, i.e., the optimal fixed $(\mathbf{P}_h^\star, \alpha_h^\star, \mathbf{T}_h^\star)$ are computed when $(\mathbf{W}, \mathbf{B})$ are given. Similarly as in the fixed strategy, one can easily verify that the optimal $(\mathbf{P}_h^\star, \alpha_h^\star, \mathbf{T}_h^\star)$ are again given by (11.48)-(11.50) but with $\mathbf{Y}_{\mathrm{T}}$,$\mathbf{C}_{\mathrm{T}}$, $\mathbf{D}_{\mathrm{T}}$,$\mathbf{Y}_{\mathrm{P}}$, and $\mathbf{X}_{\mathrm{P}}$ defined as

$$\mathbf{Y}_{\mathrm{T}} = \mathbf{I}_{LL_{\mathrm{T}}} + \mathbb{E}_{\mathbf{G}_{\mathrm{ch}}}\left[\bar{\mathbf{B}}_1 + \bar{\mathbf{B}}_1^H + \bar{\mathbf{B}}_2\right], \tag{11.71}$$

$$\mathbf{C}_{\mathrm{T}} = \mathbb{E}_{\mathbf{G}_{\mathrm{ch}}}\left[\boldsymbol{\mathcal{G}}_{\mathrm{T}}\right] + \mathbb{E}_{\mathbf{G}_{\mathrm{ch}}}\left[\overline{\mathbf{B}\boldsymbol{\mathcal{G}}}\right], \tag{11.72}$$

$$\mathbf{D}_{\mathrm{T}} = \mathbb{E}_{\mathbf{G}_{\mathrm{ch}}}\left[\mathbf{I}_{\mathrm{BT}}\mathbf{B} + \bar{\mathbf{B}}_3\mathbf{B}\right], \tag{11.73}$$

$$\mathbf{Y}_{\mathrm{P}} = \frac{\mathrm{Tr}\left(\mathbb{E}_{\mathbf{G}_{\mathrm{ch}}}\left[\mathbf{W}\mathbf{R}_{\bar{\mathbf{n}}}\mathbf{W}^H\right]\right)}{LE_{\mathrm{TX}}}\mathbf{R}_{\mathrm{TX}} + \mathbb{E}_{\mathbf{G}_{\mathrm{ch}}}\left(\boldsymbol{\mathcal{G}}^H\boldsymbol{\mathcal{G}}\right) - \mathbf{C}_{\mathrm{T}}^H\mathbf{Y}_{\mathrm{T}}^{-1}\mathbf{C}_{\mathrm{T}}, \tag{11.74}$$

and

$$\mathbf{X}_{\mathrm{P}} = \mathbb{E}_{\mathbf{G}_{\mathrm{ch}}}\left[\boldsymbol{\mathcal{G}}^{H}(0)\right] + \mathbb{E}_{\mathbf{G}_{\mathrm{ch}}}\left[\boldsymbol{\mathcal{G}}_{\mathrm{B}}^{H}\mathbf{B}\right] - \mathbf{C}_{\mathrm{T}}^{H}\mathbf{Y}_{\mathrm{T}}^{-1}\mathbf{D}_{\mathrm{T}}. \tag{11.75}$$

Second, the computation of the optimal adjustable $(\mathbf{W}_h^{\star}, \mathbf{B}_h^{\star})$ for given $(\mathbf{P}, \alpha, \mathbf{T})$ is completely identical as in the adjustable strategy.

11.8 PRS: proposition 1

Proposition 1. *For any nonsingular matrix* $\mathbf{C}$ *with Gaussian integer elements, i.e.,* $\mathrm{C}_{i,j} \in \mathbb{Z}[j]$*, the elements of its inverse* $\mathbf{C}^{-1}$ *are also Guassian integeres if and only if* $|\det(\mathbf{C})| = 1$.

Proof. This proposition has been proved for a real-valued nonsingular integer matrix $\mathbf{C}$ in [102]. The inverse $\mathbf{C}^{-1}$ for a nonsingular $\mathbf{C}$ can be constructed from the adjoint matrix, $\mathrm{adj}(\mathbf{C})$, i.e.,

$$\mathbf{C}^{-1} = \frac{1}{\det(\mathbf{C})}\mathrm{adj}(\mathbf{C}). \tag{11.76}$$

(1) *Sufficient condition:* As $\mathbf{C}$ consists of Gaussian integer elements, then (i) the elements of the adjoint matrix are also Gaussian integers, since its elements are equal to the different cofactors of $\mathbf{C}$. Moreover, when $|\det(\mathbf{C})| = 1$, $\det(\mathbf{C})$ must be an element of the set $\{1, -1, j, -j\}$. Consequently, $\mathbf{C}^{-1}$ also has Gaussian integer elements.

(2) *Necessary condition:* When both $\mathbf{C}$ and $\mathbf{C}^{-1}$ consist of Gaussian integer elements, then both $\det(\mathbf{C})$ and $\det\left(\mathbf{C}^{-1}\right)$ are Gaussian integers. Denote $\det(\mathbf{C}) = x_1 + jy_1$ and $\det\left(\mathbf{C}^{-1}\right) = x_2 + jy_2$ with $x_1, x_2, y_1, y_2 \in \mathbb{Z}$. Because $\det\left(\mathbf{C}^{-1}\right) = \frac{1}{\det(\mathbf{C})}$, the following relations hold:

$$x_2 = \frac{x_1}{x_1^2 + y_1^2}, \;\; y_2 = \frac{-y_1}{x_1^2 + y_1^2}. \tag{11.77}$$

Since all parameters in (11.77) must be integer-valued, it can be verified that either $(x_1, y_1) = (x_2, y_2) = (\alpha, 0)$ or $(x_1, y_1) = -(x_2, y_2) = (0, \alpha)$ with $\alpha = \pm 1$ such that $|\det(\mathbf{C})| = \left|\det\left(\mathbf{C}^{-1}\right)\right| = 1$. □

11.9 PRS: proposition 2

Proposition 2. *When all entries of the sequence* $\{\mathbf{c}(k)\}$ *are independently and uniformly drawn from the set* $\mathcal{C}_{\mathrm{PRS}} = \{0, \cdots, \sqrt{M} - 1\} + j\{0, \cdots, \sqrt{M} - 1\}$ *and* $\mathbf{b}(k)$ *is constructed according to*

$$\mathbf{b}(k) = \left[\mathbf{T}^{-1}(0)\left(\mathbf{c}(k) - \sum_{o=1}^{L_{\mathrm{T}}}\mathbf{T}(m)\mathbf{b}(k-o)\right)\right]_{\sqrt{M}}, \tag{11.78}$$

where $[\cdot]_{\sqrt{M}}$ *equals the element-wise modulo-*$\sqrt{M}$*reduction of the real and the imaginary part, and (i) all entries of the matrix* $\mathbf{T}^{-1}(0)$ *and all matrices* $\mathbf{T}(m)$ *are Gaussian integers and (ii)* $\left|\det(\mathbf{T}^{-1}(0))\right| = 1$*, then also all entries of the sequence* $\{\mathbf{b}(k)\}$ *are independently and uniformly drawn from* $\mathcal{C}_{\mathrm{PRS}}$*.*

Proof. Equation (11.78) can be interpreted as a finite-state machine with input, state, and output at instant k given by $\mathbf{c}(k)$, $\mathbf{s}(k) = \left[\mathbf{b}^T(k-1)\cdots\mathbf{b}^T(k-L_{\mathrm{T}})\right]^T$, and $\mathbf{b}(k)$, respectively. Next all components of the initial state $\mathbf{s}(0)$ are assumed to belong to the set $\mathcal{C}_{\mathrm{PRS}}$. As the elements of $\mathbf{T}^{-1}(0)$ and $\mathbf{T}(m)$ with $m = 1,\ldots,L_{\mathrm{T}}$ are Gaussian integers and $\mathbf{c}(k) \in \mathcal{C}_{\mathrm{PRS}}^{N_{\mathrm{T}}}$ by assumption, it is proven by induction that $\mathbf{b}(k) \in \mathcal{C}_{\mathrm{PRS}}^{N_{\mathrm{T}}}$ and $\mathbf{s}(k) \in \mathcal{C}_{\mathrm{PRS}}^{L_{\mathrm{T}}N_{\mathrm{T}}}$ for $k \in \{0,\cdots,K\}$.

The joint probability mass function of $\mathbf{b}(0),\mathbf{b}(1),\ldots,\mathbf{b}(K)$ conditioned on $\mathbf{s}(0)$ can be expressed as

$$\Pr\left[\mathbf{b}(0){=}\boldsymbol{\beta}(0),\ldots,\mathbf{b}(K){=}\boldsymbol{\beta}(K)|\mathbf{s}(0){=}\boldsymbol{\sigma}(0)\right]{=}\prod_{k=0}^{K}\Pr\left[\mathbf{b}(k){=}\boldsymbol{\beta}(k)|\mathbf{s}(k){=}\boldsymbol{\sigma}(k)\right] \tag{11.79}$$

with $\boldsymbol{\beta}(k) \in \mathcal{C}_{\mathrm{PRS}}^{N_{\mathrm{T}}}$ and $\boldsymbol{\sigma}(k) = \mathcal{C}_{\mathrm{PRS}}^{L_{\mathrm{T}}N_{\mathrm{T}}}$ for $k \in \{0,\cdots,K\}$. When $\mathbf{s}(k) = \boldsymbol{\sigma}(k)$, the only value of $\mathbf{c}(k) \in \mathcal{C}_{\mathrm{PRS}}^{N_{\mathrm{T}}}$ giving rise to $\mathbf{b}(k) = \boldsymbol{\beta}(K)$ is $\mathbf{c}(k) = \boldsymbol{\gamma}(k)$, where $\boldsymbol{\gamma}(k) = \left[\mathbf{T}(0)\boldsymbol{\beta}(k) + \left[\mathbf{T}(1)\cdots\mathbf{T}(L_{\mathrm{T}})\right]\boldsymbol{\sigma}(k)\right]_{\sqrt{M}}$. Hence,

$$\Pr\left[\mathbf{b}(k) = \boldsymbol{\beta}(k)|\mathbf{s}(k) = \boldsymbol{\sigma}(k)\right] = \Pr\left[\mathbf{c}(k) = \boldsymbol{\gamma}(k)\right] = M^{-N_{\mathrm{T}}}, \tag{11.80}$$

where the right-most equation results from the statistical properties of $\mathbf{c}(k)$. Thus (11.79) becomes

$$\Pr\left[\mathbf{b}(0) = \boldsymbol{\beta}(0),\ldots,\mathbf{b}(K) = \boldsymbol{\beta}(K)|\mathbf{s}(0) = \boldsymbol{\sigma}(0)\right] = M^{-(K+1)N_{\mathrm{T}}}, \tag{11.81}$$

which depends neither on $(\boldsymbol{\beta}(0),\ldots,\boldsymbol{\beta}(K))$ nor on $\boldsymbol{\sigma}(0)$. This indicates that all entries of the vectors $\mathbf{b}(0),\ldots,\mathbf{b}(K)$ are independently and uniformly drawn from $\mathcal{C}_{\mathrm{PRS}}$. □

11.10 PRS: derivation of $\mathrm{BER}^{(l)}$ expression for ST PRS

This appendix discusses the detailed derivation of (7.52), which is an approximation of (7.51).

First, all pairs of symbols $\left((\mathbf{c}_{\mathrm{ex}})_l, (\hat{\mathbf{c}}_{\mathrm{ex}})_l\right)$ in the extended symbol constellation that correspond to the pair $(\mathrm{c}_l, \hat{c}_l)$ after the modulo operator are expressed as $\left(\mathrm{c}_l + \mathrm{d}_l\sqrt{M}, \hat{c}_l + \hat{\mathrm{d}}_l\sqrt{M}\right)$ with $\left(\mathrm{d}_l, \hat{\mathrm{d}}_l\right) \in \mathcal{C}_{\mathrm{PRS}}^2$. All symbols $\mathbf{a}(k-m)$ that contribute to isi_l are collected in the vector $\mathbf{a}_{\mathrm{ISI}}$. This appendix employs the notations $p_l(\mathfrak{r})$ and $p_l(\mathfrak{r}|\mathfrak{s})$ to respectively denote the probability mass functions $\Pr(\mathrm{r}_l = \mathfrak{r})$ and $\Pr(\mathrm{r}_l = \mathfrak{r}|\mathrm{s}_l = \mathfrak{s})$, where $\mathbf{r}$ and $\mathbf{s}$ are vectors of discrete

random variables. The probability $\Pr\left(\mathrm{c}_l = \mathfrak{c}, \hat{c}_l = \hat{\mathfrak{c}}\right)$ can then be rewritten as

$$p_l\left(\mathfrak{c}, \hat{\mathfrak{c}}\right) = \sum_{\left(\mathfrak{d}, \hat{\mathfrak{d}}\right) \in \mathbb{Z}[j]^2} \sum_{\mathfrak{a}_{\mathrm{ISI}}} p_l\left(\mathfrak{c}, \hat{\mathfrak{c}}, \mathfrak{d}, \hat{\mathfrak{d}}, \mathfrak{a}_{\mathrm{ISI}}\right) \tag{11.82}$$

$$= \sum_{\left(\mathfrak{d}, \hat{\mathfrak{d}}\right) \in \mathbb{Z}[j]^2} \sum_{\mathfrak{a}_{\mathrm{ISI}}} p_l\left(\hat{\mathfrak{c}}, \hat{\mathfrak{d}} | \mathfrak{c}, \mathfrak{d}, \mathfrak{a}_{\mathrm{ISI}}\right) p_l\left(\mathfrak{d} | \mathfrak{c}, \mathfrak{a}_{\mathrm{ISI}}\right) p_l\left(\mathfrak{c}, \mathfrak{a}_{\mathrm{ISI}}\right). \tag{11.83}$$

Next, the symbols $\mathfrak{c}_{\mathfrak{d}} = \mathfrak{c} + \mathfrak{d}\sqrt{M}$ and $\hat{\mathfrak{c}}_{\hat{\mathfrak{d}}} = \hat{\mathfrak{c}} + \hat{\mathfrak{d}}\sqrt{M}$ in the extended symbol set are defined, allowing to rewrite $p_l\left(\hat{\mathfrak{c}}, \hat{\mathfrak{d}} | \mathfrak{c}, \mathfrak{d}, \mathfrak{a}_{\mathrm{ISI}}\right)$ as

$$p_l\left(\hat{\mathfrak{c}}, \hat{\mathfrak{d}} | \mathfrak{c}, \mathfrak{d}, \mathfrak{a}_{\mathrm{ISI}}\right) = \Pr\left(\mathfrak{c}_{\mathfrak{d}} + \mathrm{isi}_l\left(\mathfrak{a}_{\mathrm{ISI}}\right) + \left(\mathbf{n}_{\mathrm{v}}\right)_l \in \mathcal{D}\left(\hat{\mathfrak{c}}_{\hat{\mathfrak{d}}}\right)\right), \tag{11.84}$$

where $\mathcal{D}(\cdot)$ represents the decision area of a symbol in the extended symbol set, and the notation $\mathrm{isi}_l\left(\mathfrak{a}_{\mathrm{ISI}}\right)$ emphasizes the dependence of isi_l on the vector $\mathbf{a}_{\mathrm{ISI}}$. Because the right-hand side of (11.84) is affected by only the difference $\hat{\mathfrak{c}} + \hat{\mathfrak{d}}\sqrt{M} - \mathfrak{c} - \mathfrak{d}\sqrt{M} - \mathrm{isi}_l\left(\mathfrak{a}_{\mathrm{ISI}}\right)$, (11.84) reduces to

$$p_l\left(\hat{\mathfrak{c}}, \hat{\mathfrak{d}} | \mathfrak{c}, \mathfrak{d}, \mathfrak{a}_{\mathrm{ISI}}\right) = \Pr\left(\mathfrak{c} + \mathrm{isi}_l\left(\mathfrak{a}_{\mathrm{ISI}}\right) + \left(\mathbf{n}_{\mathrm{v}}\right)_l \in \mathcal{D}\left(\hat{\mathfrak{c}}_{\mathfrak{d}_-}\right)\right), \tag{11.85}$$

where $\hat{\mathfrak{c}}_{\mathfrak{d}_-} = \hat{\mathfrak{c}} + \mathfrak{d}_-\sqrt{M}$ with $\mathfrak{d}_- = \hat{\mathfrak{d}} - \mathfrak{d}$. After substituting (11.85) into (11.83) and replacing the sum over $\left(\mathfrak{d}, \hat{\mathfrak{d}}\right) \in \mathbb{Z}[j]^2$ by a summation over $\left(\mathfrak{d}, \mathfrak{d}_-\right) \in \mathbb{Z}[j]^2$, only $p_l\left(\mathfrak{d} | \mathfrak{c}, \mathfrak{a}_{\mathrm{ISI}}\right)$ in (11.83) depends on $\mathfrak{d}$. As the summation of $p_l\left(\mathfrak{d} | \mathfrak{c}, \mathfrak{a}_{\mathrm{ISI}}\right)$ over all $\mathfrak{d}$ amounts to 1, $p_l\left(\mathfrak{c}, \hat{\mathfrak{c}}\right)$ from (11.83) can be written as

$$p_l\left(\mathfrak{c}, \hat{\mathfrak{c}}\right) = \sum_{\mathfrak{d}_- \in \mathbb{Z}[j]} \sum_{\mathfrak{a}_{\mathrm{ISI}}} F\left(\mathfrak{c} - \hat{\mathfrak{c}}_{\mathfrak{d}_-}, \mathfrak{a}_{\mathrm{ISI}}, \left(\mathbf{n}_{\mathrm{v}}\right)_l\right) p_l\left(\mathfrak{c}, \mathfrak{a}_{\mathrm{ISI}}\right), \tag{11.86}$$

where $F\left(\mathfrak{c} - \hat{\mathfrak{c}}_{\mathfrak{d}_-}, \mathfrak{a}_{\mathrm{ISI}}, \left(\mathbf{n}_{\mathrm{v}}\right)_l\right)$ is a shorthanded notation for $\Pr(\mathfrak{c} + \mathrm{isi}_l\left(\mathfrak{a}_{\mathrm{ISI}}\right) + \left(\mathbf{n}_{\mathrm{v}}\right)_l \in \mathcal{D}\left(\hat{\mathfrak{c}}_{\mathfrak{d}_-}\right))$. Plugging (11.86) into (7.51) subsequently yields

$$\mathrm{BER}^{(l)} = \sum_{\mathfrak{a}_{\mathrm{ISI}}} \sum_{\mathfrak{c} \in \mathcal{C}_{\mathrm{PRS}}} G(\mathfrak{c}, \mathfrak{a}_{\mathrm{ISI}}) \Pr\left(\mathrm{c}_l = \mathfrak{c}, \mathbf{a}_{\mathrm{ISI}} = \mathfrak{a}_{\mathrm{ISI}}\right), \tag{11.87}$$

where

$$G\left(\mathfrak{c}, \mathfrak{a}_{\mathrm{ISI}}\right) = \sum_{\hat{\mathfrak{c}}_{\mathfrak{d}_-} \in \mathbb{Z}[j]} \frac{N_{\neq}\left(\mathfrak{c}, \hat{\mathfrak{c}}_{\mathfrak{d}_-}\right)}{\log_2(M)} F\left(\mathfrak{c} - \hat{\mathfrak{c}}_{\mathfrak{d}_-}, \mathfrak{a}_{\mathrm{ISI}}, \left(\mathbf{n}_{\mathrm{v}}\right)_l\right) \tag{11.88}$$

and the function $N_{\neq}\left(\mathfrak{c}, \hat{\mathfrak{c}}\right)$ is generalized to the extended symbol set, i.e., $N_{\neq}\left(\mathfrak{c}, \hat{\mathfrak{c}}\right) = N_{\neq}\left(\mathfrak{c}, \hat{\mathfrak{c}}_{\mathfrak{d}_-}\right)$ for all $\mathfrak{d}_- \in \mathbb{Z}[j]$. Unfortunately, the summation over all $\hat{\mathfrak{c}}_{\mathfrak{d}_-}$ in (7.51) consists of an infinite number of terms, prohibiting the exact evaluation of $\mathrm{BER}^{(l)}$. However, the properties of the binary reflected Gray mapping impose not only that horizontally and vertically neighboring symbols in the

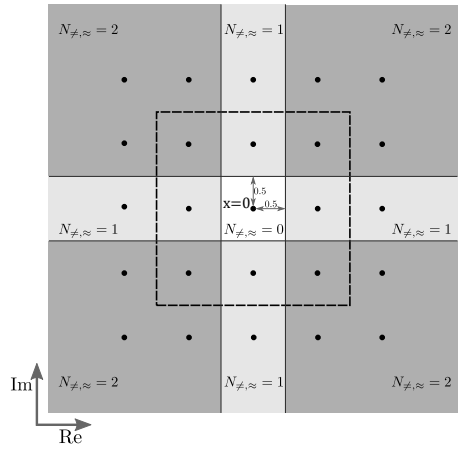

Figure 11.1: Visualization of the approximation $N_{\neq,\approx}(x)$. The white, light gray, and dark gray areas represent the areas for which $N_{\neq,\approx}(x) = 0$, $N_{\neq,\approx}(x) = 1$, and $N_{\neq,\approx}(x) = 2$, respectively.

extended symbol set only differ one bit, but also that diagonally neighboring symbols differ only in two bits, justifying the approximation $N_{\neq}(\mathfrak{c}, \hat{\mathfrak{c}}_{\mathfrak{d}\_}) \approx N_{\neq,\approx}\left(\mathfrak{c} - \hat{\mathfrak{c}}_{\mathfrak{d}\_}\right)$, where

$$N_{\neq,\approx}(x) = \begin{cases} 0 & x = 0 \\ 1 & (\mathrm{Re}[x] = 0) \vee (\mathrm{Im}[x] = 0) \\ 2 & \text{otherwise} \end{cases}. \tag{11.89}$$

The approximation $N_{\neq,\approx}(x)$ is visualized in Fig. 11.1. Interestingly, the number of errors in the decision areas adjacent to $x = 0$ within the dashed square is not altered by the approximation meaning that $N_{\neq}(\mathfrak{c}, \hat{\mathfrak{c}}_{\mathfrak{d}\_}) = N_{\neq,\approx}\left(\mathfrak{c} - \hat{\mathfrak{c}}_{\mathfrak{d}\_}\right)$ when the difference $\mathfrak{c} - \hat{\mathfrak{c}}_{\mathfrak{d}\_}$ is within the dashed square. For $M = 4$, the approximation is actually an upper bound as only additional errors are introduced. Replacing in (11.88) $N_{\neq}\left(\mathfrak{c}, \hat{\mathfrak{c}}_{\mathfrak{d}\_}\right)$ by $N_{\neq,\approx}\left(\mathfrak{c} - \hat{\mathfrak{c}}_{\mathfrak{d}\_}\right)$ yields the function $G_{\approx}(\mathbf{a}_{\mathrm{ISI}})$ that no longer depends on $\mathfrak{c}$, i.e.,

$$G_{\approx}(\mathbf{a}_{\mathrm{ISI}}) = \sum_{x \in \mathbb{Z}[j]} \frac{N_{\neq,\approx}(x)}{\log_2(M)} F(x, \mathbf{a}_{\mathrm{ISI}}, (\mathbf{n}_{\mathrm{v}})_l) \tag{11.90}$$

The infinite summation over x in (11.90) can than be replaced by the summation over the two regions characterized by $N_{\neq,\approx}(x) = 1$ and $N_{\neq,\approx}(x) = 2$,

respectively. This results in

$$G_{\approx}(\mathfrak{a}_{\mathrm{ISI}}) = Q\left(\frac{0.5 - \mathrm{Re}\left[\mathrm{isi}_l(\mathbf{a}_{\mathrm{ISI}})\right]}{\sigma_{(\mathbf{n}_{\mathrm{v}})_l}}\right) + Q\left(\frac{0.5 + \mathrm{Re}\left[\mathrm{isi}_l(\mathbf{a}_{\mathrm{ISI}})\right]}{\sigma_{(\mathbf{n}_{\mathrm{v}})_l}}\right) + Q\left(\frac{0.5 - \mathrm{Im}\left[\mathrm{isi}_l(\mathbf{a}_{\mathrm{ISI}})\right]}{\sigma_{(\mathbf{n}_{\mathrm{v}})_l}}\right) + Q\left(\frac{0.5 + \mathrm{Im}\left[\mathrm{isi}_l(\mathbf{a}_{\mathrm{ISI}})\right]}{\sigma_{(\mathbf{n}_{\mathrm{v}})_l}}\right), \quad (11.91)$$

where $Q(\cdot)$ represents the tail distribution of the standard normal distribution and $\sigma_{(\mathbf{n}_{\mathrm{v}})_l}$ equals the standard deviation of the real part of, which is given by $\sigma_{(\mathbf{n}_{\mathrm{v}})_l} = \sqrt{\frac{\left(\mathbf{W}\mathbf{R}_{\tilde{\mathbf{n}}}\mathbf{W}^H\right)_{l,l}}{8\Delta^2}}$. Substituting $G_{\approx}(\mathfrak{a}_{\mathrm{ISI}})$ for $G(\mathfrak{c}, \mathfrak{a}_{\mathrm{ISI}})$ in (11.87) yields the approximation of $\mathrm{BER}^{(l)}$. Moreover, the rotational symmetry of the QAM constellation can be exploited by remarking that $\Pr(\mathfrak{a}_{\mathrm{ISI}}) = \Pr(-\mathfrak{a}_{\mathrm{ISI}}) = \Pr(j\mathfrak{a}_{\mathrm{ISI}}) = \Pr(-j\mathfrak{a}_{\mathrm{ISI}})$, simplifying the approximation to

$$\mathrm{BER}^{(l)} \approx \frac{1}{\log_2(M)}\mathbb{E}_{\mathbf{a}_{\mathrm{ISI}}}\left[4\mathrm{Q}\left(\frac{0.5 - \mathrm{Re}\left[\mathrm{isi}_l(\mathbf{a}_{\mathrm{ISI}})\right]}{\sigma_{(\mathbf{n}_{\mathrm{v}})_l}}\right)\right]. \quad (11.92)$$

Because $N_{\neq,\approx}(x)$ maintains the number of bit errors in the decision areas adjacent to the decision area of the data symbol, the approximation (11.92) is expected to be very accurate when $\mathrm{isi}_l(\mathbf{a}_{\mathrm{ISI}})$ and $\sigma_{(\mathbf{n}_{\mathrm{v}})_l}$ are small compared to 1, e.g., in case of powerful equalization and large SNR.

11.11 Robust PRS: linear MMSE estimation from pilot symbols

This appendix discusses how the channel estimate in the κth frame is derived based on the pilot symbols. The structure of each frame is already shown in Fig. 8.2: each frame contains not only a block of pilot symbols and a block of data symbols, but also two guard intervals to avoid that any interference from the pilot symbols is present in the processing of the data symbols and vice versa. As for the pilot symbols, only the signals received at the $N_{\mathrm{p}} - L_{\mathrm{H}} + 1$ consecutive instants, where the channel memory is entirely filled with pilot symbols, are exploited for channel estimation. In Fig. 8.2, the associated interval of time indices for frame κ is given by $[k_{\mathrm{p},\kappa} + L_{\mathrm{H}}^{(2)}, k_{\mathrm{p},\kappa} + N_{\mathrm{p}} - 1 - L_{\mathrm{H}}^{(1)}]$. This restriction yields the $N_{\mathrm{R}} \times (N_{\mathrm{p}} - L_{\mathrm{H}} + 1)$ observation matrix $\mathbf{Y}_\kappa$, which can be written as

$$\mathbf{Y}_\kappa = \mathbf{H}_\kappa \mathbf{A}_\kappa + \mathbf{N}_\kappa, \quad (11.93)$$

where the ith column of the $N_{\mathrm{T}} L_{\mathrm{H}} \times (N_{\mathrm{p}} - L_{\mathrm{H}} + 1)$ pilot symbol matrix $\mathbf{A}_\kappa$ equals $[\mathbf{a}_{p,\kappa}^H(L_{\mathrm{H}} + i - 2), \cdots, \mathbf{a}_{p,\kappa}^H(i-1)]^H$. Here, the vector $\mathbf{a}_{p,\kappa}(n)$ denotes the $N_{\mathrm{T}} \times 1$ pilot symbol vector transmitted during the nth symbol interval in the κth block. Moreover, the relationship from (11.93) can also be represented as

$$\mathbf{y}_\kappa = \mathbf{A}\mathbf{h}_\kappa + \mathbf{n}_\kappa, \quad (11.94)$$

where $\mathbf{A} = \mathbf{A}_\kappa^T \otimes \mathbf{I}_{N_\mathrm{R}}$ and $\mathbf{y}_\kappa$, $\mathbf{n}_\kappa$, and $\mathbf{h}_\kappa$ are obtained by stacking the columns of $\mathbf{Y}_\kappa$, $\mathbf{N}_\kappa$, and $\mathbf{H}_\kappa$, respectively. Because all noise samples are assumed to be uncorrelated, the covariance matrix of the noise contribution $\mathbf{n}_\kappa$ is given by $\mathbf{R}_{\mathrm{n}_\kappa} = N_0 \mathbf{I}_{N_\mathrm{R}(N_\mathrm{P}-L_\mathrm{H}+1)}$. From (11.94), one can compute the linear MMSE estimate of $\mathbf{h}_\kappa$ as $\hat{\mathbf{h}}_\kappa = \mathbf{X}\mathbf{y}_\kappa$ with

$$\mathbf{X} = \left(N_0 \mathbf{R}_{\mathrm{h}_\kappa}^{-1} + \mathbf{A}^H \mathbf{A}\right)^{-1} \mathbf{A}^H, \tag{11.95}$$

where $\mathbf{R}_{\mathrm{h}_\kappa}$ is the covariance matrix of $\mathbf{h}_\kappa$. To express this covariance matrix, the $L_\mathrm{H} \times L_\mathrm{H}$ matrices $\mathbf{U}(i)$ are defined as

$$(\mathbf{U}(i))_{m,m'} = \mathbb{E}\left[(\mathbf{H}_{\kappa+i}(m))_{l,l'} \left(\mathbf{H}_\kappa(m')\right)^*_{l,l'}\right] \tag{11.96}$$

for $(m, m') \in \left\{-L_\mathrm{H}^{(1)}, \cdots, L_\mathrm{H}^{(2)}\right\}^2$. The covariance matrix $\mathbf{R}_{\mathrm{h}_\kappa}$ is then given by $\mathbf{R}_{\mathrm{h}_\kappa} = \mathbf{U}(0) \otimes \mathbf{I}_{N_\mathrm{R} \times N_\mathrm{T}}$. Next, the vector $\bar{\mathbf{h}}_\kappa$ represents the perfect CSI and is defined as $\bar{\mathbf{h}}_\kappa = \mathbf{h}_\kappa$ in the case of configuration C2 and as $\bar{\mathbf{h}}_\kappa = [\mathbf{h}_\kappa^H \cdots \mathbf{h}_{\kappa-\mathcal{K}}^H]^H$ in the case of configurations C1 and C3. Based on this definition and the decomposition $\hat{\mathbf{h}}_\kappa = \mathbf{X}\mathbf{A}\mathbf{h}_\kappa + \mathbf{X}\mathbf{n}_\kappa$, one can express the available CSIT as follows

$$\hat{\bar{\mathbf{h}}}_\kappa = \mathbf{E}\bar{\mathbf{h}}_\kappa + \mathbf{F}\bar{\mathbf{n}}_\kappa, \tag{11.97}$$

where

$$\mathbf{E} = \begin{cases} \mathbf{I}_{\mathcal{K}+1} \otimes (\mathbf{X}\mathbf{A}) & \text{C1} \\ \mathbf{X}\mathbf{A} & \text{C2}\,, \\ [\mathbf{0}\ \ \mathbf{I}_\mathcal{K} \otimes (\mathbf{X}\mathbf{A})] & \text{C3} \end{cases} \tag{11.98}$$

$\mathbf{F}$ is similarly obtained by substituting $\mathbf{X}$ for $\mathbf{X}\mathbf{A}$ in (11.98), and $\bar{\mathbf{n}}_\kappa$ is equal to $\mathbf{n}_\kappa$ in the case of configuration C2, whereas it results from stacking the vectors $\mathbf{n}_\kappa, \cdots, \mathbf{n}_{\kappa-\mathcal{K}}$ in the case of configurations C1 and C3. The relationship in (11.97) demonstrates that $\hat{\bar{\mathbf{h}}}_\kappa$, conditioned on $\bar{\mathbf{h}}_\kappa$ is Gaussian with mean $\mathbf{E}\bar{\mathbf{h}}_\kappa$ and covariance matrix $N_0 \mathbf{F}\mathbf{F}^H$. Moreover, the vector $\bar{\mathbf{h}}_\kappa$ itself is a zero-mean Gaussian random vector with covariance matrix $\mathbf{R}_{\bar{\mathrm{h}}_\kappa} = \bar{\mathbf{U}} \otimes \mathbf{I}_{N_\mathrm{R} \times N_\mathrm{R}}$, where $\bar{\mathbf{U}}$ is equal to the $(\mathcal{K}+1)\,L_\mathrm{H} \times (\mathcal{K}+1)\,L_\mathrm{H}$ block matrix with the $L_\mathrm{H} \times L_\mathrm{H}$ block at position $(i, j) \in \{1, \cdots, \mathcal{K}+1\}$ equal to $\mathbf{U}(i-j)$. Next, it can be verified that, $\bar{\mathbf{h}}_\kappa$, conditioned on $\hat{\bar{\mathbf{h}}}_\kappa$ is also Gaussian distributed with a mean $\boldsymbol{\mu}_{\bar{\mathrm{h}}_\kappa|\hat{\bar{\mathrm{h}}}_\kappa}$ and covariance matrix $\mathbf{R}_{\bar{\mathrm{h}}_\kappa|\hat{\bar{\mathrm{h}}}_\kappa}$ with

$$\boldsymbol{\mu}_{\bar{\mathrm{h}}_\kappa|\hat{\bar{\mathrm{h}}}_\kappa} = \mathbf{R}_{\bar{\mathrm{h}}_\kappa|\hat{\bar{\mathrm{h}}}_\kappa} \mathbf{E}^H (N_0 \mathbf{F}\mathbf{F}^H)^{-1} \hat{\bar{\mathbf{h}}}_\kappa \tag{11.99}$$

and

$$\mathbf{R}_{\bar{\mathrm{h}}_\kappa|\hat{\bar{\mathrm{h}}}_\kappa} = \left(\mathbf{R}_{\bar{\mathrm{h}}_\kappa}^{-1} + \mathbf{E}^H \left(N_0 \mathbf{F}\mathbf{F}^H\right)^{-1} \mathbf{E}\right)^{-1}. \tag{11.100}$$

Based on (8.15) and (8.16), it follows that the elements of $\mathbf{E}_{\mathrm{GG}}(\hat{\bar{\mathbf{h}}}_\kappa)$ and $\mathbf{E}_{\mathrm{GT}}(\hat{\bar{\mathbf{h}}}_\kappa)$ from respectively (8.19) and (8.20) can be straightforwardly expressed

in terms of the a posteriori expectations and covariances of the elements of $\mathbf{h}_\kappa$ for given $\hat{\bar{\mathbf{h}}}_\kappa$. These a posteriori moments are obtained by extracting the proper elements from the a posteriori mean and the a posteriori covariance matrix of $\bar{\mathbf{h}}_\kappa$ given in respectively (11.99) and (11.100).

11.12 Robust PRS: orthogonal pilot sequences

As an example, the considered pilot sequence is derived from a ZC sequence [103, 104]. The pilot sequence for the first antenna is constructed by cyclically extending a ZC sequence of length $N_\mathrm{p} - L_\mathrm{H} + 1$ with $L_\mathrm{H} - 1$ symbols, which yields a pilot sequence of length N_p. The pilot sequence for the lth antenna is obtained by applying $(l-1)L_\mathrm{H}$ cyclic shifts to the ZC sequence from the first antenna, and adding a cyclic extension of $L_\mathrm{H} - 1$ symbols. For $N_\mathrm{p} - L_\mathrm{H} + 1 \geq N_\mathrm{T} L_\mathrm{H}$, all rows from $\mathbf{A}_\kappa$ are orthogonal, yielding $\mathbf{A}_\kappa \mathbf{A}_\kappa^H = \bar{E}_\mathrm{p} \mathbf{I}_{N_\mathrm{T} L_\mathrm{H}}$, where $\bar{E}_\mathrm{p} = (N_\mathrm{p} - L_\mathrm{H} + 1)E_\mathrm{p}$ and E_p is the transmitted energy per pilot symbol.

Bibliography

[1] J. Mietzner, R. Schober, L. Lampe, W. H. Gerstacker, and P. A. Hoeher, "Multiple-antenna techniques for wireless communications - a comprehensive literature survey," *IEEE Communications Surveys Tutorials*, vol. 11, no. 2, pp. 87–105, 2009.

[2] D. Vande Ginste, D. De Zutter, D. Deschrijver, T. Dhaene, P. Manfredi, and F. Canavero, "Stochastic Modeling-Based Variability Analysis of On-Chip Interconnects," *IEEE Trans. Compon., Hybrids, Manuf. Technol.*, vol. 2, no. 7, pp. 1182–1192, Jul. 2012.

[3] P. Manfredi, D. Vande Ginste, and D. De Zutter, "An Effective Modeling Framework for the Analysis of Interconnects Subject to Line-Edge Roughness," *IEEE Microwave Wireless Compon. Lett.*, vol. 25, no. 8, pp. 502–504, Aug. 2015.

[4] P. Manfredi, D. Vande Ginste, D. De Zutter, and F. G. Canavero, "Generalized Decoupled Polynomial Chaos for Nonlinear Circuits With Many Random Parameters," *IEEE Microwave Wireless Compon. Lett.*, vol. 25, no. 8, pp. 505–507, Aug. 2015.

[5] V. Stojanovic and M. Horowitz, "Modeling and Analysis of High-Speed links," in *Proc. of the IEEE 2003 Custom Integrated Circuits Conf., 2003.*, Sep. 2003, pp. 589–594.

[6] R. Payne, P. Landman, B. Bhakta, S. Ramaswamy, S. Wu, J. Powers, U. Erdogan, A.-L. Yee, R. Gu, L. Wu, Y. Xie, B. Parthasarathy, K. Brouse, W. Mohammed, K. Heragu, V. Gupta, L. Dyson, and W. Lee, "A 6.25-gb/s binary transceiver in 0.13-/spl mu/m cmos for serial data transmission across high loss legacy backplane channels," *Solid-State Circuits, IEEE Journal of*, vol. 40, pp. 2646 – 2657, 01 2006.

[7] Y. Ban, "Feed-forward equalizer for high speed serial electrical communication up to 100 gb/s," in *2018 IEEE MTT-S International Wireless Symposium (IWS)*, 2018, pp. 1–4.

[8] G. P. Fettweis, "The Tactile Internet: Applications and Challenges," *IEEE Trans. Veh. Technol.*, vol. 9, no. 1, pp. 64–70, Mar. 2014.

[9] Y. Frans, J. Shin, L. Zhou, P. Upadhyaya, J. Im, V. Kireev, M. Elzeftawi, H. Hedayati, T. Pham, S. Asuncion, C. Borrelli, G. Zhang, H. Zhang, and K. Chang, "A 56-Gb/s PAM4 Wireline Transceiver Using a 32-Way Time-Interleaved SAR ADC in 16-nm FinFET," *IEEE J. Solid-State Circuits*, vol. 52, no. 4, pp. 1101–1110, Apr. 2017.

[10] Y. Ban, T. De Keulenaer, Z. Li, J. Van Kerrebrouck, J. H. Sinsky, B. Kozicki, J. Bauwelinck, and G. Torfs, "A Wide-Band, 5-Tap Transversal Filter With Improved Testability for Equalization up to 84 Gb/s," *IEEE Microwave Wireless Compon. Lett.*, vol. 25, no. 11, pp. 739–741, Nov. 2015.

[11] J. Zhang, Q. B. Chen, K. Qiu, A. C. Scogna, M. Schauer, G. Romo, J. L. Drewniak, and A. Orlandi, "Design and Modeling for Chip-to-Chip Communication at 20 Gbps," in *2010 IEEE Int. Symp. on Electromagnetic Compatibility*, Jul. 2010, pp. 467–472.

[12] F. Loi, E. Mammei, S. Erba, M. Bassi, and A. Mazzanti, "A 25mw highly linear continuous-time fir equalizer for 25gb/s serial links in 28-nm cmos," *IEEE Transactions on Circuits and Systems I: Regular Papers*, vol. 64, no. 7, pp. 1903–1913, 2017.

[13] *Multipath: Wideband Channel*. John Wiley & Sons, Ltd, 2008, ch. 7, pp. 153–185. [Online]. Available: https://onlinelibrary.wiley.com/doi/abs/10.1002/9780470751749.ch7

[14] H. Nyquist, "Certain topics in telegraph transmission theory," *Transactions of the American Institute of Electrical Engineers*, vol. 47, no. 2, pp. 617–644, 1928.

[15] D. A. Shnidman, "A generalized nyquist criterion and an optimum linear receiver for a pulse modulation system," *The Bell System Technical Journal*, vol. 46, no. 9, pp. 2163–277, 1967.

[16] G. L. Stuber, J. R. Barry, S. W. McLaughlin, Ye Li, M. A. Ingram, and T. G. Pratt, "Broadband mimo-ofdm wireless communications," *Proceedings of the IEEE*, vol. 92, no. 2, pp. 271–294, 2004.

[17] N. Benvenuto and S. Tomasin, "Iterative Design and Detection of a DFE in the Frequency Domain," *IEEE Trans. Commun.*, vol. 53, no. 11, pp. 1867–1875, Nov. 2005.

[18] G. M. Guvensen and A. O. Yilmaz, "A General Framework for Optimum Iterative Blockwise Equalization of Single Carrier MIMO Systems and Asymptotic Performance Analysis," *IEEE Trans. Commun.*, vol. 61, no. 2, pp. 609–619, Feb. 2013.

[19] A. Scaglione, P. Stoica, S. Barbarossa, G. B. Giannakis, and H. Sampath, "Optimal designs for space-time linear precoders and decoders," *IEEE Transactions on Signal Processing*, vol. 50, no. 5, pp. 1051–1064, 2002.

[20] J. Proakis and M. Salehi, *Digital Communications.* McGraw-Hill, 2008.

[21] *Digital Communications via Linear, Distorting Channels.* John Wiley & Sons, Ltd, 2005, pp. 9–121. [Online]. Available: https://onlinelibrary.wiley.com/doi/abs/10.1002/0471439002.ch2

[22] G. Forney, "Maximum-Likelihood Sequence Estimation of Digital Sequences in the Presence of Intersymbol Interference," *IEEE Trans. Inform. Theory*, vol. 18, no. 3, pp. 363–378, May 1972.

[23] S. Verdu, "Minimum Probability of Error for Asynchronous Gaussian Multiple-Access Channels," *IEEE Trans. Inform. Theory*, vol. 32, no. 1, pp. 85–96, Jan. 1986.

[24] W. van Etten, "Maximum Likelihood Receiver for Multiple Channel Transmission Systems," *IEEE Trans. Commun.*, vol. 24, no. 2, pp. 276–283, Feb. 1976.

[25] W. van Etten, "An optimum linear receiver for multiple channel digital transmission systems," *IEEE Transactions on Communications*, vol. 23, no. 8, pp. 828–834, 1975.

[26] C.-C. Yeh and J. R. Barry, "Adaptive Minimum Bit-Error Rate Equalization for Binary Signaling," *IEEE Trans. Commun.*, vol. 48, no. 7, pp. 1226–1235, Jul. 2000.

[27] ——, "Adaptive Minimum Symbol-Error Rate Equalization for Quadrature-Amplitude Modulation," *IEEE Trans. Signal Process.*, vol. 51, no. 12, pp. 3263–3269, Dec. 2003.

[28] A. Hjorungnes, M. L. R. de Campos, and P. S. R. Diniz, "Jointly optimized transmitter and receiver fir mimo filters in the presence of near-end crosstalk," *IEEE Trans. Signal Process.*, vol. 53, no. 1, pp. 346–359, 2005.

[29] M. L. Honig, P. Crespo, and K. Steiglitz, "Suppression of Near- and Far-End Crosstalk by Linear Pre- and Post-Filtering," *IEEE J. Select. Areas Commun.*, vol. 10, no. 3, pp. 614–629, Apr. 1992.

[30] J. Salz, "Digital Transmission Over Cross-Coupled Linear Channels," *AT & T Technical Journal*, vol. 64, no. 6, pp. 1147–1159, Jul. 1985.

[31] A. Hjørungnes, P. S. R. Diniz, and M. L. R. de Campos, "Jointly Minimum MSE Transmitter and Receiver FIR MIMO Filters in the Presence of Near-End Crosstalk and Additive Noise," in *Circuits and Systems, 2003. ISCAS '03. Proc. of the 2003 Int. Symp. on*, vol. 4, May 2003, pp. IV–13–IV–16 vol.4.

[32] C. Toker, S. Lambotharan, and J. A. Chambers, "Joint Transceiver Design for MIMO Channel Shortening," *IEEE Trans. Signal Process.*, vol. 55, no. 7, pp. 3851–3866, Jul. 2007.

[33] L. Jacobs, M. Guenach, and M. Moeneclaey, ""linear mimo equalization for high-speed chip-to-chip communication"," in *2015 IEEE International Conference on Communications (ICC)*, 2015, pp. 4978–4983.

[34] M. Joham, D. A. Schmidt, J. Brehmer, and W. Utschick, "Finite-Length MMSE Tomlinson-Harashima Precoding for Frequency Selective Vector Channels," *IEEE Trans. Signal Process.*, vol. 55, no. 6, pp. 3073–3088, Jun. 2007.

[35] E. Shamash and K. Yao, "On the structure and performance of a linear decision fedback equalizer based on the minimum error probability criterion," in *1974 IEEE Proceedings of International Communications Conference*, Jun. 1974.

[36] A. Chevreuil and L. Vandendorpe, "Mimo mmse-dfe: a general framework," in *Ninth IEEE Signal Processing Workshop on Statistical Signal and Array Processing (Cat. No.98TH8381)*, 1998, pp. 368–371.

[37] L. Jacobs, M. Guenach, and M. Moeneclaey, ""application of mimo df equalization to high-speed off-chip communication"," in *IEEE EUROCON 2015 - Intern. Conference on Computer as a Tool (EUROCON)*, 2015, pp. 1–4.

[38] S. Roy and D. D. Falconer, "Multi-user decision-feedback space-time equalization and diversity reception," in *1999 IEEE 49th Vehicular Technology Conference (Cat. No.99CH36363)*, vol. 1, 1999, pp. 494–498 vol.1.

[39] C. A. Belfiore and J. H. Park, "Decision Feedback Equalization," *Proceedings of the IEEE*, vol. 67, no. 8, pp. 1143–1156, 1979.

[40] J. Salz, "Optimum mean-square decision feedback equalization," *The Bell System Technical Journal*, vol. 52, no. 8, pp. 1341–1373, 1973.

[41] N. Al-Dhahir and A. H. Sayed, "The Finite-Length Multi-Input Multi-Output MMSE-DFE," *IEEE Trans. Signal Process.*, vol. 48, no. 10, pp. 2921–2936, Oct. 2000.

[42] J. Frigon and B. Daneshrad, "Multiple-input multiple-output (mimo) receiver for wideband space-time communications," in *12th IEEE Intern. Symp. on Personal, Indoor and Mobile Radio Communications. PIMRC 2001. Proceedings (Cat. No.01TH8598)*, vol. 1, 2001.

[43] A. Lozano and C. Papadias, "Layered space-time receivers for frequency-selective wireless channels," *IEEE Transactions on Communications*, vol. 50, no. 1, pp. 65–73, 2002.

[44] L. Jacobs, M. Guenach, and M. Moeneclaey, "Mimo pre-equalization and dfe for high-speed off-chip communication," in *2016 13th Intern. Multi-Conference on Systems, Signals Devices (SSD)*, 2016, pp. 177–182.

[45] G. D. Golden, C. J. Foschini, R. A. Valenzuela, and P. W. Wolniansky, "Detection algorithm and initial laboratory results using V-BLAST space-time communication architecture," *Electronics Letters*, vol. 35, no. 1, pp. 14–16, Jan. 1999.

[46] D. Duttweiler, J. Mazo, and D. Messerschmitt, "An Upper Bound on the Error Probability in Decision-Feedback Equalization," *IEEE Trans. Inform. Theory*, vol. 20, no. 4, pp. 490–497, 1974.

[47] M. Tomlinson, "New automatic equaliser employing modulo arithmetic," *Electronics Letters*, vol. 7, no. 5, pp. 138–139, Mar. 1971.

[48] H. Harashima and H. Miyakawa, "Matched-transmission technique for channels with intersymbol interference," *IEEE Trans. Commun.*, vol. 20, no. 4, pp. 774–780, Aug. 1972.

[49] H. Miyakawa and H. Harashima, "A method of code conversion for a digital communication channel with intersymbol interference," *Trans. Inst. Electron. Commun. Eng. Japan, A*, vol. 52, pp. 272–273, 1969.

[50] R. F. Fischer, *Precoding Schemes*. John Wiley & Sons, Ltd, 2005, pp. 123–218. [Online]. Available: https://onlinelibrary.wiley.com/doi/abs/10.1002/0471439002.ch3

[51] W. H. Gerstacker, R. F. H. Fischer, and J. B. Huber, "Blind equalization for digital cable transmission with Tomlinson-Harashima precoding and shaping," in *Communications, 1995. ICC '95 Seattle, 'Gateway to Globalization', 1995 IEEE Int. Conf. on*, vol. 1, Jun. 1995, pp. 493–497 vol.1.

[52] G. D. Forney and M. V. Eyuboglu, "Combined equalization and coding using precoding," *IEEE Commun. Mag.*, vol. 29, no. 12, pp. 25–34, 1991.

[53] R. F. H. Fischer, C. Windpassinger, A. Lampe, and J. B. Huber, "Tomlinson-Harashima Precoding in Space-Time Transmission for Low-Rate Backward Channel," in *2002 Int.Zurich Seminar on Broadband Communications Access - Transmission - Networking (Cat. No.02TH8599)*, Feb. 2002, pp. 1–6.

[54] F. A. Dietrich, P. Breun, and W. Utschick, "Tomlinson-Harashima Precoding: A Continuous Transition from Complete to Statistical Channel Knowledge," in *GLOBECOM '05. IEEE Global Telecommunications Conf., 2005.*, vol. 4, Dec. 2005, pp. 2379–2384.

[55] R. F. Fischer, C. Windpassinger, A. Lampe, and J. B. Huber, "Space-time transmission using tomlinson-harashima precoding," *ITG FACHBERICHT*, pp. 139–148, 2002.

[56] M. Joham, J. Brehmer, A. Voulgarelis, and W. Utschick, "Multiuser spatio-temporal tomlinson-harashima precoding for frequency selective vector channels," in *ITG Workshop on Smart Antennas (IEEE Cat. No.04EX802)*, 2004, pp. 208–215.

[57] S. Wahls and H. Boche, "On spatio-temporal tomlinson harashima precoding in iir channels: Mmse solution, properties, and fast computation," in *2011 IEEE International Conference on Acoustics, Speech and Signal Processing (ICASSP)*, 2011, pp. 3248–3251.

[58] M. Joham, J. Brehmer, and W. Utschick, "Mmse approaches to multiuser spatio-temporal tomlinson-harashima precoding," *Itg Fachbericht*, pp. 387–394, 2004.

[59] R. F. H. Fischer, C. Stierstorfer, and J. B. Huber, "Precoding for Point-to-Multipoint Transmission over MIMO ISI Channels," in *Int. Zurich Seminar on Communications, 2004*, Feb. 2004, pp. 208–211.

[60] P. Kabal and S. Pasupathy, "Partial-Response Signaling," *IEEE Trans. Commun.*, vol. 23, no. 9, pp. 921–934, Sep. 1975.

[61] L. Jacobs, J. Bailleul, P. Manfredi, M. Guenach, D. Vande Ginste, and M. Moeneclaey, "On Partial Response Signaling for MIMO Equalization on Multi-Gbit/s Electrical Interconnects," in *26th European Signal Processing Conference(EUSIPCO 2018)*, Sep. 2018.

[62] N. Eiselt, D. Muench, A. Dochhan, H. Griesser, M. Eiselt, J. J. V. Olmos, I. T. Monroy, and J. P. Elbers, "Performance Comparison of 112-Gb/s DMT, Nyquist PAM4, and Partial-Response PAM4 for Future 5G Ethernet-Based Fronthaul Architecture," *Journal of Lightwave Technology*, vol. 36, no. 10, pp. 1807–1814, May 2018.

[63] A. Lender, "The duobinary technique for high-speed data transmission," *IEEE Transactions on Communication and Electronics*, vol. 82, no. 2, pp. 214–218, 1963.

[64] M. R. Ahmadi, J. Moon, and R. Harjani, "Constrained Partial Response Receivers for High-Speed Links," *IEEE Trans. Circuits Syst. II*, vol. 55, no. 10, pp. 1006–1010, Oct. 2008.

[65] R. F. H. Fischer, "Lattice-Reduction-Aided Equalization and Generalized Partial-Response Signaling for Point-to-Point Transmission over Flat-Fading MIMO Channels," in *4th Int. Symp. on Turbo Codes Related Topics; 6th Int. ITG-Conference on Source and Channel Coding*, Apr. 2006, pp. 1–6.

[66] R. F. H. Fischer and C. Siegl, "Lattice-reduction-aided equalisation for transmission over intersymbol-interference channels," *Electronics Letters*, vol. 41, no. 17, pp. 969–970, Aug. 2005.

[67] ——, "On the Relation between Lattice-Reduction-Aided Equalization and Partial-Response Signaling," in *2006 Int. Zurich Seminar on Communications*, 2006, pp. 34–37.

[68] A. K. Lenstra, H. W. Lenstra, and L. Lovasz, "Factoring Polynomials with Rational Coefficients," *MATH. ANN*, vol. 261, pp. 515–534, 1982.

[69] Q. Zhou and X. Ma, "Improved Element-Based Lattice Reduction Algorithms for Wireless Communications," *IEEE Trans. Wireless Commun.*, vol. 12, no. 9, pp. 4414–4421, Sep. 2013.

[70] J. Park, J. Chun, and F. T. Luk, "Lattice Reduction Aided MMSE Decision Feedback Equalizers," *IEEE Trans. Signal Process.*, vol. 59, no. 1, pp. 436–441, Jan. 2011.

[71] M. Niroomand and M. Derakhtian, "A Low Complexity Diversity Achieving Decoder Based on a Two-Stage Lattice Reduction in Frequency-Selective MIMO Channels," *IEEE Trans. Wireless Commun.*, vol. 16, no. 4, pp. 2465–2477, Apr. 2017.

[72] I. Berenguer, J. Adeane, I. J. Wassell, and Xiaodong Wang, "Lattice-Reduction-Aided Receivers for MIMO-OFDM in Spatial Multiplexing Systems," in *2004 IEEE 15th Int. Symp. on Personal, Indoor and Mobile Radio Communications (IEEE Cat. No.04TH8754)*, vol. 2, Sep. 2004, pp. 1517–1521 Vol.2.

[73] A. Goldsmith, S. A. Jafar, N. Jindal, and S. Vishwanath, "Capacity limits of mimo channels," *IEEE Journal on Selected Areas in Communications*, vol. 21, no. 5, pp. 684–702, 2003.

[74] X. Zhang, D. P. Palomar, and B. Ottersten, "Statistically Robust Design of Linear MIMO Transceivers," *IEEE Trans. Signal Process.*, vol. 56, no. 8, pp. 3678–3689, Aug. 2008.

[75] M. Sternad, A. Ahlen, and E. Lindskog, "Robust decision feedback equalizers," in *1993 IEEE Intern. Conf. on Acoustics, Speech, and Signal Processing*, vol. 3, 1993, pp. 555–558 vol.3.

[76] F. A. Dietrich, P. Breun, and W. Utschick, "Robust Tomlinson-Harashima Precoding for the Wireless Broadcast Channel," *IEEE Trans. Signal Process.*, vol. 55, no. 2, pp. 631–644, Feb. 2007.

[77] A. Maleki-Tehrani, B. Hassibi, and J. M. Cioffi, "Adaptive equalization of multiple-input multiple-output (mimo) frequency selective channels," in *Conference Record of the Thirty-Third Asilomar Conference on Signals,*

Systems, and Computers (Cat. No.CH37020), vol. 1, 1999, pp. 547–551 vol.1.

[78] M. Guenach, L. Jacobs, B. Kozicki, and M. Moeneclaey, "Performance analysis of pre-equalized multilevel partial response modulation for high-speed electrical interconnects," *Computers & Electrical Engineering*, vol. 58, pp. 30 – 48, 2017.

[79] W. Murray, *Newton-Type Methods.* John Wiley & Sons, Inc., 2010. [Online]. Available: http://dx.doi.org/10.1002/9780470400531.eorms0569

[80] R. Pascanu, Y. N. Dauphin, S. Ganguli, and Y. Bengio, "On the saddle point problem for non-convex optimization," 2014.

[81] J. J. Choi, S. Oh, and R. J. Marks, "Training Layered Perceptrons Using Low Accuracy Computation," in *[Proceedings] 1991 IEEE Int. Joint Conference on Neural Networks*, Nov. 1991, pp. 554–559 vol.1.

[82] B.-G. Song and J. A. Ritcey, "Joint Pre and Postfilter Design for Spatial Diversity Equalization," *IEEE Trans. Signal Process.*, vol. 45, no. 1, pp. 276–280, Jan. 1997.

[83] S. Boyd and L. Vandenberghe, *Convex Optimization.* Cambridge University Press, 2004.

[84] F. J. Solis and R. J. B. Wets, "Minimization by Random Search Techniques," *Math. Oper. Res.*, vol. 6, no. 1, pp. 19–30, Feb. 1981. [Online]. Available: http://dx.doi.org/10.1287/moor.6.1.19

[85] E. Agrell, T. Eriksson, A. Vardy, and K. Zeger, "Closest Point Search in Lattices," *IEEE Trans. Inform. Theory*, vol. 48, no. 8, pp. 2201–2214, Aug. 2002.

[86] N. Vucic, H. Boche, and S. Shi, "Robust Transceiver Optimization in Downlink Multiuser MIMO Systems with Channel Uncertainty," in *2008 IEEE Int. Conf. on Communications*, May 2008, pp. 3516–3520.

[87] J. Wang and D. P. Palomar, "Worst-Case Robust MIMO Transmission With Imperfect Channel Knowledge," *IEEE Trans. Signal Process.*, vol. 57, no. 8, pp. 3086–3100, Aug. 2009.

[88] T.-J. Ho and B.-S. Chen, "Robust Minimax MSE Equalizer Designs for MIMO Wireless Communications With Time-Varying Channel Uncertainties," *IEEE Trans. Signal Process.*, vol. 58, no. 11, pp. 5835–5844, Nov. 2010.

[89] S. A. Kassam and H. V. Poor, "Robust techniques for signal processing: A survey," *Proceedings of the IEEE*, vol. 73, no. 3, pp. 433–481, 1985.

[90] H. Tang, W. Chen, and J. Li, "Achieving optimality in robust joint optimization of linear transceiver design," *IEEE Transactions on Vehicular Technology*, vol. 65, no. 3, pp. 1814–1819, 2016.

[91] M. B. Shenouda and T. N. Davidson, "On the Design of Linear Transceivers for Multiuser Systems with Channel Uncertainty," *IEEE J. Select. Areas Commun.*, vol. 26, no. 6, pp. 1015–1024, Aug. 2008.

[92] A. Pascual Iserte, A. I. Perez-Neira, and M. A. Lagunas Hernandez, "Exploiting transmission spatial diversity in frequency selective systems with feedback channel," in *2003 IEEE International Conference on Acoustics, Speech, and Signal Processing, 2003. Proceedings. (ICASSP '03).*, vol. 4, 2003, pp. 85–88.

[93] R. W. Lucky, "Automatic Equalization for Digital Communication," *The Bell System Technical Journal*, vol. 44, no. 4, pp. 547–588, Apr. 1965.

[94] I. M. Stancu-Minasian, *Fractional Programming*, 1st ed. Springer Netherlands, 1997. [Online]. Available: https://doi.org/10.1007/978-94-009-0035-6

[95] N. Vucic and H. Boche, "Robust transceiver optimization for frequency selective MIMO channels," in *2008 IEEE 9th Workshop on Signal Processing Advances in Wireless Communications*, Jul. 2008, pp. 391–395.

[96] J. Bailleul, L. Jacobs, P. Manfredi, D. V. Ginste, and M. Moeneclaey, "Equalization of multi-Gb/s chip-to-chip interconnects affected by manufacturing tolerances," *Computers & Electrical Engineering*, vol. 62, pp. 17 – 28, Aug. 2017.

[97] J. Bailleul, L. Jacobs, P. Manfredi, D. V. Ginste, M. Guenach, and M. Moeneclaey, "MIMO Time-Domain Equalization for High-Speed Continuous Transmission Under Channel Variability," *IEEE Trans. Commun.*, vol. 66, no. 8, pp. 3394–3406, Aug. 2018.

[98] J. Bailleul, L. Jacobs, M. Guenach, and M. Moeneclaey, "Optimized Precoded Spatio-Temporal Partial-Response Signaling Over Frequency-Selective MIMO Channels," *IEEE Transactions on Wireless Communications*, vol. 19, no. 9, pp. 5938–5950, 2020.

[99] J. Bailleul, L. Jacobs, P. Manfredi, D. Vande Ginste, and M. Moeneclaey, "MMSE equalization of multi-Gb/s chip-to-chip interconnects with M-PAM signaling affected by manufacturing tolerances," in *2016 Symp. on Communications and Vehicular Technologies (SCVT)*, Nov. 2016, pp. 1–6.

[100] L. Jacobs, J. Bailleul, P. Manfredi, M. Guenach, D. V. Ginste, and M. Moeneclaey, "MIMO Equalization for Multi-Gbit/s Access Nodes Affected by Manufacturing Tolerances," in *GLOBECOM 2017 - 2017 IEEE Global Communications Conference*, Dec. 2017, pp. 1–6.

[101] J. Bailleul, L. Jacobs, M. Guenach, and M. Moeneclaey, "Robust Spatio-Temporal Partial-Response Signaling over a Frequency-Selective Fading MIMO Channel with Imperfect CSI," in *30st Annual IEEE Int. Symp. on Personal, Indoor and Mobile Radio Communications*, Sep. 2019, pp. 1–7.

[102] A. Schrijver, *Theory of Linear and Integer Programming.* John Wiley and Sons, Jun. 1998.

[103] D. Chu, "Polyphase codes with good periodic correlation properties (corresp.)," *IEEE Trans. Inform. Theory*, vol. 18, no. 4, pp. 531–532, Jul. 1972.

[104] R. Frank, S. Zadoff, and R. Heimiller, "Phase shift pulse codes with good periodic correlation properties (corresp.)," *IRE Transactions on Information Theory*, vol. 8, no. 6, pp. 381–382, Oct. 1962.